

Unveiling Electronic Correlations in Layered Molecular Conductors by Optical Spectroscopy

Von der Fakultät Mathematik und Physik
der Universität Stuttgart zur Erlangung der Würde eines Doktors
der Naturwissenschaften (Dr. rer. nat.) genehmigte Abhandlung

vorgelegt von
Andrej Pustogow
aus Berlin

Hauptberichter: Prof. Dr. Martin Dressel
Erster Mitberichter: Prof. Dr. Hidenori Takagi
Zweiter Mitberichter: Prof. Dr. Vladimir Dobrosavljević

Tag der mündlichen Prüfung: 24.11.2017
Prüfungsvorsitzende: Prof. Dr. Maria Daghofer

1. Physikalisches Institut der Universität Stuttgart
2017

Gloria et Virtute

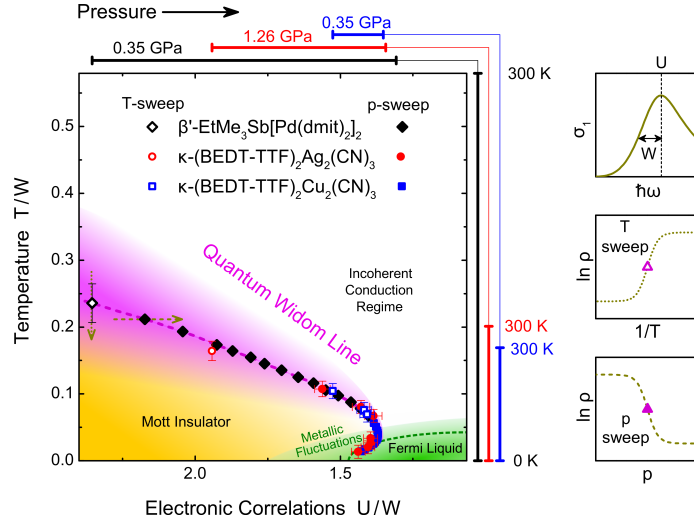
*To all who supported me – and even more to those who
distracted me from work.*

Zusammenfassung

Diese Arbeit handelt von den elektronischen Eigenschaften korrelierter Elektronensysteme, insbesondere optischen Untersuchungen nahe des Mott Metall-Isolator-Übergangs (*engl.* metal-insulator transition, MIT).

In paramagnetischen Mott-Isolatoren führt die starke Coulomb-Abstoßung zur gegenseitigen Blockade der Elektronen, welche ihre Bewegung einschränkt. Als ein Musterbeispiel korrelierter Elektronensysteme ist der physikalische Hintergrund des isolierenden Mott-Zustands seit mehr als einem halben Jahrhundert kontrovers und heiß diskutiert [1]. Dennoch entging sein Verhalten bei niedrigen Temperaturen bisher präziser Erforschung, da es üblicherweise von antiferromagnetischer Ordnung überdeckt wird [2]. In Mott Quanten-Spin-Flüssigkeiten wird die magnetische Ordnung jedoch bis zum absoluten Nullpunkt unterdrückt [3], was einzigartige Einblicke in das Wesen des ursprünglichen Mott-Zustands ermöglicht. Speziell erlaubt die Abwesenheit von Antiferromagnetismus experimentellen Zugang zur Region nahe der Phasengrenze, wo ein Koexistenzbereich von metallischen und isolierenden Zuständen theoretisch vorhergesagt [4, 5], allerdings bisher noch nie im Labor nachgewiesen wurde. Der Mott MIT ist bei niedrigen Temperaturen von erster Ordnung und wird oberhalb des kritischen Endpunkts zu einem kontinuierlichen Übergang, der als die Quantum-Widom-Line (QWL) identifiziert wurde. Auf diese Weise verhält er sich analog zu superkritischen Flüssigkeiten und Gasen [6, 7]. Erst vor Kurzem wurde gezeigt, dass der Widom-Line-Formalismus bei stark korrelierten Mott-Systemen angewendet werden kann [5], sowie bei der Pseudogap in hoch- T_c Kupraten [8, 9]. Im generischen Phasendiagramm weist die QWL eine sonderbare Umkehrung auf, die bei niedrigen Temperaturen zu einer positiven Steigung des MIT führt, ähnlich dem Pomeranchuk-Effekt in ^3He [10]. In dieser Arbeit untersuchen wir die optischen Eigenschaften dreier organischer Quanten-Spin-Flüssigkeiten mit unterschiedlich starker effektiver Korrelation U/W , wobei U die lokale Coulomb-Abstoßung ist und W die Bandbreite. Beide Größen sind durch die optischen Übergänge zwischen den Hubbard-Bändern experimentell zugänglich. Diese Materialien realisieren das

Abbildung 0.0.1: Quantitatives Phasendiagramm des unverfälschten Mott-Isolators [13]. Die Bandbreite W und Coulomb-Abstoßung U wurden durch das spektroskopisch gemessene Mott-Hubbard-Band (oben rechts) bestimmt. Auf renormierten Skalen – effektive Korrelationen U/W und Temperatur T/W – wurden die Widerstands-Daten $\rho(T, p)$ [14, 15] zu einer gemeinsamen Quantum-Widom-Line vereint.

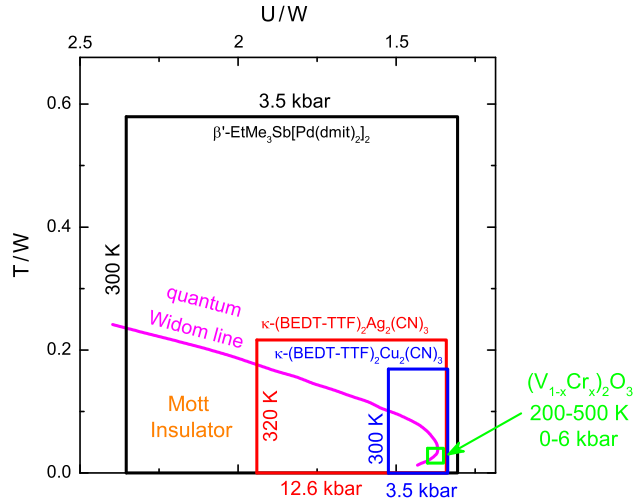


Hubbard-Modell vorbildlich innerhalb eines einzelnen elektronischen Bands [11, 12]. Wie in Abb. 0.0.1 dargestellt, entspricht in der frequenzabhängigen Leitfähigkeit $\sigma_1(\omega)$ das Maximum der Mott-Hubbard-Übergänge dem Parameter U und W ist die halbe Breite.

Anhand der temperaturabhängigen optischen Daten von β' -EtMe₃Sb[Pd(dmit)₂]₂ konnten wir demonstrieren, dass die QWL tatsächlich die universelle Abgrenzung des Mott-Zustands mit einer wohldefinierten Bandlücke ist, die ihn vom inkohärenten Hochtemperaturregime abgrenzt. Die elektrodynamischen Eigenschaften bei niedrigen Frequenzen hängen stark von der Position im Temperatur-Druck Phasendiagramm ab. Nahe der Phasengrenze können wir die theoretisch vorhergesagten metallischen Fluktuationen [4, 5] innerhalb der Bandlücke von κ -(BEDT-TTF)₂Cu₂(CN)₃ identifizieren, wodurch wir eine mehr als ein Jahrzehnt andauernde Kontroverse über das mit Abkühlung zunehmende, niederenergetische spektrale Gewicht in diesem isolierenden Material [16, 17] auflösen. Insbesondere schließen wir einen signifikanten Beitrag von Spinon-Quasiteilchen nahe des Mott MIT aus [18, 19], übereinstimmend mit aktuellsten dynamischen Molekularfeld-Theorie-Berechnungen [20].

Durch Kombination unserer optischen Ergebnisse mit druckabhängigen Transport-Daten [14, 15] und theoretischen Rechnungen erstellen wir ein universelles Phasendiagramm, das *alle* Mott-Isolatoren auf quantitativen Skalen vereint (Abb. 0.0.1). Vor allem erweitern wir den Einblick durch Verwendung allgemeingültiger Skalen, T/W und U/W , über konventionelle T - p Darstellungen hinaus, was einen direkten Vergleich der effektiven Temperatur und Korrelationsstärke zwischen verschiedenen Verbindungen sowie mit theoretischen Resultaten erlaubt, welche stets in Einheiten der Bandbreite W berechnet werden [4, 5]. Zudem zeigen wir, dass unser neuartiger

Abbildung 0.0.2: Der jeweils beobachtete Bereich im Phasendiagramm ist für verschiedene Materialien [14, 15] dargestellt. Aufgrund der größeren Bandbreite W [24–26] kann für das Übergangsmetall-Oxid $(V_{1-x}Cr_x)_2O_3$, das eine sehr ähnliche Phasengrenze wie die organischen Verbindungen aufweist [27], bei vergleichbaren, oder sogar höheren Drücken und Temperaturen nur eine deutlich kleinere $T/W-U/W$ Fläche (grünes Rechteck) untersucht werden.



Ansatz unmittelbar auf verschiedene Mott-Systeme ausgedehnt werden kann, unter anderem nicht-frustrierte κ -(BEDT-TTF) $_2X$ [21–23] und anorganische Materialien. In Übergangsmetall-Oxiden wie V_2O_3 ist W um einiges größer als in organischen Verbindungen [24–26], weshalb der beobachtete $T/W-U/W$ Bereich im Phasendiagramm trotz vergleichbarer Temperaturen und Drücke deutlich kleiner ist. Wie aus Abb. 0.0.2 ersichtlich, erlaubt die kleine Bandbreite organischer Materialien die Erforschung extrem hoher Temperatur-Bereiche im Phasendiagramm – unerreichbar für Oxide, da 10^3-10^4 K oberhalb ihres Schmelzpunkts liegen. Ein Vergleich von $T_c \approx 10$ K mit den Energie-Skalen U and W ergibt, dass die Cooper-Paare in κ -(BEDT-TTF) $_2X$ ähnlich, wenn nicht sogar stärker gebunden sind als in den Kupraten, was die grundlegende Bedeutung des Mott-Zustands für Hochtemperatur-Supraleitung unterstreicht – dem heiligen Gral der heutigen Festkörperphysik.

Nicht minder interessant ist die Entwicklung stark renormalisierter Fermi-Flüssigkeiten unter dem Einfluss unterschiedlich starker elektronischer Korrelationen. Wir haben diese Problemstellung anhand der κ -[(BEDT-STF) $_x$ (BEDT-TTF) $_{1-x}$] $_2Cu_2(CN)_3$ Familie untersucht, in der chemische Substitution der organischen Moleküle den Übergang von einer Quanten-Spin-Flüssigkeit zum metallischen Zustand bewirkt. In Abb. 0.0.3 (a) identifizieren wir den von der Bandbreite getriebenen Mott MIT; insbesondere wird die *Geburt* kohärenter Quasiteilchen aus dem spektralen Gewicht der Hubbard-Bänder enthüllt.

Diagramm (b) verdeutlicht die charakteristische quadratische Energieabhängigkeit der Streurate auf gemeinsamen Skalen sowohl für den temperaturabhängigen Widerstand, als auch die frequenzabhängigen optischen Daten [28, 29]. Unsere Daten bestätigen die Kadowaki-Woods Relation [30] für unterschiedlich starke Korrelatio-

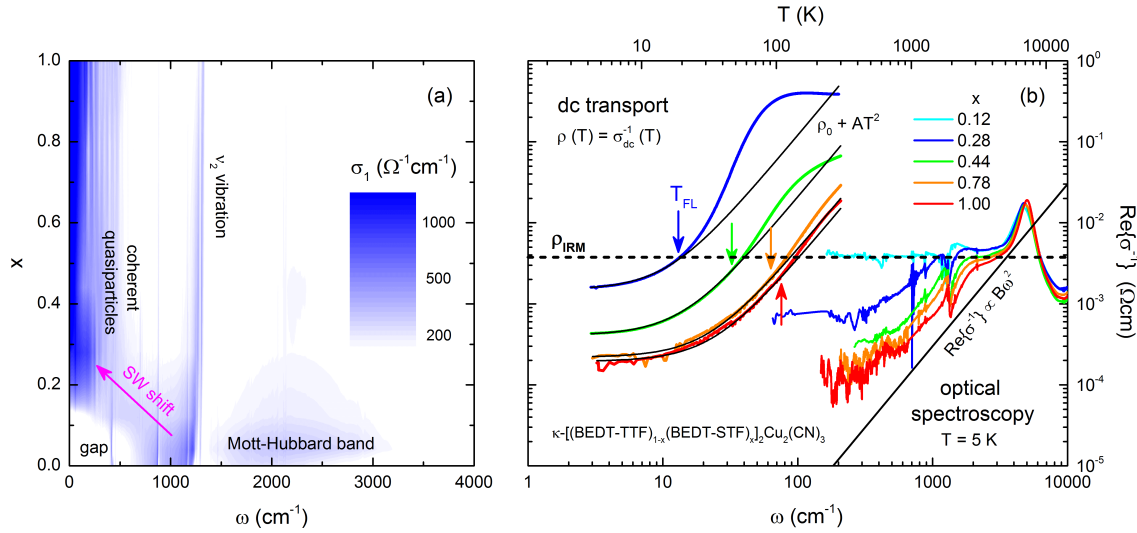


Abbildung 0.0.3: (a) Die κ - $[(\text{BEDT-STF})_x(\text{BEDT-TTF})_{1-x}]_2\text{Cu}_2(\text{CN})_3$ Familie weist einen Bandbreite-getriebenen Mott MIT wie aus dem Lehrbuch auf. Mit abnehmenden Korrelationen verschiebt sich das spektrale Gewicht Schritt für Schritt vom Mott-Hubbard-Band in Richtung $\omega = 0$ und bildet dadurch die Grundlage für einen kohärenten Quasiteilchen-Zustand. Die wenig beeinflusste Mode bei 1300 cm^{-1} ist eine Molekülvibration. Der temperatur- und frequenzabhängige Widerstand $\text{Re}\{\sigma^{-1}\}(\omega)$ offenbart die quadratische Energieabhängigkeit der Streurate und die fundamentale Begrenzung der Fermi-Flüssigkeit durch das Ioffe-Regel-Mott (IRM) Limit.

nen und belegen damit die durchgängige Gültigkeit der intrinsischen Eigenschaften einer Fermi-Flüssigkeit im Verlauf des Mott MIT – wohlgermerkt mit renormalisierten Parametern. Erstaunlicherweise finden wir Hinweise auf belastbare (*engl.* resilient) Quasiteilchen sogar oberhalb von T_{FL} [31] bis zum Ioffe-Regel-Mott (IRM) Limit [32], welches wir als die fundamentale Begrenzung einer Fermi-Flüssigkeit in den T - und ω -abhängigen elektrodynamischen Eigenschaften begründen [28]. Nahe $T = 0$ treffen sich der Verlust von Kohärenz, Supraleitung bei Normaldruck ($T_c = 2.9 \text{ K}$) und die Öffnung der Mott-Bandlücke bei $x = 0.12$. In diesem Sinne verbindet das IRM-Limit nicht nur die wohldefinierten Mott- und Fermi-Flüssigkeitszustände, sondern beflügelt auch ausgeprägte Quantenfluktuationen als den Klebstoff unkonventioneller Supraleitung.

Bisher haben wir uns auf die Mott-Physik in halb-gefüllten Materialien konzentriert; viertel-gefüllte $(\text{BEDT-TTF})_2X$ hingegen sind empfänglich für Ladungsordnungsinstabilitäten, daher sind ihre elektronischen Korrelationen und supraleitenden Eigenschaften von gleichem Interesse. Bemerkenswerterweise hat eine auf dem erweiterten Hubbard-Modell basierende theoretische Arbeit vorhergesagt, dass Ladungsfluktuationen d -Wellen-Supraleitung vermitteln [33], was von mannigfaltigen experimentel-

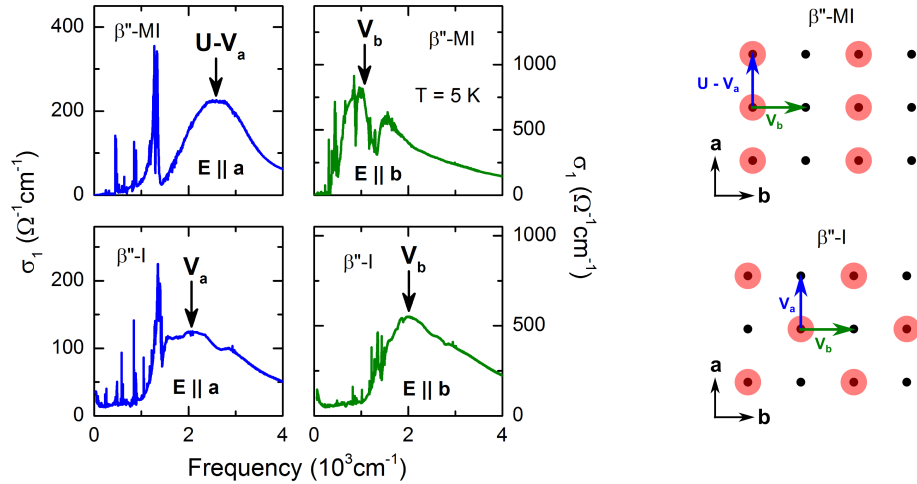
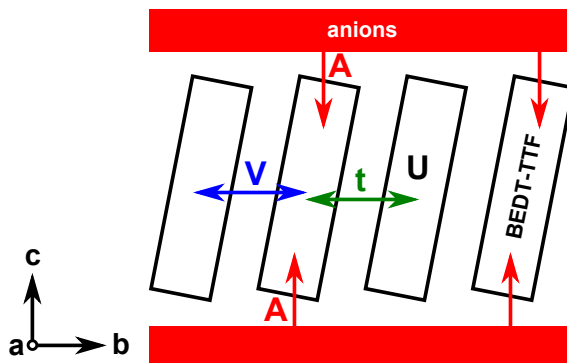


Abbildung 0.0.4: Die elektronischen Anregungen von β'' -MI weisen eine ausgeprägte Polarisationsabhängigkeit auf, in Einklang mit strukturellen Details, welche ein streifenförmiges Ladungsmuster nahelegen [39, 40]. Für Übergänge von ladungsreichen zu anderen ladungsreichen Molekülen entlang a muss aufgrund stärkerer lokaler Abstoßung U eine höhere Coulomb-Energie aufgewendet werden als für Übergänge von ladungsreich zu ladungsarm. Die Spektren von β'' -I sind in Einklang mit der Kristallstruktur [39, 40] eher isotrop, was auf ein Schachbrett-Muster hinweist.

len Ergebnissen untermauert wurde [34–38]. Daher haben wir eine umfangreiche optische Studie an β'' -(BEDT-TTF) $_2$ SF $_5$ RSO $_3$ durchgeführt und herausgefunden, dass die Umverteilung der Molekülladung 2δ in der Tat mit der Coulomb-Wechselwirkung skaliert, womit wir das in Ref. [38] vorhergesagte Phasendiagramm experimentell bestätigen. Zudem weisen wir die Koexistenz von Ladungsordnung und Supraleitung für $R = \text{CH}_2\text{CF}_2$ nach, indem wir die ladungssensitiven Molekülschwingungen unterhalb von $T_c = 5$ K messen. Unsere Experimente an deuterierten Kristallen ergeben eine direkte Verbindung zwischen diesen beiden Zuständen, da T_c und 2δ zugleich größer werden.

Durch die Analyse der anisotropen elektronischen Anregungen erlauben unsere optischen Untersuchungen handfeste Rückschlüsse auf das Muster der Ladungsverteilung, dargestellt in Abb. 0.0.4. Während das Mott-Hubbard-Band in β'' -MI ($R = \text{CHF}_2$) stark anisotrop ist und auf ein Streifenmuster von ladungsreichen und -armen Molekülen hinweist, sind die Anregungen in β'' -I ($R = \text{CH}_2$) aufgrund eines Schachbrettmusters annähernd isotrop. Wie bereits früher angemerkt [39, 40], legen die Kristallstrukturen nahe, dass positivere BEDT-TTF Moleküle näher zum negativen Endstück der SF $_5$ RSO $_3$ Anionen liegen als die ladungsarmen Gitterplätze. Außerdem offenbaren druckabhängige Transport-Ergebnisse eine unkonventionelle Erhöhung der Übergangstemperatur T_{CO} [41], was verstärkte Wechselwirkungen trotz

Abbildung 0.0.5: Unsere experimentellen Ergebnisse legen nahe, dass Ladungsordnung in einigen $(BEDT-TTF)_2X$ Verbindungen nicht ausschließlich durch nächste-Nachbar Coulomb-Abstoßung hervorgerufen, sondern vom äußeren Anionenpotential A induziert wird. Unter Druck nehmen die nominellen Korrelationen V/W ($W \propto t$) zwar ab, das Verhältnis $(V+A)/W$ kann jedoch zunehmen, was die Erhöhung von T_{CO} erklärt.



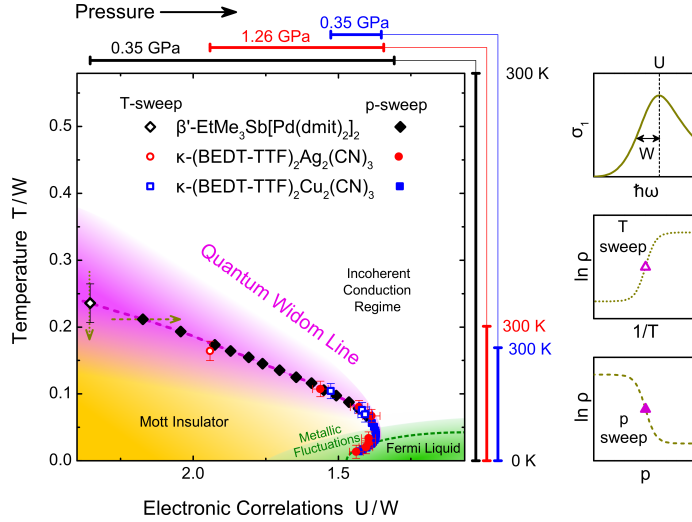
größerer Bandbreite bedingt. Wie in Abb. 0.0.5 skizziert, erklären wir diese interessanten Beobachtungen durch einen maßgeblichen Einfluss der Anionen auf die molekulare Ladungsverteilung durch äußere Modulation des elektrostatischen Potentials.

Abstract

This thesis deals with the electronic properties of correlated electron systems, in particular optical investigations close to the Mott metal-insulator transition (MIT). In paramagnetic Mott insulators, strong Coulomb repulsion leads to a *traffic jam* of electrons, arresting their motion. As a paradigm of correlated electron systems, the physical content of the Mott insulating state has remained the subject of much controversy and debate for more than half a century [1]. Still, its low-temperature behaviour evaded precise experimental exploration because it is typically concealed by antiferromagnetic order [2]. In Mott quantum spin liquids, however, no magnetic order is stabilized down to $T \rightarrow 0$ [3], offering unique insight into the nature of the genuine Mott state. In particular, the absence of antiferromagnetism allows to experimentally access the region close to the phase boundary where theory predicted a coexistence region of metallic and insulating phases [4, 5], not observed in experiment so far. The Mott MIT is first-order type at low temperatures and turns into a crossover above the critical endpoint, where it is identified as the quantum Widom line (QWL). Thus, it shows analogy to supercritical liquids and gases [6, 7]. Only very recently, the Widom line formalism was shown to apply to strongly correlated Mott systems [5] and the pseudogap in high- T_c cuprates [8, 9]. In the generic phase diagram, the QWL exhibits a peculiar back-bending resulting in a positive slope of the metal-insulator boundary at low temperatures, reminiscent of the Pomeranchuk-effect in ^3He [10].

Here we explore the optical response of three organic quantum spin liquids with different degrees of effective correlation U/W , where U is the on-site Coulomb repulsion and W the bandwidth, experimentally accessible via the optical transitions between the Hubbard bands. These materials are prototype realizations of the single-band Hubbard model [11, 12], thus the maximum of the Mott-Hubbard band in the frequency-dependent conductivity $\sigma_1(\omega)$ corresponds to U whereas the half-width determines W , as sketched in Fig. 0.0.6. From the temperature evolution of the Mott gap in β' - $\text{EtMe}_3\text{Sb}[\text{Pd}(\text{dmit})_2]_2$ we demonstrate that the QWL is indeed the

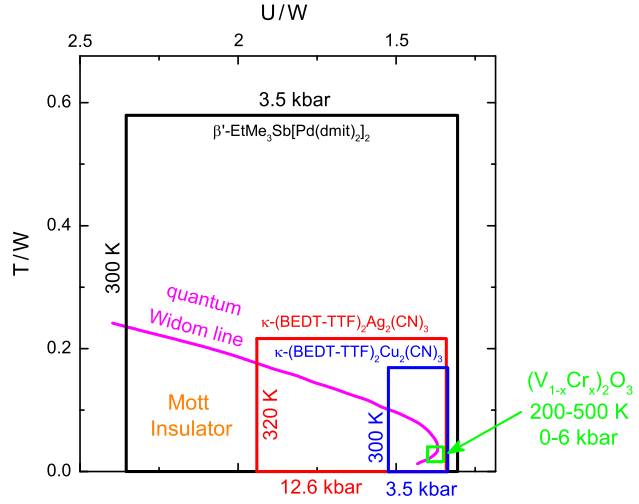
Figure 0.0.6: Quantitative phase diagram of genuine Mott insulators [13]. The bandwidth W and Coulomb repulsion U were determined from the Mott-Hubbard band (top right) measured by optical spectroscopy. Using renormalized scales – electronic correlations U/W and temperature T/W – we collapsed the quantum Widom lines of several organic Mott insulators, determined from the dc resistivity $\rho(T, p)$ [14, 15], on one universal curve.



true boundary of the gapped Mott state, separating it from the incoherent high-temperature regime. The low-frequency electrodynamics depend strongly on the position in the temperature-pressure phase diagram. In particular, in the vicinity of the phase boundary, metallic fluctuations can be identified within the Mott gap of κ -(BEDT-TTF) $_2$ Cu $_2$ (CN) $_3$ establishing the theoretical predictions [4, 5]. By this, we resolve more than one decade of controversy on the unconventional increase of low-frequency spectral weight upon cooling in this insulating material [16, 17] and rule out a significant contribution of spinons close to the MIT [18, 19], consistent with state of the art dynamical mean-field theory results [20].

Combining our optical data with pressure-dependent transport studies [14, 15] and theoretical calculations, we construct a universal phase diagram valid for *all* Mott insulators on quantitative scales, presented in Fig. 0.0.6. In particular, we advance beyond conventional T - p plots and use renormalized scales T/W and U/W which allow for direct comparison of effective temperature and correlation strength between different compounds. Moreover, this procedure also links experiment with theory, where the temperature, frequency and energy scales used in calculations are always in units of W [4, 5]. We furthermore show that our novel scaling approach can be extended in a straight-forward fashion to different Mott systems, including non-frustrated κ -(BEDT-TTF) $_2X$ [21–23] and inorganic materials. In transition metal oxides, such as V $_2$ O $_3$ for instance, W is significantly larger than in organic compounds [24–26], hence the covered T/W - U/W region in the phase diagram is significantly smaller although comparable temperatures and pressures were applied. As illustrated in Fig. 0.0.7, the small bandwidth of organics enables to access an extremely high temperature region in the phase diagram never achievable by oxides

Figure 0.0.7: The respective range covered in the phase diagram is illustrated for different materials [14, 15]. A larger bandwidth W implies that only a smaller area can be accessed for the same applied pressures and temperatures. The transition-metal oxide $(V_{1-x}Cr_x)_2O_3$ [27] exhibits a very similar Mott insulator-metal boundary as the organic compounds. Despite comparable and even larger p and T , these data cover just a tiny $T/W-U/W$ part (green rectangle) due to much larger W [24–26] compared to the organics.



since this would require temperatures around 10^3-10^4 K, which is above their melting point. Comparison of $T_c \approx 10$ K with the energy scales U and W yields that, on renormalized scales, the pairing interaction is of similar, if not higher strength in κ -(BEDT-TTF) $_2X$ as compared to the cuprates. This emphasizes an inherent relation between the Mott-Hubbard state and high-temperature superconductivity, the holy grail of condensed matter physics in present time.

Of equal interest is the evolution of the strongly renormalized Fermi liquid exposed to a varying degree of electronic correlations. We approached this issue by studying the κ -[(BEDT-STF) $_x$ (BEDT-TTF) $_{1-x}$] $_2Cu_2(CN)_3$ series where the quantum spin liquid Mott state is turned metallic by chemical modification of the donor layers. To that end, we identify the bandwidth-tuned nature of this Mott MIT in Fig. 0.0.8 (a), which unveils the *birth* of quasiparticles from the spectral weight of the Hubbard bands. The characteristic quadratic energy dependence of the scattering rate is revealed both in the temperature-dependent dc resistivity and the frequency-dependent optical response [28, 29], which are compared on common scales in panel (b). Our data confirm the validity of the Kadowaki-Woods ratio [30] for different correlation strength, proving that a Fermi liquid remains well-defined upon approaching the Mott MIT, yet with strongly renormalized parameters. Strikingly, indications for resilient quasiparticles are observed even above T_{FL} [31] up to the Ioffe-Regel-Mott (IRM) limit [32], which we establish as the fundamental boundary of the Fermi liquid not only in the dc response, but also in the frequency domain [28]. Close to $T = 0$ the loss of coherence coincides with the appearance of ambient-pressure superconductivity ($T_c = 2.9$ K) and the opening of the Mott gap at $x = 0.12$. Therefore, the IRM limit connects not only the well-defined Mott and Fermi liquid states, but also facili-

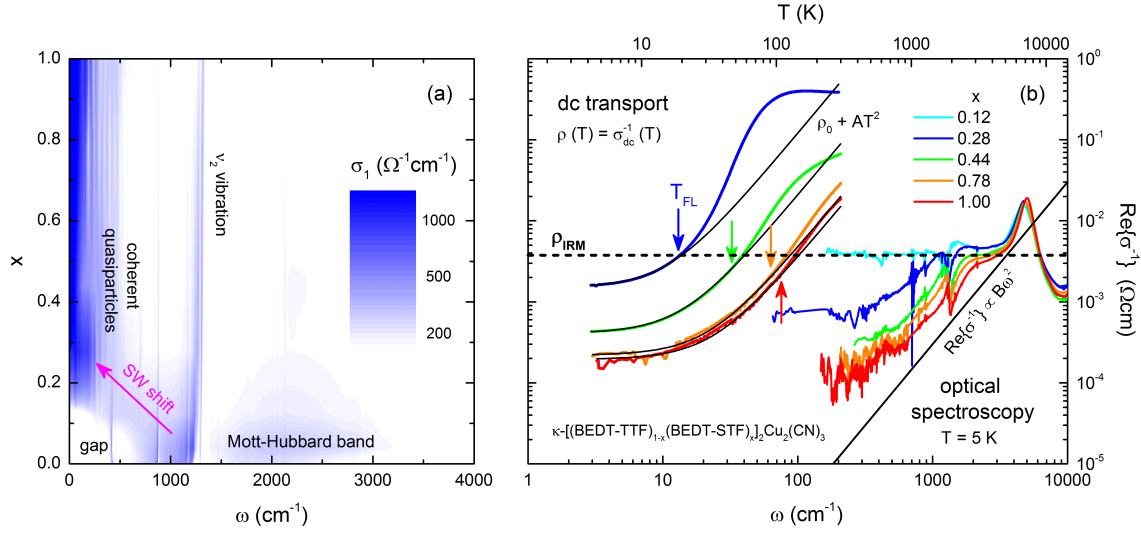


Figure 0.0.8: (a) The κ -[(BEDT-STF) $_x$ (BEDT-TTF) $_{1-x}$] $_2$ Cu $_2$ (CN) $_3$ series reveals a prototype bandwidth-tuned Mott-MIT. Upon reducing the correlations, the spectral weight is successively shifted from the Mott-Hubbard band towards $\omega = 0$ forming a coherent quasiparticle peak. The non-changing feature at 1300 cm^{-1} is a molecular vibration. (b) The frequency-dependent resistivity $\text{Re}\{\sigma^{-1}\}(\omega)$ is compared to temperature-dependent dc transport $\rho(T)$ on a common energy scale. The quadratic energy dependence of scattering, characteristic of a Fermi liquid, is fundamentally confined by the Ioffe-Regel-Mott (IRM) limit in both the dc and optical response.

tates pronounced quantum fluctuations providing the pairing glue of unconventional superconductivity.

While having focussed above on the Mott physics in half-filled materials, quarter-filled (BEDT-TTF) $_2$ X prone to charge order instabilities are of equal interest regarding their electronic correlations and superconducting properties. Strikingly, a theory based on the extended Hubbard model predicted that charge fluctuations mediate d -wave pairing [33], which was corroborated by numerous experimental results [34–38]. We thus performed a comprehensive optical study on β'' -(BEDT-TTF) $_2$ SF $_5$ RSO $_3$ and find that the molecular charge disproportionation 2δ indeed scales with the Coulomb repulsion, providing experimental evidence for the tentative phase diagram proposed in Ref. [38]. Moreover, we establish the coexistence of charge order and superconductivity for $R = \text{CH}_2\text{CF}_2$ by measuring the charge-sensitive vibrations below $T_c = 5$ K. From experiments on deuterated samples we conclude a direct relationship between these two phases since both T_c and 2δ increase at the same time.

Our optical studies enable firm conclusions on the particular charge pattern by evaluating the anisotropic electronic excitations, as illustrated in Fig. 0.0.9. While the Mott-Hubbard band shows strong anisotropy in β'' -MI ($R = \text{CHF}_2$), indicative of

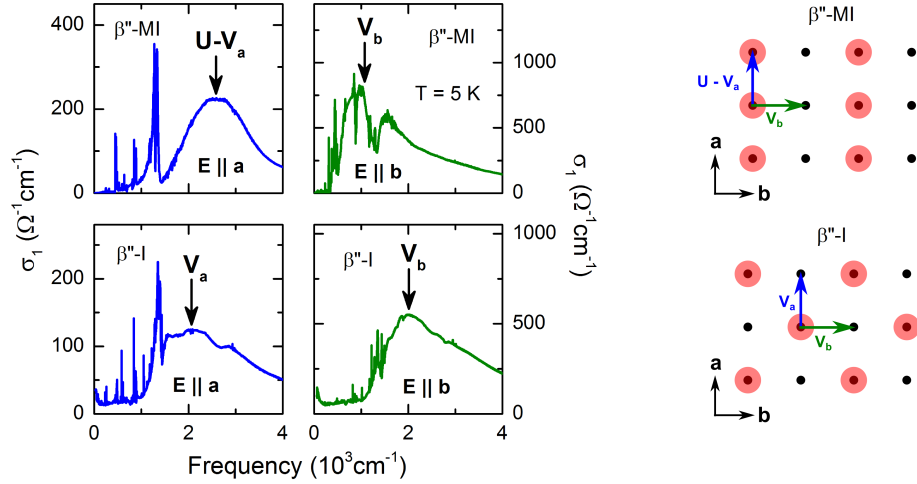
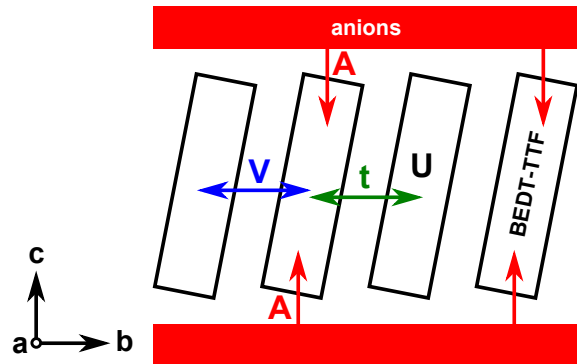


Figure 0.0.9: There is a pronounced polarization dependence of the electronic excitations in $\beta''\text{-MI}$ where structural details suggest a stripe-like charge pattern [39, 40]. Upon transition from a charge-rich to another charge-rich site along a , a larger Coulomb energy has to be paid than for transitions between charge-rich and charge-poor molecules due to the larger on-site repulsion U . The spectra of $\beta''\text{-I}$ are more isotropic, indicative of a checkerboard-like arrangement, in agreement with the crystal structure [39, 40].

a stripe-like arrangement of charge-poor and charge-rich molecules, the excitations are almost isotropic for $\beta''\text{-I}$ ($R = \text{CH}_2$) with a checkerboard pattern. As already pointed out previously [39, 40], the crystal structures infer that more positively charged BEDT-TTF molecules are closer to the negative end of the SF_5RSO_3 anions than the charge-poor sites. In addition, pressure-dependent transport results reveal an unconventional enhancement of the transition temperature T_{CO} [41] implying enhanced interactions despite a concomitant increase of the bandwidth. We explain these interesting observations by a significant involvement of the anions in molecular charge disproportionation via an external modulation of the electrostatic potential, as sketched in Fig. 0.0.10.

Figure 0.0.10: Our experimental results suggest that charge order in several $(\text{BEDT-TTF})_2X$ compounds is not a pure effect of inter-site Coulomb repulsion, but imposed from the externally modulated anion potential A . When pressure is applied, the nominal correlations V/W ($W \propto t$) are reduced. As A becomes more important, the ratio $(V+A)/W$ increases, explaining the enhancement of T_{CO} .



Publications

Some of the results presented in this thesis (including the Appendix) have already been published

- **A. Pustogow**, T. Peterseim, S. Kolatschek, L. Engel, and M. Dressel,
“Electronic correlations versus lattice interactions: Interplay of charge and anion orders in $(\text{TMTTF})_2\text{X}$ ”
In: *Phys. Rev. B*, vol. 94, no. 19, p. 195125, (2016).

Some of the results are currently under review

- **A. Pustogow**, M. Bories, A. Löhle, R. Rösslhuber, E. Zhukova, B. Gorshunov, S. Tomić, J. A. Schlueter, R. Hübner, T. Hiramatsu, Y. Yoshida, G. Saito, R. Kato, T.-H. Lee, V. Dobrosavljević, S. Fratini, and M. Dressel,
“Quantum Spin Liquids Unveil the Genuine Mott State”
In: *arXiv preprint*, arXiv:1710.07241 (2017).

Additional scientific publications which are not presented here

- **A. Pustogow**, Y. Li, I. Voloshenko, P. Puphal, C. Krellner, I. I. Mazin, M. Dressel and R. Valentí,
“Nature of optical excitations in the frustrated kagome compound Herbertsmithite”
In: *Phys. Rev. B*, vol. xx, no. xx, p. xxxxxx(R), in press
- M. Dressel, P. Lazić, **A. Pustogow**, E. Zhukova, B. Gorshunov, J. A. Schlueter, O. Milat, B. Gumhalter, and S. Tomić,
“Lattice vibrations of the charge-transfer salt $\kappa\text{-(BEDT-TTF)}_2\text{Cu}_2(\text{CN})_3$: Comprehensive explanation of the electrodynamic response in a spin-liquid compound”
In: *Phys. Rev. B*, vol. 93, no. 8, p. 081201(R), (2016).

-
- M. Pinterić, P. Lazić, **A. Pustogow**, T. Ivek, M. Kuvezdić, O. Milat, B. Gumhalter, M. Basletić, M. Culo, B. Korin-Hamzić, A. Löhle, R. Hübner, M. Sanz Alonso, T. Hiramatsu, Y. Yoshida, G. Saito, M. Dressel, and S. Tomić,
 “Anion effects on electronic structure and electrodynamic properties of the Mott insulator κ -(BEDT-TTF)₂Cu₂(CN)₃ ”
 In: *Phys. Rev. B*, vol. 94, no. 16, p. 161105(R), (2016).
 - R. Swietlik, B. Barszcz, **A. Pustogow**, M. Dressel,
 “Raman spectroscopy evidence of domain walls in the organic electronic ferroelectrics (TMTTF)₂X (X = SbF₆, AsF₆, PF₆) ”
 In: *Phys. Rev. B*, vol. 95, no. 8, p. 085205, (2017).
 - P. Puphal, M. Bolte, D. Sheptyakov, **A. Pustogow**, K. Kliemt, M. Dressel, M. Baenitz, C. Krellner,
 “Strong magnetic frustration in Y₃Cu₉(OH)₁₉Cl₈: a distorted kagome antiferromagnet”
 In: *J. Mater. Chem. C*, vol. 5, no. 10, pp. 2629-2635, (2017).
 - I. Voloshenko, M. Herter, R. Beyer, **A. Pustogow**, and M. Dressel,
 “Pressure-dependent optical investigations of Fabre salts in the charge-ordered state”
 In: *J. Phys. Condens. Matt.*, vol. 29, no. 11, p. 115601, (2017).
 - P. Lazić, M. Pinterić, **A. Pustogow**, K. Treptow, T. Ivek, O. Milat, B. Gumhalter, N. Doslić, M. Dressel, and S. Tomić,
 “Importance of van der Waals interactions and cation-anion coupling in an organic quantum spin liquid”
 In: *arXiv preprint*, arXiv:1710.01942 (2017)
 - M. Hemmida, H.-A. Krug von Nidda, B. Miksch, L. L. Samoilenko, **A. Pustogow**, J. A. Schlueter, A. Loidl, and M. Dressel,
 “Weak Ferromagnetism and Spin Glass in κ -(BEDT-TTF)₂Hg(SCN)₂Br”
 In: *arXiv preprint*, arXiv:1710.04028 (2017)

Contents

Zusammenfassung	v
Abstract	xi
1 Mot(t)ivation	1
2 Theoretical Background	7
2.1 Light-Matter Interaction	7
2.1.1 Optical Response Functions	10
2.1.2 Kramers-Kronig Relations	11
2.1.3 Observables	13
2.2 Electronic Band Picture	14
2.2.1 Metals and Insulators	15
2.2.2 Drude-Sommerfeld Model	17
2.2.3 Lorentz and Fano models	20
2.2.4 Matthiessen Rule and Ioffe-Regel-Mott Limit	21
2.3 Correlated Electron Systems	22
2.3.1 Fermi Liquid Theory and Extended Drude Formalism	22
2.3.2 The Mott Metal-Insulator Transition	25
2.3.3 Extended Hubbard Model	28
2.3.4 Mott Insulators and Quantum Spin Liquids	31
2.3.5 Charge Order in 1/4-Filled Systems	33
3 Materials: Pairing and Frustration in quasi 2D (BEDT-TTF)₂X	37
3.1 Molecular Conductors	37
3.1.1 Quasi Two-Dimensional (BEDT-TTF) ₂ X	39
3.1.2 Packing-Motifs	41
3.2 Charge-Sensitive Molecular Vibrations	41
3.3 Mott Physics in 1/2-Filled Organic Quantum Spin Liquids	45

3.4	Charge Order and Superconductivity in 1/4-filled (BEDT-TTF) ₂ X	51
4	Experiments and Data Extraction	59
4.1	Measurement Setup	59
4.1.1	Fourier-Transform Infrared Spectroscopy	59
4.1.2	Optical Cryostats	62
4.2	Geometry of Optical Measurements	65
4.2.1	Reflectivity Measurements and Extrapolation	66
4.2.2	Transmission Measurements	68
4.2.3	Sample Preparation	70
4.3	Determination of Band Parameters and Fitting Procedures	70
4.3.1	Mott-Hubbard Band Analysis	71
4.3.2	Vibrational Modes	73
4.3.3	Power-Law Exponents	73
4.4	dc Transport	74
4.5	SQUID Magnetometry	75
5	Results I: Genuine Mott Physics in 1/2-filled (BEDT-TTF)₂X	79
5.1	Quantum Spin Liquids Unveil the Genuine Mott State	80
5.1.1	Electrodynamic Response of Quantum Spin Liquids	80
5.1.2	Revealing Electronic Correlations and Pomeranchuk Effect	85
5.1.3	Unified Phase Diagram of the Mott Insulator	93
5.1.4	Mott-Hubbard DMFT Calculations	99
5.1.5	Mott Physics in κ -(BEDT-TTF) ₂ Cu[N(CN) ₂]Br _x Cl _{1-x}	99
5.1.6	Superconductivity and Fermi Liquid on the Metallic Side	106
5.1.7	Summary and Discussion	110
5.2	Low-Energy Excitations of Quantum Spin Liquids	113
5.2.1	Power-Law Conductivity in κ -(BEDT-TTF) ₂ Cu ₂ (CN) ₃	113
5.2.2	Spinons Below the Mott Gap of β' -EtMe ₃ Sb[Pd(dmit) ₂] ₂	118
5.2.3	Summary and Discussion	122
5.3	Mott Transition in κ -[(BEDT-STF) _x (BEDT-TTF) _{1-x}] ₂ Cu ₂ (CN) ₃	124
5.3.1	Bandwidth-Tuned Mott Transition	125
5.3.2	Ioffe-Regel-Mott Limit: Universal Boundary of the Fermi Liquid	132
5.3.3	Summary and Discussion	141
6	Results II: Charge Order and Superconductivity at 1/4-Filling	143
6.1	Charge Order and Superconductivity in β'' -(BEDT-TTF) ₂ SF ₅ RSO ₃	144

6.1.1	Charge Order Revealed by Molecular Vibrations	148
6.1.2	Electronic Excitations and Charge Pattern	154
6.1.3	Phase Diagram: Reversed Bandwidth-Tuning by Pressure . . .	158
6.1.4	Coexistence of Charge Order and Superconductivity	167
6.1.5	Deuteration Effect on Charge Order and Superconductivity . .	171
6.1.6	Summary and Discussion	175
6.2	Negligible Charge Fluctuations in θ -(BEDT-TTF) ₂ I ₃	177
6.3	Charge Order in β'' -(BEDT-TTF) ₄ [(H ₃ O)Ga(C ₂ O ₄) ₃] · C ₆ H ₅ NO ₂ . . .	180
6.3.1	Electronic Excitations and Fermi Liquid Behaviour	182
6.3.2	Charge Order	188
6.3.3	Summary and Discussion	194
6.4	Conclusion and Outlook	195
A Appendix		199
A.1	The Interplay of Charge and Anion Orders in (TMTTF) ₂ X	200
A.1.1	Introduction	200
A.1.2	Materials and Experiments	201
A.1.3	Results and Analysis	205
A.1.4	Charge Order	205
A.1.5	Anion Order	208
A.1.6	Tetramerization	209
A.1.7	Deuteration	212
A.1.8	Conclusions	215
A.1.9	Supplement	216
	A.1.9.1 Charge-Sensitive Vibrations	216
	A.1.9.2 The Dimeric ν_4 Mode	219
A.2	Correlation-Dependent Luttinger-Liquid Dynamics in 1D	222
A.2.1	Abstract	222
A.2.2	Introduction	222
A.2.3	Experimental Details	224
A.2.4	Results	225
A.2.5	Temperature-Dependent Luttinger Exponent.	227
A.2.6	Conclusion	229
A.3	Charge Order on the Nanoscale in α -(BEDT-TTF) ₂ I ₃	230
A.3.1	Introduction	230
A.3.2	Material Properties	231
A.3.3	Near-Field Optical Properties	233

A.3.4	Spatially Inhomogeneous Transition in a Non-Uniform Sample	234
A.3.5	Conclusions	238
B	Acknowledgments	241
	Bibliography	245
	Declaration of originality	279

1. Mot(t)ivation

When common people think about condensed matter physics, the first things that come into their mind are the versatile applications essential for our daily life, ranging from functional materials towards carbon-based implementations and electronic devices. From the physicists point of view, however, this field bears much more fascinating phenomena than just the mere thermodynamic, ductile and conducting properties at ambient conditions ($T = 295$ K, $p = 1$ bar = 10^5 Pa). Approaching the topic from the other extreme, high-energy physics was extremely efficient over the last century to provide a comprehensive understanding of the fundamental interactions between elementary particles that assemble our universe, eventually leading to the Standard Model. Yet, this concept alone is not sufficient to describe collective excitations of many-body systems, as pointed out in his famous article by P. W. Anderson [42]. In this regard, the essence of solid state physics relies in emergent phenomena associated with diverse quasiparticles, such as excitons, magnons, and phonons to mention just a few, arising from electronic, magnetic and lattice interactions.

In this thesis we focus primarily on electron-electron interactions via their charge and magnetic degrees of freedom. While in most materials band theory provides an excellent description of the conduction properties, there are some systems that exhibit insulating behaviour despite their nominally metallic band structure. It is known, since the early works of Mott and Hubbard, that sufficiently strong Coulomb interactions are able to localize the charge carriers in solids, even in absence of long-range magnetic order [1]. This is a manifestation of the imbalance in the particle-wave duality of conduction electrons [14], which is driven by the competition between the Coulomb repulsion U (localized, particle-like) and the bandwidth W (delocalized, wave-like). When the insulator *melts*, which is achieved either by reducing the strength of interactions or by doping away from half-integer fillings, the resulting metallic state retains a strongly correlated character, as renormalized low-energy quasiparticles coexist with precursor features of the Mott insulator [2, 43]. Many

narrow-band materials of interest are today identified as strongly correlated metals close to the Mott regime [44]. In this regard, electronic transport is commonly discussed in the context of the Ioffe-Regel-Mott limit, confining coherent quasiparticles of a Fermi liquid to a regime with less than one scattering event per lattice site [32]. While numerous studies have concentrated on the complex behavior of correlated metals [45], the Mott transition itself has seemingly managed to keep some of its secrets concealed. This metal-insulator transition (MIT) is a weakly first-order phase transition confined to temperatures of only few percent of the bandwidth. As a result, the approach to this transition is masked, in most examples, by magnetic instabilities also taking place at comparable temperatures. For that reason, we study quantum spin liquids in which antiferromagnetism is suppressed down to $T = 0$. The region in the close vicinity of the low-temperature phase boundary, which exhibits a positive slope in the $T - p$ phase diagram reminiscent of the Pomeranchuk effect in ^3He [10], is of particular interest since a coexistence of metallic and insulating phases was predicted by theory [4, 5], but never observed in experiment. At elevated temperatures, however, the Mott MIT shows great similarity to conventional liquids and gases [6, 7]. While it is a well-defined first-order phase transition below the critical endpoint, in the supercritical region it is a crossover identified as the quantum Widom line (QWL) [5]. Our results establish the QWL as the genuine boundary of the gapped Mott state; at higher temperatures, electrons behave like in a thermally activated semiconductor with incoherent transport properties.

In order to examine the nature of the Mott transition in half-filled systems, we choose layered organic compounds, specifically $(\text{BEDT-TTF})_2X$, as they belong to the few systems where the single-band Hubbard model is truly realized [11, 12] – in many transition-metal oxides, including the high-temperature superconducting cuprates [46], the band structure is more complex [47, 48] impeding a clean analysis. Moreover, the small bandwidth of organic charge transfer salts allows us to investigate incoherent phenomena in the high-temperature limit due to more strongly pronounced thermal effects on the band structure.

The method of choice is optical spectroscopy as it directly maps the electronic transitions between the Hubbard bands and, therefore, provides experimental access to the intrinsic parameters of the Mott transition, namely the Coulomb repulsion and bandwidth. This allows us to *quantitatively* compare the degree of electronic correlations U/W between different compounds. While it is well-established in theory that the phase diagram is controlled by the parameters T/W and U/W [4, 5], experimental studies were usually confined to $T - p$ plots until now. To that end,

we elaborated a novel paradigm to connect the Widom lines of different compounds utilizing the optically determined band parameters. We thus present, for the first time, a universal phase diagram of *all* Mott insulators on quantitative scales. A possible extension of this Mott-Hubbard scaling towards the metallic side of the MIT is discussed, providing a direct link to high-temperature superconductivity.

We also study Mott-Hubbard interactions in quarter-filled organic materials where, apart from the on-site term U , the inter-site Coulomb repulsion V becomes important. For sufficiently strong correlations V/W , a charge-ordered state is realized in α , β'' - and θ -type (BEDT-TTF) $_2X$ at low temperatures. Vibrational spectroscopy on charge-sensitive modes provides a convenient tool to monitor the local molecular charge [49, 50]. Combining these results with the anisotropic electronic excitations enables us to assign the spatial charge pattern. There is growing evidence, however, that in many materials the electrostatic potential of the anions plays a crucial role for charge disproportionation between the organic molecules [51].

These compounds are of particular interest as unconventional superconductivity is stabilized in the near vicinity of the charge-ordered phase, suggestive of a possible relation of the attractive pairing mechanism to charge fluctuations [33, 38]. We thus performed a profound endeavour to prove that these two states are coexisting rather than competitive. To date, already more than 100 organic superconductors are known [52]; just a small minority of them reveals conventional pairing according to the BCS theory. It is, thus, highly desirable to understand the underlying interactions that account for superconductivity at low temperatures and drive the Mott metal-insulator transition.

1. Chapter: Here, we give reasons for the continuous interest in condensed matter physics and, specifically, strongly correlated electron systems subject to Mott-Hubbard interactions.
2. Chapter: The theoretical background provides a solid basis to understand the fundamental interactions of light and matter, in particular the conduction electrons in solids. The theoretical concepts of the Mott insulator, quantum spin liquids and charge order are introduced in the framework of the extended Hubbard model.
3. Chapter: At this point, the general properties of the studied material class of organic conductors are presented on basis of published literature.
4. Chapter: The reader receives a circumstantial introduction to the experimental methods and data extraction. A general overview of the measurement setups

and the basic principle of optical spectroscopy is given, specifically focussing on Fourier-Transform infrared (FTIR) spectroscopy. Moreover, the characteristics of the observed data are discussed and how the relevant physical quantities were extracted, such as assignment of the site charge from molecular vibrations. In particular, the determination of electronic interactions from the frequency-dependent optical conductivity is an integral part throughout this thesis.

5. Chapter: This part reports the main result of this work, namely the construction of a unified phase diagram of genuine Mott insulators on quantitative scales. In this regard, we present a novel route that facilitates classification and comparison of the correlation strength between different compounds, and with theory. We also suggest to translate this concept to the metallic and superconducting regions of the phase diagram. The controversial role of spin excitations in the Mott state is discussed for several quantum spin liquid materials. Using the extended Drude formalism, the correlation-dependent renormalization of the Fermi liquid parameters is revealed for a series of chemically modified compounds subject to the bandwidth-tuned Mott transition. The importance of the Ioffe-Regel-Mott limit for the realm of coherent quasiparticles is pointed out.
6. Chapter: In the second chapter on the results we investigate $(\text{BEDT-TTF})_2X$ compounds with quarter-filled bands subject to charge order and discuss a possible relation to unconventional superconductivity. In particular, we prove the coexistence of these two phases. Indications are found that the role of anions for charge order is more important than anticipated, maybe not only for the compounds under study, but many more – or even all – organic charge-transfer systems.

Diese Arbeit ist wie folgt gegliedert:

1. Kapitel: An dieser Stelle begründen wir das stete Interesse an der Physik kondensierter Materie und, im Speziellen, stark korrelierten Elektronensystemen unter dem Einfluss von Mott-Hubbard Wechselwirkungen.
2. Kapitel: Der theoretische Hintergrund dient als solides Fundament für das Verständnis der grundlegenden Wechselwirkungen zwischen Licht und Materie,

insbesondere im Hinblick auf die Leitungselektronen in Festkörpern. Die theoretischen Konzepte des Mott-Isolators, von Quanten-Spin-Flüssigkeiten sowie Ladungsordnung werden anhand des erweiterten Hubbard-Modells eingeführt.

3. Kapitel: Hier werden die wichtigsten Eigenschaften der untersuchten Materialien aus der Fachliteratur vorgestellt.
4. Kapitel: Der Leser erhält eine ausführliche Einführung in die experimentellen Methoden und Datenanalyse. Ein grundlegender Überblick über die Messgeräte und -verfahren wird mit Fokus auf Fourier-Transformations-Infrarot-Spektroskopie (FTIR) gegeben. Zudem werden die wichtigsten Aspekte der Messergebnisse und die Extraktion der relevanten physikalischen Größen, zum Beispiel die Bestimmung der Molekülladung anhand der Schwingungsmoden, diskutiert. Insbesondere ist die Ermittlung der elektronischen Wechselwirkungen durch die optische Leitfähigkeit ein wesentlicher Bestandteil dieser Arbeit.
5. Kapitel: Dieser Abschnitt präsentiert die Konstruktion eines einheitlichen Phasendiagramms für unverfälschte Mott-Isolatoren auf quantitativen Skalen als die wichtigste Errungenschaft dieser Arbeit. Diesbezüglich stellen wir eine neuartige Methode vor, die die Klassifizierung und den Vergleich der Korrelationsstärke zwischen verschiedenen Verbindungen sowie mit theoretischen Ergebnissen ermöglicht. Wir regen an, dieses Konzept auch auf die metallischen und supraleitenden Teile des Phasendiagramms auszudehnen. Die kontroverse Rolle von Spin-Anregungen im Mott-Zustand wird anhand verschiedener Quanten-Spin-Flüssigkeits-Materialien diskutiert. Mithilfe des erweiterten Drude-Formalismus enthüllen wir die korrelationsabhängige Renormierung der Fermi-Flüssigkeits-Parameter im Zuge des von der Bandbreite getriebenen Mott-Übergangs in chemisch modifizierten Verbindungen. Die Bedeutung des Ioffe-Regel-Mott-Limits für die Stabilisierung kohärenter Quasiteilchen wird aufgezeigt.
6. Kapitel: Im zweiten Ergebnis-Abschnitt untersuchen wir viertel-gefüllte (BEDT-TTF)₂X Verbindungen im Hinblick auf Ladungsordnung und diskutieren eine mögliche Verknüpfung mit unkonventioneller Supraleitung. Insbesondere belegen wir die Koexistenz dieser beiden Phasen. Wir finden Hinweise dafür, dass die Rolle der Anionen für Ladungsordnung wichtiger ist als üblicherweise angenommen, vielleicht nicht nur für die untersuchten Systeme, sondern für viele andere – oder sogar alle – organische Ladungs-Transfer Salze.

2. Theoretical Background

Information presented in this chapter is based mainly on Ref [53]. Therefore, only statements from other sources will be cited specifically.

2.1 Light-Matter Interaction

Since matter consists of charged particles, in particular negatively charged electrons surrounding the positively charged nuclei, it is susceptible to static and dynamic electric and magnetic fields, \mathbf{E} and \mathbf{B} . First, however, we consider electromagnetism in vacuum which is circumstantially described by Maxwell's equations

$$\nabla \cdot \mathbf{E} = \frac{\rho}{\epsilon_0} \quad (2.1.1)$$

$$\nabla \cdot \mathbf{B} = 0 \quad (2.1.2)$$

$$\nabla \times \mathbf{E} = -\frac{\partial \mathbf{B}}{\partial t} \quad (2.1.3)$$

$$\nabla \times \mathbf{B} = \mu_0 \mathbf{j} + \mu_0 \epsilon_0 \frac{\partial \mathbf{E}}{\partial t}, \quad (2.1.4)$$

where ρ and \mathbf{j} are the charge and current densities, respectively. The vacuum permittivity ϵ_0 and permeability μ_0 are related to the speed of light $c = \frac{1}{\sqrt{\epsilon_0 \mu_0}}$. In absence of charges and currents, combining these equations yields a wave equation of the electric and magnetic fields

$$\frac{1}{c^2} \frac{\partial^2 \mathbf{E}}{\partial t^2} - \nabla^2 \mathbf{E} = 0 \quad (2.1.5)$$

$$\frac{1}{c^2} \frac{\partial^2 \mathbf{B}}{\partial t^2} - \nabla^2 \mathbf{B} = 0 \quad (2.1.6)$$

which is nothing but an electromagnetic wave propagating with the speed of light. There, the electric and magnetic fields oscillate in-phase and are polarized perpendicular to each other and the propagation direction.

Inside a material, application of an electric field \mathbf{E} , for instance, induces a polarization \mathbf{P} and current flow inside the material in order to counterbalance the electrostatic potential. Similarly, an external magnetic field \mathbf{B} influences the magnetic moments, such as electron and nuclear spins, giving rise to a magnetization \mathbf{M} . Therefore, the charge and magnetic responses affect the actual field strength inside the material. The corresponding auxiliary fields are $\mathbf{D} = \epsilon_0\mathbf{E} + \mathbf{P}$ and $\mathbf{H} = \frac{1}{\mu_0}\mathbf{B} + \mathbf{M}$, respectively. As a result, an electromagnetic wave is attenuated and propagates slower through the material than in vacuum, i.e. $v_{medium} = \frac{1}{\sqrt{\epsilon\epsilon_0\mu\mu_0}} < c$, where ϵ and μ are the relative permittivity and permeability, respectively. Since the field strengths are related via the speed of light $|\mathbf{E}| = c|\mathbf{B}|$ and in most materials $\mu \approx 1$, the charge response is dominated by the electric field component and thus predominantly appears parallel to the polarization of \mathbf{E} .

A photon, i.e. an electromagnetic wave packet, carries a quantum of energy E related to its wavelength λ and frequency ν , the product of which gives the speed of light $c = \lambda\nu$. The photon energy can be expressed in various units

$$E = \hbar\omega = h\nu = \frac{hc}{\lambda} = eU = k_B T, \quad (2.1.7)$$

where $h = \hbar/2\pi$, U , k_B and T denote Planck's constant, an electrostatic potential difference (voltage), Boltzmann's constant and temperature, respectively. In this thesis, wave numbers $[\omega] = \text{cm}^{-1}$ are used as the preferred energy unit¹. Fig. 2.1.1 compares the energy scales of the electromagnetic spectrum in the optical range. While interband transitions are observed at high frequencies (near-infrared, visible, UV), phonons and molecular vibrations show up in the mid- (MIR) and far-infrared (FIR) ranges. Superconductivity appears at even lower energy scales and related spectral features (superconducting gap) can be addressed in the far-far-infrared (FFIR) and THz regions. For very small transition temperatures, e.g. $T_c < 1$ K in heavy fermion superconductors [54], also the gap frequency is shifted to lower energies such that optical methods are not applicable due to the large wavelength ($\lambda \geq 1 \text{ cm}^{-1}$). Strikingly, the fingerprints of electronic correlations and their influence on the electrodynamic properties are found from the lowest end of the optical range up to the visible and UV [45]: while the scattering rate of heavy Fermion metals is suppressed down to a few GHz (10^{-1} cm^{-1}) due to the large effective mass m^* [55], the energy gap in Mott insulating copper oxides, such as the geometrically frustrated quan-

¹Strictly speaking, I will use the letter ω for any kind of frequency; the units in brackets denote whether it corresponds to inverse wavelength $\frac{1}{\lambda}$ (cm^{-1}), frequency ν (Hz) or angular frequency ω (rad s^{-1} or just s^{-1}).

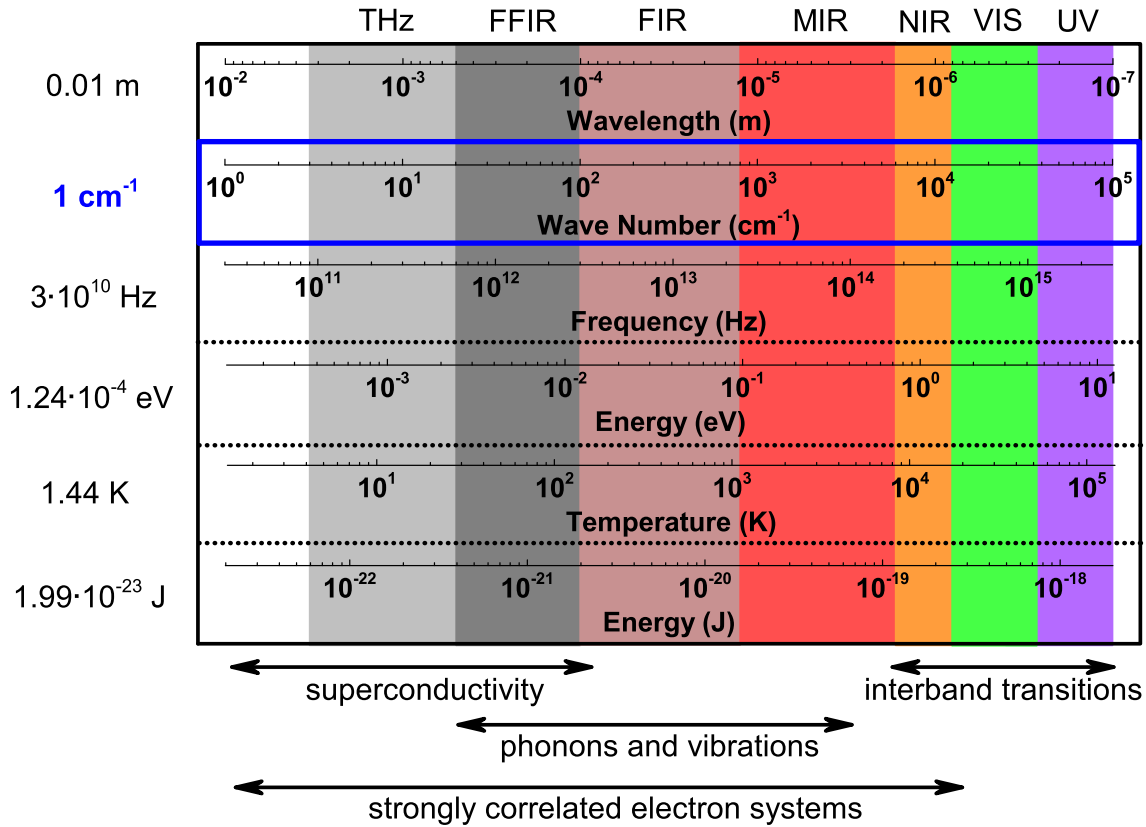


Figure 2.1.1: The electromagnetic spectrum in the optical range expressed in various units. The conversion factor with respect to wave numbers cm^{-1} is listed on the left. Interband transitions are among the typical physical phenomena that can be observed in the ultraviolet (UV), visible (VIS) and near-infrared (NIR) ranges. Lattice phonons and intramolecular vibrations typically show up in the far- (FIR) and mid-infrared (MIR) while the energy gap of a superconductor can be detected in the far-far-infrared (FFIR) and THz by optical spectroscopy. The effects of electronic correlations appear from lowest energies up to the VIS, depending on the interaction strength. A more detailed, yet by no means complete, list of observed phenomena can be found in Fig. 3 of Basov *et al.* [45].

tum spin liquid candidate Herbertsmithite, emanating from strong on-site Coulomb repulsion is about several eV (10^4 cm^{-1}) [48]. Thus, optical spectroscopy probes the relevant energy scales to study manifold material properties and phenomena of interest in contemporary solid state physics.

2.1.1 Optical Response Functions

Although there are diverse techniques to scrutinize the optical range, such as time-resolved pump-probe, Raman, (angle-resolved) photo-emission and fluorescence spectroscopies, here we focus on classical optical spectroscopy. In this method, the light intensity is far below the saturation threshold, so the electronic system remains close to equilibrium and linear response theory can be applied. Therefore, the optical response of a material is circumstantially described by two frequency-dependent, Kramers-Kronig consistent linear response functions. These can be either the real and imaginary parts of the complex dielectric function $\hat{\epsilon} = \epsilon_1 + i\epsilon_2$, refractive index $\hat{N} = n + ik$ or optical conductivity $\hat{\sigma} = \sigma_1 + i\sigma_2$. In the following, only non-magnetic materials ($\mu = 1$) will be discussed, yielding the mutual relations

$$\hat{\epsilon} = 1 + \frac{i\hat{\sigma}}{\omega\epsilon_0} = \hat{N}^2 \quad (2.1.8)$$

$$\sigma_1 = \epsilon_0\omega\epsilon_2 = 2\epsilon_0\omega nk \quad (2.1.9)$$

$$\sigma_2 = \epsilon_0\omega(1 - \epsilon_1) = \epsilon_0\omega(1 - n^2 + k^2). \quad (2.1.10)$$

In general, the results herein will be presented by σ_1 and σ_2 , as they are related to the current density induced by the external electric field $\mathbf{j} = \hat{\sigma}\mathbf{E}$, which is nothing but Ohm's law. The real part of the frequency-dependent optical conductivity $\sigma_1(\omega)$ approaches the dc conductivity $\sigma_{dc} = \frac{1}{\rho}$ in the limit $\omega \rightarrow 0$, where ρ is the material-specific resistivity.

While the optical conductivity is particularly useful in characterizing charge transport and energy dissipation related to absorption of electromagnetic radiation, the refractive index describes the propagation of light through dispersive media via the wave vector $\hat{q} = \frac{\omega}{c}\hat{N}$. In case of negligible absorption ($k = 0$) we obtain the relation $q = \frac{2\pi n}{\lambda} = \frac{2\pi}{\lambda_{\text{medium}}}$ implying that the wavelength is reduced in the material. Due to energy conservation, the frequency remains unchanged and we can calculate the speed of light in matter

$$v_{\text{medium}} = \lambda_{\text{medium}}\nu = \frac{\lambda\nu}{n} = \frac{c}{n}, \quad (2.1.11)$$

where the real part of the refractive index n determines the degree of slowing-down in matter. The inequality of propagation speeds between different media gives rise to manifold refraction processes observed in daily life, such as in lenses, optical fibers or a rainbow, to mention just a few.

For structures much larger than the wavelength, geometrical optics are circumstan-

tially described by Fresnel's formulas and Snell's law

$$n_1 \sin \theta_1 = n_2 \sin \theta_2, \quad (2.1.12)$$

where the indices 1 and 2 denote the different materials touching at the interface. While measurements at various angles of incidence are the essence of ellipsometry, which enables to determine the complete dielectric function even for optically anisotropic materials, the optical cryostats employed in this PhD project limited experiments to normal incidence. In this case, Fresnel's equations acquire the simple form

$$R = \frac{I_{refl}}{I_0} = \frac{(1 - n)^2 + k^2}{(1 + n)^2 + k^2}, \quad (2.1.13)$$

where the reflectivity R is defined as the ratio between reflected and incident intensities, I_{refl} and I_0 , respectively.

2.1.2 Kramers-Kronig Relations

The response of a material \hat{X} on an external stimulus \hat{f} is circumstantially described by the linear response function \hat{G} . Let us focus here on a basic description including several assumptions, such as the local approximation (the response $\hat{X}(\mathbf{r})$ is considered only at the particular position of the field $\hat{f}(\mathbf{r})$), an isotropic and homogeneous medium (\hat{G} is a scalar) and, as already mentioned above, the linear response theory. A more profound derivation can be found in Chapter 3.2 of Ref. [53].

Considering that the origin of the time scale should not be of physical relevance and, thus, the response function depends only on $t - t'$, the relation reads

$$\hat{X}(t) = \int_{-\infty}^{\infty} \hat{G}(t - t') \hat{f}(t') dt'. \quad (2.1.14)$$

Another important physical aspect is causality, that is, the response happens *after* the stimulus. Therefore, we restrict ourselves to integration from $-\infty$ up to t , as $\hat{G}(t - t') = 0$ for $t < t'$. Since we are interested in the frequency-dependent response rather than the time evolution of the system — which, of course, is of equal interest on its own — in the following, we discuss the spectral response function in Fourier space

$$\hat{G}(\omega) = \int \hat{G}(t - t') e^{i\omega(t-t')} dt. \quad (2.1.15)$$

After some math, we obtain the relation $\hat{X}(\omega) = \hat{G}(\omega)\hat{f}(\omega)$. In one-to-one correspondence to Ohm's law $\mathbf{j} = \hat{\sigma}\mathbf{E}$, the frequency-dependent generalized susceptibility $\hat{G} = G_1 + iG_2$ manifests as the complex conductivity $\hat{\sigma}(\omega) = \sigma_1 + i\sigma_2$. Application of Cauchy's theorem leads to the following relation between the real and imaginary parts of the response function

$$G_1(\omega) = \frac{1}{\pi} \mathcal{P} \int_{-\infty}^{\infty} \frac{G_2(\omega')}{\omega' - \omega} d\omega' \quad (2.1.16)$$

$$G_2(\omega) = -\frac{1}{\pi} \mathcal{P} \int_{-\infty}^{\infty} \frac{G_1(\omega')}{\omega' - \omega} d\omega', \quad (2.1.17)$$

where \mathcal{P} is the Cauchy principal value. Thus, G_1 and G_2 are Hilbert transforms of each other, i.e. knowing one of them over the entire frequency range allows to determine the other one by simple integration.

Upon eliminating negative frequencies by making use of $\hat{\sigma}(\omega) = \hat{\sigma}^*(-\omega)$, we end up with the form for the real and imaginary parts of the optical conductivity

$$\sigma_1(\omega) = \frac{2}{\pi} \mathcal{P} \int_0^{\infty} \frac{\omega' \sigma_2(\omega')}{\omega'^2 - \omega^2} d\omega' \quad (2.1.18)$$

$$\sigma_2(\omega) = -\frac{2\omega}{\pi} \mathcal{P} \int_0^{\infty} \frac{\sigma_1(\omega')}{\omega'^2 - \omega^2} d\omega', \quad (2.1.19)$$

where σ_1 describes the energy loss due to absorption processes and σ_2 corresponds to the phase change of an electromagnetic wave propagating through a dispersive medium.

As we will see in section 4, in most cases it is only possible to determine the absolute value of the reflected intensity R which is, a priori, not sufficient to determine σ_1 and σ_2 . The complex reflection coefficient $\hat{r} = \sqrt{R}e^{i\phi_r}$, however, can be separated into real and imaginary parts of its logarithm, $\ln \sqrt{R}$ and the phase ϕ_r , which are mutually related via the Kramers-Kronig dispersion relations

$$\ln \sqrt{R(\omega)} = \frac{2}{\pi} \mathcal{P} \int_0^{\infty} \frac{\omega' \phi_r(\omega')}{\omega'^2 - \omega^2} d\omega' \quad (2.1.20)$$

$$\phi_r(\omega) = -\frac{2\omega}{\pi} \mathcal{P} \int_0^{\infty} \frac{\ln \sqrt{R(\omega')}}{\omega'^2 - \omega^2} d\omega'. \quad (2.1.21)$$

Therefore, the Kramers-Kronig relations allow us to determine the complete response function $\hat{\sigma}$ from reflectivity measurements only. Since the integration is performed from $\omega = 0$ up to ∞ — which will never be covered completely — the accuracy of the result also depends on the extent of the captured frequency range and the extrap-

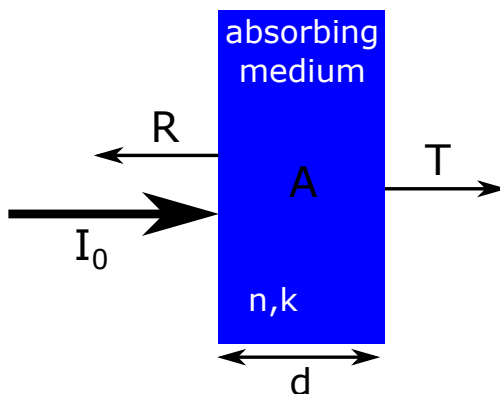


Figure 2.1.2: Upon shining light on a piece of matter, the material-specific components of the refractive index, $n(\omega)$ and $k(\omega)$, determine its colour, gloss and opacity. The reflectivity R , absorption A and transmission T , defined as the intensity ratio with respect to the incoming light I_0 , can be measured in optical experiments. These three observables are related to each other via the sample thickness d and energy conservation.

olation of data outside the measured region. More information on these technical details is given in section 4.2.1.

2.1.3 Observables

Optical spectroscopy allows to determine the frequency-dependent response functions experimentally. As sketched in Fig. 2.1.2, there are three main observables, reflectivity R , absorption A and transmission T , defined as the respective portion of the incoming light intensity I_0 , i.e. $R = \frac{I_{refl}}{I_0}$, $A = \frac{I_{abs}}{I_0}$ and $T = \frac{I_{trans}}{I_0}$. Energy conservation implies

$$R + A + T = 1, \quad (2.1.22)$$

so it is sufficient to measure two of these quantities, typically R and T , to determine the third one and, thus, the complete response function. In principle, A can also be accessed experimentally through heating of the material caused by the absorption of electromagnetic radiation at distinct frequencies. However, this bolometric method requires a thermodynamic approach rather than typical optical measurement setups, therefore it will not be considered in the following.

For an absorption process in the atomic limit, i.e. by a single layer with infinitesimal thickness, the intensity is attenuated by a specific factor. Adding several layers in series causes the contributions to add up multiplicatively. Consequently, the total absorption depends exponentially on the sample thickness, which is described by the

Lambert-Beer law,

$$I(d) = I_0 e^{-\alpha d} = 1 - A, \quad (2.1.23)$$

where α is the absorption coefficient related to the optical response functions via

$$\alpha = \frac{4\pi k}{\lambda} = \frac{\omega \epsilon_2}{cn} = \frac{\sigma_1}{\epsilon_0 cn}. \quad (2.1.24)$$

Therefore, the transmitted intensity T decreases exponentially with the distance d penetrated into the material. While α describes the attenuation per unit length², one can define the optical density αd as a measure of the transmission through a sample of given thickness. The implications for experiments are explained in detail in section 4.2.

2.2 Electronic Band Picture

While in single atoms and molecules the electrons are confined to discrete orbitals, in a periodic crystal the electronic states are extended in momentum space, yielding more or less dispersing *bands* [56, 57]. Fig. 2.2.1 (a) exemplarily shows the band structure around the Fermi energy E_F in the first Brillouin zone, i.e. for crystal momenta³ $\mathbf{k} \in [-\frac{\pi}{a}, \frac{\pi}{a}]$, where a is the unit cell parameter. Close to the minima and maxima around $\mathbf{k} = 0$, the band dispersion can be approximated by a parabola, yielding

$$E = \frac{\hbar^2 \mathbf{k}^2}{2m_{band}} \quad \rightarrow \quad m_{band} = \left(\frac{1}{\hbar^2} \frac{d^2 E}{d\mathbf{k}^2} \right)^{-1}, \quad (2.2.1)$$

where m_{band} is the band mass. In this range, charge motion in a solid can be approximated with the energy-momentum relation of a non-relativistic particle propagating in free space ($E = \frac{\mathbf{p}^2}{2m_e}$); the interaction with the crystal lattice is expressed as a mass renormalization, $m_{band} \neq m_e$, that can be anisotropic depending on the structure. Near the band gap the effective mass can be approximated as the ratio of bandwidth W_0 and band gap Δ which yields $m_{band} \approx 0.01 - 0.1 m_e$ for typical semiconductors,

²To be precise, α is the attenuation upon propagating half a wavelength in the material, i.e. for one half-cycle of the electric field.

³In a crystal, it is convenient to express the momentum in reciprocal space by the wave vector: $\mathbf{p} = \hbar \mathbf{k} = \frac{2\pi \hbar}{x}$, where x is the real-space coordinate.

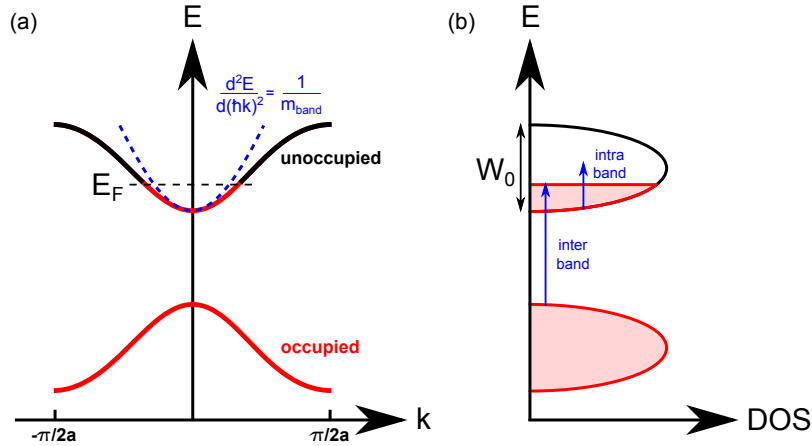


Figure 2.2.1: (a) Electronic band structure in reciprocal space around the Fermi energy E_F which determines the boundary of occupied (red) and unoccupied (black) states. The band dispersion can be approximated by a parabola around the extrema, where the curvature is inversely related to the band mass m_{band} . (b) The schematic density of states (DOS) indicates the bandwidth W_0 and possible electronic transitions in the crystal (blue arrows). Since, in general, an electron can be excited from an occupied to an unoccupied state, transitions are only possible across E_F at thermodynamic equilibrium. While inter-band excitations always appear at finite energy, intra-band transitions extend to zero frequency.

in good agreement with experimental values of, for instance, Si, InSb or GaAs [56]. The free electron mass is recovered at energies far away from the gap.

Fig. 2.2.1 (b) schematically illustrates the density of states (DOS) and the corresponding bandwidth W_0 . By absorbing a photon, an electron is excited from an occupied state (red) below E_F to an unoccupied state above E_F . The vacancy created at the original state is called a *hole* which can be considered as a positive charge with otherwise similar properties as an electron. In this context, optical spectroscopy is inherently associated with the creation of electron-hole pairs. While intra-band excitations within the partially occupied band range from zero energy up to the bandwidth W_0 , the onset of inter-band excitations is generally at finite energy above the band gap.

2.2.1 Metals and Insulators

In the electrostatic limit, i.e. for an applied dc voltage, charge motion is only possible for partially filled bands as it requires occupied and unoccupied states touching at the Fermi level [56, 57]. This criterion distinguishes metals from insulators, as sketched in Fig.2.2.2.

On the one hand, in an insulator there is a well-defined single-particle gap Δ be-

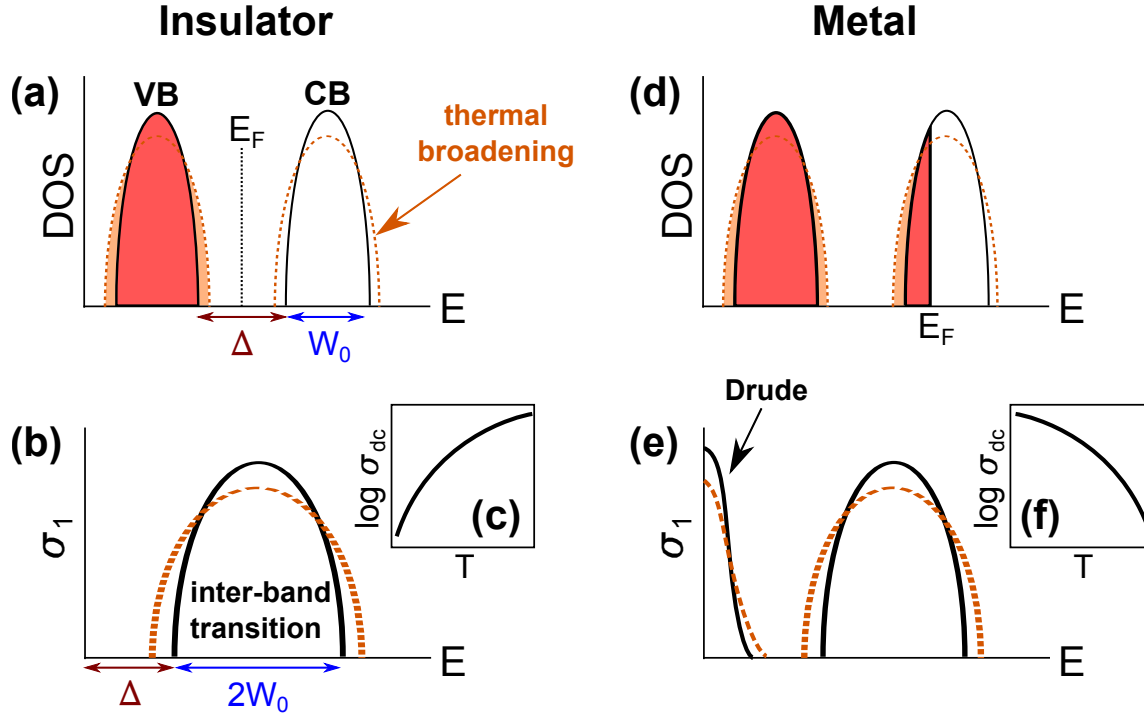


Figure 2.2.2: Fundamental differences between metals and insulators. (a) An insulator is characterized by a completely filled valence band (VB) and an empty conduction band (CB). The Fermi energy E_F is located between the two bands and charge transport requires excitation across the gap Δ . As a result, both the optical conductivity within the gap (b) and the dc conductivity are small (c). Thermal broadening of the bands leads to a reduction of Δ and, therefore, to an enhancement of σ_{dc} with temperature. (d) On the other hand, partially-filled bands imply metallic properties with gapless charge excitations and large density of states (DOS) at E_F , which shows up as a Drude peak in σ_1 (e). (f) The corresponding dc conductivity is large and decreases with temperature due to enhanced scattering and a reduction of the DOS.

tween the completely filled valence band (VB) and the unoccupied conduction band (CB)⁴. Charge carriers are immobile unless they are excited across the gap; dc transport is basically zero for $T \ll \Delta$. Upon increasing temperature, the bands become broader which effectively reduces the gap Δ . Thermal activation leads to well-known Arrhenius behaviour of dc transport [58]

$$\rho(T) = \sigma_{dc}^{-1}(T) = \rho_0 e^{\frac{\Delta}{2k_B T}} \quad (2.2.2)$$

which corresponds to hopping between localized states and is sketched in Fig. 2.2.2

⁴The valence band is the highest occupied band whereas the conduction band is the non-occupied band lowest in energy. For metals this distinction is meaningless since the band at E_F is partially occupied, fulfilling both criteria.

(c).

On the other hand, in a metal there is considerable spectral weight at E_F (panel d) and the related intraband excitations at zero energy cause a large dc conductivity

$$\sigma_{dc} = \frac{N\tau e^2}{m} = \frac{\epsilon_0 \omega_p^2}{\gamma} \quad (2.2.3)$$

which, according to the Drude model, depends on the particle density N , quasiparticle lifetime τ and mass m or, equivalently, the scattering rate $\gamma = \frac{1}{\tau}$ and plasma frequency $\omega_p = \sqrt{\frac{Ne^2}{\epsilon_0 m}}$. In presence of an electric field, charge carriers are accelerated until they are scattered by a defect, phonon or another particle. Since for an applied electric field \mathbf{E} such relaxation processes happen at specific time and length scales, we can define the drift velocity

$$\mathbf{v}_d = Ne \mathbf{j} = \frac{e\tau \mathbf{E}}{m} = \mu \mathbf{E} \quad (2.2.4)$$

where $\mu = \frac{e\tau}{m}$ is the charge carrier mobility. The reduction of $\sigma_{dc}(T)$ upon increasing temperature in a metal coincides with a reduction of the low-frequency conductivity due to broadening of the zero frequency contribution, as depicted in Fig. 2.2.2 (e).

For an insulator (panel b), an opposite tendency is expected since the inter-band transition centered at finite frequency is also subject to broadening upon increasing temperature. The reduction of the peak intensity goes hand in hand with an enhancement of the band tails. Considering the Drude expression of σ_{dc} in Equ. 2.2.3, the thermal enhancement of charge transport in an insulator stems mainly from the increasing in-gap density of states. Thus, electric conduction in insulators is governed by the particle density N accessible by thermal energy $k_B T$, whereas in typical metals the temperature dependence stems predominantly from the changes in scattering rate $\gamma(T)$ rather than the density of states. In the low-frequency limit, $\omega \ll \gamma \leq W_0/\hbar$, $\sigma_1(\omega)$ usually resembles the same temperature dependence as the dc conductivity.

2.2.2 Drude-Sommerfeld Model

Let us now have a closer look at the frequency dependence of the optical conductivity in the context of the Drude-Sommerfeld model. The central assumption is that the

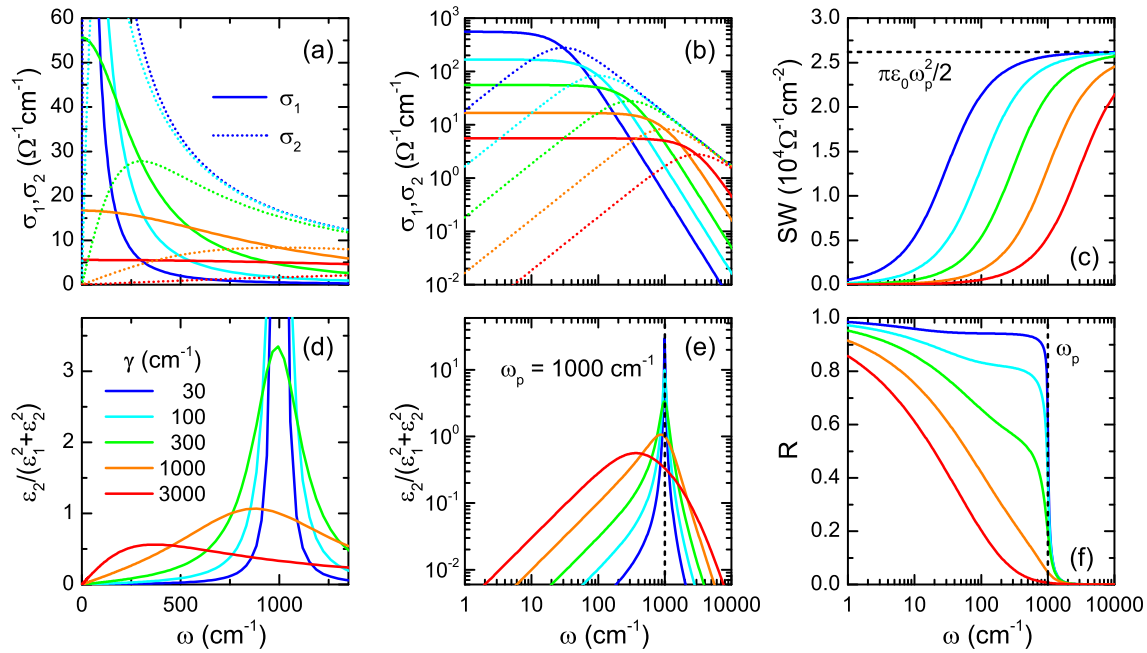


Figure 2.2.3: Frequency-dependent quantities of the Drude-Sommerfeld model calculated according to Equ. 2.2.5 for fixed plasma frequency $\omega_p = 1000 \text{ cm}^{-1}$ and varying scattering rate γ as a measure of temperature. (a,b) Linear and logarithmic plots of the real and imaginary parts of the optical conductivity. While σ_1 approaches σ_{dc} towards $\omega = 0$, σ_2 peaks at $\omega = \gamma$. (c) In the high-frequency limit well above γ , the integrated spectral weight $SW(\omega)$ saturates at a value proportional to ω_p^2 , which is related to N/m . At low frequencies, however, the SW is suppressed with γ (temperature). Note, here we integrated over $\frac{1}{\lambda}$ rather than angular frequency $\omega = \frac{2\pi c}{\lambda}$, so the unit $\Omega^{-1} \text{cm}^{-2}$ is smaller by a factor $2\pi c$ compared to Equ. 2.2.6 which yields $\Omega^{-1} \text{cm}^{-1} \text{s}^{-1}$. (d,e) The dielectric loss function peaks at ω_p and the width (FWHM) equals γ . In the overdamped case, $\gamma \geq \omega_p$, the maximum shifts towards lower frequencies. (f) The optical reflectivity R shows a pronounced plasma edge at ω_p that is washed out with enhanced scattering.

system relaxes to equilibrium within an average relaxation time τ , yielding

$$\hat{\sigma}(\omega) = \sigma_1(\omega) + i\sigma_2(\omega) = \frac{\sigma_{dc}}{1 + i\omega\tau} = \frac{\sigma_{dc}}{1 + \omega^2\tau^2} - i \frac{\omega\tau\sigma_{dc}}{1 + \omega^2\tau^2}, \quad (2.2.5)$$

which is illustrated on linear and logarithmic scales in Fig. 2.2.3 (a) and (b). The real part $\sigma_1(\omega)$ approaches the dc conductivity on low frequencies and shows a marked drop at the scattering rate, i.e. for $\omega = \gamma = \frac{1}{\tau}$. Upon increasing the temperature, scattering events become more frequent due to thermal fluctuations and phonons, increasing γ and reducing σ_{dc} . Importantly, the thermally enhanced scattering rate causes a broadening of the Drude peak, but does not affect the area below $\sigma_1(\omega)$. Thus, the spectral weight SW (c) integrated over the entire bandwidth is conserved,

yielding the optical sum rule

$$SW(\omega) = \int_0^\omega \sigma_1(\omega') d\omega' \quad \xrightarrow{\gamma \leq W_0/h \ll \omega \approx \infty} \quad \frac{\pi}{2} \epsilon_0 \omega_p^2, \quad (2.2.6)$$

where we take into account transitions within the conduction band only, i.e. we do not consider inter-band excitations.⁵ Focusing on low frequencies, the SW is reduced in a similar way as σ_1 when scattering increases with temperature (Fig. 2.2.3 c); well above γ it approaches a constant value proportional to ω_p^2 . In a classical analogue, the plasma frequency ω_p corresponds to a collective oscillation of the negatively charged electrons with respect to the positively charged nuclei. Thus, it reflects the total number of charge carriers N which is preserved upon intra-band excitations. Strictly speaking, the plasma edge observed in experiment corresponds to the screened plasma frequency $\omega_{p,screen}^2 = \frac{Ne^2}{\epsilon_\infty \epsilon_0 m}$, which is renormalized by the high-frequency dielectric constant ϵ_∞ .

Another useful quantity to evaluate the frequency-dependent optical response is the dielectric loss function $\hat{\epsilon}^{-1}$, in particular the negative of its imaginary part

$$-Im \left\{ \frac{1}{\hat{\epsilon}} \right\} = \frac{\epsilon_2}{\epsilon_1^2 + \epsilon_2^2} \quad \xrightarrow{\text{Drude model}} \quad \frac{\omega_p^2 \omega \gamma}{(\omega^2 - \omega_p^2)^2 + \omega^2 \gamma^2} \quad (2.2.7)$$

which is plotted on linear and logarithmic scales in Fig. 2.2.3 (d) and (e). For $\gamma < \omega_p$, it peaks at ω_p allowing for determination of N/m ; the full-width at half-maximum equals the scattering rate γ . In case of overdamping ($\gamma \geq \omega_p$), which corresponds to incoherent transport, the maximum appears at lower frequencies. Thus, one can define the coherence parameter

$$\kappa = \frac{\omega_p}{2\gamma} \quad (2.2.8)$$

as a measure of a well-defined Drude peak, the hallmark of coherent transport. A critical value κ^* , which is close to unity, corresponds to the crossover from incoherent conduction processes to a *good* metal. This is particularly useful in the course of a metal-insulator transition when a zero-frequency contribution evolves gradually as the gap closes.

⁵Note that Equ. 2.2.6 is valid for any kind of excitations in the solid where charge is involved, including inter-band transitions and vibrational modes. For phonons, the charge density Ne and mass m differ significantly from purely electronic excitations since the nuclei contribute to charge motion as well. Due to the large mass M involved, the intensity $\sigma_1 \propto \omega_p^2 = \frac{Ne^2}{\epsilon_0 M}$ is typically much smaller for such processes.

2.2.3 Lorentz and Fano models

While the Drude-Sommerfeld model describes the electrodynamic response of free electrons in metals, it can be generalized by introducing a restoring force that binds the electrons to the nuclei. The result is the Lorentz model which describes damped harmonic oscillations

$$\hat{\sigma}(\omega) = \frac{Ne^2}{m\tau} \left(\frac{\omega^2}{(\omega_0^2 - \omega^2)^2 + \frac{\omega^2}{\tau^2}} + i\omega\tau \frac{\omega_0^2 - \omega^2}{(\omega_0^2 - \omega^2)^2 + \frac{\omega^2}{\tau^2}} \right) \quad (2.2.9)$$

with the resonance frequency ω_0 . All related quantities and sum rules are defined similarly as above. The main difference is the following: while in the Drude model the optical conductivity is centered at $\omega = 0$, for the Lorentz oscillator $\sigma_1(\omega)$ peaks at ω_0 and vanishes quadratically towards low and high frequencies. The scattering rate γ is the full-width at half-maximum and the plasma frequency can be determined in a similar way as shown in Fig. 2.2.3. We can apply the Lorentz model to fit phonons and molecular vibrations as well as other kinds of charge excitations, such as inter-band transitions. Note, however, the electronic states in a solid are not confined to discrete energy levels, but extend over a finite bandwidth; the structure of the joint density of states leads to deviations from Lorentzian shape.

Apart from that, the interaction of an energy level, like a phonon, with the electronic background, e.g. a broadband electronic excitation in the same frequency range, may result in an asymmetric line shape. Such behaviour can be described with the Fano model [59] by introducing a dimensionless coupling parameter q

$$\hat{\sigma}(\omega) = \frac{Ne^2}{m} \left(\omega \frac{\frac{\omega}{\tau}(q^2 - 1) + 2q(\omega^2 - \omega_0^2)}{(\omega_0^2 - \omega^2)^2 + \frac{\omega^2}{\tau^2}} + i\omega \frac{(q^2 - 1)(\omega_0^2 - \omega^2) - 2\frac{\omega}{\tau}}{(\omega_0^2 - \omega^2)^2 + \frac{\omega^2}{\tau^2}} \right). \quad (2.2.10)$$

The extreme case is an antiresonance centered at ω_0 for $q = 0$ (strong coupling) whereas a Lorentzian line shape is restored for $q \rightarrow \pm\infty$ (no coupling). In the compounds investigated in this thesis, typically negative values of q are found corresponding to an intensity redistribution from the high-frequency to the low-frequency wing of the mode; in other materials also $q > 0$ was observed, see e.g. Ref. [60]. Importantly, such an asymmetry involves that the resonance frequency deviates from the maximum of $\sigma_1(\omega)$ making a standard Lorentzian fit inaccurate.

2.2.4 Matthiessen Rule and Ioffe-Regel-Mott Limit

Although distinct scattering processes may dominate charge transport in specific temperature ranges⁶, there is always more than one source of scattering. Under the assumption that these contributions are independent of each other, Matthiessen's rule states that they can be simply added up yielding the total scattering rate

$$\gamma_{total} = \gamma_{imp} + \gamma_{el-el} + \gamma_{el-ph} + \dots \quad (2.2.11)$$

analogous to an electric circuit with several resistors connected in series. Due to the initial T^5 dependence of electron-phonon scattering (γ_{el-ph}) that stems from a rapid expansion of the scattering phase space with temperature⁷, the resistance is dominated by impurities (γ_{imp}) and electron-electron (γ_{el-el}) interactions at low temperatures. At high temperatures, the phonon contribution becomes dominant and increases linearly with T since it only depends on the number of excited phonons [57]. Except for impurity scattering, all contributions mentioned above would, in principle, continue increasing with temperature. An upper limit, however, is approached when a particle is scattered once per lattice site. This is the Ioffe-Regel-Mott (IRM) limit⁸ which reads

$$\rho_{IRM} = \frac{hd}{e^2} \quad (2.2.12)$$

where d is the inter-layer separation of a two-dimensional electron system [32]. Indeed, such resistivity saturation at high temperatures is observed in conventional metals, such as Nb_3Sn or Nb_3Sb . On the other hand, the IRM-criterion is violated in many materials subject to strong electronic interactions, for instance heavy fermion compounds [61–63], high-temperature superconductors (see e.g. the review by Gunnarsson *et al.* [64]) or many other unconventional systems including organic conductors (e.g. θ -(BEDT-TTF)₂I₃ [65]). While quasiparticles are well-defined below ρ_{IRM} , the Fermi liquid concept breaks down for a larger scattering rate and the typical $\rho \propto T^2$ behaviour is lost; materials in which the resistivity continues increasing at higher temperatures are commonly referred to as *bad metals* [66]. In strongly interacting systems a linear temperature dependence is commonly observed up to high temperatures and well above ρ_{IRM} , which was recently ascribed to universal

⁶In principle, scattering is also present at finite energy, so these considerations extend to the frequency-dependent optical response.

⁷This is the well-known Bloch-Grüneisen form where the T^5 behaviour appears far below the Debye temperature Θ_D and linear temperature dependence is found above.

⁸Among the commonly used terms are Mott-Ioffe-Regel limit or just Ioffe-Regel limit.

diffusion processes related via the uncertainty principle, i.e. $\gamma \approx k_B T / \hbar$ [67, 68]. In quantum critical systems, a linear temperature dependence of $\gamma(T)$ is observed down to low temperatures, which is under current discussion in the context of fluid dynamics of viscous electron liquids.

2.3 Correlated Electron Systems

Although the description of electrons as free fermionic particles is very appealing in a pedagogical sense and it facilitates understanding the basic principles of thermodynamics, the concept is usually too simplified for studying condensed matter. In a solid, electrons are not free particles any more as they interact with each other and the lattice. Still, they can be treated as renormalized quasiparticles in the framework of the Landau Fermi liquid theory [56, 57, 69]. In addition, moderate interactions are the essence of conventional superconductivity which is perfectly understood by the BCS theory. For strong correlations, however, these concepts break down giving rise to exotic phenomena, such as the Mott metal-insulator transition (MIT) and unconventional superconductivity [2, 44].

2.3.1 Fermi Liquid Theory and Extended Drude Formalism

The Drude model described above considers a gas of non-interacting charged particles with a specific mass⁹ subject to scattering events on the time scale τ . In a solid, however, electrons *do* interact with each other making this simple approach obsolete. The powerful framework of Landau's Fermi liquid theory resolved this issue by introducing the quasiparticle (QP) concept [56, 57, 69]. There is one-to-one correspondence between an interacting electron and a non-interacting quasiparticle that behaves like a free particle with modified thermodynamic properties: the electronic heat capacity, compressibility and spin susceptibility are renormalized by the Fermi liquid parameters F_i^j . Most importantly, the effective mass m^* of the interacting charge carriers is enhanced with respect to the band mass m_{band} [69], which is expressed as a reduction of the plasma frequency

$$\omega_p^2 = \frac{Ne^2}{\epsilon_0 m^*} = \left(\frac{m_{band}}{m^*} \right) \omega_{p,0}^2 \quad (2.3.1)$$

⁹In condensed matter physics, this is essentially the band mass m_{band} that arises due to interaction with the periodic potential of the lattice.

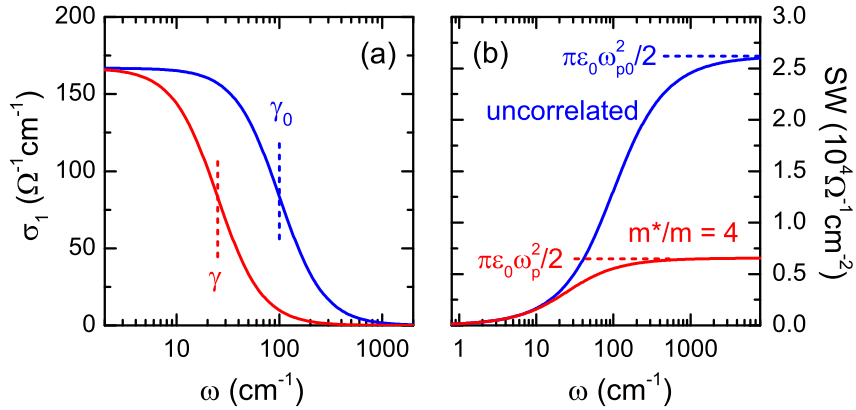


Figure 2.3.1: In presence of electronic correlations both the scattering rate and plasma frequency are renormalized by the effective mass. (a) While the dc conductivity remains unchanged, the roll-off of the Drude conductivity is shifted towards lower frequency due to the reduced scattering rate. (b) The overall spectral weight of the Drude response of correlated electrons is reduced and levels off at the renormalized plasma frequency.

and, consequently, the spectral weight of the Drude response is reduced. In this regard, coupling to the other conduction electrons, or local moments as in the case of Kondo systems, slows down the motion of a single charge, equivalent to a QP with larger dynamic mass. In such heavy fermion materials the mass enhancement can be as much as $\frac{m^*}{m_{band}} \approx 10^3$ [54].

Slower quasiparticle motion implies larger time scales between scattering events, hence also the scattering rate is renormalized, i.e. reduced, by the effective mass ($\gamma = \left(\frac{m_{band}}{m^*}\right) \gamma_0$). While the two effects compensate each other in the dc conductivity, since $\frac{\omega_p^2}{\gamma} = \frac{\omega_{p,0}^2}{\gamma_0}$, the frequency-dependence of the optical conductivity acquires the form

$$\hat{\sigma}(\omega) = \frac{\epsilon_0 \omega_p^2}{\gamma} \frac{1}{1 + i\omega/\gamma} = \frac{\epsilon_0 \omega_{p,0}^2}{\gamma_0} \frac{1}{1 + i\omega m^*/(m_{band} \gamma_0)}. \quad (2.3.2)$$

This immediately explains the low-frequency spectral weight reduction since the roll-off of the renormalized Drude response shifts towards lower energy as the scattering rate decreases, which is illustrated in Fig. 2.3.1. Note, the total spectral weight of a fixed number of charge carriers, including both the *coherent* quasiparticles discussed here as well as incoherent electron-hole excitations, is always conserved. Therefore, the reduction of SW at low frequencies is accompanied by an increase at higher energies. In the course of the Mott MIT, for instance, the SW is shifted from low to high energies as correlations become more pronounced [45].

Let us now consider the temperature and frequency dependence of scattering pro-

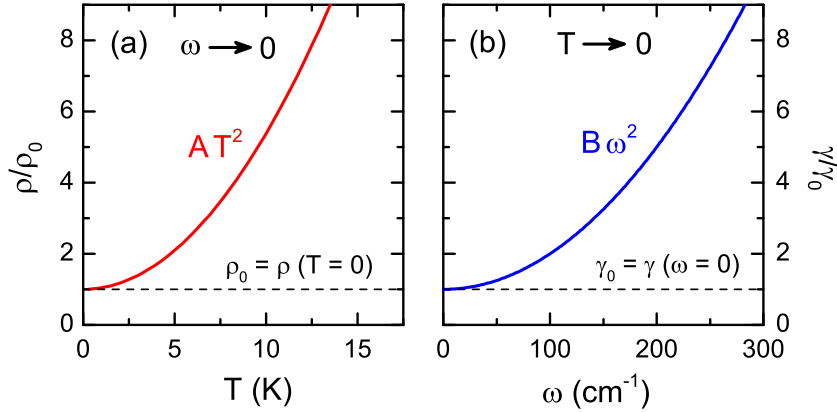


Figure 2.3.2: (a) The dc resistivity shows quadratic temperature dependence if scattering between quasiparticles is the dominant contribution. $\rho(T) \propto T^2$ is the most common way to identify Fermi liquid behaviour. (b) The frequency-dependent scattering rate determined from optical spectroscopy shows ω^2 dependence in the Fermi liquid state. The zero-frequency offset $\gamma_0(T)$ shows similar temperature dependence as the dc resistivity. According to Fermi liquid theory, the prefactors of the quadratic function should be linearly related via $A = 4\pi^2 B$ (cf. Equ. 2.3.6).

cesses between the quasiparticles. The QP life time τ strongly increases in the vicinity of the Fermi surface and the scattering phase space increases quadratically with energy [57]

$$\gamma = \frac{1}{\tau} \propto (E - E_F)^2. \quad (2.3.3)$$

Therefore, an increase of thermal energy $k_B T$ causes a quadratic enhancement of the dc resistivity via the scattering rate. In transport experiments, $\rho(T) \propto T^2$ behaviour is interpreted as a fingerprint of the Fermi liquid state, as illustrated in Fig.2.3.2 (a). One can define a characteristic temperature T_{FL} below which the QP concept is applicable; above T_{FL} the breakdown of the Fermi liquid is indicated by a deviation from the T^2 dependence of the resistivity, which usually crosses over to a more linear temperature behaviour. In experiments, T_{FL} is typically lower than 100 K since phononic effects become dominant at higher temperatures. In a similar way, energy can be expressed in units of frequency ($E = \hbar\omega$) implying $\gamma(\omega) \propto \omega^2$ (Fig. 2.3.2 b) up to a characteristic frequency ω_{FL} [28, 31] above which incoherent scattering between, for instance, the Mott-Hubbard bands sets in.

The frequency-dependent scattering rate and effective mass are extracted from the

optical conductivity

$$\gamma(\omega) = \epsilon_0 \omega_{p,0}^2 \text{Re} \left\{ \frac{1}{\hat{\sigma}} \right\} \quad (2.3.4)$$

$$\frac{m^*}{m_{band}}(\omega) = \frac{\epsilon_0 \omega_{p,0}^2}{\omega} \text{Im} \left\{ -\frac{1}{\hat{\sigma}} \right\}, \quad (2.3.5)$$

where $\text{Re}\{\hat{\sigma}^{-1}\}$ can be considered as the frequency-dependent resistivity related to $\gamma(\omega)$ in a similar way as the dc resistivity to $\frac{1}{\tau}$.

Combining the influence of temperature and frequency, one can write a general formula of the scattering rate [29, 70]

$$\gamma(T, \omega) = \gamma_0 + C [A(k_B T)^2 + B(\hbar\omega)^2], \quad (2.3.6)$$

where A , B and C are constants independent of temperature and frequency; γ_0 stems from residual scattering processes at $T = 0$ and $\omega = 0$ due to impurities. For a genuine Fermi liquid the prefactors should be related via $A/B = (2\pi)^2$, which has been unambiguously demonstrated only for Sr_2RuO_4 so far [71]. Values deviating from this were reported for other compounds [29] (and references therein).

2.3.2 The Mott Metal-Insulator Transition

Although the classification of metals and insulators according to the band structure (see Section 2.2.1) is appropriate in most cases, partially-filled bands do not automatically imply metallic properties. Let us consider now what happens upon adding free carriers (holes or electrons) to completely occupied or unoccupied bands, which is commonly called doping. At low particle density N the charges are far apart from each other and feel the long-range Coulomb repulsion

$$V(r) \propto r^{-1}, \quad (2.3.7)$$

which decays with the inter-particle distance r . Upon increasing N , at some point screening becomes relevant which causes the electrostatic potential to decay exponentially with r . As a result, the charge carriers become spatially confined which, according to the uncertainty principle, enhances the kinetic energy. At some critical density, referred to as Mott's criterion, metallic transport sets in

$$N^{-1/3} < C a_0^*, \quad (2.3.8)$$

where a_0^* denotes the effective Bohr radius and C is a constant around $2 - 4$ [56, 57]. In this regard, metallic properties and even unconventional superconductivity [72] emerge as soon as the wave functions of the charge carriers start overlapping.

Charge carrier doping turned out to be particularly successful in turning semiconductors metallic and, even more interesting, in introducing high-temperature superconductivity in the cuprates [46]. In this thesis, however, we will focus on another manifestation of the Mott metal-insulator transition where not the charge density N is tuned, but the electronic bandwidth W proportional to the transfer integral t . Going back to textbook examples and lectures, e.g. the simple case of the hydrogen atom, we find that electronic wavefunctions decrease exponentially with distance

$$t(r) \propto e^{-r}. \quad (2.3.9)$$

In particular, a reduction of the lattice constant, for instance by physical or chemical pressure¹⁰, increases the wave function overlap and enhances screening. Thus, the effective Bohr radius on the right side of Equ. 2.3.8 is modified rather than N . Note the different decay rate of t as compared to Coulomb repulsion implying that the bandwidth increases more strongly as the lattice contracts upon pressure¹¹.

Fig. 2.3.3 gives an overview of the bandwidth-tuned Mott transition. When correlations are small, electrons are delocalized over many units cells forming a coherent Fermi liquid state. As Coulomb repulsion between the charge carriers becomes more important, for instance due to reduction of the bandwidth W with respect to U (on-site Coulomb repulsion) or V (inter-site Coulomb repulsion), the range of motion is successively reduced until each particle is bound to a lattice site. Therefore, the Mott transition can be considered as a competition of the wave- and particle-like properties of an electron. While in a half-filled system with one electron (hole) per site the on-site Coulomb repulsion has to be overcome to create a double occupancy, the nearest-neighbour (inter-site) repulsion becomes important at quarter-filling. The first case is the well-known Mott insulator whereas the second scenario corresponds to electronic charge order¹².

¹⁰While physical pressure and strain correspond to application of an external force to the material, either compressive or tensile, chemical pressure denotes the exchange of lattice components (atoms, molecules) by larger or smaller units, which also changes the distance between the charge carriers.

¹¹This argument is specifically relevant for inter-site Coulomb repulsion V since the on-site term U is assumed to depend only on the local electronic structure of the lattice sites rather than the distance between them.

¹²Charge order resulting from strong inter-site Coulomb repulsion is not restricted to nearest-neighbour sites, but can, in principle, occur at any commensurate band filling $n = \frac{k}{l}$, where k and l are integers. $n = 0$ for a completely unoccupied band while $n = 2$ for a completely filled band.

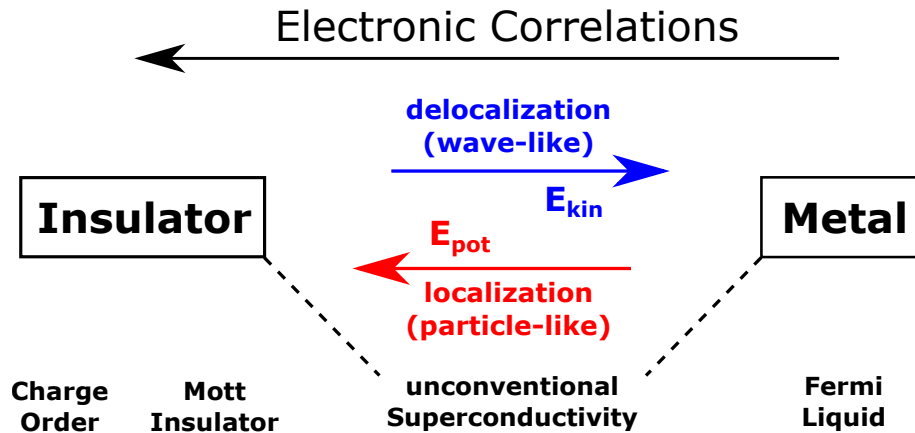


Figure 2.3.3: In the course of the bandwidth-tuned Mott transition itinerant charge carriers slow down until they are finally localized. While electrons exhibit wave-like properties when delocalized in a metal, they are bound to the lattice sites in the Mott state and, thus, behave more like particles. Electronic correlations can be quantified by the ratios U/W and V/W , where U and V are the on- and inter-site Coulomb repulsion, respectively; W is the bandwidth. The former is the dominant term in a Mott insulator originating from a half-filled band whereas the latter becomes important for charge ordering at quarter-filling; both are considered as the pairing glue of unconventional superconductivity.

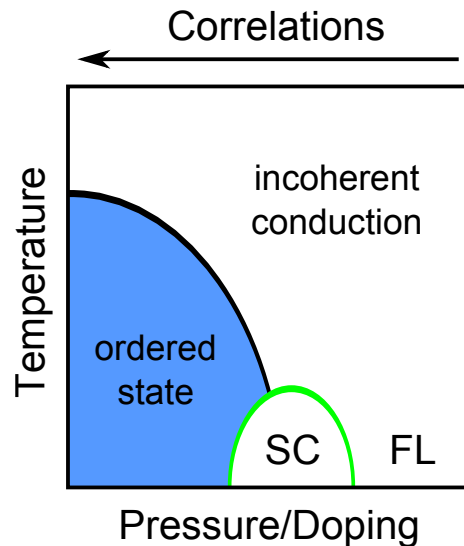


Figure 2.3.4: Many correlated electron systems exhibit a very similar phase diagram. For strong correlations, i.e. large U/W or V/W , an ordered state is stabilized at low temperatures. When the bandwidth is enhanced, either by physical or chemical pressure, or by doping, the ordered phase melts. As the transition temperature vanishes, strong quantum fluctuations of the magnetic or charge degrees of freedom lead to unconventional superconductivity.

Various strongly correlated materials follow the phase diagram depicted in Fig. 2.3.4. An ordered state (charge order, magnetic order, etc.) with insulating transport properties dominates for strong correlations. Upon increasing the bandwidth, the insulating phase is continuously suppressed until metallic behaviour is recovered. Strong quantum fluctuations are predicted to appear at the verge between the ordered state and the metal, providing the pairing glue for unconventional superconductivity. In the cuprates, spin fluctuations are believed to mediate high-temperature superconductivity [46]. Just very recently, attractive coupling between charges arising from their mutual, purely repulsive Coulomb interaction could be demonstrated experimentally using carbon nanotubes [73]. Such an excitonic mechanism is naturally related with charge fluctuations arising from the competition of W and U (V) at the Mott (charge order) transition.

2.3.3 Extended Hubbard Model

In many cases, the effect of electronic interactions on the physical properties can be adequately described by the extended Hubbard model

$$H = -t \sum_{\langle i,j \rangle, \sigma} (c_{i\sigma}^\dagger c_{j\sigma} + H.c.) + U \sum_i n_{i\uparrow} n_{i\downarrow} + V \sum_{\langle i,j \rangle} n_i n_j, \quad (2.3.10)$$

where $c_{i\sigma}^\dagger$ and $c_{i\sigma}$ are the creation and annihilation operators of a particle at site i with spin σ ; $n_i = c_{i\sigma}^\dagger c_{i\sigma}$ is the number operator. The first term corresponds to the kinetic energy whereas the second and third parts represent the electrostatic contributions. The transfer integral t , proportional to the bandwidth W_0 , is a measure of the nearest-neighbour hopping probability. While the second term quantifies the on-site Coulomb repulsion U , which arises upon creating a double occupancy obeying the Pauli principle, the third term corresponds to the inter-site Coulomb repulsion V and counts the number of charges on nearest-neighbour sites. The implications of Equ. 2.3.10 on the total energy of a two-dimensional system with a partially filled band are illustrated in Fig. 2.3.5. There is only one electron at site (a) and all of its nearest neighbours are unoccupied, so the Coulomb energy is zero and hopping is possible in each direction. On the other hand, the movement of the charge at position (b) is restricted to the downwards direction (blue arrow) since the upper, right and left nearest-neighbour sites are fully occupied by two electrons with antiparallel spins each, which is the maximum according to the Pauli principle.

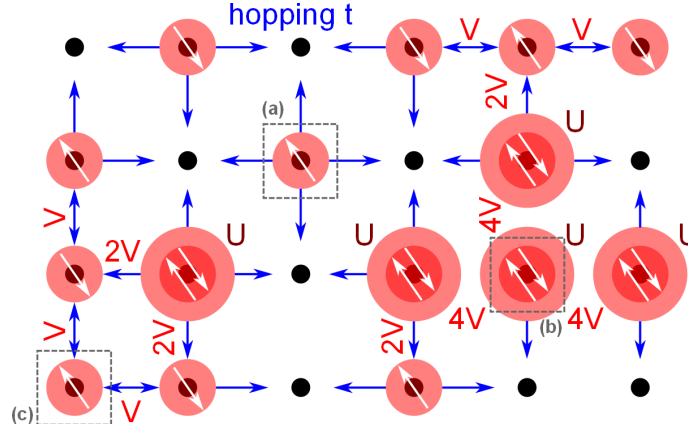


Figure 2.3.5: Visualization of the extended Hubbard model on a square lattice. The transfer integral t is a measure of the hopping probability between neighbouring sites. As indicated by the blue arrows, a charge can only move from an occupied site to a singly-occupied or empty site; the Pauli exclusion principle allows a maximum of two electrons with antiparallel spins (white arrows) per site. It is evident that the charge on site (b) is restricted to downward movement only. The on- and off-site Coulomb energies are indicated in dark and light red, respectively. For large U/t , the electron on site (c) will not be able to hop up or right. When V becomes dominant, even the movement of the charge at (a) to its neighbouring empty sites will be suppressed. These correlation effects become particularly important at commensurate filling, such as $n = 1$ (Mott insulator) or $n = 0.5$ (charge order).

The on-site Coulomb energy amounts to U , whereas the inter-site contribution V arising from the neighbouring charges is $4V$ for each pair of doubly occupied sites. Finally, the electron in the lower left corner of the displayed part of the lattice (c) has two singly occupied nearest neighbours yielding a potential energy V per pair. If it moves to one of its neighbouring sites, the on-site Coulomb energy is increased by U and also the inter-site repulsion is modified. Note, the spins of nearest neighbours tend to align antiparallel to allow for possible hopping processes satisfying the Pauli principle, which will be discussed in section 2.3.4.

Overall, Fig. 2.3.5 illustrates how charge motion is affected by the band filling and the electrostatic repulsion. If there are too many particles, no current can flow due to the Pauli principle and, similarly, electrons remain localized if the kinetic energy is not large enough to overcome the Coulomb repulsion. The same arguments apply for holes.

The effects of Coulomb repulsion are maximized at commensurate band filling $n = \frac{k}{l}$, as depicted in Fig. 2.3.6 where we generally assume $V < U$. In the half-filled case (left), metallic behaviour is expected in the absence of correlations ($U = V = 0$). When the on-site Coulomb repulsion U exceeds the bandwidth and becomes the

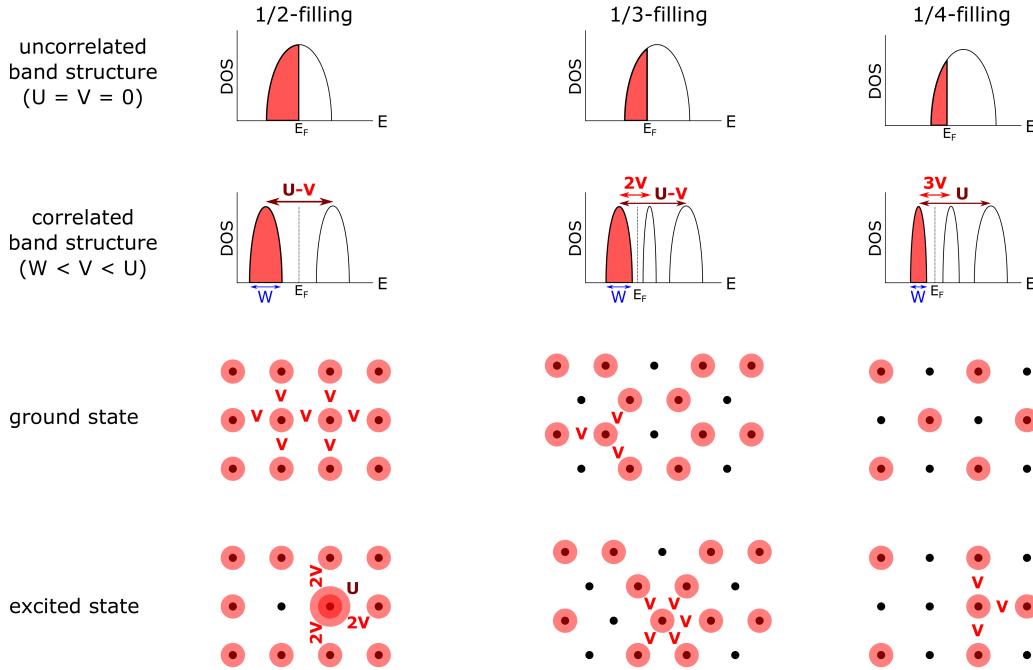


Figure 2.3.6: Elementary excitations at commensurate band filling. Sufficiently strong on-site Coulomb repulsion with respect to the bandwidth, i.e. large U/W , drives a half-filled system into the Mott insulating state. In the ground state, each site is singly occupied minimizing the potential energy. Excitation of an electron across the Mott-Hubbard gap, i.e. moving it to its neighbouring site and creating a double occupancy and a hole, is associated with a potential energy cost ($U - V$).

dominant energy scale, charge motion is suppressed yielding one electron localized at each site. As a result, the density of states splits up into the occupied lower (LHB) and unoccupied upper (UHB) Hubbard bands separated by the potential energy ($U - V$) that has to be paid upon creating a charge excitation. Note, the bandwidth of the Hubbard bands W is generally smaller than the bare bandwidth W_0 , with $W = W_0/\sqrt{2}$ in the limit of strong correlations [74]. In more dilute systems, the inter-site Coulomb repulsion V triggers charge ordering with different patterns depending on the specific lattice geometry and band filling. For $n = 1/3$ on a two-dimensional triangular lattice, for instance, the electrons arrange in a honeycomb-like structure since it minimizes V (middle panels of Fig. 2.3.6). There are two kinds of elementary excitations: a potential energy of $2V$ is required to move a charge to an unoccupied site and a barrier of $(U - V)$ has to be overcome to create a double-occupancy. Similarly, the excitation energies amount to $3V$ and U for a quarter-filled square lattice where the charges are arranged in a checkerboard-like pattern in the ground state, involving zero Coulomb energy according to Equ.2.3.10.

2.3.4 Mott Insulators and Quantum Spin Liquids

In the Mott insulating state charge motion is suppressed by U and the electrons are localized, hence only the first two terms of Equ. 2.3.10 with $U' = U - V$ are sufficient to describe the relevant physics¹³. Still, quantum mechanics allows for tunneling processes between neighbouring sites even for $U \gg W$. Since also this *virtual* hopping has to satisfy the Pauli principle, the spins tend to align antiferromagnetically to enable a double occupancy [2]; in contrast to a ferromagnet, where all spins are parallel, nearest neighbours are aligned antiparallel to each other [56, 57], as sketched in Fig. 2.3.7 (a) and (b), respectively. The exchange interaction arising from these

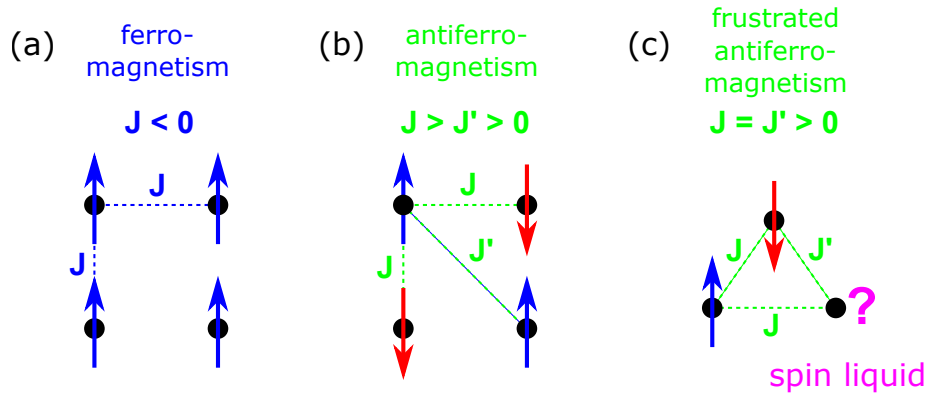


Figure 2.3.7: (a) Parallel alignment of the spins is favourable for $J < 0$ leading to ferromagnetic order. (b) Antiferromagnetic interaction ($J > 0$) on a square lattice causes long range magnetic order. Note that the diagonal term J' favours an opposite alignment of the lower right spin, but, as long as J is significantly larger, antiparallel alignment of nearest neighbours remains the most favourable configuration. (c) In a geometrically frustrated lattice, such as triangular (shown here), kagome or hyperkagome arrangements, not all antiferromagnetic bonds can be satisfied simultaneously. Even for large exchange interaction no magnetic order is realized for $J = J'$, which gives rise to a spin liquid state.

virtual hopping processes is proportional to

$$|J| \propto \frac{t^2}{U} = U \left(\frac{t}{U} \right)^2, \quad (2.3.11)$$

where t is the transfer integral [2]. Since the Mott insulating state implies that $U \gg W > t$,¹⁴ the energy scales of J are much smaller than U and antiferromagnetism appears at temperatures well below the Mott transition. The thermodynamic

¹³This is the original form of the *Hubbard model*; introducing inter-site terms V_i makes it *extended*.

¹⁴The bandwidth scales with the transfer integral t times the number of nearest neighbours n . In a d -dimensional square lattice one obtains the simple relation $W = 2nt$, where $n = 2d$, which yields $W = 8t$ in two dimensions. For a two-dimensional triangular lattice one obtains $W = 9t$.

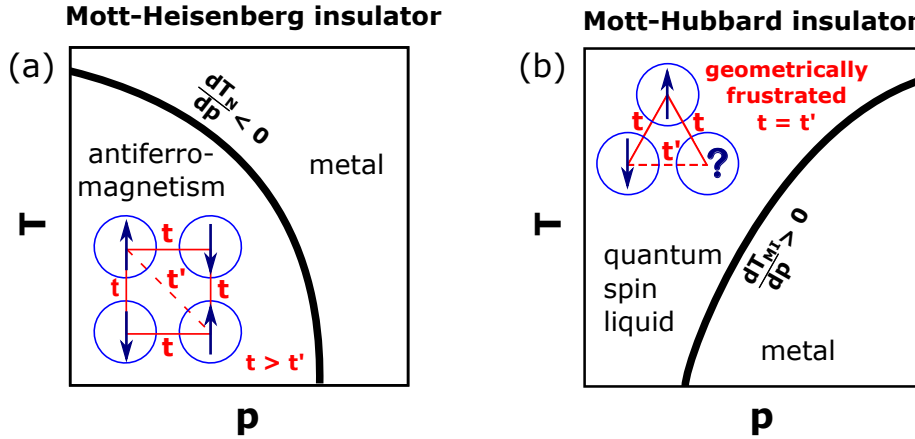


Figure 2.3.8: (a) According to the Clausius-Clapeyron relation, $\frac{dT}{dp} = \frac{dV}{dS}$, the boundary between the antiferromagnetic (small entropy) and metallic (large entropy) states in a Mott-Heisenberg insulator has a negative slope in the T - p phase diagram. (b) Due to strong spin fluctuations down to $T = 0$, the entropy of the quantum spin liquid is even larger than in the metal and the phase transition acquires a positive slope reminiscent of the Pomeranchuk effect in ${}^3\text{He}$ [10]. Therefore, suppression of magnetic order reveals the genuine Mott-Hubbard state with thermodynamic properties distinct from a Mott-Heisenberg insulator.

properties close to $T = 0$ are dominated by magnetic order and, hence, the entropy is strongly reduced compared to the metallic state. Since the volume decreases and entropy increases with pressure, the Clausius-Clapeyron equation $\frac{dT}{dp} = \frac{\Delta V}{\Delta S}$ [75] implies that the boundary between the antiferromagnetic state and the metal acquires a negative slope in the T - p phase diagram (Fig. 2.3.8 a).

In case of a triangular arrangement of the charges, illustrated in Fig. 2.3.7 (c), not all spins can be aligned antiparallel at once inhibiting long range magnetic order. Over the past few years numerous frustrated systems have been found where antiferromagnetism is suppressed down to the lowest measured temperature [15, 76–81], or with T_N significantly smaller than the exchange interaction [82]. Therefore, such a geometrically frustrated lattice gives rise to a magnetically disordered state with large entropy down to low temperatures due to the spin degrees of freedom. Theory describes this quantum spin liquid (QSL) state with the resonating valence bond formalism [83] that was also considered in the context of high-temperature superconductivity in the cuprates [84]. In particular, exotic spin excitations were predicted, such as gapless spinons forming a Fermi surface [18, 85–87].

In the T - p phase diagram, the large entropy of fluctuating spins even exceeds the entropy of the metallic state which causes a positive slope of the insulator-metal boundary. This reminds of the Pomeranchuk effect in ${}^3\text{He}$ where the solid becomes

liquid upon cooling [10]. While such behaviour is counterintuitive from our daily life experience when dealing with classical states of matter, different paradigms and interactions have to be considered in quantum systems. In the particular case of the bandwidth-tuned Mott transition, the charge solid (insulator) becomes liquid (metallic) upon cooling and with applied pressure.

The above arguments apply to low temperatures, where the competition of U (V) and W determines the ground state properties. Upon increasing the temperature, however, the dynamic and thermodynamic properties of the transition change significantly. The first-order nature of the MIT extends only up to the critical endpoint (T_{crit}, p_{crit}) , above which it is more a crossover. In the supercritical region, the boundary of the Mott state is identified as the quantum Widom line (QWL). This concept originates from the description of supercritical liquids and gases [6, 7], and it was shown to apply also for the bandwidth-tuned Mott MIT [5] as well as the pseudogap in hole-doped cuprates [8, 9]. As illustrated in Fig. 2.3.9, the QWL shows a characteristic back-bending and acquires a negative slope at high temperatures. The sketched density of states (DOS) indicates that the fully gapped Mott state is confined by the first-order transition at low temperatures and the QWL at high T . At even higher temperatures, T becomes the dominant energy scale which is characterized by incoherent conduction processes. It is interesting to note that the qualitative shape of the DOS does not change significantly upon tuning the correlations U/W . Apart from that, one should keep in mind that the relatively large dc conductivity stems from thermal activation, i.e. the temperature dependence of dc transport is still that of an insulator. Only at sufficiently low temperatures, and small enough correlations, first a bad metallic behaviour develops and then a coherent Fermi liquid response with a well-defined quasiparticle peak stabilizes.

As we see from the horizontal and vertical axes, all physical properties should be, in principle, determined by the parameters U , W and T . It will be shown with the experimental results on the Mott transition in quantum spin liquids that this consideration is certainly applicable for the quantum Widom line. Moreover, also the implications on the scaling properties on the metallic side will be discussed, in particular on the bad metallic, Fermi liquid and superconducting regimes.

2.3.5 Charge Order in 1/4-Filled Systems

In quarter-filled systems, sufficiently strong inter-site Coulomb repulsion V leads to long range charge order (CO) with a schematic phase diagram as shown in Fig. 2.3.10. When approaching the CO state, charge fluctuations appear and become more and

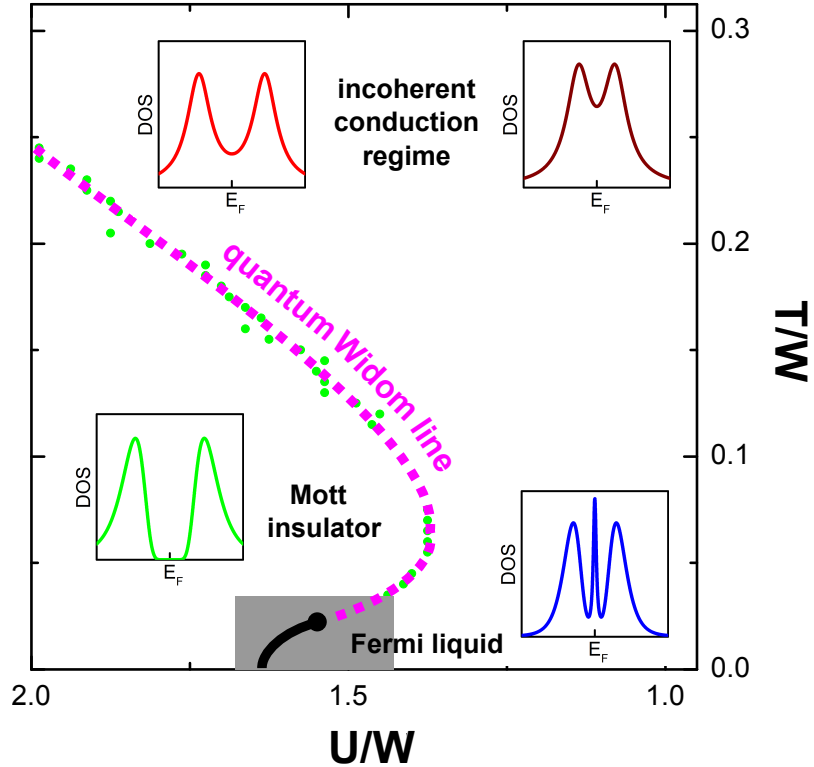


Figure 2.3.9: The generic phase diagram of the Mott insulator calculated by dynamical mean-field theoretical methods (green symbols [5]). The peculiar positive slope in the low-temperature regime (grey) is discussed in Fig. 2.3.8 (b). Above the critical endpoint, however, the well-defined first-order transition becomes a continuous crossover, referred to as the quantum Widom line (QWL). The slope becomes negative in the high-temperature regime, where thermal activation leads to incoherent conduction processes as T becomes the dominant energy scale. Hence, the QWL defines the boundary of the fully gapped Mott state, as indicated by the sketched density of states (DOS).

more pronounced in the vicinity of the phase transition. On the verge, when CO is suppressed towards $T = 0$, possibly forming a quantum critical point [88], these quantum fluctuations are believed to mediate unconventional superconductivity (SC) with d -wave symmetry of the Cooper pairs [33]. In analogy to SC that emerges in magnetically ordered systems, where a coexistence regime was identified for several systems [89, 90], it is a highly non-trivial question whether CO and SC coexist or compete. Thus, experimental verification of a possible phase coexistence, which is still lacking for quarter-filled CO systems, may reveal important information on the mutual relationship between charge order and superconductivity.

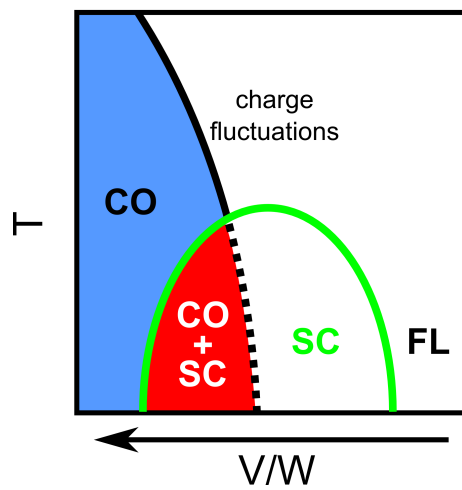


Figure 2.3.10: In strongly correlated compounds at quarter filling superconductivity (SC) emerges as charge order (CO) is suppressed upon reducing V/W . It is believed that charge fluctuations mediate the formation of Cooper pairs with d -wave symmetry [33]. A possible coexistence of the two phases, like it was observed for antiferromagnetic systems [89, 90], may shed light on their mutual relationship, in particular, whether they are competitive states or not. Charge fluctuations have not been established experimentally in the superconducting state so far.

3. Materials: Pairing and Frustration in quasi 2D $(\text{BEDT-TTF})_2X$

The effects of electronic correlations were investigated in various layered organic charge transfer salts with quasi two-dimensional electronic properties. The vast majority of experiments was performed on $(\text{BEDT-TTF})_2X$ compounds with different anions X . This chapter introduces this material class and illustrates the important structural and physical aspects, and how they can be accessed in experiment. Two main features are pointed out: on the one hand, the band shape in the optical conductivity provides access to crucial parameters like Coulomb repulsion and bandwidth while, on the other hand, narrow intra-molecular vibration modes are specifically useful as they are related to the molecular charge. Finally, previously published experimental results are presented in order to introduce the compounds under study and relate the material properties to the theoretical models presented in Chapter 2.

3.1 Molecular Conductors

Carbon-based molecular conductors are versatile materials that allow for synthesis of miscellaneous compounds with desired structural and electronic properties. Organic compounds have the general advantage of growing at comparably low-temperatures which enables low cost production at large scale, in principle. The reader may recognize that, apart from natural oil and gas as our main sources of energy, many devices of daily use are made from organics, such as smartphone displays consisting of organic light-emitting diodes (OLED). The focus of this thesis, however, is basic research and the understanding of complex, exotic states of matter rather than potential applications.

The materials under study are charge-transfer salts consisting of organic radicals, i.e. molecules with unpaired valence electrons, and anions with closed shells. In case of (BEDT-TTF)₂X, the monovalent anions X^- imply that the remaining positive charge is redistributed between the two organic molecules, which nominally yields BEDT-TTF^{+0.5}. As explained in section 2.2.1, the low-energy electronic and electrodynamic properties are determined by the unpaired electrons that imply partially filled bands. The anions, however, determine the specific arrangement of organic entities with respect to each other, in particular the distance between the sites which is the crucial parameter for the transfer integrals and the electrostatic potential (cf. section 2.3.2). Importantly, the large extension and separation of the molecules, as compared to atoms and inter-atomic distances, brings about rather small energy scales. While crystals built from single atoms as the lattice sites imply U , V and W in the range of several eV, the related energies are of order 10^{-1} eV here. Thus, the small energy scales allow to study significantly larger ranges in the generic T/W vs U/W phase diagram (Fig. 2.3.9); vice versa, smaller pressure¹ and temperature ranges are sufficient to cover the regime of interest. Moreover, these compounds represent the single-band (extended) Hubbard model in its purest form as the anion bands are far away from the Fermi level. In this regard, molecular conductors are ideal model systems to study the intrinsic interactions that drive exotic phenomena like competing orders, metal-insulator transitions, strongly correlated metals and unconventional superconductivity. In particular, the conclusions drawn here apply one-to-one to other Mott systems, potentially resolving the conundrum of high-temperature superconductivity in hole-doped cuprates.

Beyond that, novel states of matter can be accessed, such as the Fulde-Ferrel-Larkin-Ovchinnikov (FFLO) state established in several quasi 2D organic superconductors [92–98]. Furthermore, light- and field-induced superconductivity [99] as well as optically tunable, transient modulation of on-site Coulomb repulsion U [100] have been reported recently in layered molecular conductors.

Fig. 3.1.1 shows diverse structures of molecular conductors based on organic radicals. In (TMTTF)₂X compounds the donor molecules arrange in stacks separated by anions. The transfer integrals are highly anisotropic, with the largest overlap and electrical conductivity along the stacks, which leads to quasi one-dimensional electronic properties. Note that correlations are always present in 1D preventing the formation of a coherent quasiparticle peak in the spectral function. Peculiar

¹Typically a few kbar are enough to drive the systems from the insulating state towards superconducting and metallic behaviour. This allows to use He gas pressure cells in order to perform pressure sweeps and constant temperature as, for instance, in Refs. [14, 91].

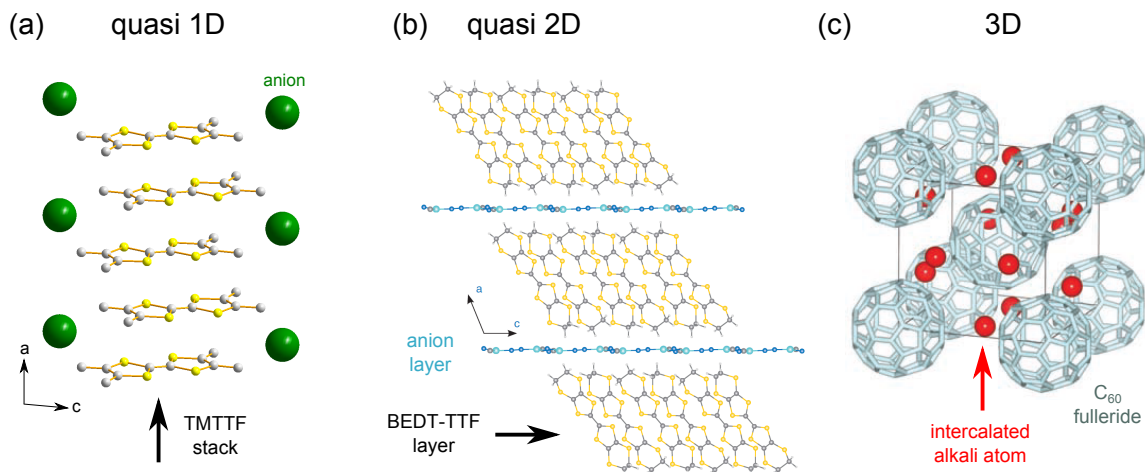


Figure 3.1.1: Depending on the crystal structure, the dimensionality of the electronic system varies between different organic charge-transfer salts. (a) Quasi one-dimensional TMTTF or TMTSF stacks are formed in the Bechgaard-Fabre salts. (b) $(\text{BEDT-TTF})_2X$ compounds consist of alternating layers of organic molecules and anions which yields quasi two-dimensional electronic properties. (c) Alkali fullerenes, such as K_3C_{60} , form three-dimensional structures. Note, here the organic molecules are electron acceptors rather than donors like the compounds in (a) and (b). Reproduced from [51, 101, 102].

phenomena such as Luttinger liquid behaviour and spin charge separation have been observed in experiment [103]. $(\text{BEDT-TTF})_2X$ consist of alternating layers of anions and organic molecules. Weak coupling between the conducting planes brings about quasi two-dimensional transport properties, providing a perfect playground for electrostatic and magnetic interactions (Heisenberg model etc.) in 2D. On the other hand, also three-dimensional arrangements can be realized, for example in alkali fullerenes [102, 104]. Although correlations are generally reduced at higher dimensions², a similar Mott MIT as in $\kappa\text{-(BEDT-TTF)}_2\text{Cu}[\text{N}(\text{CN})_2]\text{Cl}$ [105] could be observed recently in Cs_3C_{60} [106]. Moreover, possible light-induced superconductivity up to room temperature was concluded from transient pump-probe results upon exciting specific C_{60} phonon modes [107].

3.1.1 Quasi Two-Dimensional $(\text{BEDT-TTF})_2X$

Although considerable effort was devoted to the investigation of quasi one-dimensional $(\text{TMTTF})_2X$ compounds, which will be listed in the Appendix, the main focus of this thesis was directed towards layered $(\text{BEDT-TTF})_2X$ with quasi two-dimensional

²With dimensionality also the number of interacting sites increases and, hence, the bandwidth is enhanced; the Coulomb terms remain similar.

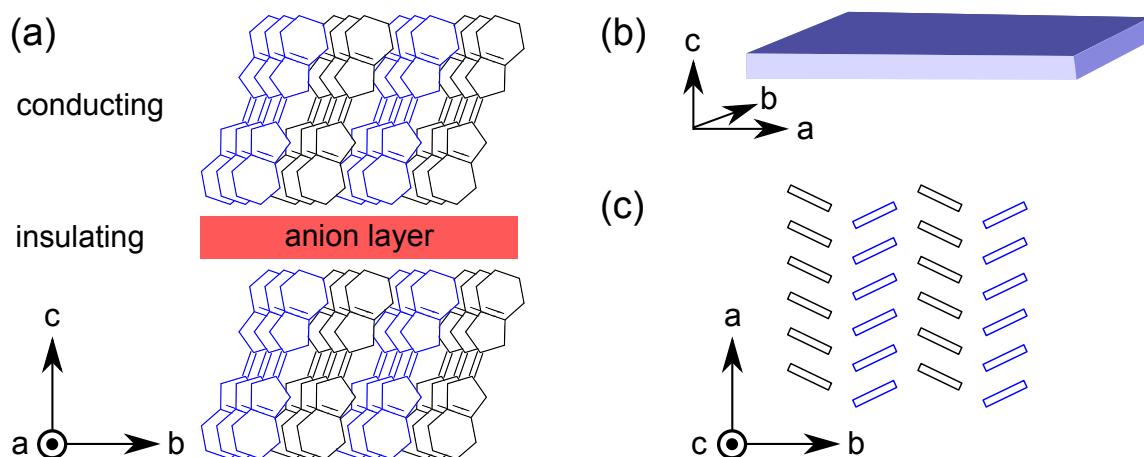


Figure 3.1.2: (a) The $(BEDT-TTF)_2X$ compounds investigated in this thesis consist of alternating layers of organic molecules and anions. For β' - $EtMe_3Sb[Pd(dmit)_2]_2$, the organic $Pd(dmit)_2$ entities accept the charges of the inter-layer $EtMe_3Sb$ cations. In both cases, the mobile charge carriers reside on the planes of organic molecules which implies quasi two-dimensional electronic properties. (b) Typical single crystals grow in plate-like shape where the out-of-plane axis (here c) is the smallest dimension. (c) Within the conducting layers the molecules are tilted with respect to each other. The distinct arrangement has large influence on the electronic properties.

electronic properties. The crystal structure and typical sample geometry are depicted in Fig. 3.1.2. Charge transport happens predominantly within the planes of organic molecules while the anion layers can be, in a crude approximation, considered as spacers that separate the conducting sheets³. However, the anions modify not only the inter-layer transfer integrals, but also the in-plane spacing and arrangement between the BEDT-TTF sites. While in (a) the out-of-plane direction is denoted as c , different intra-layer packing (c) can modify the unit cell size such that in some systems the nomenclature of axes is different. The two-dimensional wave function overlap leads to the growth of typically plate-like single-crystals with the out-of-plane axis being the thinnest side.

The samples were grown by electrochemical methods and samples were, in most cases, provided by external collaborators. While all β'' - $(BEDT-TTF)_2SF_5R_3SO_3$ samples were synthesized by J.A. Schlueter (Argonne Nat. Lab. and Nat. Science Foundation), who also provided κ - $(BEDT-TTF)_2Cu_2(CN)_3$, the material β'' -Ga was supplied by Y. Ihara (Hokkaido Univ., Sapporo). β' - $EtMe_3Sb[Pd(dmit)_2]_2$ was provided by R. Kato (RIKEN, Saitama) and κ - $(BEDT-TTF)_2Ag_2(CN)_3$ by T. Hiramatsu, Y. Yoshida and G. Saito (Meijo Univ.). κ - $[(BEDT-STF)_x(BEDT-TTF)_{1-x}]_2Cu_2(CN)_3$

³As we will later see, in some cases the anionic potential becomes non-trivial, which was especially prominent in the $(TMTTF)_2X$ compounds [51].

with different substitution ratios x was grown by Y. Saito (Hokkaido Univ., Sapporo and Univ. Stuttgart). A. Löhle and R. Hübner (Univ. Stuttgart) successfully synthesized κ -(BEDT-TTF)₂Cu₂(CN)₃ and κ -(BEDT-TTF)₂Ag₂(CN)₃.

3.1.2 Packing-Motifs

As already mentioned in the previous section, the anions determine also the in-plane packing. Diverse arrangements have been realized, the most important ones for this work are sketched in Fig. 3.1.3. Generally, one can distinguish two different branches, one of which leads to single molecular arrangement, the other one involves BEDT-TTF dimers. On the one hand, the α , β'' and θ structures have more or less separate molecules which results in quarter-filled hole bands due to the nominal charge BEDT-TTF^{+0.5}. According to section 2.3.2, these materials classes are prone to charge order instabilities for sufficiently strong electronic correlations V/W . On the other hand, in the dimerized β , β' , λ and κ phases the orbitals of two BEDT-TTF molecules combine within a dimer causing a splitting of the nominally 3/4-filled electronic band into one completely occupied band and another one occupied by one electron. Hence, these materials are effectively half-filled giving rise to Mott physics and the related antiferromagnetic exchange interactions.

In the course of a phase transition, the in-plane arrangements can be modified such that the degree of dimerization is modified. Naturally, the different structures imply an optical response and transport properties specific for each phase and the respective crystal directions. Hence, optical spectroscopy is ideally suited to distinct between the various in-plane packings.

3.2 Charge-Sensitive Molecular Vibrations

The BEDT-TTF molecule consists of 26 atoms and thus exhibits 72 vibrational degrees of freedom. These eigenmodes have been extensively characterized by means of Raman and optical spectroscopy, as well as theoretical calculations [50, 109–112]. Similar as lattice phonons, molecular vibrations are nothing but harmonic oscillations with restoring force $\mathbf{F} = -k\mathbf{x}$, where the resonance frequency ω_0 depends on the spring constant k and the mass m of the involved atoms and chemical moieties, i.e. $\omega_0 = 2\pi\nu \propto \sqrt{k/m}$ [57]. Therefore, the oscillation is faster for stronger restoring force and slower for heavier particles. Motions of the ethylene end groups containing the light hydrogen atoms are observed at high frequencies whereas carbon and sulfur

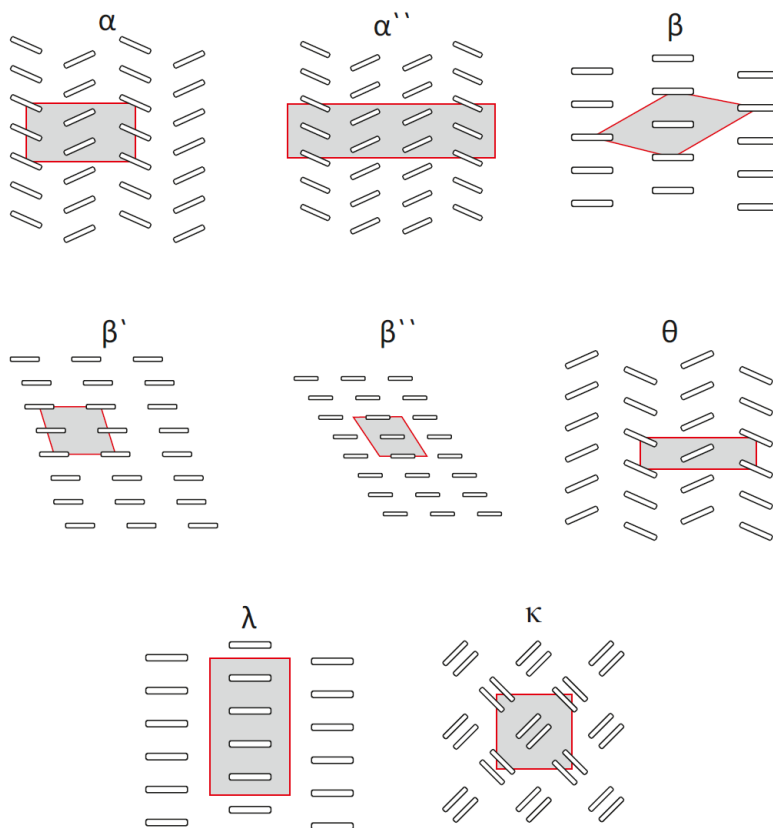


Figure 3.1.3: Various arrangements between the molecules are stabilized within the conducting layers (i.e. *in-plane*) of quasi two-dimensional organic charge-transfer salts (not all shown). Naturally, these structures are closely related with the anion packing between the layers. The electronic properties are strongly modified and generally anisotropic. In particular, the nominally quarter-filled bands ($0.5 e$ per organic molecule) split up into one completely-filled and another half-filled band due to dimerization in the β , β' , λ and κ phases. Reproduced from Ref. [108].

atoms vibrate at lower energies. Substitution with different isotopes causes a shift and/or splitting of the respective modes.

The spring constant k depends on the chemical bond strength, which is related to the amount of charge between the vibrating atoms. Thus, the resonance frequencies are different between neutral BEDT-TTF and its radical cation. The charge-rich C=C double bonds are subject to the most pronounced changes and, hence, the C=C stretching vibrations are most sensitive to changes of the molecular charge. Since optical spectroscopy requires a dipole moment to which the incoming photons can couple, symmetric vibrations usually do not show up in the spectra and can be only detected by Raman experiments. Therefore, we focus here on the infrared-active ν_{27} mode that can be excited for polarization along the molecular long axis (i.e. $E \parallel c$).

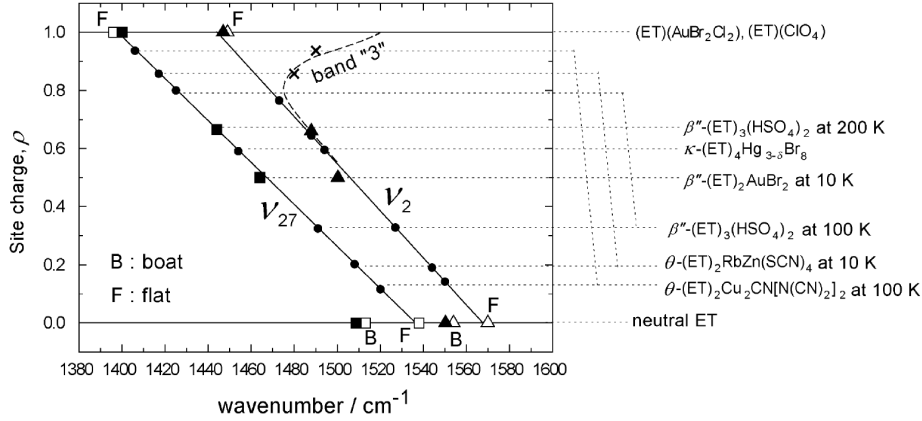


Figure 3.2.1: In an extensive infrared study Yamamoto *et al.* compared the resonance frequency ω_0 of the intramolecular $\nu_{27}(b_{1u})$ vibration for compounds with different BEDT-TTF charge. In the important range between the neutral and monovalent cationic states ω_0 depends linearly on the molecular charge (see Equ.3.2.1). The symmetric $\nu_2(a_g)$ C=C breathing mode is not infrared-active and can only be observed in Raman experiments. Reproduced from Ref. [49].

A linear frequency-charge relation was reported by Yamamoto *et al.* [49]:

$$\nu_{27}(\rho) = 1538 \text{ cm}^{-1} - \rho \cdot 140 \text{ cm}^{-1}/e, \quad (3.2.1)$$

which is illustrated in Fig.3.2.1. Here, ρ denotes the molecular charge. The resonance frequency decreases by 140 cm^{-1} upon removing an electron from the neutral BEDT-TTF molecule.

In the normal state with equally charged BEDT-TTF^{+0.5} molecules, this vibrational feature appears around $1460 - 1470 \text{ cm}^{-1}$ in the spectra of typical (BEDT-TTF)₂X charge transfer salts, as sketched in Fig- 3.2.2 (a) and (c). Interactions with the lattice (Davydov splitting) and the electronic background (emv coupling) can cause minor shifts and broadening of the resonance leading to a small splitting of the main feature due to inequivalent lattice sites. Such effects are typically in the range of $\Delta\nu \leq 10 \text{ cm}^{-1}$ which puts a lower bound to the detectable charge inequality $2\delta = \rho_{rich} - \rho_{poor} \leq 0.07e$. In a system with significant charge disproportionation $2\delta > 0.1 e$, the ν_{27} mode is clearly split into several peaks located at distinct frequencies corresponding to the molecular charge $\rho_0 \pm \delta$. The easiest scenario with only two different site charges arranged in an alternating checkerboard-like pattern is depicted in Fig. 3.2.2 (b) and (d).

Note that, in general, the charge distribution may be more complicated. Since the

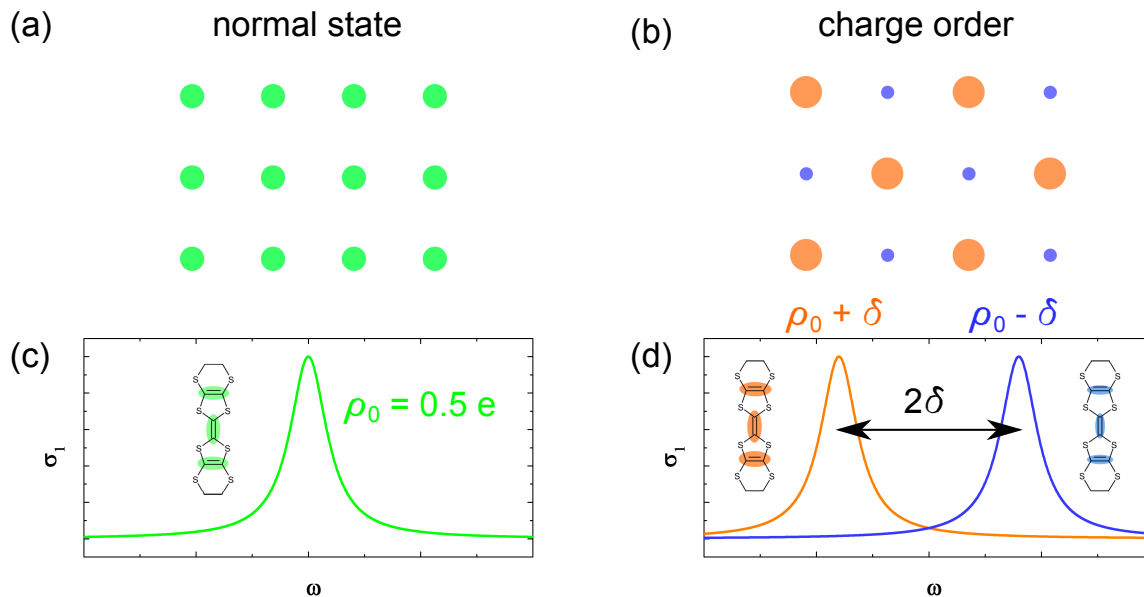


Figure 3.2.2: In the normal state (a), all BEDT-TTF molecules have the same charge $\rho_0 = +0.5e$. Since the resonance frequency of the charge-sensitive ν_{27} vibration mode is the same for each molecule, there is one single peak in the optical conductivity (c). In the charge-ordered state (b), the charge-poor and -rich molecules have a site charge of $\rho_{rich} = \rho_0 + \delta$ and $\rho_{poor} = \rho_0 - \delta$ which brings about two distinct peaks separated by $\Delta\nu = 2\delta \cdot 140 \text{ cm}^{-1}/e$ (see Equ.3.2.1).

intensity of the vibration mode⁴ depends strongly on ρ , the fraction of molecules with charge ρ_i can not be determined straight forward from the relative spectral weight. While a mode splitting reveals the existence of differently charged molecular sites, this probe is insensitive to the specific CO pattern. Also, the resonance frequency of the modes may be shifted due to interaction with the lattice implying that the absolute values of frequency do not agree with Equ. 3.2.1. However, it is safe to assume that the anions do not change their valency — otherwise the material would become unstable — and charge conservation requires an average charge $\bar{\rho} = \frac{1}{N} \sum_{i=1}^N \rho_i \equiv 0.5 e$ per BEDT-TTF molecule. Therefore, the relative frequency differences between the split peaks are usually enough information to determine the charge arrangement. Comparison with other charge-sensitive measurement techniques, for instance X-ray diffraction or NMR spectroscopy, allows to discern between different scenarios.

All arguments discussed above can be applied straight forward to the closely related (TMTTF)₂X compounds and, therefore, similar intramolecular vibrations are used to determine the molecular charge [113] (see Appendix A.1). This method is

⁴A 100-fold increase of the ν_{27} intensity between neutral and mono-cationic BEDT-TTF was reported in Ref.[50].

particularly useful to study the charge dynamics of the correlated electrons since one probes at significantly higher frequency than the energy of the low-temperature ground state, providing an undisturbed measure of the local charge. It should be pointed out that this is a specific advantage of the molecular materials under study, which can not be applied straight forward to determine the atomic charge in, for instance, transition-metal oxides, where charge ordering phenomena are of similar importance.

3.3 Mott Physics in 1/2-Filled Organic Quantum Spin Liquids

The Mott physics and magnetic properties of dimerized quasi two-dimensional molecular conductors with effectively half-filled bands have been studied intensely over the last decades. Here, we focus on the three compounds β' -EtMe₃Sb[Pd(dmit)₂]₂, κ -(BEDT-TTF)₂Ag₂(CN)₃ and κ -(BEDT-TTF)₂Cu₂(CN)₃ with an almost ideal triangular arrangement of organic dimers within the conducting planes. As indicated in Fig. 3.3.1, the inter-dimer transfer integrals t and t' are very similar in size which causes strong geometrical frustration⁵. Despite exchange interactions J of several 10² K, antiferromagnetic order is suppressed down to mK temperatures and these materials are considered as quantum spin liquid (QSL) candidates [15, 76, 78]. Exotic spin excitations, in particular the so-called *spinons*, are predicted to occur at low energies while the charge degrees of freedom remain localized in the Mott insulating state [18, 85, 86, 116]. Such a disentanglement of the spin and charge degrees of freedom is known to appear in one-dimensional systems, where the fundamental excitations are split into spinons and holons, both of which can propagate freely through the lattice [103].

Due to $t_d \gg t, t'$, the on-site Coulomb repulsion, which can be approximated with the intra-dimer transfer integral $U \approx 2t_d$ [117], is significantly larger than the bandwidth $W = 9t$. Hence, correlations in these compounds are sufficiently strong to stabilize the Mott insulating state. The overall energy scales of U and W are of order 0.1 eV, so several 100 K already have a significant impact on the conduction properties via thermal broadening of the Hubbard bands. Consequently, the boundary of the Mott state – the quantum Widom line (QWL) – can be mapped on comparably small temperature and pressure scales, as shown in Fig. 3.3.2 for β' -

⁵The itinerant exchange mechanism projects the geometrical frustration of the transfer integrals directly on the antiferromagnetic exchange interaction $t/t' \propto J/J' \approx 1$.

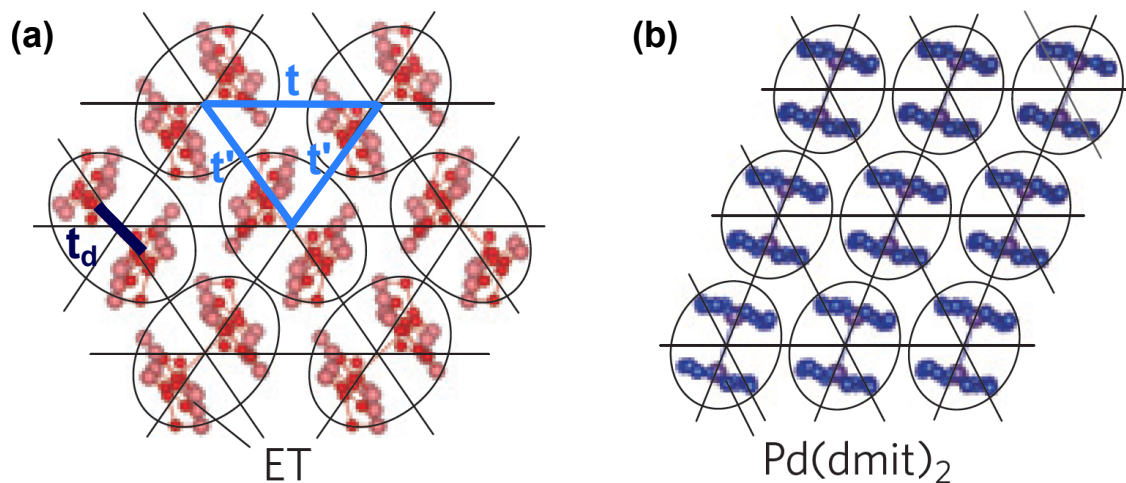


Figure 3.3.1: (a) The dimers of organic molecules are arranged in a triangular pattern for $\kappa\text{-(BEDT-TTF)}_2\text{Ag}_2(\text{CN})_3$ and $\kappa\text{-(BEDT-TTF)}_2\text{Cu}_2(\text{CN})_3$. The strength of dimerization is determined. The inter-dimer transfer integrals t , t' are almost equal, which leads to geometrical frustration and the suppression of antiferromagnetic order down to lowest temperatures, which is discussed in the context of quantum spin liquids [15, 76, 78]. (b) Also in $\beta'\text{-EtMe}_3\text{Sb}[\text{Pd(dmit)}_2]_2$ the dimers are arranged on a frustrated triangular lattice [114, 115]. Modified from Ref. [14].

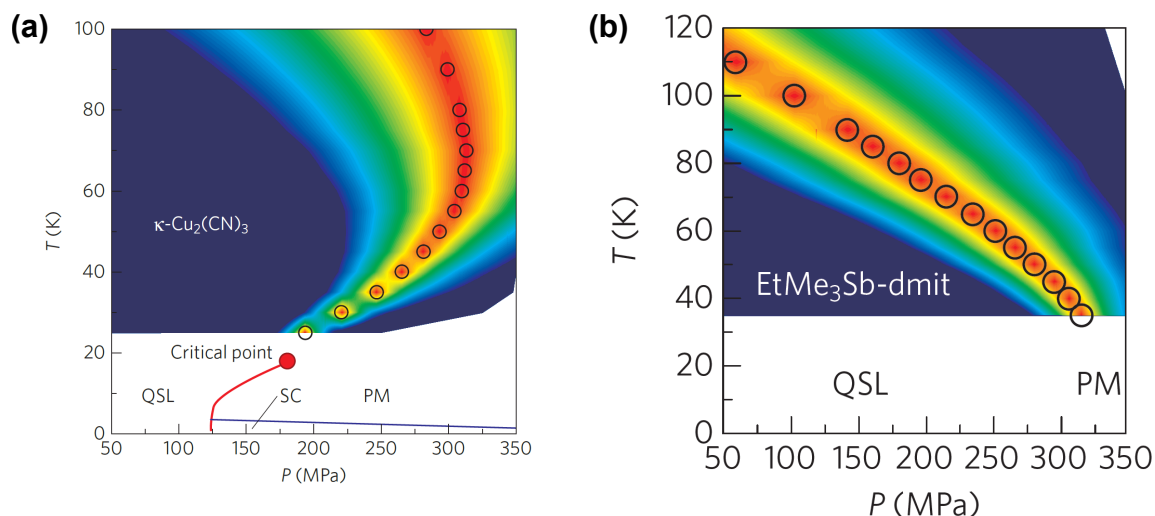


Figure 3.3.2: In the supercritical region the boundary of the gapped Mott state is a crossover rather than a well-defined first-order transition, identified as the quantum Widom line (red color) which is determined from pressure-dependent dc transport on $\kappa\text{-(BEDT-TTF)}_2\text{Cu}_2(\text{CN})_3$ (a) and $\beta'\text{-EtMe}_3\text{Sb}[\text{Pd(dmit)}_2]_2$ (b). The former compound nicely reveals the back-bending in the vicinity of the metallic state. Reproduced from Ref. [14].

$\text{EtMe}_3\text{Sb}[\text{Pd(dmit)}_2]_2$ and $\kappa\text{-(BEDT-TTF)}_2\text{Cu}_2(\text{CN})_3$ [14]. Panel (b) nicely reveals the back-bending of the QWL in the supercritical region consistent with theoretical

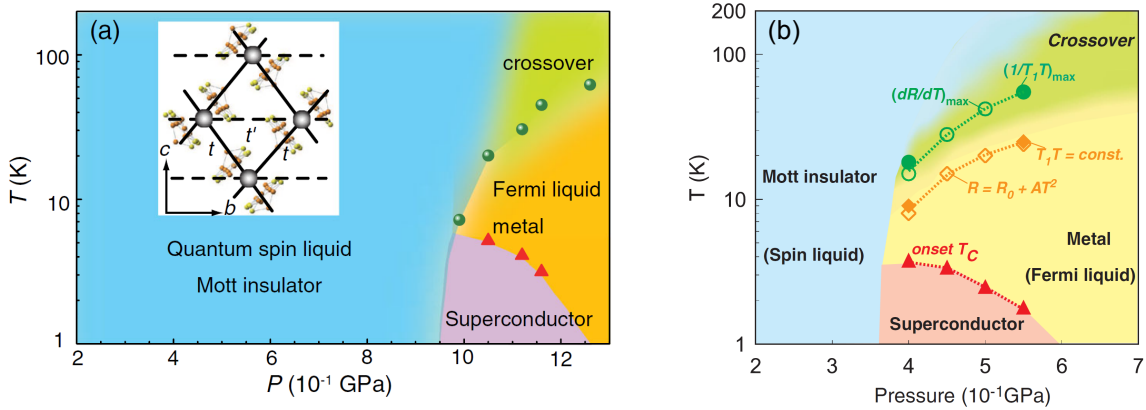


Figure 3.3.3: At low temperatures the geometrically frustrated quantum spin liquid compounds κ -(BEDT-TTF) $_2$ Ag $_2$ (CN) $_3$ (a) and κ -(BEDT-TTF) $_2$ Cu $_2$ (CN) $_3$ (b) show phase diagrams very similar to Fig. 2.3.8 (b). Specifically, the large entropy of the spin degrees of freedom involves a positive slope of the phase boundary between the Mott and metallic states. Superconductivity is stabilized below 5 K as a result of strong quantum fluctuations. Reproduced from Refs. [15, 118].

calculations (cf. Fig. 2.3.9).

Pressure-dependent dc transport measurements (Fig. 3.3.3) revealed that κ -(BEDT-TTF) $_2$ Ag $_2$ (CN) $_3$ is more strongly correlated than κ -(BEDT-TTF) $_2$ Cu $_2$ (CN) $_3$ since the metallic and superconducting states are recovered only at higher pressure in the former compound [15, 118]. The low-temperature first-order Mott MIT shows a positive slope due to the spin degrees of freedom, very similar to Fig. 2.3.8 (b). On the metallic side, a Fermi liquid phase with strongly renormalized quasiparticles resides next to the superconducting phase. At higher temperatures, bad metallic behaviour and incoherent conduction processes dominate the transport properties. Fig. 3.3.4 shows the phase diagram in the vicinity and above the critical endpoint of the Mott MIT of κ -(BEDT-TTF) $_2$ Cu[N(CN) $_2$]Cl. While at lower temperatures it is a well-defined first-order transition, in the supercritical region the boundary of the Mott state is a crossover. Importantly, the behaviour resembles that of κ -(BEDT-TTF) $_2$ Cu $_2$ (CN) $_3$, with the characteristic back-bending of the QWL. Since this compound is less frustrated than the QSL materials ($t/t' \approx 0.44$), antiferromagnetic (AFM) order is stabilized below $T_N = 25$ K [89]⁶.

Optical studies revealed striking differences between κ -(BEDT-TTF) $_2$ Cu $_2$ (CN) $_3$ and κ -(BEDT-TTF) $_2$ Cu[N(CN) $_2$]Cl [16], which is shown in Fig. 3.3.5. In the course of the AFM phase transition, the Mott-Hubbard band of the latter compound is significantly narrowed and a charge gap opens below 0.1 eV. The spectral weight reduction

⁶Having in mind that $J \approx 200$ K, there is still considerable frustration since $T_N \ll J$.

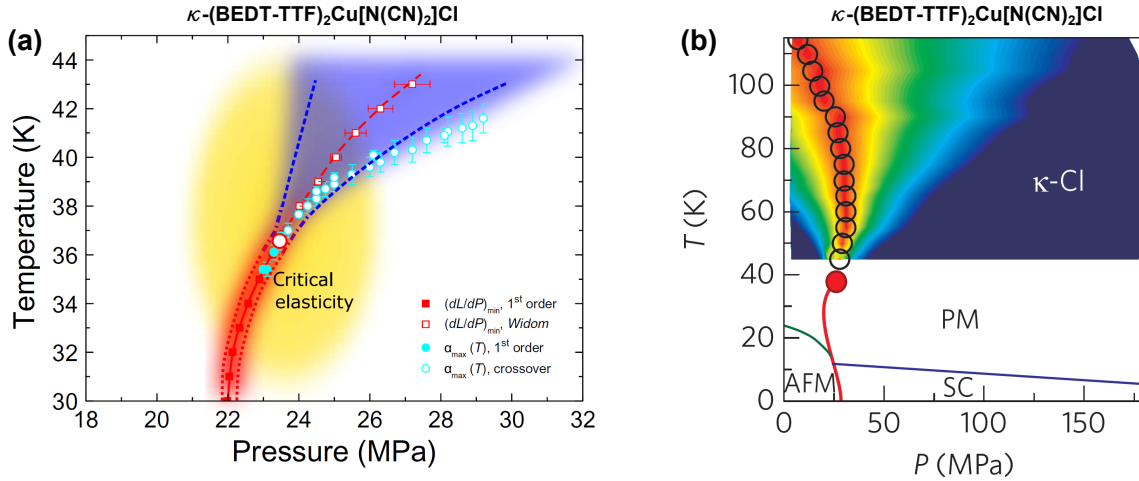


Figure 3.3.4: Phase diagram of κ -(BEDT-TTF)₂Cu[N(CN)₂]Cl determined from dilatometry (a) and dc transport (b) measurements under pressure. The boundary of the Mott state reveals the characteristic positive slope, cf. Fig. 2.3.8. While it is a well-defined first-order transition below the critical endpoint around 36 K, it becomes a crossover at higher temperatures identified as the quantum Widom line. Reproduced from Refs. [14, 91].

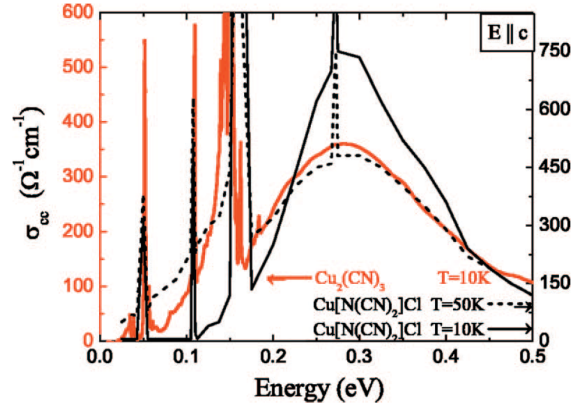


Figure 3.3.5: A well-defined gap develops in the optical conductivity of κ -(BEDT-TTF)₂Cu[N(CN)₂]Cl when the antiferromagnetic state is entered, which causes a strong reduction of the low-energy spectral weight. The quantum spin liquid compound κ -(BEDT-TTF)₂Cu₂(CN)₃ does not show such behaviour; the low-frequency wing of the Mott-Hubbard band decays smoothly towards $\omega = 0$. Reproduced from Ref. [16].

at low energies is accompanied by an enhancement of σ_1 in the mid-infrared range. On the other hand, there is no discrete phase transition in the QSL Mott state of the former material, and the conductivity reduces gradually towards low frequencies. Such *gapless* behaviour seems to be related to the fluctuating spin sector. To explain the different low-frequency responses, Ng *et al.* predicted a coupling of the spin de-

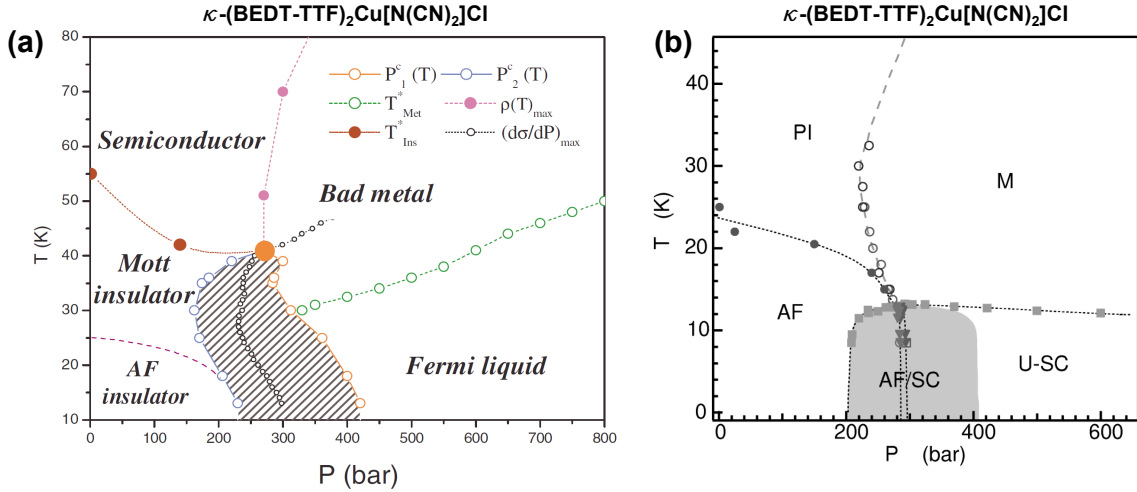


Figure 3.3.6: (a) The low-temperature phase diagram of κ -(BEDT-TTF) $_2$ Cu[N(CN) $_2$]Cl reveals the different slopes of the antiferromagnetic ($dT_N/dp < 0$) and Mott ($dT_{MI}/dp > 0$) transitions, which is explained in Fig. 2.3.8. Hysteresis reveals the first-order nature of the transitions at low temperature. (b) There is a coexistence regime of antiferromagnetism and superconductivity. Reproduced from Refs. [89, 105].

degrees of freedom with the charge response through an emergent gauge field, causing power-law absorption within the Mott gap [18]. Although such peculiar behaviour could not be verified so far, there have been ongoing, controversially discussed studies including different QSL compounds [17, 119].

As shown in Fig. 3.3.6 (a), for κ -(BEDT-TTF) $_2$ Cu[N(CN) $_2$]Cl a hysteretic range of coexistence was observed at the insulator-metal boundary below the critical endpoint, indicative of the first-order nature of the MIT [105]. When contrasting the low-temperature phase diagram to that of κ -(BEDT-TTF) $_2$ Cu $_2$ (CN) $_3$, the slope of the metal-insulator transition becomes negative upon approaching the antiferromagnetic state, opposite to the QSL compound. This is a direct manifestation of the reduced spin entropy in the magnetically ordered phase, cf. Fig. 2.3.8 (a). Note, the slope of the phase boundary becomes negative only in the vicinity of AFM - the spin-disordered state at higher temperatures exhibits the same kind of Mott physics as the QSL.

Let us now focus on the superconducting (SC) state of these dimerized systems. It is interesting to note that a range of coexistence between the AFM and SC phases was reported for κ -(BEDT-TTF) $_2$ Cu[N(CN) $_2$]Cl [89], which is depicted in Fig. 3.3.6 (b). The superconducting dome peaks at approximately the same pressure where $T_N \rightarrow 0$ which indicates a relation to strong quantum fluctuations. Fig. 3.3.7 (a) shows a generic phase diagram that qualitatively connects the Mott insulating, antiferromag-

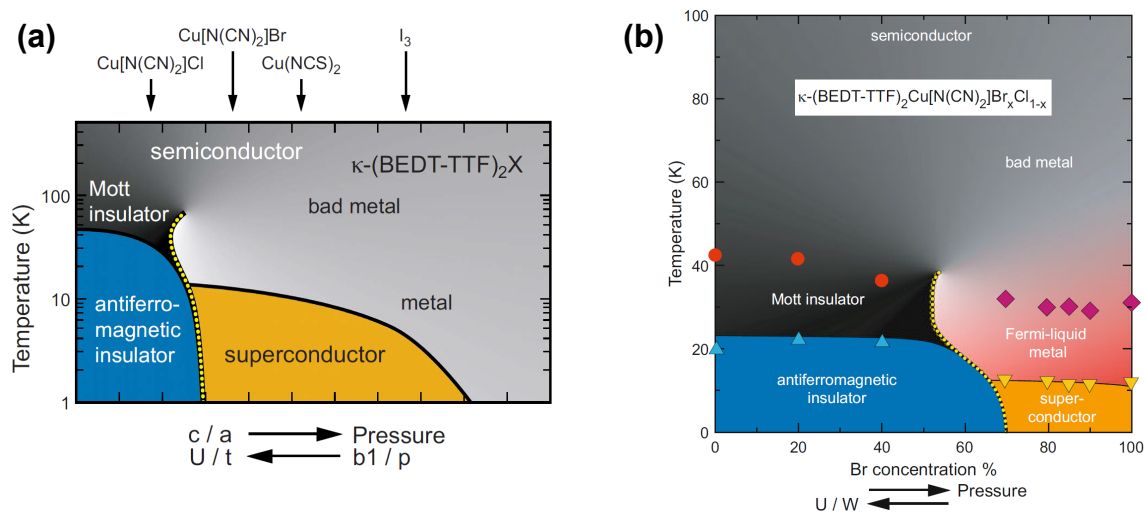


Figure 3.3.7: (a) Several compounds from the $\kappa-(BEDT-TTF)_2X$ series are summarized in a common phase diagram [120–123]. Note, the vast majority of the phase diagrams reported so far are confined to qualitative conclusions rather than absolute numbers U/t or U/W , inhibiting quantitative comparison between different materials and with theory. (b) Specifically, the bandwidth-tuned Mott transition is triggered by small variations like partial chemical substitution of a halogen atom in $\kappa-(BEDT-TTF)_2Cu[N(CN)_2]Br_xCl_{1-x}$. Reproduced from Refs. [21, 23].

netic, superconducting and metallic states of several $\kappa-(BEDT-TTF)_2X$ compounds. Empirically assembled pressure-dependent data suggest that, depending on the specific anions, the degree of electronic correlations U/W implies a distinct ambient pressure position in the phase diagram [120–123]. Furthermore, it was found that chemical alloying of different anions has a similar effect on the electronic correlations as applied pressure. Due to great similarity of the anion structure, such bandwidth-tuning could be realized for the $\kappa-(BEDT-TTF)_2Cu[N(CN)_2]Br_xCl_{1-x}$ series [21, 23]; the phase diagram with respect to Br content x is shown in Fig. 3.3.7 (b). Similarly, small modifications of the BEDT-TTF molecules, such as introduction of different isotopes or isovalent substitution of S by O or Se, may have a significant influence on the electronic system. While ^{13}C or ^{17}O are typically used in NMR spectroscopy or to disentangle specific vibration modes, deuteration may even have an influence on the chemical bonding and, hence, the physical properties. It was shown for several organic superconductors of different structures that the D analogue leads to an increase of correlations U/W [122, 124] and the enhancement of T_C rules out conventional BCS pairing [40]. Detailed considerations on the microscopic origin of deuteration effects in quasi one-dimensional $(TMTTF)_2X$ can be found in the Appendix (section A.1.7) and Ref. [51]. Isovalent substitution of BEDT-TTF by BEDT-STF and

BETS (S atoms partially replaced by Se) provides direct access to tune the in-plane transfer integrals and, thus, the bandwidth [125, 126].

3.4 Charge Order and Superconductivity in 1/4-filled (BEDT-TTF)₂X

As we have seen in Section 2.3.5, materials at quarter filling are prone to charge order instabilities. In terms of the extended Hubbard model (Equ. 2.3.10), the parameter V/W allows to drive the material through the metal-insulator transition. In the course of this bandwidth-tuning, a strongly correlated metallic state governed by fluctuating charge order arises in the vicinity of the charge-ordered insulating region. Theoretical calculations predicted that these charge fluctuations mediate unconventional superconductivity at low temperatures [33, 127]. Similar as in the high- T_C copper oxides, the superconducting gap has nodes. While due to the characteristic geometry of the CuO_2 planes the order parameter in the cuprates acquires $d_{x^2-y^2}$ symmetry, d_{xy} pairing is predicted for quarter-filled organic conductors with a checkerboard charge order pattern. Experimental studies on β'' -(BEDT-TTF)₂SF₅CH₂CF₂SO₃ [37, 128] and α -(BEDT-TTF)₂I₃ [129] indicated deviations from BCS behaviour. However, they do not provide conclusive evidence on the symmetry of the superconducting gap. Apart from that, superconductivity in β'' -(BEDT-TTF)₂SF₅CH₂CF₂SO₃ was found to resemble the characteristic features of the Fulde-Ferrel-Larkin-Ovchinnikov (FFLO) state, recently established in an NMR study [98].

Quarter-filled organic conductors from the α -, β'' - and θ -(BEDT-TTF)₂X families have been suggested as prime examples of charge-order-driven superconductivity [33, 127], following the generic phase diagram in Fig. 3.4.1 (a). Note the reduced units T/t and V/t ($t \propto W$). Yet, comparison between materials of different lattice structure may lead to severe complications and it is a priori not possible to construct a unified $T - p$ phase diagram from the experimental data valid for all these structures (cf. Fig. 3.1.2). In this regard, it is highly desirable to have a series of closely related materials at distinct positions of the phase diagram.

As summarized in the phase diagram in Fig. 3.4.1 (b), the β'' -(BEDT-TTF)₂SF₅RSO₃ family provides such a well-bounded laboratory. These compounds share a common arrangement of BEDT-TTF stacks aligned along the crystallographic a -direction, which is illustrated in Fig. 3.4.2. Upon modifying the anion layer by substituting the chemical moiety R , qualitatively different transport properties are realized. While

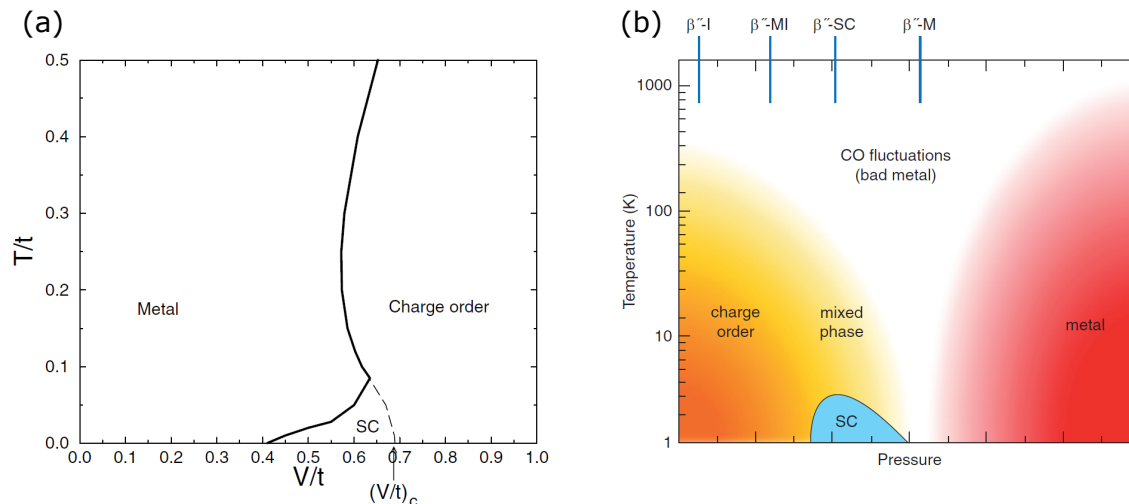


Figure 3.4.1: (a) Theory predicted unconventional superconductivity in quarter-filled correlated electron systems mediated by charge fluctuations. As the interactions V/t are reduced, a non-Fermi liquid state emerges in the vicinity of the insulating charge-ordered region. There, charge fluctuations prevail down to lowest temperatures and serve as pairing glue for d -wave superconductivity [33, 127]. (b) Experimentally, a similar phase diagram was suggested for the β'' -(BEDT-TTF)₂SF₅RSO₃ series, where β'' -I, β'' -MI, β'' -SC and β'' -M correspond to $R = \text{CH}_2, \text{CHF}_2, \text{CH}_2\text{CF}_2$ and CHF , respectively. Reproduced from Refs. [33, 38].

insulating behaviour is present up to room temperature for $R = \text{CH}_2$ (β'' -I), there is a metal-insulator transition around 180 K for CHF_2 (β'' -MI) [39, 131]. The compounds with $R = \text{CH}_2\text{CF}_2$ (β'' -SC) and CHF (β'' -M) are metallic at all temperatures and the former one even becomes superconducting below $T_C \approx 5$ K [132].

The specific β'' arrangement implies anisotropic transport properties due to different transfer integrals between the molecules within one stack and on adjacent stacks. Since the molecular faces are tilted with respect to the stacks, the wave function overlap is largest along the b direction. Hence, the conductivity is largest perpendicular to the stacks and acquires a minimum along the stacks⁷. Still, the in-plane transport properties are of the same order of magnitude whereas the resistivity perpendicular to the organic layers is higher by a factor $10^2 - 10^3$.

The strong anisotropy of the charge dynamics extends to finite frequencies up to the mid-infrared spectral range. Fig. 3.4.3 shows the optical response at room temperature along the three principal axes of β'' -SC [36, 37, 133]. Apart from sharp molecular vibrations at low frequencies, the out-of-plane reflectivity is flat and featureless, and

⁷The direction of minimum conductivity does not exactly coincide with the crystallographic a -direction, but is tilted by a small angle. In this thesis, however, for simplicity the notation $E \parallel a$ will be used for both the a -axis and the direction of minimum conductivity.

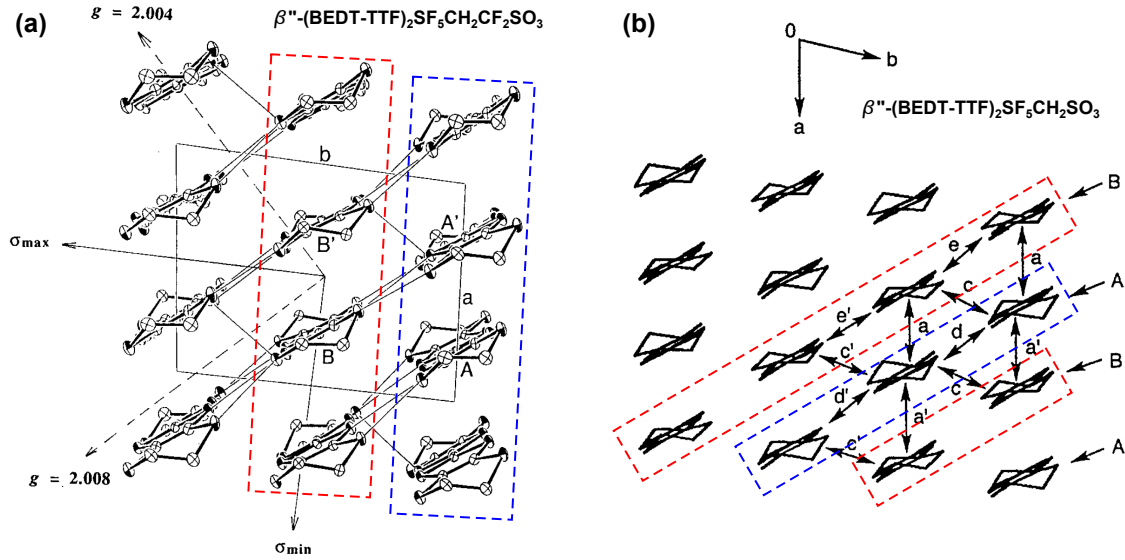


Figure 3.4.2: Two inequivalent lattice sites, denoted as A and B, are identified within the conducting layers of $\beta''\text{-(BEDT-TTF)}_2\text{SF}_5\text{RCH}_2\text{CF}_2\text{SO}_3$. While the A and B molecules are arranged in stacks along a for $R = \text{CH}_2\text{CF}_2$, CHFCF_2 and CHF (a), equivalent molecules form coplanar arrays in the $-a + b$ direction for $R = \text{CH}_2$ (b). Due to anisotropic wave function overlap, the conductivity is largest along the crystallographic b -axis and smallest perpendicular to it. Although σ_{min} is not exactly parallel to a , for simplicity $E \parallel a$ and $E \perp b$ will be used synonymously in this thesis. Modified from Refs. [39, 130].

the optical conductivity is very small, reminiscent of an insulator. Within the plane, both directions show metallic behaviour with non-zero conductivity towards $\omega \rightarrow 0$. The largest response is observed for $E \parallel b$, where the reflectivity shows a plasma edge around 6000 cm^{-1} and σ_1 peaks around $1000 - 2000 \text{ cm}^{-1}$. At room temperature, the spectra of the other compounds of the $\beta''\text{-(BEDT-TTF)}_2\text{SF}_5\text{RCH}_2\text{CF}_2\text{SO}_3$ series are qualitatively similar and will be presented in chapter 6.

As elaborated in section 3.2, the intramolecular ν_{27} vibration provides access to the site-specific BEDT-TTF charge. Therefore, considerable efforts [36] were devoted to low-temperature infrared experiments perpendicular to the conducting planes. The charge-sensitive ν_{27} mode of $\beta''\text{-SC}$ and $\beta''\text{-M}$ is plotted in Fig. 3.4.4. Apparently, the two distinct modes of the superconducting compound reveal charge fluctuations which possibly provide the pairing glue for unconventional superconductivity [37, 38, 134]. Although it remains rather broad down to low temperatures, no significant peak splitting is observed for the metallic compound, consistent with a Fermi liquid state without considerable quantum fluctuations.

Apart from vibrational spectroscopy, there are a few other methods to determine the BEDT-TTF charge. On the one hand, nuclear magnetic resonance (NMR)

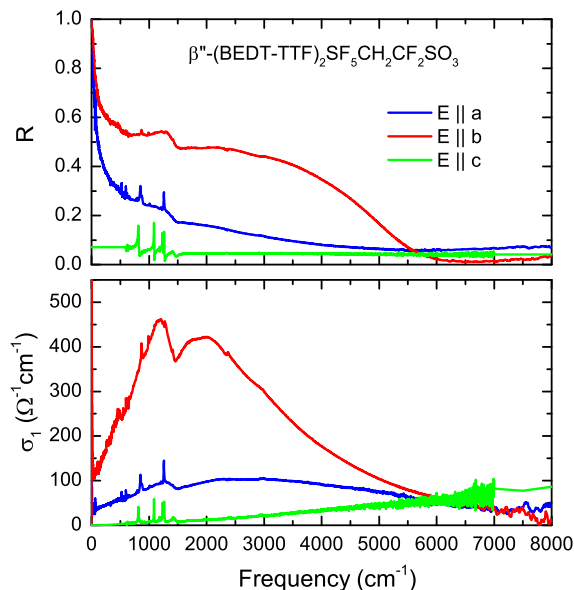


Figure 3.4.3: Anisotropic reflectivity (upper panel) and optical conductivity (lower panel) of β'' -(BEDT-TTF) $_2$ SF $_5$ CH $_2$ CF $_2$ SO $_3$ reproduced from Refs. [36, 37]. The largest response is observed along the crystallographic b direction. While $E \parallel a$ shows less pronounced, but still metallic properties, the out-of-plane reflectivity ($E \parallel c$) is flat and σ_1 vanishes towards $\omega = 0$ which is typical insulating behaviour. The narrow peaks below 1500 cm^{-1} correspond to vibrational features.

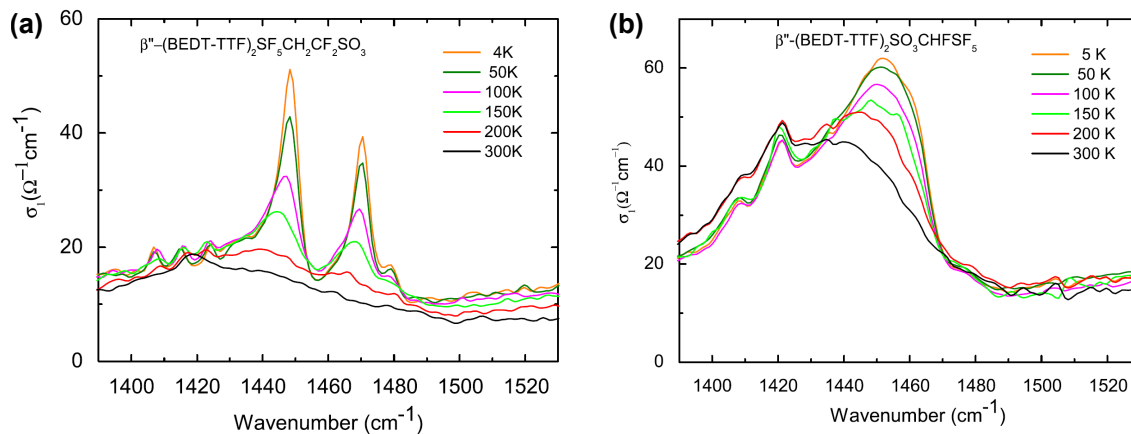


Figure 3.4.4: The charge-sensitive ν_{27} mode was measured down to low temperatures in out-of-plane geometry $E \parallel c$ for β'' -SC and β'' -M. While there are two distinct peaks for the superconducting compound (a), reminiscent of charge fluctuations [37], no splitting is observed for β'' -M (b). Reproduced from Ref. [36].

measures the spin density per molecule (see e.g. Ref. [135]); the concept is analogous as described for (TMTTF)₂X [136]. On the other hand, the inter-atomic distances within the organic molecule can be also used to approximate the charge density. Using the Guionneau-Day equation [137], the molecular charge of the four β'' -(BEDT-TTF)₂SF₅RSO₃ compounds was estimated from the atomic coordinates yielding more positive charge on *A* compared to the *B* sites [39, 131]. Note that the charge pattern in β'' -I is checker-board-like (i.e. diagonal stripes along $-a + b$) rather than stripe-like, and there is significant dimerization of the transfer integrals along the *a*-direction [39, 138]. In this regard, these materials show more (β'' -SC) or less (β'' -M) strongly pronounced charge fluctuations in the metallic state and, as we will later see, static charge order (β'' -I and β'' -MI) in the insulating phase [36–38, 50, 134]. Most importantly, these results suggest that the theoretical considerations about a possible relation between charge order and superconductivity work also in real materials since both effects are observed.

A specific question regarding β'' -SC arises whether there is coexistence or competition between charge order and superconductivity, which has been reported for antiferromagnetic (κ -(BEDT-TTF)₂Cu[N(CN)₂]Cl, see Ref [89], cf. Fig. 3.3.6) and spin-density wave (TMTSF₂PF₆, see Ref. [90]) states, for instance. There, magnetic order is triggered by the effectively half-filled bands due to strongly dimerized organic molecules. In hole-doped copper-oxides, however, charge density wave order was revealed at doping levels of 12.5 %, i.e. at 1/8 filling, where a strongly competitive character with respect to $d_{x^2-y^2}$ superconductivity was identified [139]; very recent ultrafast pump-probe experiments demonstrated an enhancement of T_c upon melting the competing order [140]. Therefore, it is highly desirable to answer whether or not such competition is also observed for charge fluctuations at quarter filling, which will be tackled in section 6.1.4.

An obvious test of the suggested phase diagram are pressure-dependent transport investigations, as performed on β'' -(BEDT-TTF)₂SF₅CH₂CF₂SO₃ by Hagel *et al.* [41]. Fig. 3.4.5 summarizes the unexpected results gained from that study. Interestingly, insulating behaviour sets in around 10 kbar which can not be simply understood in the context of the extended Hubbard model. The observed hysteresis indicates a possible involvement of the lattice; also for β'' -(BEDT-TTF)₂SF₅CHF₂CF₂SO₃ hysteresis was found between the cooling and heating runs [40]. While microscopic charge disproportionation is mostly considered to be a pure effect of the competition between inter-site Coulomb interaction V and bandwidth W , compression would always lead to a reduction of V/W and, therefore, stabilization of metallic behaviour.

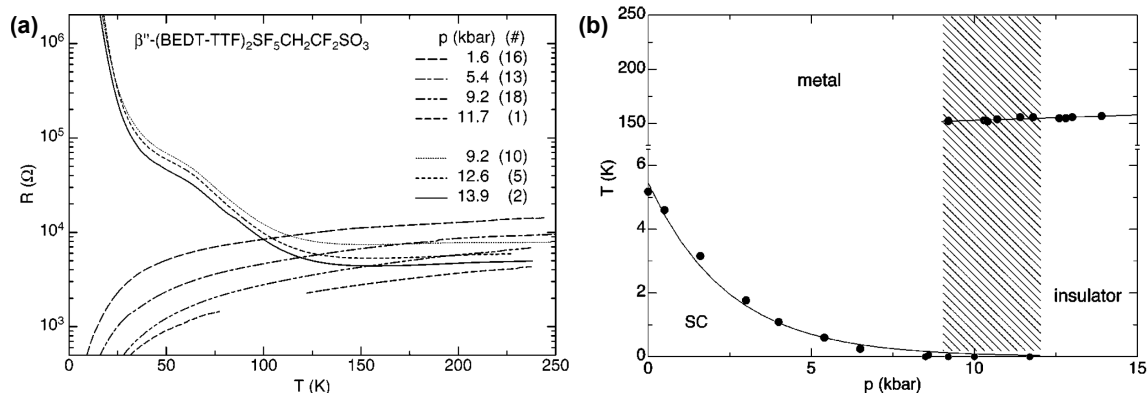


Figure 3.4.5: (a) Although in β'' -(BEDT-TTF)₂SF₅CH₂CF₂SO₃ the resistivity at high temperatures is generally reduced upon application of pressure, a metal-insulator transition appears with increasing transition temperature. (b) A hysteric coexistence regime indicates the first-order type of this transition. Superconductivity is reduced with pressure and, finally, vanishes as insulating behaviour sets in. Reproduced from Ref. [41].

In reality, however, the organic layers are not free in space but sandwiched between the anions. Considering the respective structures, the charge pattern appears to be closely related with the anion arrangement. In Ref. [39] it was pointed out that the BEDT-TTF A molecules have more H-O short contacts to the anions than the B sites. Thus, a possibly significant role of the anionic Coulomb repulsion will be discussed in this thesis.

For the θ -(BEDT-TTF)₂X series similar enhancement of the charge-ordered insulating phase was observed in pressure-dependent studies, as summarized in Fig. 3.4.6 (c). Mori *et al.* explained it with a modification of the dihedral angle θ causing a reduced wave function overlap between the BEDT-TTF molecules [52, 141, 142]. Interestingly, both the high-temperature resistivity and metal-insulator transition temperature *increase* with pressure. In this specific case, physical pressure *reduces* the bandwidth $W \propto t$ which goes hand in hand with larger electronic correlations V/W . Going back to Fig. 3.4.5 (a), however, there is an important difference to β'' -SC. While the transition temperature increases with pressure the resistivity is generally reduced (apart from the onset of the MIT). The larger conductivity indicates that the bandwidth is enhanced, as one would primarily expect upon reduction of the lattice spacing. Thus, the situation of the β'' -(BEDT-TTF)₂SF₅RSO₃ family is different than for the θ -compounds which will be thoroughly discussed in section 6.1.3.

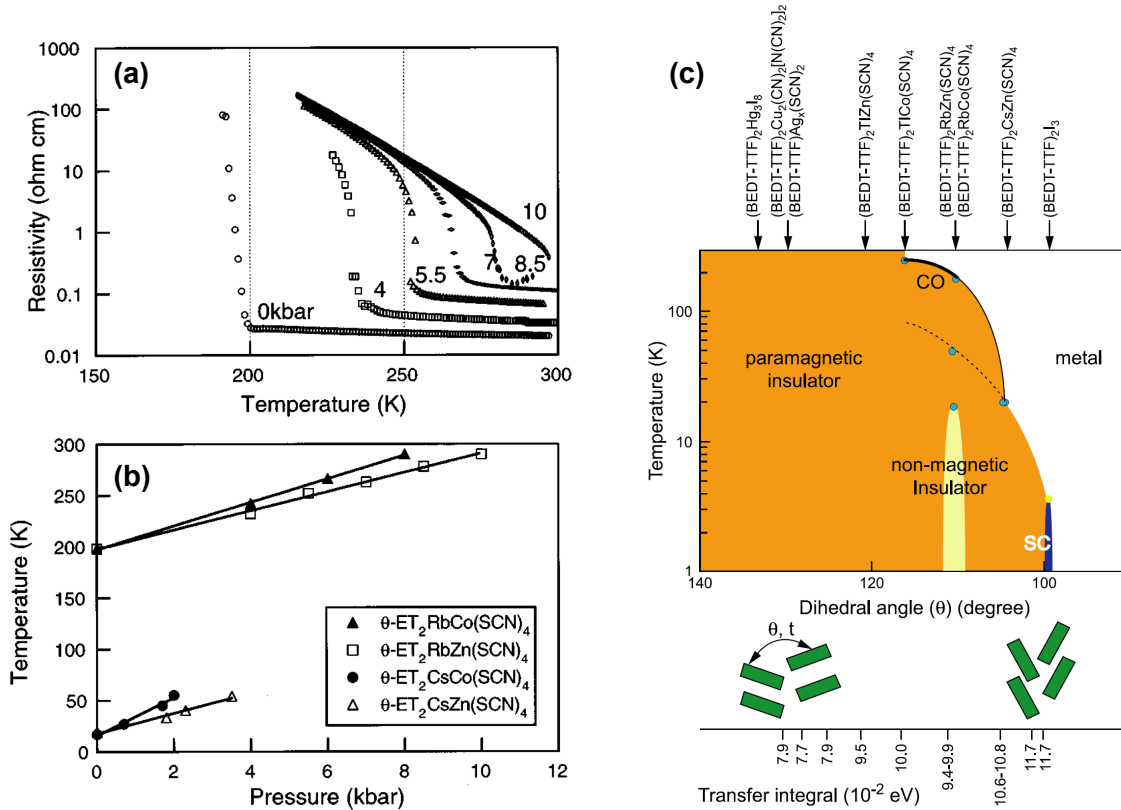


Figure 3.4.6: (a) Upon application of pressure, the resistivity of θ -(BEDT-TTF)₂MM'(SCN)₄ ($M = \text{Rb}, \text{Cs}$ and $M' = \text{Co}, \text{Zn}$; here shown for $MM' = \text{RbZn}$) is significantly enhanced [141]. (b) Also the charge order metal-insulator transition temperature increases with pressure. (c) This behaviour was explained by a reduction of the transfer integral due to modification of the dihedral angle θ between the BEDT-TTF molecules within the conducting layer upon application of pressure, establishing a general phase diagram for θ -(BEDT-TTF)₂X. Reproduced from Refs. [123, 141].

4. Experiments and Data Extraction

Different kinds of experiments were performed in this thesis to investigate the temperature- and frequency-dependent charge response. The largest focus was directed towards the optical properties in order to determine the influence of strong electronic correlations on the band shape, vibrational features, quasiparticle scattering and metal-insulator transitions. Where necessary, spectroscopic investigations were complemented by temperature- and also pressure-dependent dc transport to determine the transition temperatures. Also the magnetic properties of β'' -(BEDT-TTF) $_2X$ were studied by SQUID magnetometry.

4.1 Measurement Setup

This section is devoted to the principles of optical spectroscopy [53] and the setup employed here. Limitations, such as temperature and spectral ranges, as well as sample dimensions will be discussed in detail.

4.1.1 Fourier-Transform Infrared Spectroscopy

The central component of a Fourier-Transform infrared (FTIR) spectrometer is the Michelson interferometer sketched in Fig. 4.1.1. The light emitted from a broadband source, such as a light bulb, is divided into two parts at the beamsplitter. On the upper arm, it is reflected from the fixed mirror and then propagates back through the beamsplitter towards the detector. On the other arm, the mirror position can be modified which leads to interference effects with the light from the upper arm. Depending on the displacement Δx , different wavelengths interfere constructively or destructively. The frequency resolution depends on the maximum displacement and step size of Δx .

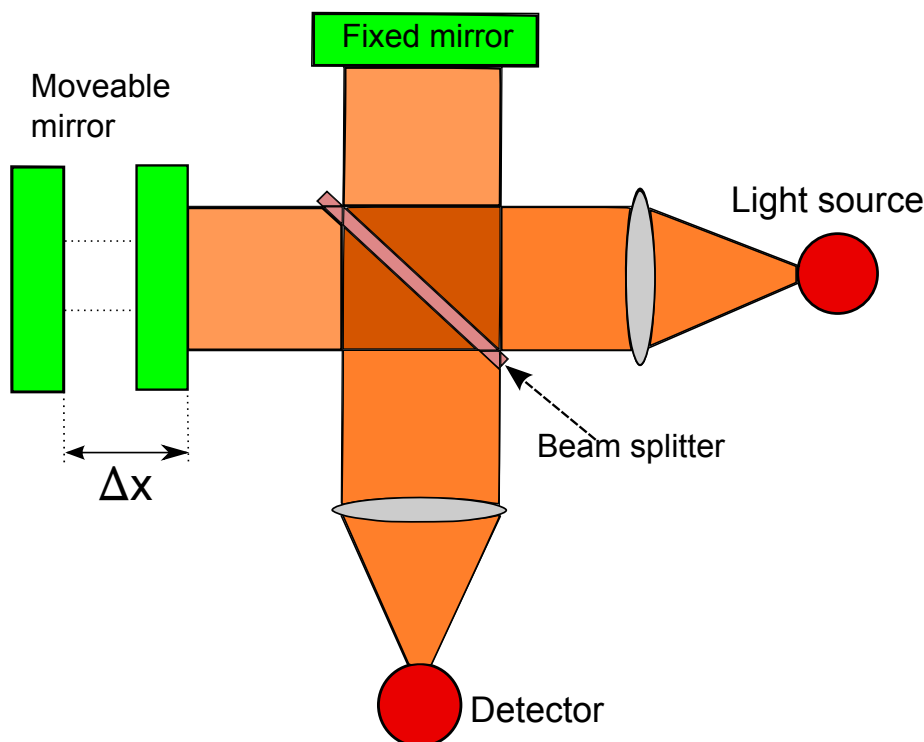


Figure 4.1.1: Basic principle of a Michelson interferometer which is the central ingredient of the employed commercial FTIR spectrometers. The light is divided into two parts at the beam splitter. After being reflected from a fixed and a movable mirror, the two beams are recombined leading to interference effects depending on the position Δx of the movable mirror. Broadband light sources and detectors are used to cover a wide spectral range. Modified from Ref. [143].

The FTIR interferogram and corresponding spectrum is illustrated in Fig. 4.1.2 for different kinds of light sources. For a laser, the spectrum consists of a sharp peak which expresses as a periodic sinusoidal modulation in the interferogram. Adding a second laser at frequency causes beating of the two components. In a real experiment, however, broadband light sources, such as a globar lamp covering the entire mid-infrared range, are used which leads to a more complicated interferogram. Conversion from mirror position Δx to frequency is done by Fourier transformation.

Various light sources, beamsplitters, detectors and windows used here are listed in Table 4.1.1. The intrinsic material properties, such as the gap size and vibrational features, confine the specific range of use for a given material which should be, of course, transparent. While at high frequencies ionic compounds like KBr, ZnSe and SiO₂ are used, carbon-based polymers are employed in the far-infrared and at lower frequencies.

Light detection was realized by semiconducting materials with varying band gap.

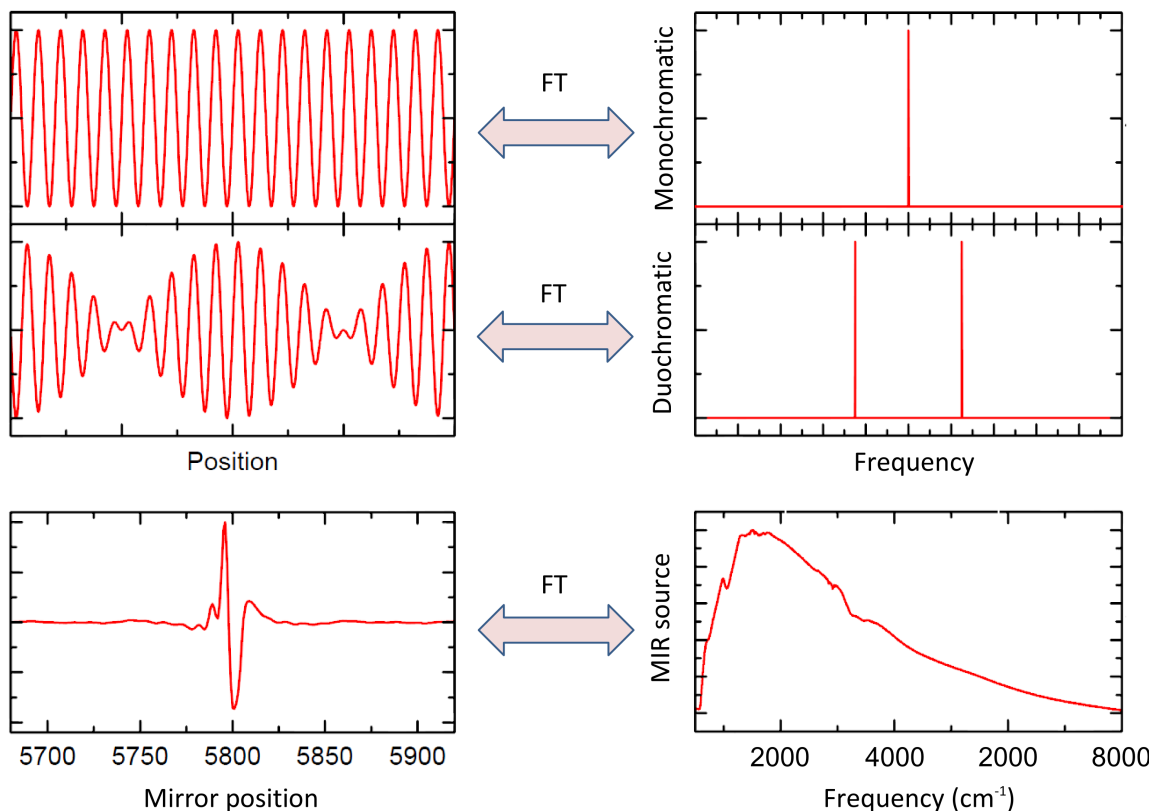


Figure 4.1.2: The interferogram (left) is shown for different spectra (right). In a monochromatic light source like a laser the spectrum consists only of one very narrow peak which expresses as a simple cosine function with respect to the mirror position. For two different frequencies, beating is observed in the measured interferogram. The bottom panels show a typical spectrum of a thermal light source (e.g. Globar). Modified from Ref. [143].

Since at high frequencies the thermal broadening of the linewidth is much smaller than the probed energy ($k_B T \ll \hbar\omega$), the detectors can operate at ambient conditions. At lower frequencies, however, temperature causes significantly blurred band gap which reduces the sensitivity. Hence, the detectors need to be cooled in the infrared and lower frequency ranges. While the near- and mid-infrared detectors, based on InSb and MCT (mercury cadmium telluride), respectively, are cooled by liquid nitrogen (77 K), the bolometer employed in the far-infrared is cooled by liquid He down to 4 K. To measure below 100 cm^{-1} it is even necessary to pump on the He bath to lower the temperature down to 1.5 K in its superfluid phase. Typically, the detectors remained cold for 8 - 12 hours once filled with cryoliquids. If the experiment required, they were refilled.

Frequency range	Light source	Beamsplitter	Detector	Window material
10 – 60 cm^{-1}	Hg Lamp	50 μm Mylar	Si Bolometer 1.5 K	Polyethylen, Polypropylen
30 – 100 cm^{-1}	Hg Lamp	23 μm Mylar	Si Bolometer 1.5 K	Polyethylen, Polypropylen
50 – 700 cm^{-1}	Hg Lamp	6 μm Mylar	Si Bolometer	Polyethylen
500 – 8.000 cm^{-1}	Globalar	Ge on KBr	MCT 77 K, DTGS	KBr, ZnSe KRS-5
2.000 – 12.000 cm^{-1}	Tungsten Lamp	CaF_2	InSb 77 K	KBr KBr
2.000 – 12.000 cm^{-1}	Tungsten Lamp	CaF_2	Si Photovoltaic	KBr, SiO_2

Table 4.1.1: Due to their characteristic frequency dependence, different light sources, beam splitters, detectors and windows have been used in optical experiments. Modified from Ref. [143].

4.1.2 Optical Cryostats

Depending on the sample size, geometry and absorption properties of the material under investigation, and the studied temperature and frequency range, three different kinds of cryostats were employed to study the optical response of molecular conductors in this thesis. The main focus was on reflectivity measurements at normal incidence in a temperature range of 5 - 300 K, which could be performed in all of these setups.

The *working horse* was a Cryovac coldfinger cryostat placed in the focus of an infrared microscope (Hyperion 1000) attached to an FTIR spectrometer which focused the infrared light on a sub-mm spot, as sketched in Fig. 4.1.3 (a). The smallest aperture corresponds to a spot size of 50 μm diameter which made it perfectly suitable for studying even small organic single crystals. Due to the small focal length (few cm), the microscope cryostat was designed in a very compact way. As a result, the sample was placed only 1 cm distant from the window at room temperature. Thermal radiation from the window limited the lowest accessible temperature to 5 K which was, in most cases, sufficient to cover the thermal region of interest since phase transitions occurred typically at several 10 K to few 100 K. Although transmission experiments were in principle possible, here we confined to reflectance geometry. Importantly, the spectral range extended from the far-infrared up to the visible (100

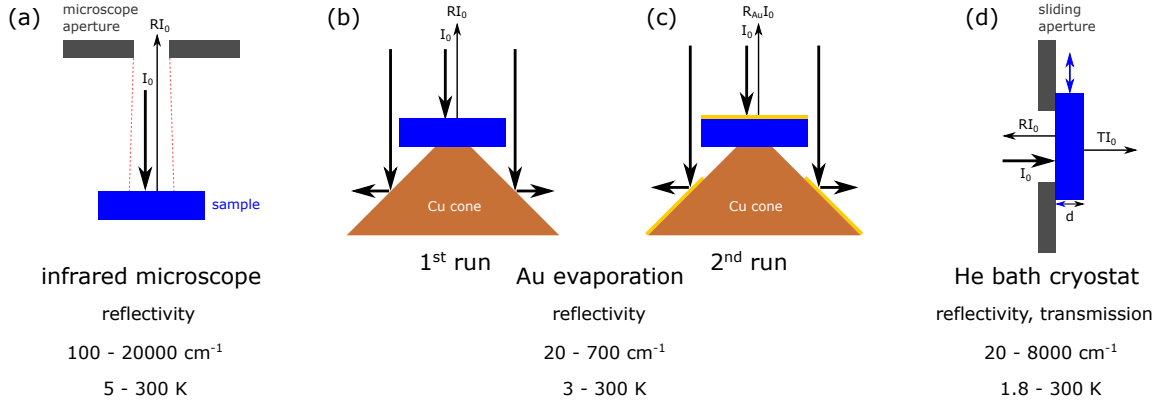


Figure 4.1.3: Three different types of cryostats were employed for low-temperature optical measurements. (a) Small samples (spot size 0.05 – 0.5 mm) required to use the infrared microscope, equipped with a pan-shaped flow cryostat. There, sample and mirror are mounted on independently movable stages which allows to align them parallel to each other in normal incidence geometry. Since the sample is just ≈ 1 cm distant from the window, that is coupled to room temperature, the heat radiation limits the minimum temperature to 5 K. (b,c) In order to get reliable reflectivity values in the far-infrared range, unaffected by diffraction effects due to the small sample size, the gold evaporation technique was applied [144]. For that, the sample was mounted on a cone and the reflectivity was measured once before and once after gold evaporation. At the end, the two values were divided yielding the absolute reflectivity of the material. (d) A sliding aperture system was used in the He bath cryostat, which allowed to measure both R and T . By inserting He exchange gas to the sample chamber, temperatures down to 2 K could be achieved. Experiments were performed from the far-far-infrared up to the near-infrared spectral ranges.

- 20000 cm^{-1}), which allowed to perform broadband optical reflectivity measurements with the sample mounted in one single apparatus.

At lower frequencies the small sample size (several 100 μm) becomes comparable to the wavelength ($\lambda = 100\mu\text{m}$ at $\omega = 100 \text{ cm}^{-1}$) which brings about diffraction problems. Therefore, the gold evaporation technique was employed to obtain reliable reflectivity data in the far- and far-far-infrared spectral ranges [144]. As illustrated in Fig. 4.1.3 (b), the sample was mounted on a copper cone. The light spot was chosen larger than the single crystal such that the incoming light that does not hit the sample is reflected away and, hence, only the intensity reflected back from the sample reaches the detector. In this configuration, polarized spectra were recorded at all temperatures of interest, typically starting at low T and heating towards 300 K. Additionally, the intensity of a gold mirror (I_{Ref}) also mounted in the cryostat was measured as a reference at each temperature. After finishing the first run and arriving

at room temperature, a thin gold layer (several 100 nm¹) was deposited on the sample surface (c) by thermal evaporation of several gold wires attached to a tungsten heating wire. Subsequently, spectra of the gold-coated sample were measured in the same sequence as in the first run, i.e. starting again at the lowest temperature. Afterwards, the sample reflectivity is computed as

$$R = \frac{I_{sample} I_{Ref,gold}}{I_{sample,gold} I_{Ref}}, \quad (4.1.1)$$

where the index *gold* indicates the measurement run with the gold coated sample. Note that the reference mirror is mounted far away from gold evaporation and no gold was deposited on it. After all, the shape of the single crystal cancels out exactly since the sample acts as its own mirror. While providing reliable reflectivity values, the drawback of this technique is that organic materials typically do not survive this procedure; while the external shape remains intact, the electronic properties may be modified due to the strong heating upon gold evaporation². Thus, the gold evaporation experiment was usually performed as the last step.

The two setups described so far provide a reliable broadband reflectivity, the temperature is limited to 5 K due to the fact that the sample resides in vacuum and heat exchange is limited to the gluing points. In particular when a material becomes insulating, the heat load introduced from the thermal radiation of the window or the light source (which is also just a heat emitter) can not be dissipated efficiently. Therefore, measurements in the superconducting state of, e.g., β'' -(BEDT-TTF)₂SF₅CH₂CF₂SO₃ required to use the He bath cryostat that can be cooled down to 2 K with exchange gas in the sample chamber. As sketched in Fig. 4.1.3 (d), a sliding aperture was used which was inconvenient to use for a sample size smaller than 0.5 × 0.5 mm; for a reasonable signal-noise ratio, single crystals should have at least mm-size. Since both the sample and reference intensities depend on the same aperture size and shape (circular), diffraction effects cancel out. This setup is suitable for measurements in both reflection and transmission geometries – not at the same time, of course. The next section explains the preferred type of measurement for different absorption properties of the sample.

¹The thickness of the deposited gold layer was larger than the skin depth.

²Consider a piece of wood that turns into coal upon heating in an oxygen-free atmosphere.

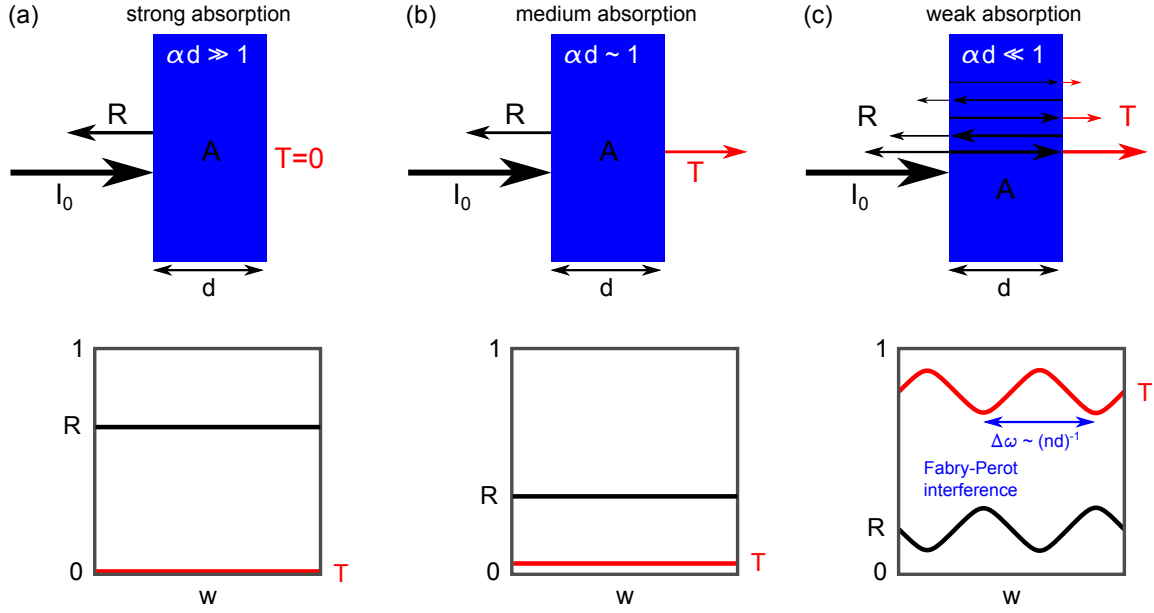


Figure 4.2.1: The geometrical and absorption properties of a sample determine the possible measurement geometry. The lower panels show exemplary reflectivity and transmission spectra for the respective situation. (a) For a strongly absorbing and sufficiently thick specimen ($\alpha d \gg 1$) the transmission is negligibly small allowing for reflectivity measurements only. (b) In case of intermediate absorption ($\alpha \approx \gg 1$) both reflectivity and transmission can be probed. (c) Weakly absorbing materials ($\alpha d \ll 1$) bring about multiple internal reflections contributing to R and T . Parallel alignment of the front and back surfaces of the sample gives rise to interference effects. As a result, well-defined Fabry-Perot oscillations appear in the reflectivity and transmission spectra; the periodicity is inversely related to the sample thickness d and refractive index n .

4.2 Geometry of Optical Measurements

Depending on the material properties, sample size and geometry, different schemes of optical measurements are preferred, applicable or even impossible. Fig. 4.2.1 sketches three regimes of optical density αd as a measure of the intensity absorbed upon propagation through the sample (cf. Equ. 2.1.23).

Panel (a) illustrates the regime of strong absorption ($\alpha d \gg 1$) with basically zero transmission through the sample. Such a situation represents the large majority of experiments conducted in this thesis and is usually realized in the low-frequency response of metals as well as at the resonance of interband transitions and vibrational features. While such large optical densities rule out any transmission experiments, reflectivity can be measured very accurately. Having a data set over a broad frequency range enables to calculate the complex optical response functions via the Kramers-Kronig relations (cf. section 2.1.2). The extrapolations outside the measured range

will be discussed in section 4.2.1.

In a regime of intermediate absorption (b), for example when a gap opens in the course of a metal-insulator transition, it is possible to probe both R and T on the very same sample, in different measurement runs, of course. Transmission can be determined reliably in the range $T = 10^{-3}$ - 10^{-1} allowing for direct calculation of σ_1 and σ_2 from R and T using the Fresnel equations at normal incidence (Equ. 2.1.13) and the Lambert-Beer-law (Equ. 2.1.23).

For a very small optical density ($\alpha d \ll 1$), however, the reflected signal is affected by contributions from the sample back side making it difficult to determine the exact value of R . Due to lacking absorption, the light is multiply reflected inside the sample giving rise to interference effects. In case of parallel sample surfaces and normal incidence, this is nothing but a (weakly) damped Fabry-Perot resonator. Accordingly, characteristic oscillations appear in both reflectivity and transmission spectra, with a periodicity $\Delta\omega = \frac{2\pi c}{2nd}$, i.e. inversely related to the optical path upon propagation through the sample and back again. Therefore, such an experiment allows to determine the real part of the refractive index n very accurately, given the sample thickness is known. Vice versa, measuring the reflectivity on a thick sample allows for precise determination of d from the Fabry-Perot resonances observed for a thin sample. Moreover, combination of Equ. 2.1.13 and 2.1.23 enables to obtain n and k directly from single-peak fits of the oscillating transmission [145]. While such a procedure results in very accurate absolute values of σ_1 and σ_2 , as it requires just a single measurement, the frequency resolution is limited to the separation of the maxima and minima of T . In principle, a similar procedure is also applicable in reflection geometry. However, this can only work if R is probed on a free-standing single crystal since reflections from any material behind the sample may contribute to the measured signal.

4.2.1 Reflectivity Measurements and Extrapolation

Typically, the optical density αd of the investigated samples was large in the measured frequency range such that the intensity at the sample back side was basically zero. As discussed above, for such strongly absorbing materials the reflectivity is determined very accurately. Still, the raw data of the respective frequency ranges are usually slightly offset as the measurements were performed in different setups (see section 4.1) using the corresponding light sources, beam splitters, windows and detectors. Fig. 4.2.2 (a) illustrates the assembly of the broadband reflectivity by multiplicatively shifting the raw data to match with the mid- and far-infrared ranges

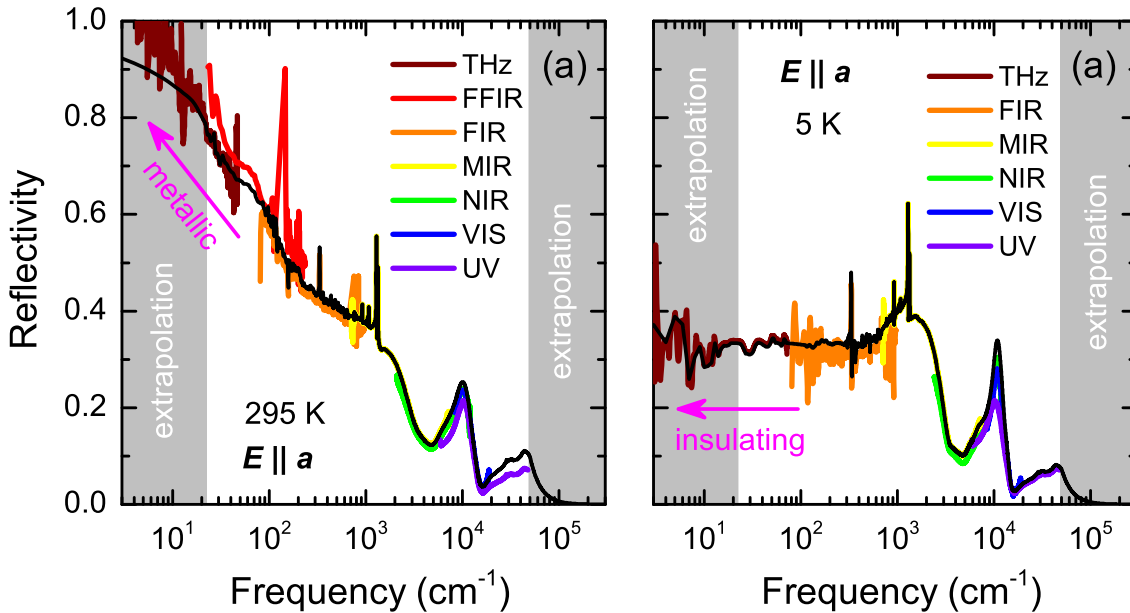


Figure 4.2.2: (a) The broadband optical reflectivity (here shown for β' - $\text{EtMe}_3\text{Sb}[\text{Pd}(\text{dmit})_2]_2 E \parallel a$ at 295 K) was assembled from several measurements covering a distinct frequency range each. Due to measurements in different setups (cf. section 4.1.2), the raw data (colour) may be slightly offset with respect to each other. They were merged by shifting R multiplicatively, yielding the final reflectivity curve (black). Outside the measured range, the data were extrapolated towards low- and high frequencies (grey areas) as described in the text. (b) The optical conductivity was determined from the reflectivity and phase shift Φ , which was calculated upon performing the corresponding Kramers-Kronig integration on $R(\omega)$ (cf. Equ. 2.1.21).

where the absolute values are most reliable. The merged reflectivity curve was then multiplied by the reflectivity of gold [146], which the reference mirrors were made from.

Since the Kramers-Kronig relations imply integration from $\omega = 0$ up to infinity, the data have to be extrapolated several orders of magnitude outside the measured range. While at high frequencies the common ω^{-4} decay was assumed up to 10^6 cm^{-1} , the low-frequency behaviour of the reflectivity depends strongly on the conduction properties. Since there are no additional excitations inside the gap of an insulator that appear towards $\omega \rightarrow 0$, the reflectivity should remain constant. On the other hand, a metallic Drude response yields the characteristic Hagen-Rubens response with $R = 1 - \sqrt{\omega}$ well below the scattering rate. Low-frequency extrapolation was performed down to 10^{-3} cm^{-1} .

In the course of a metal-insulator transition, many spectra are between these two limiting cases – at least in the measured frequency range – so a generalized Hagen-

Rubens response was applied

$$R(\omega) = a - b\omega^{-n}, \quad (4.2.1)$$

which reproduces metallic and insulating behaviour for $n = 1$ ($a = 1$) and $n = 0$ ($a < 1$, $b = 0$), respectively. In the intermediate cases, a smooth extrapolation is realized upon varying n to fit the slope of the reflectivity³. For the lowest measured reflectivity data point $R_0 = R(\omega_0)$ the factor b is determined as $\frac{a-R_0}{\omega_0^n}$. If dc or dielectric transport data were available, the constant a was iteratively modified such that the temperature-dependent trend of $\sigma_1(\omega = 0, T)$ matched with that of $\sigma_{dc}(T)$ ⁴. These modifications, however, influence only the data points at the lowest frequencies, typically $\omega < 100 \text{ cm}^{-1}$. The data in the most relevant FIR and MIR ranges, used for analysis and interpretation of the intrinsic physics, were not affected significantly. Fig. 4.2.2 (b) shows the optical conductivity calculated from the reflectivity shown in panel (a).

4.2.2 Transmission Measurements

When absorption is reduced ($\alpha d \leq 1$) the material becomes transparent and the optical transmission can be accessed experimentally. In case of small transmission ($T = 10^{-3}$ - 10^{-1}), the proportion of intensity transmitted through the sample, reflected at its back side and transmitted in the same direction as the primary reflection is smaller than the error bar of the reflectivity measurement. Hence, the back-side contribution does not affect $R(\omega)$ significantly, which remains a reliable measurement quantity. Having both reflectivity and transmission⁵ in the same frequency range allows for direct calculation of the optical conductivity without using the Kramers-Kronig relations.

Fig. 4.2.3 shows the reflection and transmission and the corresponding optical conductivity of a thin Herbertsmithite-like crystal. Due to the large optical gap of more than 3 eV, this material is transparent in the entire visible region; the weak absorption feature around 14000 cm^{-1} , which covers the red spectral range, leads to the characteristic blue-green colour [48].

³Typically, the reflectivity was plotted on a lin-log scale to view the whole data set simultaneously.

⁴Due to significant uncertainty in determining the geometry factor of organic samples, the absolute values of σ_{dc} involve considerable inaccuracy.

⁵Of course, one also needs to determine the sample thickness which can be done either with an optical microscope or by evaluating the Fabry-Perot resonances in a different frequency range.

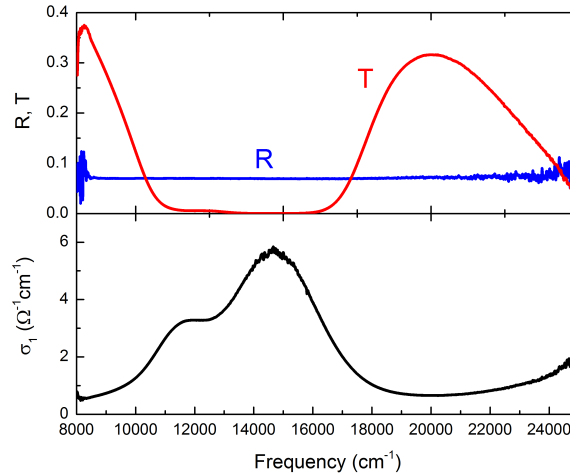


Figure 4.2.3: (a) Due to the opening of the Mott gap at low temperatures, the absorption is significantly reduced at low frequencies. Thus, it was possible to measure both the reflectivity and transmission. (b) $\sigma_1(\omega)$ was calculated directly from R and T without using the Kramers-Kronig relations and the corresponding extrapolations. The data shown here correspond to a Herbertsmithite-like compound [48].

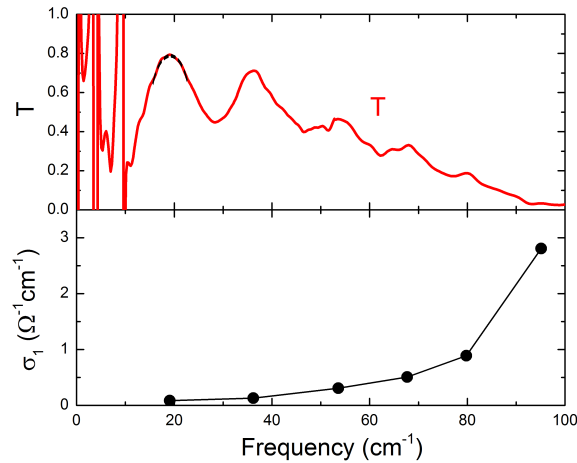


Figure 4.2.4: (a) For very weak absorption, for instance deep within the gap of a Mott insulator ($\omega \ll \Delta$), the transmission becomes comparable to the reflectivity or even larger. As a result, Fabry-Perot oscillations appear in the spectrum due to interference of multiple reflections within the material. (b) Upon fitting the oscillations close to the extrema, the optical conductivity can be determined self-consistently from the transmission data only. The frequency resolution, however, is limited by the number of extrema as the fit is accurate only close to the maxima and minima. The data shown here correspond to a Herbertsmithite-like compound [48].

Fig. 4.2.4 shows the transmission at much lower frequencies, deep inside the Mott gap, which is significantly larger and exhibits pronounced Fabry-Perot oscillations. Also the reflectivity shows such oscillating character and, thus, can not be determined

accurately any more. As indicated, the transmission can be fitted locally around the extrema by simple Fabry-Perot oscillations. The absorption coefficient, however, is different at each minimum or maximum reflecting the frequency dependence of the optical conductivity⁶. Therefore, one obtains one pair of n and k per extremum, resulting in an optical conductivity as plotted in Fig. 4.2.4 (b).

4.2.3 Sample Preparation

The organic single crystals investigated here typically grow in plate-like shape with dimensions ranging from $0.3 \times 0.1 \times 0.05$ mm (β'' -Ga) to $4 \times 3 \times 0.5$ mm (β'' -(BEDT-TTF)₂SF₅CH₂SO₃). For reflection measurements in the microscope cryostat the samples were glued by conductive carbon paste onto a small piece of copper to facilitate handling of these fragile materials. The orientation was chosen appropriately to access the respective crystal axes (in-plane or out-of-plane). The copper plate was then attached to the sample holder by silver paint and the sample and mirror intensities were aligned to maximum.

For the gold evaporation technique, the sample was glued on a copper cone which was then aligned to be parallel to the reference mirror. In transmission geometry, up to two samples were mounted on the sample holder of the He bath cryostat.

Specific modifications will be described circumstantially together with the results.

4.3 Determination of Band Parameters and Fitting Procedures

After obtaining the optical conductivity from the experimental raw data, several specific methods were applied to extract the relevant quantities, such as the Coulomb repulsion terms U and V , as well as the bandwidth W . It will also be discussed how the resonance frequencies of vibration modes, the crucial parameters for determination of the molecular charge, were determined via fitting procedures according to the Fano and Lorentz models. In addition, different ways of plotting the data will be reminded briefly in the context of physical quantities that show a power-law frequency or temperature dependence.

⁶Although one can define a charge gap in on linear scales, e.g. by defining the band edge as the intercept of the largest slope of $\sigma_1(\omega)$ or any other criterion, the optical conductivity is not zero *inside* the gap. Instead, it decreases towards $\omega = 0$ until it finally approaches σ_{dc} at $\omega = 0$, which is small, but finite at $T > 0$.

4.3.1 Mott-Hubbard Band Analysis

As discussed in section 2.3.3, the parameters of the extended Hubbard model express in the density of states (DOS) which is mapped in the optical conductivity via interband transitions. Specifically, the transitions from the lower (LHB) to the upper (UHB) Hubbard band in the DOS, form a distinct feature in the optical spectrum, denoted as the Mott-Hubbard band. The maximum position ω_{max} corresponds to the effective Coulomb repulsion, e.g. $U_0 - V_0$ for a Mott insulator emerging from a nominally half-filling band. This effective potential energy upon the transfer of one electron to its neighbouring site is crucial for charge transport; for simplicity, it will be denoted just as U in the following. As mentioned in section 2.3.3, the width of the Hubbard bands W is smaller than the bare bandwidth W_0 ; the Mott-Hubbard band observed in optical spectroscopy has a width of $2W$ ⁷ since transitions across the Mott gap occur from the bottom of the LHB to the top of the UHB. As W is different from W_0 by a factor $\sqrt{2}$ at most [74], the optically determined U/W ratio remains a good approximation of the intrinsic correlation strength. It should be pointed out that there is no other method that simultaneously probes the band shapes of both the LHB and UHB⁸. Therefore, this is the only way to access the correlations of a Mott insulator experimentally, which can be then compared to theoretical calculations.

Fig. 4.3.1 (a) shows a typical spectrum of a Mott insulator where the condition for the single-band Hubbard model – there is only one band close to the Fermi energy – is satisfied well at low frequencies. At higher energies, however, different kinds of inter-band excitations come into play which leads to an asymmetric background on top of which the Mott-Hubbard band appears. Obviously, applying the FWHM criterion to extract the bandwidth does not work as the high-frequency part is superimposed by additional contributions. Therefore, W was extracted as the half-width at half-maximum (HWHM) on the low-frequency side and U is approximated as the maximum position. This method takes into account that the ground state physics is governed mainly by the low-energy properties; it was applied in the analysis of the three quantum spin liquid compounds β' -EtMe₃Sb[Pd(dmit)₂]₂, κ -(BEDT-TTF)₂Ag₂(CN)₃ and κ -(BEDT-TTF)₂Cu₂(CN)₃ presented in section 5.1. In the course of the Mott MIT, spectral weight is successively shifted from high to

⁷Depending on the applicability to the respective data sets, it will be either the full-width at half-maximum (FWHM) or another criterion that can be applied in a consistent way.

⁸While photoemission spectroscopy is typically the method of choice to determine the band structure, it probes only the occupied states, i.e. the LHB in case of a Mott insulator. However, one needs to map also the UHB to describe the complete effect of correlations, not to mention about the technical difficulties of measuring ARPES on charge-transfer salts.

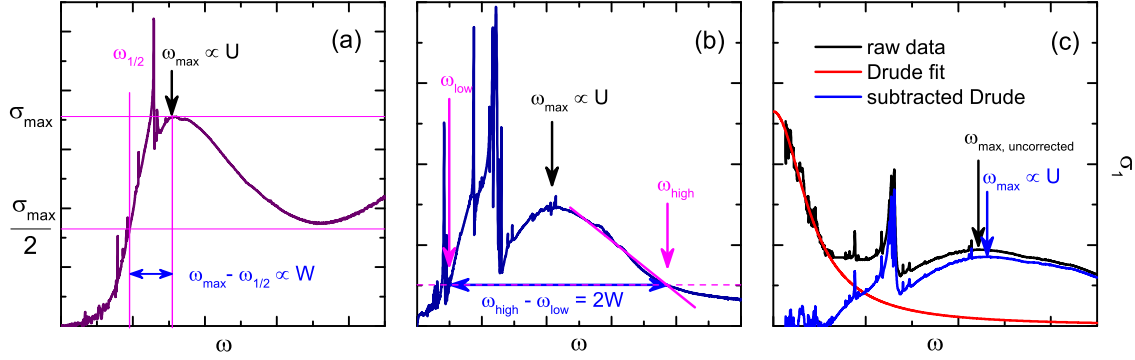


Figure 4.3.1: The bandwidth W and Coulomb repulsion U were extracted in two different ways from the Mott-Hubbard bands in the optical conductivity. (a) For insulators, such as the quantum spin liquid compounds, U was determined from the peak position ω_{max} whereas W was taken as the half-width at half-maximum. (b) On the other hand, for materials subject to a metal-insulator transition, in particular the κ -STF_x series, the high-frequency tail was linearized and the point where σ_1 starts to deviate from this line defines ω_{high} . At the low-frequency side, the frequency at which the conductivity is equal to $\sigma_1(\omega_{high})$ corresponds to ω_{low} . The bandwidth is defined as $W = \frac{1}{2}(\omega_{high} - \omega_{low})$. (c) In the metallic state, a low-frequency Drude contribution was subtracted in order to localize the real peak position $\omega_{max} \propto U$.

low energies, as observed in the κ -STF_x series (section 5.3). As a result, a finite contribution arises at $\omega = 0$ which would imply that the above procedure yields the same values of U and W since the optical conductivity below the maximum of the Mott-Hubbard band is always larger than $\sigma_1/2$. Thus, another criterion was applied to determine the bandwidth, which is illustrated in Fig. 4.3.1 (b). The upper boundary of the band was determined as the frequency where the linearly approximated decay of the band starts to deviate from σ_1 . The lower band edge was then defined as the point $\sigma_1(\omega_{low}) = \sigma_1(\omega_{high})$ on the low-frequency side. The bandwidth is then determined simply as $W = (\omega_{high} - \omega_{low})/2$. In particular, $\omega_{low} = 0$ for a metallic response, but not necessarily $W = U$. This procedure naturally results in slightly different values (10 - 15 %) of W as compared to the extraction from the low-frequency HWHM. One should, however, have in mind that the error bar is of similar size ($\approx 10\%$); within one set of data one should use the one method consistently to allow for quantitative comparison.

In case of a large Drude contribution, U could not be determined simply as the maximum position of the Mott-Hubbard band due to the frequency-dependent contribution of the Drude tail. Such a background shifts ω_{max} towards lower frequency. Upon fitting and subtracting the low-frequency Drude response, the real position of the maximum is recovered. W is determined similarly as in the previous paragraph.

4.3.2 Vibrational Modes

Vibrational modes were fitted according to the Lorentz or Fano models (cf. section 2.2.3). In case of strongly insulating behaviour, e.g. in the out-of-plane response of layered molecular conductors, the electronic background is small and weakly frequency-dependent. Hence, the vibrational features are symmetric and can be fitted with a standard Lorentz function. On the other hand, the large optical conductivity of the Mott-Hubbard and Drude contributions in the far- and mid-infrared spectral ranges is typically subject to strong frequency-dependent modifications upon a metal-insulator transition. The vibration modes are, thus, strongly affected by the electronic background and, generally, acquire an asymmetric shape. Fig. 4.3.2 illustrates how the background was approximated, which increases with frequency in this case; the overall fit including a Fano function with negative coupling parameter q approximates the feature very well.

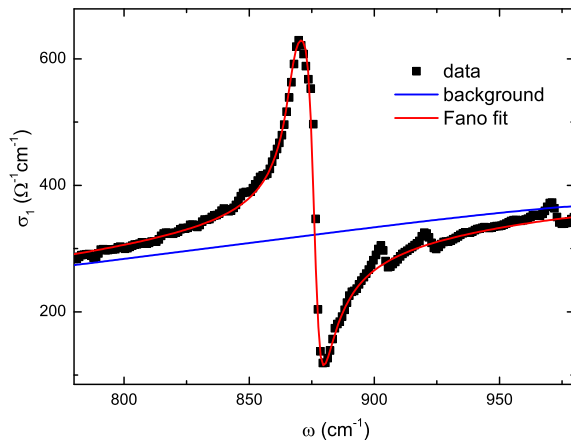


Figure 4.3.2: Exemplary Fano fit of an asymmetric vibration mode on an electronic background increasing with frequency. The experimental data points correspond to the optical conductivity of κ -(BEDT-TTF) $_2$ Cu $_2$ (CN) $_3$ ($E \parallel c$) at 20 K. Since the high-frequency wing of the feature is lowered and vice versa for the low-frequency part, a negative coupling parameter q was necessary for the fit.

4.3.3 Power-Law Exponents

Since many physical properties (resistivity, optical conductivity, spin susceptibility, etc.) are related to external tuning parameters (temperature, frequency, pressure, etc.) via power laws, typical procedures of data representation will be quickly reca-

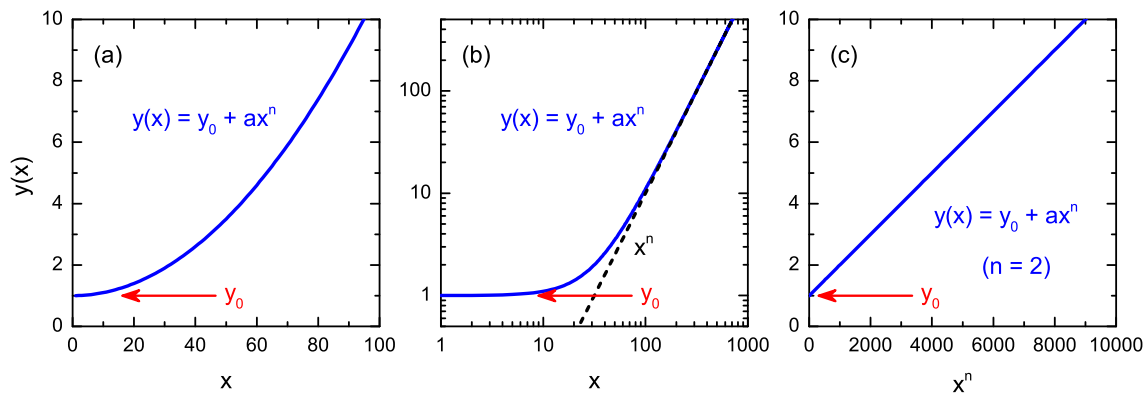


Figure 4.3.3: (a) A simple power-law function y with a constant offset y_0 is plotted on linear scales. (b) The double-logarithmic representation facilitates identification and extraction of the exponent n , which is nothing but the linear slope in the log-log plot. (c) For a known exponent, plotting versus x^n yields a line which is particularly useful for determining the prefactor a . Here, we used the exponent $n = 2$.

pitulated. Fig. 4.3.3 illustrates a simple power law function

$$y(x) = y_0 + ax^n \quad (4.3.1)$$

with an offset y_0 , prefactor a and exponent n .

Of course, iterative fitting is always an option to find the underlying parameters. Using the correct scales, however, facilitates data presentation and analysis. While linear representation allows only for identification of the offset, at sufficiently high frequencies ($ax^n \gg y_0$) the slope of the log-log plot reveals the specific exponent. A large frequency range, several decades if possible, is required for a high accuracy of the determined exponent. When the exponent is known, it is useful to plot y versus x^n which enables to determine the prefactor a from the slope.

4.4 dc Transport

In addition to optical experiments, most samples were characterized by dc transport experiments. In particular, the resistivity was measured *in situ* to check that the β'' -(BEDT-TTF) $_2$ SF $_5$ CH $_2$ CF $_2$ SO $_3$ single crystal was indeed superconducting during acquisition of optical spectra, as presented in section 6.1.4. The vast majority of these temperature-dependent resistivity measurements, however, were performed by master students and colleagues; the respective contributions will be mentioned appropriately. At this point, I would like to emphasize the work of Anja Löhle

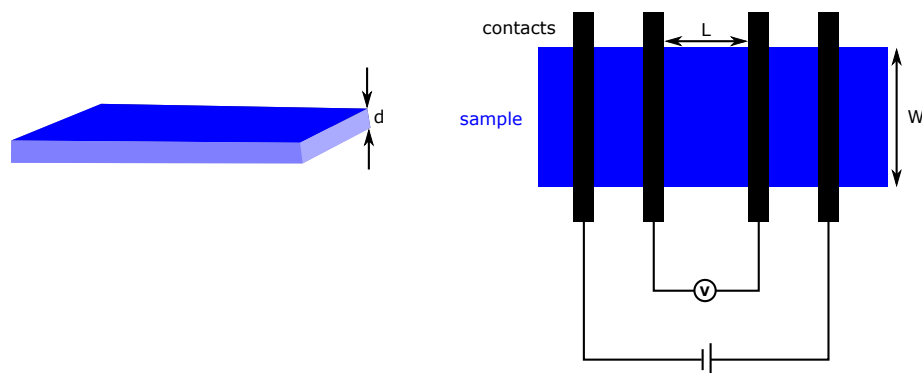


Figure 4.4.1: The material-specific resistivity is determined from the sample resistance normalized to the geometry, i.e. the channel length L and cross section A . For a rectangular shape $A = Wd$. Four contacts are used, where the outer two are connected to the current source whereas the voltage is measured at the inner two. Such a configuration ensures that no contact resistance is measured, which is particularly important for metallic samples with low resistance.

who complemented the optical results presented here by comprehensive pressure-dependent resistivity measurements, whenever necessary also with applied magnetic field. While, for the sake of completeness, I will show some plots of her results to complement my optical data, a detailed analysis of the transport investigations will be presented in her PhD thesis, which should be finalized soon after this work.

As shown in Fig. 4.4.1, the standard four-point method was applied to determine the material-specific resistivity ρ from the sample resistance R via

$$\rho = \frac{A}{L}R, \quad (4.4.1)$$

where L is the channel length and A is its cross section, typically the product of the width W and thickness d for rectangular shape.

4.5 SQUID Magnetometry

Similar as the electrical transport properties, the magnetic susceptibility χ yields important information on the general properties of the electronic system. This measurement quantity is particularly sensitive to the spin state giving unique insight on magnetic ordering, such as ferro- or antiferromagnetic arrangement of the magnetic moments (cf. Fig. 2.3.7), which may appear on top of a possible charge redistribution, for instance.

In general, parallel alignment of the spins leads to a net magnetization oriented

To avoid the use of glue or any other adhesive material to fix the specimen in the middle of a plastic tube, the material was put into a small piece of aluminum foil⁹. This simple metal is well-suited for magnetic measurements due to its small paramagnetic susceptibility that does not change much between room temperature and 2 K. After finishing the experiment, the sample was taken out and the aluminum was measured again with the same sequence (identical magnetic field, cooling rate, waiting time, etc.). The sample mass was determined before and afterwards to exclude residues in the reference. Finally, the magnetic moment of the sample was determined as

$$\mu = \mu_{total} - \mu_{Al}, \quad (4.5.1)$$

i.e. the difference between the first measurement (Al + sample) and the aluminum reference.

In order to obtain the magnetic susceptibility in units emu/mol, the magnetic moment has to be normalized with respect to the sample mass and magnetic field

$$\chi = \frac{\mu}{NB} = \frac{M\mu}{mB}, \quad (4.5.2)$$

where N is the number of moles determined from the ratio of the sample mass m and molar mass M ¹⁰. Since one (BEDT-TTF)₂X formula unit contains two organic molecules, the value of χ automatically corresponds to one unpaired electron.

As we are primarily interested in the temperature-dependent susceptibility of the correlated charge carriers, we have to subtract the temperature-independent diamagnetic contribution of the core electrons

$$\chi_{el}(T) = \chi(T) - \chi_{core}, \quad (4.5.3)$$

which yields the pure response of the unpaired electrons. The contribution of the paired core electrons χ_{core} can be approximated by summing up Pascal's constants of all atoms and bonds [148]. In organic conductors, such as θ -(BEDT-TTF)₂I₃, χ_{core} is in the same range as the contributions of Pauli paramagnetism and Landau diamagnetism¹¹ from the conduction electrons [149]. For small samples, however, there

⁹The mass of the aluminum foil was typically a few mg, i.e. in the same order of magnitude as the sample mass. Ideally, it should not exceed the sample mass too much since the larger total magnetic moment requires to use a high range in the measurement setup, which implies reduced sensitivity and larger noise in the final data after subtraction of the Al reference.

¹⁰To keep the units consistent, the magnetic field has to be inserted in cgs units, i.e. 1 G = 10⁻⁴ T. Conversion to SI units is done simply by multiplying 4 π , i.e. 1 emu/mol = 4 π cm³/mol [147].

¹¹In uncorrelated metals the contributions of the conduction electrons are of similar size

is also considerable inaccuracy due to subtraction of the reference which complicates assignment of absolute values. To circumvent this issue, the SQUID data determined here were shifted by a constant value to match the temperature dependence of the susceptibility measured by electron spin resonance (ESR), which inherently probes the response of unpaired spins only. The applied shift accounts for both the diamagnetic and experimental corrections.

$\chi_{Landau} = -\frac{1}{3}\chi_{Pauli}$ [57].

5. Results I: Genuine Mott Physics in 1/2-filled (BEDT-TTF)₂X

Quasi two-dimensional organic conductors with dimerized molecules possess effectively half-filled electronic bands. Since the occupied states of the anions are sufficiently far away from E_F , these materials are ideal candidates to study the physics of genuine Mott insulators on the single-band Hubbard model [11, 12]. Comprehensive optical measurements are carried out to map the electrodynamic response, particularly the transitions between the Hubbard bands. In the first section we investigate the three quantum spin liquids β' -EtMe₃Sb[Pd(dmit)₂]₂, κ -(BEDT-TTF)₂Ag₂(CN)₃ and κ -(BEDT-TTF)₂Cu₂(CN)₃ in order to probe the pristine Mott state in the absence of magnetic order. Extracting the bandwidth W and Coulomb repulsion U allows us to determine the degree of electronic correlations U/W and compose, for the first time, a unified phase diagram of *all* Mott insulators on quantitative scales. Close to the insulator-metal transition we identify metallic fluctuations that become more pronounced upon cooling due to the back-bending of the quantum Widom line, which is established as the true boundary of the gapped Mott state. Comparing the spin liquids with antiferromagnetic compounds yields consistent behaviour in the Mott state whereas the response is strikingly different below T_N . A phenomenological method is used to collapse the phase boundaries on the metallic side for various κ -(BEDT-TTF)₂X, suggesting a general relation of all temperature scales, including T_{MI} and T_c , to the underlying Coulomb interaction U .

Focussing on the region deep inside the Mott gap we find a power-law increase of the optical conductivity with frequency. The exponents and energy ranges differ from the theoretical prediction of spinon excitations [18]; thus we assign them to the low-frequency wing of the Mott-Hubbard band. Upon subtracting this background from the data of β' -EtMe₃Sb[Pd(dmit)₂]₂, a broad absorption is revealed in the THz and far-infrared range which extends up to $\hbar\omega \approx J$ at high energies. It is tempting to assign this feature to spinons, which are well-defined quasiparticles only

for sufficiently small charge excitations [20].

In the third section we scrutinize the bandwidth-tuned Mott transition in κ -[(BEDT-STF)_{*x*}(BEDT-TTF)_{1-*x*}]₂Cu₂(CN)₃. The optical response nicely demonstrates the spectral weight shift upon increasing the chemical substitution *x*. We identify a quadratic frequency dependence of the scattering rate reminiscent of coherent quasiparticles in a Fermi liquid. The effective mass is enhanced upon approaching the Mott transition, obeying the Kadowaki-Woods ratio [30]. The fingerprints of the Fermi liquid, among which we also identify resilient quasiparticles [31], are on fundamental grounds confined by the Ioffe-Regel-Mott limit, both in the dc and optical response.

5.1 Quantum Spin Liquids Unveil the Genuine Mott State

The Widom line identifies the locus in the phase diagram where a supercritical gas crosses over from gas-like to a more liquid-like behaviour. A similar transition exists in correlated electron liquids, where the interplay of Coulomb repulsion, bandwidth and temperature triggers between the Mott insulating state and an incoherent conduction regime. Here we explore the electrodynamic response of three organic quantum spin liquids with different degrees of effective correlation, where the absence of magnetic order enables unique insight into the nature of the genuine Mott state down to the most relevant low-temperature region. Combining optical spectroscopy with pressure-dependent dc transport and theoretical calculations, we succeeded to construct a phase diagram valid for *all* Mott insulators on a quantitative scale. In the vicinity of the low-temperature phase boundary, we discover metallic fluctuations within the Mott gap, exhibiting enhanced absorption upon cooling that is not present in antiferromagnetic Mott insulators. Our findings reveal the phase coexistence region and Pomeranchuk-like anomaly of the Mott transition, previously predicted but never observed.

5.1.1 Electrodynamic Response of Quantum Spin Liquids

Since section 5.1 bases upon a submitted manuscript [13], a considerable amount of information was contained in the associated supplementary materials document. In order to facilitate comprehension by the reader, these supplementary data are separated and will be shown at the place where they become relevant, if possible.

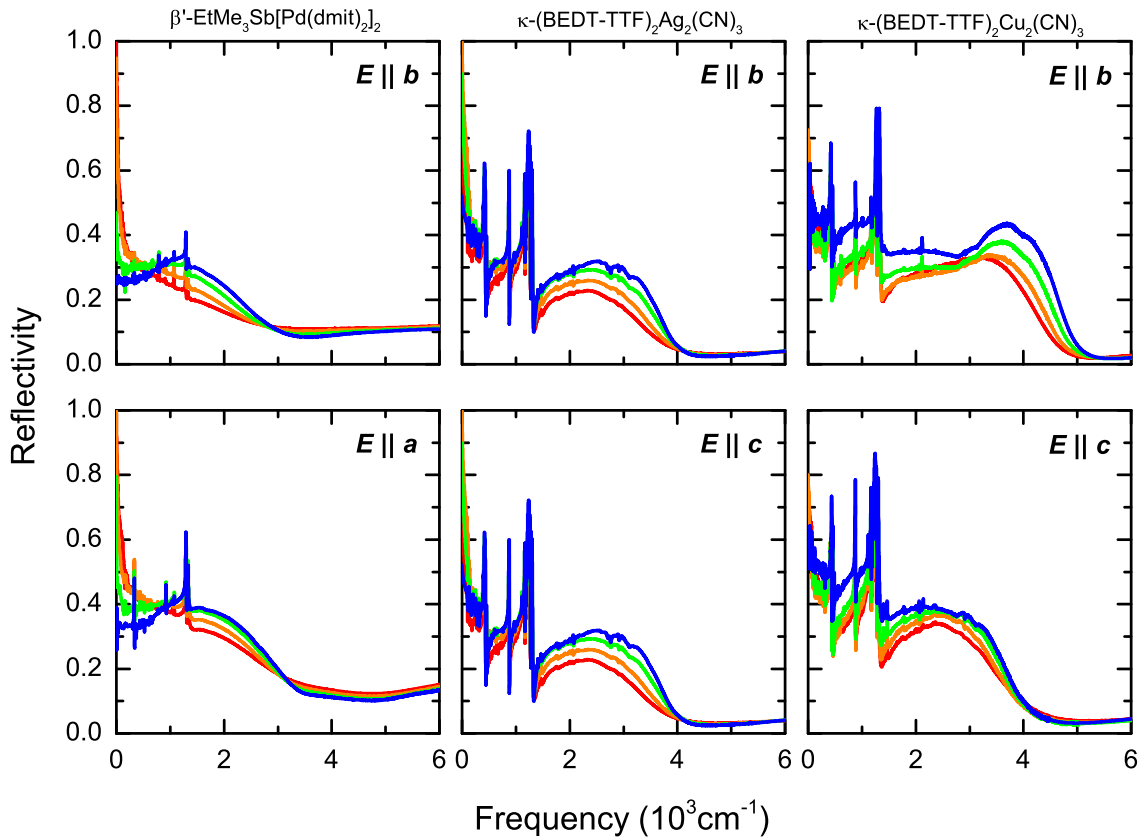


Figure 5.1.1: The temperature-dependent optical reflectivity is plotted for the three Mott insulating quantum spin liquid compounds β' -EtMe₃Sb[Pd(dmit)₂]₂, κ -(BEDT-TTF)₂Ag₂(CN)₃ and κ -(BEDT-TTF)₂Cu₂(CN)₃. The upper panels show the in-plane directions with smallest dc conductivity ($E \parallel b$) whereas the lower panels illustrate the directions of largest conductivity ($E \parallel a$ and $E \parallel c$, respectively). For convenience, only selected temperatures are shown.

Therefore, we present the optical spectroscopy results and explain their basic features right in the beginning without deeper analysis. The most significant findings will be elaborated in detail in the following subsections.

Parts of the optical experiments were carried out and presented in the course of the Master thesis of M. Bories [150]. Fig. 5.1.1 illustrates the broadband reflectivity measured along both in-plane crystal axes of the three studied quantum spin liquid compounds β' -EtMe₃Sb[Pd(dmit)₂]₂ (abbreviated EtMe), κ -(BEDT-TTF)₂Ag₂(CN)₃ (abbreviated AgCN) and κ -(BEDT-TTF)₂Cu₂(CN)₃ (abbreviated CuCN) at selected temperatures. The most relevant absorption processes appear below ≈ 0.5 eV and can be separated into two classes. On the one hand, the broad features correspond to electronic excitations whereas, on the other hand, the narrow resonances stem from lattice phonons and vibrations. In order to assign the bands to the respective

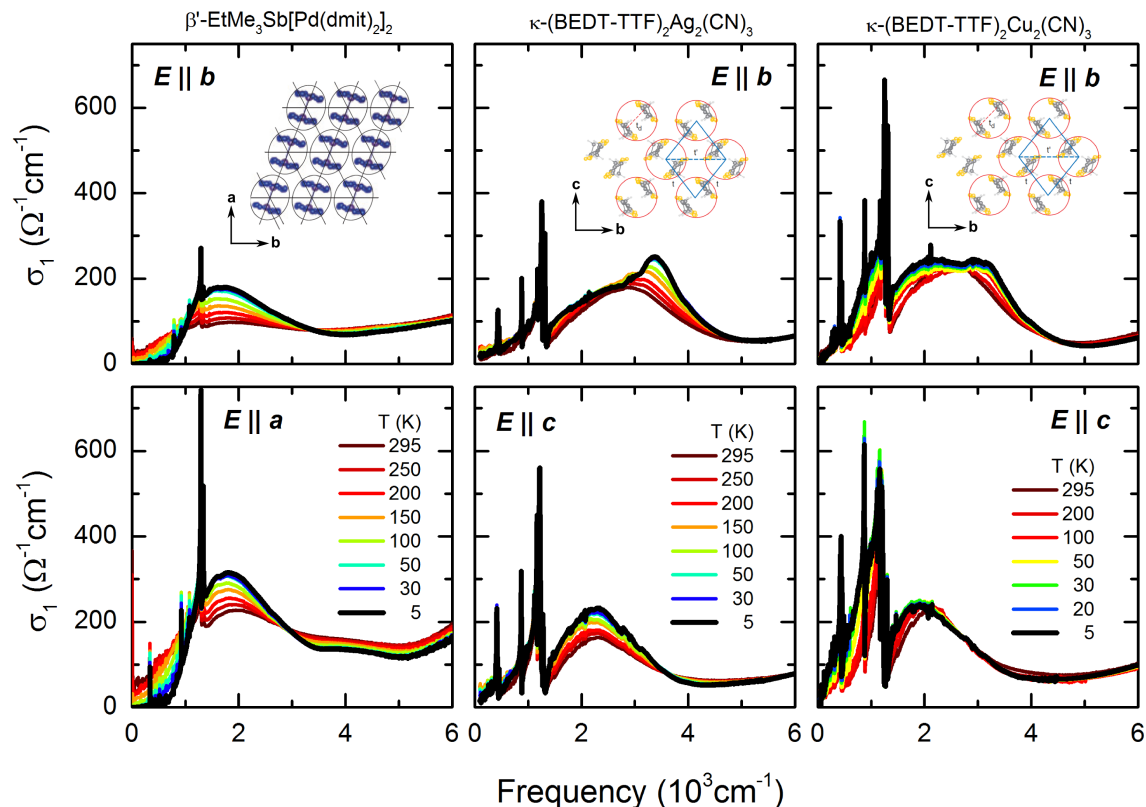


Figure 5.1.2: All spectra are dominated by the electronic transition from the lower to the upper Hubbard bands. The side band occurring around 3500 cm^{-1} for $E \parallel b$ in CuCN and AgCN, and at 4000 cm^{-1} for $E \parallel a$ in EtMe, results from intra-dimer excitations. Apart from phonons and molecular vibrations, the low-frequency optical conductivity shows qualitatively similar properties and temperature dependencies for both polarizations.

physical processes, $\sigma_1(\omega)$ was determined from the broadband reflectivity R using the Kramers-Kronig relations, as circumstantially described in section 4.2.1.

In Fig. 5.1.2 we plot the temperature-dependent optical conductivity for both in-plane polarizations of the three compounds under inspection. In their overall appearance, the spectra are very similar for both polarizations with the most prominent charge excitations around 2000 cm^{-1} . In the two κ -salts, however, the peak splits into a low- and high-energy part for the polarization $E \parallel b$. The latter corresponds to intra-dimer excitations while the former one is related to charge transfer between the dimers; as a result of strong Coulomb repulsion, the conduction band is split into the lower and upper Hubbard bands with transitions between them around 2000 cm^{-1} [21, 151, 152]. Due to the overlapping features, the determination of the maximum of the inter-dimer excitations was less accurate than for the c-direction where the intra-dimer charge transfer is less pronounced. In the case of EtMe, the intra-dimer

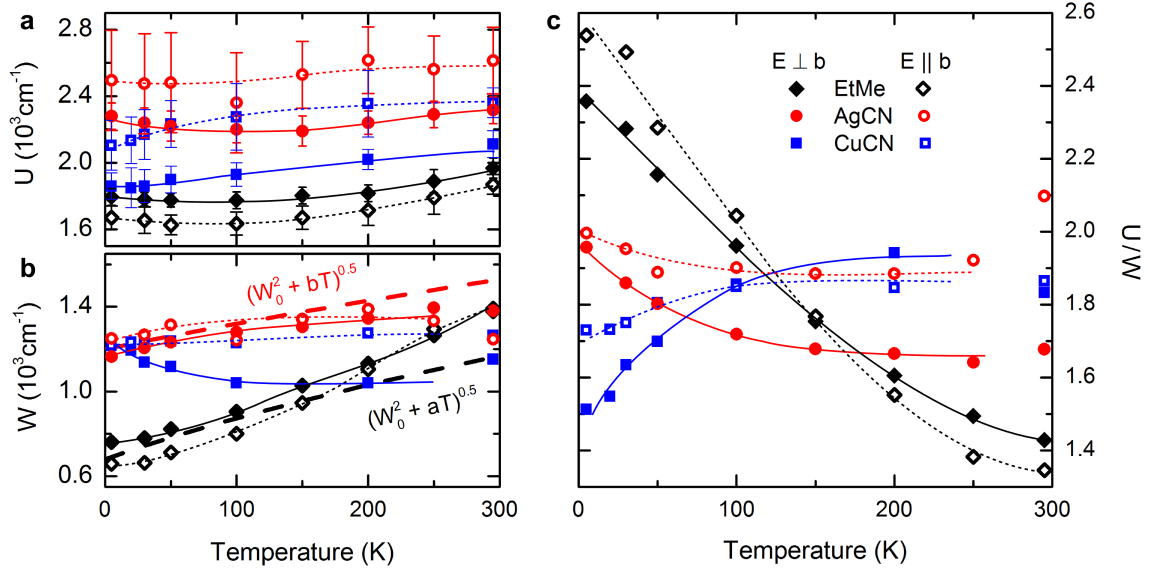


Figure 5.1.3: (a) Temperature dependence of the maximum of the Mott-Hubbard band, which is proportional to U . Due to overlapping inter- and intra-band transitions, the error bar is larger for $E \parallel b$. (b) Half-width at half-maximum of the Mott-Hubbard band $\omega_{max} - \omega_{1/2} \approx W$. The thick dashed lines correspond to a low-temperature approximation of the bandwidth broadening expected for purely thermal excitations [74], which works reasonably well for EtMe and AgCN up to $T \approx 150$ K. (c) The ratio of U and W serves as a measure of electronic correlations and is plotted as a function of T . At the lowest temperature, EtMe is most strongly correlated, followed by AgCN and CuCN. For both crystallographic directions we find a comparable temperature dependence. Dashed and solid lines are guides to the eye.

excitation band appears at much higher frequencies (around 4000 cm^{-1} for $E \parallel a$) because of its stronger dimerization (cf. Table 5.1.1).

We extracted the Mott Hubbard band parameters for both polarizations according to section 4.3.1 from the peak position (U) and the half-width at half-maximum at the low-frequency tail (W), which is plotted in Fig. 5.1.3. Most importantly, the U/W ratio in panel (c) shows qualitatively similar behaviour for both crystal directions. We infer from the lowest temperature data that electronic correlations expressed by U/W decrease in the order EtMe–AgCN–CuCN. The $(U/W)_{exp}$ values in Table 5.1.1 are taken from $E \parallel c$ due to the generally smaller error bar. At low temperatures, the thermal broadening of the bandwidth of EtMe and AgCN nicely follows the theoretically expected temperature dependence [74]. Additional smearing at elevated temperatures might be related to thermal population of low-frequency inter-molecular vibrations. At the lowest temperature, the absolute U/W value is slightly larger along $E \parallel b$ implying stronger correlations. As we will see in

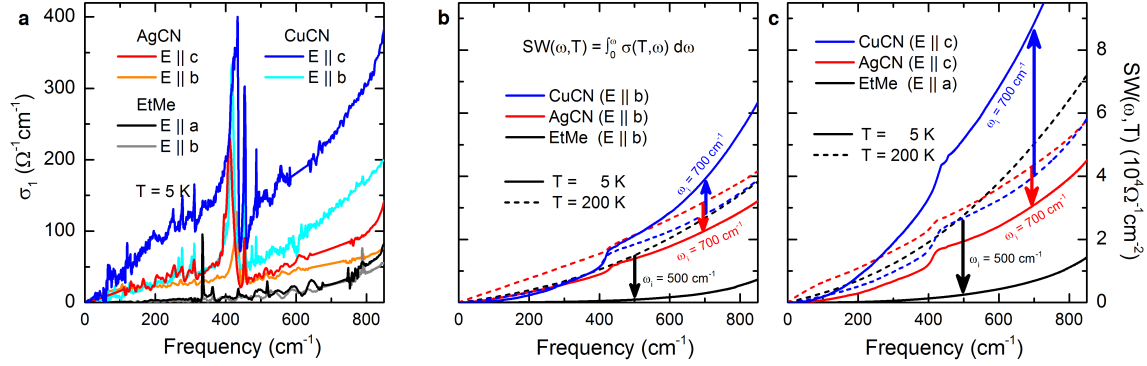


Figure 5.1.4: (a) Low-frequency conductivity of EtMe, AgCN and CuCN for both polarizations shown at the lowest measured temperature. (b,c) Despite the anisotropy, there is no significant difference in the temperature dependence of σ_1 and the spectral weight SW (b,c), as indicated by the arrows. While the SW decreases for the former two compounds, it is enhanced for the latter one upon cooling, which is unexpected for an insulator (cf. Fig. 2.2.2). The arrows denote the frequency ω_i at which the temperature dependence of the spectral weight was compared (500 cm^{-1} for EtMe, 700 cm^{-1} for CuCN and AgCN).

section 5.1.3, this anisotropy is substantially smaller than the insecurity in combining the Widom lines from transport measurements.

Although there is some anisotropy in the dc response [153–155] and optical conductivity, the overall temperature dependence of charge transport is similar for both in-plane crystal axes. As shown in Fig. 5.1.4 (a), in CuCN and AgCN the low-frequency optical conductivity is higher along the c -direction compared to $E \parallel b$, similar to the dc results [153, 154]. This anisotropy is also expressed in the maximum positions of the bands; similar to the transport gap, U is larger for $E \parallel b$ (see Fig. 5.1.3). This observation is explained by the fact that the bandwidth is largest along the c -direction. There is also small anisotropy for EtMe. The overall temperature evolution of the low-frequency response – the behaviour of $\sigma_1(\omega)$ maps onto the spectral weight, that sums up the low-energy excitations due to integration over an extended frequency range – plotted in Fig. 5.1.4 (b) and (c), however, is robust and does not depend on the polarization which assures our assumption that we probe the intrinsic behaviour of the two-dimensional electron gas subject to strong correlations. Having two independent measurements strengthens our conclusions.

For EtMe and AgCN insulating behaviour is consistently found in the dc [154, 155] and low-frequency optical conductivity. For CuCN, however, the sub-gap spectral weight exhibits an anomalous increase upon cooling reminiscent of metallic behaviour despite its insulating transport properties [153]. This non-thermal absorption is known for already more than 10 years [16] and was verified by independent optical

investigations [17]; it triggered an ongoing discussion about the low-energy excitations in this compound and whether they are related to coherent spinons [18]. In the following section, however, we resolve this mystery and assign it to a generic property of the low-temperature Mott metal-insulator-transition, i.e. originating from charge rather than magnetic excitations.

5.1.2 Revealing Electronic Correlations and Pomeranchuk Effect

The Mott metal-insulator transition (MIT) stands out among the key unresolved phenomena in interacting electron systems [2, 43, 44]. Sufficiently strong Coulomb repulsion is able to localize the charge carriers accompanied by a splitting of the nominally half-filled band into the lower (LHB) and upper (UHB) Hubbard bands separated by the Mott gap (Fig. 5.1.5 b). When temperature becomes the dominant energy scale, i.e. comparable to the bandwidth W and on-site Coulomb interaction U , the Hubbard bands are strongly blurred by thermal broadening resulting in an incoherent conduction regime (Fig. 5.1.5 d). While the Mott transition is a well-defined, first-order MIT below the critical endpoint, it shows analogy to the liquid-gas crossover in the supercritical high-temperature region [6, 7], recently associated with quantum critical scaling [14]. In this part of the phase diagram, the quantum Widom line (QWL) defines the boundary of the fully gapped Mott state [5]. A similar description applies to the pseudogap in doped Mott insulators, which underpins the decisive role of Mott physics for high-temperature superconductivity in cuprates [8]. At low temperatures ($k_B T < 10^{-2}W$) magnetic instabilities typically mask the Mott MIT; the antiferromagnetic ground state dominates the low-energy excitations and, due to the Clausius-Clapeyron relation $dp/dT = \Delta S/\Delta V$, the small entropy implies a negative slope of the phase transition (Fig. 5.1.5 f). To circumvent this problem, we study Mott insulators that are currently under scrutiny for their quantum spin liquid ground state (QSL) as a result of large geometrical frustration and disorder [3, 11, 15, 76, 156, 157]. The absence of antiferromagnetism enables us to investigate the genuine Mott state down to $T \rightarrow 0$; due to the large spin degrees of freedom, the phase transition acquires a positive slope reminiscent of the Pomeranchuk effect in ^3He , where the solid (insulator) becomes liquid (metal) upon cooling (Fig. 5.1.5 e). While from theory it is known that the phase diagram is controlled by the ratios T/W and U/W [4, 5], where temperature and Coulomb repulsion are normalized to the bandwidth, experimental studies have not advanced beyond $T - p$ plots so far, inhibiting a quantitative comparison (i) between different compounds and (ii) with

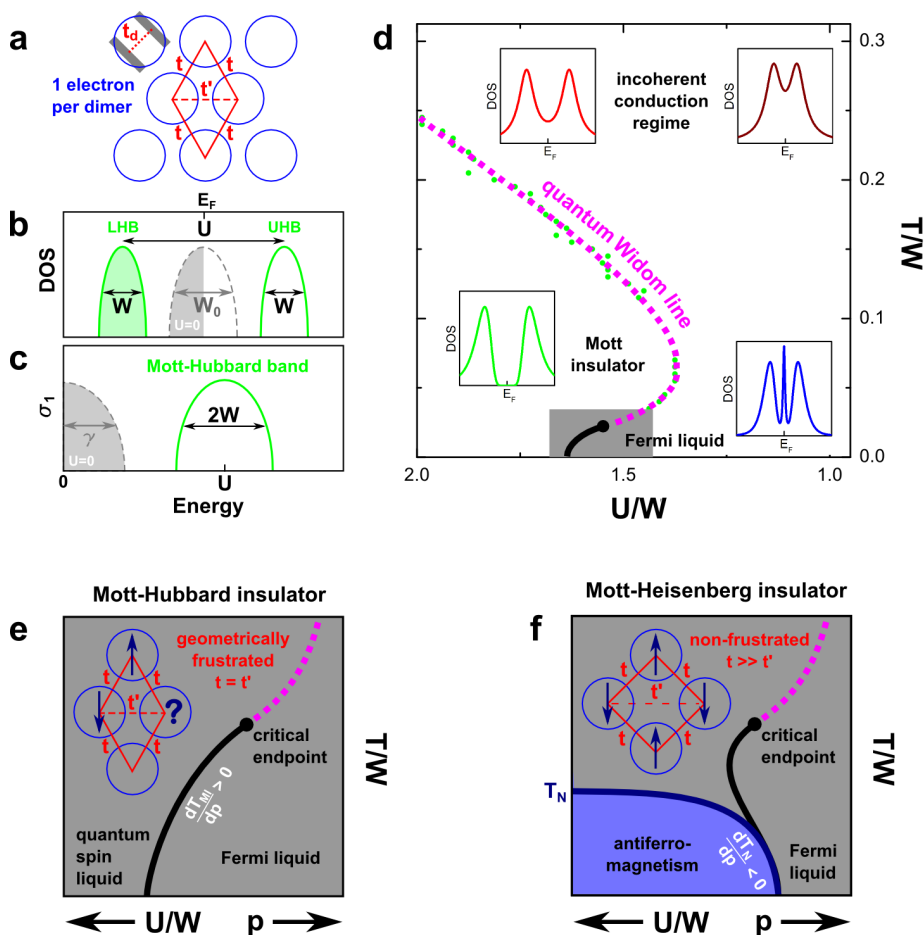


Figure 5.1.5: (a) The compounds under study have a layered structure with dimers (blue circles) of organic molecules (gray bars) arranged on a triangular lattice, where $t_d > t(t')$ are the intra- and inter-dimer transfer integrals. (b) Density of states (DOS) of the Mott insulator. The separation of the lower and upper Hubbard bands (green) is a measure of the Coulomb repulsion U (cf. Fig. 2.3.6). Although generally smaller, the width W of the Hubbard bands remains a good measure of the bare bandwidth $W_0 = 9t$ in the absence of correlations [74]. (c) The peak position $\hbar\omega_{max}$ of $\sigma_1(\omega)$ corresponds to U and the half-width equals W . In the metallic case ($U = 0$) this transforms to a zero-frequency conductivity; for small, but finite scattering the width equals the scattering rate γ of the Drude response while for bad metals the upper bound W_0 is approached. (d) Schematic phase diagram of the Mott insulator with the sketched DOS for different regions. While in the high-temperature regime charge transport is dominated by incoherent thermal excitations and the Hubbard bands are strongly blurred, a well-defined charge gap opens in the Mott insulating state and a Drude peak appears on the metallic side at low temperatures. The boundary between the conducting regime and the fully gapped Mott state is the so-called quantum Widom line (dashed pink). The back-bending at low temperatures is nicely reproduced by DMFT calculations (green points). (e,f) Zoom to the low-temperature region around the insulator-metal boundary which acquires a positive slope in a frustrated Mott insulator and a negative one for antiferromagnetism (cf. section 2.3.4).

theory. For several organic charge transfer salts we succeeded to determine U and W from the optical spectra and combine our findings with pressure-dependent dc transport and dynamical mean-field theory calculations. By identifying the relevant scales that control the transition, our approach allows us to put *all* Mott insulators – including non-frustrated compounds and transition metal oxides – on one universal phase diagram in a quantitative way. Moreover, our optical data provide evidence for charge fluctuations close to the phase boundary on the insulating side, enhanced upon cooling due to the Pomeranchuk-like anomaly. Although theoretically predicted, this phase coexistence has never been observed before.

For our investigation, we selected three well-known organic Mott insulators β' -EtMe₃Sb[Pd(dmit)₂]₂ (abbreviated EtMe), κ -(BEDT-TTF)₂Ag₂(CN)₃ (abbreviated AgCN) and κ -(BEDT-TTF)₂Cu₂(CN)₃ (abbreviated CuCN). These compounds form a layered structure with dimers of organic molecules on a triangular lattice carrying one electron each, resulting in half-filled, quasi two-dimensional electronic systems, which are well described in terms of the single-band Hubbard model [11, 12]. Charge transport is related to hopping between neighbouring sites, proportional to the transfer integrals t and t' (Fig. 5.1.5 a) and, thus, the bandwidth.

Panel (d) displays the prototypical phase diagram of a Mott insulator; the gap closes at the QWL (green data points determined by DMFT calculations, see section 5.1.4), which corresponds to a certain relation between U , W and T . Since both scales (effective temperature T/W and electronic correlations U/W) are expressed in units of W , the underlying physics is adequately described by only two parameters: the on-site Coulomb repulsion U and the bandwidth W . As we will later see (section 5.1.3), the reversal of the QWL provides a fixed point to collapse the Widom lines of different compounds onto one universal curve. Strictly speaking, the bandwidth of the Hubbard bands W is generally smaller than the bare bandwidth W_0 of the uncorrelated system. However, the effective values U/W remain a good approximation of the intrinsic U/W_0 ratio even for strong correlations [74]. In order to determine the density of states (DOS) and optical conductivity spectra for varying correlation strength U/W , we performed complementary DMFT calculations utilizing the continuous time quantum Monte Carlo (CTQMC) quantum impurity solver (section 5.1.4). The results affirm, in particular, that the maximum of the Mott-Hubbard band is proportional to the Coulomb repulsion U and the U/W ratio extracted from the band shape is closely related to the bare correlations U/W_0 .

Empirically, the on-site Coulomb repulsion can be approximated with the strength of the intra-dimer transfer integrals $U_0 \approx 2t_d$ [117, 120], which is used in Table 5.1.1.

Table 5.1.1: Electronic parameters (in units of meV) of several organic charge-transfer salts with different correlation strength. κ -(BEDT-TTF)₂Cu[N(CN)₂]Br is metallic and becomes superconducting below $T_c = 11.8$ K. κ -(BEDT-TTF)₂Cu[N(CN)₂]Cl is a Mott insulator that orders antiferromagnetically at $T_N = 25$ K; only 300 bar are sufficient to cross the insulator-to-metal transition. The spin liquid compounds CuCN and AgCN exhibit no magnetic order down to 20 mK [15, 78], although the exchange coupling $J = 250$ K is rather strong. The coupling within the dimers t_d is a measure of the Coulomb repulsion U [117]. The overlap integrals t and t' characterize the frustration on the triangular lattice. The relative strength of correlations is given by U/t and U/W_0 ($W_0 = 9t$ for a triangular lattice). The last column lists parameters solely determined from our optical measurements. The sizable renormalization of the bandwidth expected due to electronic correlations [74, 158, 159] causes the extracted U/W to be generally larger than the calculated U/W_0 . Data from Refs. [15, 22, 114, 115, 117, 156, 160].

	t_d	t	t'	t/t'	U/t	W_0	U/W_0	U/W_{exp}
κ -Br	200	78	33	0.42	5.1	500	0.8	–
κ -Cl	200	73	32	0.44	5.5	476	0.84	1.5
CuCN	200	55	45	0.83	7.3	450	0.89	1.52
AgCN	200	53	48	0.90	10.5	454	1.16	1.96
EtMe	200	28	26	0.92	32	244	3.72	2.35

There, we additionally compare the inter-dimer transfer integrals t , t' as a measure of the geometrical frustration of the spin-liquid compounds under investigation. For completeness reasons, we also list those of the related charge-transfer salts κ -(BEDT-TTF)₂Cu[N(CN)₂]Cl and κ -(BEDT-TTF)₂Cu[N(CN)₂]Br; these are well-studied compounds with a significantly weaker frustration t'/t that order antiferromagnetically or become metallic and even superconducting at low temperatures, depending on the U/W ratio [21–23, 151, 161]. U/W obtained from ab initio density functional theory (DFT) and extended Hückel calculations based on the respective crystal structure indicates that correlations increase considerably when going from CuCN via AgCN to EtMe. Deviations of the absolute value, however, stem from the limitations of the respective theoretical models.

Optical spectroscopy is the method of choice to experimentally determine the band parameters, since it directly maps the band shape by observing the transitions between the Hubbard bands, as illustrated in Fig. 5.1.5 (c). By measuring the infrared reflectivity of EtMe, AgCN and CuCN single crystals at different temperatures, we obtain the optical conductivity $\sigma_1(\omega)$ plotted in Fig. 5.1.6. Since the optical properties are rather isotropic within the highly-conducting plane (cf. Fig. 5.1.2), we focus on the polarization along the direction of the largest conductivity. The most

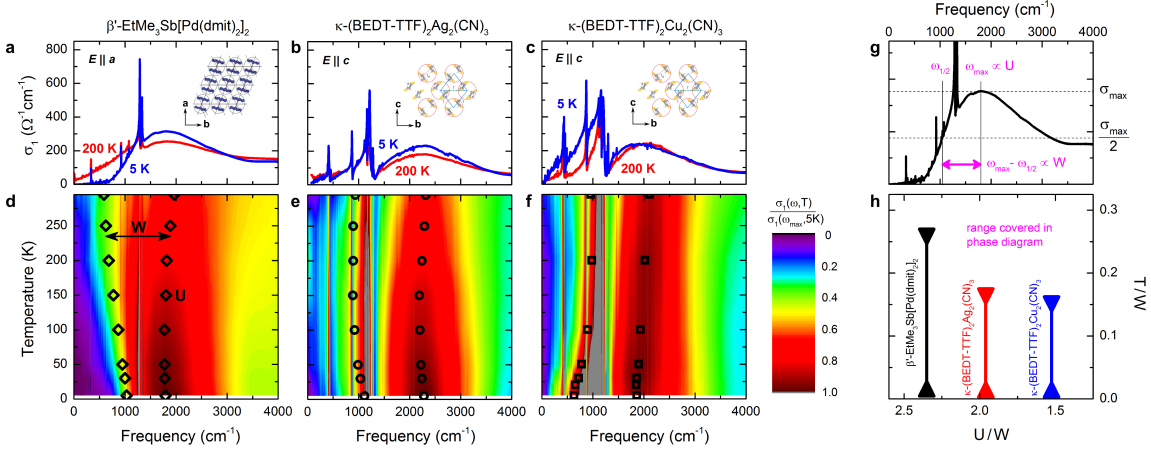


Figure 5.1.6: (a)–(c), The dominant feature in the optical conductivity that contains all information of the intrinsic Mott physics is the Mott-Hubbard band centered around 2000 cm^{-1} . At low frequencies, narrow phonon modes appear on top. Note that the band shape and the low-frequency conductivity show distinct behaviour for each compound which is related to the respective position in the phase diagram. (d)–(f), The contour plots of $\sigma_1(\omega, T)$ illustrate the temperature-dependent changes of the Mott-Hubbard band, where the open black symbols denote the maximum and half-maximum positions. (g) The Coulomb repulsion U corresponds to the band maximum position ω_{max} while the half-width at half maximum is proportional to the electronic bandwidth $W/\hbar = \omega_{max} - \omega_{1/2}$. (h) The U/W ratio at the lowest temperature defines the horizontal position in the phase diagram; the vertical bars correspond to the experimentally accessed temperature range (5–300 K) normalized to k_B and the respective bandwidth. Hence, the EtMe data extend over the largest T/W range and correlations decrease via AgCN and CuCN.

prominent feature is the Mott-Hubbard band centered around 2000 cm^{-1} , also seen in related materials [21, 151, 162, 163]. Our CTQMC calculations (section 5.1.4) reproduce the overall shape, asymmetry and intensity of the bands very well, establishing the dominant role of Mott physics in these compounds. The narrow peaks below 1500 cm^{-1} correspond to molecular vibrations and lattice phonons [101, 164], which can be clearly separated from the overall change of the Mott-Hubbard band in the contour plots.

As indicated in Fig. 5.1.6 (d)–(f), the maximum and half-height frequencies, and thus the bandwidth determined as $W/\hbar = \omega_{max} - \omega_{1/2}$, change upon cooling. Due to the band asymmetry, we extract the bandwidth from the low-frequency wing of the Mott-Hubbard band for it is related to the intrinsic low-energy excitations of the ground state (Fig. 5.1.6 (g) and section 4.3.1). While the Mott-Hubbard bands of EtMe and AgCN are subject to narrowing upon cooling, a pronounced shift towards low frequencies and unusual broadening are observed for CuCN. In order to disentangle thermal effects and to focus on quantum Mott physics, we first analyze the data

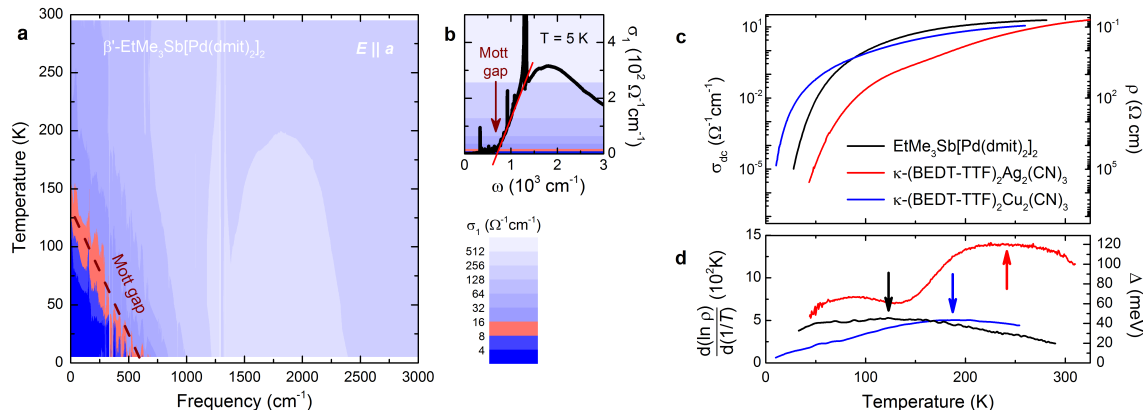


Figure 5.1.7: (a) The temperature- and frequency-dependent optical conductivity of EtMe is displayed on a logarithmic blue-white scale. The region highlighted in red indicates σ_1 at the gap frequency, which is determined by linear extrapolation of the steepest slope (panel b). The Mott gap opens around 125 K and continuously grows upon cooling ($\Delta = 650 \text{ cm}^{-1}$ at $T = 5 \text{ K}$). (c) As these spin liquid compounds do not undergo any ordering, the dc conductivity drops with decreasing temperature without evidence of a sharp phase transition, in agreement with Refs. [153, 154]. (d) The temperature-dependent transport gap $\Delta(T)$ acquires a broad maximum corresponding to an inflection point in the Arrhenius plot of $\rho(T)$. For EtMe (black) the transport gap peaks around 120 K coinciding with the opening of the Mott gap shown in panel (a), thus it reflects the quantum Widom line. Also for CuCN (blue) the maximum of $\Delta(T)$ agrees with the crossover temperature reported in Ref. [14].

at the lowest temperatures where thermal broadening is negligible; the temperature dependence of the low-frequency conductivity will be discussed in the context of Fig. 5.1.8.

From the spectroscopic data measured at $T = 5 \text{ K}$, we conclude that electronic correlations are largest in EtMe despite the small U . Indeed, the small bandwidth in this material implies that (i) it is located most left in the U/W phase diagram, (ii) the experimentally accessed temperatures (5–300 K) cover a broader vertical T/W range and (iii) the electronic compressibility is largest because pressure has a larger effect on U/W . The two κ -compounds have larger energy scales and, thus, extend over smaller T/W and U/W ranges. Consequently, in a unified phase diagram the three materials are arranged in the order EtMe–AgCN–CuCN on the descending horizontal U/W scale (Fig. 5.1.6 h), consistent with ab initio density functional theory (DFT) and extended Hückel calculations listed in Table 5.1.1 [15, 114, 115, 117, 156, 160].

A closer inspection of the temperature-dependent optical conductivity of EtMe (Fig. 5.1.7 a and b), reveals a well-defined Mott gap that opens around 125 K and continuously grows up to 650 cm^{-1} when the temperature is lowered to 5 K. This coincides

well with the crossover temperature from Ref. [14] extrapolated to $p = 0$ establishing the QWL as the true boundary between the Mott state with a well-defined charge gap and the incoherent conduction regime in the supercritical region.

Panels (c) and (d) of Fig. 5.1.7 display the temperature-dependent dc conductivity (measured by A. Löhle, R. Rösslhuber and R. Kato) and the corresponding transport gap Δ calculated from the logarithmic resistivity derivative $\frac{d \ln \rho}{1/T}$ according to Equ. 2.2.2, respectively. For all three compounds $\Delta(T)$ goes through an absolute maximum at a particular temperature that coincides with the opening of the optical gap of EtMe, thus we associate it with the QWL. There is similar agreement between Ref. [14] and the pressure-dependent dc transport results for CuCN revealing the QWL at 185, 135 and 123 K for $p = 0, 2.17$ and 2.38 kbar, respectively (Fig. 5.1.13). Although for AgCN there is another, smaller feature at 90 K, Mott physics is reflected by the global maximum of $\Delta(T)$ implying that the QWL is crossed around 245 K. Therefore, the maximum of the transport gap allows us to identify the QWL even though no clear-cut optical gap is observed for CuCN and AgCN, probably due to the smaller U/W ratio. We also notice that the size of the transport gap maximum scales with the Coulomb repulsion U determined by optical spectroscopy.

As the relevant energy scales in the phase diagram are of the order of 10^2 K or less, fingerprints of the ground state are expected in the low-frequency electrodynamic response, i.e. in the THz or far-infrared spectral ranges. A closer look on the temperature evolution of the optical conductivity well below ω_{max} (Fig. 5.1.8 c) illustrates the insulating nature of the ground state of EtMe, where the sub-gap absorption diminishes upon cooling as thermal band broadening is reduced. The integrated spectral weight, plotted in panel (d),

$$SW(\omega) = \int_0^{\omega_i} \sigma_1(\omega') d\omega' \quad \xrightarrow{\hbar\omega < U-W} \quad SW(\omega_i) \propto \frac{N}{m^*}, \quad (5.1.1)$$

provides a robust measure of these low-energy excitations enabling a more quantitative analysis beyond dc transport. This quantity determines the absorption strength up to a given cutoff frequency ω_i , chosen to be below the band edge ($U - W$) in order to probe the low-energy excitations only, and yields valuable information on correlation effects [53]. Here, N is the charge carrier density and m^* indicates the effective mass, renormalized by the band structure and electronic interactions.

While the overall spectral weight grows with decreasing correlations (Fig. 5.1.4), the temperature evolution $SW(\omega_i, T)$ plotted in Fig. 5.1.8 reveals unexpected behaviour. Although less pronounced than in EtMe (c), also AgCN (b) behaves like a typical

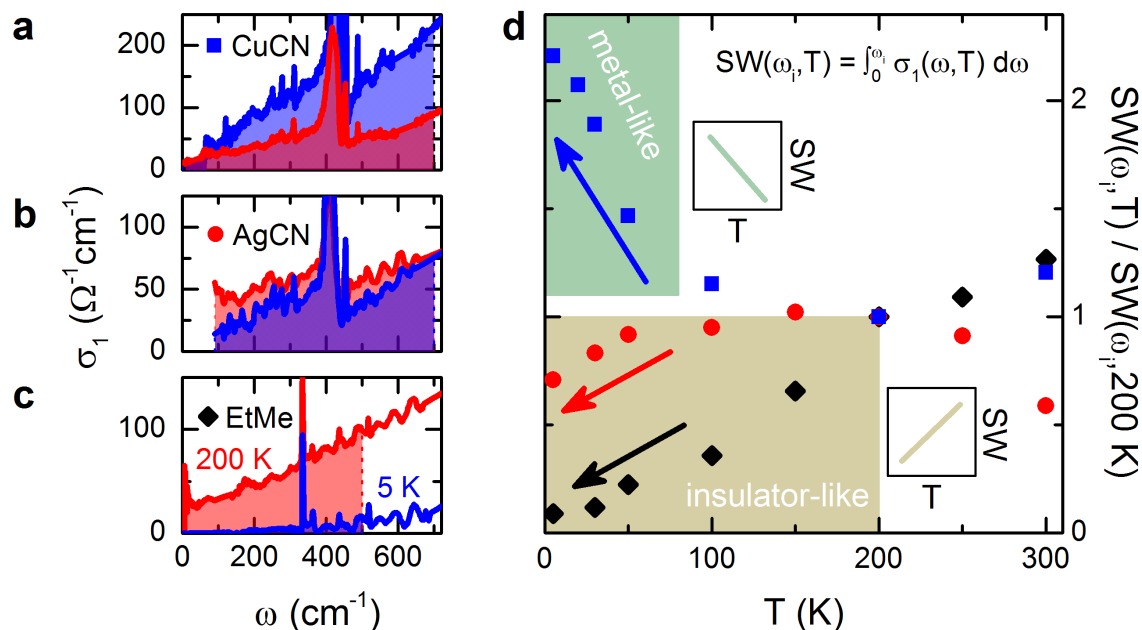


Figure 5.1.8: (a)-(c) The low-frequency optical conductivity exhibits distinct behaviour between 200 and 5 K. The shaded area indicates the corresponding spectral weight $SW(\omega_i, T)$ restricted to the region deep inside the Mott gap ($\omega_i = 500 \text{ cm}^{-1}$ for EtMe, 700 cm^{-1} for AgCN and CuCN). (d) For EtMe and AgCN the SW freezes out, consistent with thermally-activated excitations across the gap diminishing at low temperatures. In contrast, for CuCN the spectral weight strongly increases upon cooling, giving evidence for a novel absorption channel. The onset of this pronounced non-thermal enhancement appears at the same temperature as the back-bending of the quantum Widom line ($T_{\text{back}} = 70 \text{ K}$, cf. Fig. 5.1.9). The squares denote the ranges of metallic (increase of SW for $T \rightarrow 0$) and insulating behaviour (decrease of SW for $T \rightarrow 0$).

insulator, where the in-gap states are depleted upon cooling. The opposite behaviour is found in the case of CuCN, which exhibits a temperature dependence characteristic of metals (a): the low-frequency optical conductivity increases upon lowering the temperature [16, 17]. This is unexpected considering that no Drude peak is present, the hallmark of coherent transport, and that at zero frequency all compounds – including CuCN – are electrical insulators as determined from dc transport (Fig. 5.1.7 c).

This apparent contradiction can be understood by the exceptional position of CuCN in the phase diagram: this compound is more proximate to the insulator-metal boundary than EtMe and AgCN as it shows weaker correlations compared to the other two compounds (cf. Fig. 5.1.6 h). Due to the Pomeranchuk-like anomaly, the insulator-metal boundary gets closer to the ambient pressure position as the temperature is lowered below the back-bending point of the QWL (cf. Fig. 5.1.5 e). Thus,

we assign the strong non-thermal enhancement of the low-energy spectral weight below $T_{back} = 70$ K to metallic fluctuations in the Mott state that appear upon entering the coexistence region close to the phase boundary, which has been predicted theoretically [4, 5] but never observed. From the trend of our data we expect the anomalous slope of the Mott MIT to extend to the lowest measured temperature. Going back to Fig. 5.1.7 (d), the transport gap of CuCN gradually decreases and seems to vanish for $T \rightarrow 0$ consistent with a weakening of the insulating behaviour. Therefore, the QWL not only marks a crossover in the conduction properties at elevated temperatures but is also manifest in the sub-gap region of the low-temperature optical absorption of CuCN.

If this was a fundamental property manifest in the vicinity of the metallic state, it should also occur in the optical data of other compounds that are sufficiently close to the Mott insulator-metal boundary. To that end, in section 5.1.5 we reassess the optical data of the κ -(BEDT-TTF)₂Cu[N(CN)₂Br_xCl_{1-x}] series, where increasing the Br content drives the bandwidth-tuned Mott MIT towards superconductivity and a correlated Fermi liquid state [21–23, 161]. Due to the substantially weaker frustration t'/t , these systems order antiferromagnetically at low temperatures, leading to a phase diagram like in Fig. 5.1.5 (f). Above T_N , however, these compounds behave similarly as the frustrated Mott insulator CuCN and exhibit a comparable non-thermal enhancement of the SW corroborating our conclusions above. When antiferromagnetism is stabilized, however, a well-defined gap opens and the low-energy states are depleted; these intrinsic properties clearly distinguish the thermo- and electrodynamic properties of magnetically ordered and QSL Mott states.

5.1.3 Unified Phase Diagram of the Mott Insulator

Recalling the generic phase diagram of the Mott insulator presented in Fig. 5.1.5 (d), the position of the quantum Widom line (QWL) delimiting the gapped Mott state is a function of U , W and T only. A direct implication is that, in principle, each compound dominated by Mott-Hubbard interactions should exhibit the same QWL when the horizontal (U/W) and vertical (T/W) axes are renormalized by the bandwidth. Therefore, knowledge of U and W allows to collapse the experimental data of all Mott insulators in one unified phase diagram sharing a universal quantum Widom line. Compounds with a smaller bandwidth extend over a broader region while higher energy scales imply a more confined range such that larger temperature and pressure scales are necessary to cover the same U/W – T/W area.

Making use of our conclusions from the optical spectroscopy results presented in

the previous section, in particular Fig. 5.1.6 (h), we relate the transport results of the three frustrated Mott insulators to each other and combine them to a universal QWL. In the $T - p$ phase diagrams shown in Furukawa *et al.* [14], which have been reproduced in Fig. 5.1.9 (a) and (b), the back-bending point of the QWL is located at a lower temperature for EtMe ($T_{back} < 30$ K) as compared to CuCN ($T_{back} = 70$ K). This agrees well with the smaller bandwidth of EtMe providing evidence for the T/W scaling of the phase diagram. Keeping in mind that EtMe is located much deeper in the Mott insulating regime due to the larger correlations U/W , it is remarkable that the pressure at the back-bending point ($p_{back} \approx 3$ kbar) is similar to that of CuCN, consistent with the large compressibility of EtMe concluded from its generally smaller energy scales U and W . For AgCN, a similar compressibility but larger Coulomb repulsion compared to CuCN was concluded in a very recent study [15], also in line with our optical results. Altogether, the excellent agreement between optics, pressure-dependent transport and the theoretically determined band parameters (Table 5.1.1) strongly encourages our T/W vs. U/W scaling approach. In Fig. 5.1.9 (c) we proceed with the scaling procedure to connect the quantum Widom lines of EtMe and CuCN based on the pressure-dependent dc transport results from Furukawa *et al.* [14] and the data shown in Fig. 5.1.7 (d) and Fig. 5.1.13. Since CuCN has a larger bandwidth, we have to squeeze its T and p scales in order to match the QWL with that of EtMe. A good match between the EtMe and CuCN data sets can be reached for $2 < T_{EtMe} = T_{CuCN} < 4.5$. The best fit, however, is achieved for a bandwidth ratio of 3.4 when also the normalized resistance values, i.e. the color scale in Fig. 1 (d) and (f) from Ref. [14], are in agreement. For AgCN, we extracted the QWL from the pressure-dependent resistivity reported in Ref. [15] and the ambient pressure result from Fig. 5.1.7 (d), and then appropriately scaled to match with the EtMe and CuCN data. Taking CuCN as our reference material, we rescale the temperature and pressure of EtMe by factors 3.4 and 6, respectively; AgCN has a temperature scaling factor of 1.2 compared to CuCN, almost equal compressibility and is shifted to the left on the horizontal axis¹ due to the larger U . The ambient conditions are located at -1.66 GPa for EtMe and -0.83 GPa for AgCN on the CuCN pressure scale implying the following linear pressure scaling relations:

$$p_{CuCN} = -0.83\text{GPa} + 0.95p_{AgCN} = -1.66\text{GPa} + 6p_{EtMe}. \quad (5.1.2)$$

Due to the different experimental approach of Shimizu *et al.* [15], who measured

¹We emphasize that also for AgCN the optical results are in good agreement with the conclusions of Ref. [15]: AgCN has a similar bandwidth W but larger Coulomb repulsion U compared to CuCN.

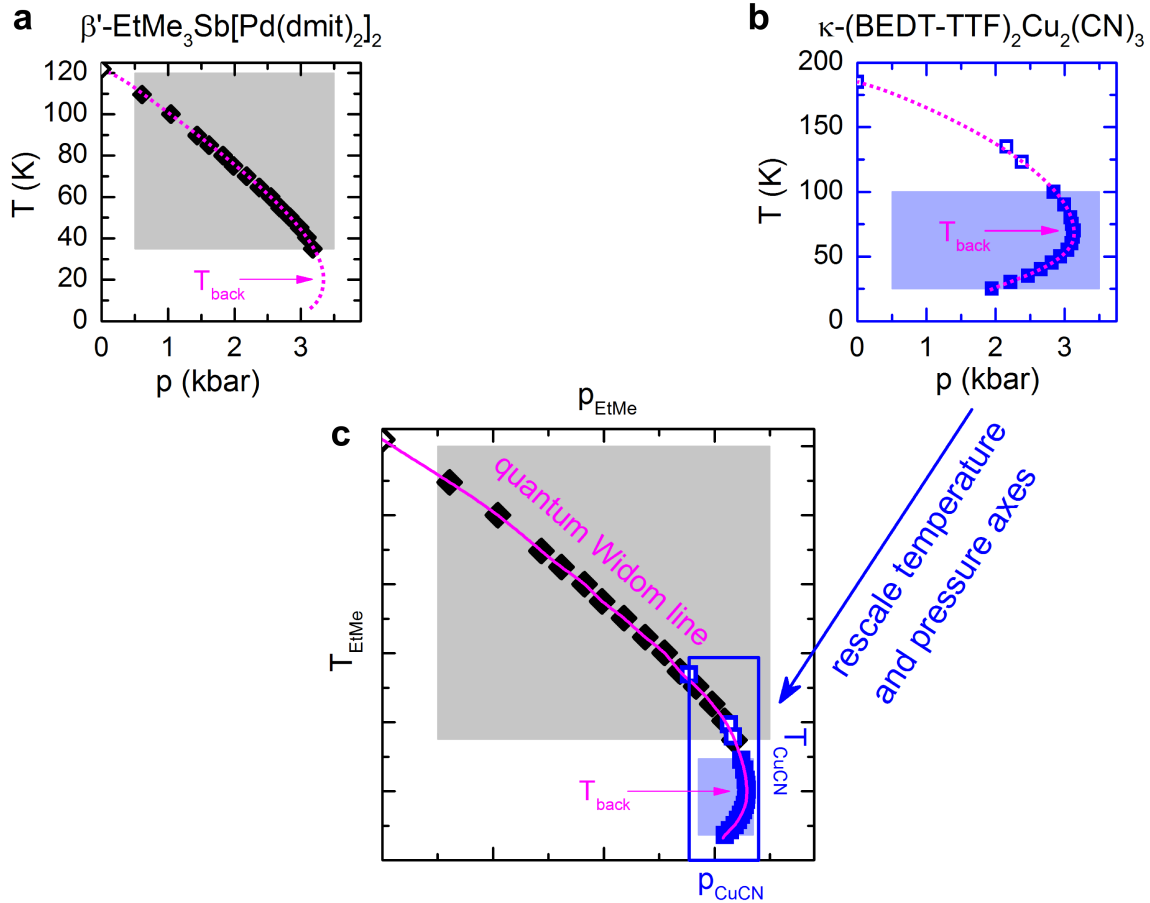


Figure 5.1.9: (a,b) The temperature and pressure range covered by the dc transport experiments of Furukawa *et al.* [14] is highlighted in grey and blue for EtMe and CuCN, respectively; the solid symbols correspond to the quantum Widom line (QWL) determined by pressure sweeps at constant temperature. The dotted magenta lines illustrate the interpolation of the QWL through the maximum of the transport gap $\Delta(T)$ (open symbols, data from Fig. 5.1.7 (d) and Fig. 5.1.13). (c) Using the back-bending at T_{back} as a fixed point, the two data sets can be connected smoothly by stretching and squeezing of the respective axes, resulting in a universal QWL (solid magenta line). As indicated by the blue rectangle, temperature and pressure of CuCN are scaled down by factors of 3.4 and 6 compared to EtMe, respectively. This implies that EtMe has a smaller bandwidth, larger compressibility and its ambient pressure position is located more left in the phase diagram than for CuCN, in excellent agreement with the optical results from Fig. 5.1.6 (h).

temperature sweeps at constant pressure rather than pressure sweeps at constant temperature, the QWL determination was not as accurate for AgCN, leading to larger error bars. Note that they concluded an absolute pressure shift of 0.6 GPa between AgCN and CuCN² while our procedure results in a shift of approximately 0.9 GPa, as shown in Equ. 5.1.2.

Our comprehensive optical and transport results render possible the construction of the unified phase diagram of Fig. 5.1.10 that, on a quantitative scale, should be valid for *all* frustrated Mott insulators. The universal quantum Widom line includes data points of EtMe, CuCN [14] and AgCN [15] determined either from the inflection points of $\ln \rho(p)$ at constant temperature or the maxima of $\frac{d \ln \rho}{1/T}$ at constant pressure. The left T/W and bottom U/W scales correspond to the optically determined Mott-Hubbard band parameters (cf. Fig. 5.1.6 h). Considering the comparatively simple method of data extraction based on the single-band Hubbard model, the qualitative and even quantitative agreement between optical and transport results is remarkable³. The horizontal and vertical bars on the top and right axes denote the pressure and temperature ranges (5–300 K) covered by the experimental data of each compound, respectively. The normalized pressure and temperature scales enable us to compare conveniently the experimental findings with results obtained from dynamical mean field theory (DMFT) calculations (Fig. 5.1.5 d). The overall shape of the QWL, i.e. the characteristic back-bending at low temperatures, reminding of the Pomeranchuk effect, is consistently found in both experiment and theory. Even on a quantitative level, the U/W and T/W values match remarkably well considering the present level of theory⁴, i.e. the single-band Hubbard model is a valid effective low-energy description for the different compounds under study.

Having assembled, for the first time, the genuine phase diagram of the Mott insulator,

²Their assumption is based on pressure-dependent transport studies of CuCN employing oil as pressure medium [118]. It is known that such setups suffer from a pressure loss at low temperatures when the oil freezes, making the pressure determination at low temperatures less accurate. On the other hand, the data of Furukawa *et al.* [14] on CuCN were measured in a He gas cylinder where the applied pressure can be adjusted and determined very accurately even at low temperatures. This explains the different pressure scale compared to Kurosaki *et al.* [118], where superconductivity sets in at 0.35 GPa while the insulator-superconductor phase boundary of CuCN is located around 0.125–0.15 GPa in Refs. [14, 165].

³While there is excellent quantitative consistency for AgCN and CuCN, the T/W range covered by EtMe is larger than inferred from the optically determined bandwidth. Note, however, that the rescaling of transport data involves considerable insecurity since the QWL reversal of EtMe is not captured by Ref. [14].

⁴The QWL back-bending appears around $U/W \approx 1.4$ and $k_B T/W \approx 0.06$ for the DMFT calculation plotted in Fig. 5.1.5 (d). Keeping in mind the general overestimation of the critical U/W_0 and T/W_0 related to the iterated perturbation theory, these values are in good consensus with the experimental result of Fig. 5.1.10.

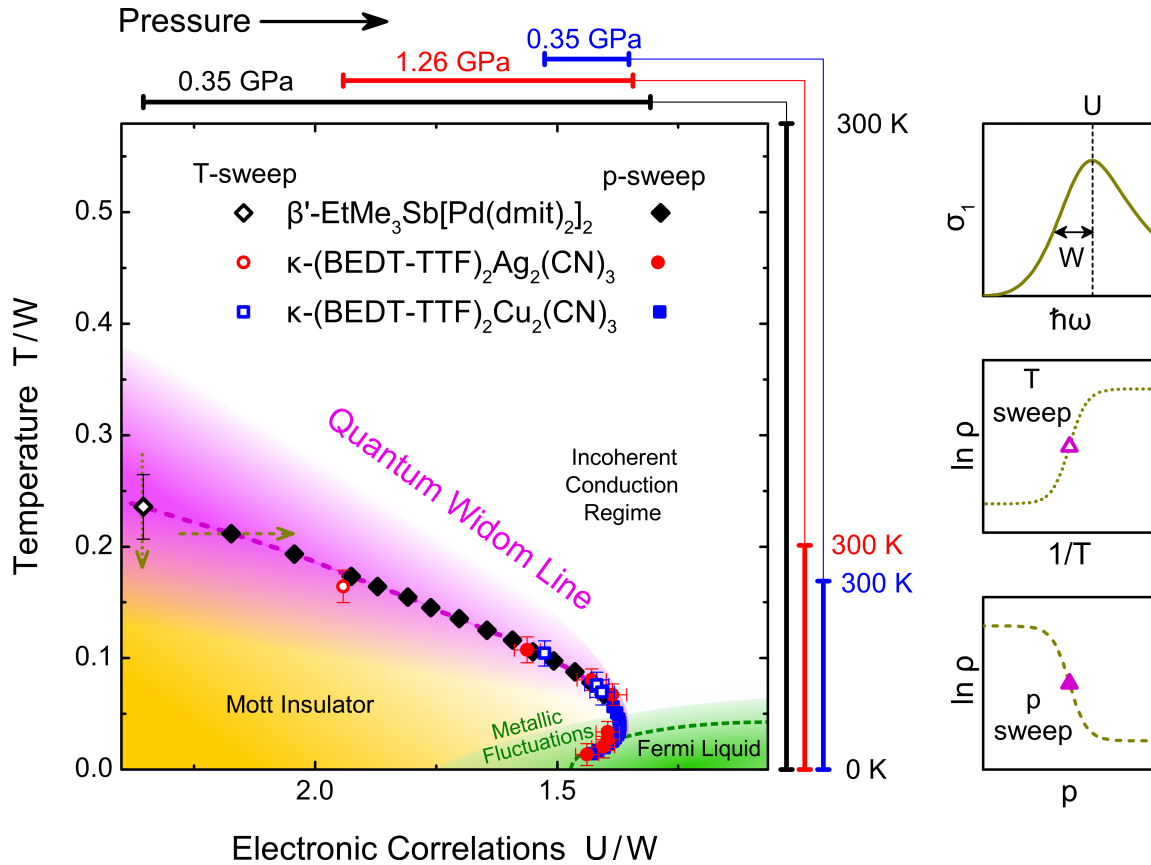


Figure 5.1.10: Quantitative phase diagram of pristine Mott insulators. The temperature $k_B T$ and Coulomb repulsion U are normalized to the bandwidth W extracted from optical spectroscopy; note that the direction of the bottom axis is reversed in order to mimic pressure. Since in these quantum spin liquids magnetic order is suppressed, the large residual entropy causes a pronounced back-bending of the quantum Widom line at low temperatures leading to metallic fluctuations (semi-transparent green area) in the Mott state close to the phase boundary. As the effective correlations decrease further, a metallic phase forms (green area) with Fermi liquid properties [23]. The universal phase diagram guided by the quantum Widom line is constructed on basis of our optical (Fig. 5.1.6 h) and transport (Figs. 5.1.7 (d) and 5.1.13) data as well as the pressure-dependent transport studies [14, 15] on EtMe (black diamonds), AgCN (red circles), and CuCN (blue squares). Upon rescaling temperature (right bars) and pressure (top bars), the quantum Widom line is found to be universal for all compounds. The curvature, as well as the T/W and U/W values match well with theoretical calculations. On the right we illustrate how U and W are determined from our optical spectra and the quantum Widom line from the electrical resistivity $\rho(T, p)$ measured as a function of temperature (open symbols) and pressure (solid symbols), indicated by arrows in the main graph.

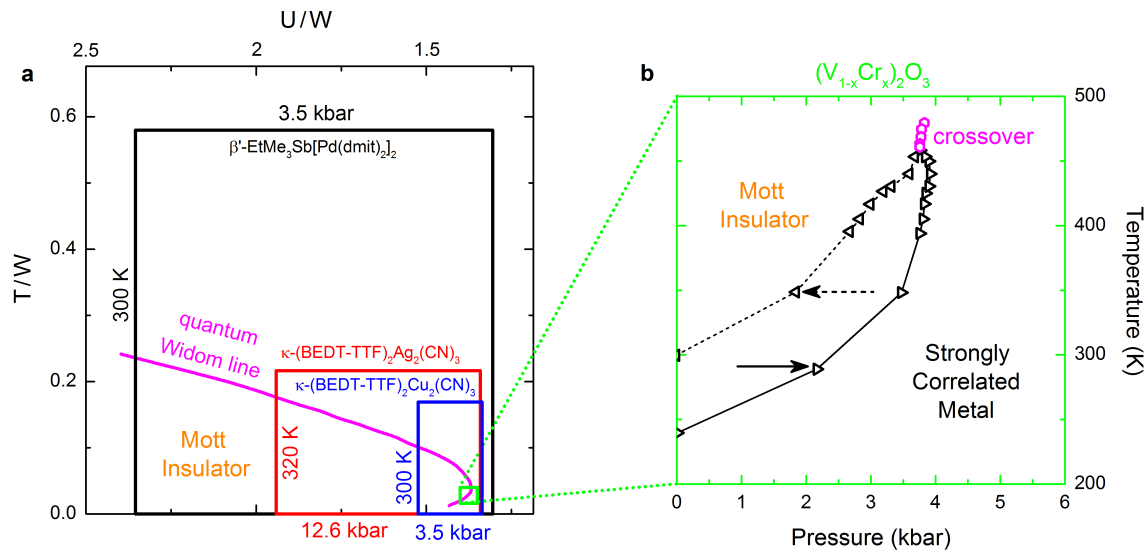


Figure 5.1.11: (a) Using comparable pressure and temperature scales, each compound covers the unified phase diagram of Fig. 5.1.10 to a different extent. We illustrate the respective T/W and U/W regions by colored frames. As the bandwidth increases in the order EtMe (black) – AgCN (red) – CuCN (blue), the corresponding range is successively reduced, both vertically and horizontally. (b) Experimentally determined phase boundary of $(\text{V}_{1-x}\text{Cr}_x)_2\text{O}_3$ as a function of pressure and temperature is reproduced from Ref. [27]. By including these data in panel (a) (green frame), it becomes obvious that a much smaller region is covered despite even larger temperature and pressure scales. This is a direct consequence of the higher energy scales, U and W , of inorganic transition-metal oxides.

this calls for verification and extension to different materials classes. In Fig. 5.1.11 we illustrate that, upon proper renormalization to the intrinsic energy scales, also the inorganic Mott insulator $(\text{V}_{1-x}\text{Cr}_x)_2\text{O}_3$ fits well into the unified phase diagram, yet covering just a small range due to its large bandwidth. This compound exhibits a transition from a paramagnetic metal to a Mott insulator upon chromium substitution. In Fig. 5.1.11 (b) the pressure and temperature dependence of the phase transition is plotted as obtained from dc transport measurements at variable pressure [27]. From optical experiments [24–26] it can be estimated that the bandwidth is approximately higher by a factor of 25 compared to EtMe; the Coulomb repulsion U is around 2.6 eV. Performing the proper scaling, we can match the phase boundary of vanadium sesquioxide with the universal QWL, covering a significantly smaller region in the phase diagram. Note that $T = 300$ K on the EtMe temperature scale corresponds to several 10^3 or even 10^4 K for vanadium oxides, cuprates or similar materials, which is well above their melting points. Thus, the small bandwidth of the organic compounds allows us to reach a temperature regime far beyond the grasp of transition metal oxides, giving unique insight into incoherent conduction processes

outside the realm of quasiparticles.

5.1.4 Mott-Hubbard DMFT Calculations

In Fig. 5.1.12 we present the DOS (a) and optical conductivity (b) calculated by dynamical mean-field theory (DMFT) using the continuous time quantum Monte Carlo (CTQMC) impurity solver⁵. As expected, and in agreement with the experimental spectra presented in Figs. 5.1.2 and 5.1.6, the maximum of $\sigma_1(\omega)$ shifts to higher energies as U increases. Importantly, the asymmetric shape of the Mott-Hubbard band observed in experiment is nicely reproduced. As shown in the inset of (b), the maximum position of the optical conductivity is related linearly to the Coulomb repulsion U establishing our approach to extract the electronic interactions from the experimentally observed Mott-Hubbard band. The theoretical σ_1 scale is calculated in units of the Ioffe-Regel-Mott (IRM) limit $\sigma_{1,IRM} = e^2/(hd)$, where h is Planck's constant and d the inter-layer distance, which allows for quantitative comparison with our experimental data. Here, the IRM limit is around $210 \text{ } \Omega^{-1}\text{cm}^{-1}$ for EtMe and $260 \text{ } \Omega^{-1}\text{cm}^{-1}$ for the two κ -compounds [114, 117, 168]. Thus, the experimental values are reproduced by our CTQMC calculations up to the same order of magnitude.

Note, that we used a Bethe lattice here while a triangular lattice was assumed for the determination of the quantum Widom line shown in Fig. 5.1.5 (d). As a result, the absolute values of $U/W_{0,CTQMC}$ might have an offset and different critical ratio at the Mott MIT; the general Mott physics, however, is captured by both approaches, as demonstrated in Ref. [4]. To obtain a reliable QWL, the iterated perturbative theory (IPT) was applied as our impurity solver, which has been shown to have accurate results compared to numerically exact CTQMC but suffer from less numeric error, especially in triangular lattice systems [4, 5].

5.1.5 Mott Physics in κ -(BEDT-TTF)₂Cu[N(CN)₂]Br_xCl_{1-x}

In the following, the quantum spin liquids are compared to the less-frustrated κ -(BEDT-TTF)₂Cu[N(CN)₂]Br_xCl_{1-x} series (abbreviated κ -Br_xCl_{1-x}) that shows magnetic order in the insulating state at low temperatures. While $T_N \approx 25 \text{ K}$ for $x = 0$ and 0.4, the compound with $x = 0.7$ is subject to an insulator-metal transition at $T_{MI} \approx 50 \text{ K}$ and becomes superconducting below $T_c = 12 \text{ K}$ [21–23]. In particular, we will show that the non-thermal sub-gap absorption is also present in the Mott

⁵As the calculations were carried out externally by T.-H. Lee and V. Dobrosavljević, we refrain from discussing the computational details here; an interested reader may consult Refs. [4, 5, 166, 167].

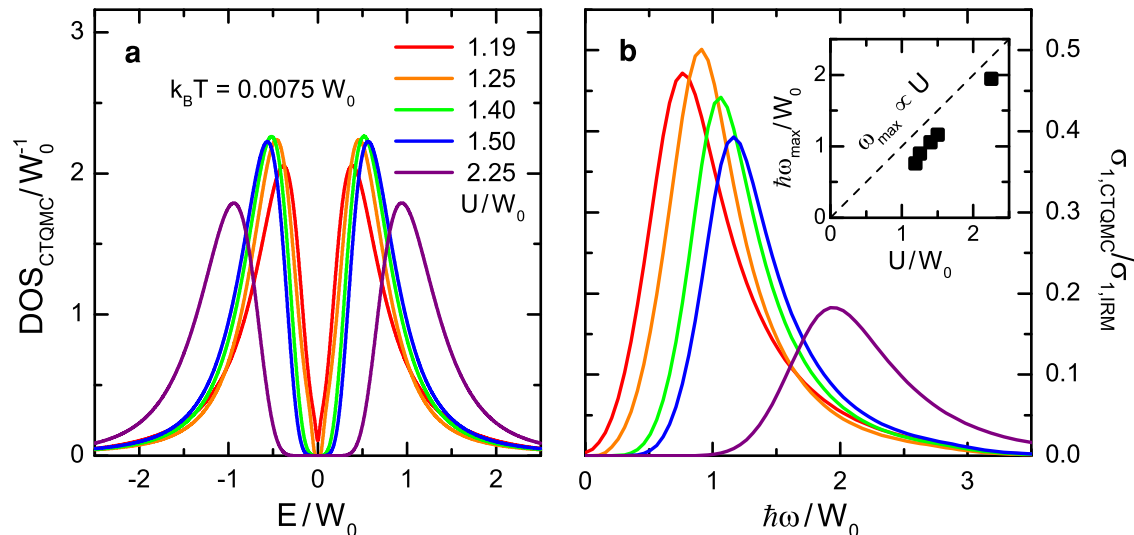


Figure 5.1.12: The density of states (DOS) and optical conductivity were calculated by dynamical mean-field theory using the continuous time quantum Monte Carlo (CTQMC) impurity solver by T.-H. Lee and V. Dobrosavljević. The asymmetric shape of the Mott-Hubbard bands observed in our optical experiments (Figs. 5.1.2 and 5.1.6) is reproduced both in the DOS (a) and σ_1 (b) for different correlation strength U/W as indicated. The calculated optical conductivity is plotted in units of the Ioffe-Regel-Mott limit. The assumed $k_B T/W = 0.0075$ corresponds to the low-temperature limit of our experiments. Inset: The linear relation between the maxima of σ_1 and the Coulomb repulsion U reassures our analysis based on Fig. 5.1.6 (g). Note, that due to the implicit assumptions of the theoretical model, the band edge is generally much steeper than in the materials under study. Here we utilized a Bethe lattice, while for the iterated perturbation theory applied in Fig. 5.1.5 (d) a triangular lattice was assumed, leading to different U/W values.

state of $\kappa\text{-Br}_x\text{Cl}_{1-x}$, corroborating our conclusions about metallic fluctuations in the vicinity of the Mott insulator-metal boundary.

In Fig. 5.1.13 (a) we plot the phase diagram of the three $\kappa\text{-Br}_x\text{Cl}_{1-x}$ compounds based on their transport [14, 23] and optical properties [21, 22]. Due to similar bandwidth we use the same temperature and pressure scale as for CuCN and indicate the respective positions for each compound. At elevated temperatures Mott physics is dominant and the $\kappa\text{-Br}_x\text{Cl}_{1-x}$ compounds follow the same QWL (black line) as CuCN. At low temperatures, however, antiferromagnetic (AFM) order forms, causing qualitatively different behaviour than in the QSL compound. In particular, the Pomeranchuk-like back-bending of the QWL (open white squares indicate the phase boundary of CuCN) is suppressed by antiferromagnetic fluctuations such that the insulator-metal boundary (dashed pink) acquires a negative slope close to the AFM state. Note that in the presence of strong geometrical frustration in CuCN the

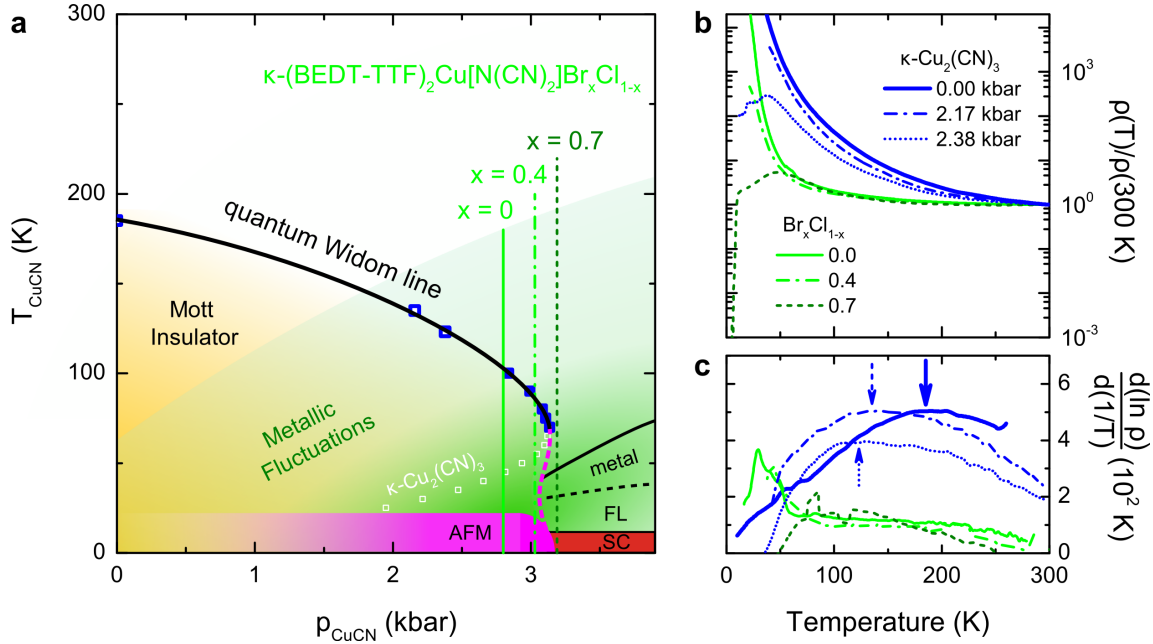


Figure 5.1.13: (a) The black line corresponds to the common high-temperature quantum Widom line of $\kappa\text{-(BEDT-TTF)}_2\text{Cu}_2(\text{CN})_3$ (blue squares, cf. Figs. 5.1.9 and 5.1.10) and $\kappa\text{-(BEDT-TTF)}_2\text{Cu}[\text{N}(\text{CN})_2]\text{Br}_x\text{Cl}_{1-x}$. The solid, dashed-dotted and dashed green lines refer to the ambient pressure positions of the compounds with $x = 0, 0.4$ and 0.7 , respectively [14, 21–23]. As indicated in semi-transparent green colour, metallic fluctuations appear both in the Mott state and in the incoherent regime above and on the right of the quantum Widom line. Since geometrical frustration is much smaller than in CuCN, antiferromagnetic (AFM) order sets in below $T_N \approx 25$ K for $x \leq 0.4$, as indicated in pink. The associated AFM fluctuations suppress the back-bending of the quantum Widom line (QWL) and cause a negative slope of the insulator-metal boundary in the vicinity of the ordered state (dashed pink line). The open white squares indicate how the low-temperature phase boundary would form in absence of AFM, realized by the geometrically frustrated CuCN. Thus, magnetic order suppresses the metallic phase up to higher pressure (i.e. smaller U/W ratio) compared to a pristine Mott insulator. (b) The resistivity data reveal that increasing the Br-content x effectively enhances the bandwidth leading to metallic and superconducting behaviour at low temperatures. We also plot the pressure-dependent resistivity of CuCN (blue) for $p = 0, 2.17$ and 2.38 kbar. (c) The logarithmic resistivity derivative of the $\kappa\text{-Br}_x\text{Cl}_{1-x}$ compounds is qualitatively different from the quantum spin liquids. A pronounced peak occurs around T_N . The transport gap maximum of CuCN (open blue squares in a) shifts to lower temperature upon pressure.

metallic state is stabilized with respect to the Mott state up to larger correlations U/W , i.e. smaller pressure, than in the less-frustrated κ -Br_{*x*}Cl_{1-*x*}. Thus, AFM and its fluctuations suppress the Fermi liquid and affect thermodynamics more strongly than the pure interplay of charge excitations and Coulomb repulsion.

The transport properties shown in Fig. 5.1.13 (b) reveal the typically smaller resistivity of κ -Br_{*x*}Cl_{1-*x*} in accordance with the location much closer to the metallic state due to weaker correlations U/W . This effect is seen very clearly in frame (c) as the transport gap is significantly smaller than in CuCN. In the vicinity of its reversal point the QWL acquires a nearly vertical slope over a broad temperature range (for $x = 0$, see Fig. 1 (e) from Ref. [14]). Hence, the contribution to the transport gap related with Mott physics manifests as a broad plateau above 50 K. The bandwidth tuning effect becomes obvious as (i) the size of the transport gap is much smaller than in the three quantum spin liquid compounds under study with stronger correlations, and (ii) the high-temperature tail of the plateau is suppressed for larger Br-content x . When entering the AFM state, however, the resistance shoots up drastically which expresses as a sharp maximum centered at T_N in the transport gap. The onset happens well above the magnetic transition, indicating magnetic fluctuations getting pronounced at $T_N < T < 50$ K.

To compare the electrodynamic properties in the context of the Mott physics discussed in section 5.1.2, we confine ourselves to a temperature right above the onset of magnetic fluctuations. In Fig. 5.1.14 (a) we plot the optical conductivity of the three quantum spin liquids and the three κ -Br_{*x*}Cl_{1-*x*} compounds at $T = 50$ K $> T_N$. To facilitate comparison, we renormalized the Mott-Hubbard band to the maximum conductivity $\sigma_{1,max}$ and frequency ω_{max} , respectively. Additionally, we smoothed the data as the frequency shift moves the vibrational features differently for each compound making the picture confusing. As a general trend, the in-gap conductivity is enhanced for smaller correlations. $\sigma_1(\omega)$ calculated by DMFT shown in Fig. 5.1.12 (b) was normalized in the same way and, similarly, exhibits a pronounced broadening of the band and increasing sub-gap absorption for reduced U/W .

In Fig. 5.1.15 (a) we plot the spectral weight SW integrated up to a cut-off frequency $\omega_i < U - W$ for both in-plane directions of the QSL compounds; the overall temperature evolution is the same for both polarizations⁶ as already inferred from

⁶Although the onset temperature and the general trend of the non-thermal enhancement is the same for both polarizations of CuCN, the b -direction shows a smaller SW increase than observed for $E \parallel c$. We might speculate whether this reflects less pronounced metallic fluctuations due to slightly stronger correlations along $E \parallel b$, i.e. a larger distance from the insulator-metal boundary in the phase diagram.

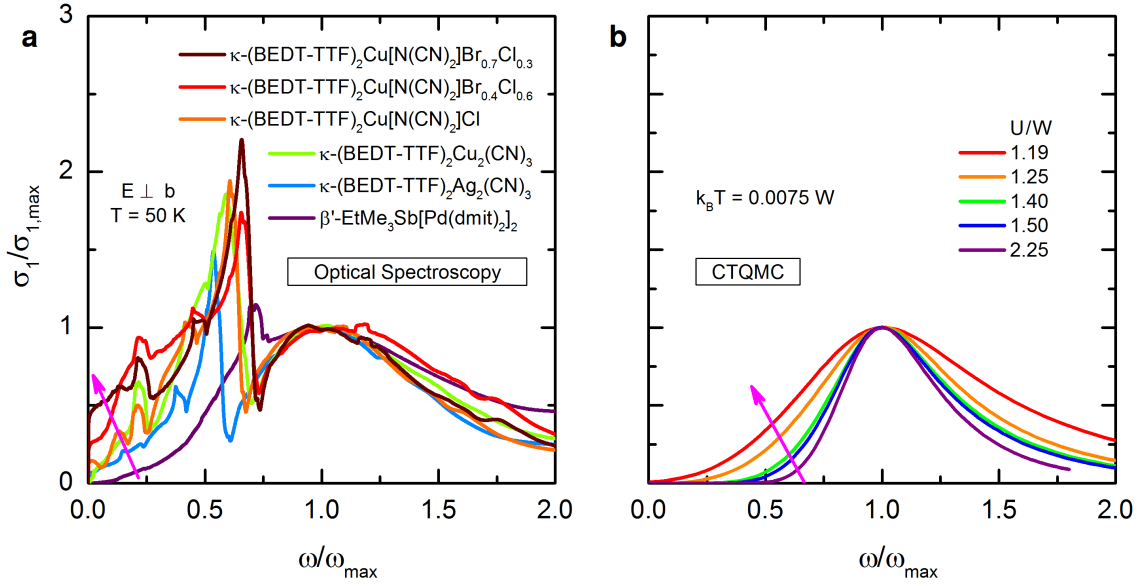


Figure 5.1.14: (a) Normalized optical conductivity of several two-dimensional Mott insulators with different correlation strength U/W ; the data are smoothed and normalized to the maximum conductivity $\sigma_{1,max}$ of the Mott-Hubbard band and the corresponding frequency ω_{max} . The $T = 50$ K data for EtMe, AgCN and CuCN are complemented by spectra of κ -Br _{x} Cl _{$1-x$} with $x = 0$ and 0.4 above their magnetic order ($T_N = 25$ K), as well as $x = 0.7$ [21, 22]. (b) Bandwidth-tuning affects the experimental optical conductivity in a similar way as the dynamical mean-field theory result using the continuous time quantum Monte Carlo (CTQMC) impurity solver. Most important is the enhancement of the low-frequency conductivity when correlations are reduced, as indicated by the magenta arrows.

Fig. 5.1.4. We calculated the SW for the highest conductivity direction of the κ -Br _{x} Cl _{$1-x$} series ($\omega_i = 700$ cm⁻¹) and conclude that these materials show a similar non-thermal enhancement of the in-gap absorption like it was observed for CuCN (Fig. 5.1.8 d). In a very similar way, the low-frequency SW increases upon cooling down to 50 K although the dc resistivity (Fig. 5.1.13 b) resembles an insulating behaviour. There is only little difference between $x = 0$ and 0.4 , on the one hand, as both are located in the Mott insulating region, and the compound with $x = 0.7$, on the other hand, which is in the incoherent regime above $T_{MI} \approx 50$ K. We conclude that the non-thermal enhancement of the SW is caused by metallic fluctuations that occur on both sides of the quantum Widom line in the vicinity of the metallic phase, i.e. in the Mott state and the incoherent regime, as pointed out in Fig. 5.1.13 (a). This precursor of coherent quasiparticles appears to be a robust feature observed in Mott insulators with and without magnetic order, and varying degree of geometrical frustration. Also, the effect of antiferromagnetism can be clearly separated since

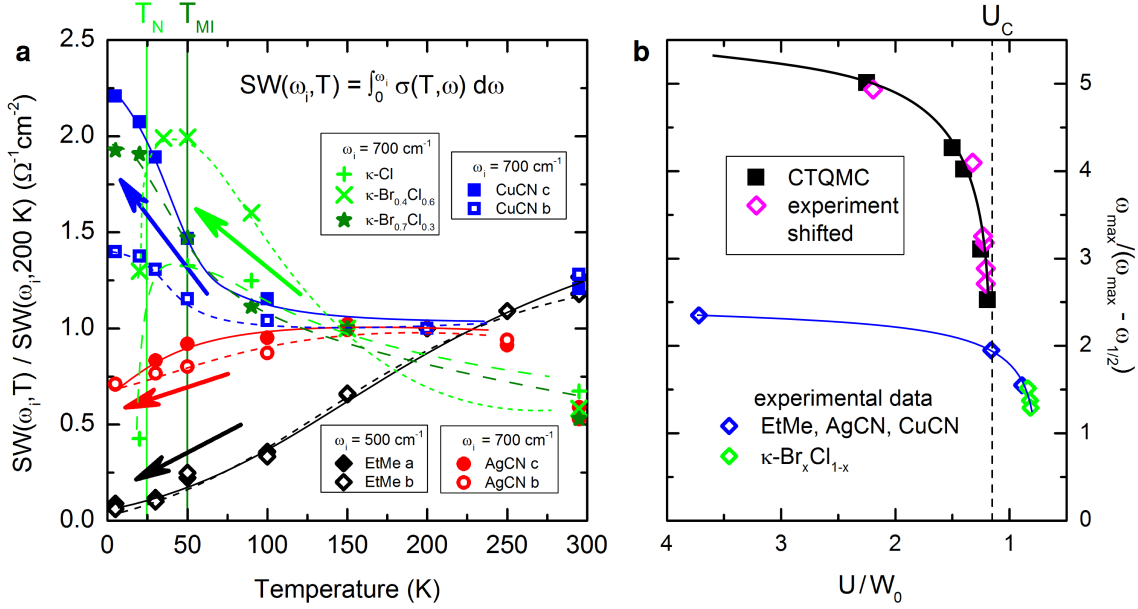


Figure 5.1.15: The optical parameters are compared between quantum spin liquids (QSL), antiferromagnetic (AFM) Mott insulators and theory. (a) Temperature evolution of the spectral weight SW of the three QSL compounds EtMe , AgCN and CuCN . In extension to Fig. 5.1.8 (d), both polarizations are plotted yielding a similar temperature evolution. In addition, the SW of the antiferromagnetic Mott insulators from the $\kappa\text{-Br}_x\text{Cl}_{1-x}$ series is included [21, 22]. Above T_N these systems behave similarly as CuCN supporting our conclusion of the non-thermal absorption. As magnetic order sets in for $x = 0$ and 0.4 , the SW drops drastically due to the opening of the AFM gap. (b) Correlation dependence of the maximum of the Mott-Hubbard band with respect to its width contrasting the experimental data from Figs. 5.1.3 and 5.1.6 (blue) and the $\kappa\text{-Br}_x\text{Cl}_{1-x}$ series (green) with the continuous time quantum Monte Carlo results (black) from Fig. 5.1.12 (b). Note the reversed axis of ordinates. The discrepancy between experiment and theory is most likely due to several assumptions of the model. Still, the trends agree very well: i.e. the experimental data can be rescaled to match exactly with theory (magenta symbols). Hence, we conclude that the underlying Mott physics is reproduced reasonably well by the CTQMC calculations.

for $x = 0$ and 0.4 the SW rapidly drops below T_N when the antiferromagnetic gap opens. Apparently, charge fluctuations are suppressed more strongly by AFM order than by the intrinsic Coulomb interactions of the Mott state.

Finally, we compare the band shape of the experimentally determined optical conductivity with the spectra calculated by DMFT. Fig. 5.1.15 (b) shows the ratio of the Mott-Hubbard band maximum ω_{max} and the half-width on its low-frequency wing $\omega_{max} - \omega_{1/2}$, i.e. U/W as determined in Fig. 5.1.6, with respect to the degree of electronic correlations U/W_0 . For the experimental data, we plot the lowest tem-

perature values⁷ versus the theoretically calculated (DFT, extended Hückel) U/W_0 values from Table 5.1.1. The $\kappa\text{-Br}_x\text{Cl}_{1-x}$ data were extracted similarly as for the quantum spin liquids. At first glance, there is a considerable quantitative discrepancy between experimental and the CTQMC data since, apparently, the theoretical bands are narrower and the calculations imply the onset of Mott insulating behaviour at a larger U_c/W_0 . However, there are many assumptions of the theoretical model that may cause deviations of the absolute values, such as the Bethe lattice instead of a triangular lattice, the dimer approximation, electron-lattice coupling, screening etc. Therefore, it is reasonable to shift the experimental curve to a different onset U_c/W_0 and rescale the absolute values. As the result of such a transformation, the experimental data match perfectly with the theoretical ones and their curvature compares very well. Hence, our theoretical model that only includes the charge dynamics of the Mott insulator qualitatively reproduces the electrodynamic response of our optical spectroscopy results.

We further notice that the relation between $\omega_{max}/(\omega_{max} - \omega_{1/2})$ and U/W seems to be non-linear. Strictly speaking, this would imply that extraction of correlation strength from the band shape in a linear fashion (cf. section 4.3.1 and Fig. 5.1.6 h) is oversimplified; particularly in the limit of large U/W_0 the correlation strength is underestimated or, equivalently, the bandwidth is overestimated⁸. Having more experimental data points would certainly help to understand the details of the influence of Mott-Hubbard interactions on the band structure. Until then, however, the presented approach remains – to the knowledge of the author – the most useful effective method to experimentally determine the correlation strength on the insulating side of the Mott transition. On the metallic side, of course, one can investigate the renormalization of the Fermi liquid parameters, such as the effective mass enhancement m^*/m_{band} of coherent quasiparticles [44, 45].

⁷We use the 5 K values of the QSL materials and the 50 K data of the $\kappa\text{-Br}_x\text{Cl}_{1-x}$ compounds since they show magnetic order and metallic behaviour at the lowest temperatures.

⁸Going back to Fig. 5.1.10, this may explain the quantitative mismatch of the T/W scale for EtMe as W is overestimated for the compound with strongest correlations. Effectively, one would then have to stretch the U/W scale of EtMe, such that the ambient pressure position is more *left* in the phase diagram. Due to the small slope of the Widom line of this compound, the general characteristics of the phase diagram would not change within the error bars.

5.1.6 Metallic Side of the Unified Phase Diagram: Superconductivity and Fermi Liquid

The unified phase diagram introduced as the main result of section 5.1.3 shows that, in the realm of the single-band Hubbard model, the only relevant energy scale in a Mott insulator is the Coulomb repulsion; for a given U , the bandwidth⁹ W determines the horizontal and vertical coordinates in the phase diagram via U/W and T/W . While this is a remarkable finding on its own, we have not elaborated a potential relation to the metallic part of the phase diagram so far, which accomodates a Fermi liquid state with strongly renormalized quasiparticles and unconventional superconductivity adjacent to the Mott state. At $T = 0$ the bandwidth determines the ground state properties to be either on the insulating ($U/W > U_c/W$) or metallic ($U/W < U_c/W$) side of the phase boundary. Since there W is of the same order of magnitude as U , the range of renormalized temperature T/W is also fixed by the Coulomb repulsion. Hence, also the characteristic transition temperatures delimiting the metallic¹⁰ (T_{MI}), Fermi liquid (T_{FL}) and superconducting (T_c) phases should, in principle, depend directly on the size of U .

In order to establish whether these considerations base on a robust footing, let us examine some experimental data in the region of interest. As we have pointed out repeatedly in this thesis, one of the few materials classes where the single-band Hubbard model is valid is the (BEDT-TTF)₂X family, in particular the effectively half-filled κ -phase charge-transfer salts. Therefore, in addition to AgCN and CuCN, the pressure-dependent physical properties of the materials with $X = \text{Cu}[\text{N}(\text{CN})_2]\text{Cl}$, $\text{Cu}[\text{N}(\text{CN})_2]\text{Br}$, $\text{Cu}(\text{SCN})_2$ and I_3 were extracted from literature [105, 169–175]. Fig. 5.1.16 presents the pressure dependence of T_{MI} , T_{FL} and T_c of all these κ -compounds. Although the data points are scattered over a large temperature and pressure range, several general trends are identified. Continuing the reasoning of the previous sections, the critical pressure necessary to drive a Mott insulator metallic scales with the correlation strength, as nicely seen for the compounds AgCN, CuCN and κ -Cl where p_0 becomes smaller as U/W is reduced. Having crossed the low-temperature Mott insulator-metal phase boundary, the metallic and Fermi liquid states are stabilized with pressure and the characteristic temperatures T_{MI} and T_{FL}

⁹For convenience, we use W instead of W_0 in the following. The distinction between bare and renormalized bandwidth will not be of importance any more.

¹⁰Above the Fermi liquid phase the resistivity resembles metallic behaviour until it hits a maximum at T_{MI} and turns insulating. Since $\rho(T)$ crosses the Ioffe-Regel-Mott limit close to T_{FL} , associated with the collapse of well-defined quasiparticles, this electronic state is typically referred to as a *bad metal*.

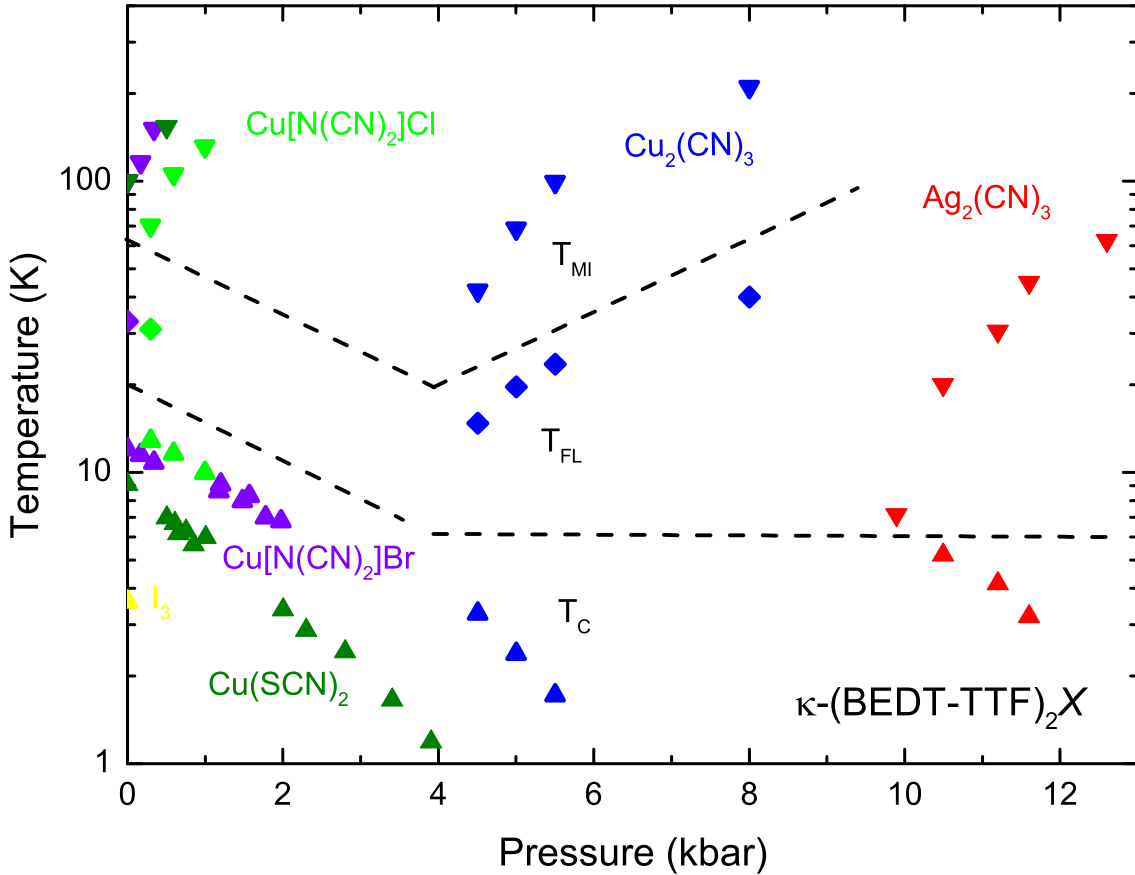


Figure 5.1.16: The pressure-dependent properties of several κ -(BEDT-TTF) $_2X$ compounds exhibit qualitatively similar trends. Depending on the respective degree of electronic correlations, a different amount of pressure has to be applied to drive the insulator-metal transition; while κ -(BEDT-TTF) $_2\text{Cu}[\text{N}(\text{CN})_2]\text{Cl}$ becomes (super-)conducting already at a few 100 bar, larger pressure is necessary for CuCN and AgCN. Once on the metallic side of the low-temperature phase boundary, the general behaviour is very similar for all compounds: the metallic and Fermi liquid states expand to higher temperatures while superconductivity is suppressed quickly, as denoted by T_{MI} , T_{FL} and T_C , respectively. The dashed lines indicate the temperature ranges of the respective transitions. The data were reproduced from Refs. [15, 105, 118, 169–175].

increase quickly towards 100 K and above. On the other hand, opposite behaviour is found for superconductivity, where T_C decreases continuously with pressure and vanishes for a few kbar.

These observations are not new and have been summarized in phenomenological phase diagrams already 20 years ago [120, 122]. While the superconducting state was studied in great detail, not much attention was devoted to the metallic and Fermi liquid phases, not to mention the quantitative scales. Furthermore, the discussed range was typically confined to temperatures below the back-bending of the

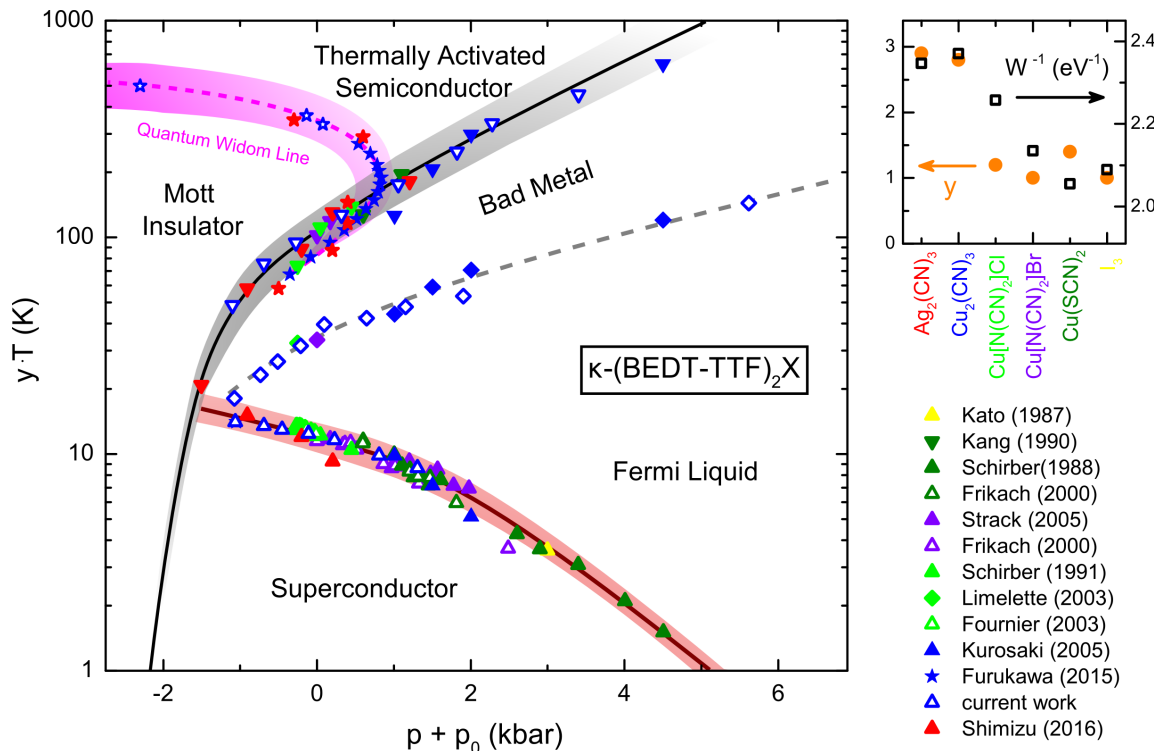


Figure 5.1.17: The pressure-dependent transition and crossover temperatures of several $\kappa\text{-(BEDT-TTF)}_2X$ compounds were collapsed on top of each other in a quantitative phase diagram on common scales. Since U and W were not available for all materials in a similar quality as for EtMe , AgCN and CuCN , we applied a linear pressure shift p_0 on the horizontal axis to account for the different U/W values; the vertical temperature scale was adjusted by multiplying a phenomenological value y . As a result, a simultaneous match of the limiting temperatures of the Mott (T_{QWL}), (bad) metallic (T_{MI}), Fermi liquid (T_{FL}) and superconducting (T_c) states was achieved. y follows the trend of the inverse bandwidth W^{-1} indicating a relation with the discussed T/W scaling in section 5.1.3. The symbols of different colour, shape and interior denote the respective references [15, 105, 118, 169–175]; additional CuCN transport data from A. Löhle are included (open blue).

quantum Widom line, which was not yet identified as the high-temperature boundary of the gapped Mott state at that time. In this regard, keeping in mind the results of the previous sections, Fig. 5.1.17 presents an attempt to collapse the characteristic temperatures of all these compounds in one phase diagram on common scales. For CuCN we added the dc measurements from A. Löhle which are in agreement with Refs. [14, 118] but more detailed and, importantly, include all transition temperatures in one data set. While we concluded in section 5.1.3 that the proper rescaling is performed as U/W and T/W on the horizontal and vertical axes, respectively, the Mott-Hubbard band parameters of the $\kappa\text{-(BEDT-TTF)}_2X$ series were not at hand in a comparable quality for all materials like for the three quantum spin liquid com-

pounds presented in the previous sections. Moreover, the range covered in Fig. 5.1.17 corresponds to a small part of Fig. 5.1.10 only; since the according modifications of U/W are pretty small, the error bars of optical spectroscopy become significant. Thus, a different approach was elaborated where the changes in U/W are adjusted by an additive pressure shift p_0 under the assumption of equal compressibility¹¹ and temperature is scaled multiplicatively by the phenomenological factor y . Overall, a remarkable fit can be achieved for all compounds, collapsing the respective transition temperatures simultaneously on universal lines. While p_0 decreases in the order AgCN–CuCN–Cl–Br–SCN–I₃, y seems to be linked to the inverse bandwidth W^{-1} , here taken from DFT calculations (Table 5.1.1 and Ref. [176]). Thus, this effective scaling procedure is consistent with the overall correlation strength¹².

At this point I take the liberty to formulate the following statements:

Mott-Hubbard scaling reaches beyond the gapped Mott state and, altogether, determines the phase boundaries of the metallic, Fermi liquid and superconducting states.

If this statement proves true, it has far-reaching consequences for electronic systems at half filling¹³ with sufficiently strong correlations:

(i) Coulomb repulsion is the only relevant energy scale for coherent transport. Distinct combinations of T , W and U determine the degree of charge localization at which the Mott criterion $N^{-1/3} < Ca_0^*$ is overcome. In the insulating state the charge moves only a little around its lattice site. When its effective range of motion a_0^* starts overlapping with the neighbouring site, metallic transport sets in.

(ii) The Fermi liquid state with well-defined coherent quasiparticles forms (not far) below the Ioffe-Regel-Mott limit realized at a certain threshold U/W ratio defining the characteristic temperature T_{FL} . This is not surprising considering that a linear relation between T_{MI} and m_{band}/m^* was found consistently in DMFT results and experiment, linking the Fermi liquid to Mott-Hubbard interactions [177, 178].

(iii) The pairing glue of unconventional superconductivity bases upon quantum fluctuations¹⁴ proportional to U . Comparing the critical temperatures of κ -(BEDT-

¹¹In the course of constructing the unified phase diagram (Fig. 5.1.10) we indeed found a pressure scaling factor between AgCN and CuCN close to unity (Equ. 5.1.2).

¹²In case that the compressibility is not equal, however, the parameter y may partially reflect the different size of U since a squeeze of the horizontal scale in order to adapt for (small) variations of U/W requires adjustment of both p_0 and y .

¹³In principle, this concept should apply for any commensurate band filling $n = 1/2, 1/3, 1/4$ etc.

¹⁴Note, the phenomenological discussion above does not include spin fluctuations, which are of major importance for d -wave pairing [46]. However, recalling that the itinerant exchange mechanism implies $J \propto U(W/U)^2$ (cf. Equ. 2.3.11), also the magnetic exchange interaction originates from Mott-Hubbard interactions; at the Mott transition U_c/W is a constant, hence J depends directly on the absolute scale of U .

$TTF)_2X$ with Mott systems from different materials classes, such as Cs_3C_{60} ($T_c > 30$ K, $U \approx 1$ eV [106, 179–181]) or the cuprates ($T_c \approx 100$ K, $U \approx 4$ eV [46, 47, 182]), we indeed find that superconductivity is enhanced with U .

We notice that the universal lines in Fig. 5.1.17 imply a specific relation between T_{MI} and T_c fixed by the correlation strength. Combining (ii) and (iii) one may deduce that superconductivity is strengthened by the effective mass enhancement evident from the reduction of T_{MI} upon approaching the Mott transition. The specific relation between m^*/m_{band} and T_c would indicate an increase of the superfluid density triggered by the effective mass divergence; in overdoped cuprates the situation is different with the phase stiffness being the limiting parameter [183]. Such a distinction would also explain the markedly different phase diagrams of the bandwidth- and doping-tuned Mott transition – while superconductivity with the maximum T_c is adjacent to the insulating Mott state for the former, it has a dome-like shape for the latter with vanishing T_c towards the insulating phase. However, solid statements beyond phenomenological observations require more detailed studies and information on a potentially intrinsic relation of these temperature scales to each other, on the one hand, and the effective mass, on the other hand. Thus, we leave this issue open for future work.

5.1.7 Summary and Discussion

Inspired by theoretical calculations [4, 5] and recent experimental results [14, 15] on pristine Mott insulators we elaborated a novel scheme in order to collapse all data sets in one universal phase diagram on quantitative scales. In particular, we demonstrate in section 5.1.3 that, upon proper renormalization of the horizontal (electronic correlations U/W) and vertical (effective temperature T/W) axes to the bandwidth W , the boundary of the gapped Mott state – identified as the quantum Widom line – can be merged on one universal curve. Hence, the physics of *all* genuine Mott insulators is unequivocally described by the Coulomb repulsion U and the bandwidth W , which express as the separation and the width of the Hubbard bands, respectively, accessed via optical spectroscopy.

Scrutinizing frustrated Mott insulators with a quantum spin liquid ground state we were able to probe the intrinsic properties of the low-temperature Mott state in absence of magnetic order. Close to the phase boundary around $T = 0$ theory predicted a coexistence regime; however, such metallic fluctuations have not been established experimentally in the insulating state up to now. In this regard, we could trace the back-bending of the Mott insulator-metal boundary down to lowest temperatures

and unequivocally identify the Pomeranchuk-like anomaly in the electrodynamics of κ -(BEDT-TTF)₂Cu₂(CN)₃ (section 5.1.2); at finite frequencies, the material becomes more metallic upon cooling although remaining an insulator in the dc-limit. This way we finally solved the long-standing dispute of excess conductivity and counterintuitive temperature dependence in the optical conductivity of this spin-liquid compound [16–18]. The anomalous slope of the Mott insulator-metal boundary seems to persist down to lowest temperatures. Such emerging metallic character may reflect the phase coexistence and spatially inhomogeneous structures caused by (weak) disorder in the vicinity of the phase transition. This interesting issue could be studied by systematically adding extrinsic disorder by heavy-ion irradiation [184, 185]. The Anderson-Mott transition is subject of interest for decades [186], but here we provide a new possibility by exploring the dynamical properties of the fully frustrated case down to low temperatures and scaling the results in a quantitative manner.

In order to test the findings revealed by quantum spin liquid compounds, we reassessed the results on the less frustrated κ -(BEDT-TTF)₂Cu[N(CN)₂]Br_xCl_{1-x} series (section 5.1.5). Due to weaker frustration these materials order antiferromagnetically at low temperatures. However, the non-thermal absorption reminiscent of metallic fluctuations was found also in the Mott insulating state above T_N , corroborating our main conclusions. The different ground states, however, reveal that antiferromagnetism suppresses metallicity more strongly than the interplay of bandwidth and Coulomb repulsion in a genuine Mott insulator.

The last part (section 5.1.5) was devoted to the metallic side of the phase diagram. Experimental results of diverse κ -(BEDT-TTF)₂X salts with different correlation strength were combined in one phase diagram on common scales using a phenomenological approach featuring similar characteristics as the generic U/W – T/W scaling. As a result, we find that the various phases and the boundaries in between can be matched exactly on top of each other, revealing universal behaviour of the Mott insulating, superconducting, Fermi liquid and (bad) metallic states, all of which being inherently related to the Coulomb repulsion. In particular, a possible connection of the bandwidth-tuned Mott transition to high-temperature superconductivity is discussed.

By combining pressure-dependent transport data with optical conductivity, we can map the quantum Widom line up to an energy range never achievable in transition metal oxides, for they have a considerably larger bandwidth compared to the organic compounds studied here. Several thousands of Kelvins and pressures beyond the accessible experimental range are required to cover the entire phase diagram in

Fig. 5.1.10 by similar experiments in vanadium oxides, for instance (cf. Fig. 5.1.11). In the overlapping region close to the reversal of the quantum Widom line, however, the behaviour agrees rather well [24–27] indicating that the bandwidth is the proper scaling parameter and the underlying physics of genuine Mott insulators is universal. To further confirm the generality of our findings, it is desirable to extend these investigations to spin liquid compounds of different symmetry, e.g. kagome and other geometries; the intrinsic properties of the Mott MIT should prevail.

For transition metal compounds charge-carrier doping is the far more common way to go from the Mott insulating to the metallic regime, most prominent in the high-temperature superconducting cuprates. Despite enormous efforts devoted to this issue over the last 30 years, no general agreement was reached on a generic phase diagram [46, 182] that is in-depth understood comparable to the bandwidth-controlled Mott transition (Refs. [4, 5] and the current work). Very recently, theoretical studies identified the pseudogap in hole-doped cuprates as a Widom line and ascribe the transport, dynamic and thermodynamic crossovers to a common origin linked to the intrinsic Mott state [8, 9]. A similar rescaling approach as proposed in section 5.1.6 might be appropriate to reveal the inherent relationship between Coulomb repulsion, doping and superconductivity in transition-metal oxides.

5.2 Low-Energy Excitations of Quantum Spin Liquids

In the previous section we discussed the characteristic charge response of genuine Mott insulators and found general similarity, which allowed us to construct, for the first time, a quantitative phase diagram that connects experimental results of various materials and theoretical predictions. While the infrared data are in excellent agreement with the single band Hubbard model, this treatment did not consider spin excitations at all. Therefore, magnetic properties are simply not relevant for the Mott transition at intermediate and elevated temperatures, which is driven by the competition of Coulomb repulsion and kinetic energy. Still, we have also seen that magnetic order has a strong influence on the low-temperature thermodynamic and electrodynamic properties, as discussed in the context of κ -(BEDT-TTF)₂Cu[N(CN)₂]Br_xCl_{1-x} (section 5.1.5, in particular Fig. 5.1.13). Naturally, antiferromagnetic (AFM) interactions are expected to become pronounced at low energies only since $J \approx t^2/U \ll U$. Apart from the distinct thermodynamic properties of the AFM insulator-metal transition, also the optical spectrum is markedly different as it shows a hard gap on the contrary to the frustrated Mott insulators discussed in section 5.1.2. These characteristic low-energy properties of quantum spin liquids (QSL) were recently considered in the context of coherent spin excitations [16, 17, 119, 187], proposed not only to couple to the charge degrees of freedom [18, 85, 116] but even promote superconductivity [188] and alter the intrinsic properties of the Fermi liquid [19]. However, these claims have remained, in large parts, unproven until now and there is an ongoing controversy in which part of the phase diagram related phenomena may become stable, or even relevant. A recent DMFT study established that coherent spin excitations remain well-defined only deep within the insulating state; as the electrons become itinerant close to the Mott transition, spinons are strongly damped [20]. Here, we will discuss the electrodynamic properties of two QSL compounds far below the Mott gap and resolve which contributions correspond to the charge response, and which might be a candidate for the long-sought spinons.

5.2.1 Power-Law Conductivity in κ -(BEDT-TTF)₂Cu₂(CN)₃

At first, we investigate the low-frequency properties of κ -(BEDT-TTF)₂Cu₂(CN)₃, abbreviated as CuCN, which have been summarized in Ref. [187]¹⁵. The electro-

¹⁵While the data are certainly correct, we have reconsidered the interpretation to a large extent, as presented in section 5.1.2.

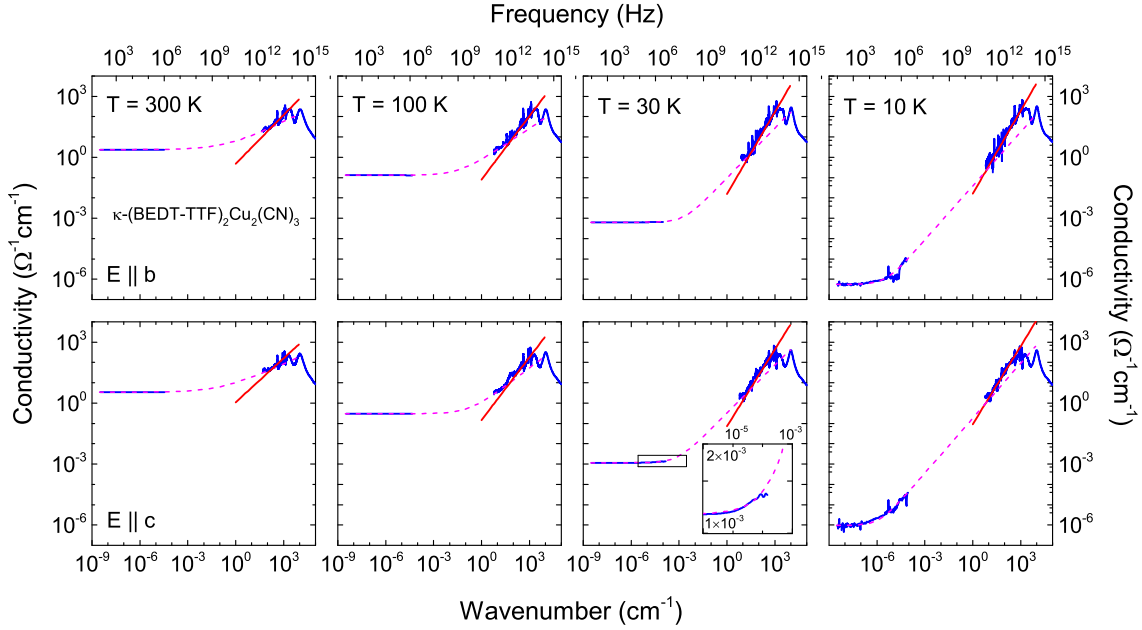


Figure 5.2.1: Overall optical conductivity of CuCN for the two polarizations $E \parallel b$ (upper panels) and $E \parallel c$ (bottom panels) for several temperatures as indicated. The dashed magenta lines are fits by $\sigma_1(\omega) = \sigma_0 + \omega^{\beta_1}$ to connect the two ranges, extending to a power-law with a different exponent β_2 in the THz range (solid red line). The inset is an enlargement of the frame in order to demonstrate the conductivity rise in the MHz range.

dynamic response of this organic spin-liquid candidate has been measured in an extremely wide energy range (10^{-13} to 2 eV) as a function of temperature (5 to 300 K), as illustrated in Fig. 5.2.1. $\sigma_1(\omega)$ is plotted from the dielectric range up to optical frequencies and, hence, connects the dc results [153] with the optical data (cf. Figs. 5.1.2 and 5.1.6). Due to technical reasons, the intermediate microwave region could not be accessed so far. As the temperature is lowered, the optical conductivity is strongly suppressed below the far-infrared ($\omega < 100 \text{ cm}^{-1}$), consistent with the insulating dc transport properties. The mere fact that the non-thermal enhancement of the in-gap absorption (Fig. 5.1.8 a) happens, for the most part, at energies above the exchange coupling $J \approx 250 \text{ K}$ implies that this cannot stem from exotic spin excitations. We explained it by metallic fluctuations that appear in the close vicinity of the Mott insulator-metal boundary and become more pronounced upon cooling due to the back-bending of the quantum Widom line (section 5.1.2).

We find that the data can be connected smoothly across the GHz-range by a straight line in the double-logarithmic plot, i.e. a power law in frequency $\sigma_1(\omega) = \sigma_0 + \omega^{\beta_1}$. Around the THz region the exponent changes to $\beta_2 > \beta_1$, which is pointed out in Fig. 5.2.2. It is interesting to note that the power-law ascend continues up to the

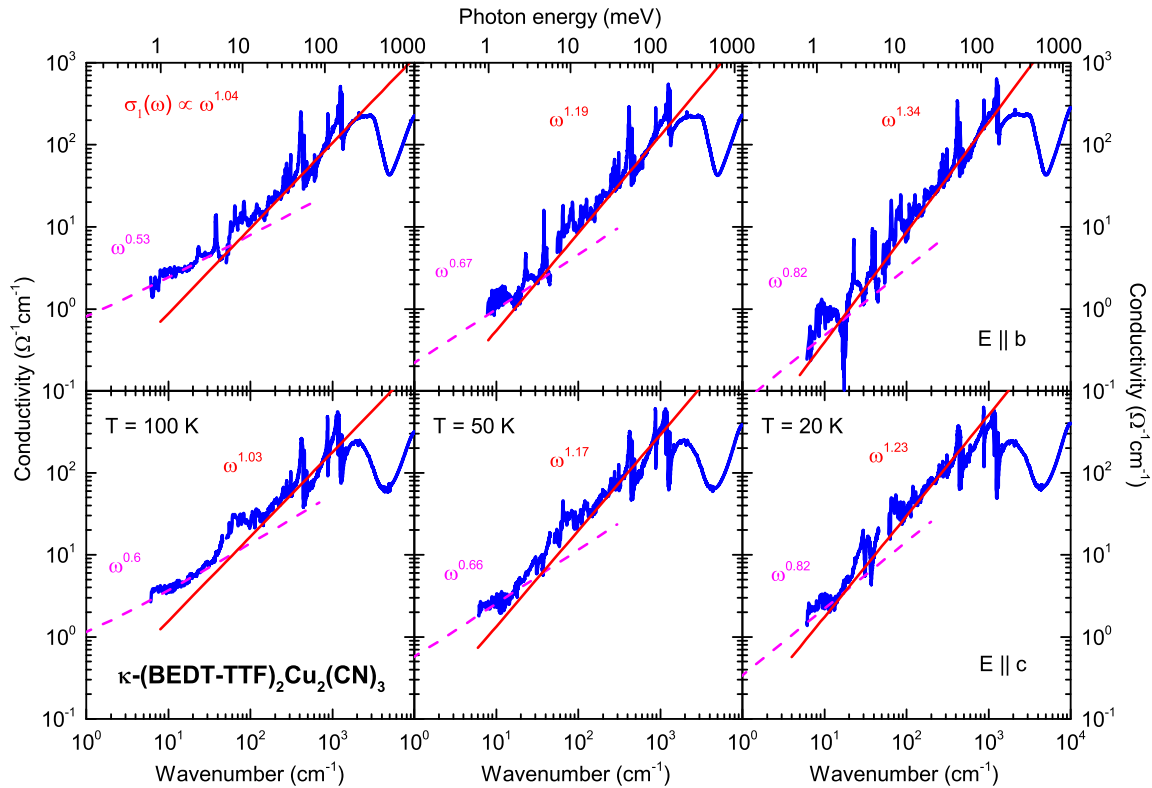


Figure 5.2.2: Optical conductivity of CuCN measured at $T = 100$, 50 , and 20 K for the two crystallographic directions (upper and lower panels as indicated). The dashed magenta lines correspond to the power-law behavior extending to low-frequencies, the solid red lines indicate the high-frequency power laws.

mid-infrared range without considerable discontinuities. Hence, it is most probably related with the smooth edge of the Mott-Hubbard band.

The original idea was that the power-law conductivity is related to a coherent spinon Fermi surface that couples to the low-energy charge excitations via an emergent gauge field [18, 189]. However, the experimental power laws around 0.9–1.4 [17, 119] are well below the theoretical prediction of $\beta_1 = 2$ below ($\hbar\omega < k_B T$) and $\beta_2 = 3.33$ ($\hbar\omega > k_B T$). Since also the energy range where they appear extends far above J , we are inclined to discard the idea of spinons in the electrodynamic response of CuCN.

Fig. 5.2.3 summarizes the optical conductivity and the extracted power-law exponents of all three studied QSL compounds. While $\kappa\text{-(BEDT-TTF)}_2\text{Ag}_2(\text{CN})_3$ (abbreviated as AgCN) behaves rather similar as CuCN, the power-law exponents of $\beta'\text{-EtMe}_3\text{Sb}[\text{Pd}(\text{dmit})_2]_2$ (abbreviated as EtMe) are significantly larger, reaching $\beta_1 = 1.8$ and $\beta_2 = 4.2$ with a much more pronounced temperature dependence because a well-defined Mott gap forms upon cooling (cf. Figs. 5.1.2, 5.1.6 and 5.1.7).

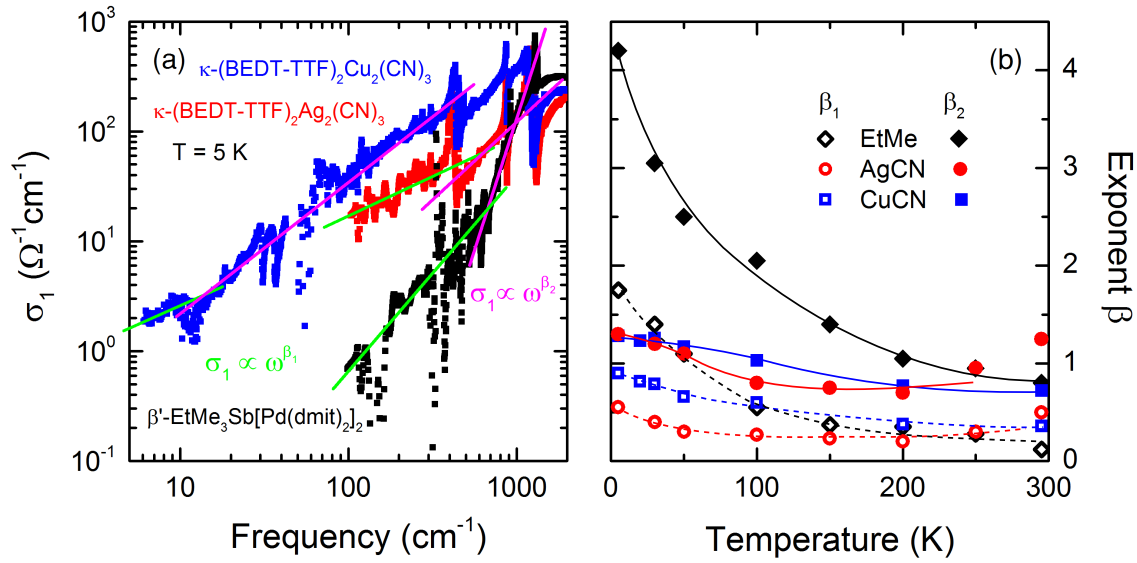


Figure 5.2.3: (a) The in-gap conductivity of EtMe, AgCN and CuCN can be approximated by power laws, as indicated by the straight lines in the log-log plot. Two different exponents are identified in different frequency regions. (b) The power-law exponents become larger upon cooling and level off at low temperatures. The theoretically predicted ω^2 behaviour could not be verified. Instead, the exponents reflect the steepness of the respective edge of the Mott-Hubbard band, which is most pronounced in EtMe due to the opening of a well-defined gap (cf. Fig. 5.1.7).

Summarizing, the measured exponents vary from compound to compound, reaching a maximum for EtMe, which is the most correlated system. Thus, our results suggest that the power-law exponent β is a measure of the U/D ratio in these compounds. In all these systems the power laws we observe do not coincide with the theoretical prediction for quantum spin liquids neither at high nor at low frequencies. The closest match with the predicted power laws would be achieved at 10 K in EtMe where, however, the crossover ω_c from β_1 to β_2 appears above 600 cm^{-1} , which is considerably larger than the theoretical prediction $k_B T \approx 14 \text{ cm}^{-1}$ at this temperature. This seems to rule out the spinon picture also for the other compounds, at least in the simplest form derived in Refs. [18, 116], a conclusion that is in accord with previous optical experiments on CuCN where a similar dependence of the excess conductivity was reported [16, 17]. Instead, the observations summarized in the above paragraph suggest a deep connection between the power laws in the sub-gap absorption and the respective position in the phase diagram, as the exponent β scales with the U/W ratio in these compounds.

Note that we cannot rule out a minor spinon contribution with a $\beta = 2$ power law masked by the dominant charge response, which decays only by $\omega^{1.4}$ towards zero

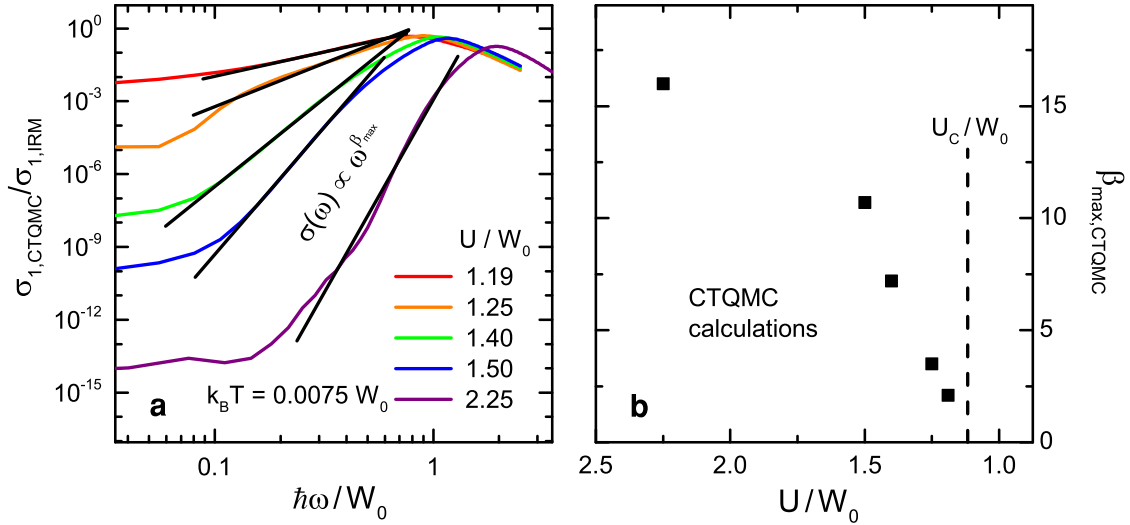


Figure 5.2.4: (a) Enhanced correlations imply a steeper band edge, illustrated by the double-logarithmic representation of $\sigma_1(\omega)$ calculated by the CTQMC method. σ_1 is plotted in units of the Ioffe-Regel-Mott limit σ_{IRM} . (b) As a result, the exponent increases with larger U/W_0 ; note the reversed direction of the axis, similar to Fig. 5.1.10. At the critical correlations U_c the spectra approach a metallic behaviour. Note that due to the implicit assumptions of the theoretical model, the band edge is generally much steeper than in the materials under study (cf. Fig. 5.2.3).

energy. At high frequencies, spinons should not play a role since the excitation energy exceeds the antiferromagnetic exchange coupling J . For compounds with a much larger charge gap, such as Herbertsmithite, the spinon contribution might become significant in the far-infrared and THz range. However, also there the experimentally observed exponent $\beta = 1.4$ is smaller than the predicted value.

In order to illustrate the correlation dependence of the steepness of the band edge, we plot the calculated CTQMC spectra from Fig. 5.1.12 on double-logarithmic scales and extracted the power-law exponents in Fig. 5.2.4. Indeed, the Mott-Hubbard bands become more narrow and exhibit a steeper edge and larger β for enhanced U/W_0 , very similar to the experimental spectra in Fig. 5.2.3. This indicates that the charge response alone is not only capable of explaining the transitions between the Hubbard bands in the mid-infrared, but it also captures the key features of the sub-gap absorption. Having such a good agreement without considering magnetic excitations at all strongly suggests that spinons are simply not relevant in this range.

5.2.2 Spinons Below the Mott Gap of β' -EtMe₃Sb[Pd(dmit)₂]₂

As inferred from the results and conclusions of the previous section and Ref. [20], spinons are not well-defined close to the Mott transition. As soon as the electrons become delocalized, the spin has to follow the charge movement, which destroys the coherence of the postulated spinon Fermi surface. Therefore, we analyze in this part the low-energy absorption of EtMe deep inside the Mott gap, in particular we extend our investigations to energies well below the antiferromagnetic exchange coupling $J \approx 250$ K [156]. In Fig. 5.2.5 we present polarized far-infrared transmission spectra of two single crystals with different thickness ($d = 50$ and $70 \mu\text{m}$), where Y. Saito assisted in data acquisition. We consistently find that the signal shape is very similar for both polarizations, except the larger absorption (smaller T) for $E \parallel a$, as already inferred from Fig. 5.1.2. Upon cooling, the material becomes successively more transparent below the Mott gap around 650 cm^{-1} that opens when cooling below 125 K, and well-defined Fabry-Perot oscillations appear. The sharp dips, nicely visible in the insets that show semilogarithmic scales, are due to vibrational features. Altogether, the data are in excellent agreement with Fig. 5.1.7. Interestingly, the increase of T towards low frequencies comes to a halt below 200 cm^{-1} , indicative of a rather broad absorption mechanism which we will discuss in the following.

In Fig. 5.2.6, we compare the resulting optical conductivity with the Kramers-Kronig and THz data, the latter ones being measured by B. Gorshunov and E. Zhukova in Moscow. There is good agreement between the values of $\sigma_1(\omega)$ determined by the different methods (cf. section 4.2): (i) from the Kramers-Kronig result using the extrapolated reflectivity, (ii) directly calculated from transmission and reflection, and (iii) from fitting the Fabry-Perot (FP) oscillations of the transmission signal using the independently-determined sample thickness. While between $200\text{--}500 \text{ cm}^{-1}$ the optical conductivity shows power-law behaviour ω^n with $n = 1.75$, the slope becomes much steeper upon approaching the maximum of the Mott-Hubbard band at higher frequencies (cf. Fig. 5.2.3). When continuing this to lower frequencies, however, the absorption is, in fact, significantly larger over a broad range $5 < \omega < 200 \text{ cm}^{-1}$, as inferred from the transmission data. Hence, there must be an additional absorption channel that adds on top of the low-frequency tail of the Mott-Hubbard band.

In Fig. 5.2.7, we plot the dielectric result together with the optical conductivity at higher frequencies. Since lower temperature data were not yet provided in the MHz range, we use the $T = 30$ K results here keeping in mind that σ_1 will be further reduced upon cooling, as deduced from the dc transport data presented in Fig. 5.1.7 (c). In the range between MHz and optical frequencies a stretched exponential is

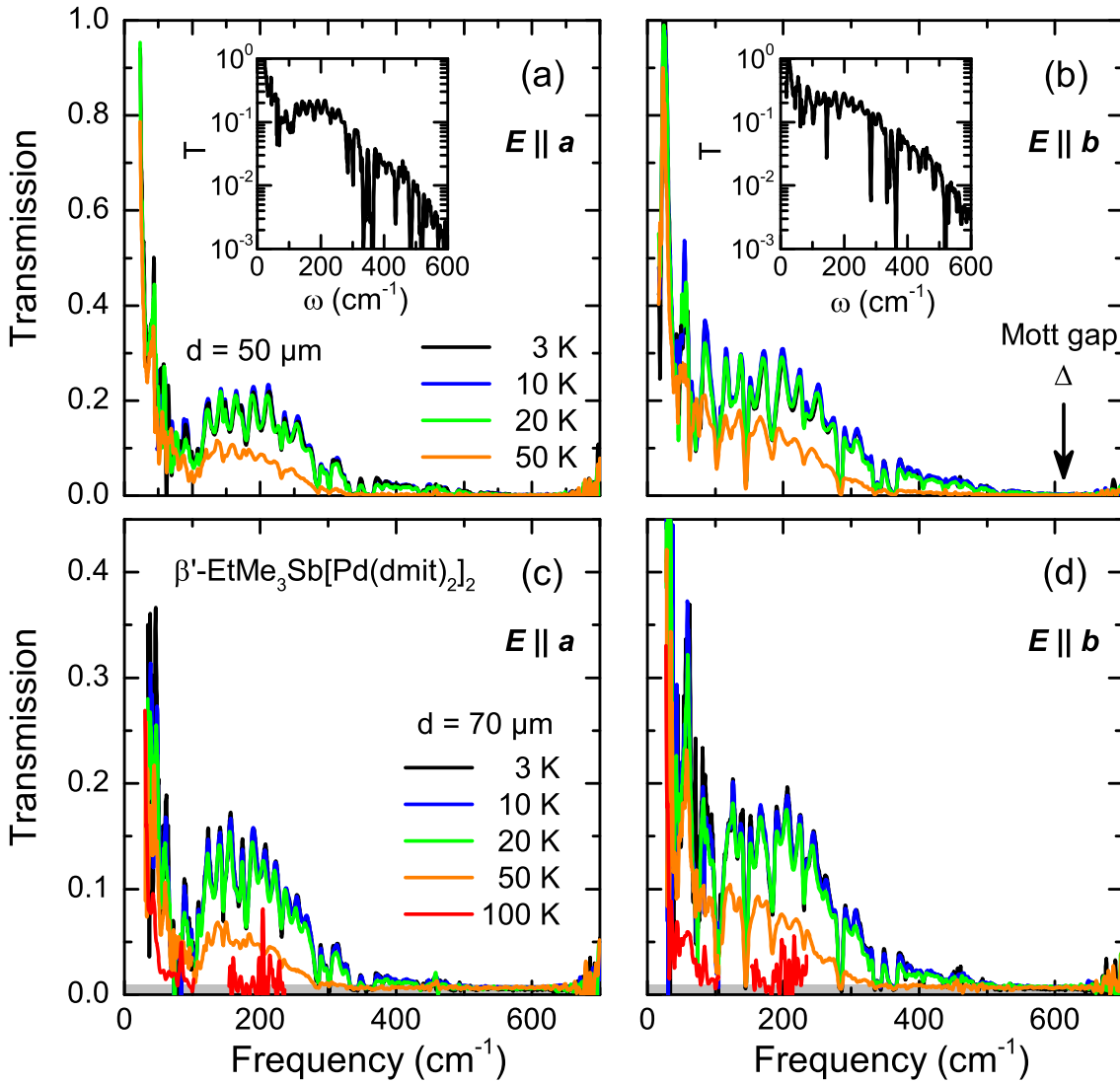


Figure 5.2.5: Polarized in-plane transmission spectra of EtMe measured on two single crystals of $50 \mu\text{m}$ (a,b) and $70 \mu\text{m}$ (c,d) thickness; note the different vertical scales. When the Mott gap opens below 125 K , the transmitted intensity becomes large enough to be measured; the transmission continues increasing down to the lowest temperatures. The sharp absorption features due to molecular vibrations and lattice phonons can be nicely observed in the semi-logarithmic plots in the insets of (a) and (b). Pronounced Fabry-Perot oscillations appear at the lowest temperatures, which allowed to determine σ_1 and σ_2 accurately around the extrema. The insets in (a) and (b) show the continuous increase of the transmission at 3 K from the Mott gap Δ towards zero frequency. A broad absorption feature is found below 200 cm^{-1} for both polarizations.

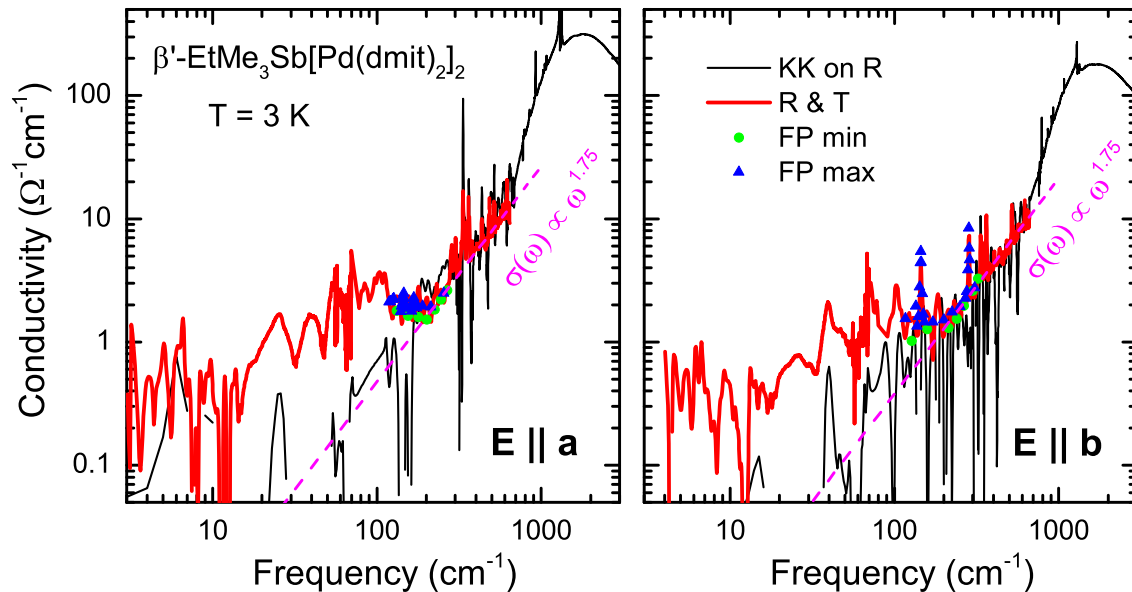


Figure 5.2.6: The low-frequency conductivity of EtMe determined by different methods gives similar results, making the observed features very robust. Apart from being pretty noisy for small σ_1 , below 100cm^{-1} the Kramers-Kronig result is not reliable any more as it depends strongly on the extrapolation. Apart from the absolute values, there is no appreciable anisotropy between the two in-plane crystal axes a and b . From $200\text{--}500\text{ cm}^{-1}$ a power law can be fitted to the data which crosses over to a larger slope reminiscent of the Mott-Hubbard band. For $\omega < 200\text{ cm}^{-1}$, however, σ_1 exceeds the extrapolated power-law descent towards lower frequencies indicative of an additional absorption mechanism.

plotted as a guide to the eye to illustrate an upper boundary for $\sigma_1(\omega)$ expected from the Mott-Hubbard band decay at high energies and the dielectric data. Indeed, the optical conductivity in the THz range is considerably larger than the presumable contribution from the correlated charge carriers. When we tentatively compare this feature to the predicted frequency dependence of a coherent spinon Fermi surface with two distinct power laws below and above $\omega = k_B T/\hbar$, the low-energy end of the THz data is exactly in the range where the behaviour should change from ω^2 to $\omega^{3.33}$. It appears that the quadratic descent towards lower energy would catch up the interpolated value of the correlated electrons rather quickly, i.e. already in the GHz range. When the electronic conductivity exceeds the spinon contribution, the related Fermi surface is likely to be damped away. Thus, the realm of coherent spinons is, in this picture, limited to a frequency range $0.1\text{ cm}^{-1} < \omega < 200\text{ cm}^{-1} \approx J$. Close to $T = 0$, however, this range is enlarged towards lower energies as the correlated charge carrier contribution asymptotically approaches the $\omega^{1.75}$ decay of the Mott-Hubbard band; the lower bound of the potentially spinon-dominated optical conductivity is then established by the crossing with the ω^2 line (green dashed) which will, therefore,

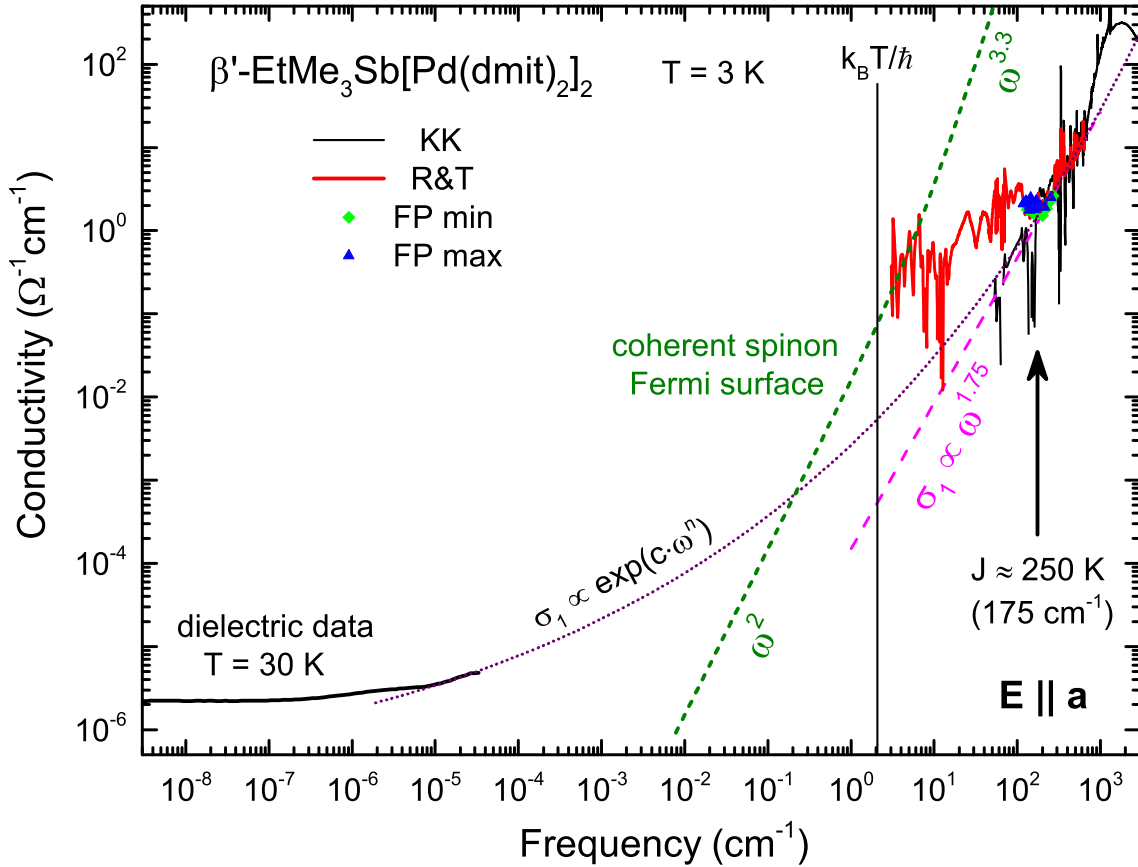


Figure 5.2.7: Dielectric and optical data are plotted in a broad range from radio frequencies up to the infrared. The optical conductivity in the THz and far-infrared ranges ($2 < \omega < 200 \text{ cm}^{-1}$) is much larger than the background, which was approximated in two different ways. On the one hand, the power law from the optical region was continued down to lower frequencies. On the other hand, we used a stretched exponential $\exp(c \cdot \omega^n)$ with $n = 0.1$ to smoothly connect the dielectric range with the optical data. The dashed green line represents the theoretically predicted frequency-dependence of a coherent spinon Fermi surface coupled to the optical conductivity via an emergent gauge field. The effective range of spinons presumably extends from the crossing of the ω^2 line with the electronic background conductivity up to the antiferromagnetic exchange coupling energy $\hbar\omega \approx J$.

not extend towards σ_{dc} as long as the electronic part exhibits a slower decay rate.

After subtracting the electronic power-law background, which is displayed in Fig. 5.2.8, the broad feature in the optical conductivity below 200 cm^{-1} is nicely revealed. Apart from a few phonons it is pretty much isotropic and, apparently, confined to a frequency range determined by the antiferromagnetic exchange $J \approx 250 \text{ K} \approx 175 \text{ cm}^{-1}$. Thus, we tentatively assign this in-gap contribution to spinons which occur when J is the dominant energy scale and the electronic conductivity is sufficiently suppressed at low temperatures. This result is consistent with the ω^2 behaviour predicted by

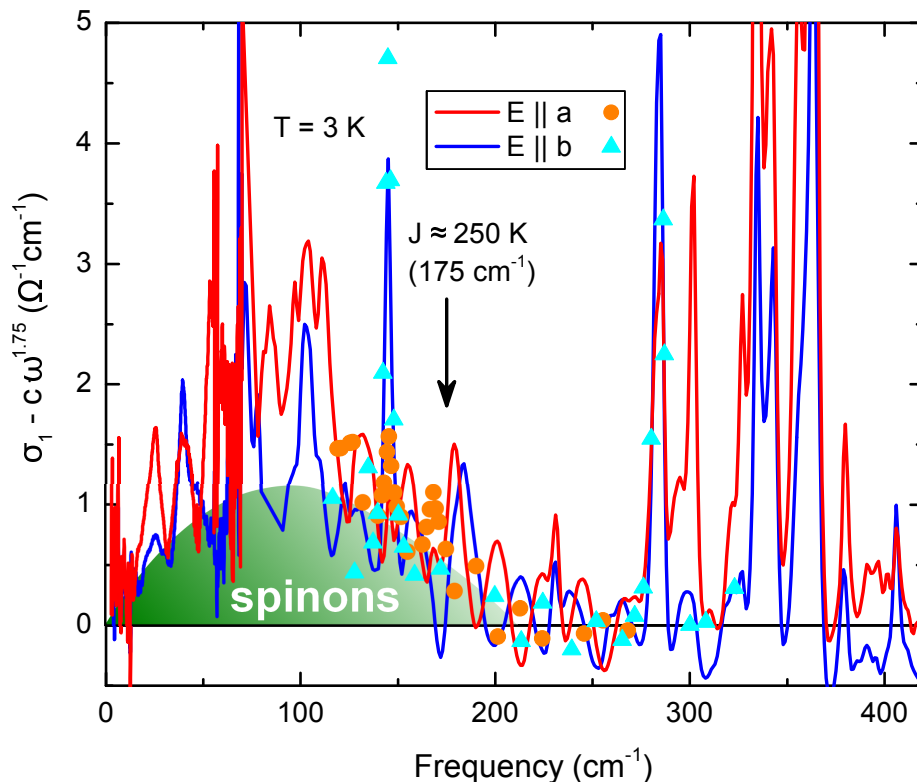


Figure 5.2.8: After subtracting the power-law background related with the Mott-Hubbard band, we obtain a broad low-energy feature below $\approx 200 \text{ cm}^{-1}$, which is close to the antiferromagnetic exchange energy of EtMe. Hence, we associate it with the coherent spinon Fermi surface predicted by theory [18, 116]. The dome-like shape of the spinon contribution arises due to the ω^2 decay towards $\omega \rightarrow 0$. This feature becomes visible when the background conductivity is sufficiently suppressed due to opening of the Mott gap. The strong, narrow modes at higher frequencies correspond to vibrational features.

Lee *et al.* [18, 116] since it decays faster towards $\omega = 0$ than the power-law background of the optical data and the hopping-related dielectric data that level off at σ_{DC} . Although present at finite frequencies deep within the Mott gap, spinons affect neither the optical range nor the dc response where the physics of correlated electrons prevails.

5.2.3 Summary and Discussion

We have scrutinized the low-energy properties of the three Mott quantum spin liquids β' -EtMe₃Sb[Pd(dmit)₂]₂, κ -(BEDT-TTF)₂Ag₂(CN)₃ and κ -(BEDT-TTF)₂Cu₂(CN)₃ on basis of their optical conductivity. For all these compounds the absorption decreases in a power-law fashion below the Mott-Hubbard band for $\omega \rightarrow 0$. Two distinct exponents are identified, a smaller one that extends towards the dielectric

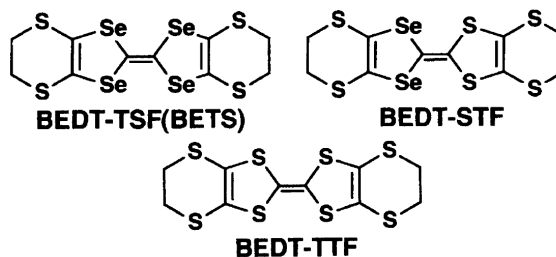
range and a larger one in the far-infrared, which amount to $\beta_1 = 1.8$ and $\beta_2 = 4.2$ for EtMe and 0.9–1.4 for CuCN and AgCN. Although particularly the values of the former material are not far from the theoretical prediction $\beta_1 = 2$ below and $\beta_2 = 3.33$ above $\hbar\omega = k_B T$ [18], the crossover observed in experiment appears far above the thermal energy ($600 \text{ cm}^{-1} \gg k_B T / \hbar \approx 2 \text{ cm}^{-1}$) and is even larger than the exchange coupling of $J \approx 250 \text{ K}$ [156]. In order to gain a deeper understanding of the band shape in these prototype Mott insulators, we compare the results with dynamical mean-field theory (DMFT) calculations. There, the sub-gap conductivity also reveals a power-law in frequency which successively increases with the strength of electronic correlations U/W , reproducing the experimental situation very well. Therefore, we rule out the proposed spinon contribution as a source of this peculiar behaviour since it is, apparently, described well in the context of charge excitations on the single-band Hubbard model without considering magnetic interactions at all. Motivated by these findings, we inspect more closely the energy range well below the exchange coupling J deep within the insulating Mott state of EtMe. Interestingly, we indeed find a contribution to $\sigma_1(\omega)$ that is considerably larger than the extrapolated low-frequency tail of the Mott-Hubbard band. Upon subtracting the power-law background, we obtain a broad mode delimited by J at its high-energy end; the strong decrease for $\omega \rightarrow 0$ is consistent with the ω^2 dependence expected for spinons. Since this feature vanishes faster towards the dielectric range and the dc limit than the charge excitations of the correlated electrons, the effective range of well-defined spinons is confined to the microwave and THz energy ranges. This is in excellent agreement with recent DMFT results stating that the controversially discussed spinon Fermi surface is damped away upon approaching the Mott MIT [20]. As soon as the electrons start moving as a whole, the spin excitations are not separated from the charge any more.

5.3 Mott Transition and Fermi Liquid in

$$\kappa\text{-}[(\text{BEDT-STF})_x(\text{BEDT-TTF})_{1-x}]_2\text{Cu}_2(\text{CN})_3$$

In this final part of chapter 5 we inspect more closely the nature of the bandwidth-tuned Mott metal-insulator transition (MIT) and its influence on the metallic state nearby. Similar as for the $\kappa\text{-}(\text{BEDT-TTF})_2\text{Cu}[\text{N}(\text{CN})_2]\text{Br}_x\text{Cl}_{1-x}$ (abbreviated $\kappa\text{-Br}_x\text{Cl}_{1-x}$) series, we employ chemical substitution and drive the materials conducting and even superconducting. As extensively discussed in section 5.1.5, modification of the anion layer ($\text{Cl} \rightarrow \text{Br}$) effectively reduces the electronic correlations U/W which causes a strong enhancement of the low-energy spectral weight and the emergence of a coherent quasiparticle response with well-defined Fermi liquid properties at low frequencies and temperatures [21–23, 161]. However, these compounds show sufficiently weaker geometrical frustration than the three quantum spin liquid (QSL) materials investigated in section 5.1, involving antiferromagnetic (AFM) order at low temperatures. Since this masks the genuine Mott transition, we will focus here on the most-studied QSL candidate $\kappa\text{-}(\text{BEDT-TTF})_2\text{Cu}_2(\text{CN})_3$ (abbreviated CuCN) subject to prototype Mott-Hubbard interactions in the entire phase diagram. We utilize a different approach compared to $\kappa\text{-Br}_x\text{Cl}_{1-x}$ and modify the conducting plane rather than the anions. Previous studies have shown that isovalent substitution of BEDT-TTF by BEDT-STF and BETS (see Fig. 5.3.1), where the S atoms are partially replaced by Se with more extended orbitals, leads to an enhancement of the intra-layer transfer integrals, effectively reducing the correlations U/W [125, 126]. Fig. 5.3.1 illustrates these three organic molecules. To that end, our observations unequivocally reveal the bandwidth-tuned Mott MIT in $\kappa\text{-}[(\text{BEDT-STF})_x(\text{BEDT-TTF})_{1-x}]_2\text{Cu}_2(\text{CN})_3$ (abbreviated $\kappa\text{-STF}_x$) with a strongly renormalized Fermi liquid state on the metallic side. This system is an ideal playground to study the effective mass enhancement upon approaching the Mott state from the metal and, when crossing the phase boundary from the insulating side, tracing the evolution of charge excitations and the shape of the Mott-Hubbard band.

Figure 5.3.1: By exchanging the inner sulfur atoms by selenium, the molecular wave functions become more extended. Chemical substitution of BEDT-TTF by BEDT-STF or BETS has a strong influence on the transfer integrals, resulting in considerable bandwidth-tuning [125, 126]. Reproduced from Ref. [125].



5.3.1 Bandwidth-Tuned Mott Transition

From dc transport experiments we find a prototype Mott MIT in κ -STF $_x$, very similar to the pressure-dependent results on CuCN [118]. Also the pressure dependence of the compounds with $x = 0.04$ and 0.12 revealed essentially the same behaviour, just with a $p = 0$ starting position more *right* in the phase diagram. Strikingly, a BEDT-STF-substitution of $x = 0.12$ results in superconductivity at ambient pressure, which was verified by independent dc and SQUID measurements. The comprehensive transport studies as a function of pressure and magnetic field were carried out by A. Löhle and will be circumstantially discussed in her PhD thesis. Optical experiments on κ -STF $_x$ at ambient pressure were conducted in great parts by M. Sanz Alonso in the course of her MSc thesis [190]. Additional spectroscopic and transport investigations on the compound with stoichiometry $x = 0.78$ were performed by Y. Saito; the BSc student K. Treptow participated in data analysis. Here, we present a comprehensive analysis of the fingerprints of the Mott MIT on the electrodynamic properties and, in particular, the band shape (cf. 5.1); in the following section, we inspect the Fermi liquid state via the extended Drude formalism.

Fig. 5.3.4 illustrates the optical conductivity of κ -STF $_x$ with $x = 0, 0.04, 0.12, 0.28, 0.44, 0.78$ and 1.00 at 5 K. With increasing substitution ratio a significant increase of the low-energy conductivity is observed going hand in hand with the emerging metallicity in the dc transport properties. This reminds strongly of the situation in κ -Br $_x$ Cl $_{1-x}$, which is plotted in Fig. 5.1.14 [21–23, 161]. At the same time, the maximum of the Mott-Hubbard band shifts towards higher frequencies. As shown in the inset of panel (a), the SQUID measurements revealed superconductivity with $T_c = 2.9$ K for $x = 0.12$. Therefore, such a small substitution is already enough to drive the material towards the Mott transition, corresponding to a hydrostatic pressure around 1–2 kbar (cf. section 5.1.3 and Refs. [14, 165]). In this regard, the introduction of BEDT-STF in the conducting plane has a considerably stronger effect on the bandwidth and electronic correlations than the modifications within the anion layers of κ -Br $_x$ Cl $_{1-x}$. The contour plot in Fig. 5.3.4 (b) nicely demonstrates the spectral weight (SW) redistribution from the Mott-Hubbard band to a narrow Drude peak at $\omega = 0$ upon the Mott MIT. Superconductivity appears exactly in the range between $x = 0.1$ and 0.2 where the Mott gap closes, but coherent quasiparticles are not yet stabilized.

Let us turn now to the temperature dependence of the optical conductivity in the strongly correlated metallic region discussed in section 5.1.6. Since for $x = 0.28$ dc transport reveals both the transitions from the incoherent semiconductor to the bad

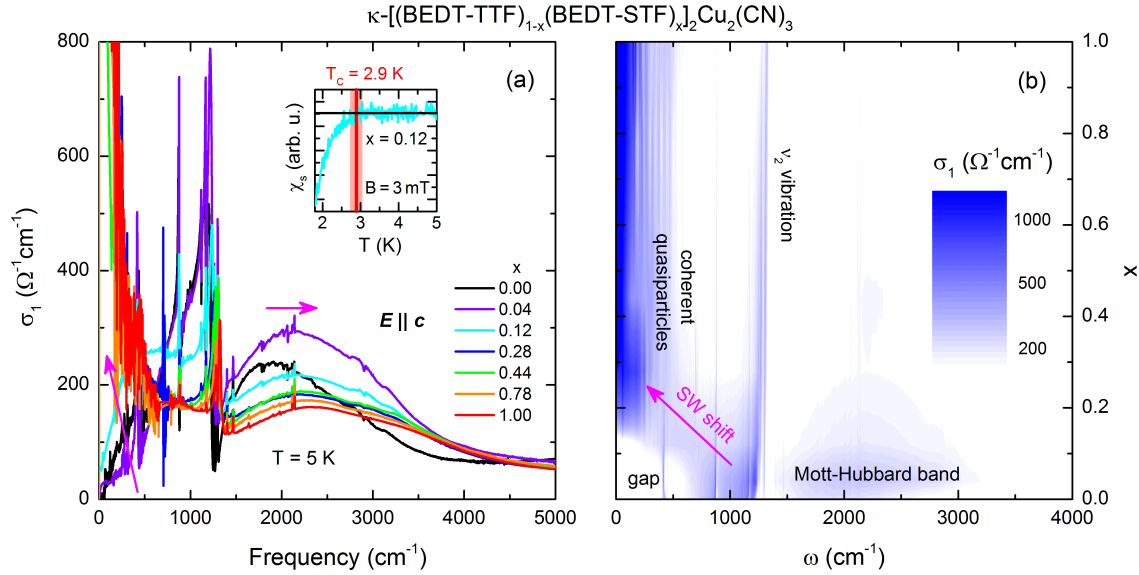


Figure 5.3.2: (a) Similar as in CuCN, the most prominent feature of the optical conductivity of κ -STF_x is the Mott-Hubbard band around 2000 cm⁻¹. Upon increasing x , this feature shifts towards higher energies. At the same time, a strong zero-frequency conductivity emerges indicating the transition from a gapped Mott insulator to a strongly correlated metallic state with renormalized quasiparticles. Inset: superconductivity with $T_c = 2.9$ K is stabilized at $x = 0.12$. (b) The contour plot (σ_1 is plotted on a logarithmic blue-white scale) illustrates the spectral weight shift from high to low energies as the BEDT-STF-content is increased. As correlations become less pronounced, the Mott gap closes and coherent quasiparticles are stabilized at low frequencies.

metal ($T_{MI} = 166$ K) and, then, to the coherent Fermi liquid state ($T_{FL} = 15$ K), we plot the corresponding spectra in Fig. 5.3.3 (a). While at high temperatures $\sigma_1(\omega)$ looks very similar as for the insulating parent compound CuCN, in good agreement with the sketched density of states in the schematic phase diagram in Fig. 5.1.5 (d), the spectral weight is successively shifted towards low frequencies upon cooling, overall very similar to the *SW* redistribution upon tuning the correlations at low temperatures. Specifically, we find that the low-energy optical conductivity remains broad and undefined in the bad metallic phase and strongly increases towards T_{FL} , where a well-defined, narrow Drude response is formed. This feature is associated with the condensation of coherent quasiparticles in the Fermi liquid state.

Fig. 5.3.3 (b) depicts the integrated spectral weight which initially shows an insulating-like low-frequency curvature that changes to a steep metallic increase at low temperatures. As illustrated in the inset, the *SW* is almost temperature-independent above 10^4 cm⁻¹ indicating that the band mass is conserved. The two distinct slopes at 5 K that level off at around 500 cm⁻¹ and 4000 cm⁻¹ correspond to the plasma edges of

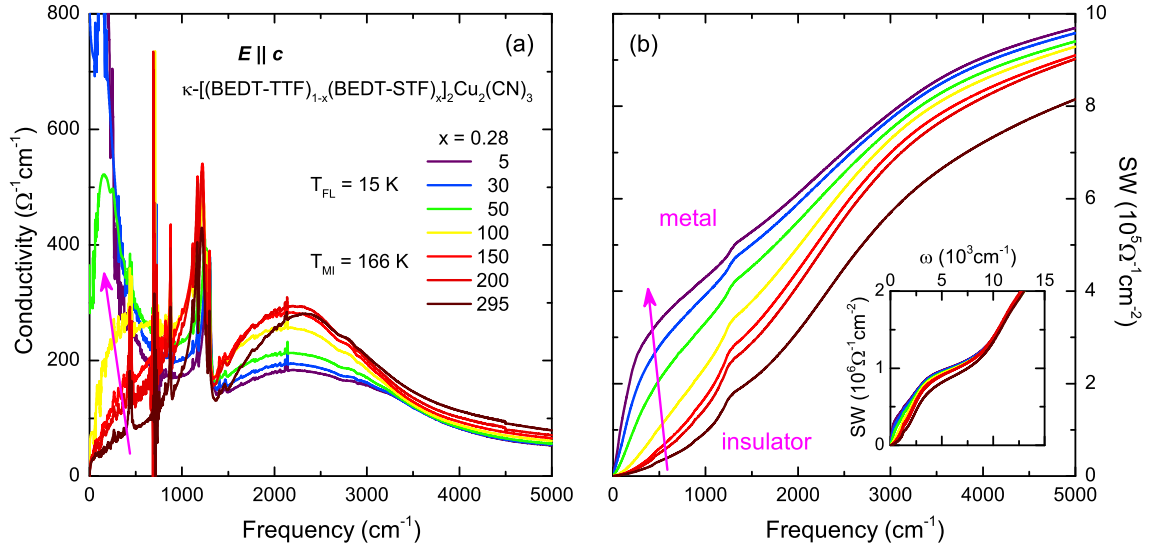


Figure 5.3.3: (a) The optical conductivity of the STF-substituted compound with $x = 0.28$ reveals the transition from an insulator at room temperature to a bad metal below $T_{MI} = 166$ K and a Fermi liquid below $T_{FL} = 15$ K. The in-gap conductivity becomes more pronounced upon cooling and, at the lowest temperature, a coherent quasiparticle peak condenses at low frequencies. (b) Correspondingly, the integrated spectral weight $SW(\omega)$ is shifted from high to low energies, which is typical for a metallic response (cf. 2.2.1). Note the qualitatively different slope and curvature at low frequencies due to insulating and metallic responses. Inset: $SW(T)$ collapses to one line above 10^4cm^{-1} proving that the increase at low frequencies is compensated at higher energies, thus the total SW is conserved.

the coherent and incoherent charge carriers, respectively. However, the uncertainty of the plasma frequency is pretty large, and extraction from the absolute value of the SW according to the sum rule (Equ. 2.2.6) is problematic as there is no perfectly flat plateau and the result depends strongly on the cut-off frequency. Therefore, we recall the behaviour of the dielectric loss function (Equ. 2.2.7), which peaks at ω_p , as nicely observed in the experimental data in Fig. 5.3.4 (a). We further notice, that there is another feature at lower frequencies related to the correlated electrons. As illustrated in the inset, we can approximate the low energy decay of the dominant peak by a power law and, upon subtracting it from the data, reveal a well-defined Drude plasmon reminiscent of coherent transport, which is plotted for all temperatures in panel (b). Upon lowering the temperature, this mode becomes well-defined and narrows significantly. Extracting the temperature dependence of the coherence parameter $\kappa = \omega_{p,coh}/\gamma_{coh}$ – the width (γ_{coh}) is significantly reduced with respect to the peak position ($\omega_{p,coh}$) – we find that the metallic state appears for $\kappa \geq 0.5$ and the Fermi liquid is stabilized close to unity. This value compares well with the results

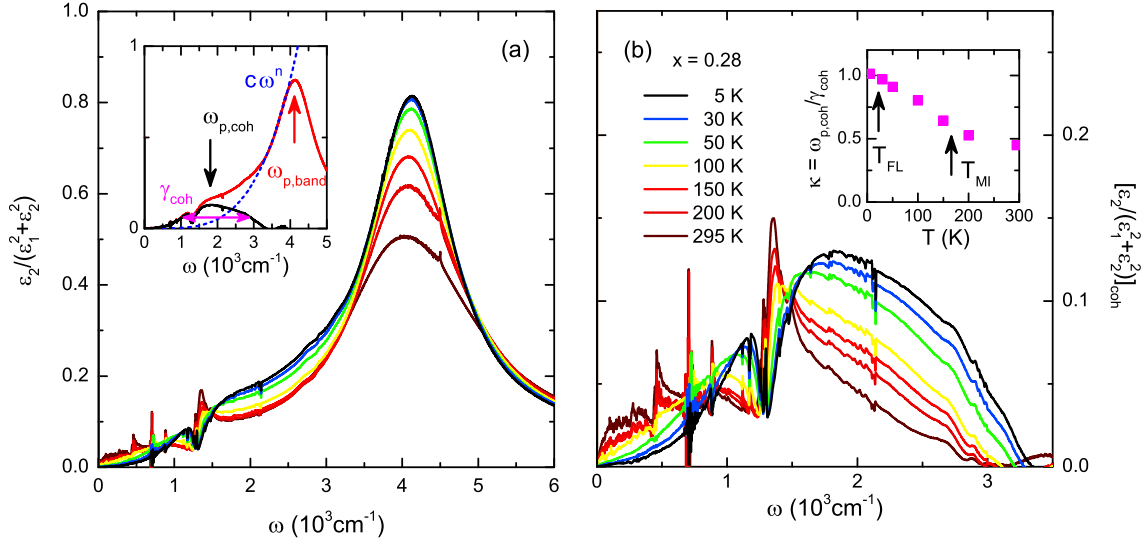


Figure 5.3.4: (a) In the dielectric loss function (cf. section 2.2.1) of $\kappa\text{-STF}_x$ ($x = 0.28$) the dominant contribution around 4000cm^{-1} corresponds to the plasma resonance $\omega_{p,\text{band}}$ of the correlated electrons on the organic molecules. Apart from a small blue shift, it narrows significantly upon cooling and a second feature appears at low frequencies, which is assigned to the formation of a metallic contribution in the course of the insulator-metal transition ($T_{\text{MI}} = 166 \text{K}$). As indicated in the inset, subtracting a power-law fit from the main mode reveals the plasma resonance of the coherent Drude peak centered at $\omega_{p,\text{coh}}$ with a full-width at half-maximum of γ_{coh} . (b) The transition from an overdamped feature at low frequencies to a well-defined Drude plasmon demonstrates the onset of metallic transport below T_{MI} . Inset: the ratio of resonance frequency and width, $\kappa = \omega_{p,\text{coh}}/\gamma_{\text{coh}}$, is a measure of charge carrier coherence.

of Pashkin *et al.* where $\kappa \approx 0.85$ for the dimensional crossover in $(\text{TMTTF})_2\text{X}$ from one-dimensional transport to 2D [191].

Now we evaluate the correlation dependence of the plasmon peak for the compounds with different chemical composition, as presented in Fig. 5.3.5. We find a consistent increase of the plasma frequency with larger x , which was also observed in $\alpha\text{-(BEDT-TTF)}_2\text{I}_3$ upon substitution with BEDT-STF and BETS [125]. The enhancement of $\omega_{p,\text{coh}}$ due to formation of a well-defined Drude plasmon in the loss function resembles very much the experimental results on doped cuprates [192]. In the inset we plot the extracted values of ω_p and utilize it to calculate the band mass which is, apparently, reduced with x . We explain it simply as a result of the increased bandwidth since this brings about a larger curvature $E = \frac{\hbar^2 \mathbf{k}^2}{2m_{\text{band}}}$. We do not exclude an influence of a modified unit cell volume that enters the plasma frequency via the charge carrier density N ; however, no structural data were available at this point. Note, that we discuss here the screened plasma frequency $\omega_{p,\text{screen}} = \sqrt{\frac{Ne^2}{\epsilon_\infty \epsilon_0 m}}$ related to the high-

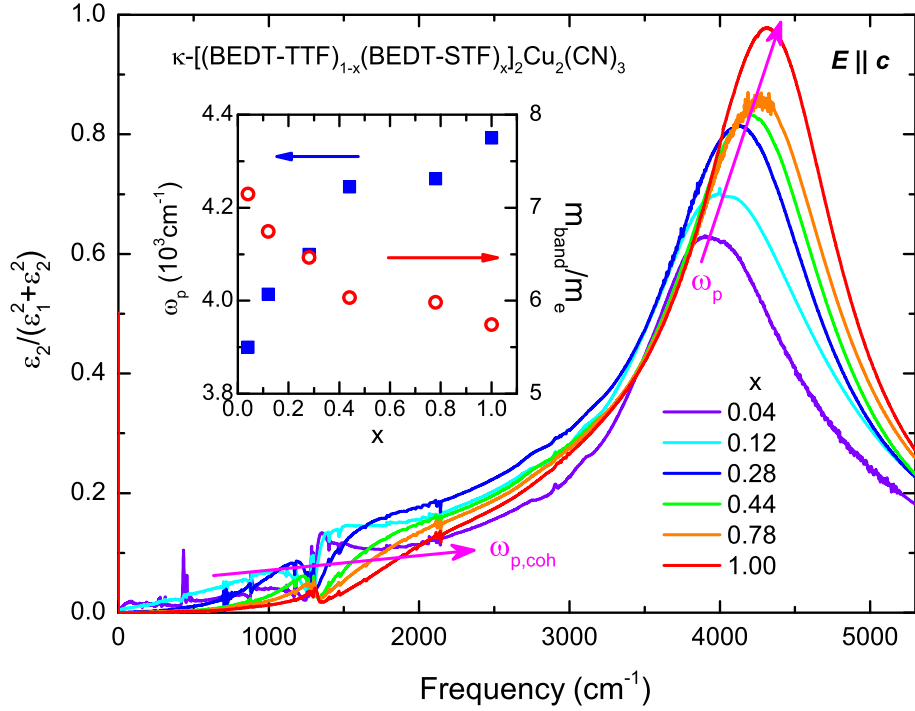


Figure 5.3.5: The loss function at $T = 5$ K reveals the bandwidth-tuned insulator-metal transition in κ -STF $_x$. Upon increasing x , the main plasmon shifts towards higher frequency and the coherent contribution becomes more pronounced indicating the formation of coherent quasiparticles. Inset: the enhancement of $\omega_{p,band}$ is equivalent to a reduction of the band mass m_{band} which results from the increased curvature d^2E/dk^2 due to larger bandwidth. A similar effect was reported for the material α -A $_2$ I $_3$, where $A = \text{BEDT-TTF}$, BEDT-STF and BETS [125].

frequency dielectric constant ϵ_∞ , that may also change upon chemical substitution. No consistent trend, however, is found at frequencies above the plasma edge; ϵ peaks around 10^4cm^{-1} at values of 2.5–3.5. Using these numbers, we obtain a bare band mass around 2 times the free electron mass, in agreement with the theoretical value of 2.3 for κ -Br $_x$ Cl $_{1-x}$ reported in Ref. [161], which is more realistic than the large m_{band}/m_e scale in the inset of Fig. 5.3.5.

Finally, we extracted the Mott-Hubbard band parameters of κ -STF $_x$ from the optical conductivity presented in Fig. 5.3.4, which is plotted in Fig. 5.3.6. Since it was not possible to use the method applied to the insulating compounds in section 5.1 due to the strong zero-frequency contribution of the Drude peak, we determined the bandwidth as 1/2 of the full width of the Mott-Hubbard band, as sketched in the inset (cf. section 4.3.1). In particular, the band edge at the high-frequency tail ω_{high} was defined from a linear cut-off; continuing $\sigma_1(\omega_{high})$ to the low-frequency tail yields ω_{low} . Thus, $2W$ corresponds to $\omega_{high} - \omega_{low}$ and, in the case of a strong

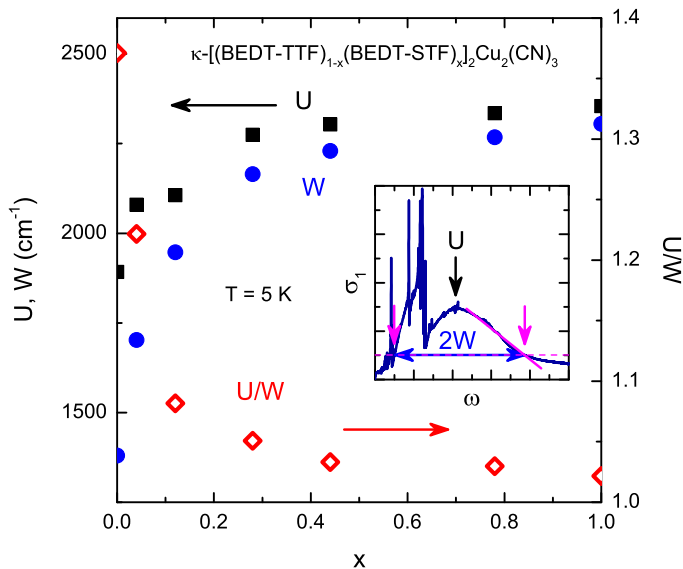


Figure 5.3.6: The bandwidth W and Coulomb repulsion U were determined from the optical data presented in Fig. 5.3.4. Although both W and U are enhanced with increasing the STF-content x , electronic correlations U/W are significantly reduced, providing evidence for the bandwidth-tuned Mott transition in these materials. Inset: the Coulomb repulsion is the maximum of the Mott-Hubbard band whereas the bandwidth was determined from the linearized cut-off at the high-frequency tail. The band shape was analyzed after subtracting the Drude component at low frequencies (cf. section 4.3.1).

Drude contribution¹⁶, it just equals ω_{high} . U was extracted after subtracting the low-frequency Drude peak, the frequency-dependent background of which slightly shifts the maximum of $\sigma_1(\omega)$.

As a result, we find that both the bandwidth W and Coulomb repulsion U are enhanced upon increasing the STF ratio. While this is exactly what we expected for W and the transfer integrals, U is typically assumed to be an atom/molecule-specific constant in the simplest models. However, in κ -(BEDT-TTF)₂X and other organic compounds with significant dimerization, the on-site term is related to the intra-dimer transfer integral t_d . In this dimer model, where one lattice site consists of two organic molecules carrying in total one electron, the Coulomb energy can be approximated as $U \approx 2t_d$ [117, 120]. This relation holds as long as the intra-dimer wave function overlap exceeds the inter-dimer hopping ($t_d \gg t, t'$) but is significantly smaller than the molecular on-site term $U_{BEDT-TTF}$, which is fulfilled for all compounds discussed here. To that end, the enhancement of U results naturally from the increase of all transfer integrals upon substituting BEDT-TTF by BEDT-STF. Most

¹⁶As a matter of course, the resulting Mott-Hubbard band parameters of CuCN are slightly different than in section 5.1.

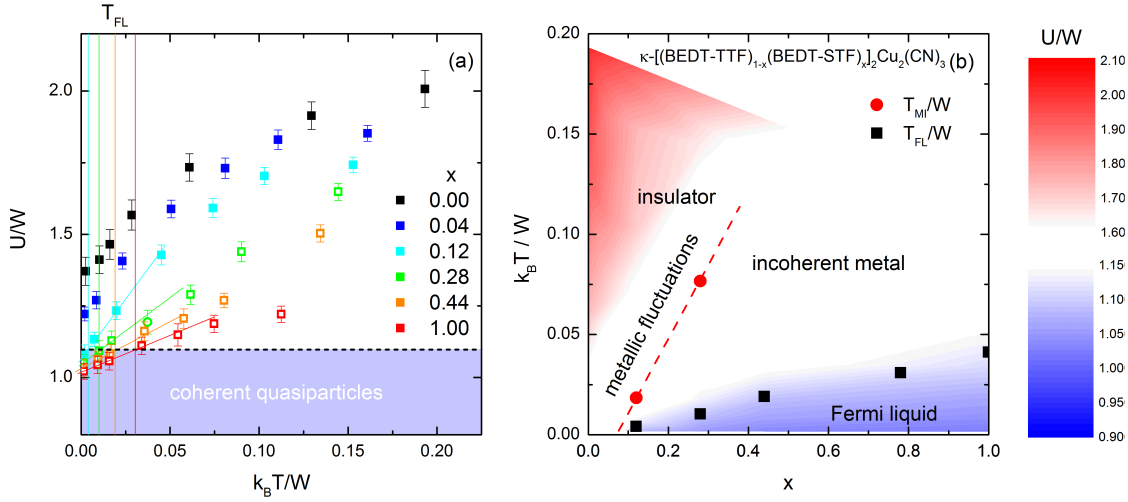


Figure 5.3.7: (a) The temperature-dependent Mott-Hubbard band shape U/W determined at all temperatures and substitutions is plotted with respect to $k_B T/W$. The characteristic Fermi liquid temperature determined by dc transport, indicated by the vertical lines, is enhanced with increasing x . There seems to be a specific U/W ratio below which coherent transport sets in (dashed black line). (b) The contour plot illustrates coherent (blue), incoherent (white) and strongly insulating (red) regions in the phase diagram of κ -STF $_x$. As already inferred from (a), the Fermi liquid phase is stabilized at a specific band shape. This implies that coherent quasiparticles become unstable below a certain density of states at $\omega = 0$ linked to a threshold U/W value.

importantly, however, the effective strength of electronic correlations proportional to U/W is successively reduced with increased x , consistent with the improved metallicity in these compounds. By this, we established the intrinsic bandwidth-tuning nature of the Mott MIT in κ -STF $_x$.

When comparing the temperature dependence of the band shape, which is illustrated in Fig. 5.3.7, we observe that the peak-to-width ratio of the Mott-Hubbard band is intertwined with the electronic state. In particular, the Fermi liquid state seems to be intrinsically related to a U/W ratio below a certain threshold. Thus, the coherent quasiparticles are stabilized only for sufficiently broad bands and large density of states at E_F . In the language of the single-band Hubbard model, this criterion is satisfied for the combination of (i) small temperatures – compared to the bandwidth, i.e. small T/W – and (ii) weak correlations. Both T_{FL} and T_{MI} increase towards higher temperature as U/W is reduced for larger x . To that end, we find that the metallic side of the phase diagram is, indeed, closely related to the strength of electronic correlations, underpinning the notions expressed in section 5.1.6. Thus, the Coulomb repulsion establishes a universal energy scale that – in a quantitative way – determines not only the metal-insulator transition, but also the regions where

superconducting, bad metallic and Fermi liquid properties are realized; the characteristic temperatures are unequivocally related to U and U/W . Extraction of the Mott-Hubbard band parameters provides a powerful tool to directly access the relevant quantities that quantitatively determine the entire phase diagram of the genuine Mott insulator.

5.3.2 Ioffe-Regel-Mott Limit: Universal Boundary of the Fermi Liquid

Having established the bandwidth-tuned nature of the Mott MIT in κ -[(BEDT-STF)_{*x*}(BEDT-TTF)_{1-*x*}]₂Cu₂(CN)₃, and the inherent relationship between electronic interactions and the Fermi liquid state, we proceed with the extended Drude analysis. In this regard, the frequency-dependent scattering rate $\gamma(\omega)$ and effective mass $\frac{m^*}{m_{band}}$ were determined according to Eqs. 2.3.4 and 2.3.5 using the plasma frequencies determined from the dielectric loss function in the previous section. In Fig. 5.3.8 we plot the temperature-dependent scattering rate of κ -STF_{*x*} with $x = 1$ on double-logarithmic scales to point out its fundamental frequency dependence¹⁷. While $\gamma(\omega)$ levels off at a constant value towards $\omega \rightarrow 0$ at high temperatures, it develops a pronounced frequency dependence upon cooling, in particular below $T_{FL} = 95$ K. At the lowest temperatures the scattering rate is reduced by two orders of magnitude and it scales as ω^2 over a broad range from the far-infrared up to the Mott-Hubbard band, which peaks at 2350 cm^{-1} for this compound (cf. Fig. 5.3.6). This quadratic behaviour is reminiscent of quasiparticle scattering in a Fermi liquid [28, 29] and extends up to $\omega_{FL} \approx 2000 \text{ cm}^{-1}$, above which γ is more or less constant with temperature in the mid-infrared range.

It is interesting to note that this value corresponds almost exactly to the Ioffe-Regel-Mott (IRM) limit – for comparison, the optical conductivity at the maximum of the Mott Hubbard band in Fig. 5.3.4 (a) is close to $\sigma_{1,IRM} = 260 \text{ cm}^{-1}$ of the parent compound CuCN [168]. Also the spectral shape of $\sigma_1(\omega)$ and the integrated spectral weight (cf. Fig. 5.3.3 b) of these compounds is very similar to DMFT results on doped Mott insulators that show Fermi liquid behaviour [31]. Upon closer inspection of Fig. 5.3.8 we indeed find that the ω^2 increase of the scattering rate does not vanish exactly at T_{FL} ; there is just a constant contribution $\gamma_0(T)$ added on top masking the quadratic increase in the log-log plot. The quadratic increase of $\gamma(\omega)$ towards the IRM limit, however, persists even above the characteristic Fermi liquid temperature

¹⁷ $\gamma(\omega)$ is expressed in units of angular frequency, i.e. $\gamma(s^{-1}) = 2\pi\gamma(Hz) = 100 \cdot 2\pi c\gamma(\text{cm}^{-1})$.

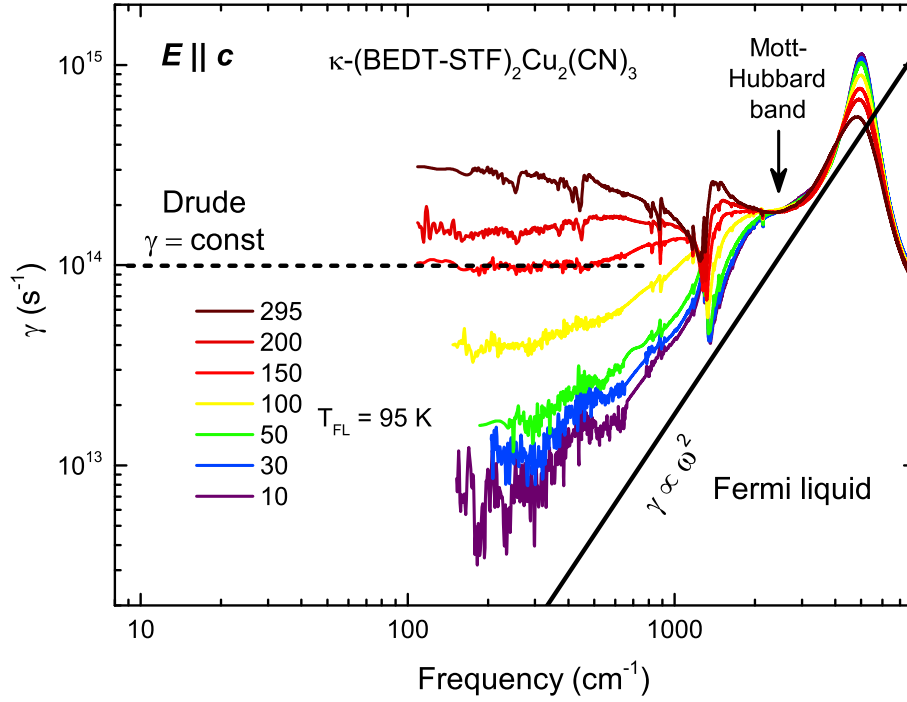


Figure 5.3.8: The frequency-dependent scattering rate of κ -STF $_x$ ($x = 1$) was calculated according to the extended Drude formalism (Equ. 2.3.4). At high temperatures $\gamma(\omega)$ is essentially frequency-independent corresponding to conventional Drude behaviour. Upon cooling through $T_{FL} = 95$ K, the scattering rate approaches the characteristic ω^2 dependence predicted for a Fermi liquid. Note, all curves merge around the maximum of the Mott-Hubbard band where γ approaches the Ioffe-Regel-Mott limit; quasiparticle scattering is the dominant contribution only at frequencies below $\omega_{FL} \approx 2000$ cm^{-1} . The feature between 1000 – 2000 cm^{-1} corresponds to the ν_2 vibration.

(Fig. 5.3.9 a), in good agreement with the picture of resilient quasiparticles discussed in Ref. [31]. In other words, the strong decrease of the scattering rate towards $\omega \rightarrow 0$ at low temperatures originates from the formation of the narrow contribution centered at zero frequency, which corresponds to the coherent quasiparticle peak in the spectral function. As temperature is increased, this feature broadens until it is completely dissolved when the IRM limit is crossed.

While we plot $\gamma(\omega)$ on a quadratic frequency scale in Fig. 5.3.9 (a), the effective mass with respect to the optically determined band mass is shown on a linear scale in panel (b). While $\frac{m^*}{m_{band}}$ is not well-defined at the highest temperature, it successively grows upon cooling and finally levels off at a constant value below ω_{FL} . We associate this plateau with m^* as it apparently extends down to the dc limit. The peak around the plasma frequency, which is well above the maximum of the Mott-Hubbard band, corresponds to the high energy region where electronic correlations are not important

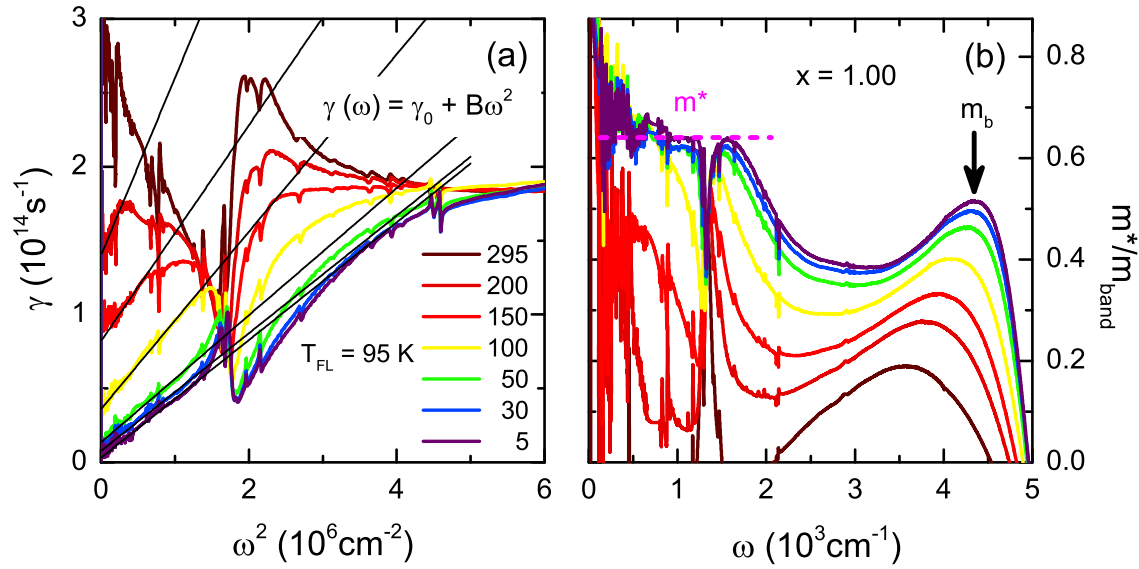


Figure 5.3.9: (a) The scattering rate is plotted versus ω^2 to reveal the characteristic frequency dependence of a Fermi liquid. Already above T_{FL} $\gamma(\omega)$ develops a quadratic-like behaviour, the frequency range ω_{FL} of which is successively expanded upon cooling. At the lowest temperature, the slope approaches the final value B_0 and the ω^2 dependence extends even above the ν_2 vibration before it saturates at the Mott-Hubbard band. The data were fitted at each temperature by $\gamma(\omega) = \gamma_0 + B\omega^2$ (thin black lines). (b) Below T_{FL} the effective mass becomes well-defined and acquires a constant value over a broad frequency range which coincides with the region where $\gamma(\omega) \propto \omega^2$.

any more. We assign this value to the uncorrelated band mass, denoted as m_b to avoid confusion; the effective mass enhancement is, therefore, expressed independently from ω_p .

The extended Drude analysis was carried out for all metallic κ -STF_x compounds; the lowest temperature results for $\gamma(\omega)$ and $\frac{m^*}{m_{band}}(\omega)$ are summarized in Fig. 5.3.10. We notice that the superconducting compound ($x = 0.12$), that does not exhibit a well-distinguishable T^2 dependence of the dc resistivity, shows a more or less constant scattering rate with an absolute value around γ_{IRM} towards low frequencies. Hence, the Fermi liquid response is almost completely suppressed by strong quantum fluctuations at the Mott transition. For the other compounds we find a monotonous decrease of the slope with increasing x accompanied by a reduction of the effective mass renormalization $\frac{m^*}{m_b}$. Note that the upper boundary of the Fermi liquid behaviour, ω_{FL} , extends at the same time, similar as the characteristic temperature T_{FL} of dc transport. The absolute values of the effective mass are smaller than those reported for κ -Br_xCl_{1-x} by Merino *et al.* [161], which is consistent with the location of the latter materials in the close vicinity of the Mott transition, where m^* is

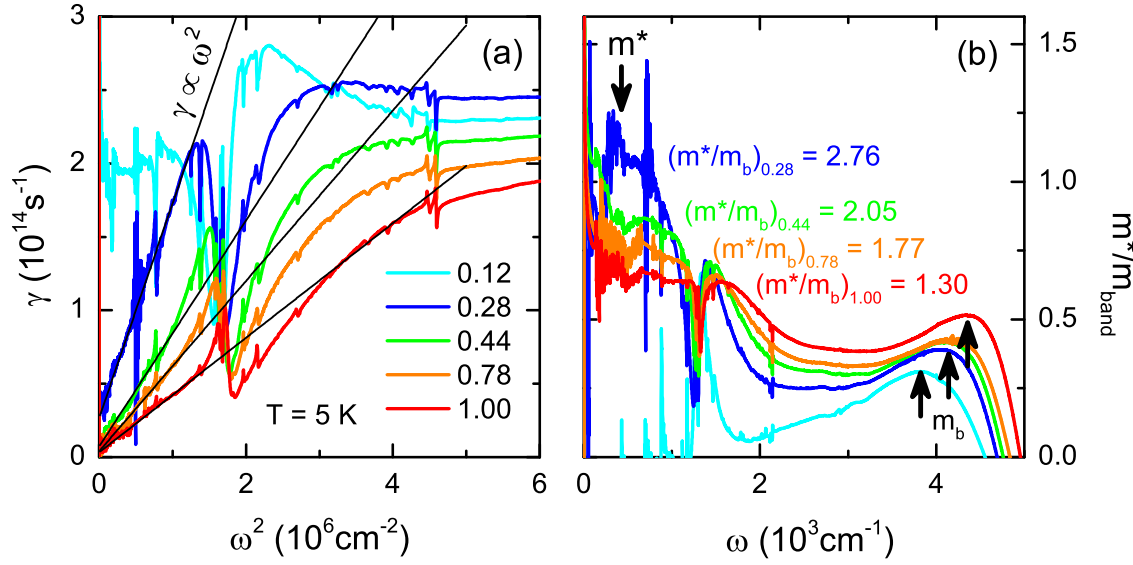


Figure 5.3.10: (a) $\gamma(\omega)$ is plotted at the lowest temperature for all STF substitutions that show metallic dc transport properties. At low frequencies, the scattering rate is constant for $x = 0.12$ indicating simple Drude behavior rather than a well-defined Fermi liquid response. The absence of coherent quasiparticles in the measured frequency range may be caused by strong quantum fluctuations in the vicinity of the Mott state which drive the superconducting transition. Nevertheless, a small window of coherence at lower energies can not be ruled out. For $x \geq 0.28$ the quadratic frequency dependence is observed as a hallmark of the Fermi liquid state. With increasing STF content the slope B is reduced and the $\gamma(\omega) \propto \omega^2$ range expands to higher frequency. (b) While the effective mass is ill-defined for $x = 0.12$, a plateau can be observed for higher STF ratio which coincides with the FL range in (a). We define $\frac{m^*}{m_{\text{band}}}$ as the ratio of the plateau value and the maximum around 4000 cm^{-1} . Thus, the mass enhancement becomes more pronounced as the Mott transition is approached.

expected to diverge.

In Fig. 5.3.11 we plot the temperature dependence of the fit parameters γ_0 and B . The quadratic prefactor B acquires a constant value upon entering the Fermi liquid regime. One could speculate whether the increasing tendency with T indicates enhanced correlations at higher temperatures, which would be in line with the decrease of the upper frequency boundary ω_{FL} . The zero-frequency extrapolation of the scattering rate shows a similar T^2 dependence as the dc resistivity, which is contrasted in Fig. 5.3.12. Interestingly, the T^2 behaviour persists even above T_{FL} for the optically determined $\gamma_0(T)$ which is another indication for the existence of resilient quasiparticles in κ -STF $_x$ [31].

When comparing the scales, we notice that the T^2 slope of the dc data is higher

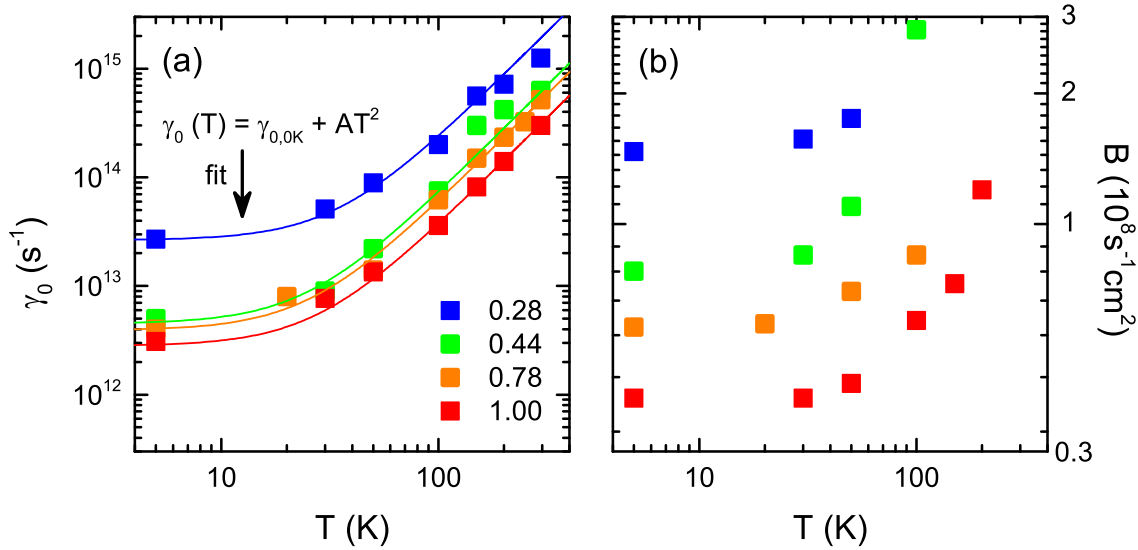


Figure 5.3.11: (a) The zero-frequency extrapolation $\gamma_0(T)$ obtained from the frequency-dependent fits ($\gamma(\omega) = \gamma_0 + B\omega^2$) at each temperature follows a T^2 dependence with prefactor A . Interestingly, this behaviour extends to higher temperatures than the quadratic temperature dependence in dc transport. (b) The prefactor B is constant at low temperatures and starts to increase above T_{FL} .

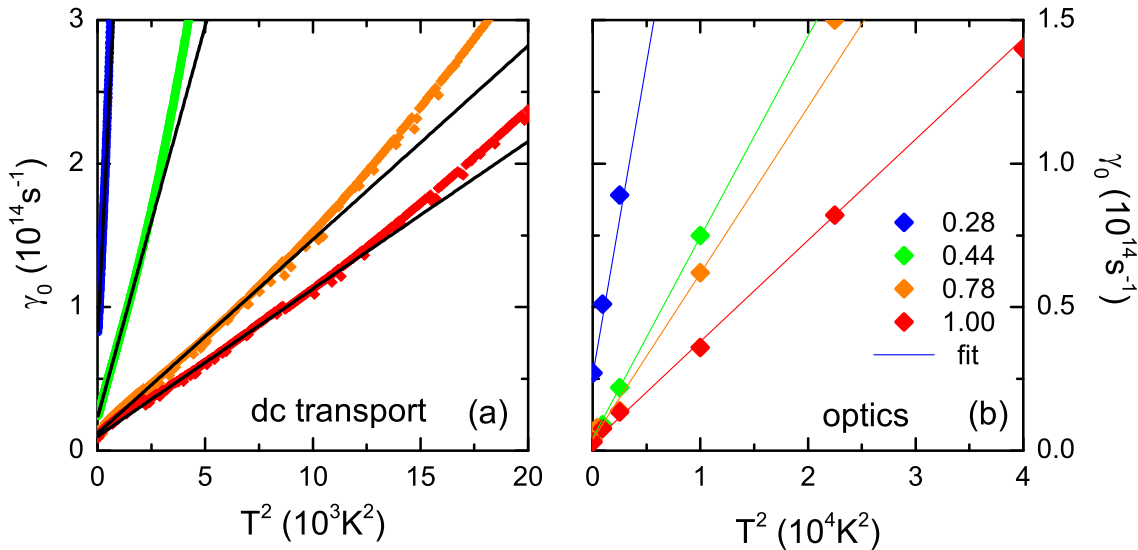


Figure 5.3.12: (a) The scattering rate of the dc conductivity was calculated using the same $\omega_{p,band}$ as in Fig. 5.3.8. (b) The $\omega \rightarrow 0$ extrapolation is plotted versus T^2 . Note the different scales of (a) and (b) implying a 5 to 10 times smaller prefactor A_{opt} compared to the dc result (a). On the one hand, this discrepancy may indicate differences of the intrinsic scattering processes at zero and finite frequency [29] or, on the other hand, it could reflect inaccurate absolute values of σ_{dc} due to uncertainty in determination of the geometry factor in the dc measurements. The latter argument explains small differences, in the worst case up to 100%, but certainly not one order of magnitude.

by a factor 5–10, which can be to some extent¹⁸ explained by problems in the determination of absolute values of the resistivity due to uncertainty in the geometry factor. Such a huge difference, however, possibly hints towards different scattering mechanisms in the dc and optical regimes, as discussed in Ref. [29]. So far, we did not mention a potential influence of disorder, which naturally appears in the course of chemical substitution¹⁹. To lowest order, however, this causes just an additional broadening of the Mott-Hubbard band which is self-consistently included in the renormalized scales U/W and T/W ; therefore, it does not affect the high-frequency properties too much. Low-energy effects such as superconductivity and dc transport are much more susceptible to disorder. Our latest pressure-dependent transport experiments have revealed that the maximum T_c is reduced with increasing x .

Now that we determined all relevant quantities, we discuss their basic relations in the context of general Fermi liquid properties in Fig. 5.3.13. Panels (a) and (b) demonstrate the overall consistency of our data with the Kadowaki-Woods ratio $A/\gamma_{Sommerfeld}^2$ since $B \propto A$ and $\gamma_{Sommerfeld} \propto m^*/m_b$. Importantly, both the quadratic prefactor and the effective mass were determined from the same set of optical data, making the $B \propto (m^*/m_b)^2$ relation even more reliable. It was demonstrated in Ref. [30] that, upon proper renormalization to some compound-specific parameters²⁰, this ratio is universal for a broad range of materials. In this sense, our data provide a unique example where the Fermi liquid was studied with respect to different strength of electronic correlations. We thus prove that the Fermi liquid approximation remains valid upon approaching the Mott transition, yet with more strongly renormalized quasiparticles. This finding negates exotic suggestions of spinons becoming relevant at the Mott MIT, which would express as a breakdown of the Kadowaki-Woods ratio due to different divergence rates of A and m^*/m_b [19]. Therefore, our result is consistent with theory [20] and section 5.2.2, stating that coherent spinons and the postulated Fermi surface are confined to a region deep in the Mott insulating state.

Fig. 5.3.13 (c) demonstrates the enhancement of the effective mass, the quadratic prefactor B and the inverse Fermi liquid frequency ω_{FL} with increasing correlations.

¹⁸The inaccuracy of absolute resistivity values in the studied organic materials is typically around a factor of two.

¹⁹Even for $x = 1.00$ the asymmetric shape of the BEDT-STF molecules causes considerable disorder.

²⁰The charge carrier density and inter-layer distance, which are among the scaling parameters utilized in Ref. [30], do not change drastically upon substitution of BEDT-TTF by BEDT-STF. Therefore, additional rescaling is not necessary when comparing between different κ -STF $_x$.

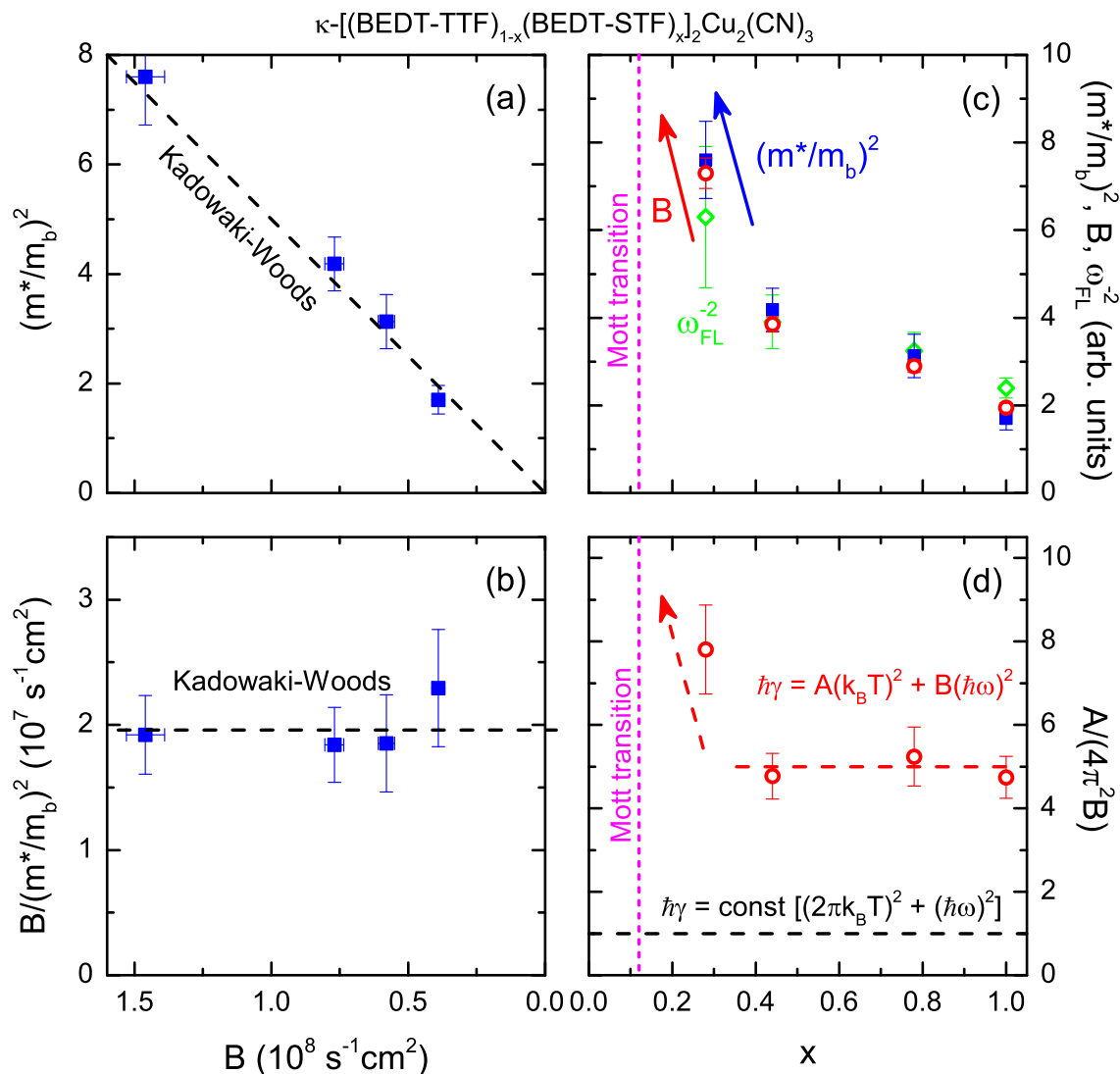


Figure 5.3.13: (a,b) The prefactor B depends quadratically on the effective mass, implying that the Kadowaki-Woods ratio [30] holds for κ -STF $_x$. Thus, the intrinsic properties of a Fermi liquid are conserved also for different correlation strength. (c) Both B and m^*/m_b are enhanced towards the Mott metal-insulator transition; due to the limited set of data we cannot conclude on the details of the increase and a possible power-law divergence. The inverse of the characteristic Fermi liquid frequency follows the effective mass enhancement, as indicated by the included data points of ω_{FL}^{-2} . (d) The ratio between the prefactors A and B of the quadratic T and ω dependence of the scattering rate are larger by a factor 5 compared to the theoretical prediction $A/B = 4\pi^2$ for a Fermi liquid with purely inelastic scattering. The ratio seems to be enhanced close to the Mott transition, indicating a stronger influence of *non-metallic* contributions to quasiparticle scattering [29]. Note that the zero-frequency extrapolation of the optical data, i.e. A_{opt} , was used giving a self-consistent value independent of the plasma frequency; the dc value of A is larger by another factor 5 – 10 for these compounds. Apart from experimental inaccuracy in the absolute values $\rho(T)$, this might be related to distinct scattering mechanisms in the dc and frequency-dependent response [29], possibly related to disorder.

Extending this data set in future studies would allow us to study the details of a possible power-law divergence – or its absence – of m^*/m_b at the Mott transition. Finally, panel (d) compares the prefactors A and B , both extracted from the optical data, in the context of Gurzhi scaling [28, 29]. Similar as reported for the κ -Br $_x$ Cl $_{1-x}$ family, where a value around 1.5 was found [22, 23, 123], the κ -STF $_x$ series exhibits an A/B ratio larger by a factor 5 compared to the theoretical prediction of $(2\pi)^2 \approx 40$ for a genuine Fermi liquid with purely elastic scattering between the quasiparticles [70]. This pristine response was observed in experiment only for Sr $_2$ RuO $_4$ so far [71]. While a value smaller than this number indicates an additional elastic contribution, such as scattering from local moments in f -electron systems [193, 194], a ratio exceeding $(2\pi)^2$ corresponds to a *non-metallic* term in the self-energy. We may speculate whether this could be related to pronounced quantum fluctuations arising from Mott-Hubbard interactions, possibly reflecting in the increase of A/B upon approaching the MIT. Another consideration may rely on the small energy scales of the organic compounds. Alternatively, we can continue the discussion of disorder effects here; however, if disorder was responsible for the large value, the effect would probably be most pronounced for larger substitutions rather than small x , as observed here.

Finally, we plot the temperature-dependent resistivity and the inverse of the optical conductivity, i.e. the frequency-dependent resistivity, on a common energy scale in Fig. 5.3.14. We point out the general similarity between $\rho(T)$ and $\sigma^{-1}(\omega)$ despite their distinct energy ranges. While the characteristic Fermi liquid T^2 behaviour of the dc resistivity is lost already well below the IRM limit, the fingerprints of resilient quasiparticles in the frequency-dependent response survive up to the temperature where ρ_{IRM} is crossed [28, 31] (e.g. $T_{IRM} \approx 150$ K for $x = 1.00$). As one can nicely see, the compound that reveals superconductivity at ambient pressure and is located almost exactly at the Mott MIT ($x = 0.12$) exhibits a scattering rate exactly at the IRM limit, which explains the absence of coherent quasiparticles down to lowest temperatures. After all, Fig. 5.3.14 nicely illustrates the quadratic energy dependence of the scattering processes establishing the Fermi liquid behaviour of κ -STF $_x$. Upon increasing the correlations, the curves shift vertically and the E^2 response is lost at the Ioffe-Regel-Mott limit. The main difference between dc transport and optics is that the resistivity continues increasing above ρ_{IRM} whereas, in the frequency domain, the scattering rate levels off around the Mott-Hubbard band. Since at these large energies no coherent quasiparticles exist, we can draw a general $\sigma^{-1} \sim k_B T - \hbar\omega$ regime in which the Fermi liquid is stable.

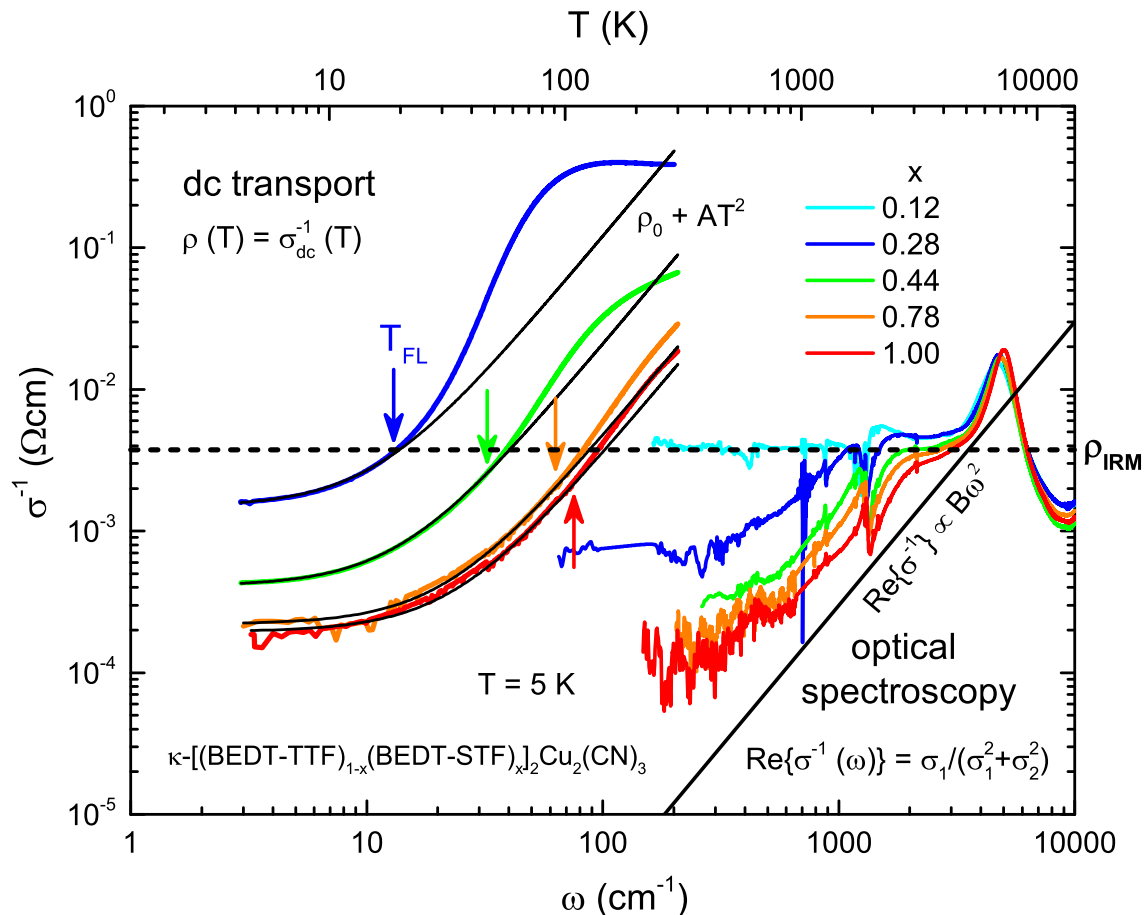


Figure 5.3.14: The temperature-dependent dc resistivity as well as the real part of the inverse optical conductivity (i.e. frequency-dependent resistivity) are plotted on a common energy scale. The characteristic T^2 and ω^2 behaviour is generally observed for $\text{Re}\{\sigma^{-1}\}(T, \omega)$ below a certain threshold identified as the Ioffe-Regel-Mott limit ρ_{IRM} (here calculated for the lattice parameter of $\kappa\text{-(BEDT-TTF)}_2\text{Cu}_2(\text{CN})_3$). Thus, the IRM-limit manifests in both frequency- and temperature-dependent conductivity as the fundamental upper boundary of the Fermi liquid state with coherent quasiparticles. While the T^2 dependence of the dc resistivity holds only up to $T_{FL} < T_{IRM}$, the fingerprints of the Fermi liquid persist up to the IRM limit in the frequency-dependent scattering properties, indicative of resilient quasiparticles [31]. As the compound with $x = 0.12$ is located very close to the Mott transition, the resistivity equals almost exactly ρ_{IRM} and the Fermi liquid is not stabilized.

5.3.3 Summary and Discussion

We identified the κ -[(BEDT-STF) $_x$ (BEDT-TTF) $_{1-x}$] $_2$ Cu $_2$ (CN) $_3$ series, where the BEDT-TTF molecules of κ -(BEDT-TTF) $_2$ Cu $_2$ (CN) $_3$ are successively substituted by BEDT-STF with more extended orbitals, as a prime example of the bandwidth-tuned Mott transition. As the ratio x increases, a pronounced spectral weight shift from the Mott-Hubbard band to low energies is observed, corroborating the dc transport results that reveal the onset of metallicity for $x \geq 0.12$. Even ambient-pressure superconductivity with $T_c = 2.9$ K was established at the critical substitution. Upon advancing into the highly conducting region, a bad metallic regime at high temperatures up to T_{MI} and a strongly correlated Fermi liquid state below T_{FL} are stabilized. Both phases expand towards higher temperatures with increasing STF content. Optical spectroscopy allows us to study the charge carrier coherence in a more subtle way than simple dc transport. The dielectric loss function reveals the formation of a well-defined Drude plasmon at low temperatures reminiscent of coherent quasiparticles. Moreover, the band mass m_{band} is reduced for larger x as a result of the enhanced width of the Mott-Hubbard bands and the concomitant increase of the curvature d^2E/dk^2 . Extracting the relevant quantities U and W , we establish a decrease of electronic correlations with increasing substitution ratio in κ -STF $_x$. Strikingly, we observe that the stabilization of the bad metallic and Fermi liquid phases depends inherently on the band shape U/W , corroborating our considerations elaborated in section 5.1.6. In this sense, the on-site Coulomb interaction and the bandwidth are the relevant energy scales circumstantially describing the insulating Mott state as well as the metallic part of the phase diagram; optical spectroscopy enables to determine these quantities in a quantitative way.

In the last part, we focus on the frequency-dependent properties of the Fermi liquid state, accessed via the extended Drude formalism. In particular, the scattering rate $\gamma(\omega)$ exhibits the expected ω^2 behaviour below T_{FL} with a strongly enhanced effective mass upon approaching the Mott MIT of κ -STF $_x$. The prefactor B of the quadratic frequency dependence exhibits the expected proportionality to $(m^*/m_b)^2$ verifying that the Kadowaki-Woods ratio is universal even for a varying degree of electronic correlations U/W , in excellent agreement with Ref. [30]. Hence, a Fermi liquid does not alter its intrinsic properties even for large renormalization of the defining parameters. As we have tested this on a system with quantum spin liquid ground state on the Mott insulating side, we prove the suggested influence of spinons on the coherent quasiparticle response [19] to be irrelevant, in good consensus with dynamical mean-field theory results [20].

Upon comparing the prefactors of the quadratic energy dependence in the dc limit (A) and the optical response (B), their ratio is larger by a factor 5 than expected for a pristine Fermi liquid [28, 29, 70]. The absence of Gurzhi scaling indicates large *non-metallic* contributions to scattering in this material, possibly related to quantum fluctuations of the Mott state. Alternative explanations may consider the small energy scales of these organic compounds or the considerable amount of disorder emanating from chemical substitution. After all, we demonstrate that the coherent quasiparticle response of a Fermi liquid is inherently constrained by the Ioffe-Regel-Mott limit, which establishes an upper bound to the T^2 and ω^2 dependence both in the transport and optical data. Even though T_{FL} is crossed well below ρ_{IRM} in the dc resistivity, the fingerprints of resilient quasiparticles remain visible in $\sigma_1(\omega)$ up to the IRM limit, in great conformity with DMFT calculations on the single-band Hubbard model [31].

6. Results II: Charge Order and Superconductivity in 1/4-Filled (BEDT-TTF)₂X

Several quarter-filled organic conductors of the (BEDT-TTF)₂X family with quasi two-dimensional electronic properties were investigated by means of optical spectroscopy accompanied by dc transport and magnetic susceptibility (SQUID) measurements. Upon analyzing the optical properties of β'' -(BEDT-TTF)₂SF₅CH₂SO₃ and β'' -(BEDT-TTF)₂SF₅CHF₂SO₃, and comparing them with the published results of β'' -(BEDT-TTF)₂SF₅CH₂CF₂SO₃ and β'' -(BEDT-TTF)₂SF₅CHFSO₃ [36, 37, 50, 128, 134], a generalized phase diagram of the β'' -(BEDT-TTF)₂SF₅RSO₃ series was established based on electronic correlations, proving the prediction of Ref. [38]. We find that both the charge disproportionation 2δ and transition temperature T_{CO} scale with inter-site Coulomb repulsion V . Strikingly, pressure-dependent dc transport reveals an increase of T_{CO} with p , uncommon for bandwidth-tuning in terms of the single-band extended Hubbard model. We associate this anomalous behaviour and, hence, the origin of charge disproportionation in these compounds to the electrostatic potential of the anions rather than pure inter-site Coulomb repulsion between the BEDT-TTF sites. Moreover, the coexistence of charge order and superconductivity was directly proven in a challenging experiment, where the charge-sensitive vibrations were probed in the superconducting state of β'' -(BEDT-TTF)₂SF₅CH₂CF₂SO₃. Complementary measurements on isotope-substituted samples¹ facilitated assignment of these modes and, strikingly, revealed a direct relation between T_c and 2δ in β'' -(BEDT-TTF)₂SF₅CH₂CF₂SO₃.

We also investigated the optical properties of the quarter-filled organic supercon-

¹The infrared-active $\nu_{27}(b_{1u})$ mode was measured for β'' -(BEDT-TTF)₂SF₅CH₂CF₂SO₃ samples with completely deuterated BEDT-TTF and for β'' -Ga crystals, where the two carbon atoms of the inner BEDT-TTF C=C bond were substituted by ¹³C.

ductors θ -(BEDT-TTF)₂I₃ and β'' -(BEDT-TTF)₄[(H₃O)Ga(C₂O₄)₃] · C₆H₅NO₂ on indications of fluctuating or partially localized charge order in the metallic state. It appears that 2δ is almost zero for the former compound while it is in a similar range as for β'' -(BEDT-TTF)₂SF₅CH₂CF₂SO₃ for the latter one, which also shows a higher T_c . In addition, the broadband electrodynamic response of β'' -(BEDT-TTF)₄[(H₃O)Ga(C₂O₄)₃] · C₆H₅NO₂ was measured and analyzed in the context of Mott-Hubbard excitations as well as the extended Drude model, yielding even more strongly renormalized quasiparticles than in κ -[(BEDT-STF)_{*x*}(BEDT-TTF)_{*1-x*}]₂Cu₂(CN)₃, which was presented section 5.3.2.

6.1 Charge Order and Superconductivity in β'' -(BEDT-TTF)₂SF₅*RSO*₃

Let us start with the β'' -(BEDT-TTF)₂SF₅*RSO*₃ family where *R* corresponds to the chemical moieties CH₂, CHF₂CF₂, CH₂CF₂ and CHF, hereafter denoted as β'' -I, β'' -MI, β'' -SC and β'' -M, respectively. The nomenclature follows Girlando *et al.* [38], who summed up the basic properties of these compounds in a tentative phase diagram, as shown in Fig. 3.4.1 (b).

Table 6.1.1 lists the basic transport and structural characteristics of the β'' -(BEDT-TTF)₂SF₅*RSO*₃ series. While for the first compound insulating properties were reported up to room temperature [39], the second one undergoes a metal-insulator transition at 170 K [40]; the other two materials are metallic at all temperatures [37]. The unit-cell volumes V_{UC} are distinct due to the different length of alkyl groups *R*: since CH₂ and CHF are only about half the size of CHF₂CF₂ and CH₂CF₂, also V_{UC} is significantly smaller, respectively. Within one of these pairs, the charge

*Table 6.1.1: Charge order transition temperatures T_{CO} for the β'' -(BEDT-TTF)₂SF₅*RSO*₃ compounds. The unit cell volume V_{UC} and inter-layer separation d_{\perp} (at 300 K), as well as the charge disproportionation 2δ determined from the atomic distances within the BEDT-TTF molecule [137] do not follow a continuous trend. Data from Refs. [39, 40, 132].*

R	CH ₂	CHF ₂ CF ₂	CH ₂ CF ₂	CHF
T_{CO} (K)	> 300	175	-	-
V_{UC} (Å ³)	1742.45	1841.9	1835.5	1761.55
d_{\perp} (Å)	17.30	17.35	17.11	17.18
2δ (e)	0.2	0.10	0.14	0.06

disproportionation 2δ determined according to the Guionneau-Day equation [137] shows decreasing tendency with unit-cell volume. Following the order in the tentative phase diagram, however, the trend of 2δ is discontinuous which is probably due to inaccuracies of this method [39, 40]. We generally notice that the inter-layer separation d_{\perp} is significantly smaller for the two metallic systems. Hence, the wave function overlap between the organic layers is reduced for β'' -I and β'' -MI which causes more pronounced two-dimensionality and stronger correlations. On the other hand, this reflects that the anions are located not between the BEDT-TTF molecules, but directly above and below them, which goes hand in hand with a smaller anion-BEDT-TTF separation.

In the following, we have a closer look on the transport and magnetic properties of the β'' -(BEDT-TTF)₂SF₅RSO₃ family. Since the $\rho(T)$ data of β'' -I and β'' -MI reported in Refs. [39, 40] are confined to liquid nitrogen temperatures ($T_{min} = 77$ K), additional dc transport experiments were organized. Under supervision of A. Löhle, the temperature-dependent resistivities of the two compounds were measured by Y. Saito and B. Heydari, respectively. Fig. 6.1.1 shows the results plotted together with $\rho(T)$ of β'' -SC and β'' -M from Ref. [37].

While β'' -MI shows metallic properties above 170 K, insulating behaviour is found at lower temperatures with a pronounced enhancement below 90 K. It is interesting to note that the absolute value of ρ is almost one order of magnitude lower than in β'' -SC and β'' -M. The reason is the specific alignment of β'' -MI along the crystallographic b -axis with largest wave function overlap. In contrast, the plotted resistivity of β'' -SC was measured along the in-plane direction with smallest conductivity ($E \parallel a$). Comparison with $E \parallel b$ data of the deuterated compound yields a similar room temperature value $\rho(300K) = 0.2 \Omega\text{cm}$ [195] and, hence good agreement for the two compounds with the longer moiety R . Although the data of β'' -M were also measured along the b -direction, the resistivity is larger, possibly indicating that smaller anion size in β'' -(BEDT-TTF)₂SF₅RSO₃ causes reduced conduction properties. However, one should have in mind the considerable inaccuracy of the geometry factor in transport measurements. The resistivity of β'' -I was measured at 45° to the b -axis and it yields the largest room temperature value. This material is first insulating and then exhibits a more metallic behaviour below $T_{MI} = 70$ K, which is shown in more detail in Fig. 6.1.2. There is sizeable hysteresis between heating and cooling runs indicating structural modifications. We also plot the transport gap Δ (inset) determined using Equ. 2.2.2, which is around 10^3 K in the range 100–200 K. In addition to dc transport, also the magnetic susceptibility was measured in the

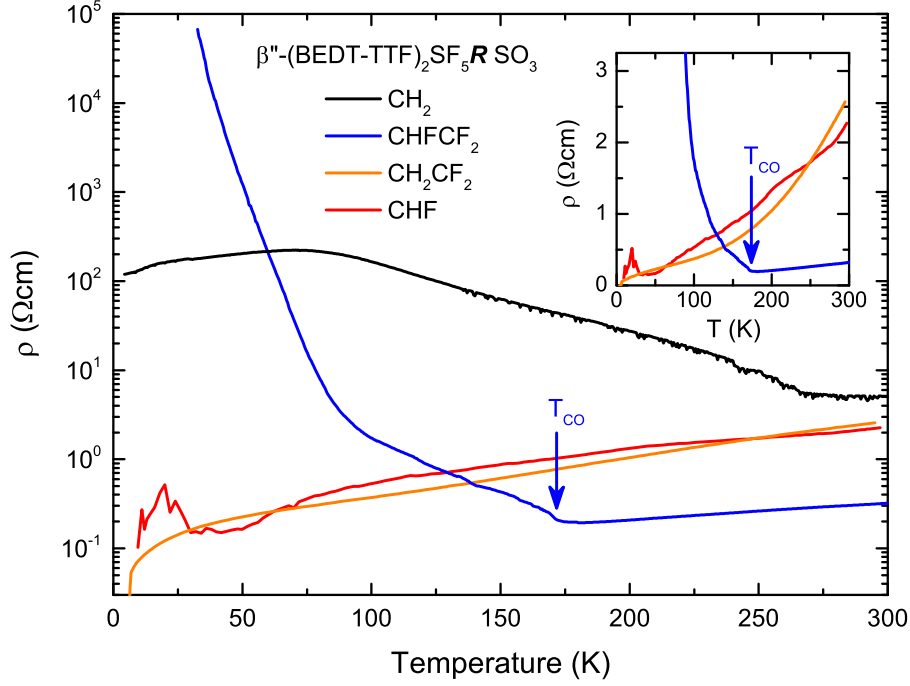


Figure 6.1.1: Temperature-dependent dc resistivity of β'' -I and β'' -MI (measurements: B. Heydari, Y. Saito and A. Löhle) is plotted together with the resistivity of β'' -SC and β'' -M (data from Ref. [37]). While the trend is discontinuous for the former two compounds, the latter two exhibit metallic properties at all temperatures; β'' -SC becomes superconducting below $T_c = 5$ K. In accord with Ref. [39], β'' -I shows insulating behaviour at high temperatures; below $T_{MI} = 70$ K the resistance decreases upon cooling. β'' -MI is subject to the largest changes, most pronounced below $T_{CO} = 170$ K when charge order sets in.

SQUID at a magnetic field of 0.1 T; the experimental details are circumstantially described in section 4.5. Part of the data were acquired within the Block-Praktikum of Ksenia Weber and Philipp Scheiger. Fig. 6.1.3 shows the electronic component χ_{el} for β'' -MI, β'' -SC and β'' -M in good agreement with the electron spin resonance data from Refs. [39, 40, 130] normalized to room temperature. The magnetic field direction was approximately perpendicular to the conducting layers, however, with a large uncertainty $\pm 20^\circ$. In the normal state, the spin susceptibility is positive due to Pauli paramagnetism. The two metallic compounds show a smooth decrease of χ_{el} by a factor 2 from 300 K down to low temperatures; it remains more or less constant below 50 K indicative of a metallic behaviour [39, 130]. The huge diamagnetic response in the superconducting state of β'' -SC is presented and discussed in Fig. 6.1.21.

The spin susceptibility of β'' -MI is constant above $T_{CO} = 170$ K consistent with the metallic transport properties. In the charge-ordered state, χ_{el} drops significantly until it is basically zero below 80 K, which coincides with the enhanced increase of

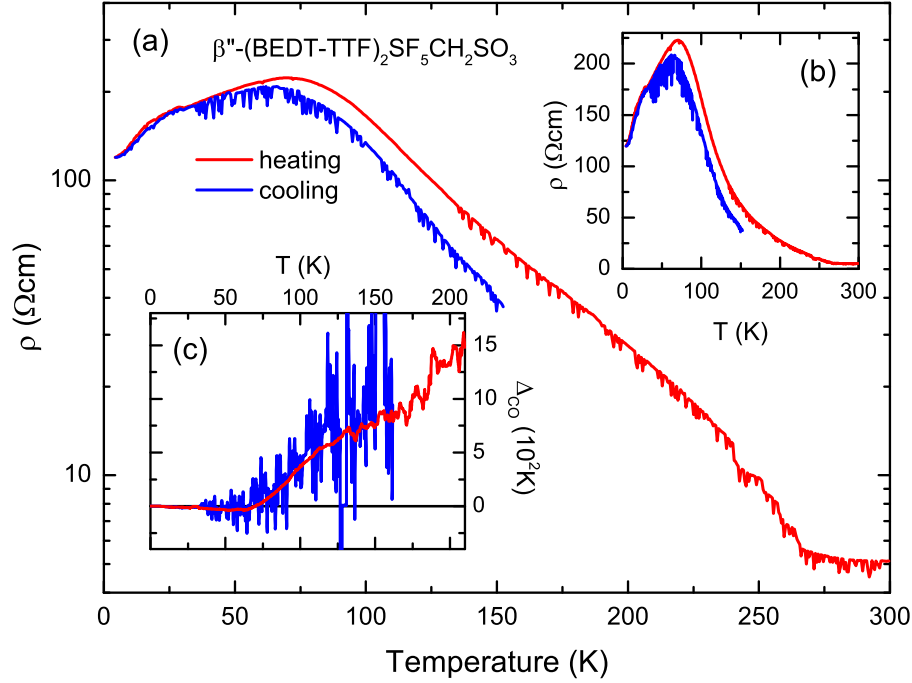


Figure 6.1.2: Temperature-dependent dc resistivity of β'' -I on semilogarithmic (a) and linear scales (b). The resistivity has a maximum around 70 K which is shifted slightly due to hysteretic behaviour between the heating and cooling runs. (c) The transport gap extracted from the Arrhenius plot according to Equ. 2.2.2 amounts to $\Delta_{\text{CO}}/k_B \approx 10^3$ K in the range 100–200 K.

resistivity. Considering the structural properties discussed in section 3.4, which indicate a stripe-like arrangement of charge-poor and -rich molecules along the crystallographic a -direction, it is tempting to assign the vanishing magnetic susceptibility to an antiferromagnetic arrangement of the spins due to increased exchange interaction along the stacks. This might appear in a similar way like the tetramerization in the anion-ordered and spin-peierls phases of quasi one-dimensional (TMTTF) $_2X$ [51]. First, however, we have to prove that the insulating state in β'' -MI and β'' -I is in fact associated with charge order. Keeping in mind the error bars of the structural determination of the molecular charge, and the circumstance that Raman investigations have been performed only at room temperature so far [39, 40], this calls for a comprehensive study of the charge-sensitive modes via infrared spectroscopy. The following section presents a consistent overview of the local site charge distributions and the electronic excitations observed in the broadband electrodynamic response of the β'' -(BEDT-TTF) $_2$ SF $_5$ RSO $_3$ family. To that end, we compare these findings to the charge-disproportionate states in the quasi one-dimensional (TMTTF) $_2X$ family, where a detailed understanding was gained over the last few years [51, 113, 196].

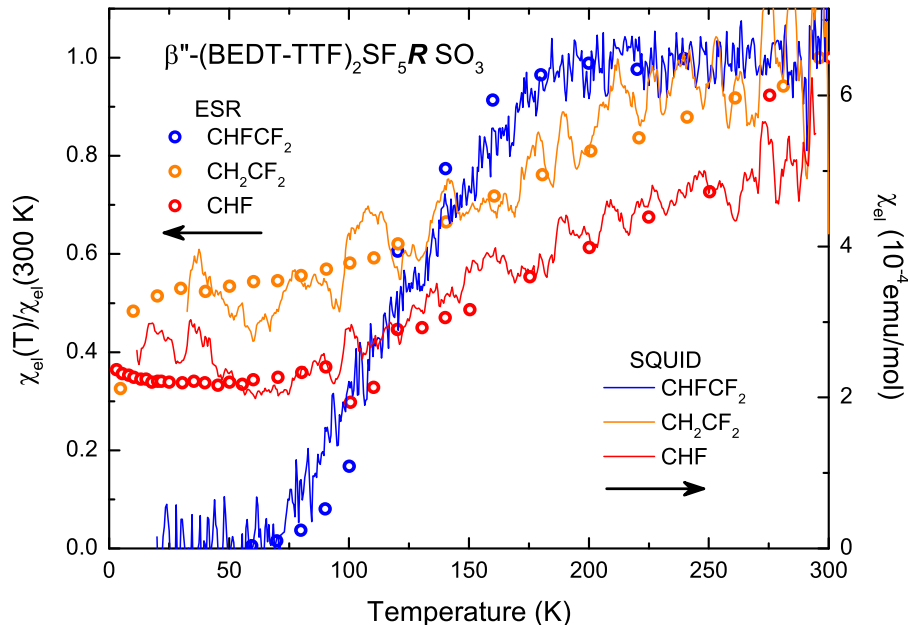


Figure 6.1.3: The spin susceptibility of β'' -MI, β'' -SC and β'' -M was measured in the SQUID magnetometer and the reference was subtracted according to Section 4.5. A constant was added to account for the diamagnetic background χ_D . The SQUID data (right scale) match well with the ESR data from Refs. [39, 40, 130] (left scale). β'' -MI shows a pronounced drop of spin susceptibility when charge order sets in below $T_{CO} = 170$ K. χ_{el} basically vanishes at low temperatures indicating spin pairing in the insulating state. The other two compounds remain metallic down to lowest temperatures and show a non-vanishing spin susceptibility arising from Pauli paramagnetism. χ_{el} decreases continuously upon cooling.

6.1.1 Charge Order Revealed by Molecular Vibrations

Broadband in- and out-of-plane optical experiments on β'' -I and β'' -MI were conducted in order to determine the charge disproportionation and pattern, as well as the strength of electronic interactions. A number of people participated in measurements and data processing: A. Rohwer, S. Kolatschek (Block-Praktikum 1), B. Röslin and S. Kern (Block-Praktikum 2), A. Böhme and S. Klein (Block-Praktikum 3), M. Sanz-Alonso, K. Treptow [197] and Y. Saito.

The strongly anisotropic optical response of these materials is plotted in Fig. 6.1.4. In both cases the spectra are very similar to β'' -SC (cf. Fig. 3.4.3). The conductivity is largest along the crystallographic b -direction with a plasma edge around 6000 – 7000cm^{-1} . The other in plane polarization ($E \parallel a$) also shows metallic response with $\omega_p \approx 3000$ – 4000cm^{-1} . Perpendicular to the conducting planes ($E \parallel c$) the overall insulating-like optical conductivity is dominated by narrow molecular vibration modes.

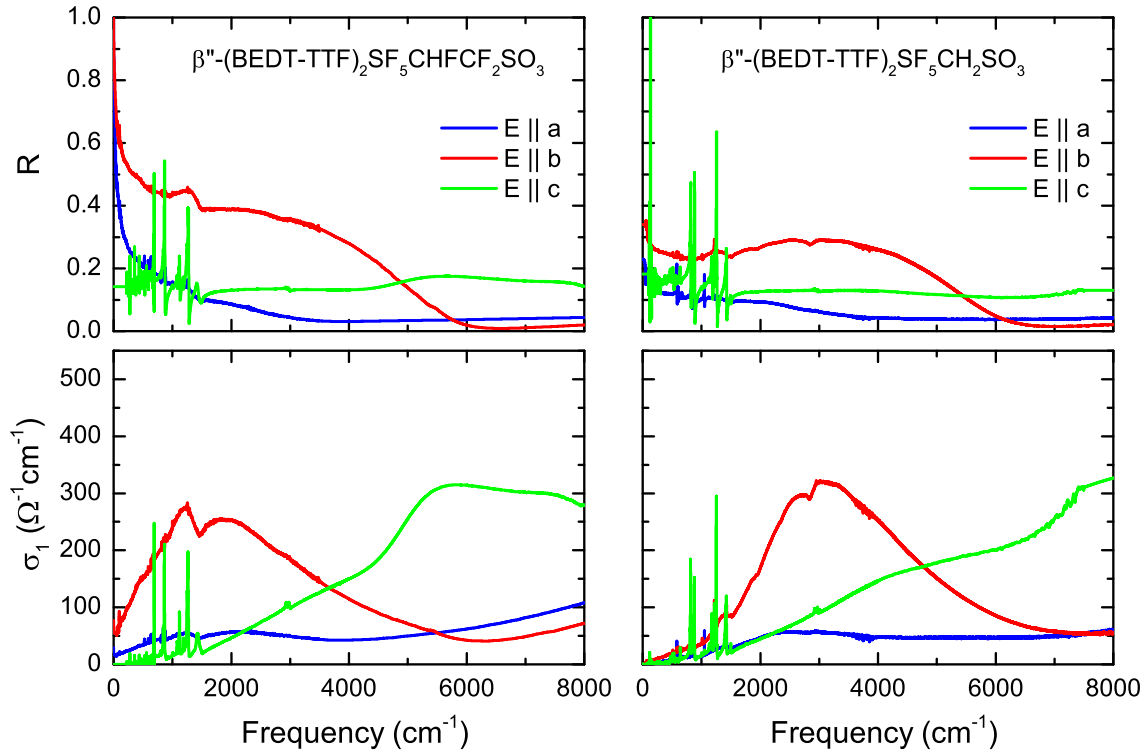


Figure 6.1.4: The optical reflectivity and conductivity of β'' -MI (left panels) and β'' -I (right panels) show very similar properties and anisotropy as β'' -SC (cf. Fig. 3.4.3). Note, for β'' -MI the polarization denoted ' $E \perp b$ ' in Refs. [198, 199] corresponds to the crystallographic c -direction rather than the in-plane component $E \parallel a$.

In order to determine the molecular charge, the charge-sensitive ν_{27} vibration around $1400\text{--}1500\text{cm}^{-1}$ was detected out-of-plane. While Fig. 6.1.5 (a) and (b) illustrate the reflectivity and optical conductivity of β'' -I over a broad range, the particular behaviour of the ν_{27} mode is plotted in panel (c). Two main peaks are identified already at room temperature corresponding to inequivalent BEDT-TTF site charges. The frequency separation reduces slightly upon cooling with $2\delta = 0.47$ e at 5 K. An additional splitting occurs below 100 K and another mode appears around 1466 cm^{-1} . Nominally, this would represent a pretty small amount of BEDT-TTF^{+0.5}. Although it would be tempting to relate the occurrence of this feature below 100 K to the onset of metallicity in the same temperature range, the weak intensity would imply a negligibly small fraction of normally charged BEDT-TTF. More firm conclusions can be drawn from the additional splitting of the peaks at 1430 and 1495cm^{-1} , respectively, that occurs at low temperatures. Apparently, there is a small, but noticeable reorganization of charge leading to a superstructure and doubling of the unit cell. The general charge pattern, however, should resemble the high-temperature

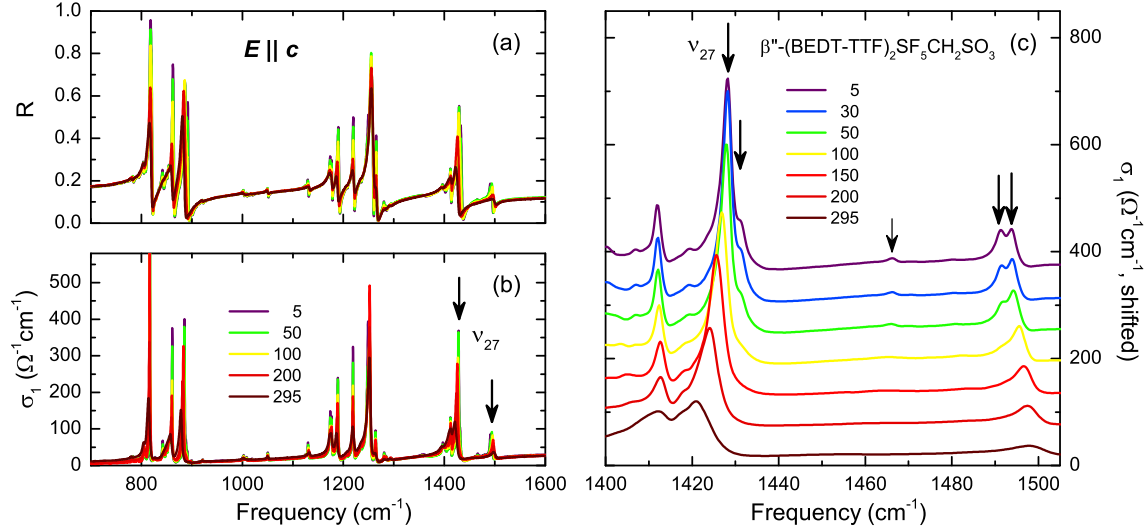


Figure 6.1.5: The out-of-plane ($E \parallel c$) optical reflectivity (a) and conductivity (b) of β'' -I is dominated by molecular vibrations on a negligibly small electronic background. Only selected temperatures are shown. (c) The charge-sensitive ν_{27} mode shows two main peaks at 1428 and 1495 cm^{-1} and a weak satellite at 1467 cm^{-1} . The splitting corresponds to a charge disproportionation of $2\delta = 0.47 e$ at 5 K. While the peak separation does not change much with temperature, the main features split up into doublets below 100 K. The data are vertically shifted.

situation, i.e. the sites remain in their original charge-poor/-rich state with a slight modification $\pm\Delta\delta$ of order 2 cm^{-1} .

The mode described above is by far not the only vibration with an appreciable dependence on the BEDT-TTF charge; several other features can be found at lower frequencies. However, the ν_{27} provides the most accurate estimate of the molecular charge due to its linear frequency-charge relation [49]. To prove the distinct ionicities of BEDT-TTF molecules in β'' -I, another feature observed in the far-infrared range will be discussed shortly. The vibration around 500–530 cm^{-1} plotted in Fig. 6.1.6 is ascribed to the $\nu_{34}(\text{b}_{1u})$ mode and shows a very similar structure as the ν_{27} vibration. The secondary splitting below 100 K can be perceived, but it is not completely resolved ($\Delta\omega = 1 \text{ cm}^{-1}$) due to the generally smaller peak separation compared to the ν_{27} mode. The two main peaks are separated by 15 cm^{-1} which corresponds to $2\delta = 0.78 e$ using the calculated frequencies of neutral BEDT-TTF and its monovalent cation listed in Ref. [50], where it is denoted as ν_{31} . Keeping in mind possible nonlinearities of $\nu_{34}(\rho)$, which may result in an overestimation of 2δ , this finding proves the significant charge disproportionation in β'' -I. Alternatively, one might assign this feature to the Raman-active $\nu_9(\text{a}_g)$ mode where 2δ would be closer to the ν_{27} result. However, the electronic background in this range is basically zero ruling out

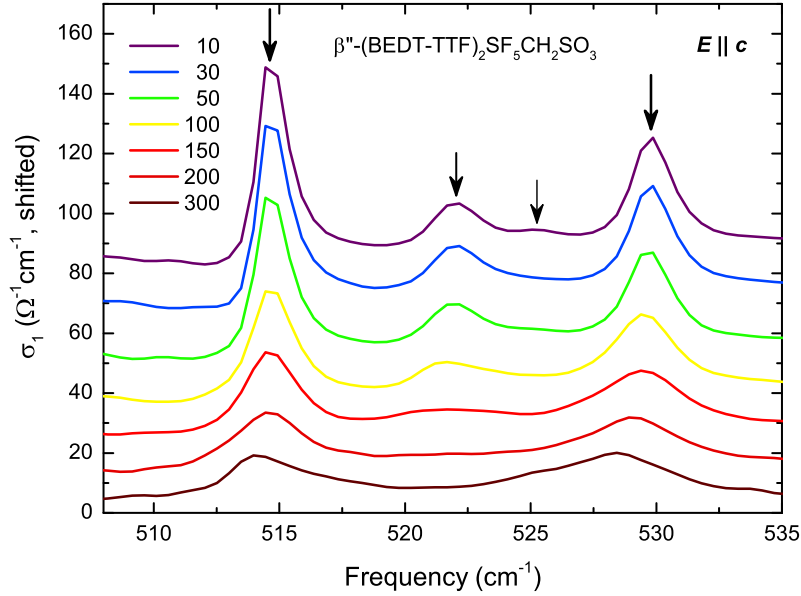


Figure 6.1.6: The out-of-plane ($E \parallel c$) optical conductivity of β'' -I in the far-infrared spectral range reveals the charge-sensitive $\nu_{34}(b_{1u})$ mode which exhibits a very similar structure as the ν_{27} mode. The splitting of the two main peaks is about 15 cm^{-1} corresponding to a charge disproportionation of $2\delta = 0.78 e$ at 5 K according to Ref. [50] (there denoted as ν_{31}). The data are vertically shifted.

significant emv coupling. Moreover, these peaks are observed only for out-of-plane polarization² which indicates b_{1u} symmetry.

Fig. 6.1.7 presents the out-of-plane ($E \parallel c$) response of β'' -MI. The metal-insulator transition is nicely revealed in the temperature dependence of the ν_{27} vibration where two distinct peaks at 1445 and 1486 cm^{-1} evolve below T_{CO} ; they are already present up to room temperature, but become very sharp when the charges are localized in the insulating state. The splitting corresponds to $2\delta = 0.29 e$ at 5 K. Two minor features appear around the frequency of BEDT-TTF^{+0.5}, where the one at 1465 cm^{-1} bears significantly more spectral weight than the intermediate peak in β'' -I discussed above. Since β'' -MI is strongly insulating at low temperatures, it becomes clear that the bare occurrence of BEDT-TTF^{+0.5} does not necessarily relate to metallic behaviour. Therefore, these intermediate features with small intensity are not considered in the following.

The observation of significantly different site charges provides direct evidence for the charge-ordered nature of the insulating state in β'' -I and β'' -MI. In Fig. 6.1.8

²A closer look revealed the appearance of the ν_{34} mode in the $E \parallel b$ spectra where, however, also the ν_{27} vibration is observed. The strongly reduced intensity of this minor crosstalk indicates that the crystal surface probed in the in-plane measurement is not perfectly along ab , but includes a small c component along b . The $E \parallel a$ spectra showed no crosstalk.

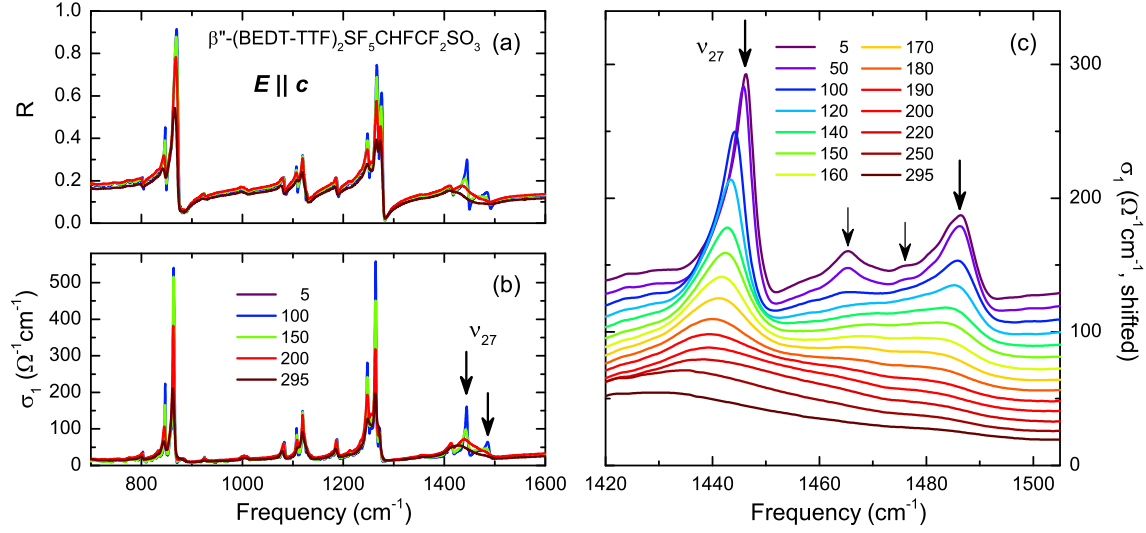


Figure 6.1.7: The out-of-plane ($E \parallel c$) optical reflectivity (a) and conductivity (b) of $\beta''\text{-MI}$ is very similar to $\beta''\text{-I}$; the response shows insulating behaviour and the dominant features are molecular vibrations. Only selected temperatures are plotted. (c) The charge-sensitive ν_{27} mode shows two main peaks at 1445 and 1486 cm^{-1} ($2\delta = 0.29 e$ at 5 K) that are already present at room temperature and narrow significantly in the charge-ordered state below $T_{\text{CO}} = 180$ K. The satellite around 1470 cm^{-1} splits into two peaks below 120 K. The data are vertically shifted.

the temperature-dependent ν_{27} spectra of all four $\beta''\text{-(BEDT-TTF)}_2\text{SF}_5\text{RSO}_3$ compounds are summarized, including the new data presented above as well as the results from Ref. [36]. The charge disproportionation decreases in the order $\beta''\text{-I} - \beta''\text{-MI} - \beta''\text{-SC} - \beta''\text{-M}$, consistent with the tentative phase diagram from Fig. 3.4.1 (b) [38]. A similar relation between 2δ and the strength of electronic correlations was reported for the CO phase in $(\text{TMTTF})_2X$ [51, 113, 196]. We also notice that the peaks become significantly broader upon reduction of 2δ reflecting that the charge localization (fluctuation) strength is strongly linked to the amount of redistributed charge. Following the arguments of Girlando *et al.* [38], who stated that there is a coexistence of fluctuating (broad modes) and localized (separated sharp peaks) charges in $\beta''\text{-SC}$, the absence of broad features in the low-temperature ν_{27} spectra of $\beta''\text{-I}$ and $\beta''\text{-MI}$ is in line with the insulating behaviour.

For a quantitative comparison, the ν_{27} resonance frequencies and the corresponding charge disproportionation are plotted in Fig. 6.1.9. The two main peaks split more or less symmetrically around the $\text{BEDT-TTF}^{+0.5}$ position. For completeness reasons, also the minor features are plotted as small, empty symbols. In all four $\beta''\text{-(BEDT-TTF)}_2\text{SF}_5\text{RSO}_3$ compounds, the temperature dependence of 2δ is rather weak. This is different compared to electronic CO in quasi one-dimensional $(\text{TMTTF})_2X$ where

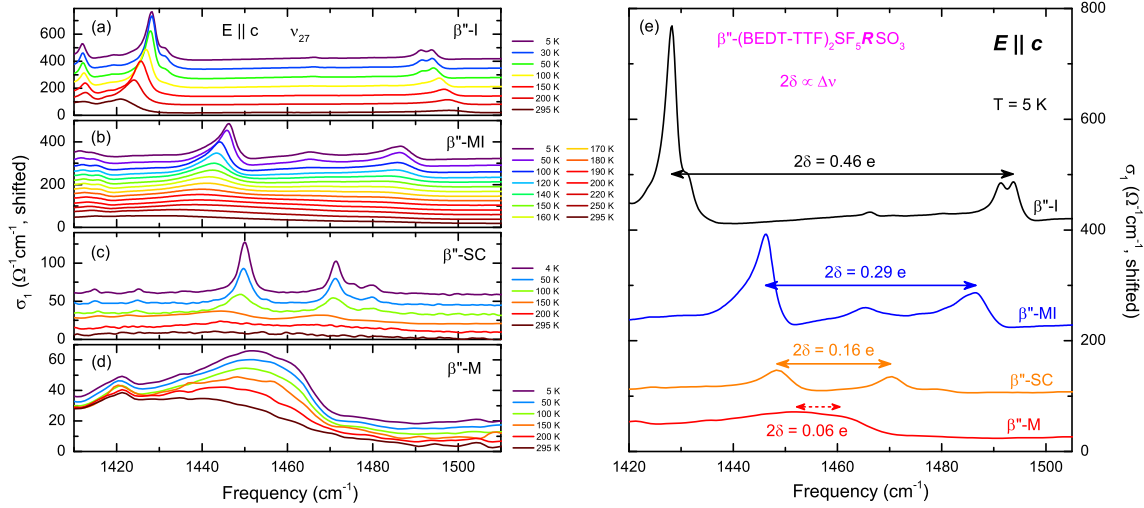


Figure 6.1.8: (a)-(d) The temperature dependence of the charge-sensitive mode ν_{27} is compared between β'' -I, β'' -MI, β'' -SC and β'' -M. The data of the former two materials are from Figs. 6.1.5 and 6.1.7 whereas for the latter two compounds the spectra were taken from Ref. [36]. While β'' -M shows only one broad feature (possibly consisting of two very close peaks) at all temperatures, the modes of the other compounds narrow significantly upon cooling. (e) The modes are compared on a common scale at the lowest temperature. The dashed red line indicates the upper boundary of the splitting in β'' -M. Apparently, the peaks become narrower and more intense as the charge disproportionation is enhanced. The data are vertically shifted.

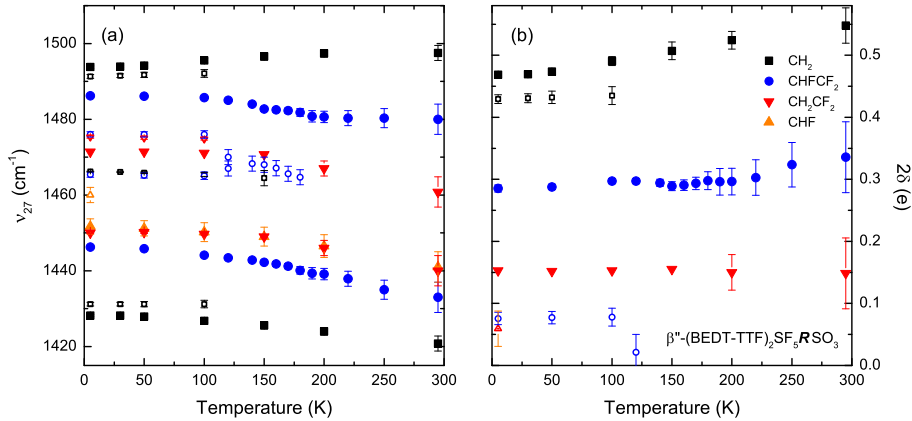


Figure 6.1.9: (a) The resonance frequencies of the ν_{27} peaks were determined by fitting the data shown in Fig. 6.1.8. One can nicely see that the peaks split more or less symmetrically around the 0.5 e position around $1460 - 1470 \text{ cm}^{-1}$. While initially most of the modes show blue-shifting upon cooling, the general structure basically remains constant below 100 K . The small open symbols denote satellite peaks. (b) The charge separation is significantly reduced in the order β'' -I - β'' -MI - β'' -SC - β'' -M, indicating a decrease of electronic correlations.

the order parameter increases in a second-order, mean-field fashion below T_{CO} [51, 113, 196, 200].

6.1.2 Electronic Excitations and Charge Pattern

Now we turn to the in-plane electrodynamic response which yields valuable information on the interaction strength and correlations. Fig. 6.1.10 shows the temperature-dependent optical properties of β'' -I. For both polarizations, the overall intensity of the Mott-Hubbard band increases upon cooling with a gap around 900 cm^{-1} in fair agreement with Δ_{CO} shown in Fig. 6.1.2. Also, we find a narrow Drude-like contribution that appears below 100 K consistent with the metallicity found in the transport properties at low temperatures, which were measured on the very same sample. Interestingly, the Mott-Hubbard band peaks around 2000 cm^{-1} for both a - and b -directions which implies an isotropic charge pattern, such as a checkerboard arrangement, rather than a stripe-like periodicity.

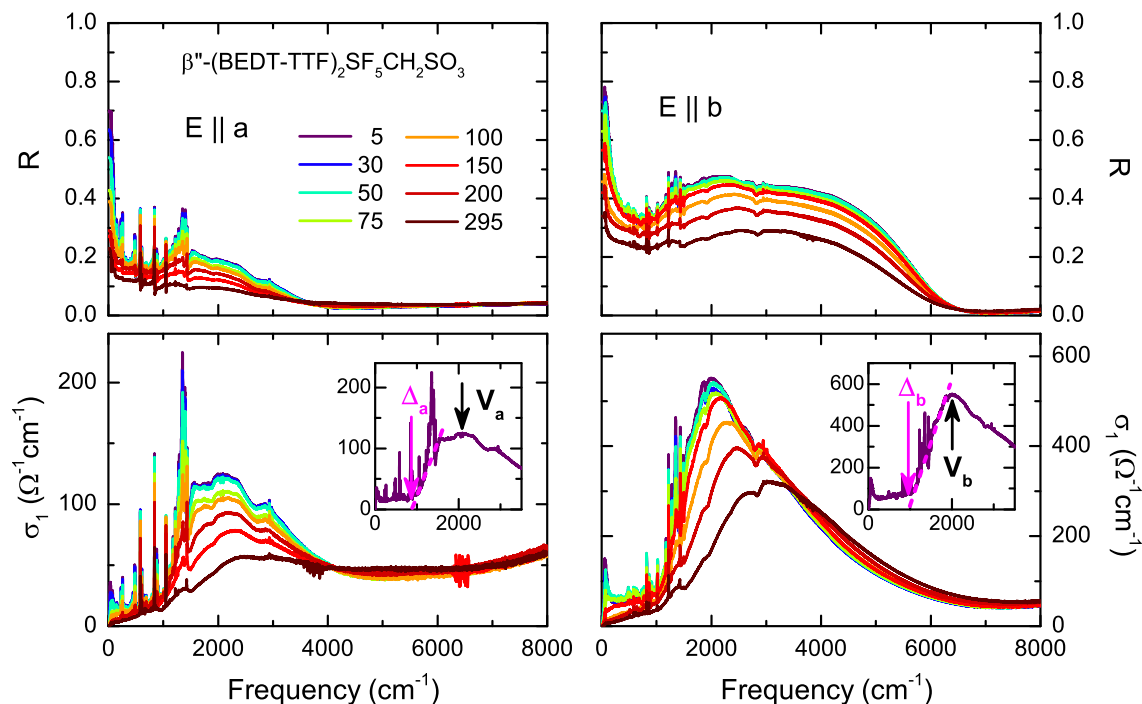


Figure 6.1.10: Broadband reflectivity and conductivity of β'' -I. The spectra show good agreement in the mid-infrared range with Refs. [201, 202]. The strong upturn of reflectivity in the far-infrared indicates a narrow Drude contribution that appears at low temperatures substantiating the metallicity observed in dc transport. The insets illustrate the the Mott-Hubbard band parameters at 5 K; although the band shape and intensities are not identical, the gap size Δ and Coulomb repulsion V are almost isotropic.

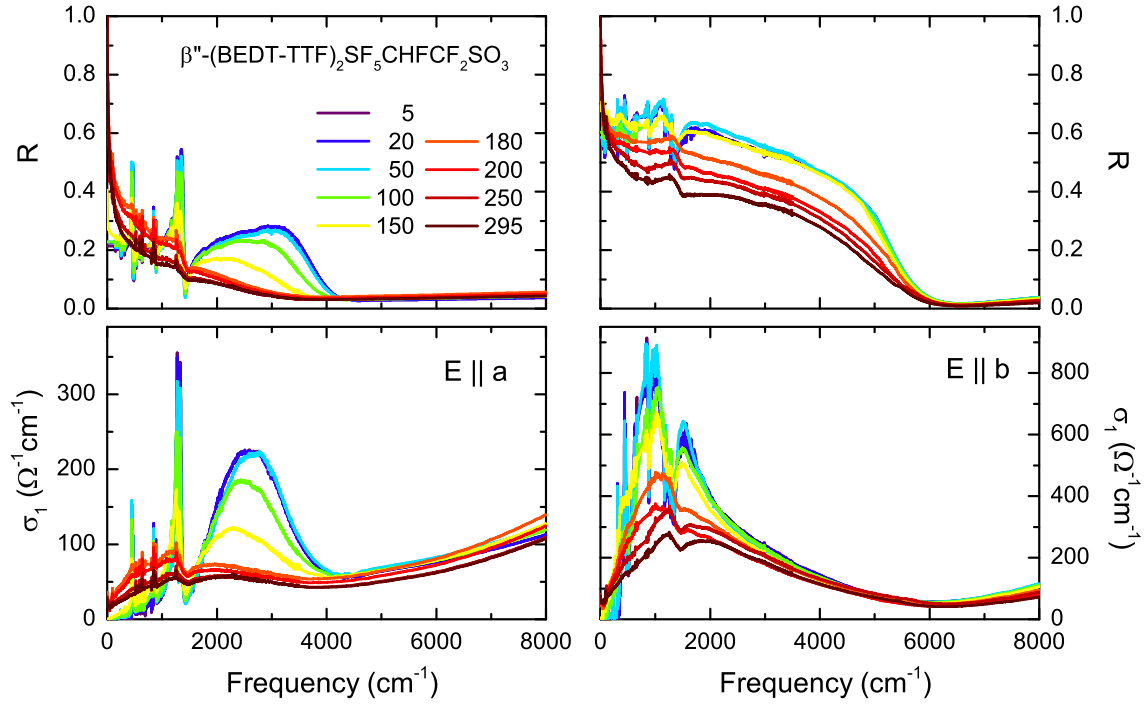


Figure 6.1.11: The in-plane optical response of β'' -MI is strongly anisotropic. Two qualitatively different kinds of electronic excitations evolve in the course of the metal-insulator transition. While the Mott-Hubbard band is centered between 2000–3000 cm^{-1} for $E \parallel a$, it peaks around 1000 cm^{-1} along the b -direction and acquires a strongly asymmetric shape.

The situation is different for β'' -MI (Fig. 6.1.11) which exhibits strongly anisotropic electronic properties. As the material becomes insulating, a sharp gap appears in the optical conductivity and the Mott-Hubbard band gets significantly enhanced. The overall gap size and Coulomb repulsion are larger for $E \parallel a$ which is pointed out in Fig. 6.1.12. There, the electronic excitations are centered around 2600 cm^{-1} and the gap is far above 1000 cm^{-1} . On the other hand, the Mott-Hubbard transitions peak around 1000 cm^{-1} for $E \parallel b$; the sharp band edge below 500 cm^{-1} shows good agreement with the transport data³. We also determined the bandwidth as the half-width at half maximum, cf. section 4.3.1, which is larger for the a -axis. Since the interaction strength is larger along this crystallographic direction, correlations are less pronounced for $E \parallel b$.

The distinct optical excitations of β'' -I and β'' -MI stem from the specific charge arrangements. It was already pointed out in Refs. [39, 40] (cf. Fig. 3.4.2) that the charge-rich A ($\rho = 0.5 + \delta$) and charge-poor B ($\rho = 0.5 - \delta$) sites in the former

³For determination of the optical gap, the steepest slope of the band edge was extrapolated to $\sigma_1 = 0$. The vibration modes that appear at exactly these frequencies are a potential source of inaccuracy.

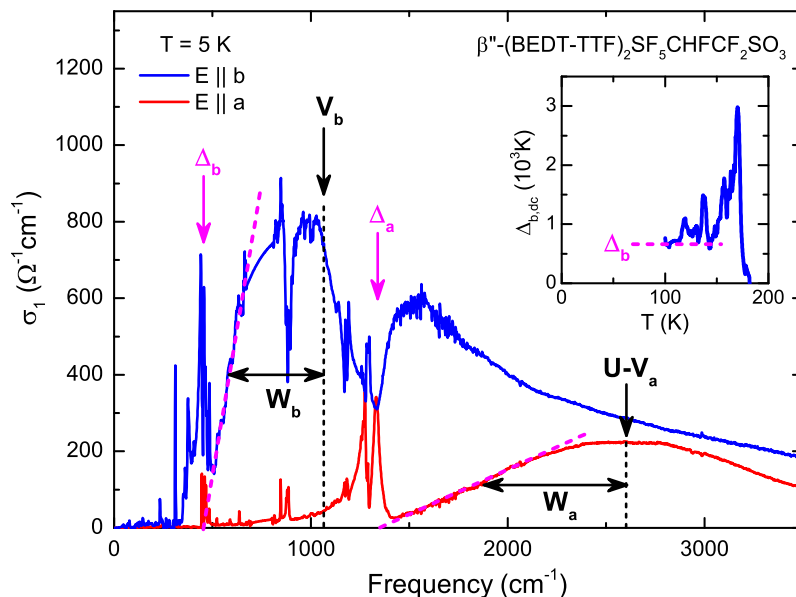


Figure 6.1.12: The strongly anisotropic optical conductivity of β'' -MI is shown for the a and b polarizations at the lowest measured temperature. The respective band parameters and gap positions (determined from linear extrapolation of the band edge) are indicated with appropriate indices. While transitions along b happen between charge-poor and -rich sites, excitations for $E \parallel a$ are between charge-rich molecules increasing the on-site Coulomb repulsion U due to creation of a double occupancy (cf. Fig. 6.1.13). Inset: The gap size coincides for the transport and optical results.

material are arranged along $-a+b$ whereas the stripes in the other three β'' -(BEDT-TTF) $_2$ SF $_5$ RSO $_3$ compounds are aligned along b . Fig. 6.1.13 contrasts the spectra of β'' -I and β'' -MI for both polarizations and sketches the respective charge pattern with the corresponding transitions. The checkerboard-like arrangement in β'' -I implies that the charge-poor and -rich molecules alternate along the a - and b -axes. Hence, nearest neighbour excitations always move a charge from an occupied to an empty site which incurs an additional inter-site Coulomb energy⁴ V . The situation is different for the stripe-like pattern of β'' -MI; transitions for $E \parallel a$ happen between charge-rich molecules reducing the inter-site repulsion V_a on the expense of the on-site Coulomb energy U due to creation of a double occupancy. Since $U \gg V_i$, the corresponding Mott-Hubbard band peaks at a higher frequency. On the other hand, excitations along b move an electron from a charge-rich to a charge-poor site, reducing the intra-stripe repulsion to the nearest neighbours in $\pm a$ direction ($2V_a$) at the cost of the inter-stripe repulsion V_b . As a result, the excitation energy $V_b - 2V_a$

⁴Strictly speaking, one has to sum up one inter-site term V_i ($i = a, b$) for each nearest neighbour projected along a and b . In the specific case of β'' -I this would be one b -contribution and two a -terms for excitation along b , and vice versa for $E \parallel a$.

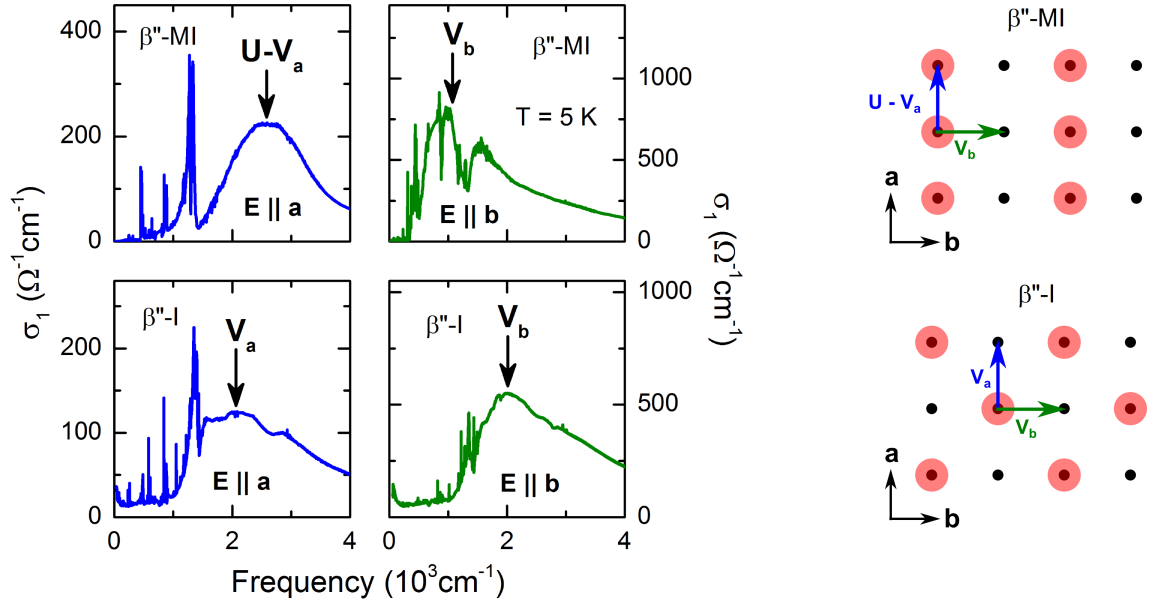


Figure 6.1.13: Different charge patterns in β'' -MI and β'' -I are inferred from optical spectroscopy results obtained here and the structural properties reported in Refs. [39, 40]. Since there is a checker-board-like pattern in the latter compound, excitations along both in-plane axes are between charge-poor and -rich molecules incurring an almost isotropic energy cost V . In the former material, such excitations appear for $E \parallel b$ whereas transitions between charge-rich sites along the a -axis create double occupancies with an additional on-site penalty U , shifting the Mott-Hubbard band to higher energy.

is significantly lower because $2V_a$ and V_b are of a comparable order of magnitude. Note, these considerations apply to the extreme case $2\delta = 1$ e; for smaller charge disproportionation each transition involves a finite on-site Coulomb repulsion $Un_i n_j$ since even on the charge-poor sites $n_i \neq 0$. However, such an on-site term does not introduce anisotropy to the checkerboard pattern of β'' -I since the amount of charge on the nearest-neighbour sites along a and b is identical.

Now that we have gained an overall understanding of the microscopic charge arrangement, the spectra of all β'' -(BEDT-TTF) $_2$ SF $_5$ RSO $_3$ compounds are summarized in Fig. 6.1.14. Note that β'' -SC shows a well-defined low-energy Mott-Hubbard band⁵ only for $E \parallel b$ – very similar to β'' -MI, but at lower frequency due to the smaller 2δ ; the transition along the a -direction appears at higher energy and is much broader than for β'' -MI, reflecting the larger bandwidth. A quantitative comparison between the materials is difficult for $E \parallel a$ due to (i) the different charge patterns and (ii) the dominant metallic background for β'' -SC and β'' -M which inhibits separation of

⁵The overall shape and generally larger intensity of the $E \parallel b$ spectra indicate that they have a common origin for all compounds, namely excitations between charge-poor and charge-rich sites.

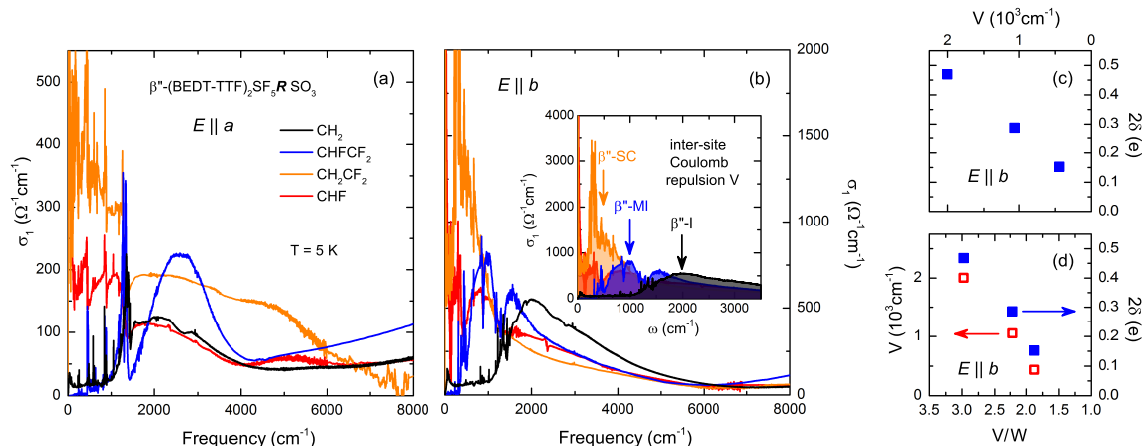


Figure 6.1.14: (a,b) Both polarizations of the in-plane optical conductivity at 5 K are summarized for the four $\beta''\text{-(BEDT-TTF)}_2\text{SF}_5\text{R SO}_3$ compounds. The inset in (b) points out the excitation energy of transitions between charge-poor and -rich sites; the inter-site Coulomb interaction V decreases in the fashion $\beta''\text{-I} - \beta''\text{-MI} - \beta''\text{-SC}$. (c) The charge disproportionation 2δ increases with V proving the physical interpretation in terms of the extended Hubbard model. (d) Also the bandwidth was determined; 2δ and V are consistently reduced with decreasing correlations V/W .

the Mott-Hubbard bands⁶. Along the b -axis, however, electronic excitations of all compounds are from charge-poor to charge-rich sites and, therefore, representative of the involved inter-site Coulomb energy V . As shown in the inset of panel (b), the interaction strength is largest for $\beta''\text{-I}$ and decreases in the order $\beta''\text{-MI} - \beta''\text{-SC} - \beta''\text{-M}$. Extracting the band parameters from the Mott-Hubbard bands yields that the charge disproportionation follows V in a monotonous, approximately linear fashion. This corroborates the main assumption that charge order in these compounds is driven mainly by Coulomb repulsion and can be treated in terms of the extended Hubbard model. The fact that the order parameter 2δ is suppressed with decreasing correlations provides conclusive evidence that the underlying physics are satisfactorily described by bandwidth tuning, as proposed by Girlando *et al.* [38].

6.1.3 Phase Diagram: Reversed Bandwidth-Tuning by Pressure

Now that we verified the respective positions in the phase diagram by determining the correlations and the charge disproportionation, pressure-dependent transport experiments on $\beta''\text{-MI}$ were conducted in order to explore the region in between.

⁶Several broad bands in the far- and mid-infrared ranges were necessary to fit the data in Ref. [37].

Fig. 6.1.15 presents the dc resistivity measured by B. Heydari for $p = 0$ –13 kbar. While for the single-band extended Hubbard model with conventional bandwidth-tuning one would expect a reduction of correlations and the transition temperature with pressure, this compound shows opposite behaviour. T_{CO} increases up to 230 K at the highest pressure which corresponds to an enhancement of $\Delta T_{CO} = 60$ K. At the same time, we find that the resistivity is reduced with p at low and high temperatures, everywhere except the range around the phase transition. Moreover, the CO transition is accompanied by considerable hysteresis that becomes more pronounced with higher pressure. This is seen more clearly in the trend of the transport gap, plotted in Fig. 6.1.16, where the heating curves are shifted by several K to higher temperatures. Note that we defined the maximum of Δ_{dc} as the transition temperature here; the gap is enhanced by almost a factor 4 from 0 to 7 kbar and

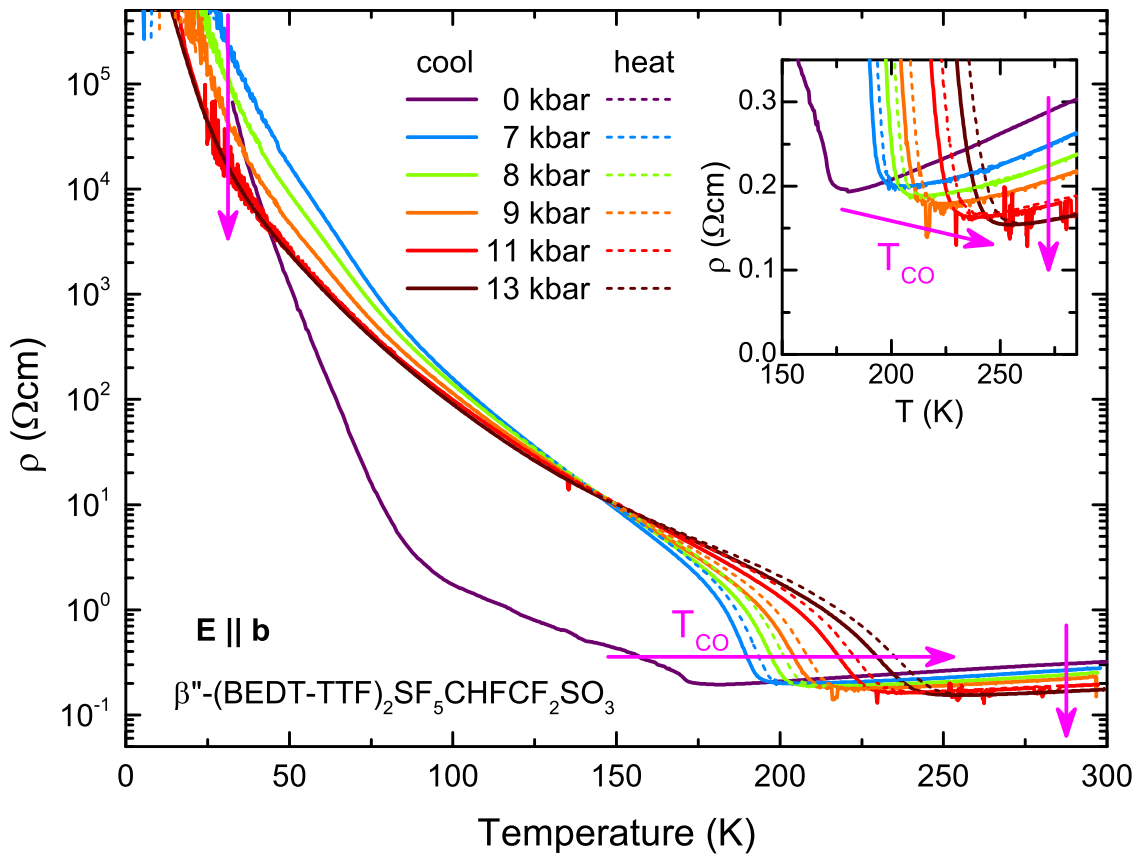


Figure 6.1.15: The electrical resistivity of β'' -MI was measured up to 13 kbar by B. Heydari. The charge order transition is significantly enhanced with pressure and reveals significant hysteresis between the cooling (solid) and heating (dashed) curves. As pointed out in the inset, the high-temperature resistivity is successively reduced with p . Similar behaviour is found also at low temperatures, as indicated by the magenta arrows.

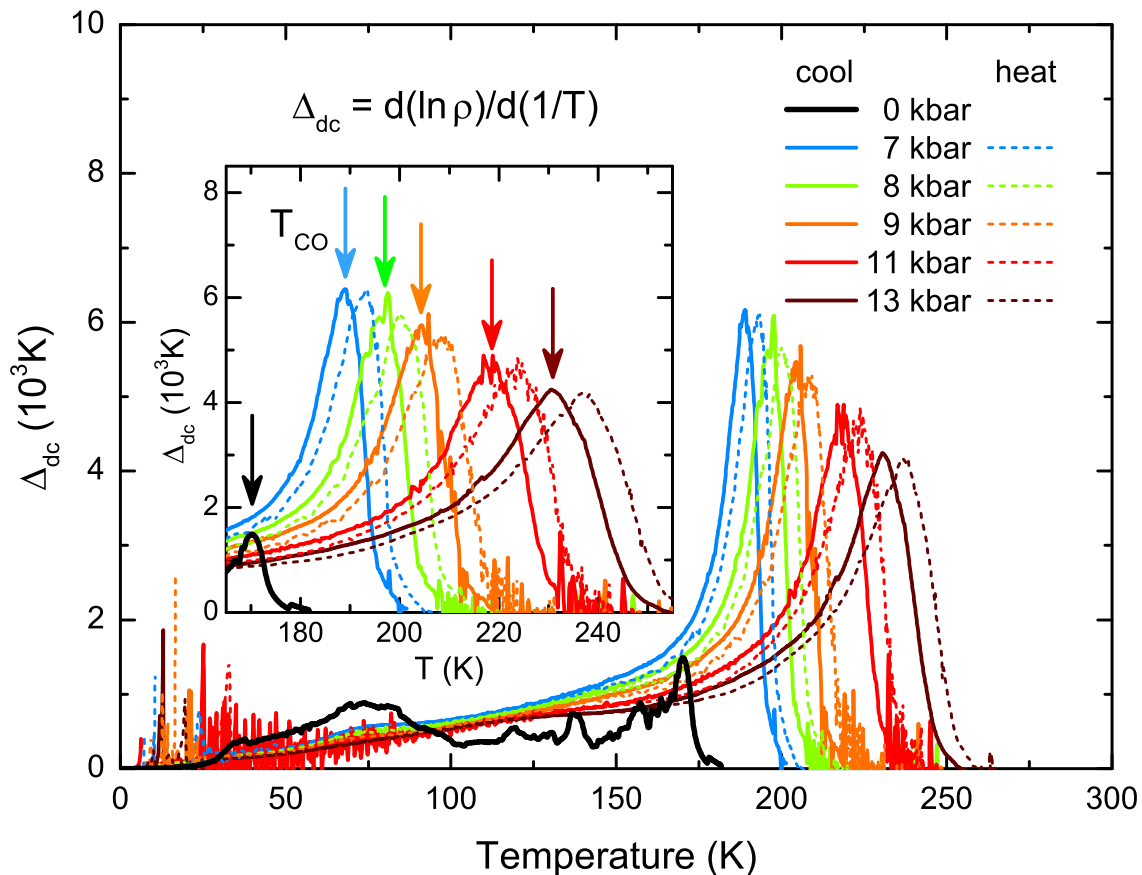


Figure 6.1.16: The transport gap of the pressure-dependent dc transport data of β'' -MI was calculated according to Equ. 2.2.2. Here we associate the maximum with the transition temperature T_{CO} , which increases with pressure. After an initial increase of the peak value, $\Delta_{dc,max}$ decreases and the transition broadens with higher pressure. The inset highlights the hysteresis between the cooling (solid) and heating (dashed) runs. The arrows indicate T_{CO} for cooling.

decreases for higher pressure. Similar behaviour is found for the plateau-like region around 100–150 K. We also notice a broadened width of the transition with pressure. The feature around 70–80 K at $p = 0$ almost vanishes at higher pressures.

Similar behaviour was observed for β'' -SC [41], as shown in Fig. 3.4.5. Initially, superconductivity is suppressed with hydrostatic pressure and when it vanishes around 10 kbar, insulating behaviour sets in with $T_{MI} \geq 150$ K. Also for this compound, the transition temperature increases with pressure while the overall resistivity decreases; hysteresis is observed between increasing and decreasing p .

It is tempting to assign the insulating behaviour observed in both compounds to a charge disproportionate state originating from a similar kind of interactions. Fig. 6.1.17 shows a tentative, combined phase diagram, where the data of β'' -SC [41] start at

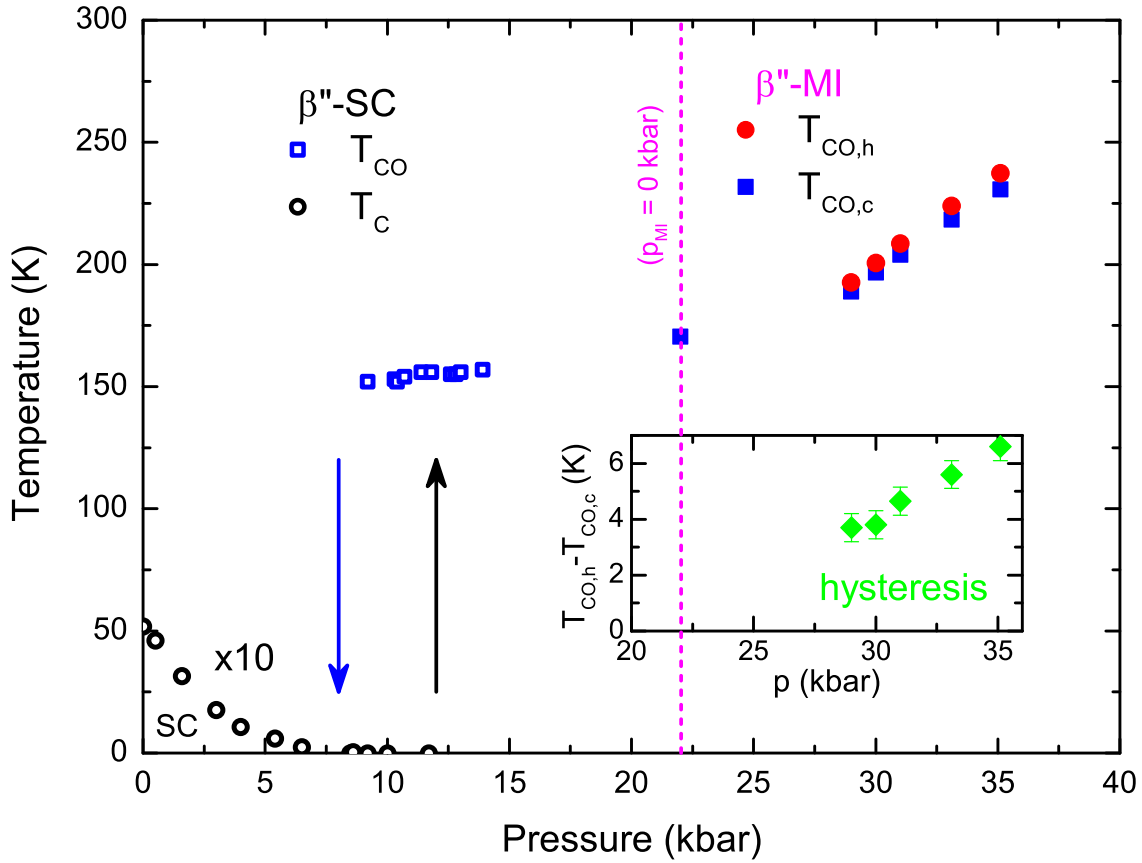


Figure 6.1.17: A combined T - p phase diagram was constructed from the data of β'' -SC [41] and the results on β'' -MI obtained here. The ambient pressure position of the latter compound was shifted by 22 kbar to obtain a smooth connection. The inset presents the hysteresis between heating (h) and cooling (c) runs, which becomes larger with increasing pressure. For β'' -SC, the two arrows indicate the hysteresis between pressure increase (black) and decrease (blue). The superconducting transition temperature is enlarged by a factor 10 for convenience.

ambient pressure and the scale of β'' -MI is shifted by $p = 22$ kbar. No additional scaling factors were applied to the p - and T -axes. Importantly, the pressure where superconductivity diminishes in β'' -SC coincides with the onset of the metal-insulator transition. It was found in previous studies [38, 134] that two different kinds of charge carriers coexist in this compound: localized electrons with disproportionate charge and fluctuating carriers that account for the metallicity. Upon cooling, the mobile component partially freezes out which explains the successive decrease of the spin susceptibility as the number of electrons contributing to Pauli paramagnetism is reduced. In this context, it is reasonable to assume that the number of fluctuating charge carriers diminishes upon application of pressure. Hence, the fraction of the

density of states accessible for superconductivity is suppressed and T_c vanishes as soon as all electrons are localized.

So far, the data were only presented in a phenomenological way omitting a deeper discussion of the physical origin of such interesting behaviour. It is not the first time that a positive slope of T_{CO} was observed in the T - p phase diagram; similar behaviour appears throughout the θ -(BEDT-TTF) $_2X$ series which was assigned to a reduction of the bandwidth due to a modified dihedral angle between the BEDT-TTF molecules within the conducting plane [141, 142]. There, the resistivity shows an increasing tendency with pressure reflecting the decrease of the transfer integrals. In the case of β'' -(BEDT-TTF) $_2SF_5RSO_3$, however, the opposite behaviour is found, with an overall enhancement of conductivity upon pressure. Thus, we conclude that the bandwidth increases in the present case implying a different physical mechanism of the pressure-enhanced MIT. Having in mind that the Coulomb repulsion between the BEDT-TTF sites can not outweigh the enhanced bandwidth, there must be an additional source of electrostatic energy that influences the molecular charge. This brings us to quasi one-dimensional (TMTTF) $_2X$ which show two distinct types of charge-disproportionate insulating states. On the one hand, a 0101 type charge pattern is found for electronically driven charge order evoked from the inter-site Coulomb repulsion within the chain. On the other hand, compounds with non-centrosymmetric anions are subject to a reorganization of the anions at low temperatures; the new superlattice periodicity causes a tetramerization of the organic stack. Since some TMTTF sites have a shorter distance to the anions, they are exposed to a significantly stronger electrostatic potential due to the negative charge of the anion. Consequently, the charge arrangement along the stacks is altered from 0101 to 0011 in the course of anion order (AO), which is circumstantially described in the Appendix A.1 and Ref. [51]. Strikingly, a distinct pressure dependence of the CO (suppressed) and AO (enhanced) states was reported together with a resistivity decreasing with p [203], which reminds very much of the behaviour observed for the β'' -(BEDT-TTF) $_2SF_5RSO_3$ compounds.

In order to evaluate whether such *anion-induced* charge ordering may be present in β'' -(BEDT-TTF) $_2SF_5RSO_3$, we now take a closer look on the properties of the anion layer (Fig. 6.1.18). It appears that the anions can be considered as dipoles with the negative charge localized predominantly on the SO_3 moiety and the other parts of the molecule being neutral. Indeed, these units are arranged in a periodic manner with the dipoles aligned parallel or antiparallel to each other. As a result, the electrostatic potential is modulated in a stripe-like fashion along the crystallographic a -direction.

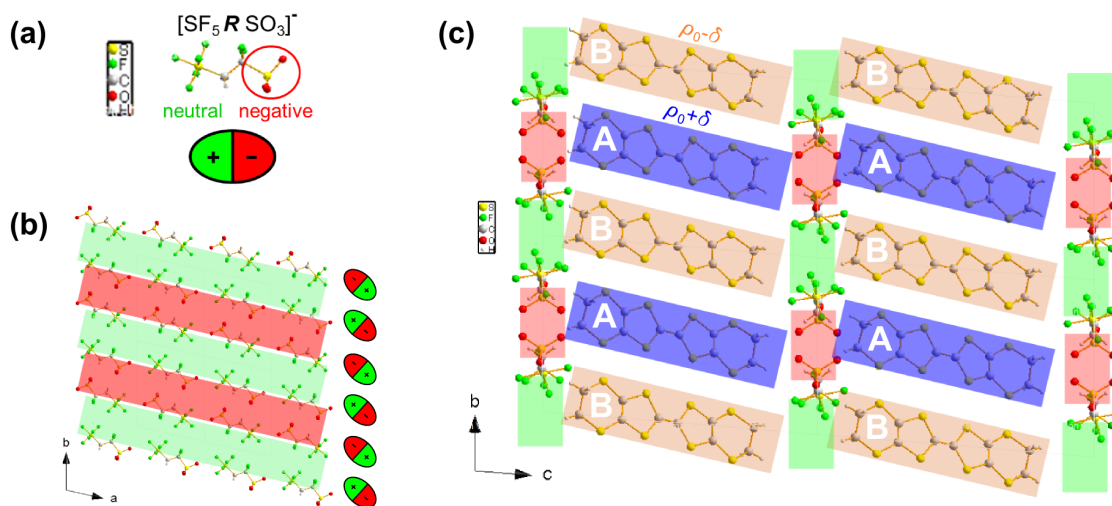


Figure 6.1.18: (a) The electronic charge of the $[\text{SF}_5\text{R SO}_3]^-$ anions is distributed in a non-uniform, dipole-like manner. While the SF_5 end-group is more or less neutral, the negative charge resides predominantly at the SO_3 moiety. (b) The in-plane view on the anion layer reveals a periodic arrangement that leads to a stripe-like potential modulation. (c) The stacks of BEDT-TTF molecules along the a -direction are arranged in such a way that the A sites are closer to the SO_3^- entity and, thus, acquire more positive charge than the B molecules, as inferred from the structural data [39, 40].

Evidently, the molecules with a larger number of anion-BEDT-TTF (O–H) short links, namely the A sites, have a more positive charge $\rho_0 + \delta$ than those further away ($\rho_0 - \delta$ on the B sites) [39, 40]. Very similar behaviour was found for SO_3 containing anions with the negative charge located closer to one layer of BEDT-TTF than to the other, such that the two layers acquire inequivalent charge resulting in a strongly polarized organic conductor with non-vanishing dipole moment [204]. Hence, these observations corroborate the importance of the anionic charge arrangement for various $(\text{BEDT-TTF})_2X$ compounds. Table 6.1.2 lists the number of O–H short links between the respective BEDT-TTF molecule and the anions. Only β'' -M shows similar number of O–H bonds for the A and B sites which explains the negligible charge disproportionation as each site is exposed to a more or less similar electrostatic potential.

Fig. 6.1.19 presents the anion patterns of all four β'' -(BEDT-TTF) $_2$ SF $_5$ RSO $_3$ compounds. The green and red regions indicate the different influence of the anions on the A and B sites. Note that the anion dipole is aligned almost along the a -direction for β'' -M reducing the net potential difference between the A and B stacks. For β'' -SC and β'' -MI the anions are rotated clockwise generating the modulated electrostatic landscape which induces the finite charge disproportionation.

Table 6.1.2: The β'' -(BEDT-TTF) $_2$ SF $_5$ RSO $_3$ compounds with different number of O–H BEDT-TTF-anion short links between the A and B sites [39, 40, 132] show finite charge disproportionation. 2δ was determined from the infrared-active ν_{27} vibration mode (cf. Figs. 6.1.8 and 6.1.9) giving a more reliable estimate of the molecular charge than the structural data.

R	CH $_2$	CHFCF $_2$	CH $_2$ CF $_2$	CHF
O–H (A B)	4 1	4 1	4 1	2 2
2δ (e)	0.47	0.29	0.16	0.06

We conclude that the inter-site Coulomb repulsion within the organic layers is not sufficient to cause an enhancement of T_{CO} with pressure, as observed for β'' -(BEDT-TTF) $_2$ SF $_5$ RSO $_3$. The structural properties suggest that there is an additional electrostatic ingredient related to the anion arrangement. Hydrostatic pressure causes an enhancement of the Coulomb energy as the anions come closer to the BEDT-TTF molecules, e.g. by rotation within the ab -plane or simply due to the reduced lattice spacing along the c -axis. Hence, the interaction strength is enhanced with pressure even though the bandwidth increases at the same time. One may modify the extended Hubbard model by adding an another potential energy term

$$H = H_{el} + H_{anion}, \quad (6.1.1)$$

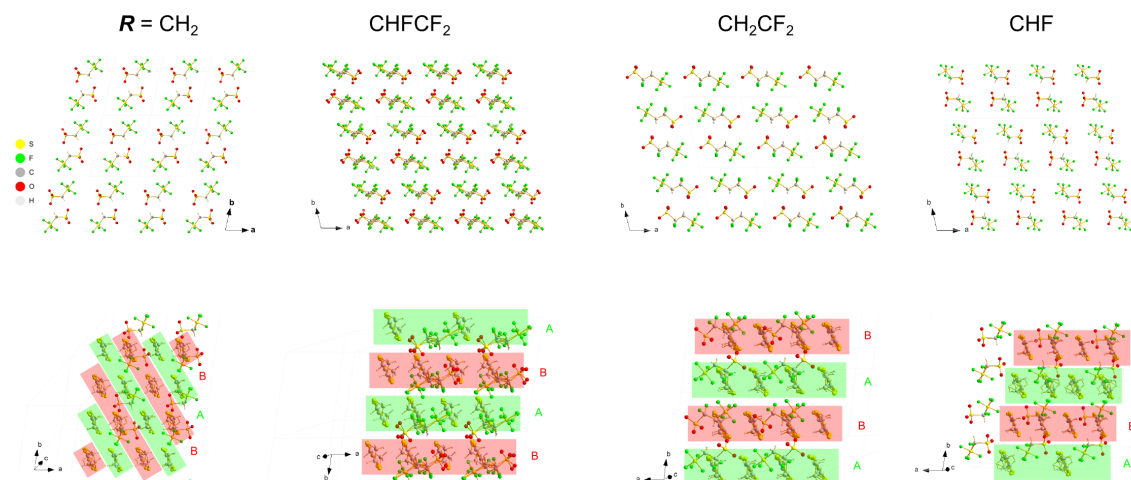


Figure 6.1.19: Anion arrangement and corresponding charge pattern for all four β'' -(BEDT-TTF) $_2$ SF $_5$ RSO $_3$. While it is stripe-like for β'' -MI, β'' -SC and β'' -M, it is more checkerboard-like (i.e. stripes along $-a + b$) for β'' -I.

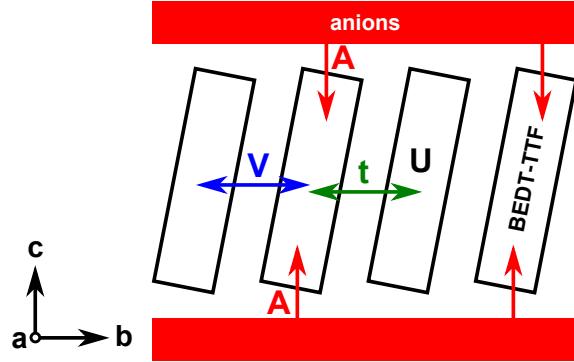


Figure 6.1.20: Schematic illustration of the origin of the various terms of Coulomb energy in $(\text{BEDT-TTF})_2X$. While U has to be paid upon creating a double-occupancy, V is the nearest-neighbour repulsion and t is the transfer integral proportional to the bandwidth W . In a real crystal, however, the BEDT-TTF layers are not free in space, but separated by the anion layers, which may contribute a periodic modulation of the electrostatic potential as indicated by A .

where H_{el} corresponds to Equ. 2.3.10 and H_{anion} to the anion contribution associated with the electrostatic component A . In a crude approximation, the nearest-neighbour BEDT-TTF-anion interactions, expressed by the number of hydrogen bonds (see Table 6.1.2) for instance, may be summed in a similar way as for the inter-site Coulomb repulsion V . Fig. 6.1.20 depicts the different terms that appear in Equ. 6.1.1. While the transfer integral t ($W \propto t$), the on-site interaction U and the nearest-neighbour repulsion V act within the BEDT-TTF layers only, the anion potential A contributes an external modulation of the electrostatic potential.

At this point, the interpretation of the unconventional pressure dependence is straightforward. In a single layer of BEDT-TTF the reduced lattice spacing implies a reduction of the nominal correlations V/W and U/W . Compression along the perpendicular direction (here the c -axis) primarily increases the anion contribution which can compensate, or even exceed the enhanced bandwidth. Overall, the deciding term for the effective correlations and the metal insulator transition⁷ is no longer V/W , but $(V + A)/W$. Note that T_{CO} may be enhanced even though the effective correlations are reduced, just because the ratio of T/W and $T/(V + A)$ is smaller, i.e. a larger temperature is required to access the same point in the $T/W - (V + A)/W$ phase diagram (see the discussion of the unified phase diagram in section 5.1).

Very recently, the charge distribution in the unit cell was calculated by H. Jeschke

⁷Here, we neglect the contribution from inter-layer hopping t_{\perp} to the bandwidth. Since these compounds are strongly anisotropic and show quasi two-dimensional electronic properties, this approximation seems reasonable. In the limit of large pressure this term may become important.

for all β'' -(BEDT-TTF)₂SF₅RSO₃ compounds by DFT methods using the experimentally determined crystal structures [205]. Even without introducing correlation effects, a significant charge disproportionation between the BEDT-TTF molecules is observed, in perfect agreement with above considerations based on our experimental results⁸. These findings suggest that the anionic potential is not simply a contribution to the Coulomb energy, but it appears to be the origin of charge order in the β'' -(BEDT-TTF)₂SF₅RSO₃ family. Considering that previous investigations attempted to describe the underlying physics to a large extent by the single-band extended Hubbard model [36, 37], i.e. completely neglecting the anions, this observation is particularly important as it points out that this approach is too simplified, at least for this materials class. The question arises to what extent charge ordering in other systems, such as α - or θ -(BEDT-TTF)₂X, is a consequence of intra-layer Mott-Hubbard interactions, or just induced externally by the anions. It is worth mentioning that even for κ - and β' -type quantum spin liquid compounds a possible involvement of the anions to disorder-related phenomena is under current discussion [154, 155, 164, 206]. Moreover, the theories constructed to describe the pairing glue of superconductivity in quarter-filled materials base upon the aforementioned Hubbard model [33]; one might speculate whether Cooper pairs *care* about the origin of charge order and the fluctuations related to it. Possibly, the mere existence of an electrostatic modulation (maybe think of it as kind of a charge density wave) is the key ingredient for an attractive interaction between the electrons. Certainly, these findings call for a general reconsideration of previous results and further comprehensive studies on related compounds.

⁸It was a great surprise when we met at the ISCOM 2017 and both of us having approached the same issue independently, yielding essentially the same conclusions.

6.1.4 Coexistence of Charge Order and Superconductivity in β'' -(BEDT-TTF) $_2$ SF $_5$ CH $_2$ CF $_2$ SO $_3$

As extensively described in sections 3.4 and 6.1, there are numerous studies on β'' -(BEDT-TTF) $_2$ SF $_5$ CH $_2$ CF $_2$ SO $_3$ investigating its charge disproportionation [36–38, 134] as well as its superconducting properties [41, 98, 128, 131, 132, 207]. The overall picture suggests that the appearance of superconductivity in this material is not just coincidence, but related — or even mediated — by charge fluctuations, which possibly arise from the modulated anion potential. Analogous to superconductivity (SC) in the vicinity of a magnetically ordered phase, where a certain range of coexistence was identified [89, 105], it is expected that also charge order (CO) and SC appear simultaneously in a specific region of the phase diagram, given that they are not competing. Yet, a direct proof of such a phase coexistence is still missing. To answer this fundamental question, the charge-sensitive ν_{27} mode was probed in the superconducting state. *In situ* dc transport measurements provided evidence for the actual sample temperature and the onset of superconductivity.

Prior to optical investigations, the superconducting properties of the β'' -SC single crystal under study were characterized by SQUID magnetometry, as shown in Fig. 6.1.21. The spin susceptibility drops markedly as the temperature is lowered below $T_c = 5$ K (inset). Note, the large difference of zero-field-cooled (ZFCH) and field-cooled (FCH) heating curves reveals the Meissner state below 2.8 K and the Shubnikov phases above that.

The low transition temperature and possible heating effects due to the infrared radiation required to use the bath cryostat with He exchange gas, depicted in Fig. 4.1.3 (d). While typical sample dimensions applicable in this setup are in the mm range or larger, the actually probed sample surface was only 0.3×1 mm 2 as it was necessary to measure along the out-of-plane direction ($E \parallel c$), which is the thinnest side of the crystal. To adopt the specimen to this cryostat, a hybrid between the Au evaporation and sliding aperture techniques was employed. As sketched in Fig. 6.1.22, the sample was glued first on an insulating sapphire plate to avoid electrical grounding. Then, four contacts were attached to the single crystal and it was mounted on a cone which allowed to align the surface parallel to the mirror in the He bath cryostat in a similar way as usually done for Au evaporation.

Fig. 6.1.23 shows the outcome of the above described experiment. While the temperature sensor nominally showed temperatures down to 2.9 K (a), the real sample temperature was about 2 K higher as a result of insufficient thermal coupling and the infrared radiation from the light source. The temperature values have been corrected

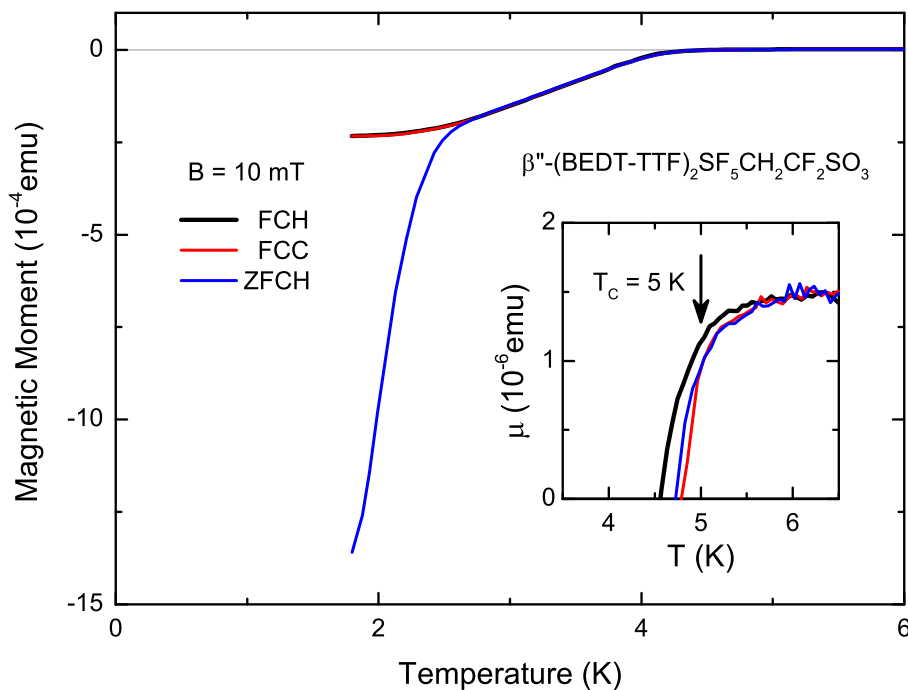


Figure 6.1.21: The β'' -SC sample investigated in the optical experiment with *in situ* dc transport was pre-characterized by SQUID magnetometry. The spin susceptibility shows strong diamagnetic shielding below $T_c = 5$ K verifying the superconducting properties characteristic of this compound [98, 132]. The difference between zero-field cooled (ZFCH) and field-cooled (FCH) heating curves indicates the crossover from the Meissner state to the Shubnikov phase around 2.8 K for an applied magnetic field of 10 mT.

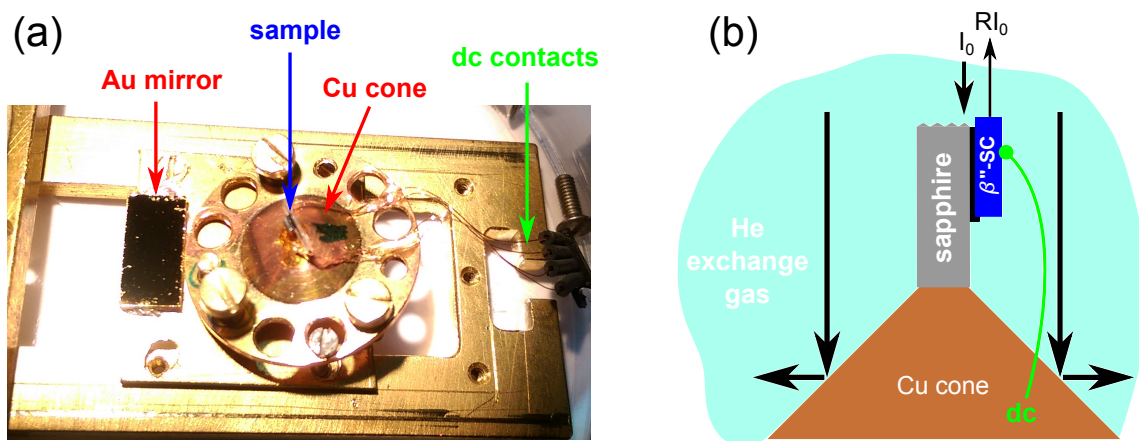


Figure 6.1.22: To allow for alignment of the β'' -(BEDT-TTF) $_2$ SF $_5$ CH $_2$ CF $_2$ SO $_3$ single crystal probed on an out-of-plane ($E \parallel c$) surface, the sample was mounted on a cone in the He bath cryostat (cf. Fig. 4.1.3 d). The necessity to measure dc transport *in situ* required to attach the sample to an insulating substrate; in the present case we employed sapphire. Altogether, this approach enabled to measure the optical reflectivity on a 0.3×1 mm 2 sample surface in a controlled way down to nominally 2 K.

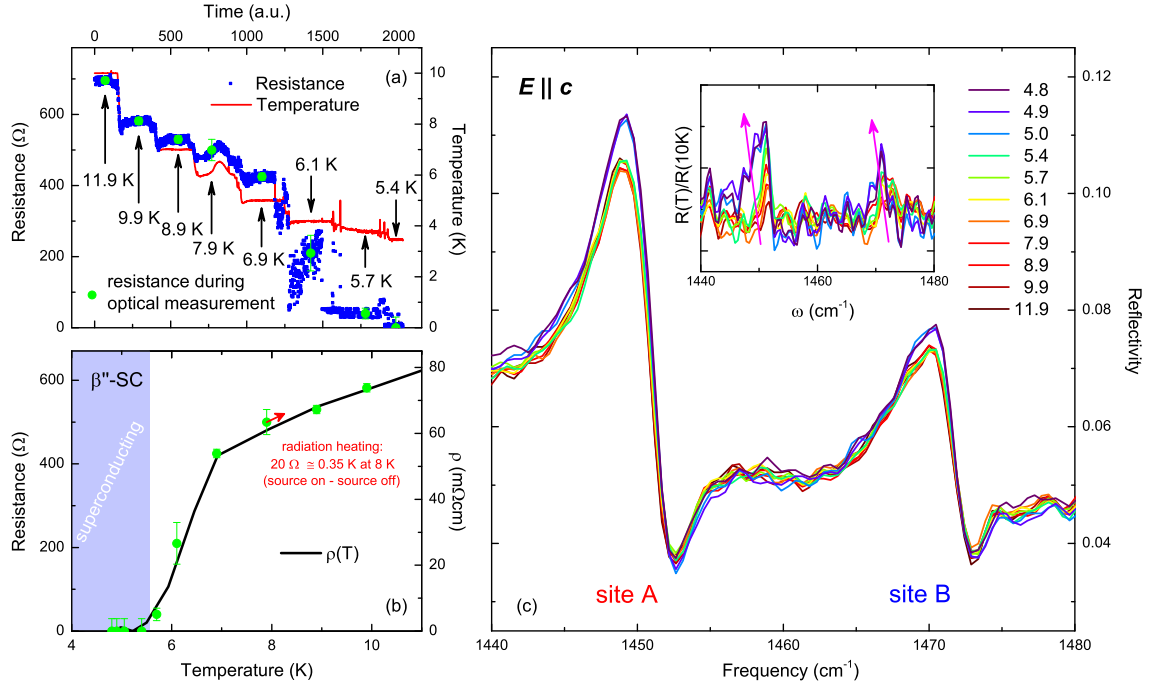


Figure 6.1.23: Simultaneous dc transport and optical measurements—reveal the coexistence of CO and SC. (a) The resistance was recorded during the optical experiment; the plateaus indicate the temperature stabilization. (b) The resistance values during the measurement (green symbols) nicely match with the resistivity from literature [37]. The heat load upon turning the infrared source on and off corresponds to a temperature change of 0.35 K. (c) The splitting of the charge sensitive ν_{27} mode persists in the superconducting state. While the resonance frequencies of the two peaks do not change, the intensity is enhanced below $T_c = 5$ K, as pointed out in the inset.

for this offset. Panel (a) nicely illustrates the time dependence of the resistivity; after ramping, the temperature was equilibrated in order to perform the optical measurement (2×2 min acquisition time, 1 cm^{-1} spectral resolution) which is corroborated by the resistivity plateaus corresponding to the stabilized temperature. Each green symbol denotes the starting point of an optical experiment. Fig. 6.1.23 (b) displays the actual sample temperature deduced from comparison of the *in situ* results with the temperature-dependent dc resistivity. Effectively, the optical experiments were performed slightly below 5 K and resistivity in fact dropped to zero. Therefore, the superconducting state was certainly entered, but the SC volume fraction was well below unity.

The optical reflectivity of the ν_{27} mode is shown in panel (c). This is the first time that the charge-sensitive vibrations are monitored while entering the superconducting state. The splitting due to the differently charged molecules on the *A* and *B* sites

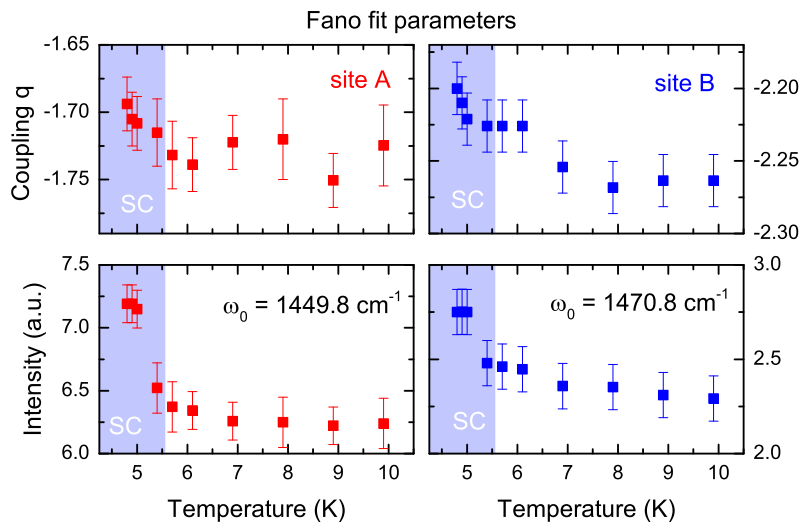


Figure 6.1.24: The two peaks in the reflectivity shown in Fig. 6.1.23 (c) were fitted by one Fano function each. While the resonance frequency and width of the modes are more or less constant within the error bars, there are significant modifications of the coupling parameter q and the intensity. This indicates a possible interaction between charge fluctuations and Cooper pairs.

remains unchanged at all measured temperatures. As highlighted by the inset, both peaks become more intense as the sample turns superconducting. In order to analyze this more quantitatively, the vibrational features were fitted by one Fano function each, the fit parameters of which are presented in Fig. 6.1.24. Although the data show appreciable error bars, a consistent trend larger than the uncertainty level is observed. An enhancement of intensity by about 10 % is clearly visible when the sample becomes superconducting. Judging from the data points in the SC state, the oscillator strength seems to saturate at a certain level rather than becoming more intense.

After all, these experimental results establish that the charge disproportionation persists in the SC state, even though not the entire sample volume was superconducting. In particular, no additional peaks appear around the frequency of BEDT-TTF^{0.5} which proves that the Cooper pairs condense on top of the differently charged A and B sites. To that end, we provide compelling evidence for a coexistence of CO and SC.

Relating this finding to the previous section, where the charge disproportionation was associated with the electrostatic potential of the anions, it would have been very surprising if a low-energy feature like superconductivity had a strong impact on the molecular charge. Note that the SC gap is of order 10 cm^{-1} [128] which is

more than one order of magnitude lower in energy than the charge fluctuation band around 500 cm⁻¹ observed in the electrodynamic response for $E \parallel b$ (cf. Fig. 6.1.14 (b) and Ref. [37]). Even though the charge carriers within the BEDT-TTF layers become superconducting, this would neither lift the charge modulation on the organic molecules nor move the anions from their original position above T_c . We interpret the enhanced intensity of the infrared-active vibration mode as a result of modified screening in the SC state. An in-depth analysis and theoretical description is still missing and subject of future efforts.

6.1.5 Deuteration Effect on Charge Order and Superconductivity

Having established the coexistence of CO and SC, let us now scrutinize whether there is a non-trivial relationship between the two phases – observing two features at the same time does not necessarily imply that they are connected to each other. It is, therefore, instructive to investigate a chemically or physically modified sample where the superconducting properties differ from the parent compound. If an appreciable effect on T_c appeared hand in hand with a change in the charge order/fluctuations, this would manifest a possible interrelation. Since pressure-dependent optical experiments are highly challenging, chemical substitution provides a more convenient route that allows for measurements at ambient conditions in a different region of the phase diagram. While the transition from an antiferromagnetic Mott insulator to a Fermi liquid with superconductivity at low temperatures could be realized in the κ -(BEDT-TTF)₂Cu[N(CN)₂]Br_xCl_{1-x} series via partially increasing the Br content in the anion layer [21–23, 161], modifications of the cations may also lead to a considerable bandwidth-tuning effect. On the one hand, selenium atoms can be introduced on the sulfur positions of BEDT-TTF resulting in more extended wave functions and, hence, significantly increased transfer integrals of BEDT-STF or BETS [125, 126]. In section 5.3 the outcome of this approach is presented in detail for the particular case of κ -[(BEDT-STF)_x(BEDT-TTF)_{1-x}]₂Cu₂(CN)₃. On the other hand, appreciable effects were observed even for isotope substitution, with the largest changes for the terminal hydrogen atoms due to a relative mass enhancement of 100% [208–210]. In particular, deuteration of κ -(BEDT-TTF)₂Cu[N(CN)₂]Br causes a *negative pressure* effect, i.e. the nominally metallic compound becomes insulating and correlations increase [122, 124]. Most likely, this stems from a modification of anion-BEDT-TTF interactions via hydrogen bonds [51].

In the specific case of β'' -SC, Schlueter *et al.* reported an unconventional enhance-

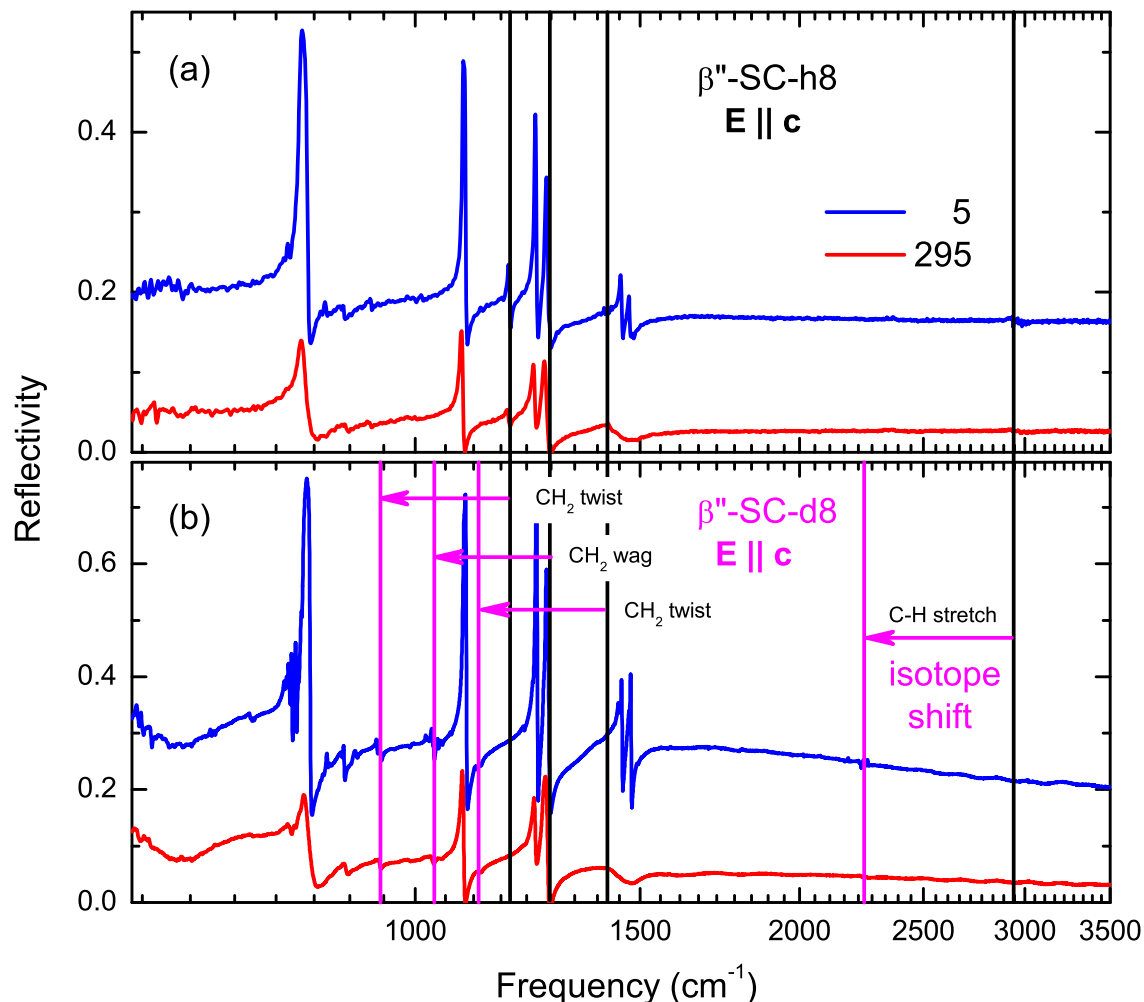


Figure 6.1.25: Comparison of the out-of-plane spectra of h8 and d8 β'' -SC yields pronounced red shifts of the CH_2 (twist, wag) and C-H (stretch) vibrations upon deuteration, consistent with literature [111, 112]. The charge-sensitive ν_{27} mode, however, does not shift considerably since it mainly involves the C=C double bond rather than hydrogen atoms.

ment of T_c upon deuteration [131], which is opposite to the expectation for phonon-mediated superconductivity in the context of the BCS theory since the transition temperature should be reduced for softened vibrations due to the larger mass. However, the charge state in this chemically modified compound has not been studied so far. To that, we measured the charge-sensitive vibrational features of a fully deuterated sample and compared it with the conventional, hydrogenated analogue. Optical experiments on β'' -(BEDT-TTF) $_2$ SF $_5$ CH $_2$ CF $_2$ SO $_3$ with BEDT-TTF-d8 (i.e. β'' -SC-d8) were performed together with Y. Saito.

Fig. 6.1.25 contrasts the out-of-plane spectra of the h8 (a) and d8 (b) compounds. Evidently, the modes that include motions of the ^2H atoms are shifted significantly

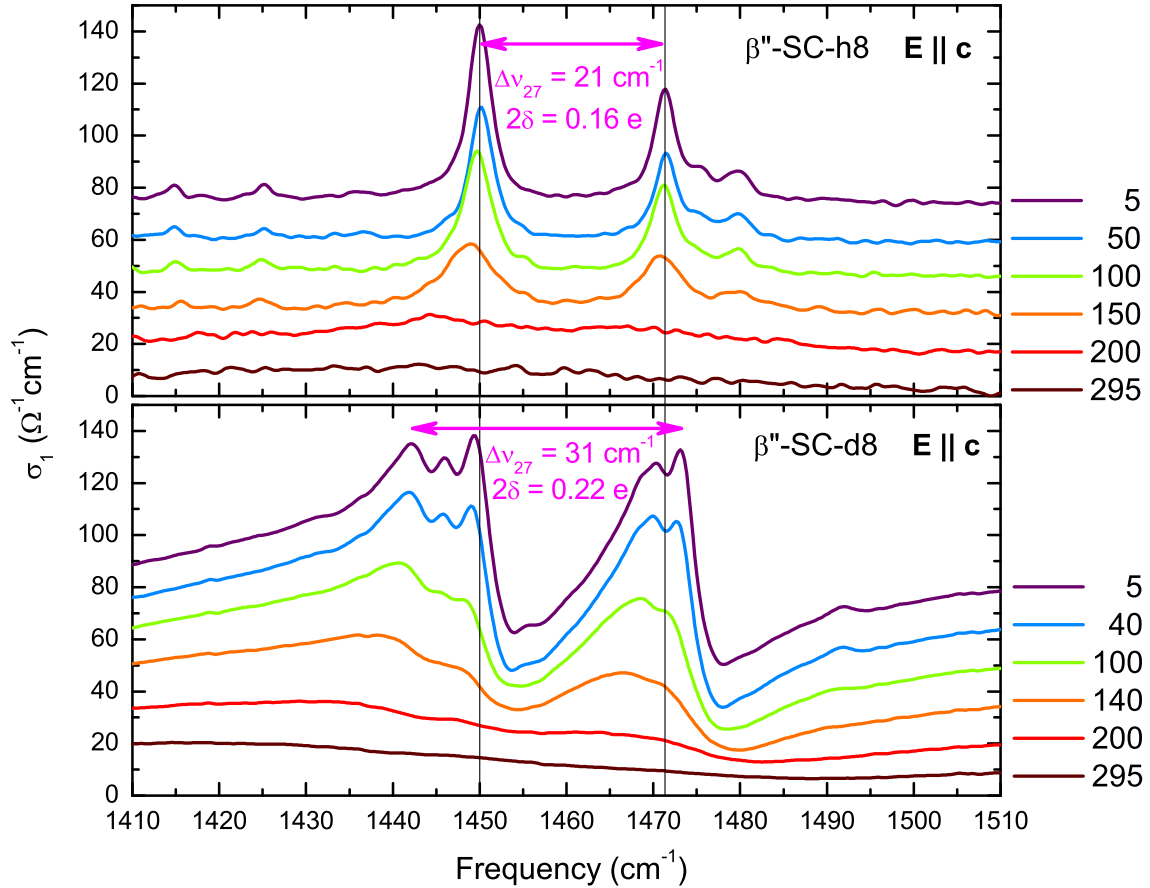


Figure 6.1.26: Although the C=C vibration is not affected by deuteration per se, the mode splitting $\Delta\nu$ is enlarged in β'' -(BEDT-TTF) $_2$ SF $_5$ CH $_2$ CF $_2$ SO $_3$ -d8. The corresponding charge disproportionation 2δ increases from 0.15 e to 0.17 e (average) and 0.22 e (maximum peak separation). Moreover, the modes are split even further implying more complex charge fluctuations. The concomitant enhancement of superconductivity ($\Delta T_c \approx 0.25$ K reported in Ref. [131]) strengthens the idea of charge fluctuations as the pairing glue of superconductivity.

to lower frequencies due to the larger mass compared to ^1H . Specifically, we identify CH $_2$ twisting and wagging vibrations below 1500 cm^{-1} , as well as C–H stretching around 2000–3000 cm^{-1} , all of which are subject to a red-shift. Since the charge-sensitive ν_{27} mode does not involve hydrogen motions, this feature remains at its original position in the spectrum around 1450 cm^{-1} . Our results agree well with previous spectroscopic studies [111, 112]. We point out that the d8-spectra show no residuals at the h8 resonance frequencies implying that the sample is completely substituted with deuterium and no remnants of ^1H are left.

Let us focus now on the ν_{27} vibration which is presented in Fig. 6.1.26, where the upper panel corresponds to β'' -SC-h8 and the lower one to β'' -SC-d8. We find that

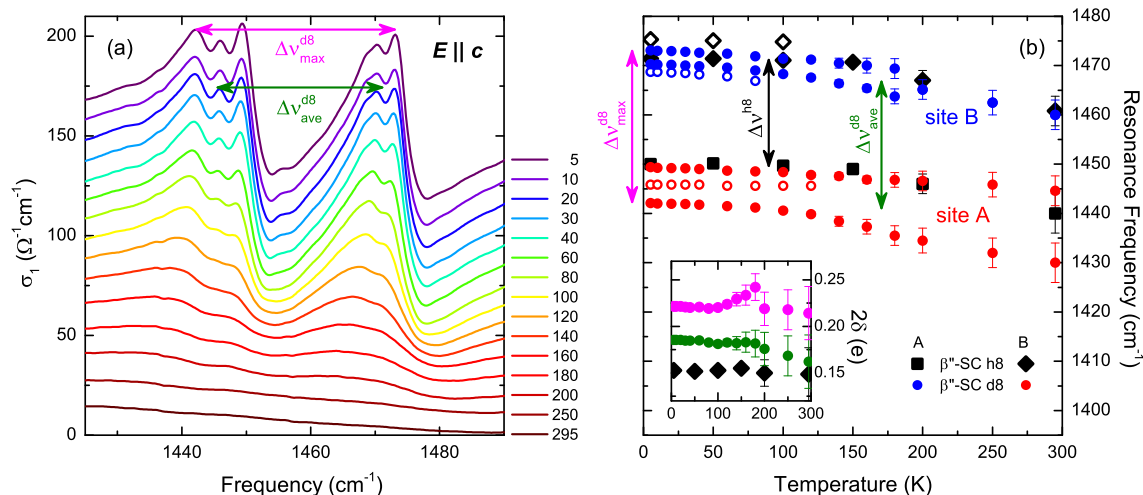


Figure 6.1.27: (a) The temperature evolution of the ν_{27} mode in β'' -SC-d8 is plotted for the entire data set. Two main branches are identified consisting of three features each. The spectra are vertically shifted for convenience. (b) The peak positions are compared to the h8 compound which shows basically similar structure, but less complex sub-splitting. Inset: the charge disproportionation is significantly larger for the deuterated material.

also the deuterated compound exhibits inequivalent site charges. Strikingly, a larger number of peaks is observed and the splitting is significantly increased; the charge disproportionation corresponding to the largest peak separation amounts to $2\delta = 0.22$ e, as compared to 0.15 e for β'' -SC-h8.

Since our optical experiments between 5 and 295 K were performed in small temperature steps, a detailed analysis could be carried out. In Fig. 6.1.27 we plot the entire data set (a) and present the temperature evolution of the peak positions (b). We can distinguish in total 6 modes arranged in two main branches corresponding to the crystallographically inequivalent *A* and *B* stacks. The overall trend upon cooling is similar to β'' -SC-h8 with a negligible temperature dependence of the charge disproportionation. The average splitting between the respective center of gravity corresponds to $2\delta = 0.18$ which is considerably larger than in β'' -SC-h8. Generally, the ν_{27} vibrational features of the deuterated compound appear at lower frequency. A possible reason for this may be the reduced kinetics of ^2H which modifies the H-bonds to the anions in such a way that the cations acquire a slightly more positive charge, at least on the C=C double bonds. The important role of hydrogen for the molecular charge has been demonstrated in the $\kappa\text{-H}_3(\text{Cat-EDT-TTF})_2$ systems studied by Mori *et al.* [211, 212]. It was found that deuteration has a tremendous effect, even switching between quantum spin liquid and charge-ordered states ($T_{\text{CO}} = 185$ K) [213].

To conclude, we found a significant enhancement of the charge disproportionation in β'' -SC upon deuteration, concomitant to an increase of T_c reported previously. Thus, we assign the strengthening of superconductivity to originate directly from the enlarged charge disproportionation. Due to the distinguished position of H-atoms in this material, being the linking units between the anions and BEDT-TTF molecules, this result provides additional evidence for the decisive role of the anions for charge order and, on top of that, superconductivity.

Despite the apparent importance of deuteration for unconventional electronic states, including the Mott transition, charge order, superconductivity, and quantum spin liquid behaviour, the field is lacking comprehensive studies to pin down the exact mechanism and significance of hydrogen bonding in strongly correlated charge-transfer salts. To that end, optical investigations on the charge-sensitive molecular vibrations in quasi one-dimensional (TMTTF) $_2X$ are under way (ongoing experiments by A. Rohwer); charge and anion orderings are understood in much more detail in these compounds [51, 113] as opposed to quasi two-dimensional (BEDT-TTF) $_2X$.

6.1.6 Summary and Discussion

We established the tentative phase diagram of β'' -(BEDT-TTF) $_2$ SF $_5$ RSO $_3$ [38], where $R = \text{CH}_2, \text{CHF}_2, \text{CH}_2\text{CF}_2$ and CHF , by extensive transport, magnetic and, particularly, optical experiments. The two-dimensional nature as well as the metallic and insulating properties of the electronic systems are revealed from the anisotropic electrodynamic response. Employing vibrational spectroscopy, we distinguish different site charges $\rho_0 \pm \delta$ associated with the charge-ordered nature of the insulating states in these materials with effectively 1/4-filled bands. The charge disproportionation 2δ increases with larger Coulomb repulsion providing evidence for the electrostatic origin of charge order. From the polarization-dependent peak position of the Mott-Hubbard band we can directly examine the specific charge pattern within the BEDT-TTF planes. In particular, the electronic excitations are strongly anisotropic for $R = \text{CHF}_2$ and CH_2CF_2 implying a stripe-like arrangement of charge-poor and charge-rich molecules along the crystallographic a -direction, in excellent agreement with our SQUID data (cf. Fig. 6.1.3), the structural properties [39, 40] and first principles density functional theory calculations [205]. Therefore, our results confirm that these four materials can be summarized in a common phase diagram in the order $\text{CH}_2 - \text{CHF}_2 - \text{CH}_2\text{CF}_2 - \text{CHF}$ [38] for decreasing electronic interactions and charge disproportionation.

Pressure-dependent transport experiments reveal an unexpected increase of the metal-

insulator transition temperature for $R = \text{CHF}_2$ and CH_2CF_2 [41]. Since this is accompanied by an enhancement of the bandwidth, as the absolute values of the resistivity are lowered, it implies an additional electrostatic potential A adding to the inter-site Coulomb repulsion V within the BEDT-TTF layer; while in the standard single-band Hubbard model V/W is reduced with pressure, the external term may cause an overall enhancement of the effective correlations $(V + A)/W$ leading to an increase of T_{MI} . Comparison with the structure yields that the BEDT-TTF sites close to the negative SO_3^- part of the anion acquire a more positive charge, and those further away a more negative one. Therefore, we explain the charge-disproportionate insulating state in the β'' -(BEDT-TTF) $_2\text{SF}_5\text{R}\text{SO}_3$ series – and probably also in other families of charge transfer salts – by an external modulation of the electrostatic potential due to the anions, in a similar way as deduced for the anion-ordered phase in (TMTTF) $_2X$ [51].

While the insulating properties of these materials are fascinating on their own, our primary interest in 1/4-filled (BEDT-TTF) $_2X$ arose from the unconventional superconductivity stabilized at low temperatures. In order to establish a relation to charge fluctuations, which were predicted to mediate Cooper pairing [33], the charge-sensitive ν_{27} vibration of β'' -(BEDT-TTF) $_2\text{SF}_5\text{CH}_2\text{CF}_2\text{SO}_3$ was measured below $T_c = 5$ K, which was verified by *in situ* transport experiments. As a result, we find that charge order persists in the superconducting state, providing evidence that these two phenomena do not compete with each other. Moreover, studies on deuterated samples revealed that T_c and 2δ increase at the same time, adding another indication for a possibly intrinsic dependence of superconductivity on charge order.

6.2 Negligible Charge Fluctuations in θ -(BEDT-TTF) $_2$ I $_3$

The θ -series is highly susceptible towards charge fluctuations and charge order [52, 141]. As a result of the highly frustrated triangular arrangement of BEDT-TTF molecules, glassy charge dynamics were identified recently [214–217]. θ -(BEDT-TTF) $_2$ I $_3$ is the only member of this family that shows metallic behaviour down to low temperatures, and even superconductivity with $T_c = 3.6$ K [218]. Previous optical and transport investigations concluded moderately correlated metallic behaviour that reveals a coherent quasiparticle response at low temperatures when the resistivity is below the Ioffe-Regel-Mott limit ρ_{IRM} [65].

To scrutinize a possible effect of charge fluctuations in this material, the temperature dependence of the charge-sensitive $\nu_{27}(\text{b}_{1u})$ mode was measured. Fig. 6.2.1 shows the out-of-plane response ($E \parallel b$) which is dominated by intramolecular vi-

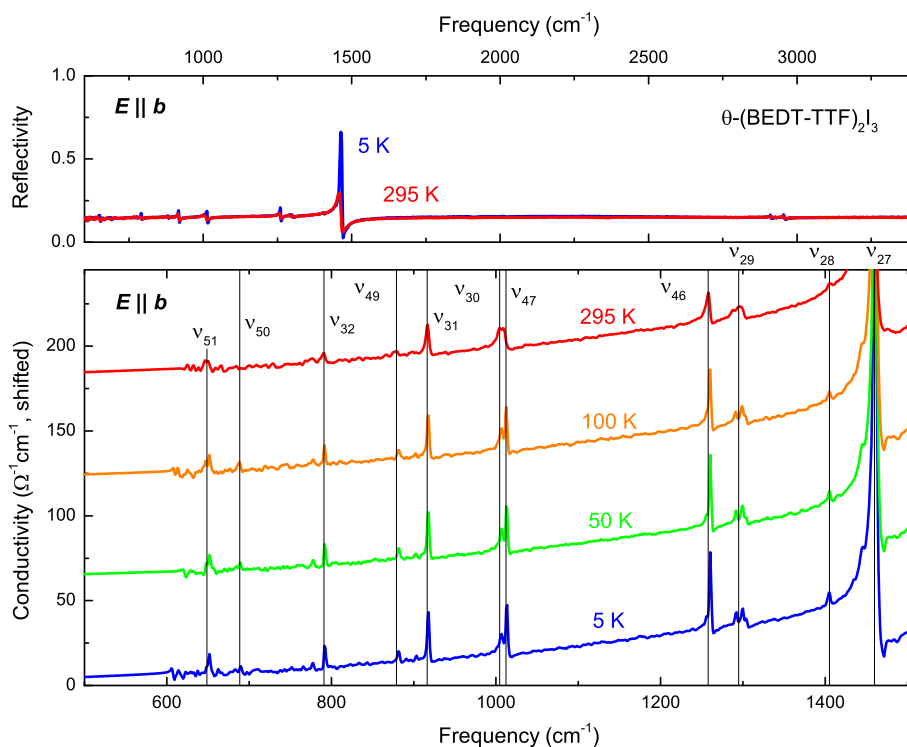


Figure 6.2.1: Perpendicular to the conducting plane ($E \parallel b$) the optical reflectivity and conductivity of θ -(BEDT-TTF) $_2$ I $_3$ reveal insulating behaviour indicative of the quasi two-dimensional electronic properties. Note the different frequency scales of the two panels. The spectrum is dominated by intramolecular vibrations on top of a vanishing electronic background. The BEDT-TTF normal modes were assigned according to Ref. [111].

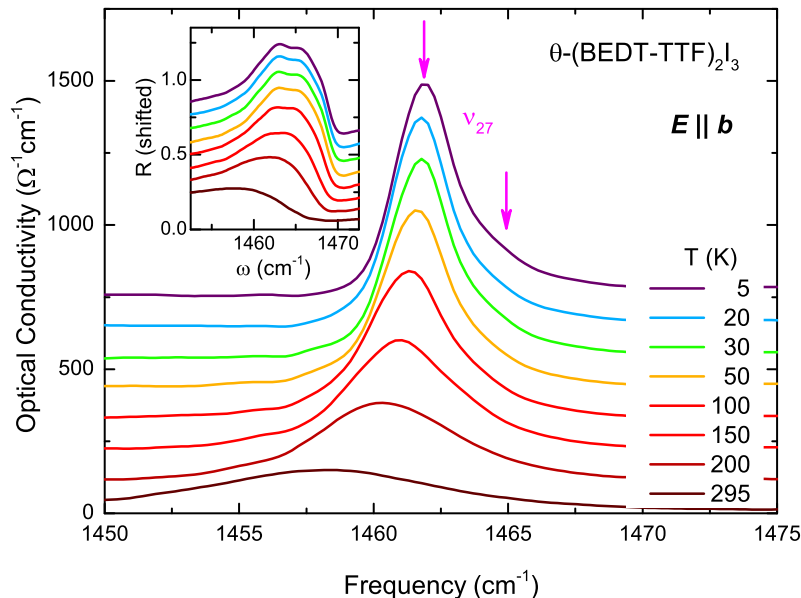


Figure 6.2.2: The charge-sensitive ν_{27} mode shows typical narrowing and blue-shifting upon cooling, as expected for a vibrational feature. At low temperatures, a minor splitting ($\Delta\nu \approx 3 \text{ cm}^{-1}$) is observed corresponding to $2\delta = 0.02 e$. This rules out sizeable charge disproportionation consistent with the absence of Mott-Hubbard bands in the in-plane response [65] and the small superconducting transition temperature $T_c = 3.6 \text{ K}$ [218].

brations. As indicated, the BEDT-TTF normal modes could be assigned in good agreement with Eldridge *et al.* [111]. The spectrum reveals mainly infrared-active vibrations consistent with the centrosymmetry of BEDT-TTF sites in the θ -type lattice structure: unlike in the κ -salts, the organic molecules are not dimerized which prevents activation of symmetric modes by out-of-phase vibration of two molecules in a dimer.

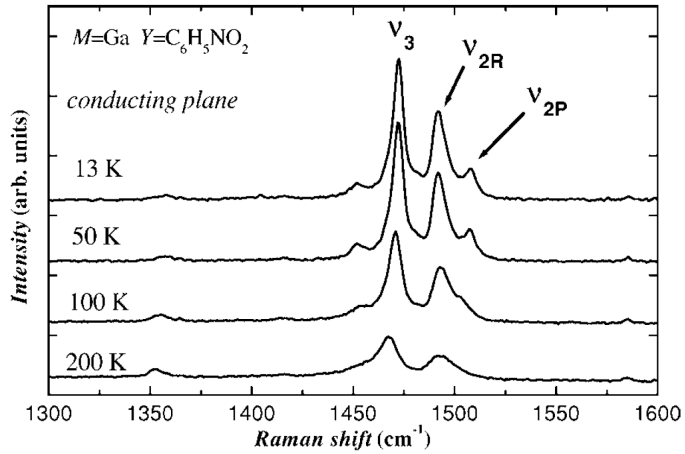
The ν_{27} mode is by far the strongest feature in the spectrum due to its large dipole moment along the molecular long axis. Fig. 6.2.2 illustrates its temperature dependence. Upon cooling, the mode gets much narrower and two distinct features can be identified, better visible in the inset showing the reflectivity rather than σ_1 . The splitting, however, is very small incurring a charge disproportionation of only $2\delta = 0.02 e$. Therefore, significant charge fluctuations can be ruled out in θ -(BEDT-TTF)₂I₃, consistent with the in-plane response at the lowest temperature that lacks a finite-energy band [65], which would have indicated appreciable Mott-Hubbard interactions. Apart from that, the small T_c indicates that this compound is located well on the metallic side of the insulator-metal transition. A comprehensive spectroscopic study of the Fermi liquid regime at low temperatures, however, is still pending as the data presented in Ref. [65] do not extend to low-enough frequencies. In particular,

an extended Drude analysis would allow for determination of the effective mass. Following the arguments of Cano-Cortés *et al.* [88], θ -(BEDT-TTF) $_2$ I $_3$ should reach a quantum critical regime upon slightly increasing the electronic correlation strength V/W . Pressure-dependent transport studies, however, revealed the transformation of the metallic state to a narrow-gap semiconductor, similar as in α -(BEDT-TTF) $_2$ I $_3$ [219]. Hence, the situation is somewhat different than in the other θ -compounds where application of pressure caused a reduction of the bandwidth and, therefore, an increase of the correlations stabilizing an insulating state [52, 141]. We may speculate whether deuteration has a similar effect on superconductivity and the charge disproportionation as in β'' -SC [131]. The physical realization of θ -(BEDT-TTF) $_2$ I $_3$ is already challenging as the α -, β'' - and κ -phases grow more favourably for this stoichiometry; the use of d8-BEDT-TTF will probably not ease this task.

6.3 Charge Fluctuations and Fermi Liquid in β'' -(BEDT-TTF) $_4$ [(H $_3$ O)Ga(C $_2$ O $_4$) $_3$] · C $_6$ H $_5$ NO $_2$

Another potential candidate to scrutinize a possible connection between superconductivity and charge fluctuations is β'' -(BEDT-TTF) $_4$ [(H $_3$ O)Ga(C $_2$ O $_4$) $_3$] · C $_6$ H $_5$ NO $_2$, in the following abbreviated as β'' -Ga. Similar as in β'' -SC, indications of charge disproportionation were found in this compound; in particular, the Raman data shown in Fig. 6.3.1 indicate $2\delta = 0.13$ e from the splitting of the charge-sensitive ν_2 mode [34, 220]. This material belongs to the tunable series composed of oxalate-based anions

Figure 6.3.1: Raman measurements are sensitive to totally symmetric intramolecular vibrations such as the breathing mode that includes C=C stretching. The charge-sensitive ν_2 feature splits below 100 K indicating a charge disproportionation $2\delta = 0.13$ e. The temperature dependence of the splitting is more pronounced than in the β'' -(BEDT-TTF) $_2$ SF $_5$ RSO $_3$ series. Reproduced from Ref. [34].



[$XM(C_2O_4)_3$]· Y , where X is a monovalent cation (e.g. NH $_4^+$ or H $_3$ O $^+$), M a threevalent, typically transition-metal cation (e.g. Cr $^{3+}$, Fe $^{3+}$ or Ga $^{3+}$) and Y denotes the neutral solvent guest molecule (e.g. C $_6$ H $_5$ NO $_2$ or C $_6$ H $_5$ CN) [34, 221–224]. Depending on the unit cell volume, the electronic properties are that of an insulator (large V_{UC}) or a metal (small V_{UC}); superconductivity is observed at the verge [34, 224]. Hence, the underlying physics seem to be consistent with the extended Hubbard model, as opposed to β'' -(BEDT-TTF) $_2$ SF $_5$ RSO $_3$ discussed in section 6.1. Furthermore, introduction of magnetic ions M , such as Cr $^{3+}$ or Fe $^{3+}$, causes a reduction of the superconducting transition temperature and the upper critical field; both $T_c = 7.5$ K and $H_{c2\parallel} = 33$ T ($H_{c2\perp} = 5.2$ T perpendicular to the conducting layers) are largest for non-magnetic Ga $^{3+}$ [34]. The extremely large upper critical field makes β'' -Ga an ideal candidate for an FFLO state with a spatially modulated superconducting order parameter [225, 226]. For comparison, $H_{c2\parallel}$ in β'' -SC [98] is below 20 T which, however, made this phase easily accessible using conventional superconducting magnets. Single crystals of β'' -Ga are extremely thin and have a needle-like shape with typical dimensions of $0.05 \times 0.2 \times 1$ mm 3 ; the thickness along the c -axis can be as

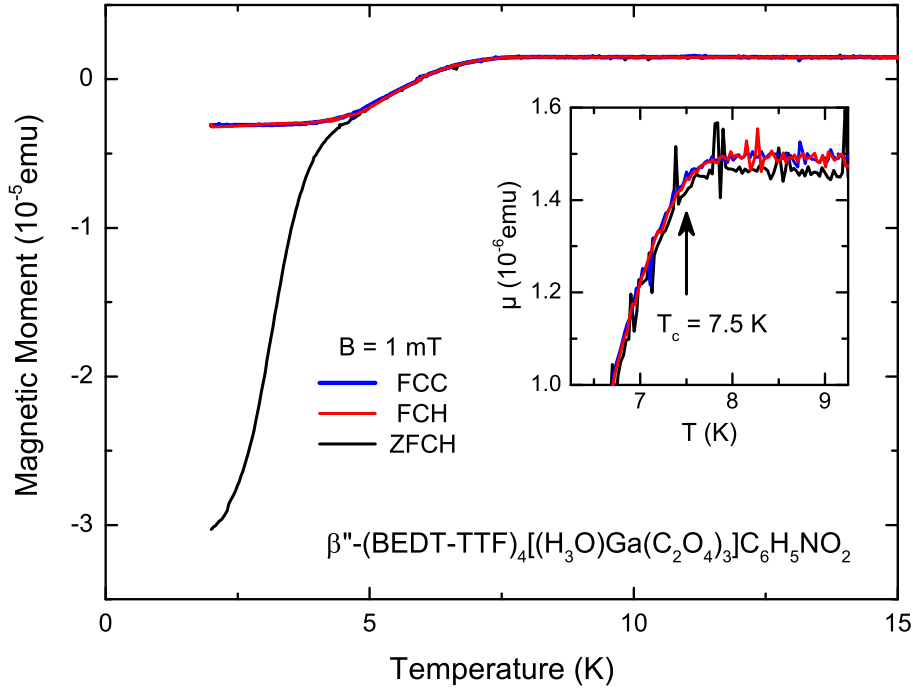


Figure 6.3.2: The magnetic response of a β'' -Ga single crystal was characterized by SQUID magnetometry. The spin susceptibility shows strong diamagnetic shielding below $T_c = 7.5$ K verifying the superconducting properties characteristic of this compound [34, 222, 223]. The crossover from the Shubnikov phase to the Meissner state slightly below 5 K is nicely observed when comparing zero-field cooled (ZFCH) and field-cooled (FCH) heating curves.

small as a few 10 μm . Samples were provided by Y. Ihara and A. Kawamoto from Hokkaido University, Japan. The conductivity is largest along the crystal long axis denoted as the a -direction.

In order to check for superconductivity, the magnetic properties of β'' -Ga were characterized by SQUID magnetometry prior to optical measurements; Fig. 6.3.2 shows the temperature dependence of a typical single crystal. Due to the extremely small sample mass ($m < 0.1$ mg), the normal-state magnetic moment was too low to be measured accurately. The strong diamagnetic shielding below 7.5 K establishes the onset of superconductivity. Very similar to β'' -(BEDT-TTF) $_2$ SF $_5$ CH $_2$ CF $_2$ SO $_3$ (cf. Fig. 6.1.21), the different trend of zero-field cooled (ZFCH) and field-cooled (FCH) heating curves reveals the Meissner state at low temperatures and the Shubnikov phase above 5 K at $B = 1$ mT.

In the following, we present and analyze the optical properties of β'' -Ga. First, the in-plane response will be discussed giving insight to the electronic excitations. Using the extended Drude model, the scattering rate and effective mass are evaluated

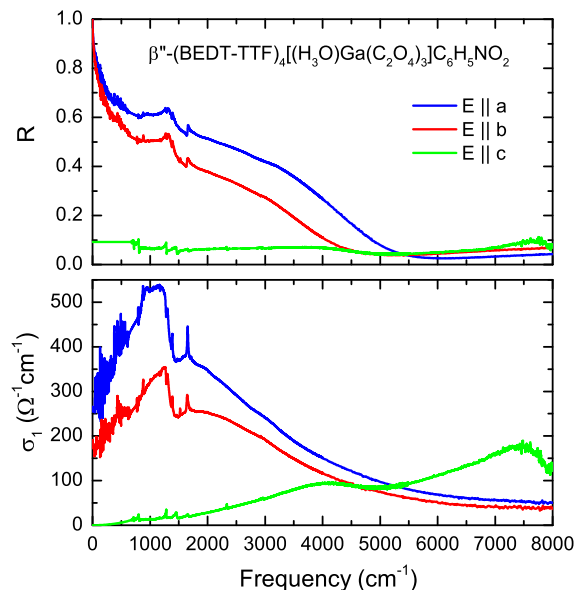


Figure 6.3.3: The optical reflectivity and conductivity of β'' -Ga is plotted along the three principal axes. Like in the other compounds discussed in this thesis, the in-plane properties are metallic while the out-of-plane direction exhibits an insulating response, which proves the quasi two-dimensional nature of the electronic system. However, there is significantly weaker anisotropy within the conducting plane as compared to the $\beta''\text{-(BEDT-TTF)}_2\text{SF}_5\text{RSO}_3$ compounds (cf. Figs. 3.4.3 and 6.1.4).

in the context of Fermi liquid behaviour. Then, the charge-sensitive vibrations are presented in order to reveal possible charge order/fluctuations, the specific charge pattern and whether it is related to the anion layer, as discussed in the previous sections of this chapter. Using partially ^{13}C substituted samples facilitates disentangling the complex spectrum in the range of the ν_{27} mode.

6.3.1 Broadband Electrodynamical Response: Electronic Excitations and Fermi Liquid Behaviour

The temperature-dependent optical reflectivity was measured for all three principal axes; the room-temperature spectra are presented in Fig. 6.3.3. As for the other compounds discussed earlier in this thesis, the optical conductivity is strongly anisotropic between the in- and out-of-plane responses establishing the quasi two-dimensional electronic properties. We note, however, that the a and b -directions show comparable shape and intensity, i.e. the in-plane anisotropy is considerably smaller than in $\beta''\text{-(BEDT-TTF)}_2\text{SF}_5\text{RSO}_3$ where a stripe-like charge arrangement was found. This is likely related with the hexagonal arrangement of the oxalate-network in the anion

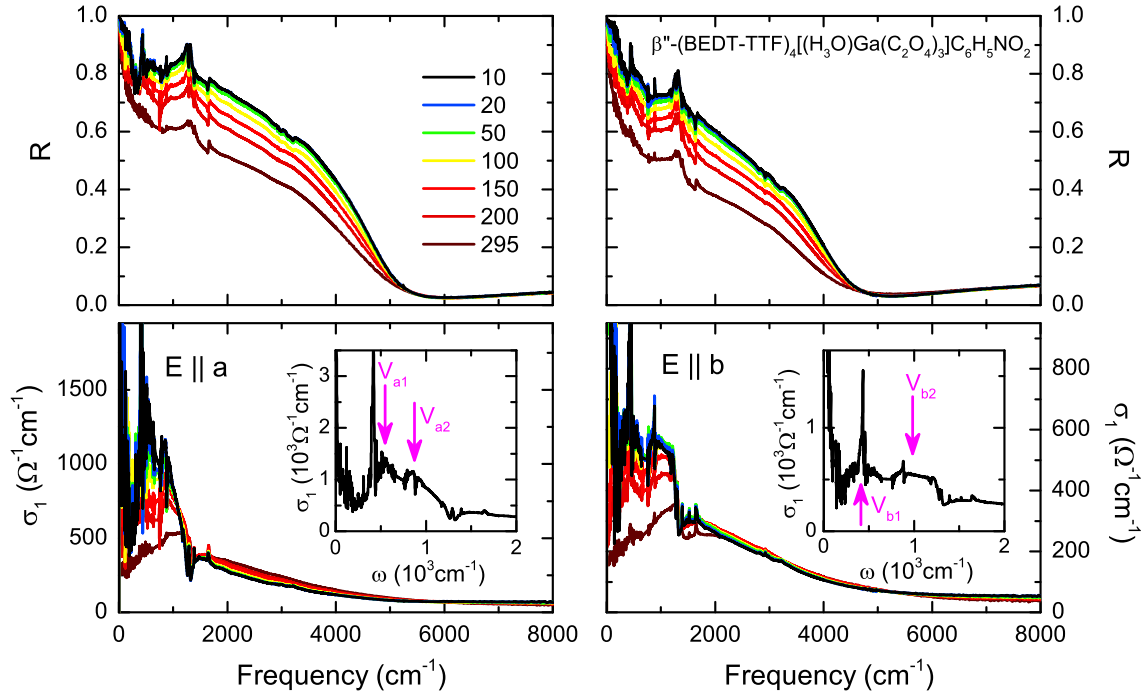


Figure 6.3.4: The temperature-dependent optical response of β'' -Ga is plotted for both in-plane polarizations. Despite a factor two difference between the absolute values of the optical conductivity along a and b , the anisotropy is much less pronounced than in the β'' -(BEDT-TTF)₂SF₅RSO₃ compounds. Two charge fluctuation bands around 500 (V_{i1} where $i = a, b$) and 900 cm^{-1} (V_{i2}) are identified in the far-infrared range for both crystal axes, as pointed out by the insets. Note, a similar feature was observed in the superconducting material β'' -SC where it appears only for $E \parallel b$ [37]. Such isotropic charge excitations indicate a different, particularly non-stripe-like, charge pattern in β'' -Ga.

layer, which does not accentuate a specific direction.

Now we turn to the temperature dependence of the in-plane response which is shown in Fig. 6.3.4. The reflectivity shows very similar shape for both polarizations with a basically temperature-independent plasma edge around 5000 cm^{-1} ; both the intensity (by a factor 2) and plasma frequency are larger along the a -direction. Overall, the optical conductivity does not change much with temperature above 2000 cm^{-1} . At low frequencies, however, σ_1 increases strongly upon cooling and develops a narrow Drude peak and two finite-energy bands around 500 and 900 cm^{-1} , the latter ones being closer together for $E \parallel a$ ($V_{a1} = 550$ and $V_{a2} = 870$ cm^{-1}) and more separated for $E \parallel b$ ($V_{b1} = 420$ and $V_{b2} = 980$ cm^{-1}). We assign these features to charge order excitations that appear in a comparable range as in β'' -SC (cf. Fig. 6.1.14 and Ref. [37]). There, such transitions appear only for $E \parallel b$ due to the stripe-like charge arrangement. Thus, the almost isotropic excitations observed for β'' -Ga imply

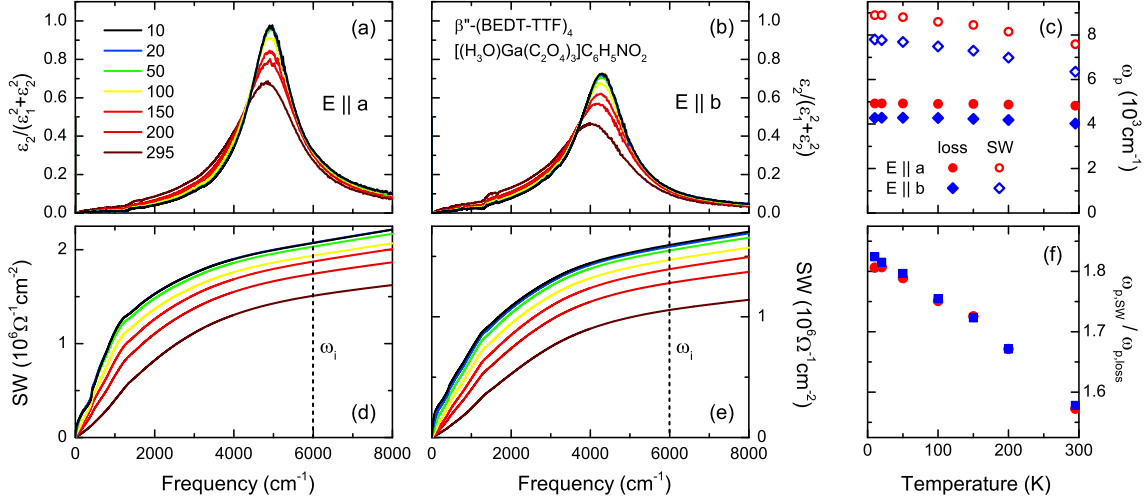


Figure 6.3.5: The plasma frequency of β'' -Ga is determined in two different ways which should, in principle, give a similar result. On the one hand, the dielectric loss function is calculated from the complex permittivity (a,b); $\omega_{p,loss}$ corresponds to the peak position. On the other hand, the spectral weight (SW) is integrated up to a cut-off frequency ($\omega_i = 6000 \text{ cm}^{-1}$) (d,e); for a single-band response it should be related to the plasma frequency via the sum rules (Equ. 2.2.6). As indicated in panels (c) and (f), the two results are distinct due to difficulty in choosing the correct ω_i for integration; the difference is very similar for the two polarizations. While $\omega_{p,loss}$ shows only weak temperature dependence (cf. Fig. 6.3.4), with values of 4925 cm^{-1} ($E \parallel a$) and 4275 cm^{-1} ($E \parallel b$) at 5 K, the plasma frequency determined from the SW exhibits a more pronounced increase with cooling.

a different charge pattern. The narrow feature on top of the 500 cm^{-1} band is likely of phononic origin.

In order to proceed the analysis according to the extended Drude formalism, we first have to determine the plasma frequency. As presented in Fig. 6.3.5, ω_p was determined both from the dielectric loss function ($Im\{-\frac{1}{\epsilon}\} = \frac{\epsilon_2}{\epsilon_1^2 + \epsilon_2^2}$, see Equ. 2.2.7 and Fig. 2.2.3) and the integrated spectral weight SW (see Equ. 2.2.6). In principle, both methods should provide the same result for a single-band response. However, the finite extent of the bands and possible contributions from higher frequencies make it difficult to define the correct cut-off frequency; 6000 cm^{-1} was used here.

Apparently, the plasma frequency deduced from the SW yields higher values as compared to the loss function result. There is, however, a direct link between the two methods since their ratio is identical for both polarization directions, as shown in panel (f). The general tendency of increasing ω_p upon cooling, which is more strongly pronounced for the SW data, may reflect the thermal contraction of the material implying a larger charge carrier density at low temperatures. On the other hand, the almost temperature-independent loss function results resemble the trend

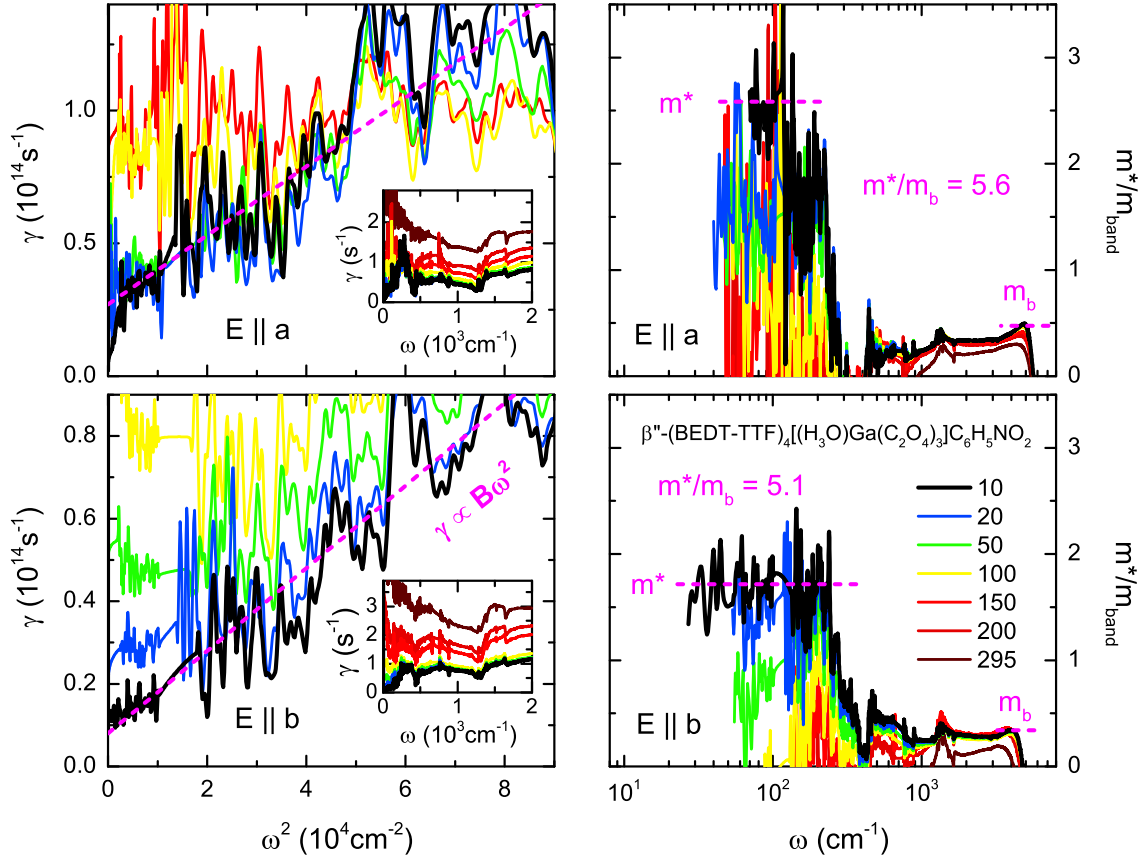


Figure 6.3.6: The frequency-dependent scattering rate (left panels) and effective mass m^*/m_{band} (right panels) were determined for both in-plane polarizations of β'' -Ga applying the extended Drude formalism (cf. Equ. 2.3.4). $\gamma(\omega)$ is plotted versus ω^2 to extract the quadratic prefactor B . The insets show a larger frequency range on linear scales highlighting the low-frequency region where the Fermi liquid fingerprints are observed. At low temperatures, m^*/m_{band} levels off at low energies with the plateau corresponding to the mass renormalization of the correlated quasiparticles.

of the reflectivity data (cf. Fig. 6.3.4) that exhibit a plasma edge almost constant in temperature.

We notice that the low-frequency curvature of the SW changes from insulating-like to metallic-like upon cooling, associated with the condensation of coherent charge carriers in a narrow Drude peak and, as we will see, the stabilization of a Fermi liquid phase. To investigate the specific fingerprints in the scattering properties and the degree of electronic correlations, we performed the extended Drude analysis. Fig. 6.3.6 presents the temperature- and frequency-dependent scattering rate $\gamma(\omega)$ and effective mass $m^*/m_{band}(\omega)$ of β'' -Ga calculated according to Equ. 2.3.4 using $\omega_{p,loss}$. As already stated above for the optical conductivity, the absolute values of these quantities are consistently larger for $E \parallel a$.

With decreasing temperature, the overall number of scattering events in the low-frequency response diminishes giving rise to a Drude regime at intermediate temperatures and a Fermi liquid phase upon approaching $T_c = 7.5$ K. Although the data are pretty noisy in the range of the quadratic frequency dependence, one nicely observes the transition from a scattering rate constant in temperature (Drude-like between $100 \text{ K} < T < 200 \text{ K}$) to a power-law behaviour ($\gamma = \gamma_0 + B\omega^2$ below 300 cm^{-1}) reminiscent of a Fermi liquid. In the same energy range, the effective mass becomes well defined just below 100 K and acquires a plateau that extends down to zero frequency – as inferred from the measured range. Therefore, our results indicate that the Fermi liquid state with well-defined quasiparticles is confined to $T < 100$ K.

In the mid-infrared ($1500\text{--}3000 \text{ cm}^{-1}$) m^*/m_{band} is almost constant at a significantly smaller value. The influence of electronic correlations manifests in an effective mass enhancement m^*/m_b around 5.6 and 5.1 for the a - and b -directions⁹, respectively. These values are even larger than those found for $\kappa\text{-}[(\text{BEDT-STF})_x(\text{BEDT-TTF})_{1-x}]_2\text{Cu}_2(\text{CN})_3$ (section 5.3) where the Mott transition was investigated at half filling. We have to keep in mind, however, that all compounds with Fermi liquid behaviour studied there ($x \geq 0.28$) are well on the metallic side whereas $\beta''\text{-Ga}$ – since it is superconducting – is located right at the verge between the insulating and metallic phases where m^* is expected to diverge. The ambient-pressure superconducting compound of the $\kappa\text{-STF}_x$ series ($x = 0.12$) did not show Fermi liquid behaviour at all since, most likely, T_{FL} was already suppressed to energies outside the measured range. Comparison of the different transition temperatures in 1/4-filled ($T_c \approx 7.5$ K in $\beta''\text{-Ga}$) and 1/2-filled ($T_{c,\text{max}} \approx 5$ K for $\kappa\text{-}[(\text{BEDT-STF})_x(\text{BEDT-TTF})_{1-x}]_2\text{Cu}_2(\text{CN})_3$) materials is beyond the scope of the present analysis since there are other parameters essential for superconductivity, such as the energy scales (V, U, W) or charge carrier densities.

Finally, let us compare the quadratic energy dependence of the scattering rate in the temperature and frequency domains, which is illustrated in Fig. 6.3.7 where the real part of the inverse conductivity for $E \parallel a$ is displayed. While for dc transport we plot simply the temperature-dependent resistivity (data from A. Löhle), by inverting the complex optical conductivity we basically obtain the frequency-dependent resistivity which is nothing but the scattering rate divided by ω_p^2 . Hence, neither of these quantities depends on the experimentally determined plasma frequency allowing for a direct, quantitative comparison. There is good agreement between the dc resistivity and the zero-frequency extrapolation of the optical data. Despite the almost ideal

⁹A similar analysis was performed as in section 5.3.2

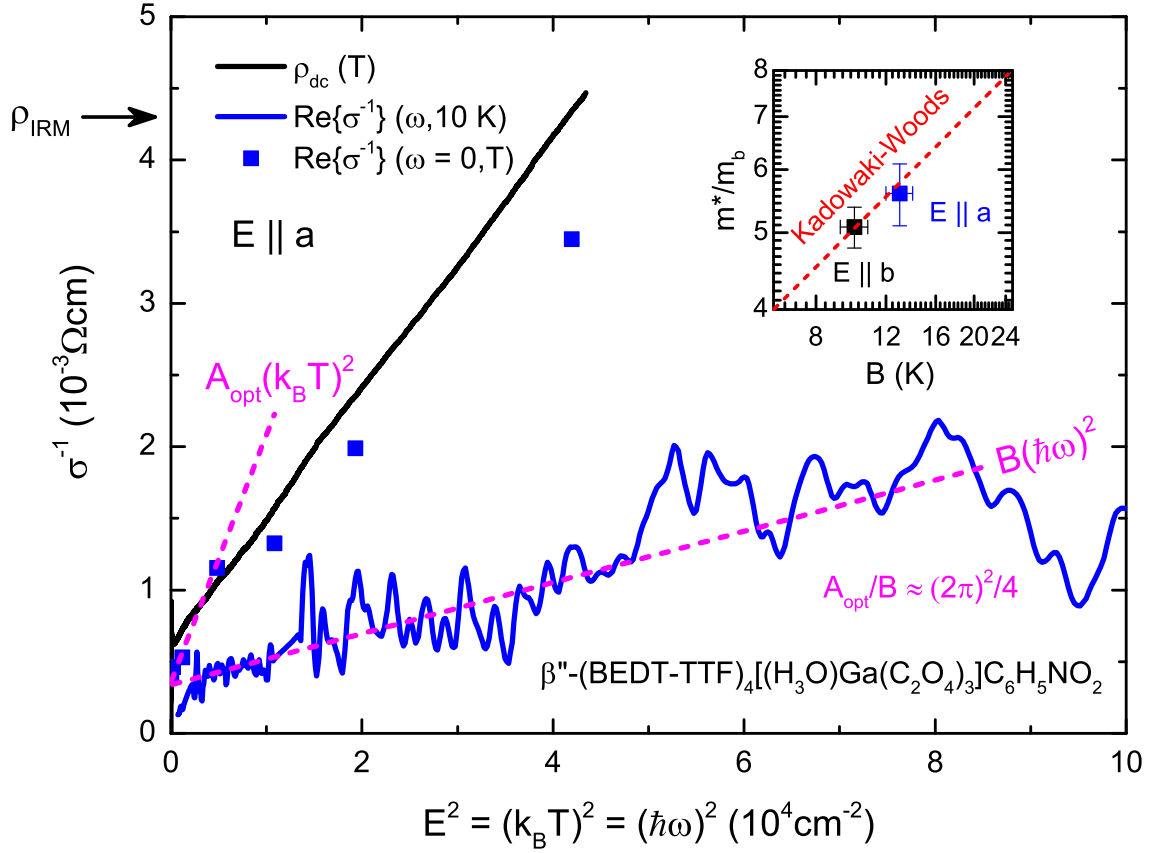


Figure 6.3.7: The real part of the inverse optical conductivity (blue line) is plotted together with the zero frequency cut-off (blue dots) and the dc resistivity (black line) with respect to squared energy to point out the Fermi liquid response. All data are for $E \parallel a$. Although the resistivity is well below the Ioffe-Regel-limit, the large range of $\rho \propto (k_B T)^2$ is probably influenced by thermal expansion rather than Fermi liquid behaviour up to 300 K. The ratio of the prefactors $A_{opt}/B \approx (2\pi)^2/4$, where A_{opt} is determined from the zero-frequency extrapolation of the optical data, deviates from the nominal prediction for a Fermi liquid. Inset: upon comparing the mass renormalization and the prefactor B for both polarizations, the results are in excellent agreement with the Kadowaki-Woods ratio, i.e. $B \propto (m^*/m_b)^2$.

$\rho_{dc} \propto AT^2$ behaviour up to room temperature, it should be stressed that the Fermi liquid phase is limited to $T < 100$ K, as inferred from the extended Drude analysis discussed above. The quadratic temperature dependence of resistivity is, most likely, just a coincidence related to the thermal expansion and activation of additional scattering channels like phonons.

To keep the analysis self-consistent¹⁰, we extract the prefactors A_{opt} and B (dashed pink lines) from the temperature-dependence of the zero-frequency extrapolation and

¹⁰It was pointed out in Ref. [29] that the T^2 prefactor A of the dc resistivity is generally not equal to A_{opt} as it might include additional scattering mechanisms.

the frequency dependence of the lowest temperature optical data, indicated by the blue squares and the blue line, respectively. Comparing these two values we obtain a ratio $A_{opt}/B = (2\pi)^2/4$ smaller by a factor four than the prediction for a pristine Fermi liquid ($A/B = (2\pi)^2$) with purely inelastic scattering between quasiparticles, which was undoubtedly reported only for Sr_2RuO_4 so far [71]. Hence, scattering in $\beta''\text{-Ga}$ can be classified close to the purely elastic limit, similar as in heavy-Fermion compounds (e.g. URu_2Si_2) and the doped Mott insulator NdTiO_3 [193, 194]. While it was argued that this might be related to scattering from the localized f -electrons of U and Nd in those materials [29], in the current case the elastic scattering events may be related to the charge density modulation which acts like a screened local moment. Note, the $(\text{BEDT-TTF})_2X$ Mott insulators at half filling exhibit A/B ratios exceeding $(2\pi)^2$ (section 5.3 and Refs. [22, 23, 123]) which, in the language of Maslov *et al.* [29], indicates a *non-metallic* contribution to the self-energy. We might speculate whether this is related to incoherent metallic fluctuations as the Fermi liquid state reaches up to the Ioffe-Regel-Mott limit in those compounds; in $\beta''\text{-Ga}$ ρ_{IRM} is crossed just at room temperature, i.e. far above T_{FL} , and the charge carriers are subject to predominantly elastic scattering.

A similar analysis was performed for the b -direction of $\beta''\text{-Ga}$ yielding $A_{opt}/B \approx (2\pi)^2/2$, also indicative of a considerable elastic contribution to the scattering rate. When comparing the effective mass enhancement and the quadratic frequency prefactor between the two polarizations of this compound, we find that the Kadowaki-Woods relation $B \propto (m^*/m_b)^2$ is nicely fulfilled (inset of Fig. 6.3.7). We point out that the a - and b -directions are subject to different plasma frequency and bandwidth and, hence, different degree of electronic correlations. Therefore, this result self-consistently proves that the Kadowaki-Woods ratio holds for variable correlation strength, underpinning the conclusions of Jacko *et al.* [30].

6.3.2 Charge Order

In order to reveal possible static or fluctuating charge order in $\beta''\text{-Ga}$ we determined the molecular charge disproportionation on basis of molecular vibrations. For that, temperature-dependent optical measurements in the mid-infrared range were performed in out-of-plane ($E \parallel c$) geometry on $\approx 100 \mu\text{m}$ thin $\beta''\text{-Ga}$ single crystals. The resulting spectra are shown in Fig. 6.3.8. The background reflectivity and conductivity resemble insulating behaviour with no big changes upon cooling. The narrow features correspond to molecular vibrations and we will focus now on the temperature evolution of the charge-sensitive ν_{27} mode, which is plotted in

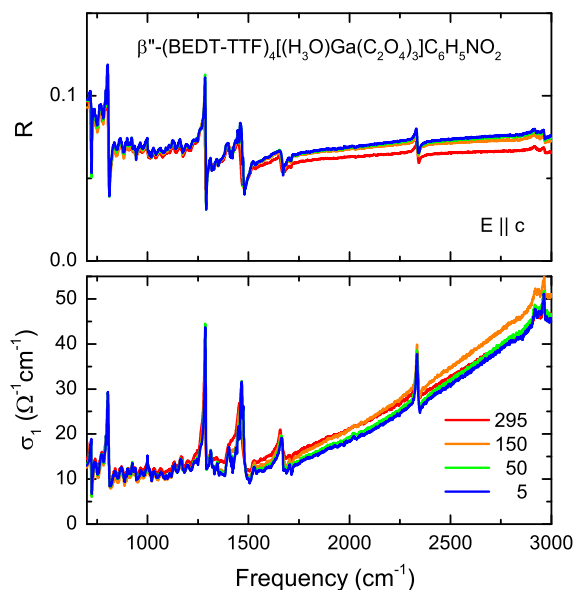


Figure 6.3.8: The out-of-plane optical reflectivity and conductivity of β'' -Ga exhibit insulating behaviour at all temperatures. The main changes are observed for the narrow vibrational features, such as the charge-sensitive ν_{27} mode around $1400\text{--}1500\text{ cm}^{-1}$.

Fig. 6.3.9. The optical spectra of this compound are not as simple to analyze as for the β'' -(BEDT-TTF)₂SF₅RSO₃ series since the anion layer contains carbon-based molecules that exhibit vibrations in a similar range as the ν_{27} mode. For instance, the C₂O₄ oxalate groups are subject to C–O motions around $1405\text{--}1420\text{ cm}^{-1}$ [227] and, on the other hand, the solvent guest molecule C₆H₅NO₂ shows vibrational features at 1400 and 1525 cm^{-1} , as well as a narrow band around 1475 cm^{-1} [228, 229], as indicated in Fig. 6.3.9. Keeping in mind the ethylene bending vibrations of the BEDT-TTF molecule at 1420 cm^{-1} , we identify the main branches of the ν_{27} mode in the range $1430\text{--}1480\text{ cm}^{-1}$. Importantly, the splitting evolves gradually upon cooling, indicative of a more second-order-like onset of charge order similar as in (TMTTF)₂X [51, 113, 196] and opposed to β'' -(BEDT-TTF)₂SF₅RSO₃, where the charge disproportionation is already present at room temperature and basically temperature-independent.

To that end, these features were fitted by a couple of Fano functions, the resonance frequencies of which are plotted in Fig. 6.3.10. There are two main branches at 1449 and 1467 cm^{-1} , each of which is split into two sub-peaks, that can be exclusively assigned to differently charged BEDT-TTF molecules with $2\delta = 0.13$ in perfect agreement with previous Raman investigations (Fig. 6.3.1 and Refs. [34, 220]). Moreover, there is a feature slightly below 1440 cm^{-1} that would correspond to an ionicity 0.2 e different than the dominant peak. However, it is well known that the intensity of the

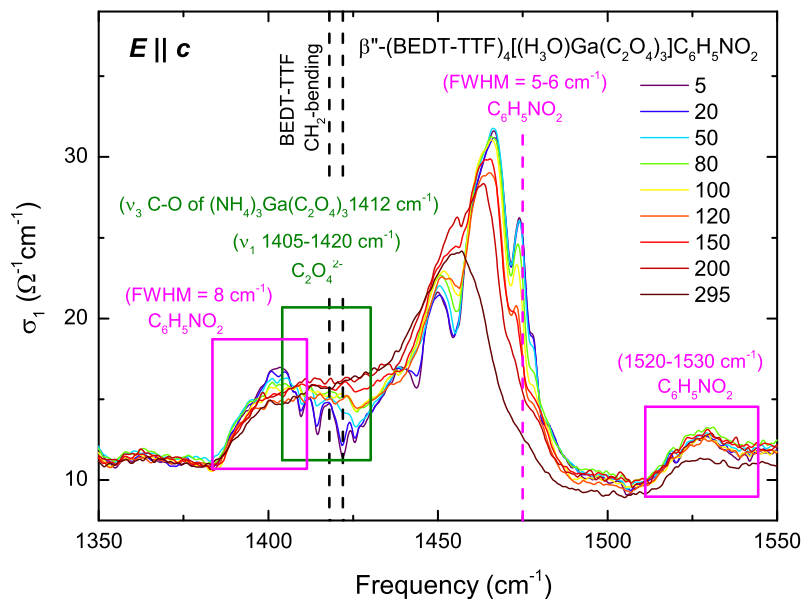


Figure 6.3.9: The optical spectra around the ν_{27} mode show a complex structure with contributions from BEDT-TTF, the anionic C_2O_4 oxalate groups [227] as well as the solvent $C_6H_5NO_2$ molecules [228, 229]. It is not trivial to disentangle the individual terms arising from to C=C or C-O motions. Except a $C_6H_5NO_2$ vibration, the range around 1430–1500 cm^{-1} is basically unaffected by the external contributions such that we can safely assign them to the ν_{27} mode, which is split into multiple peaks at low temperatures.

ν_{27} mode is strongly enhanced with ionicity [50]; in this regard, the weaker intensity of the lower-frequency peaks implies a smaller number of contributing molecules, i.e. there are more sites with less positive charge than with larger hole density. Although their argument was formulated for the more strongly charge disproportionate state below 10 K, Ihara *et al.* inferred a poor-rich-rich state with honeycomb charge arrangement [230, 231]. In analogy to that, we might consider a situation where, for example, two molecules have a less positive charge ρ_{poor} (the dominant peak at 1467 cm^{-1}) while another one (ρ_{medium}) is slightly more (1449 cm^{-1}) and the remaining one (1439 cm^{-1}) even more positively charged (ρ_{rich}). We will come back to the possible charge pattern associated with this at a later point.

In order to disentangle which peaks belong to the BEDT-TTF ν_{27} mode, the optical spectra of a ^{13}C -enriched β'' -Ga single crystal were acquired for $E \parallel c$. Note that only the two carbon atoms of the central C=C bond were substituted. Fig. 6.3.11 contrasts the temperature-dependent spectra for ^{12}C and ^{13}C . Although the main features around 1430–1470 cm^{-1} exhibit a red-shift of only 8 cm^{-1} , which is just one third of the value reported for neutral BEDT-TTF [111], one can clearly distinguish the other features which are unaffected by isotope substitution. One might speculate

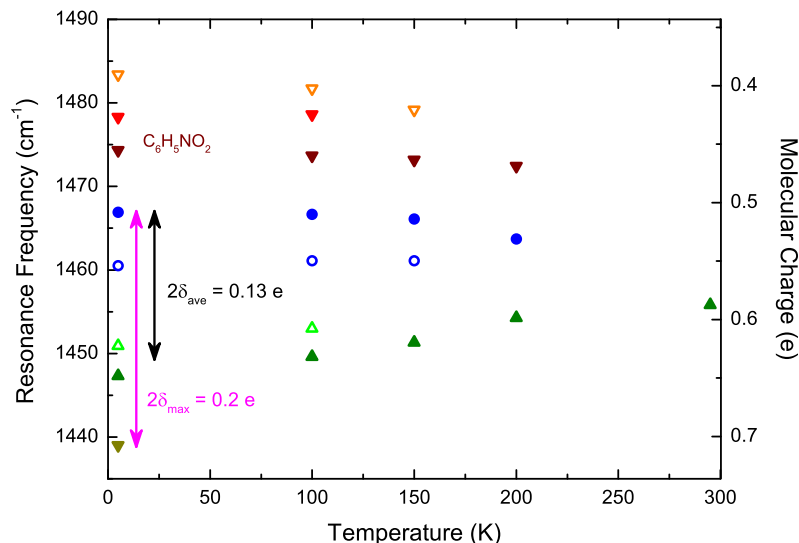


Figure 6.3.10: The ν_{27} mode was fitted with several Fano functions in the range 1430–1500 cm^{-1} at selected temperatures. The splitting between the three main branches evolves continuously upon cooling. While the features above 1470 cm^{-1} are related to $\text{C}_6\text{H}_5\text{NO}_2$ vibrations, the two main peak pairs around 1450 and 1465 cm^{-1} correspond to $2\delta_{\text{ave}} = 0.13 e$ in good agreement with Raman experiments [34, 220]. Taking into account the feature below 1440 cm^{-1} yields a charge disproportionation up to 0.2 e.

whether the bands at 1400 and 1525 cm^{-1} are related to the ν_{27} mode as they seem to shift slightly upon ^{13}C -substitution; however, the red-shift is even smaller and the resulting BEDT-TTF charge would be close to +1 e and neutral, respectively. In addition, the intensity of these features is pretty low, so we do not consider them in the following. After all, only the 1430–1470 cm^{-1} peaks exhibit a pronounced shift upon isotope substitution corroborating the above assignments.

Having identified the molecular charges as poor-poor-medium-rich based on the ν_{27} mode, one can consider the spatial distribution of the charge pattern. Similar as for β'' -(BEDT-TTF) $_2\text{SF}_5\text{RSO}_3$, we first have a look on the anion arrangement of β'' -Ga, shown in Fig. 6.3.12 (a). It appears that the negatively charged $[\text{Ga}(\text{C}_2\text{O}_4)_3]^{-3}$ groups, linked via H_3O^+ cations, form a hexagonal structure with the neutral solvent molecules in the voids. Hence, BEDT-TTF molecules adjacent to the oxalate entities are expected to acquire a more positive charge than the sites close to the solvent and H_3O^+ . In panel (b) a tentative charge pattern is suggested with two more positively charged ($\rho_{\text{rich}} = \rho_0 + \delta_1$ and $\rho_{\text{medium}} = \rho_0 + \delta_2$) and two more negatively charged molecules ($\rho_{\text{poor},1} = \rho_0 - \delta_3$ and $\rho_{\text{poor},2} = \rho_0 - \delta_4$). In order to conserve the average charge of $\rho_0 = 0.5 e$ per BEDT-TTF, we impose the constraint $\delta_1 + \delta_2 - \delta_3 - \delta_4 = 0$. Note, such a pattern with two charge-poor, one -medium and one -rich sites is consistent

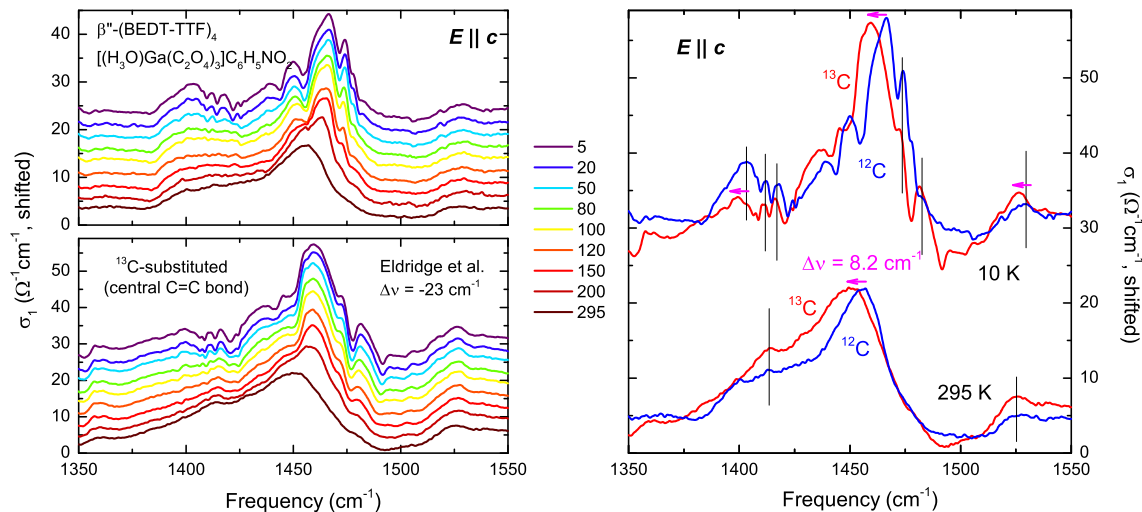


Figure 6.3.11: The out-of-plane response was measured for a ^{13}C enriched β'' -Ga sample in order to disentangle the BEDT-TTF and anion layer contributions. As indicated by the horizontal arrows and vertical black lines, the ν_{27} peaks are red-shifted while the other modes remain at the same frequencies, respectively, corroborating the assignment in Fig. 6.3.9. Small modifications are also observed for the 1400 and 1525 cm^{-1} features.

with the normal state where two inequivalent molecules are arranged pairwise along the stacks [232]. Also, the electronic excitations arising from this configuration are consistent with the spectra presented in Fig. 6.3.4. Since both a and b directions do not point along a specific stack, one always observes a mixture between intra- and inter-stack excitations. Therefore, the structural properties seem to pin the charge pattern to the anion layer, yet with a much weaker influence as compared to β'' -(BEDT-TTF) $_2$ SF $_5$ RSO $_3$. The less pronounced effect in the compound discussed here, i.e. the smaller charge disproportionation and the conventional pressure dependence of correlations¹¹ is related to the non-ideal commensurability between the anions and BEDT-TTF molecules; in β'' -SC and β'' -MI, for example, the negative ends of the separately movable SF $_5$ RSO $_3$ units point towards an A site each unlike the more rigid oxalate entities in β'' -Ga that do not map ideally onto specific BEDT-TTF molecules. To encourage an electrostatic argument, however, similar DFT calculations on the charge density distribution as carried out for the β'' -(BEDT-TTF) $_2$ SF $_5$ RSO $_3$ series [205] are also necessary here to elucidate the charge pattern potentially induced by the anions.

An anion-induced CO should also express in the structural properties. In temperature-

¹¹dc transport experiments under pressure revealed a suppression of superconductivity going hand in hand with improved metallicity. These results will be circumstantially presented in the thesis of A. Löhle.

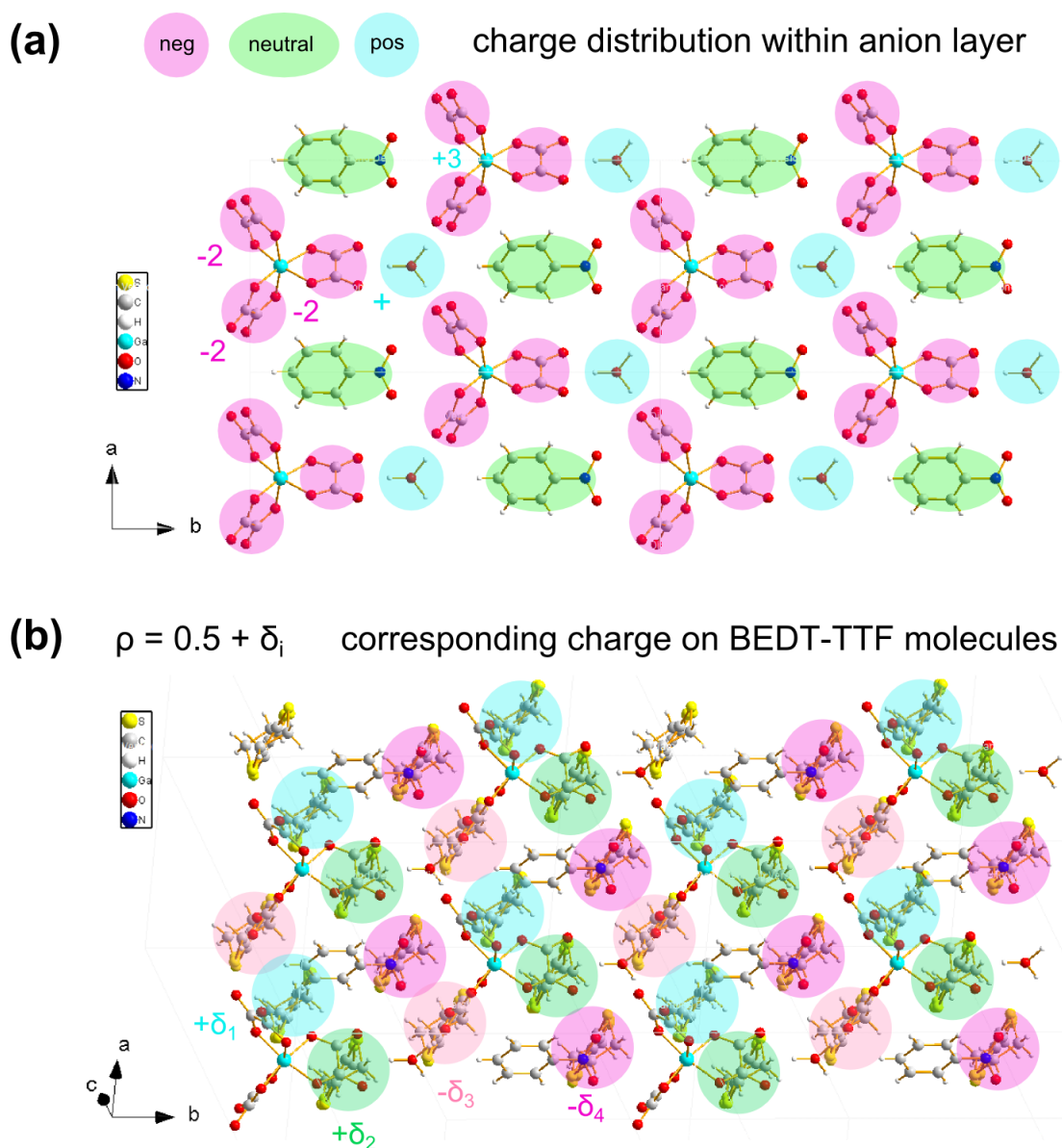


Figure 6.3.12: (a) The anion layer shows an inhomogeneous charge distribution that potentially maps onto the conducting BEDT-TTF planes. (b) A possible charge arrangement with two more negative and two more positive sites would correspond to the two ν_{27} peak pairs separated by $2\delta = 0.13 e$ as deduced from Figs. 6.3.9 and 6.3.10. Since no specific stripe pattern is formed, such a configuration is consistent with the almost isotropic electronic excitations presented in Fig. 6.3.4.

dependent x-ray results it was found that the c -axis length of the unit cell is reduced upon cooling, i.e. the anion-BEDT-TTF separation decreases when CO sets in [232]. Strikingly, no significant modification of the lattice constant within the ab -plane was observed in the CO state indicating that the main change of Coulomb interaction appears in the out-of-plane direction.

6.3.3 Summary and Discussion

A comprehensive electrodynamic study has been performed parallel and perpendicular to the conducting planes of β'' -(BEDT-TTF)₄[(H₃O)Ga(C₂O₄)₃] · C₆H₅NO₂ in order to elucidate the degree of charge disproportionation and correlation strength. From the charge-sensitive vibrations and the almost isotropic electronic excitations we conclude that the charge pattern in this compound is not stripe-like, as already suggested previously [231]. In a similar way as for the β'' -(BEDT-TTF)₂SF₅RSO₃ series, this arrangement seems to be related to the anion layer, yet with overall weaker coupling expressing in a charge disproportionation slightly smaller than in β'' -(BEDT-TTF)₂SF₅CH₂CF₂SO₃. After all, we again find that superconductivity appears in the presence of charge order, corroborating a possible relationship. The size of the charge disproportionation is much larger than in θ -(BEDT-TTF)₂I₃, where T_c is significantly smaller.

Finally, the extended Drude analysis yields a sizeable effective mass enhancement establishing the strongly correlated nature of β'' -(BEDT-TTF)₄[(H₃O)Ga(C₂O₄)₃] · C₆H₅NO₂. Comparison with Gurzhi scaling [29] indicates considerable elastic contributions to scattering, similar as for heavy fermion compounds [193] and different from the κ -[(BEDT-STF) _{x} (BEDT-TTF) _{$1-x$}]₂Cu₂(CN)₃ compounds discussed in section 5.3. We may speculate whether this is due to quasiparticles scattering off the periodic charge modulation arising from partially localized electrons.

6.4 Conclusion and Outlook

The novel concepts and experimental results presented in this thesis reveal that molecular conductors provide a unique laboratory to examine the interplay of electronic correlations, unconventional superconductivity and strongly renormalized quasiparticles.

Our comprehensive investigations on organic quantum spin liquid compounds by means of optical spectroscopy presented in section 5.1 allow us to study the Mott insulating state in its genuine form. By mapping the Mott-Hubbard excitations we can quantify the degree of electronic correlations U/W (U is the Coulomb repulsion and W the bandwidth). In particular, we establish that correlations decrease in the order β' -EtMe₃Sb[Pd(dmit)₂]₂ – κ -(BEDT-TTF)₂Ag₂(CN)₃ – κ -(BEDT-TTF)₂Cu₂(CN)₃, consistent with ab initio density functional theory (DFT) and extended Hückel results [15, 114, 115, 117, 156, 160], placing the latter material in the near vicinity of the insulator-metal boundary. There, we identify metallic fluctuations in the Mott state that become enhanced upon cooling due to the back-bending of the quantum Widom line – the supercritical boundary of the gapped Mott insulator [5–7] – and, thus, unravel the long-standing conundrum of the non-thermal sub-gap absorption in κ -(BEDT-TTF)₂Cu₂(CN)₃ [16, 17, 187]. By renormalization to the bandwidth we can connect the pressure-dependent dc transport results [14, 15] of these frustrated Mott insulators on common scales. This enables us to compose, for the first time, a comprehensive and quantitative phase diagram valid for the whole class of organic quantum spin liquid compounds (see section 5.1.3). In-depth comparison with different materials and state-of-the-art theoretical calculations establishes that our findings are in fact representative of *all* Mott insulators [13]. This novel paradigm extends to inorganic quantum spin liquid compounds as well as non-frustrated transition-metal oxides such as the cuprates, where electronic correlations of the underlying Mott state are believed to be the crucial ingredient for high-temperature superconductivity.

Comparison of the pressure-dependent results of different κ -(BEDT-TTF)₂ X compounds reveals that Mott-Hubbard interactions reach well into the metallic side of the phase diagram. Specifically, the collapse of the characteristic temperatures delimiting the bad metallic, Fermi liquid and superconducting states on universal lines suggests a direct relation to the underlying Coulomb repulsion. Translating these findings to Mott systems with larger energy scales implies a concomitant enhancement of the transition temperatures proportional to U . Future studies will show if this concept is able to explain the strongly correlated metallic states in transition-metal oxides and, in particular, high-temperature superconductors.

Through systematic electrodynamic studies on a complete set of chemically modified κ -[(BEDT-STF) $_x$ (BEDT-TTF) $_{1-x}$] $_2$ Cu $_2$ (CN) $_3$ compounds we can monitor the bandwidth-tuned Mott metal-insulator transition in great detail. We demonstrate the formation of a strongly renormalized Fermi liquid state as the spectral weight is shifted from the Mott-Hubbard band towards zero energy. Our data suggest a certain band shape with a threshold peak-to-width ratio associated with the stabilization of coherent quasiparticles. We can trace the Fermi liquid not only via the AT^2 behaviour of the dc resistivity, but also by the quadratic frequency dependence of the scattering rate, $\gamma \propto B\omega^2$, which persists even above T_{FL} indicative of resilient quasiparticles [28, 31]. By extracting the effective mass enhancement, we find that the prefactor B increases in a similar fashion as $(m^*/m_b)^2$ upon approaching the Mott MIT, establishing that the Kadowaki-Woods ratio [30] holds for different correlation strength. Comparison of the terms A and B , both extracted from the optical data, yields considerable *non-metallic* contributions as compared to purely inelastic scattering associated with Gurzhi scaling in a pristine Fermi liquid [29]. Importantly, we identify the Ioffe-Regel-Mott (IRM) limit as the universal boundary of a coherent quasiparticle state both in the dc and frequency-dependent resistivity. Ambient-pressure superconductivity ($T_c = 2.9$ K for $x = 0.12$) is stabilized at the verge between the gapped Mott state and the Fermi liquid where ρ_{IRM} is reached close to $T = 0$.

The work presented in chapter 5 demonstrates the relevance and outreach of Mott-Hubbard interactions for (i) the Mott insulating state, (ii) quasiparticle renormalization in the Fermi liquid and (iii) high-temperature superconductivity. Optical spectroscopy provides a powerful tool for a quantitative determination of the Coulomb repulsion U and bandwidth W , the fundamental parameters defining the strength of electronic correlations U/W . Choosing archetype systems with a simple electronic structure, realized in quasi two-dimensional molecular conductors [11, 12], enables profound scrutiny of the single-band Hubbard model in all its aspects.

More immediately, we expect that our results will trigger numerous experiments on other frustrated systems such as triangular, honeycomb, kagome or hyperkagome lattices, where magnetic ordering is also prevented [3, 81, 86]. The systematic approach presented here enables a quantitative classification and comparison of various materials classes, and a straight link to theory [4, 5]. Thus, we anticipate strong impact on the fields of quantum spin liquids, transition metal oxides, unconventional superconductivity and theoretical modeling of strongly correlated electron systems.

In the second part of this thesis, we applied the above formalism to experimentally

establish the phase diagram of β'' -(BEDT-TTF)₂SF₅RSO₃ proposed by Girlando *et al.* [38]. Indeed, electronic correlations decrease in the order $R = \text{CH}_2 - \text{CHF}_2 - \text{CH}_2\text{CF}_2 - \text{CHF}$ and, in particular, the charge disproportionation 2δ scales with the inter-site Coulomb repulsion V . By measuring the charge-sensitive ν_{27} vibration below $T_c = 5$ K, verified by *in situ* dc transport experiments, we provide evidence for a coexistence of charge order and superconductivity in β'' -(BEDT-TTF)₂SF₅CH₂CF₂SO₃. Our observation suggests that these two states are not competing and unconventional Cooper pairing in this material is mediated by charge fluctuations [33]. Investigation of the deuterated compound reveals that the enhancement of 2δ is accompanied by an increase of T_c [131], corroborating this picture. Considerable charge disproportionation was also observed in the organic superconductor β'' -(BEDT-TTF)₄[(H₃O)Ga(C₂O₄)₃]·C₆H₅NO₂ while the small transition temperature in θ -(BEDT-TTF)₂I₃ ($T_c = 3.6$ K) seems to be related with basically absent charge order.

Evaluating the polarization dependence of the electronic excitations we establish a stripe-like charge pattern in all β'' -(BEDT-TTF)₂SF₅RSO₃ except for $R = \text{CH}_2$ where a checkerboard-like arrangement is observed. A closer inspection of the crystal structures discloses that the molecular charge is inherently related with the distance to the negatively charged SO₃⁻ endgroup of the anions [39, 40]. Also for β'' -(BEDT-TTF)₄[(H₃O)Ga(C₂O₄)₃]·C₆H₅NO₂ we find indications for a similar situation, yet implying an almost isotropic charge pattern. Moreover, a peculiar pressure dependence is observed for $R = \text{CHF}_2$ and CH₂CF₂ where the insulating state is stabilized at higher temperatures rather than being suppressed [41]. Our findings, therefore, suggest that charge order in these compounds is induced, at least to a non-negligible extent, by the anions rather than being a pure effect of inter-site Coulomb repulsion between the BEDT-TTF molecules. We propose a similar scenario as deduced for the anion-ordered state in quasi one-dimensional (TMTTF)₂X [51].

To conclude, we provide substantial indications for a non-trivial interplay between charge order and superconductivity in quarter-filled (BEDT-TTF)₂X. Future studies may address this issue on related materials, such as deuterated compounds, and extend experiments down to lower temperatures to probe deep inside the superconducting state. In addition, we elucidate the origin of charge order and its mutual interaction with the anions. To that end, we suggest that such a situation is common rather than serendipity in the charge-transfer salts. Comprehensive structural studies down to cryogenic temperatures are a convenient route towards a better understanding of the anion-BEDT-TTF coupling strength and its influence on the

conduction properties. Another prospective direction is dielectric spectroscopy as it probes the polarizability of the material and, thus, delivers important information on the charge-disproportionate states. Also, a careful analysis of the anionic vibrations and those of the ethylene endgroups may provide detailed information.

A. Appendix

Apart from the quasi two-dimensional molecular conductors discussed in the main thesis, as a side project numerous experiments on diverse strongly correlated systems have been performed during the four years at the 1. Physikalisches Institut. While there was a considerable amount of work on inorganic quantum spin liquid compounds, including $\text{Zn}_x\text{Cu}_{4-x}(\text{OH})_6\text{Cl}_2$, $\text{Y}_3\text{Cu}_9(\text{OH})_{19}\text{Cl}_8$ and Cs_2CuCl_4 , which is partially published or currently under review¹ [48, 82, 233], the Appendix summarizes the work on different organic systems. All parts are written up in the style of research articles, as they are already published, or will be soon.

The main results on quasi one-dimensional $(\text{TMTTF})_2X$ are shown in the first two sections, where the first one presents our comprehensive optical study ($E \parallel c$) on the compounds with tetrahedral anions that has been published in Ref. [51]. The second part (section A.2) shows unpublished results presenting the electrodynamic response along the stacks ($E \parallel a$) of the six Fabre salts $(\text{TMTTF})_2X$ with anions $X = \text{PF}_6$, AsF_6 , SbF_6 , BF_4 , ClO_4 and ReO_4 . The data are discussed in the context of the correlation-dependent Luttinger liquid parameter K_ρ which is affected differently by the diverse electronic states (metallic, Mott insulating, charge-ordered, anion-ordered).

Section A.3 contains the results of our collaboration with the Basov group at the University of California, San Diego (current address: Columbia University, New York) supported by the DAAD. There, I had the opportunity to perform, for the first time, low-temperature optical near-field experiments on a strongly correlated organic conductor. In particular, we investigated the spatial evolution of the charge-ordered state of α -(BEDT-TTF)₂I₃ around $T_{\text{CO}} = 136$ K by spectroscopic experiments on the nanometer scale. Primarily, we demonstrated that this technique is indeed applicable to study the materials class of charge-transfer salts, which opens a new avenue towards understanding the details of the phase transitions. We established the coexistence of charge-ordered and metallic domains separated by sharp domain walls of

¹ $x = 1$ corresponds to the intensively studied quantum spin liquid compound Herbertsmithite.

a few 100 nm width. Our main result, however, is the observation that tensile stress, arising from the different thermal contraction of sample and substrate (Al_2O_3) upon cooling, causes the organic crystal to break into segments with an inhomogeneous internal strain distribution that stabilizes different positions in the phase diagram on spatially separated regions of the sample. A characteristic stripe-like pattern is observed with a periodicity around $2 \mu\text{m}$ which is reproduced very well by finite-element calculations. Currently, work on the manuscript is close to be finished.

A.1 Electronic Correlations *Versus* Lattice Interactions: The Interplay of Charge and Anion Orders in $(\text{TMTTF})_2X$

The quasi-one-dimensional molecular conductors $(\text{TMTTF})_2X$ commonly undergo a charge-order transition upon cooling. For tetrahedral anions ($X = \text{BF}_4^-$, ClO_4^- and ReO_4^-), in addition, anion ordering is observed. In a comprehensive infrared study, we trace the resonance frequencies of the charge-sensitive vibrational modes to determine the charge disproportionation $2\delta = \rho_{\text{rich}} - \rho_{\text{poor}}$ as a function of temperature. In combination with analogue investigations for the centrosymmetric anions, we conclude that charge order does not depend on the anion shape and symmetry, but is intrinsic to the TMTTF stack. Since correlation effects are of paramount importance, we find a universal relation between the charge imbalance 2δ and ordering temperatures T_{CO} and gaps Δ_{CO} , respectively. Below T_{AO} the charge disproportionation gradually changes. Ordering of the tetrahedral anions minimizes the electrostatic energy for the anions and organic molecules as a whole, resulting in a 0110 pattern. This way we can understand that deuteration of the methyl endgroups enhances T_{CO} but does not affect the anion ordering, which is linked to the anion-sulfur distance.

A.1.1 Introduction

Molecular-based solids act as model systems in condensed-matter science featuring low-dimensional physics as the main topic driven by theory. The discovery [234] of the first organic superconductor $(\text{TMTSF})_2\text{PF}_6$ in 1980 was the result of more than a decade of intense research triggered by W. A. Little's prediction in 1964 [235]. Since then, the family of the Bechgaard and Fabre salts has been a fruitful ground to experimentally test theoretical predictions, in particular related to the physics in reduced dimensions.

The building blocks of $(\text{TMTTF})_2X$ charge-transfer salts are organic donor molecules with nominally $\rho = +0.5$ e charge per TMTTF. As displayed in Fig. A.2.1 (a), one-dimensional stacks are formed along the a -axis separated in c -direction by monovalent anions X . The relation of intra- and interchain wave function overlap, denominated by t_{\parallel} and t_{\perp} , respectively, brings about strongly anisotropic electronic properties with phenomena only found at low-dimensions. The nominally quarter-filled bands should lead to metallic properties along the stacks while the transport perpendicular to the a -axis exhibits semiconducting behaviour. At ambient conditions this is in fact observed in the quasi-one-dimensional TMTTF-salts and in the more two-dimensional TMTSF-analogues. However, upon cooling these compounds commonly undergo various forms of phase transition depending on the subtle interplay of charge, spin and lattice degrees of freedom [103, 236]. The charge transport in TMTTF-salts is rather well understood by a sequence of band-like metallic transport of delocalized carriers, localization due to electronic interaction leading to a Mott insulating phase, charge-order driven by intersite Coulomb repulsion in quarter-filled systems [237]. While the electronically-driven charge order was extensively studied in $(\text{TMTTF})_2X$ with centrosymmetric anions $X = \text{PF}_6^-, \text{AsF}_6^-, \text{SbF}_6^-$ and TaF_6^- using NMR or optical spectroscopy [113, 191, 196, 200, 238–244], for instance, a comparable endeavor is still pending for the non-centrosymmetric anions. The case is of particular importance as anion ordering causes a new type of structural phase transition at low temperatures, as depicted in Fig. A.1.1 (b). It is of high interest to clarify the charge distribution in the anion-ordered state and to investigate its competition with charge order [208, 237, 245–252]. To that end, we have performed a detailed study of the charge arrangement in quasi-one-dimensional $(\text{TMTTF})_2X$ salts with tetrahedral anions $X = \text{BF}_4^-, \text{ReO}_4^-$ and ClO_4^- by means of vibrational spectroscopy.

A.1.2 Materials and Experiments

For the octahedral anions of $(\text{TMTTF})_2X$ the physical background is well-established [113]. With lowering the temperature, the charges first become localized around T_{ρ} , before $4k_F$ charge order (CO) along the stacks sets in for $T < T_{\text{CO}}$. Elaborate optical studies on the temperature dependence of the charge imbalance reveal a typical mean-field behaviour. With growing anion size $d(\text{TaF}_6) > d(\text{SbF}_6) > d(\text{AsF}_6) > d(\text{PF}_6)$, i.e. larger inter-chain separation and thus more pronounced one-dimensionality, the phase transition becomes less gradual and more abrupt [196, 200]. At low temperatures other transitions to various magnetic ground states occur [236]: The system exhibits either antiferromagnetic order ($X = \text{SbF}_6^-, \text{TaF}_6^-$) or a spin-Peierls tran-

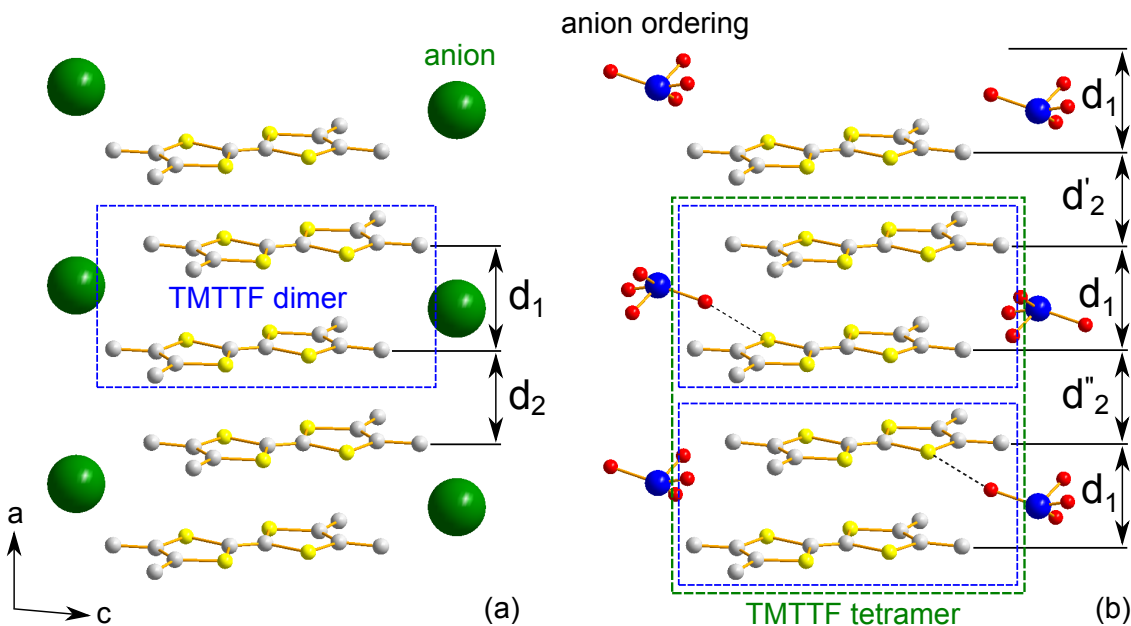


Figure A.1.1: Crystal structure of $(\text{TMTTF})_2\text{X}$, where TMTTF stands for tetramethyl-tetrathiafulvalene and X denotes a monovalent anion. (a) In the normal state the organic molecules experience a finite dimerization within the chain, with intra- and inter-dimer distances $d_1 < d_2$, respectively. Between the TMTTF stacks the anions can freely rotate around their center position, as indicated by the green spheres. (b) At low temperatures the anions become ordered in an alternating fashion with wave vector $(1/2, 1/2, 1/2)$, causing a periodic modulation of the electrostatic potential along all three crystal directions. Under high pressure and in $(\text{TMTSF})_2\text{X}$ compounds the wave vector is different. The unit cell is doubled, now containing four inequivalent molecules; pairs of dimers separated by $d'_2 < d''_2$ imply a tetramerization of the organic molecules. Two molecules have close links to anions, two of them do not.

sition (PF_6^- , AsF_6^-) [241]. In the latter case, the lattice is slightly distorted and a redistribution of charge is observed that indicates the competition between $2k_F$ tetramerization associated with the spin-Peierls state and $4k_F$ CO driven by long-range Coulomb interactions [253–256].

At elevated temperatures the transport properties of the three $(\text{TMTTF})_2\text{X}$ compounds subject to our present investigation are in line with those of the centrosymmetric anions [237]. At low temperatures, however, an additional rather sharp transition occurs, when the tetrahedral anions arrange in an ordered fashion (AO). While $\rho(T)$ exhibits a sudden jump with a well-pronounced hysteresis for $(\text{TMTTF})_2\text{ClO}_4$, it is significantly more rounded for $(\text{TMTTF})_2\text{BF}_4$ (see Fig. A.1.2). Interestingly, $\rho(T)$ increases when $(\text{TMTTF})_2\text{ReO}_4$ is cooled through T_{AO} with no sign of hysteresis; it more resembles a second-order phase transition. The respective transition temperatures are summarized in Table A.1.1. Again, the smaller the anions are, the

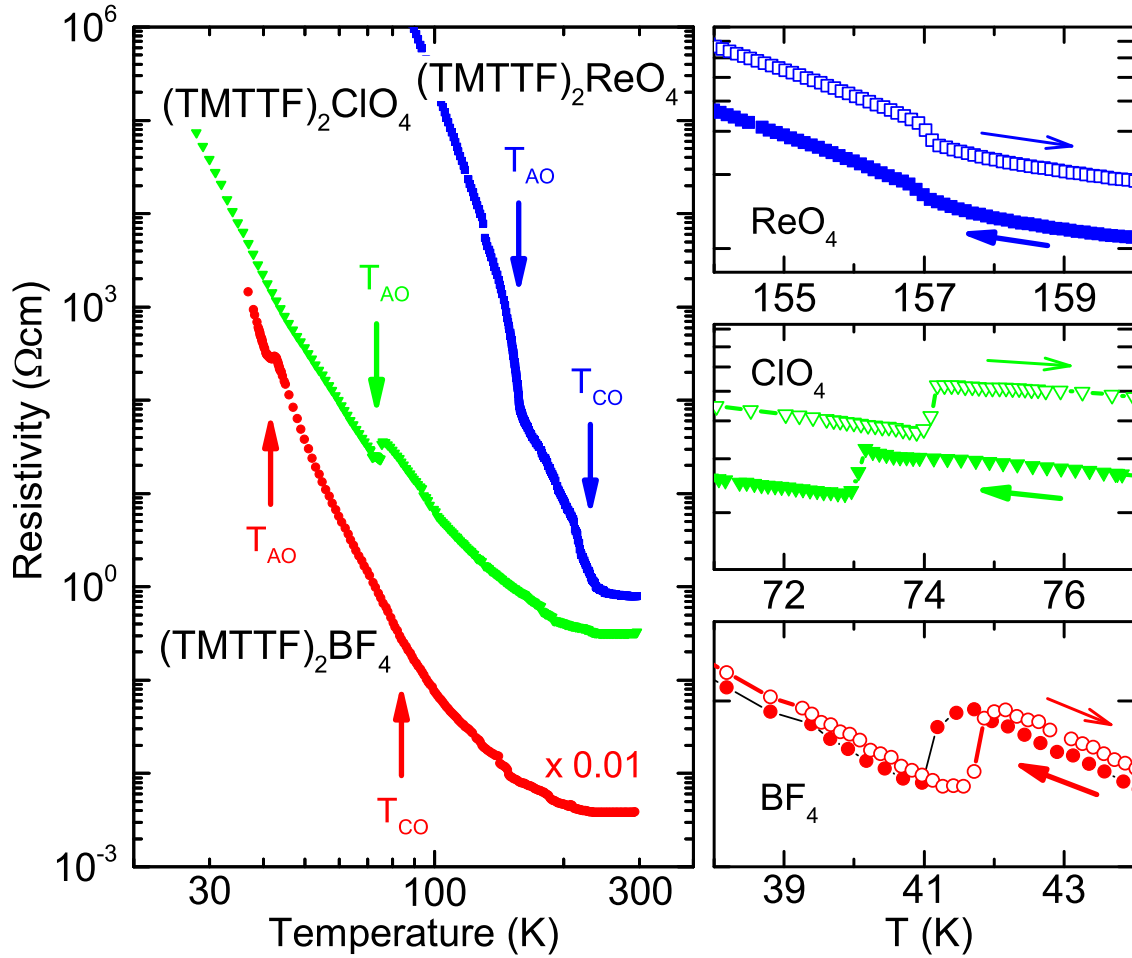


Figure A.1.2: Temperature-dependent electrical resistivity of $(\text{TMTTF})_2\text{ReO}_4$, $(\text{TMTTF})_2\text{BF}_4$, and $(\text{TMTTF})_2\text{ClO}_4$ measured along the chain direction. For clarity reasons the curve of $(\text{TMTTF})_2\text{BF}_4$ is shifted down by a factor of 100. In order to illustrate the behaviour around the anion transition temperature T_{AO} , the respective resistivities are plotted during cooling (solid symbols) and warming (open symbols).

lower the transition temperatures. More detailed structural considerations suggested the misfit between anion and cavity volumes to be the essential parameter that determines T_{AO} , i.e. how tightly the anion is squeezed between the surrounding methyl groups [257, 258].

In this series, $(\text{TMTTF})_2\text{ClO}_4$ takes up a distinct position as it does not show any CO transition above T_{AO} . Previous studies could not reveal any indication of static or fluctuating charge disproportionation neither in the metallic state nor for $T < T_{\text{AO}}$ [263]. One attempt to explain this fact considers the large sulphur-anion distance [237, 264]. Based on low-temperature x-ray studies it was also suggested that the pronounced intra-stack dimerization suppresses CO [251]. Indeed, the dimeriza-

Table A.1.1: Transition temperatures of charge and anion order, T_{CO} and T_{AO} , unit cell volume V , anion volume V_A and degree of intra-stack dimerization $(d_2 - d_1)/(d_2 + d_1)$ at 300 K of the investigated $(\text{TMTTF})_2X$ salts with tetrahedral anions X . Data from Refs. [259–262].

Anion	BF_4^-	ClO_4^-	ReO_4^-
T_{CO} (K)	84	-	230
T_{AO} (K)	41.5	73.4	157
V (\AA^3)	648.5	654.8	679.5
V_A (\AA^3)	14.4	18.4	25.4
$\frac{d_2-d_1}{d_2+d_1}$ (10^{-2})	1.13	1.89	2.10

tion is large compared to the anion and unit cell volumes of the other two compounds, cf. Tab. A.1.1. For $(\text{TMTTF})_2\text{ReO}_4$, on the other hand, dielectric [208, 247, 265], electron-spin resonance [248], magnetic susceptibility [252], NMR [249], x-ray [250, 251], and transport studies [237] provided evidence that the charge imbalance and charge-order pattern are different between the CO and AO phases. The real part of the dielectric constant $\epsilon'(T)$ shows a maximum at T_{CO} and a rapid drop at T_{AO} . This behaviour is distinct from $(\text{TMTTF})_2\text{BF}_4$ where the dielectric properties exhibit two maxima [265]. In spite of continuous efforts, nothing is known about the microscopic charge redistribution evoked from anion ordering.

In addition to extensive dc transport measurements [237], we have performed a comparative study of the optical properties of $(\text{TMTTF})_2X$, with particular emphasis on vibrational spectroscopy that allows us to locally probe the charge disproportionation on the ground of the well-established relationship between the resonance frequency of intramolecular vibrations and molecular charge [113, 266]. T. Peterseim, S. Kollatschek and L. Engel participated in optical experiments. First, we focus on the infrared active $\nu_{28}(\text{b}_{1u})$ mode that is observed for polarization along the molecular axis (i.e. $E \parallel c$), and for which the linear relation

$$\nu_{28}(\rho) = 1632 \text{ cm}^{-1} - \rho \cdot 80 \text{ cm}^{-1}/e \quad (\text{A.1.1})$$

is well-established, linking the molecular charge ρ (in units of e) to the vibrational frequency ν_{28} . In addition, we have performed reflection measurements in stacking direction ($E \parallel a$) which allows us to monitor totally symmetric vibrations, for instance the modes $\nu_3(\text{a}_g)$ and $\nu_4(\text{a}_g)$, when they appear due to electron-molecular vibrational (emv-) coupling or below the anion-ordering phase transition.

The cooling rate was typically 1 K/min and ≤ 0.3 K/min for optical and transport measurements, respectively. More experimental details can be found in the Supplement A.1.9 and Refs. [113, 237, 267].

A.1.3 Results and Analysis

Fig. A.1.3 (a-c) presents the optical conductivity of $(\text{TMTTF})_2\text{BF}_4$, $(\text{TMTTF})_2\text{ClO}_4$, and $(\text{TMTTF})_2\text{ReO}_4$ in the spectral range of the $\nu_{28}(\text{b}_{1u})$ vibration for various temperatures in a waterfall plot. Already with the naked eye a splitting of the feature can be seen for all three compounds. For a quantitative analysis, we fitted the mode and determined the resonance frequencies, in panels (d-f) they are plotted as a function of temperature. The corresponding charge disproportionation 2δ is calculated by Equ. A.1.1 and plotted in panels (g-i).

It is interesting to note that the ν_{28} modes [Fig. A.1.3 (a-c)] are rather broad compared to corresponding vibrational features observed in the Fabre salts with octahedral anions [113]. This general tendency evidences large disorder of the anions; the molecular environment is strongly modified, leading to a strong alteration of the resonance frequency.

For $(\text{TMTTF})_2\text{BF}_4$ a charge imbalance develops below T_{CO} with the maximum value $2\delta_{\text{CO}} = 0.16$ e; but around T_{AO} it comes to a halt and gets even reduced for lower temperatures. In the case of $(\text{TMTTF})_2\text{ReO}_4$, the charge disproportionation enhances rapidly before it saturates below 200 K around 0.35 e. As anion ordering sets in, the charge continues to redistribute in a mean-field fashion: 2δ eventually rises up to 0.64 e. For $(\text{TMTTF})_2\text{ClO}_4$ no particular CO transition occurs. However, for the first time we clearly observe the development of a mode splitting below T_{AO} corresponding to a charge imbalance that gradually increases to $2\delta_{\text{AO}} = 0.115$ e at the lowest temperature.

A.1.4 Charge Order

Before we discuss the behaviour observed at the anion-ordering transition, let us briefly look at the development of the charge imbalance at T_{CO} and compare it with the trend reported for the salts with octahedral anions. In the latter compounds, the transition also occurs continuously and mean-field-like, with a slight difference in abruptness depending on the anions size [113, 196, 200]. In Fig. A.1.4 (a) we plot the charge disproportionation $2\delta_{\text{CO}}$ versus the CO transition temperature T_{CO} evaluated for several Fabre salts $(\text{TMTTF})_2X$ and measurement techniques. The results of

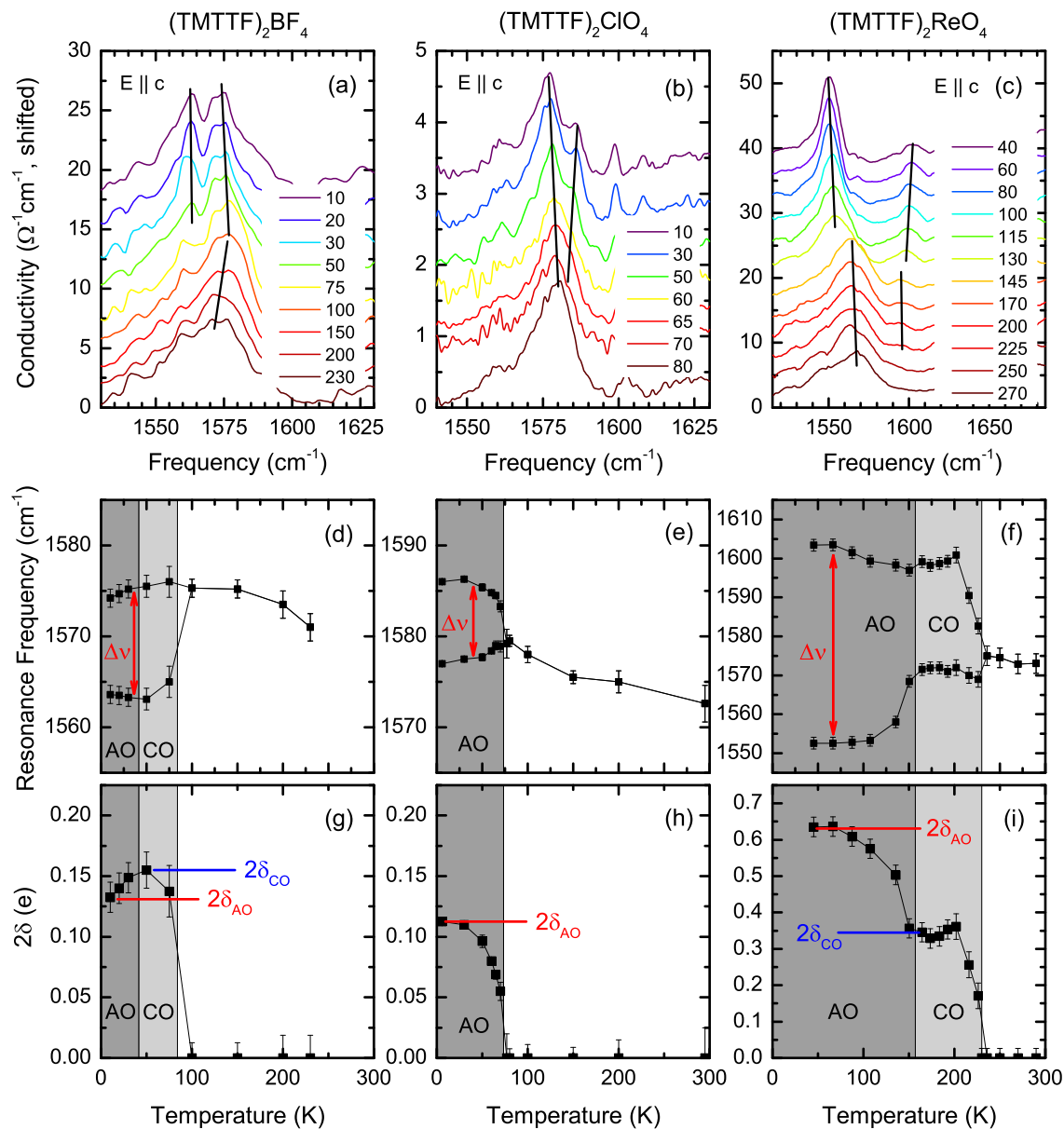


Figure A.1.3: (a)-(c) Temperature evolution of the charge-sensitive infrared-active mode ν_{28} of $(\text{TMTTF})_2X$ with tetrahedral anions X measured for $E \parallel c$. (d)-(f) At the charge-order transition the band splits into two peaks as a result of differently-charged organic molecules. (g)-(i) According to Equ. A.1.1, the charge disproportionation $2\delta = \Delta\nu/(80 \text{ cm}^{-1}/e)$ can be directly extracted from the peak separation $\Delta\nu$. While in $(\text{TMTTF})_2\text{BF}_4$ the mode splitting seems to be reduced below T_{AO} , for $(\text{TMTTF})_2\text{ReO}_4$ a strong enhancement sets in at the anion-ordered phase implying a further charge redistribution. Surprisingly, at T_{AO} there is also a splitting for $X = \text{ClO}_4^-$ in absence of electronically-driven charge order.

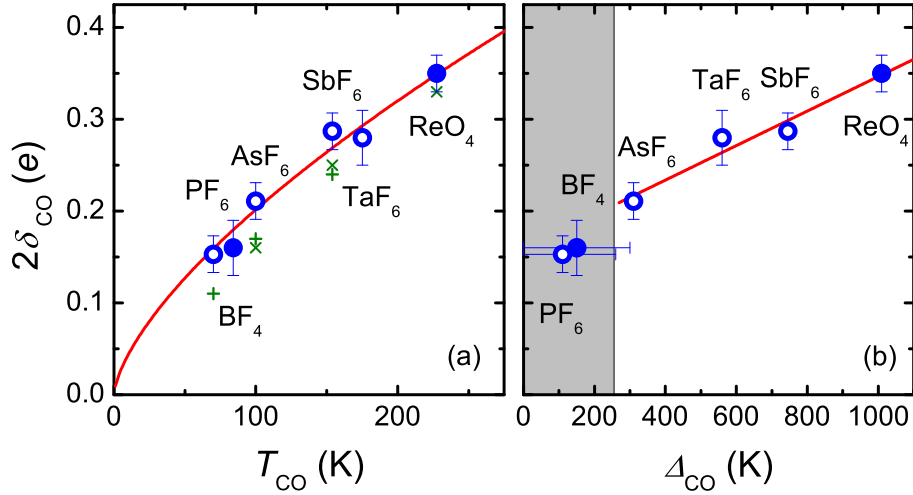


Figure A.1.4: (a) Charge imbalance related with electronically-driven charge order as function of transition temperature T_{CO} for $(\text{TMTTF})_2X$ with octahedral (open circles, Refs. [196, 200]) and tetrahedral (solid dots, this work) anions. The charge disproportionation of the different compounds follows one line, where the best fit was achieved for $2\delta_{\text{CO}} \propto T_{\text{CO}}^{2/3}$ (red line). For completeness reasons, NMR [136, 249, 269] and Raman [113, 268] values are indicated by green crosses and plus signs, respectively. Infrared-active molecular vibrations, however, are the most direct and precise tool to determine the molecular charge. (b) Charge disproportionation plotted versus the charge order gap obtained from dc transport [200, 237]. $2\delta_{\text{CO}}$ depends linearly on Δ_{CO} . The CO gap could not be extracted accurately for small T_{CO} as indicated by the grey area.

infrared [196, 200], Raman [113, 268] and NMR [136, 249, 269] investigations are in good agreement. Previous NMR studies reported much larger values [239, 240, 253, 270] which was attributed to the fact that the spin-lattice relaxation rate not only probes the spin density, but also antiferromagnetic fluctuations; therefore, more recent studies evaluated the Knight shift to determine $2\delta_{\text{CO}}$ [136, 269]. Our results on $(\text{TMTTF})_2\text{BF}_4$ and $(\text{TMTTF})_2\text{ReO}_4$ nicely fall in line with the optical data of symmetric anions indicating a general relation between T_{CO} and $2\delta_{\text{CO}}$. In panel (b) we find a linear dependence between the charge disproportionation and the CO gap Δ_{CO} extracted from transport measurements [200, 237]. Due to the small transition temperature and energy gap, no accurate value of Δ_{CO} could be determined for $X = \text{PF}_6^-$ and BF_4^- .

We conclude that the physical properties in the CO phase are dominated by isolated, one-dimensional TMTTF chains; big anions imply large separation between molecules such that long-range Coulomb repulsion V dominates over the wave function overlap t . At zero temperature $2\delta_{\text{CO}}$ is governed by V/t , and thus proportional to Δ_{CO} , while at T_{CO} thermally-activated hopping is large enough to destroy the or-

dered state. Therefore, CO is mainly an electronic effect and universal for all Fabre salts, independent of anion symmetry.

Hard x-ray photoemission spectroscopy on $(\text{TMTTF})_2\text{SbF}_6$ revealed a cooperative shift of the SbF_6^- anions towards the more positively charged TMTTF when CO causes charge depletion [271], confirming previous suggestions based on dielectric measurements and thermal contraction [272, 273]. This shift cannot be seen in $(\text{TMTTF})_2\text{PF}_6$ due to the weaker charge disproportionation. High-resolution near-edge x-ray absorption fine structure (NEXAFS) studies on $(\text{TMTTF})_2\text{AsF}_6$ indicate the strengthening of the $\text{S} \cdots \text{F}$ interaction [274]. The charge polarization increases as T_{CO} rises. It is safe to assume that an analogue scenario holds for the tetrahedral anions, too, as they undergo a CO transition. An important point should be made here: this interaction and cooperative shift of anions does not lead to a tetramerization, as observed in the case of anion order. The anion response on charge order, however, translates the phase of the charge pattern from one chain to the neighboring one. By this, the anions enhance inter-stack coupling and thus crucially contribute for stabilizing charge order in three dimensions.

A.1.5 Anion Order

First, let us revisit the case of $(\text{TMTTF})_2\text{ClO}_4$ where no CO transition is evident in resistivity (Fig. A.1.2) and any sizeable charge disproportionation was previously ruled out by x-ray investigations in the AO state [263]. In stark contrast, our infrared measurements reveal a splitting of the charge-sensitive ν_{28} mode at T_{AO} as presented in Fig. A.1.3 (b,e), corresponding to $2\delta_{\text{AO}} = 0.115$ e at the lowest temperature. Several other charge-sensitive vibrations also exhibit a splitting of the lines as shown in Figs. A.1.9, A.1.10 and A.1.11 of the Supplement A.1.9. Interestingly, according to Fig. A.1.3 (h) the temperature evolution of the charge disproportionation follows a second-order behaviour, in contrast to the dc results shown in Fig. A.1.2 that evidence an abrupt first-order phase transition at T_{AO} with a well developed hysteresis [237]. When considering the other two tetrahedral anions $X = \text{BF}_4^-$ and ReO_4^- , the change of the resonance frequency in the AO phase also implies a redistribution of charge. As seen in Fig. A.1.3 (g,i), the low-temperature value of 2δ is approached in a continuous way. For $(\text{TMTTF})_2\text{BF}_4$ the charge disproportionation decreases when entering the AO phase while it strongly increases for $(\text{TMTTF})_2\text{ReO}_4$. These values are in good agreement with x-ray studies [250] where the analysis by the Guionneau-Day-equation [137] yields an increase of 2δ from about 0.3 e at the AO transition to 0.5 e at $T = 100$ K. From NMR experiments a value of 0.33 e was estimated in the CO

phase [249]. Altogether, our data provide strong evidence that charge is redistributed at T_{AO} following a mean-field temperature dependence.

A closer look at the temperature dependence of 2δ for (TMTTF)₂BF₄ [Fig. A.1.3 (g)] reveals that the charge disproportionation diminishes for $T < T_{\text{AO}}$. We conclude that the two phases are of competing character. Independent of the CO value above T_{AO} , a certain charge pattern is assumed as the anions order.

A.1.6 Tetramerization

In order to gain insight into the spatial charge pattern and its periodicity in the AO phase, we have to consider the structural changes upon anion ordering in more detail. When cooling through T_{AO} the anion orientations and positions alter; thus the symmetry is broken and the lattice periodicity doubles, as depicted in Fig. A.1.1 (b). By specifically probing the molecular and anion orbitals in the AO state, angular-dependent measurements of the x-ray absorption near-edge structure (XANES) verified a tetramerization within the TMTTF stacks together with minor displacements and/or deformations of the ReO₄⁻ tetrahedra [275], as previously suggested by x-ray diffraction [276].

The structural change of the anions creates a strongly modulated electrostatic potential that influences the charges on the organic molecules, especially via the shortest distance of ligands to TMTTF molecules. Hence we ascribe the observed charge rearrangement to the anionic Coulomb potential in the AO phase. As shown in Fig. A.1.1 (b), the closest ligand-sulfur distance implies a charge pattern with 0110 periodicity on the tetramer rather than the 0101 arrangement in the CO phase imposed by nearest-neighbor Coulomb repulsion. Keeping that in mind, the anion-sulfur distance is probably not the best parameter to describe the origin of CO [237, 264]. It is primarily a measure of anion-cavity misfit and thus reflects more or less the anion size: large anions are generally squeezed more tightly between the stacks implying a shorter anion-S distance. However, the deciding effect for CO is not that the anion is close, but the inter-molecular distances are large. The 0110 pattern is supported by the rapid loss of ferroelectricity on the one hand [247] – as a centrosymmetric tetramer is much less polarizable than a dimer with unequal charge – and a strong decrease of spin polarizability on the other hand, which is caused by AF spin pairing due to the proximity of charge-rich molecules [252]. Fig. A.1.5 summarizes the structural and charge arrangements schematically, in agreement with Ref. [277].

As a consequence of 0110 tetramerization, the coupling of intramolecular vibrations between neighboring TMTTF is strongly enhanced. The totally symmetric $\nu_4(\text{a}_g)$

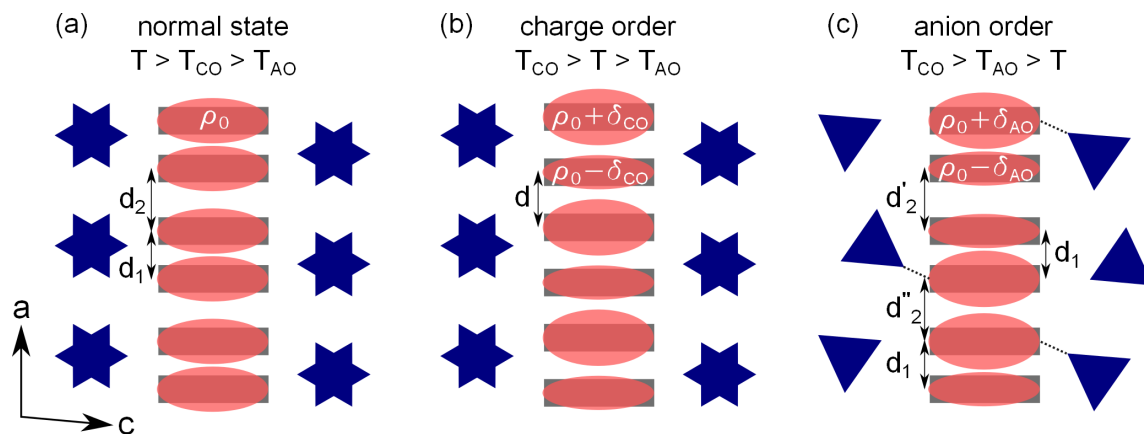


Figure A.1.5: Sketch of the molecular charge and anion arrangement in $(\text{TMTTF})_2X$ compounds at different temperatures. (a) While the stacks are dimerized at elevated temperatures, (b) the molecules are more equidistant with alternating charge-poor and -rich sites in the charge-ordered state. (c) The low-temperature ground state of $(\text{TMTTF})_2X$ with tetrahedral anions, however, is determined by ordering of the anions. Organic molecules with a ligand-sulfur short link acquire more positive charge.

mode (Fig. A.1.6) is nominally infrared-silent as it creates no dipole moment to which the oscillating electric field of a photon could couple. In a TMTTF dimer the vibrations of the two molecules can couple in- and out-of-phase. The latter scenario implies that the charge shifts periodically between the two molecules and thus creates an oscillating dipole pointing from the instantaneously charge-rich to the charge-poor molecule making it infrared-active; it shows up between $800 - 1300 \text{ cm}^{-1}$ depending on the coupling to the electronic background (see Supplement A.1.9 and Ref. [278]). The in-phase combination with resonance frequency $1400 - 1500 \text{ cm}^{-1}$ is typically not observed.

In the AO state, however, 0110 tetramerization enables the vibrational coupling of two dimers resulting in four normal modes depicted in Fig. A.1.6. In principle, these modes also exist for equally-charged molecules; the oscillator strength depends on the coupling of the dimers which is strongly affected by the wave function overlap between the two central TMTTF molecules. Therefore, larger intensity is expected for the 0110 pattern compared to the 0101 configuration or equally-charged sites.

From Fig. A.1.7 (a)-(c) we see that for all three $(\text{TMTTF})_2X$ compounds under investigation, right below T_{AO} an intense vibrational feature appears around $1410 - 1420 \text{ cm}^{-1}$. According to Fig. A.1.6 we assign it to the activated $\nu_{4,gu}$ mode, in good agreement with calculations [278]. The peak is rather broad for $X = \text{BF}_4^-$ (width of 22 cm^{-1}) and ClO_4^- (26 cm^{-1}) whereas it appears sharp and more intense for ReO_4^- (18 cm^{-1}).

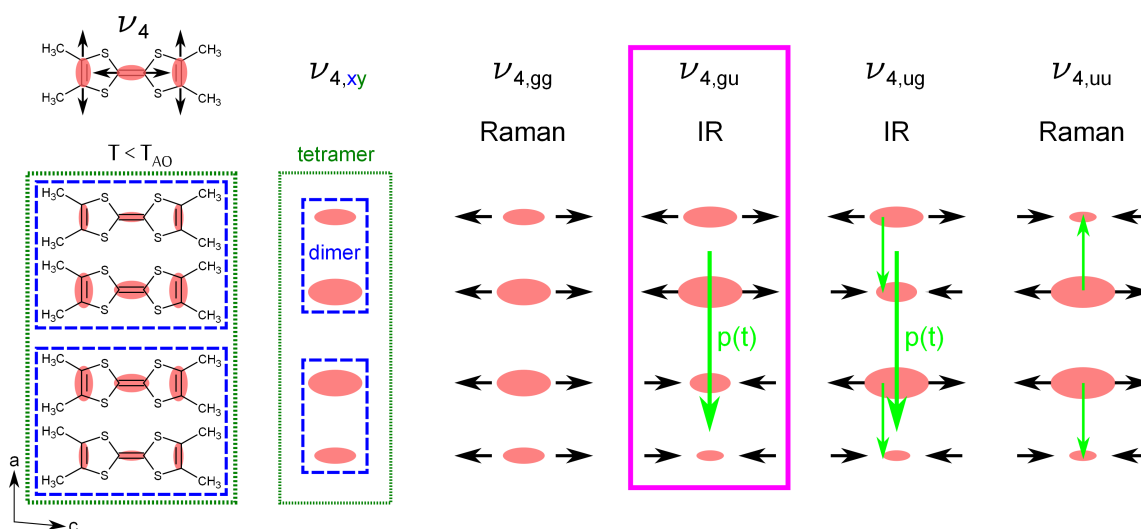


Figure A.1.6: The totally symmetric intramolecular $\nu_4(a_g)$ mode is Raman-active and typically observed by infrared spectroscopy only as the out-of-phase vibration within a dimer. Tetramerization enables the combination of dimeric vibrations. Following common spectroscopic notation, the indices x and y stand for the symmetry (g for in-phase, u for out-of-phase) of the vibration within and between the two dimers, respectively. In particular, AO activates the dimeric in-phase vibration by out-of-phase combination of two dimers within the tetramer; the $\nu_{4,gu}$ mode couples to infrared light via the oscillating dipole p (green arrow) between the dimers. Due to large wave function overlap between the charge-rich molecules in the center of the tetramer, the 0110 charge pattern increases vibrational coupling between the dimers resulting in enhanced intensity.

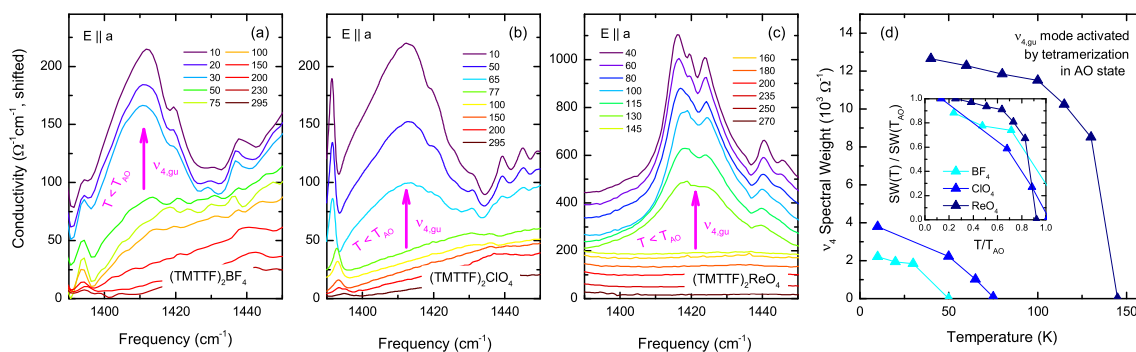


Figure A.1.7: (a)-(c) When cooling below T_{AO} , the tetrameric $\nu_{4,gu}$ mode depicted in Fig. A.1.6 appears around $1410 - 1420\text{cm}^{-1}$ providing evidence for the tetramerization of TMTTF molecules in the AO state. The data are vertically shifted for better illustration. (d) The integrated spectral weight of this mode scales with anion size and continuously grows upon cooling. Renormalization to the transition temperature and low-temperature intensity (inset) results in similar, mean-field-like curves for all compounds.

We find that the spectral weight of the mode increases, too, when going from the small BF_4^- to the large ReO_4^- . In part, this is affected by the electronic charge involved, but also implies that the tetramerization is more pronounced as the unit cell is enlarged and the intra- and inter-stack wavefunction overlap decreases. In other words, the influence of the anions on the organic molecules scales with their electrostatic potential A in respect to the transfer integral t . Fig. A.1.7 (d) illustrates that the spectral weight grows upon cooling in a mean-field behaviour, comparable to the development of the charge disproportionation 2δ (cf. Fig. A.1.3). $(\text{TMTTF})_2\text{-ClO}_4$ behaves in the same fashion as the other tetrahedral compounds although it did not undergo a CO transition previously. Thus we attribute this behaviour solely to the arrangement of the anions and not to the electronically-driven CO. The activation of the ν_4 mode provides a powerful tool for the determination of the charge arrangement within the stack; in particular, it allows us to distinguish between charge and anion order.

In analogy to the conclusion we have drawn here for the anion order, NMR studies suggested a competition between spin-Peierls and CO resulting in a charge redistribution below T_{AO} [253, 254]. We propose to extend these investigations to $(\text{TMTTF})_2X$ compounds with tetrahedral anions. It is worthwhile to recall that optical studies on $(\text{TMTTF})_2\text{PF}_6$ and $(\text{TMTTF})_2\text{AsF}_6$ exhibit a similar activation of the ν_4 vibration when entering the spin-Peierls state, also leading to a tetramerization of the TMTTF chains [113]. However, the IR intensity of the activated ν_4 mode is much smaller than for tetrahedral anions, probably due to a weaker charge redistribution effect in the SP phase. A similar argument can be drawn for $X = \text{BF}_4^-$ with small $\nu_{4,gu}$ intensity and minor change of 2δ below T_{AO} ; an incomplete charge redistribution would explain the small maximum of the dielectric constant at T_{AO} as tetramers with residual 0101 charge pattern are still polarizable [265].

A.1.7 Deuteration

Deuterated $(\text{TMTTF})_2X$ salts provide another important aspect for a better understanding of the interaction between organic molecules and anions. Replacing hydrogen by deuterium in the terminal methyl groups results in a considerable increase of T_{CO} while T_{AO} remains unaffected [208–210]. As shown in Fig. A.1.8 (a), the enhancement $\Delta T_{\text{CO}} = T_{\text{CO,D}} - T_{\text{CO,H}}$ is largest for small anions and transition temperatures. In addition, there is a linear relationship between the squared transition temperatures $T_{\text{CO,D}}^2 = T_{\text{CO,H}}^2 + D^2$ with $D = 60.2\text{K}$ (b).

The stabilisation of CO is explained by the reduction of intra-stack dimerization upon

deuteration, which is known to compete with CO [209]. In particular, theoretical calculations revealed that the critical value of Coulomb repulsion V_C , above which CO sets in, increases with dimerization [279]. Therefore, T_{CO} is enhanced when the dimerization is reduced. On the experimental side, Nogami *et al.* reported a critical value of bond dimerization $\frac{\Delta t}{\langle t \rangle} = \frac{2(t_2 - t_1)}{t_2 + t_1} = \frac{1}{4}$ at the CO transition, irrespective of the actual value of T_{CO} [251]. To proceed this discussion, we first need to understand the origin of intra-stack dimerization in (TMTTF)₂X systems.

In an isolated TMTTF chain, each molecule is equivalent; the crystal-structure periodicity of two TMTTF molecules is imposed by the anions (see Fig. A.1.1). Therefore, it is natural to ascribe the $4k_F$ bond dimerization to the presence of anions and their interaction with the organic stack. The deuteration effect implies that this happens via hydrogen bonds between the terminal methyl groups and the anion ligands, as indicated in Fig. A.1.8 (c). At elevated temperatures, the hydrogen atoms are more mobile and follow the thermal fluctuations of the anion rather quickly. Heavier deuterium atoms slow down this dynamics leading to a less effective anion-stack interaction and hence a reduced dimerization. This way we can simultaneously explain the enhancement of dimerization with temperature [251, 280] and the robust deuteration contribution D with respect to the anion geometry, as in an intuitive picture the shape of a thermally fluctuating anion is blurred. In other words, the randomly-oriented anion influences its own cavity by repeatedly bouncing against the surrounding (i.e. methyl groups), with a weaker effect for corners sluggish in reaction (i.e. deuterium atoms).

Having said that, we interpret the peculiar behaviour from Fig. A.1.8 (b) including general considerations on dc transport results [200, 237]: the energy gap extracted from the Arrhenius plot behaves mean-field-like; upon the phase transition, the CO gap Δ_{CO} adds in quadrature to the high-temperature gap Δ_0 , i.e. $\Delta = \sqrt{\Delta_0^2 + \Delta_{CO}^2}$ [281]. Similarly, we interpret the deuteration effect as a contribution that adds to the strength of CO; in other words, deuteration weakens dimerization and its negative influence on CO. The constant term D , which is independent of anion size and symmetry, is related to the critical bond dimerization $\frac{\Delta t}{\langle t \rangle} = \frac{1}{4}$. Therefore, the dimerization effect detrimental for CO has similar absolute size at the transition temperature. This explains the less pronounced deuteration effect for big anions with large T_{CO} as D is smaller in relation to V/t .²

²Another attempt to explain the larger ΔT_{CO} for smaller anions is the phononic origin of anion fluctuations. Following the arguments of Pouget [210] the lowest-energy anion vibrations are related to the anion mass. Indeed, the relative change of transition temperature $\frac{\Delta T_{CO}}{T_{CO}}$ is proportional to $m_{\text{anion}}^{-1/2}$.

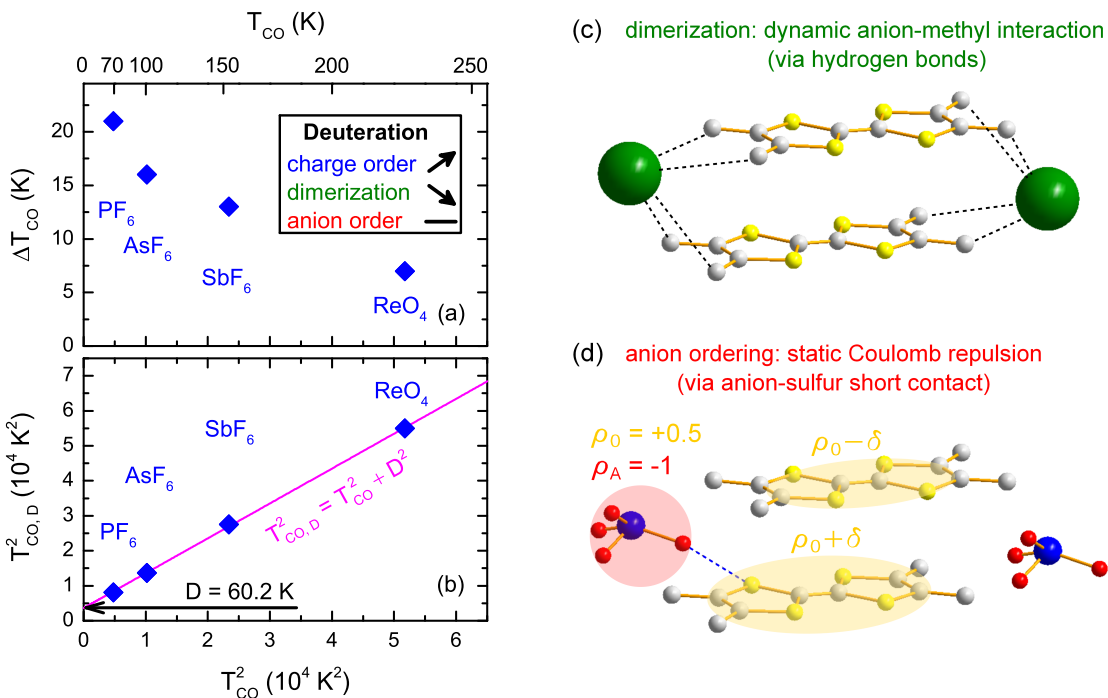


Figure A.1.8: (a) Deuteration of the methyl end groups enhances charge ordering in $(TMTTF)_2X$ (data taken from Refs. [208] and [210]) while T_{AO} remains unchanged. The stack dimerization is reduced. The change of transition temperature ΔT_{CO} is largest for small anions and small T_{CO} . (b) The deuteration effect on CO can be described as a constant value D that adds in quadrature to T_{CO} . (c) The interaction of anions and TMTTF molecules that causes dimerization takes place via the hydrogen bonds; if dimerization diminishes, T_{CO} is enhanced. (d) Since AO is mainly affected by the interaction with the molecular charge, which scales with the shortest ligand-sulfur distance, deuteration has no influence on T_{AO} .

The fact that T_{AO} remains unaffected by deuteration implies that at low temperatures the anion-TMTTF interaction does not depend on the methyl groups; in absence of thermal motion, the influence of the anions on the organic molecules takes place via the charge-rich C=C bonds. The shortest ligand-sulfur distance determines the Coulomb potential A of the anion that rearranges the molecular charge, as illustrated in Fig. A.1.8 (d). Considering the strong influence of AO on the charge pattern, this observation manifests that the AO phase is a pure effect of Coulomb interaction between anions and stack. The periodic alignment of the anions and the concomitant charge rearrangement within the organic chain minimizes the electrostatic energy of the entire system.

A.1.8 Conclusions

We have performed extensive infrared studies on (TMTTF)₂X with tetrahedral anions ($X = \text{BF}_4^-$, ClO_4^- and ReO_4^-) to explore the electronically-driven charge order and anion order. By carefully analyzing the temperature dependence of charge-sensitive vibrations, we observed delicate modifications of the charge disproportionation and pattern. We provide evidence that charge order in all (TMTTF)₂X compounds is an intrinsic feature of the organic stack solely determined by the competition between bandwidth $W = 4t$ and inter-site Coulomb repulsion V . Bigger anions imply larger inter-molecular distances such that long-range repulsion V is more pronounced with respect to t , which enhances both transition temperature and charge disproportionation.

Our high resolution optical experiments revealed a charge disproportionation in the anion-ordered state which is not associated with electronically-driven CO and follows mean-field behaviour. The activation of the totally symmetric and thus nominally infrared-inactive ν_4 vibration below T_{AO} evidences molecular tetramerization. We ascribe the large intensity of this feature to a charge rearrangement in the AO state. Long-range order of the anions periodically modulates the electrostatic potential on the TMTTF chain such that the molecular charge arranges in a 0110 pattern rather than 0101-type compared to electronically-driven charge order. CO minimizes the Coulomb repulsion within the stack whereas AO minimizes the electrostatic energy for anions and organic molecules as a whole. We explain the different origin of anion order and charge order and provide evidence for their clearly competing character.

Our observations suggest that the structural changes determining the anionic Coulomb potential A happen instantaneously at T_{AO} ; whereas the ionicity, related to the A/t ratio, develops continuously. Therefore, even if this ratio remains more or less constant below T_{AO} , 2δ increases cumulatively as the thermally-activated hopping gradually decreases towards $T = 0$.

The intra-stack dimerization at elevated temperatures is evoked from thermally-activated hydrogen-bond dynamics between the terminal methyl groups and the anion ligands. Dimerization also competes with charge order; as it is suppressed by deuteration, CO is enhanced. However, the Coulomb interaction responsible for AO acts via the anion-sulfur short-link. Our findings suggest that, in addition to a large V/t ratio, the CO state is limited to a temperature regime with small anion-stack interaction such that the organic chain can be considered as completely isolated.

A.1.9 Supplement

A.1.9.1 Charge-Sensitive Vibrations

Upon entering the charge-ordered state a number of intramolecular TMTTF vibrations are subject to splitting which allows to quantitatively determine the amount of charge disproportionation. The relation between vibration frequency and molecular charge was empirically found by numerous optical studies combined with numerical calculations [113, 266]. For some modes a linear dependence holds

$$\nu_i(\rho) = \nu_{i,0} - \Delta\nu_i \cdot \rho/e \quad (\text{A.1.2})$$

with the resonance frequency of the neutral molecule $\nu_{i,0}$ and the frequency difference between the neutral and mono-cationic states $\Delta\nu_i$. Since the molecular charge is mainly located on the C=C double bonds, the three modes sketched in Fig. A.1.9 that involve in-phase (ν_3 and ν_4) and out-of-phase (ν_{28}) C=C stretching vibrations show the strongest frequency-charge dependence. A rather large splitting is also observed for modes with C-S stretching, as for example the symmetric ν_{10} and the infrared-active ν_{33} vibrations [113, 266].

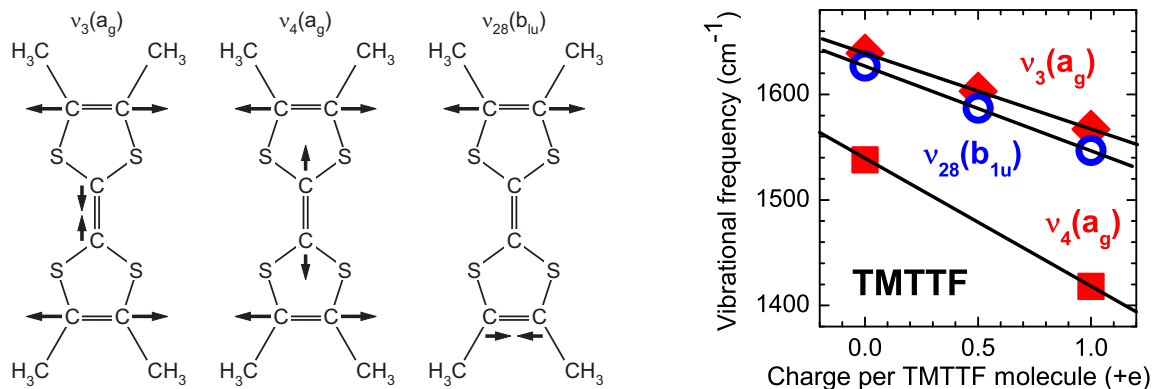


Figure A.1.9: Sketch of the three most charge-sensitive intramolecular modes which involve in- and out-of-phase stretching vibrations of the C=C double bonds. The right graph shows the dependence of resonance frequency on molecular charge.

For the three modes illustrated in Fig. A.1.9 the difference in resonance frequency between neutral TMTTF and its radical cation amounts to $\Delta\nu_3 = 72\text{cm}^{-1}$, $\Delta\nu_4 = 120\text{cm}^{-1}$ and $\Delta\nu_{28} = 80\text{cm}^{-1}$; the resonance frequencies of the neutral molecule are $\nu_{3,0} = 1639\text{cm}^{-1}$, $\nu_{4,0} = 1538\text{cm}^{-1}$ and $\nu_{28,0} = 1627\text{cm}^{-1}$, respectively. As the symmetric vibrations produce no electric dipole and can thus only contribute to the optical conductivity via coupling to the electronic background (emv-coupling), this

may alter the linearity of the $\nu(\rho)$ -relationship. Hence, the most reliable way to quantitatively determine the molecular charge is the linear frequency-charge relation of the ν_{28} mode (see Equ. A.1.1). However, to excite the dipole of this vibration it is necessary to polarize the infrared light parallel to the molecular long axis corresponding to the crystallographic c -direction. As this is commonly the thinnest side of the crystal ($z < 100\mu\text{m}$), the resulting small signal makes experiments rather challenging and requires the use of an IR microscope.

Fig. A.1.3 shows the temperature-dependent optical conductivity for the tetrahedral compounds in the range of the ν_{28} vibration. Similar investigations have been performed on the emv-coupled ν_3 mode observed for $E \parallel a$, with qualitatively the same results, which is presented in Fig. A.1.10. Furthermore, also the higher harmonic

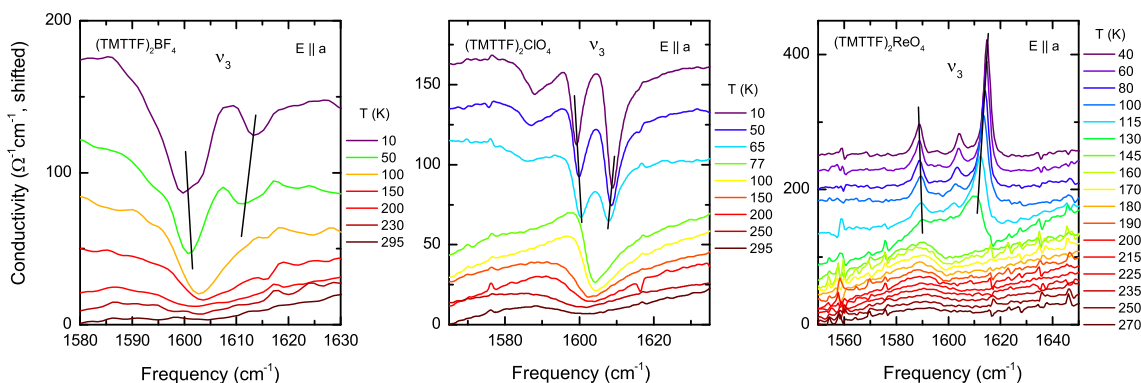


Figure A.1.10: Temperature-dependent behaviour of the totally symmetric ν_3 mode observed in a -direction of $(\text{TMTTF})_2X$ with tetrahedral anions. It becomes infrared-active by emv-coupling and, similarly as the ν_{28} mode, it splits at the CO transition. The charge rearrangement in the AO phase shows up as a splitting ($X = \text{ClO}_4^-$) and a further modification ($X = \text{ReO}_4^-$) of the ν_3 mode.

$2\nu_{10}$ ($E \parallel a$, $E \parallel c$), the sum frequencies $\nu_{10} + \nu_{11}$ and $\nu_4 + \nu_{10}$ ($E \parallel a$), and the infrared-active ν_{33} mode ($E \parallel c$) are subject to splitting upon the phase transitions (Fig. A.1.11). Keeping in mind that, the simultaneous occurrence of splitting only in these charge-sensitive modes is a strong proof of charge disproportionation in the AO state since there is no splitting observed in other vibrational modes. As already mentioned for the ν_3 mode, the linear approximation is no longer valid due to emv-coupling. Additionally, for some vibrational features the large noise impedes to extract credible $\Delta\nu$ and 2δ values. Hence, the ν_{28} resonance frequency provides the most reliable way to quantitatively determine the molecular charge.

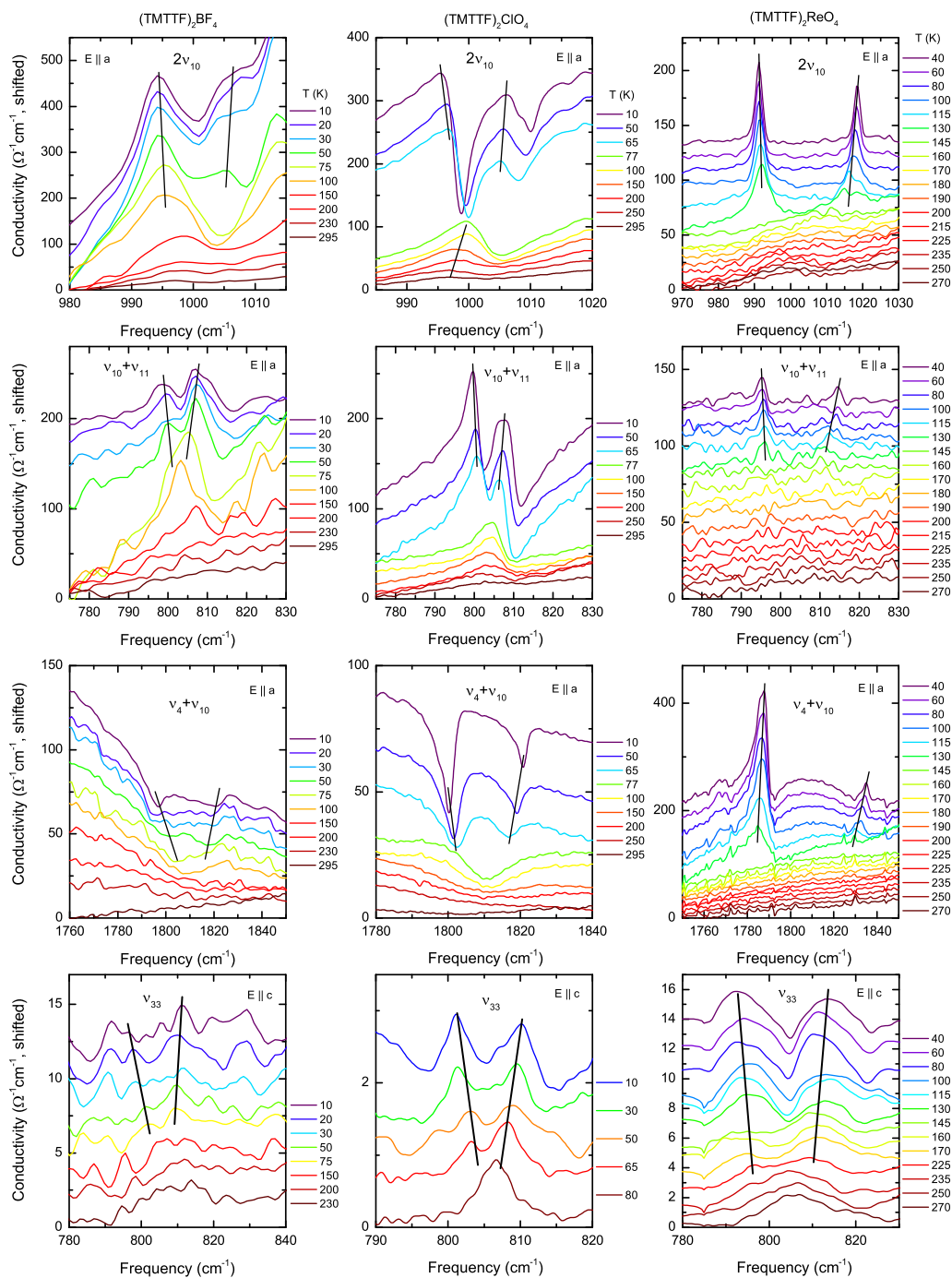


Figure A.1.11: Temperature development of the higher harmonic $2\nu_{10}$ (here plotted for $E \parallel a$, similar behaviour for $E \parallel c$), the sum frequencies $\nu_{10} + \nu_{11}$ and $\nu_4 + \nu_{10}$ ($E \parallel a$), and the infrared-active ν_{33} ($E \parallel c$). The left, central and right columns correspond to $(\text{TMTTF})_2\text{BF}_4$, $(\text{TMTTF})_2\text{ClO}_4$ and $(\text{TMTTF})_2\text{ReO}_4$, respectively. For all materials these modes show a splitting upon crossing the respective phase transition. Due to different coupling to the electronic background, some features appear as peaks, others as dips. Owing to the small signal, the data measured in c -direction are more noisy.

A.1.9.2 The Dimeric ν_4 Mode

As stated above, the symmetric ν_4 vibration creates no dipole moment and does not couple to infrared light. In (TMTTF)₂X compounds, however, the stacks of organic molecules show a considerable degree of dimerization that increases with temperature [251, 280]. In a TMTTF dimer the vibrations of the two molecules can couple in-phase ($\nu_{4,g}$) and out-of-phase ($\nu_{4,u}$). The latter combination induces an oscillating dipole as the charge is periodically shifted from one molecule to the other, making it infrared-active. The coupling between molecules depends strongly on the electronic background which has a large effect on the resonance frequency [278]. Hence, the feature is observed between 800–1300 cm⁻¹ depending on the size and position of the charge transfer band. As the compounds with tetrahedral anions are subject to anion order, the tetrameric combinations of the ν_4 mode are indicated according to the nomenclature introduced in Fig. A.1.6. In particular, tetramerization activates the dimeric in-phase vibration by out-of-phase combination between two dimers ($\nu_{4,gu}$).

Fig. A.1.12 shows the dimeric out-of-phase vibration at the lowest measured temperatures for (TMTTF)₂X with octahedral ($X = \text{PF}_6^-$, AsF_6^- and SbF_6^-) and tetrahedral ($X = \text{BF}_4^-$, ClO_4^- and ReO_4^-) anions. The pink dashed line corresponds to a fit with a Fano function to account for the asymmetric shape induced by emv-coupling. Other vibrational modes in the range between 800 – 1100 cm⁻¹ appear as antiresonances on top of the $\nu_{4,u}$ ($\nu_{4,ug}$) mode. When the feature moves to higher frequencies, as in the case of (TMTTF)₂ReO₄ (f), they turn into positive peaks.

Fig. A.1.13 shows the temperature evolution of the $\nu_{4,u}$ ($T > T_{\text{AO}}$) and $\nu_{4,ug}$ ($T < T_{\text{AO}}$) features observed in the respective crystal directions. In the absence of the charge transfer band – and therefore weak emv-coupling – perpendicular to the stacks ($E \parallel b$ and $E \parallel c$) the dimeric out-of-phase vibration is located around 1300 cm⁻¹. The temperature dependence is similar for different crystal directions. While upon cooling (TMTTF)₂BF₄ the feature first moves towards smaller frequencies, anion ordering brings about a pronounced blue-shift and intensity increase. For (TMTTF)₂-ReO₄ and (TMTTF)₂ClO₄ even a jump is observed at T_{AO} . Therefore, we conclude a strong enhancement of anion-stack interaction upon the AO transition.

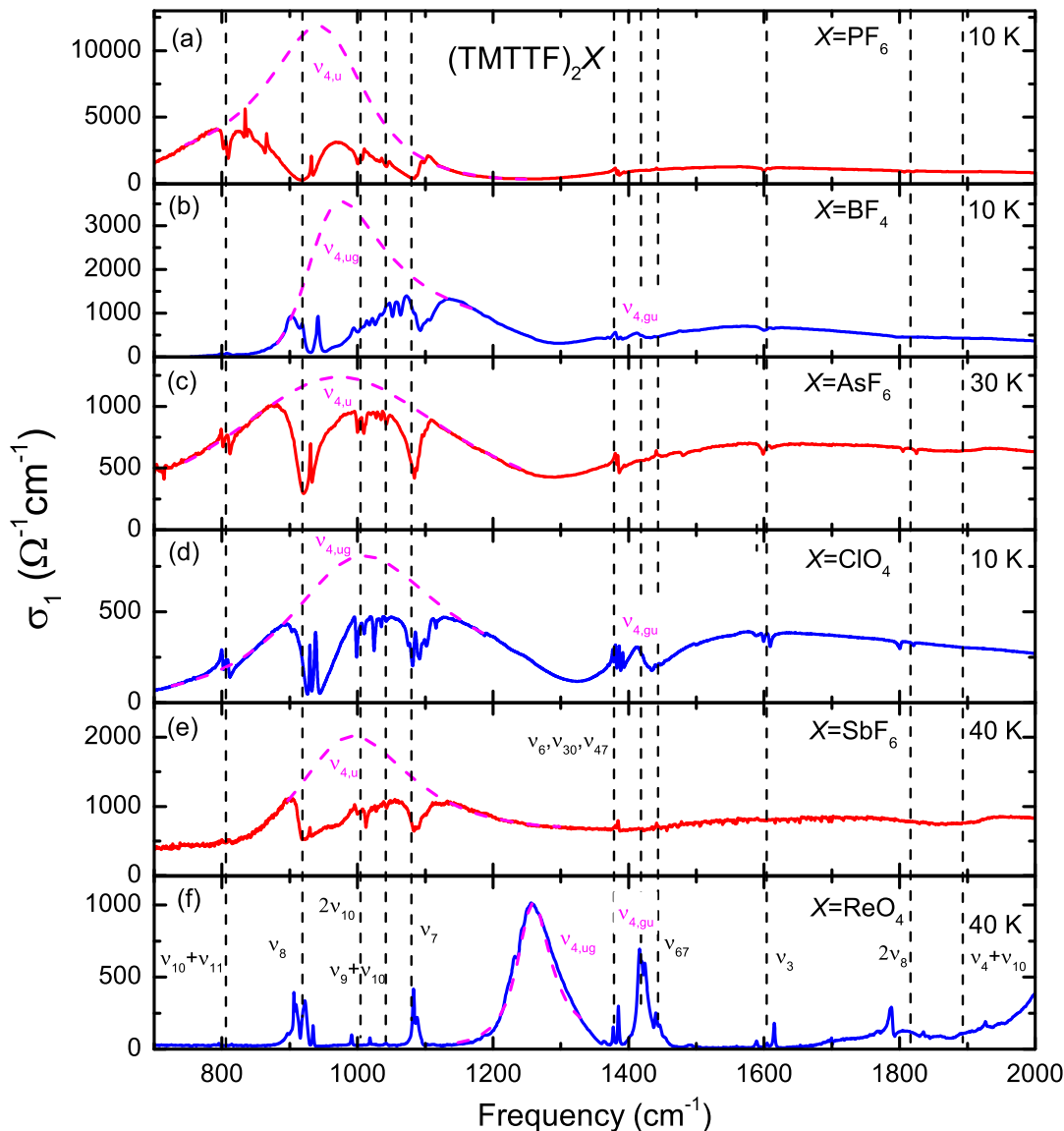


Figure A.1.12: The totally symmetric ν_4 mode is observed in the optical conductivity of $(\text{TMTTF})_2\text{X}$ with octahedral ($X = \text{PF}_6^-$, AsF_6^- and SbF_6^- , red) and tetrahedral ($X = \text{BF}_4^-$, ClO_4^- and ReO_4^- , blue) anions. The huge feature ($\nu_{4,u}$ for octahedral, $\nu_{4,ug}$ for tetrahedral anions) results from the out-of-phase vibration of the two molecules in a dimer. Due to the large gap in the spectrum of $(\text{TMTTF})_2\text{ReO}_4$, the background optical conductivity, and hence emv-coupling, is small in the range of the ν_4 mode such that it acquires a quite symmetric shape (f). For the other compounds, strong interaction with the electronic background – the charge-transfer band is located at lower energies – causes a shift towards lower frequencies and more Fano-like shape. This emv-coupling effect perfectly matches with theoretical calculations [278]. Anion order in compounds with tetrahedral anions implies the activation of an additional feature related to the ν_4 mode around 1410 cm^{-1} , as discussed in the main manuscript. Tetramerization and charge redistribution cause strong inter-dimer coupling such that the out-of-phase combination of two in-phase vibrating dimers becomes infrared-active ($\nu_{4,gu}$).

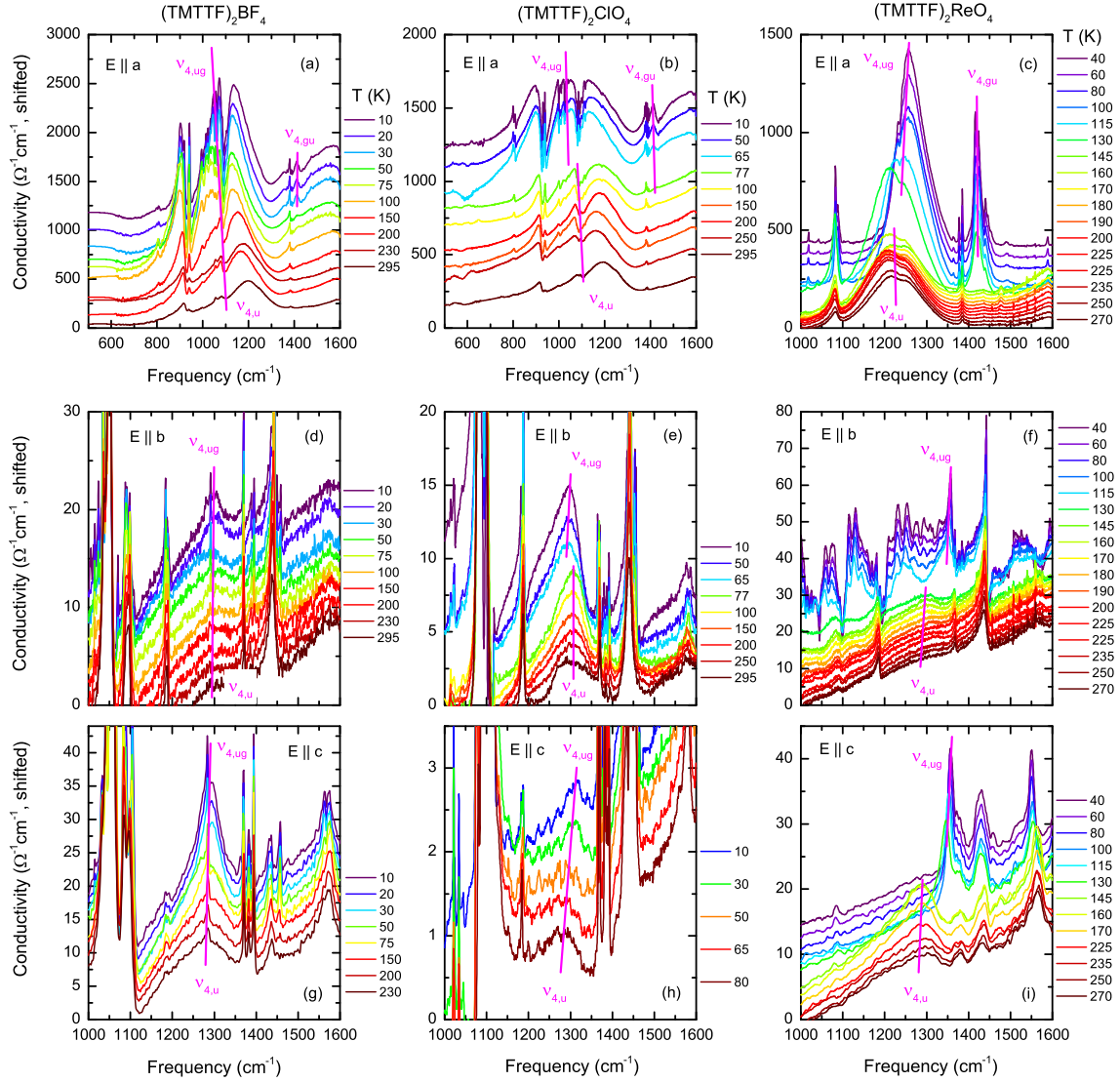


Figure A.1.13: Temperature dependence of the ν_4 mode of tetrahedral ($X = \text{BF}_4^-$, ClO_4^- and ReO_4^-) anions. The $\nu_{4,u}$ ($\nu_{4,ug}$ for $T < T_{\text{AO}}$) feature is observed in all crystal directions. In the absence of the electronic background perpendicular to the stacks ($E \parallel b$ and $E \parallel c$) it appears around 1300 cm^{-1} . Along the chains ($E \parallel a$) it shifts to lower frequencies due to strong emv-coupling. While for $X = \text{BF}_4^-$ there is a continuous blue-shift below T_{AO} , the feature shows an abrupt jump for ClO_4^- and ReO_4^- indicating the pronounced charge redistribution in the AO phase. Furthermore, anion order activates the tetrameric $\nu_{4,gu}$ vibration, which is discussed in Section IV. C of the main manuscript. It occurs only in a-direction as the tetramers are formed on the stacks. The strong increase of overall signal in (f) is due to a thin sample getting partially transparent as absorption decreases upon cooling.

A.2 Correlation-Dependent Luttinger-Liquid Dynamics Observed in One-Dimensional Electron Systems

A.2.1 Abstract

Infrared studies on the quasi one-dimensional organic compounds $(\text{TMTTF})_2X$ ($X = \text{PF}_6, \text{AsF}_6, \text{SbF}_6, \text{BF}_4, \text{ClO}_4$ and ReO_4) have been conducted from room temperature down to $T = 10$ K. The power-law revealed in the optical conductivity is a hallmark of physics in one dimension. We extract the non-universal Luttinger liquid exponent that characterizes the interacting electron system. It is sensitive to electronic correlations and influenced by the charge rearrangement.

A.2.2 Introduction

Electrons in low dimensions have been intensely investigated since the 1950's, first theoretically and later experimentally. While Fermi-liquid theory describes dimensions larger than two, the quasiparticle concept breaks down in one dimension where already arbitrarily small interactions lead to strong electronic correlations; as a result, the electronic response is governed by collective excitations commonly treated in the context of Tomonaga-Luttinger liquids [282–286]. For electrons in one-dimension unique phenomena, such as power-law behaviour and spin-charge separation, have been predicted and successfully demonstrated in recent years by investigating ultra-cold atomic gases [287, 288], carbon nanotubes [289, 290], surface structures [291, 292] or strongly anisotropic crystalline solids [293, 294].

In analogy to the Landau parameters of a Fermi liquid [69], a one-dimensional system is characterized by the non-universal Luttinger liquid exponents K_ν and velocities v_ν , where $\nu = \sigma$ and ρ for the spin and charge degrees of freedom, respectively. While $K_\nu = 1$ in the non-interacting case, it becomes smaller (larger) for repulsive (attractive) interactions, i.e. $K_\rho < 1$ for a system dominated by Coulomb repulsion. The exponents influence thermodynamics by showing up in the specific heat, temperature-independent Pauli susceptibility and electronic compressibility [295–297]. K_ρ can also be addressed via the NMR spin-lattice relaxation rate [298, 299] or resistivity studies [300, 301]; in most cases, however, the parameter is extracted from the spectral function measured by photoemission spectroscopy [292, 294]. Giamarchi suggested to consider the electrodynamic response, where a power-law decay of the

optical conductivity $\sigma(\omega)$ is expected at the high-frequency tail of the Mott-Hubbard band [302–304]

$$\sigma(\omega) \propto \omega^{-\gamma} = \omega^{4n^2K_\rho - 5} \quad , \quad (\text{A.2.1})$$

with the power-law exponent γ linearly related to the Luttinger liquid parameter K_ρ . The order of commensurability $n = \frac{1}{2p}$ depends on the band filling p , i.e. the number of electrons per site; hence, $n = 1$ and $n = 2$ for half and quarter-filled bands, respectively. In the non-interacting case ($K_\rho = K_\sigma = 1$) for complete filling ($n = 1/2$), the characteristic ω^{-3} decay of a one-dimensional band insulator [305] is restored³ via $K_\rho + K_\sigma - 5 = -3$.

Since theory was developed for strictly one-dimensional electron systems in the low-energy limit, $T = 0$ and $\omega = 0$, it was surprising that NMR, photoemission, transport and optical measurements [299–301, 306–308] could identify Luttinger liquid behaviour also in the quasi-one-dimensional Bechgaard salts where conditions are certainly not ideal. It turns out that a system behaves like being one-dimensional at energy scales larger than the transverse hopping t_\perp [304]. Consistently, a Luttinger liquid exponent $K_\rho = 0.23$ is obtained for all (TMTSF)₂X compounds. Pressure applied to the even more one-dimensional (TMTTF)₂X salts in the metallic state increases the inter-chain hopping and K_ρ until two-dimensional transport sets in [191, 309]. It was suggested [302–304, 310] that the finite inter-chain coupling t_\perp is crucial at low temperatures where the materials behave as a two- or even three-dimensional Fermi liquid. Experiments confirmed the crossover to the Luttinger liquid behaviour at elevated temperatures $k_B T > t_\perp$ [301], or finite frequencies [307]. The critical exponents are non-universal and depend on electronic interactions, however, systematic studies of the Luttinger-liquid properties turn out to be difficult as low-dimensional metals are subject to Peierls instabilities, charge order or enter a Mott insulating state.

Although Luttinger liquid physics is expected to break down for a one-dimensional band insulator, the situation is more intriguing in the case of a Mott insulator at commensurate filling brought about by electronic correlations [295]. In this work, we exploit the fact that one-dimensional physics prevails at high frequencies independent on the low-energy ground state [293, 297, 311], i.e. the characteristic power-law behaviour can be analyzed for $\hbar\omega > t_\perp, k_B T$. From the frequency-dependent low-temperature conductivity we extract the interaction-dependent Luttinger exponent

³While K_σ does not intervene for Umklapp processes at 1/2- and 1/4-filling, it has to be taken into account for a completely filled band.

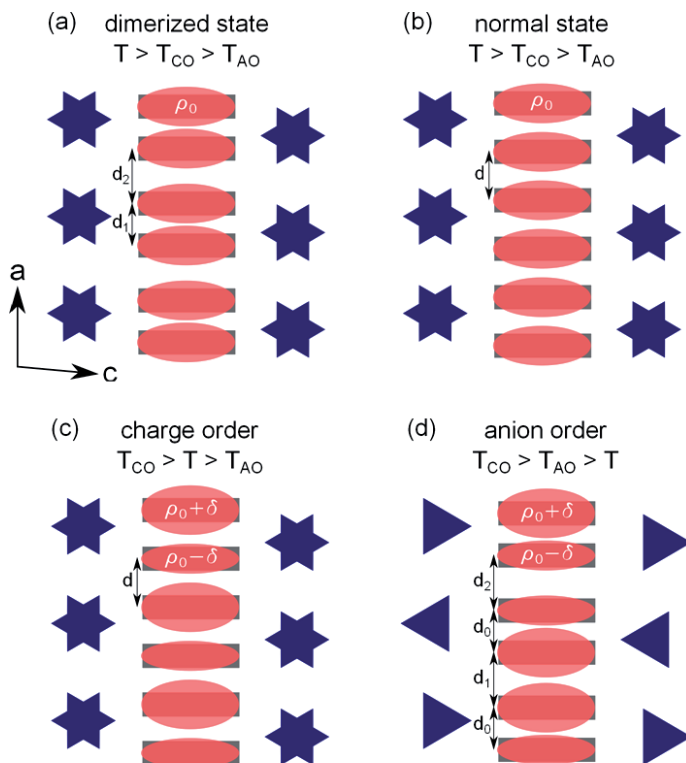


Figure A.2.1: Molecular, anion and charge arrangement of $(\text{TMTTF})_2X$ in different phases. (a) At high temperatures the TMTTF chain are slightly dimerized. (b) The stack becomes more homogeneous as the dimerization decreases upon cooling [250, 251, 280, 312]. (c) When inter-site Coulomb repulsion V becomes the dominant energy scale for $T < T_{\text{CO}}$ the molecular charge orders in an alternating fashion. (d) At high temperatures the anions do not have a well-defined orientation but fluctuate around their center position (indicated by the six-fold symmetry). At lower temperatures, when they take their final position, non-centrosymmetric anions are arranged in two orientations alternating, for instance, left or right. The resulting periodic modulation of the electrostatic potential causes severe changes of the structure and charge distribution.

as a measure of the instantaneous degree of Coulomb repulsion. In particular, we demonstrate the temperature-dependent changes of intra-chain Coulomb repulsion directly reflecting the charge rearrangement within the stacks induced by various phase transitions.

A.2.3 Experimental Details

We have performed comprehensive optical investigations of quasi-one-dimensional $(\text{TMTTF})_2X$ salts, where TMTTF stands for tetramethyltetrafulvalene and X indicates a monovalent anion, such as the octahedral PF_6 , AsF_6 , SbF_6 and tetra-

hedral BF_4 , ReO_4 , ClO_4 . T. Peterseim, S. Kolatschek and L. Engel participated in optical experiments. The compounds form stacks of organic molecules along the crystallographic a -direction separated by anions X^- (Fig. A.2.1) leading to effectively $+0.5 e$ charge per TMTTF site. The needle-like single crystals (typically $0.1 \times 0.2 \times 1 \text{ mm}^3$) were grown by electrochemical methods and characterized by dc transport. All compounds become insulating at low temperatures due to electronic correlations, but – depending on the anions – they exhibit transitions to ordered ground states in the charge and spin sector, including coupling to the lattice and anion ordering of non-centrosymmetric anions [113, 237, 255, 313, 314]. As illustrated in Fig. A.2.1, the charge arrangement and intra-stack distance vary for the different states. Therefore, such severe changes of the electronic system should also reflect in the interaction parameter K_ρ . Thus we study the temperature-dependent behaviour of the Luttinger liquid exponent upon the metal-insulator transitions. To that end the temperature-dependent reflectivity was measured in the mid- and near-infrared range by Fourier-transform spectroscopy using an infrared microscope that enabled us to perform polarization-dependent experiments on crystal surfaces of $50 \mu\text{m}$ diameter.

A.2.4 Results

The mid-infrared optical conductivity of $(\text{TMTTF})_2X$ is plotted in Fig. A.2.2 as measured at the lowest temperature with the polarization along the molecular stacks ($E \parallel a$). The spectra are dominated by the Mott-Hubbard band in the mid-infrared range with numerous vibrational features below 2000 cm^{-1} discussed at other occasions [51, 113]; here we focus on the high-frequency tail. In order to make comparison easier, the data were normalized to the maximum conductivity σ_{max} and plotted in Fig. A.2.3 in a double logarithmic fashion. All compounds exhibit a power-law decay $\sigma(\omega) \propto \omega^{-\gamma}$ as predicted in Equ. A.2.1 for a one-dimensional metal. The observation evidences that the high-frequency physics is dominated by Luttinger-liquid behaviour even when an insulating state is stabilized at low temperatures. A closer inspection reveals that the specific exponents systematically depend on the dimension of the electronic system, and also illustrates the different impact of the respective ground states. Extensive studies of the $(\text{TMTTF})_2X$ salts with centrosymmetric, octahedral anions ($X = \text{PF}_6$, AsF_6 , SbF_6 and TaF_6) have proven that inter-site Coulomb repulsion drives charge order [238, 239, 241, 242, 272, 315], while in the case of non-centrosymmetric anions an additional ordering was found [237]. As depicted in Fig. A.2.1 (d), the tetrahedral ions ($X = \text{BF}_4$, ClO_4 and ReO_4) get oriented and dis-

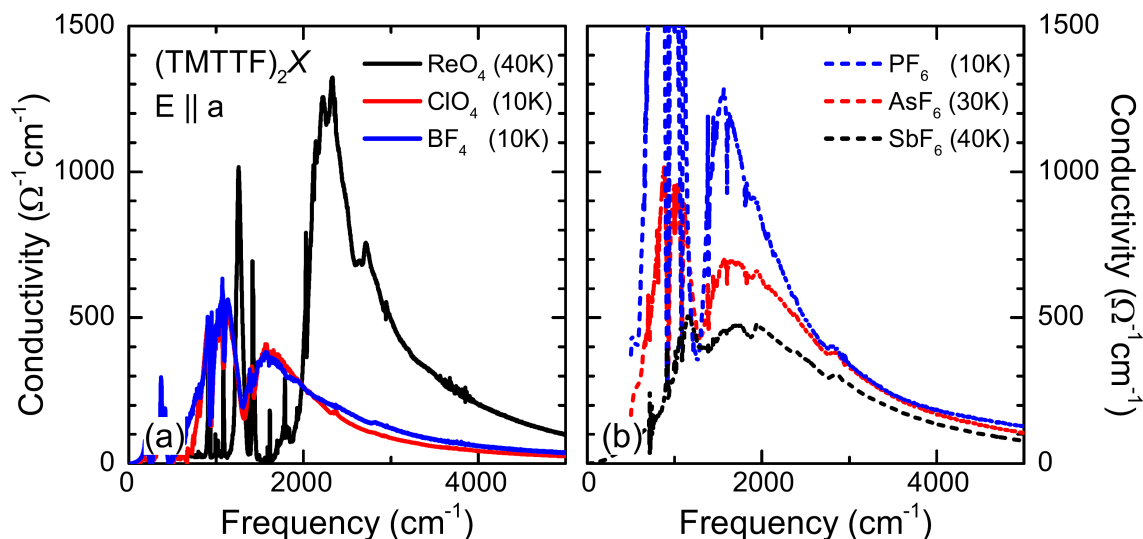


Figure A.2.2: Optical conductivity of $(\text{TMTTF})_2\text{X}$ salts with (a) tetrahedral and (b) octahedral anions at the lowest measured temperatures. Above the Mott-Hubbard band, $\sigma(\omega)$ decays according to a power law.

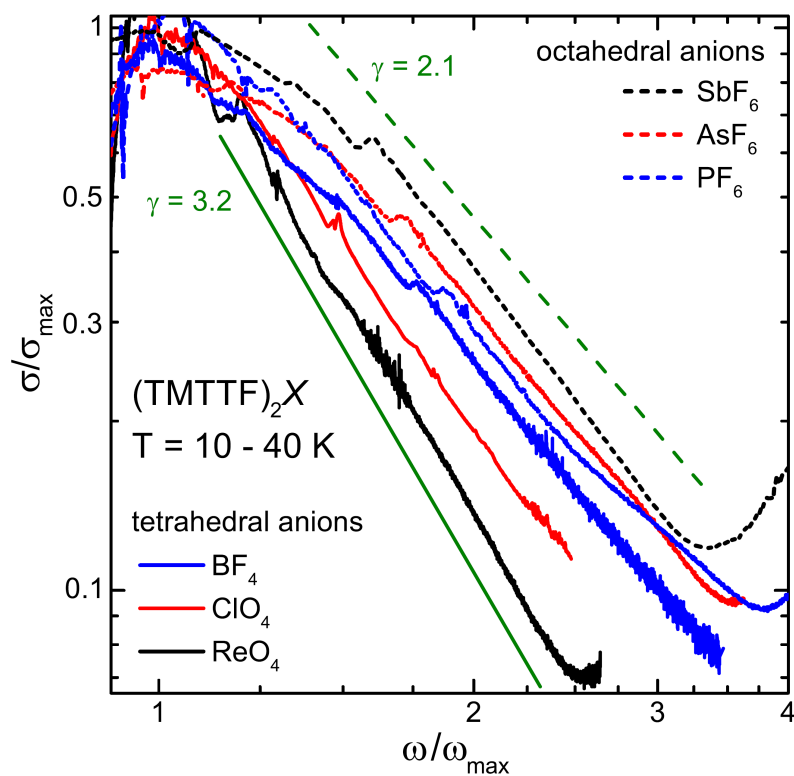


Figure A.2.3: Frequency-dependent conductivity normalized to the maximum of the charge transfer band σ_{max} at ω_{max} . The double-logarithmic presentation reveals a power-law behaviour $\sigma(\omega) \propto \omega^{-\gamma}$ with exponents ranging from $\gamma = 2.1$ for the centrosymmetric anions up to 3.2 for the non-centrosymmetric ones.

placed and thus periodically modulate the potential landscape. This way the shortest O-S distance decreases significantly [276, 313] leading to a severe deformation of the organic stack. Several studies consistently suggest that the 0101 charge order becomes redistributed to a 0011 type for $T < T_{\text{AO}}$, doubling the periodicity [208, 247, 249–251]. A considerable rearrangement of charge upon the anion-order transition could now be also confirmed for $(\text{TMTTF})_2\text{ClO}_4$ [51]. Hence, for all compounds the charge disproportionation changes at T_{AO} , providing evidence for a competition between the charge-ordered and anion-ordered states.

A.2.5 Temperature-Dependent Luttinger Exponent.

The variation in charge arrangement and electronic coupling should have an impact on the effective correlations. To that end, the power-law exponents γ of the $(\text{TMTTF})_2X$ -salts were extracted for all measured temperatures and plotted in Fig. A.2.4. At high temperatures γ takes values between 2.5 and 3 for all compounds under study in agreement with previous reports [191, 309]. For comparison, $(\text{TMTSF})_2X$ salts show a more or less temperature-independent exponent of 1.3 [307], giving evidence of the much stronger on-chain correlations in $(\text{TMTTF})_2X$. The most striking finding, however, is the pronounced temperature dependence of the Luttinger liquid parameter and the distinct variations at the phase transitions. In the metallic state the centrosymmetric compounds, $T > T_{\text{CO}}$, we find a strong increase of γ (reduction of K_ρ) with temperature. At the charge order transition the exponents exhibit a kink, marking a strong decrease towards low temperatures. The behaviour is reversed at the AO phase transition of the tetrahedral compounds, where the exponents shoot up and saturate at larger values. These observations imply that the on-chain interactions decrease upon cooling for $T > T_{\text{AO}}$, whereas they increase for $T < T_{\text{AO}}$.

In order to understand these findings better, let us consider the extended Hubbard model

$$\begin{aligned}
 H = & - t \sum_{\langle ij \rangle, \sigma} (c_{i\sigma}^\dagger c_{j\sigma} + h.c.) \\
 & + U \sum_i n_{i\uparrow} n_{i\downarrow} + V \sum_{\langle ij \rangle} n_i n_j
 \end{aligned}
 \tag{A.2.2}$$

with the transfer integral t , on-site Coulomb repulsion U and inter-site Coulomb repulsion V . The Luttinger parameter $K_\rho < 1$ is a measure of the repulsive electron-electron interactions and the respective terms in the Hubbard model. In case of

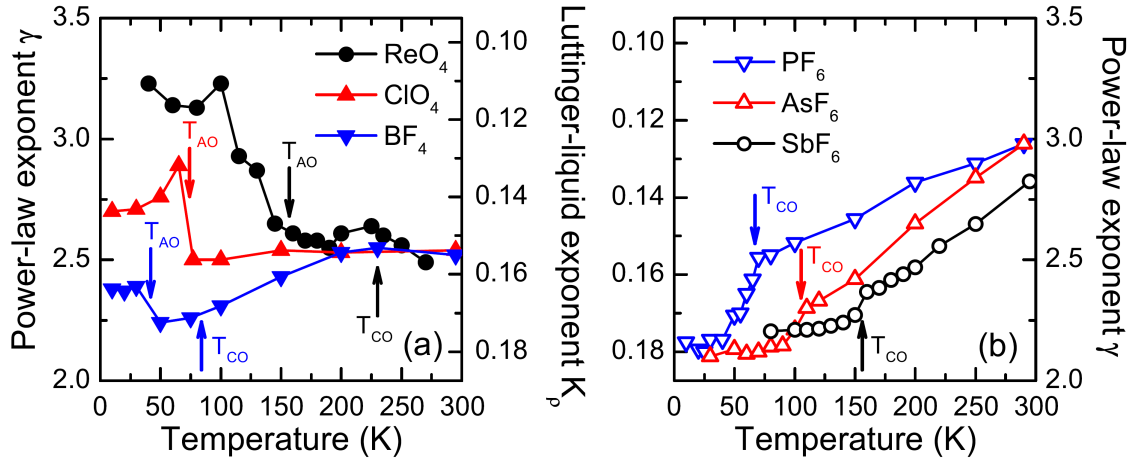


Figure A.2.4: Temperature dependence of the extracted power-law exponents of several (TMTTF)₂X compounds. (a) For tetrahedral anions γ significantly increases when entering the AO state, which corresponds to enhanced repulsive electron-electron interactions according to Equ. A.2.1. A clear dependence on anion size is observed. (b) On the other hand, for octahedral anions the exponent monotonically decreases upon cooling with a kink at T_{CO} and a steeper slope at low temperatures.

(TMTTF)₂X the low-temperature physics is dominated by inter-site Coulomb repulsion with the consequence of a charge-ordered ground state which minimizes the third term in Eq. A.2.2. The electronic repulsion on the TMTTF chain can roughly be approximated by the electrostatic potential between nearest-neighbors

$$\Delta E = \sum_{\langle ij \rangle} \frac{\rho_i \rho_j}{d_{ij}} \quad (\text{A.2.3})$$

where ρ_i denote the site charge and d_{ij} the intra-stack distance of neighboring TMTTF molecules. Modifications of the charge pattern and the degree of dimerization change the total electrostatic repulsion; for the arrangements depicted in Fig. A.2.1 we arrive at an order relation

$$\Delta E_{CO} < \Delta E_0 < \Delta E_{\text{dim}}, \Delta E_{AO} \quad (\text{A.2.4})$$

where ΔE_0 is the electrostatic energy for equally distributed charge (Fig. A.2.1 b). It directly becomes clear that, as expected, charge order reduces the Coulomb energy while dimerization and anion order cause an enhancement with respect to ΔE_0 .

Now, we can understand how variations in the microscopic charge structure change the exponents. The most trivial point is the strong thermal contraction of the organic crystals which causes a larger orbital overlap and pushes the system towards metal-

licity when lowering the temperature. Simultaneously, the electronic dimerization decreases with cooling and pressure, i.e. the difference in transfer integrals between neighboring molecules along the stack [250, 251, 280, 312]. Therefore the Coulomb repulsion decreases with lowering the temperature as reflected in the increase of K_ρ shown in Fig. A.2.4 (b). In trying to minimize electronic repulsion, charge order sets in at T_{CO} causing an even further decrease of the exponent. Hence, the Luttinger liquid exponent is a measure of the effective Coulomb repulsion and sensitive to the rearrangement of charge.

The situation is more delicate in the anion-ordered state as it implies an intertwined electronic and structural reorganization. The formation of a 0011 charge pattern implies that two charge-rich molecules are next to each other. Combined with the underlying dimerization/tetramerization (Fig. A.2.1) the electronic repulsion drastically increases, as given in Eq. A.2.4, leading to a strong increase of the exponent. It is interesting to note that a 0101 arrangement reduces Coulomb repulsion compared to the dimerized state with equally-distributed charge. A more complete examination of the relevant energies has to consider the anions and their interaction with the organic stacks, too.

A.2.6 Conclusion

From our comprehensive investigations of the temperature-dependent electrodynamic behaviour of various quasi one-dimensional organic conductors $(TMTTF)_2X$ we conclude that the power-law $\sigma(\omega) \propto \omega^{-\gamma}$ observed in the optical conductivity is very sensitive to the electronic repulsion along the molecular stack. The temperature-dependent γ is extracted from the high-frequency decay of the Mott-Hubbard band. In accord with theoretical predictions the rearrangement of charge and structure influences the effective electronic correlations and modifies the Luttinger liquid exponent K_ρ .

A.3 Charge Order on the Nanoscale in α -(BEDT-TTF)₂I₃

We present cryogenic optical nanoimaging of the complex spatial evolution of the charge order phase in α -(BEDT-TTF)₂I₃ single crystals. In particular, we observe a sharp phase boundary (width $\approx 10^{-7}$ m) between metallic and insulating regions, providing conclusive evidence on the first-order nature of this phase transition. Our results further infer that pronounced strain within single segments of 10–100 μ m size spatially modulates the electronic correlations on the sample, effectively tuning different spots on the surface to different positions in the phase diagram. Thus, we observe a local, inhomogeneous bandwidth-tuning of the order of 0.5 kbar within a range of just a few μ m. These findings point out possible issues arising from bulk measurements on inhomogeneous specimens and demonstrate the exceptional capabilities of cryogenic scanning near-field optical microscopy (cryo-SNOM) in disentangling the local electrodynamic properties.

A.3.1 Introduction

The thermodynamic stabilization and competition between structural and/or electronic states of matter are a major paradigm of condensed matter physics and materials science. Ideally, a phase transition manifests as the distinct change of a physical quantity, such as the magnetization or the resistivity, upon changing a tuning parameter like temperature or pressure. Typical bulk measurements rely on clean, single-crystalline materials with constant transition temperature over the entire sample to probe the intrinsic properties only. However, it is not always possible to obtain uniform specimens free of defects or internal strain. As a result, the actual phase transition may happen at slightly different temperatures on spatially separated parts of the sample, effectively broadening the transition as sketched in Fig. A.3.5 (a)-(c). This can mask a formally first-order transition when evaluating only the macroscopic order parameter in an inhomogeneous bulk crystal.

The way out is a spatially-resolved local probe measuring a physical quantity subject to pronounced changes upon the phase transition. Obviously, simple atomic force microscopy (AFM) is not appropriate to study metal-insulator transitions as it is not sensitive to the conduction properties of the material. Although in principle very powerful, tunneling methods have severe difficulties with insulators and the surface sensitivity makes these methods inapplicable for many materials. The method of choice is, therefore, cryogenic scanning near-field optical microscopy (cryo-

SNOM) which combines the advantages of optical spectroscopy and scanning probe techniques at low temperatures: while the electromagnetic radiation penetrates sufficiently deep into the material effectively probing the bulk material⁴, the lateral resolution is limited by the AFM tip (≈ 10 – 20 nm) which is orders of magnitude below the diffraction limit of the probed wavelengths [316].

In this work, we present the first – to the knowledge of the author – low-temperature optical near-field experiments tracing the metal-insulator transition in a bulk single-crystalline correlated electron material. While previous low-temperature studies focussed on thin films [317], single crystals were mostly studied close to room temperature, or above [318]. Generally, the field is just at its beginnings and most relevant work originated from the collaborating group [319–325]. Also other spatially-resolved techniques are mostly limited to elevated temperatures [326]. Here, we mapped the spatial evolution of the insulating state through the phase transition in the organic conductor α -(BEDT-TTF) $_2$ I $_3$, a well-known prototype material subject to electronically-driven charge order [327–329]. By probing the opening of the optical gap in the insulating state, we identify spatially separated charge-ordered and metallic regions with a sharp phase boundary, proving the first-order nature of the transition. Moreover, we analyze the complex phase arrangement emanating from internal strain and find a local suppression of charge order by more than 5 K, which corresponds to an equivalent hydrostatic pressure of 0.6 - 0.7 kbar (cf. Fig. A.3.1 f).

A.3.2 Material Properties

α -(BEDT-TTF) $_2$ I $_3$ is an organic conductor with quasi two-dimensional electronic properties consisting of alternating layers of BEDT-TTF^{+0.5} radical cations and I $_3^-$ anions. Together with strong inter-site Coulomb repulsion V the effectively quarter-filled bands lead to a charge redistribution between the organic molecules below $T_{CO} = 136$ K. A sharp phase transition was reported with the resistivity shooting up by several orders of magnitude within less than 1 K [329]. Although no sizeable hysteresis was found, the charge order transition is believed to be of first order due to the abrupt change of the order parameter (i.e. the charge disproportionation 2δ) like in other quasi two-dimensional (BEDT-TTF) $_2$ X compounds, as sketched in Fig. A.3.5 (a). In contrast, quasi one-dimensional (TMTTF) $_2$ X exhibit second-order behaviour with gradually increasing, mean-field like charge disproportionation [51, 113, 196],

⁴An electric field builds up between the tip and its mirror charge in the sample. The effective penetration depth of the near-field into the material is of order 10 nm, containing $\approx 10^3$ units cells. Thus, the surface contributes only to a small extent.

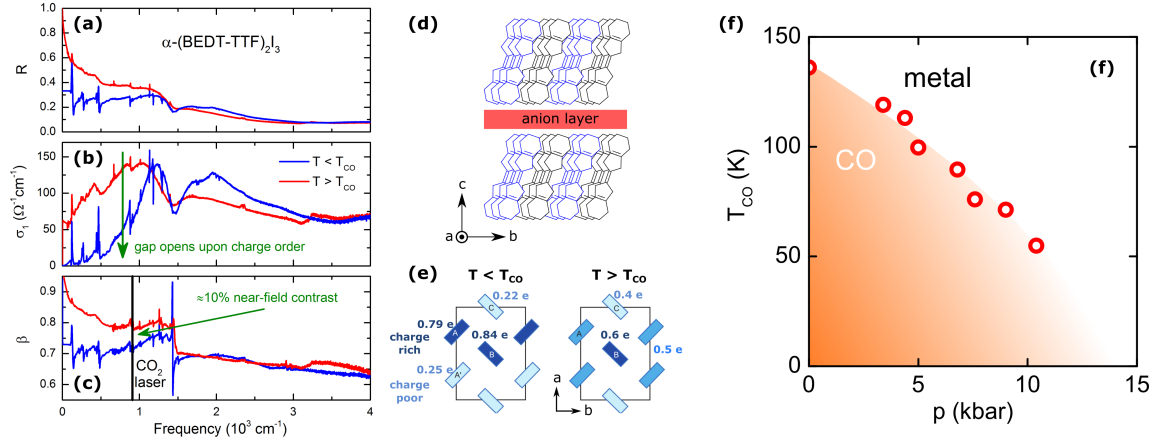


Figure A.3.1: The far field optical reflectivity (a) and conductivity (b) of α -(BEDT-TTF) $_2$ I $_3$ exhibit pronounced changes upon the charge order transition [329]. In particular, a spectral gap opens in the insulating state. (c) The near-field reflectivity β is calculated according to Equ. A.3.1. Distinct changes are also observed at the frequency of the CO $_2$ laser ($\omega_L = 910 \text{ cm}^{-1}$). (d) The crystal structure is similar as for other (BEDT-TTF) $_2$ X. (e) In the charge order phase below T_{CO} the charge-rich and -poor molecules are arranged in horizontal stripes oriented along the b -axis [330]. (f) The hydrostatic pressure phase diagram shows an initial suppression of charge order by 8 K/kbar [331].

cf. Fig. A.3.5 (b). Upon applying hydrostatic pressure to α -(BEDT-TTF) $_2$ I $_3$, the accompanying reduction of electronic correlations V/W suppresses the charge-ordered state at an initial rate of 8 K/kbar as evident from the phase diagram in Fig. A.3.1 (f). Moreover, this material has recently attracted considerable attention due to massless Dirac fermions identified around 15 kbar [331–333].

Charge order strongly affects the low-frequency optical properties as shown in Fig. A.3.1 (a) and (b). Through the metal-insulator transition, the zero-frequency Drude weight vanishes due to the opening of an optical gap [329], which causes a pronounced drop of both the reflectivity and conductivity at low frequencies. Intuitively, similar changes are expected for the near-field response. According to McLeod *et al.* [334] the near-field amplitude reflected off the sample can be approximated from the far-field dielectric function,

$$\beta = \frac{\epsilon - 1}{\epsilon + 1} \quad \text{with} \quad \epsilon = \sqrt{\epsilon_{\parallel}\epsilon_{\perp}}, \quad (\text{A.3.1})$$

where ϵ_{\parallel} and ϵ_{\perp} denote the complex dielectric function $\epsilon = \epsilon_1 + i\epsilon_2$ parallel and perpendicular to the probed surface, respectively. For the investigated crystals, the conducting ab -plane⁵ (sketch of crystal structure in Fig. A.3.1 d) is parallel to the

⁵Strictly speaking, there is small anisotropy within the conducting plane, so we averaged between

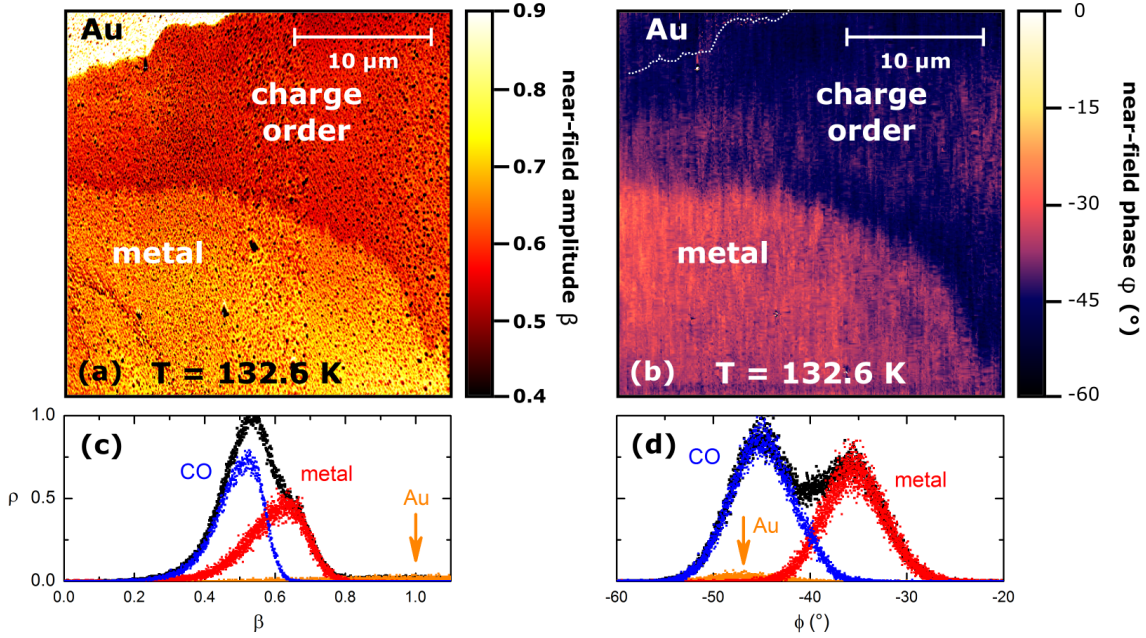


Figure A.3.2: (a) The near-field amplitude β measured with a CO_2 laser at 910 cm^{-1} reveals a clear phase boundary. In good agreement with panel (c), the metallic regions show larger amplitude than the charge order (CO) phase. (b) Also the near-field phase ϕ shows considerable contrast between the metallic and insulating regions. The position of the phase boundary matches perfectly with panel (a). (c) Intensity histogram of metallic (red) and CO (blue) regions normalized to the signal of the Au layer (30 nm thickness). (d) The respective maxima of the intensity histogram are separated by more than 10° . Interestingly, the charge-ordered region has a similar phase shift as the gold layer.

sample surface while the c -axis is perpendicular ($\epsilon_\perp = \epsilon_c$). As expected, the modeled near-field spectra also show considerable modifications upon the charge order metal-insulator transition, most pronounced at lowest energies. At the frequency of the CO_2 laser, $\omega_L = 910\text{ cm}^{-1}$, used in the near-field experiment, the contrast of β is around 15%.

A.3.3 Near-Field Optical Properties

At first, we present our data obtained from a clean and homogeneous single crystal. In Fig. A.3.2 (a) we show the near-field amplitude β at the charge order transition mapped on a $40 \times 40\ \mu\text{m}^2$ spot. There is a well-defined phase boundary between the metallic (yellow) and insulating (red) regions providing conclusive evidence for the first-order nature of the charge order transition in α -(BEDT-TTF) $_2$ I $_3$. In order

the two in-plane directions $\epsilon_\parallel = \frac{\epsilon_a + \epsilon_b}{2}$. Since the overall temperature dependence is similar, we show only the a -polarization in Fig. A.3.1 (a) and (b).

to obtain reliable absolute values of β , we normalized the scale to the intensity of the gold layer ('Au', very bright) in the top left corner. The histogram of pixel amplitudes (panel c), selectively determined for the respective areas, reveals that the charge-ordered (CO) part of the image has a near-field amplitude about $\beta = 0.5$ whereas the metallic region is centered around $\beta = 0.65$, yielding a slightly larger contrast but overall good agreement with the calculation according to Equ. A.3.1.

Fig. A.3.2 (b) presents the corresponding near-field phase⁶ ϕ that also shows well-distinguishable metallic and CO regions perfectly overlapping with the amplitude data in panel (a). The corresponding pixel histogram (panel d) has two well-separated maxima at -45° (CO) and -35° (metal). Surprisingly, there is no noticeable phase difference between the CO regions of α -(BEDT-TTF)₂I₃ and the gold layer, the border of which is indicated by the dotted white line in panel (b).

Upon changing temperature, the phase boundary propagates quickly over the entire sample and moves out of the observed area within a few 100 mK. Most probably, the laser light ($P \approx 0.5$ mW) heats up the sample creating a temperature gradient between the heat sink (the gluing point several 100 μm distant from the gold edge in top left direction) and the parts of the crystal most distant to it. Insufficient thermal coupling of this thin sample also explains the transition occurring more than 3 K below the nominal transition temperature at 136 K, which is most likely just an offset between the sample and sensor temperatures. Overall, the small coexistence range of a few 100 mK is in good agreement with literature [329] and indicates high sample quality with an essentially uniform transition temperature.

A.3.4 Spatially Inhomogeneous Charge Order Transition in a Non-Uniform Sample

As we have seen, investigating smooth sample surfaces by means of cryogenic nanoimaging yields results consistent with bulk measurements on uniform single-crystals. However, now we make use of the great advantage of this scanning probe technique and study a more inhomogeneous, multiply cracked α -(BEDT-TTF)₂I₃ sample consisting of many loosely connected segments of different size and shape. Fig. A.3.3 (a) shows the evolution of the complex phase boundaries separating the metallic and insulating regions on a $40 \times 40 \mu\text{m}^2$ spot in small temperature steps. The transition initiates in the vicinity of the gold layer in the top right part of the image slightly below the nominal transition at 136 K. Although the CO phase successively grows

⁶Consider it as the analogue to the phase change of the far-field reflectivity, commonly determined in ellipsometric and THz experiments.

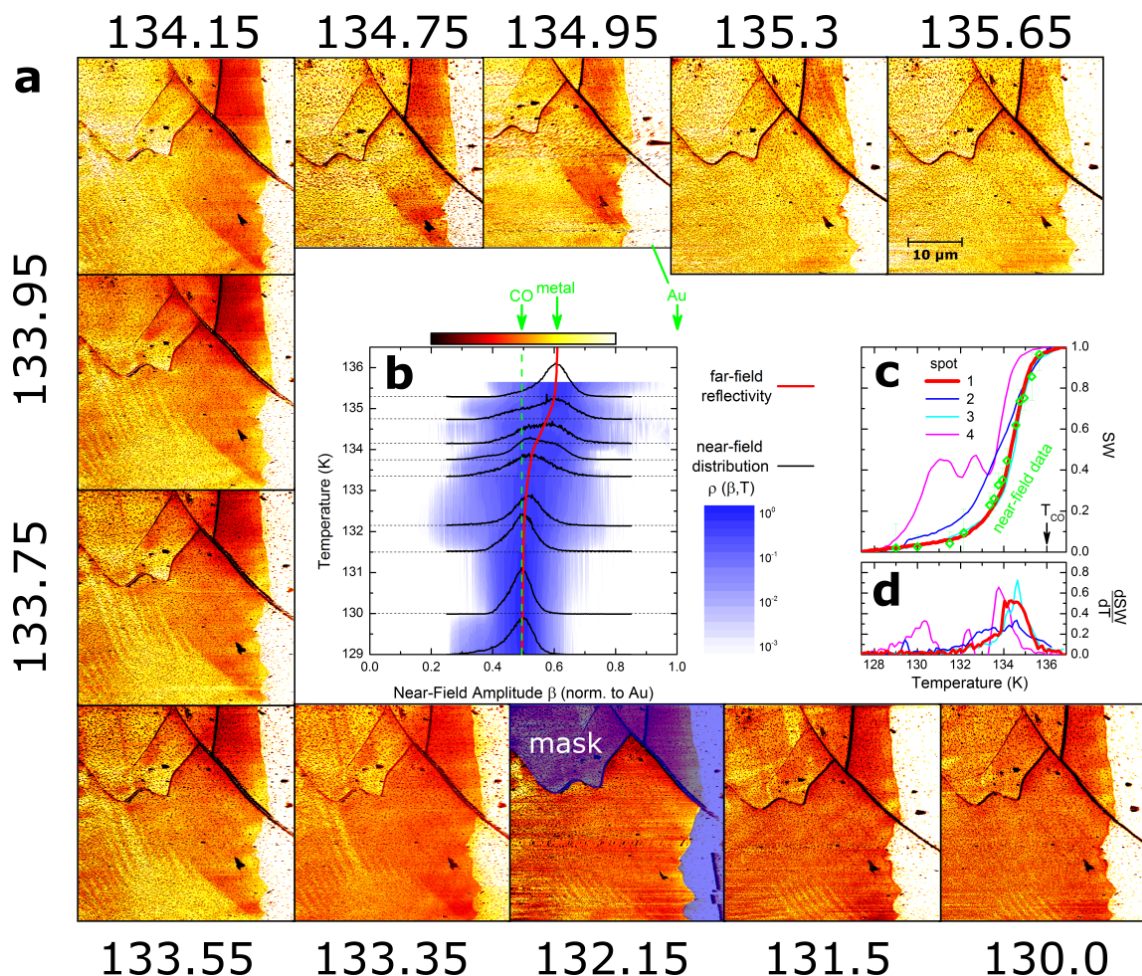


Figure A.3.3: (a) Near-field maps of a multiply-cracked α -(BEDT-TTF) $_2$ I $_3$ crystal measured close to $T_{\text{CO}} = 136$ K. Clear phase separation between metallic (yellow) and insulating (red) regions is observed with a phase coexistence over a temperature range $\Delta T \geq 6$ K. The near-field amplitude β was normalized to the signal of a 30 nm thick gold layer ('Au', bright part on the right of each image) evaporated beforehand. (b) To quantitatively analyze the temperature evolution of the two phases, we determined the pixel histograms of β on the non-masked region only, as indicated at 132.15 K. The white-blue contour plot and the black lines correspond to the amplitude distributions at the measured temperatures. In the range with the largest changes (133.5 K–135 K) a bimodal distribution of metallic and CO regions is observed. The trend nicely follows the result of our far-field experiments (red line) on the same area ('spot 1'). (c) The far-field reflectivity was measured subsequently on different parts of the sample. The low-frequency range with most pronounced changes was integrated from 600 to 800 cm^{-1} and the resulting temperature-dependent spectral weight (SW) was normalized to the high- and low-temperature plateau values, i.e. deep in the metallic and charge-ordered phases, respectively. After similar normalization, the temperature dependence of the average near-field intensity from (b) agrees perfectly with the far-field data of spot 1. (d) The derivative with respect to temperature was calculated to highlight the largest rate of change. Apparently, the transition does not happen at the same temperature on the different spots. While it is very similar and sharp for spots 1 and 3, it is much broader on spot 2. For region 4 it even seems to be interrupted.

with lower temperature, the last stripe-like metallic relicts in the bottom part of the map persist down to $T \leq 130$ K. Phase coexistence over such a large temperature range cannot be explained just by temperature gradients. Note, despite the rapidly vanishing electrical conductivity, the in-plane thermal conductivity merely changes at the phase transition (25% drop reported in Ref. [335]) due to the large phononic contribution at 135 K, which rules out temperature gradients of 5 K within a few μm .

Fig. A.3.3 (b) shows the pixel distributions of the largest single segment in the lower part of the maps (un-masked area indicated at 132.15 K) at all temperatures. The histograms exhibit a bimodal phase coexistence around the temperature range of the largest amplitude changes. The subsequent far-field reflectivity measurements plotted in panels (c) and (d) reveal distinct temperature dependence on different parts of the sample; both T_{CO} and the width of the transition vary with position. The spot overlapping with the un-masked area shows consistent behaviour with Fig. A.3.3 (b).

To quantify the dynamical phase boundary motion, we determined its distance Δ to the parallel crack indicated by the green arrow in Fig. A.3.4 (a); the temperature dependence is plotted in panel (b). While initially the insulating phase expands rather quickly, consistent with a realistic temperature gradient⁷ of several K/mm, below 134.5 K the phase boundary propagates much slower (equivalent to a gradient $dT/dx = 80$ K/mm) ruling out a thermal origin. This is corroborated by the peculiar stripe pattern with approximately $2 \mu\text{m}$ periodicity occurring in the middle of the segment, which was mapped with 20 nm resolution on a $10 \times 10 \mu\text{m}^2$ spot (Fig. A.3.4 c). The line cut of panel (d) illustrates width of the phase boundaries of several 100 nm. The general behaviour of the discussed segment is nicely illustrated by panel (e); while charge order is stabilized first at the edges of the sample, the metallic phase persists in the center involving a stripe-like pattern.

To understand this behaviour more detailed, finite-element strain calculations have been carried out on a sample being clamped to the substrate at the two bottom edges, which resembles the experimental situation very well⁸. Due to different thermal contraction of the sapphire substrate (small) [336] and α -(BEDT-TTF)₂I₃ (large) [337], the sample is subject to strong tensile stress along the a -direction, accompanied by a compression in the perpendicular directions. As a result, the crystal breaks into

⁷This is still large, but we have to keep in mind the small sample thickness $d = 15 \mu\text{m}$ and the cracks impeding heat transport.

⁸The sample was glued to the sapphire substrate from two sides, more or less parallel to the a -direction.

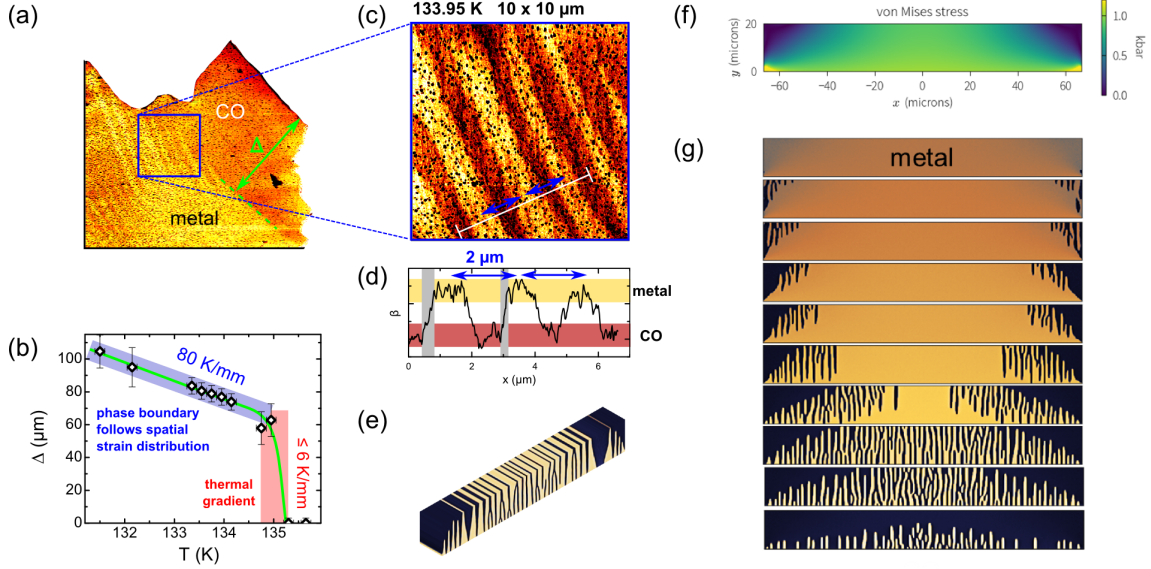


Figure A.3.4: (a) The segment analyzed in Fig. A.3.3 (b) illustrates the stripe pattern at 133.95 K. (b) The distance x between the crack (top right side) and the metal-insulator phase boundary (dashed green line), indicated by the green arrow in (a), was determined at several temperatures. Initially, a large area parallel to the crack becomes charge-ordered within a fraction of a Kelvin (≤ 0.35 K). This quick propagation of the phase boundary can be attributed to a temperature gradient of ≤ 6 K/mm. However, below 134.5 K the metallic phase retreats at a much slower rate, which would imply an unrealistically large temperature gradient. Thus, we explain the dynamics and the stripe-like pattern (a) of the phase boundary by a spatially inhomogeneous strain distribution within the sample. (c) A $10 \times 10 \mu\text{m}^2$ high-resolution map was acquired in the center of the segment with most pronounced stripes. (d) The profile indicated by the white line in (c) reveals a stripe periodicity of $2 \mu\text{m}$ and a phase boundary width of few 100 nm. (e) Three-dimensional illustration of an elongated, rectangular segment considered for the finite element strain calculation to reproduce the experimental data. (f) The calculated strain profile upon tensile stress applied at the bottom corners reveals large strain at the center of the segment and small values close to the edges. (g) The interplay of metallic and charge order phases was simulated at different temperatures throughout the phase transition. Very similar to the experimental data from Fig. A.3.3, charge order successively grows from the edges of the segment while the metallic phase is repressed towards the center. Around the phase transition, a characteristic stripe pattern appears upon minimizing the Landau free energy, in excellent agreement with experiment.

many segments, partially relieving the strain at the edges. Therefore, each segment exhibits an internal strain modulation, generally large in the center and small at the edges. As shown in Fig. A.3.4 (f), this is reproduced by the strain calculations very well. Under consideration of the relevant material parameters, such as the Young's modulus of comparable charge-transfer salts [338] and the anisotropic thermal expansion upon the charge order transition [339], also the characteristic stripe pattern is nicely obtained. Overall, the Landau free energy is minimized for alternating metallic and insulating regions which stems from the competition between the domain wall energy on the one hand, and the elastic energy on the other hand. Apparently, it is more favourable to introduce domain walls than sustaining internal strain. In particular, α -(BEDT-TTF)₂I₃ exhibits a contraction along the a -direction while the b -axis expands upon cooling through the charge order transition [339]. It has been shown that compression along b is much more effective in suppressing charge order than hydrostatic pressure [340, 341] as it causes a considerable enhancement of the transfer integrals and, thus, reduces V/W via the bandwidth [337]. This explains the pronounced effects of strain in this sample; the coexistence regime of $\Delta T_{\text{CO}} \geq 6$ K corresponds to an equivalent pressure along the b -direction of approximately 0.5 kbar. It should be stressed that the direction of stripes is primarily related to the applied strain, i.e. they form perpendicular to the direction of strain. Similar behaviour was observed in strained VO₂ thin films [342]. Also there, the TiO₂ substrate induces uniaxial strain resulting in a stripe-like modulation of the VO₂ transition temperature. In our specific case, the effects becomes very pronounced due to coincidental compression more or less parallel to the b -direction, which is most susceptible to uniaxial pressure. For a different geometry we expect qualitatively similar results, but with a different stripe periodicity, which is 2 μm in the present scenario.

A.3.5 Conclusions

To conclude, we achieved a comprehensive understanding of the spatial evolution of the charge order metal-insulator transition in α -(BEDT-TTF)₂I₃. For a homogeneous single crystal it reveals a sharp transition and we detect only one phase boundary that, most likely, originates from a small thermal gradient ($\Delta T/\Delta x \approx 5$ K/mm) on the sample. Thus, the first-order nature of the charge order transition in α -(BEDT-TTF)₂I₃ is unequivocally demonstrated, as indicated in Fig. A.3.5 (a) and (d). A clamped specimen subject to multiple cracking exhibits qualitatively different behaviour. We observe a spatially inhomogeneous suppression of the metal-insulator transition towards lower temperatures originating from a local modulation of the

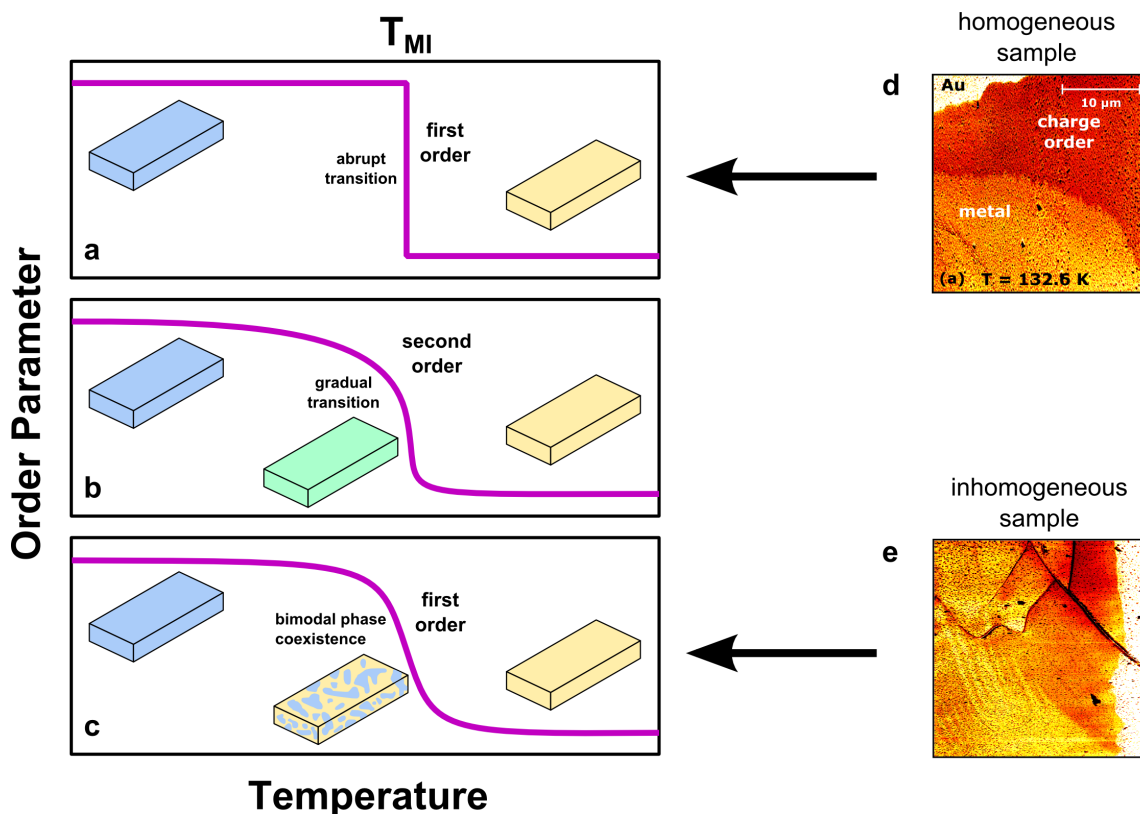


Figure A.3.5: Possible scenarios of metal-insulator transitions in solids. A general distinction can be made between abrupt first-order (a) and gradual, mean-field like second-order (b) phase transitions. (c) In case of a bimodal phase coexistence of an originally first-order transition the macroscopic order parameter looks very similar to the second-order scenario. Such a spatial phase separation may be the result of a non-uniform free energy modulation caused by internal strain or defects. (d) The homogeneous α -(BEDT-TTF) $_2$ I $_3$ single crystal investigated in this study showed a distinct phase boundary that follows the temperature gradient on the sample. Upon proper thermalization, the macroscopic transition happens instantaneously (few 100 mK) on the entire crystal, reminiscent of the situation in (a). (e) Different behaviour is found for a highly inhomogeneous sample where internal strain spatially modulates the electronic correlations, resulting in a phase coexistence over more than 5 K with a complex stripe pattern of the phase boundary. Macroscopic measurement quantities would observe a strongly broadened transition like in panel (c), inhibiting an a priori assignment of the first-order nature of the phase transition.

strain within a single segment, which acts like physical pressure. Thus, strain is relieved in the regions close to the segment boundary, i.e. the crack, whereas effective pressure is largest in the center. As a result, the metallic phase persists well below the nominal transition temperature ($\Delta T_{CO} \geq 6$ K) corresponding to uniaxial pressure around 0.5 kbar applied along b . The material reacts to this external stimulus and minimizes the Landau free energy by forming stripes perpendicular to the direction of

strain. Thus, the local probe allows us to directly monitor the inhomogeneous first-order phase transition which would show up as a broad crossover (Fig. A.3.5 c) in a bulk measurement, reminiscent of a second-order transition (panel b). In this regard, we demonstrate how powerful near-field optical microscopy can resolve the interplay of metallic and insulating phases of correlated electron systems, especially at low temperatures. In principle, this method is not limited to the opening of a spectral gap, but can be applied in a similar way to phonons and other characteristic features that exhibit pronounced changes in the optical conductivity. Further experiments on the charge-sensitive vibrations in α -(BEDT-TTF)₂I₃ are under way.

B. Acknowledgments

Finally, it is time to thank all the people who supported me during my four years at the 1. Physikalisches Institut.

- First of all I would like to thank my supervisor Prof. Dressel. Our (almost) daily discussions were very helpful to guide me through the doctorate and understand the experimental results. I am also grateful for your support and counselling towards initiating my scientific career and I am sure that – even after publishing the last of the dozen pending manuscripts – we will continue collaborating in future.
- I also would like to thank Prof. Takagi for agreeing to co-referee this work. Thank you also for your nice lecture on correlated electron systems in the winter term 2014/15. It deepened my understanding of electronic correlations.
- Similarly, I would like to thank Prof. Dobrosavljević for co-refereeing this thesis remotely from Florida. Apart from that, I appreciate your direct requests and criticism as well as your continuous search for the scientific truth, which became rare in times of glossy journals and coherent spinons.
- Simone Fratini was one of the main contributors to this work, particularly in working out the bandwidth rescaling approach. Conversations with you helped me a lot to grasp the relevant Mott physics and, besides that, the time in Corsica was great fun. Grazie mille!
- I would like to thank Sina Zapf and Tomislav Ivek, who introduced me to the lab and gave me guidance in the first year of my PhD work. I'm wondering who will be the next one to take my part as the *Küken*.
- I would like to point out support by Gabi Untereiner who manipulates samples like nobody else. I don't want to imagine how many samples I would have destroyed without your help. Thank you!

- I also thank Agni Schmidt for keeping the institute running by outstanding administrative work.

I also want to acknowledge all collaborators, people who provided samples and those who supported my work:

- At this point, I would like to thank Silvia Tomić with whom we are collaborating closely on diverse projects. I acknowledge your critical review which helped a lot to improve our manuscripts.
- I would like to thank Dmitri Basov and Alex McLeod for enabling my research visits at UCSD. It was a pleasure to visit San Diego and enjoy the pleasant weather in December 2015 and 2016, especially when returning with such a nice set of data.
- Many thanks to Elena Zhukova and Boris Gorshunov for continuous advice and performing THz experiments in Moscow and Stuttgart.
- I'm very happy about our collaboration with Roser Valentí, Ying Li and Igor Mazin, who did a great job to model our experimental results on Herbertsmithite. Roser is continuously posing relevant questions, which pushes frontiers forward and allows us to reconsider and improve our own ideas.
- I would like to thank Takaaki Hiramatsu, Yukihiro Yoshida and Gunzi Saito for providing the κ -(BEDT-TTF)₂Ag₂(CN)₃ samples.
- Similarly, I would like to thank John Schlueter for providing single crystals of κ -(BEDT-TTF)₂Cu₂(CN)₃ and β'' -(BEDT-TTF)₂SF₅RSO₃.
- I would like to thank Reizo Kato for providing β' -EtMe₃Sb[Pd(dmit)₂]₂.
- Many thanks to Yoshihiko Ihara and Atsushi Kawamoto for providing β'' -(BEDT-TTF)₄[(H₃O)Ga(C₂O₄)₃]·C₆H₅NO₂ samples and discussing the results with me.
- Anja Löhle and Ralph Hübner, thank you for growing κ -(BEDT-TTF)₂Cu₂(CN)₃ and κ -(BEDT-TTF)₂Ag₂(CN)₃ samples and discussing structural details.
- Thanks also to Pascal Puphal and Cornelius Krellner for providing Herbertsmithite and Y₃Cu₉(OH)₁₉Cl₈ single crystals.

I want also to thank the people who supported and accompanied me over the years at the institute.

- I would like to thank the entire IR-team for the nice working atmosphere and continuous support.
- My most positive memories at the institute I connect with Anja. Thank you not only for the experimental stuff (see above) but, much more important, for all the fun time. If I had to share the bed with a colleague again, you know whom I would choose.
- Many thanks to our institute daddies David(off) and Tobi, who are great experts in the lab and now in industry. I had always lots of fun with you – in many languages using the *relevant words*.
- Li brother, nobody was as mot(t)ivated as you. Your perpetual interest and critical questions were enormously helpful. Xiexie han da!
- Since my first day at the institute it was always great fun with Micha. As soon as you entered the room, conversations became *informal* instantaneously. Although many memories of that infamous Söllerhaus weekend remain tangled, our *Ehrenrunde* was legen–DARY!
- Yohei kun, it was a pleasure to work with you. Thanks for introducing me to the Japanese language and way of life – ranging from food towards the onsen. Arigatou gozai mas! Saitamaa!
- Ievgen, it was very nice to practice Russian with you on a daily basis and also ping-pong was a good thing to relax after spending too much time in the lab. I'll never forget our travels to transfer a highly valuable cargo – the Bruker 66 spectrometer – in the luggage compartment to Ettlingen.
- I also appreciated Russian conversations with Artem, with whom I also discussed intensely the physics of correlated metals.
- Last but not least, many thanks to Andrea, or how I used to call you, *Mrs. Rohwer*. I appreciated your plant watering service and all our lunch discussions about life in South Africa. All the best with your experiments; I'm highly interested in your results.

- I would like to thank all my Bachelor and Master students: Lena, Kevin, Miriam, Mathias and Tobias. Thank you for all your requests which made me think and, most importantly, your contributions to this work. I hope I could provide you some useful input for your future life.
- Certainly, *non-work-related evening activities* with Roland, Stefano, Olga, Marian and my favourite *Kellerkinder* Desirée, Markus and Björn, as well as many of the above mentioned people were a good counterpart to office and lab time. I enjoyed it a lot; hopefully we can repeat this once in a while also after having left the PI1.
- Thanks also to all the other people of the institute for many on- and off-topic conversations over the years and the nice working atmosphere (ladies first, of course): Annika, Rebecca, Helga, Audrey, Marc, Bruno, Guilherme, Mamoun, Nikolaj, Sascha, Richard, Mojtaba, Shuai, Conrad and, finally, Eric *der Wikinger*; and of course all whom I might have forgotten to mention here. Thank you!

Finally, I would like to thank my parents for supporting me since my very first day on earth in achieving my goals, which I was always free to choose without any economical or educational limitations. Many thanks also to my sister who understands my thoughts in all situations and, thus, always provides me mental support if needed. Now she is giving me a great example of growing up her son Lorian together with Dima. Also my grandparents are very important persons for me; they support (*ed*) all my decisions and always make me feel home, wherever in Europe. Meeting my cousins, aunts and uncles is everytime connected with a nice time. Of course, I would like to thank all my friends for continuously having a nice time and a lot of fun, either at parties, when running through the woods, defending the football pitch against other children (*Otk: Gewinner bleibt am Platz!*), playing chess and other board games, or simply via conversations ranging over the entire spectrum from scientific towards lowermost levels. Last but not least, I am very happy to have Sarah in my life. Although we have highly different backgrounds, you accept me as I am and supported me a lot throughout the last three years. While many people mentioned above assisted me in the lab, you helped me by distracting me from work, which is even more important than getting nice results! Thank you a lot!

Bibliography

1. Mott, N. F. *Metal-Insulator Transitions* 2nd ed. (Taylor Francis Ltd., Bristol, 1990).
2. Gebhard, F. *The Mott Metal-Insulator Transition: Models and Methods* (Springer Berlin Heidelberg, Berlin, Heidelberg, 1997).
3. Zhou, Y., Kanoda, K. & Ng, T.-K. Quantum spin liquid states. *Reviews of Modern Physics* **89**, 25003 (2017).
4. Terletska, H., Vucicević, J., Tanasković, D. & Dobrosavljević, V. Quantum Critical Transport near the Mott Transition. *Physical Review Letters* **107**, 26401 (2011).
5. Vucicević, J., Terletska, H., Tanasković, D. & Dobrosavljević, V. Finite-temperature crossover and the quantum Widom line near the Mott transition. *Physical Review B* **88**, 75143 (2013).
6. Xu, L., Kumar, P., Buldyrev, S. V., Chen, S.-H., Poole, P. H., Sciortino, F & Stanley, H. E. Relation between the Widom line and the dynamic crossover in systems with a liquid-liquid phase transition. *Proceedings of the National Academy of Sciences of the United States of America* **102**, 16558–16562 (2005).
7. Simeoni, G. G., Bryk, T, Gorelli, F. A., Krisch, M, Ruocco, G, Santoro, M & Scopigno, T. The Widom line as the crossover between liquid-like and gas-like behaviour in supercritical fluids. *Nature Physics* **6**, 503–507 (2010).
8. Sordi, G., Sémon, P., Haule, K. & Tremblay, A.-M. S. Pseudogap temperature as a Widom line in doped Mott insulators. *Scientific Reports* **2**, 547 (2012).
9. Sordi, G., Sémon, P., Haule, K. & Tremblay, A.-M. S. c-axis resistivity, pseudogap, superconductivity and Widom line in doped Mott insulators. *Physical Review B* **87**, 41101 (2013).
10. Richardson, R. C. The Pomeranchuk effect. *Reviews of Modern Physics* **69**, 683–690 (1997).

11. Powell, B. J. & McKenzie, R. H. Quantum frustration in organic Mott insulators: from spin liquids to unconventional superconductors. *Reports on Progress in Physics* **74**, 56501 (2011).
12. Hotta, C. *Theories on Frustrated Electrons in Two-Dimensional Organic Solids* 2012.
13. Pustogow, A., Bories, M., Löhle, A., Rösslhuber, R., Zhukova, E., Gorshunov, B., Tomic, S., Schlueter, J. A., Hübner, R., Hiramatsu, T., Yoshida, Y., Saito, G., Kato, R., Lee, T.-H., Dobrosavljevic, V., Fratini, S. & Dressel, M. Quantum Spin Liquids Unveil the Genuine Mott State. *under review*. arXiv: [1710.07241](https://arxiv.org/abs/1710.07241) (2017).
14. Furukawa, T., Miyagawa, K., Taniguchi, H., Kato, R. & Kanoda, K. Quantum criticality of Mott transition in organic materials. *Nature Physics* **11**, 221–224 (2015).
15. Shimizu, Y., Hiramatsu, T., Maesato, M., Otsuka, A., Yamochi, H., Ono, A., Itoh, M., Yoshida, M., Takigawa, M., Yoshida, Y. & Saito, G. Pressure-Tuned Exchange Coupling of a Quantum Spin Liquid in the Molecular Triangular Lattice κ -(ET)₂Ag₂(CN)₃. *Physical Review Letters* **117**, 107203 (2016).
16. Kézsmárki, I., Shimizu, Y., Mihály, G., Tokura, Y., Kanoda, K. & Saito, G. Depressed charge gap in the triangular-lattice Mott insulator κ -(ET)₂Cu₂(CN)₃. *Physical Review B* **74**, 201101 (2006).
17. Elsässer, S., Wu, D., Dressel, M. & Schlueter, J. A. Power-law dependence of the optical conductivity observed in the quantum spin-liquid compound κ -(BEDT-TTF)₂Cu₂(CN)₃. *Physical Review B* **86**, 155150 (2012).
18. Ng, T.-K. & Lee, P. A. Power-Law Conductivity inside the Mott Gap: Application to κ -(BEDT-TTF)₂Cu₂(CN)₃. *Physical Review Letters* **99**, 156402 (2007).
19. Senthil, T. Theory of a continuous Mott transition in two dimensions. *Physical Review B* **78**, 45109 (2008).
20. Lee, T.-H., Florens, S. & Dobrosavljević, V. Fate of Spinons at the Mott Point. *Physical Review Letters* **117**, 136601 (2016).
21. Faltermeier, D., Barz, J., Dumm, M., Dressel, M., Drichko, N., Petrov, B., Semkin, V., Vlasova, R., Mezière, C. & Batail, P. Bandwidth-controlled Mott transition in κ -(BEDT-TTF)₂Cu[N(CN)₂]Br_xCl_{1-x}: Optical studies o. *Physical Review B* **76**, 165113 (2007).

-
22. Dumm, M., Faltermeier, D., Drichko, N., Dressel, M., Mézière, C. & Batail, P. Bandwidth-controlled Mott transition in κ -(BEDT-TTF)₂Cu[N(CN)₂]Br_xCl_{1-x}: Optical studies of correlated carriers. *Physical Review B* **79**, 195106 (2009).
 23. Yasin, S., Dumm, M., Salameh, B., Batail, P., Mézière, C. & Dressel, M. Transport studies at the Mott transition of the two-dimensional organic metal κ -(BEDT-TTF)₂Cu[N(CN)₂]Br_xCl_{1-x}. *The European Physical Journal B* **79**, 383–390 (2011).
 24. Qazilbash, M. M., Schafgans, A. A., Burch, K. S., Yun, S. J., Chae, B. G., Kim, B. J., Kim, H. T. & Basov, D. N. Electrodynamics of the vanadium oxides VO₂ and V₂O₃. *Physical Review B* **77**, 115121 (2008).
 25. Perucchi, A., Baldassarre, L., Postorino, P. & Lupi, S. Optical properties across the insulator to metal transitions in vanadium oxide compounds. *Journal of Physics: Condensed Matter* **21**, 323202 (2009).
 26. Lo Vecchio, I., Baldassarre, L., D’Apuzzo, F., Lima, O., Nicoletti, D., Perucchi, A., Fan, L., Metcalf, P., Marsi, M. & Lupi, S. Optical properties of V₂O₃ in its whole phase diagram. *Physical Review B* **91**, 155133 (2015).
 27. Limelette, P., Georges, A., Jérôme, D., Wzietek, P., Metcalf, P. & Honig, J. M. Universality and Critical Behavior at the Mott Transition. *Science* **302**, 89 – 92 (2003).
 28. Berthod, C., Mravlje, J., Deng, X., Zitko, R., van der Marel, D. & Georges, A. Non-Drude universal scaling laws for the optical response of local Fermi liquids. *Physical Review B* **87**, 115109 (2013).
 29. Maslov, D. L. & Chubukov, A. V. Optical response of correlated electron systems. *Reports on Progress in Physics* **80**, 026503 (2017).
 30. Jacko, A. C., Fjærrestad, J. O. & Powell, B. J. A unified explanation of the Kadowaki-Woods ratio in strongly correlated metals. *Nature Physics* **5**, 422–425 (2009).
 31. Deng, X., Mravlje, J., Zitko, R., Ferrero, M., Kotliar, G. & Georges, A. How Bad Metals Turn Good: Spectroscopic Signatures of Resilient Quasiparticles. *Physical Review Letters* **110**, 86401 (2013).
 32. Hussey, N. E., Takenaka, K. & Takagi, H. Universality of the Mott-Ioffe-Regel limit in metals. *Philosophical Magazine* **84**, 2847–2864 (2004).
-

33. Merino, J. & McKenzie, R. H. Superconductivity Mediated by Charge Fluctuations in Layered Molecular Crystals. *Physical Review Letters* **87**, 237002 (2001).
34. Bangura, A. F., Coldea, A. I., Singleton, J., Ardavan, A., Akutsu-Sato, A., Akutsu, H., Turner, S. S., Day, P., Yamamoto, T & Yakushi, K. Robust superconducting state in the low-quasiparticle-density organic metals β'' -(BEDT-TTF)₄[(H₃O)M(C₂O₄)]. *Physical Review B* **72**, 14543 (2005).
35. Drichko, N., Dressel, M., Kuntscher, C., Pashkin, A., Greco, A., Merino, J. & Schlueter, J. Electronic properties of correlated metals in the vicinity of a charge-order transition: Optical spectroscopy of α -(BEDT-TTF)₂MHg(SCN)₄ (M=NH₄, Rb, Tl). *Physical Review B* **74**, 235121 (2006).
36. Drichko, N., Kaiser, S., Sun, Y., Clauss, C., Dressel, M., Mori, H., Schlueter, J., Zhylyayeva, E. I., Torunova, S. A. & Lyubovskaya, R. N. Evidence for charge order in organic superconductors obtained by vibrational spectroscopy. *Physica B: Condensed Matter* **404**, 490–493 (2009).
37. Kaiser, S., Dressel, M., Sun, Y., Greco, A., Schlueter, J. A., Gard, G. L. & Drichko, N. Bandwidth Tuning Triggers Interplay of Charge Order and Superconductivity in Two-Dimensional Organic Materials. *Physical Review Letters* **105**, 206402 (2010).
38. Girlando, A., Masino, M., Schlueter, J. A., Drichko, N., Kaiser, S. & Dressel, M. Charge-order fluctuations and superconductivity in two-dimensional organic metals. *Physical Review B* **89**, 174503 (2014).
39. Ward, B. H., Schlueter, J. A., Geiser, U., Wang, H. H., Morales, E., Parakka, J. P., Thomas, S. Y., Williams, J. M., Nixon, P. G., Winter, R. W., Gard, G. L., Koo, H.-J. & Whangbo, M.-H. Comparison of the Crystal and Electronic Structures of Three 2:1 Salts of the Organic Donor Molecule BEDT-TTF with Pentafluorothiometylsulfonate Anions SF₅CH₂SO₃⁻, SF₅CHFSO₃⁻, and SF₅CF₂SO₃⁻. *Chemistry of Materials* **12**, 343–351 (2000).
40. Schlueter, J. A., Ward, B. H., Geiser, U., Wang, H. H., Kini, A. M., Parakka, J., Morales, E., Koo, H.-J., Whangbo, M.-H., Winter, R. W., Mohtasham, J & Gard, G. L. Crystal structure, physical properties and electronic structure of a new organic conductor β'' -(BEDT-TTF)₂SF₅CHF₂SO₃. *Journal of Materials Chemistry* **11**, 2008–2013 (2001).

41. Hagel, J., Wosnitza, J., Pfeleiderer, C., Schlueter, J. A., Mohtasham, J. & Gard, G. L. Pressure-induced insulating state in an organic superconductor. *Physical Review B* **68**, 104504 (2003).
42. Anderson, P. W. More Is Different. *Science* **177**, 393 LP –396 (1972).
43. Edwards, P. P. & Rao, C. N. R. *Metal-Insulator Transitions Revised* (Taylor Francis, Bristol, 1995).
44. Imada, M., Fujimori, A. & Tokura, Y. Metal-insulator transitions. *Reviews of Modern Physics* **70**, 1039–1263 (1998).
45. Basov, D. N., Averitt, R. D., van der Marel, D., Dressel, M. & Haule, K. Electrodynamics of correlated electron materials. *Reviews of Modern Physics* **83**, 471–541 (2011).
46. Keimer, B., Kivelson, S. A., Norman, M. R., Uchida, S. & Zaanen, J. From quantum matter to high-temperature superconductivity in copper oxides. *Nature* **518**, 179–186 (2015).
47. Olalde-Velasco, P., Jiménez-Mier, J., Denlinger, J. D., Hussain, Z. & Yang, W. L. Direct probe of Mott-Hubbard to charge-transfer insulator transition and electronic structure evolution in transition-metal systems. *Physical Review B* **83**, 241102 (2011).
48. Pustogow, A., Li, Y., Voloshenko, I., Puphal, P., Krellner, C., Mazin, I. I., Dressel, M. & Valentí, R. Nature of optical excitations in the frustrated kagome compound Herbertsmithite. *Physical Review B* **xx**, xxxxxx(R) (in press).
49. Yamamoto, T., Uruichi, M., Yamamoto, K., Yakushi, K., Kawamoto, A. & Taniguchi, H. Examination of the Charge-Sensitive Vibrational Modes in Bis(ethylenedithio)tetrathiafulvalene. *The Journal of Physical Chemistry B* **109**, 15226–15235 (2005).
50. Girlando, A. Charge Sensitive Vibrations and Electron-Molecular Vibration Coupling in Bis(ethylenedithio)-tetrathiafulvalene (BEDT-TTF). *The Journal of Physical Chemistry C* **115**, 19371–19378 (2011).
51. Pustogow, A., Peterseim, T., Kolatschek, S., Engel, L. & Dressel, M. Electronic correlations versus lattice interactions: Interplay of charge and anion orders in (TMTTF)₂X. *Physical Review B* **94**, 195125 (2016).
52. Mori, H. Materials Viewpoint of Organic Superconductors. *Journal of the Physical Society of Japan* **75**, 51003 (2006).

53. Dressel, M. & Grüner, G. *Electrodynamics of Solids: Optical Properties of Electrons in Matter* (Cambridge University Press, Cambridge, 2002).
54. Steglich, F., Aarts, J., Breidl, C. D., Lieke, W., Meschede, D., Franz, W. & Schäfer, H. Superconductivity in the Presence of Strong Pauli Paramagnetism: CeCu_2Si_2 . *Physical Review Letters* **43**, 1892–1896 (1979).
55. Scheffler, M., Dressel, M., Jourdan, M. & Adrian, H. Extremely slow Drude relaxation of correlated electrons. *Nature* **438**, 1135–1137 (2005).
56. Kittel, C. *Introduction to Solid State Physics* 8th ed., 407–409 (John Wiley and Sons, Inc, 2005).
57. Hunklinger, S. *Festkörperphysik* 2nd ed. (Oldenbourg Wissenschaftsverlag GmbH, München, 2009).
58. Mott, N. F. & Davis, E. A. *Electronic Processes in Non-Crystalline Materials* 2nd ed. (Clarendon Press, Oxford, 1979).
59. Fano, U. Effects of Configuration Interaction on Intensities and Phase Shifts. *Physical Review* **124**, 1866–1878 (1961).
60. Damascelli, A., Schulte, K., van der Marel, D. & Menovsky, A. A. Infrared spectroscopic study of phonons coupled to charge excitations in FeSi. *Physical Review B* **55**, R4863–R4866 (1997).
61. Andres, K., Graebner, J. E. & Ott, H. R. $4f$ -Virtual-Bound-State Formation in CeAl_3 at Low Temperatures. *Physical Review Letters* **35**, 1779–1782 (1975).
62. De Visser, A., Franse, J. J. M. & Menovsky, A. A. Resistivity of single-crystalline UPt3 and its pressure dependence; Interpretation by a spin-fluctuation model. *Journal of Magnetism and Magnetic Materials* **43**, 43–47 (1984).
63. Palstra, T. T. M., Menovsky, A. A. & Mydosh, J. A. Anisotropic electrical resistivity of the magnetic heavy-fermion superconductor URu_2Si_2 . *Physical Review B* **33**, 6527–6530 (1986).
64. Gunnarsson, O., Calandra, M. & Han, J. E. Colloquium: Saturation of electrical resistivity. *Reviews of Modern Physics* **75**, 1085–1099 (2003).
65. Takenaka, K., Tamura, M., Tajima, N., Takagi, H., Nohara, J. & Sugai, S. Collapse of Coherent Quasiparticle States in θ - $(\text{BEDT-TTF})_2\text{I}_3$ Observed by Optical Spectroscopy. *Phys. Rev. Lett.* **95**, 227801 (2005).
66. Emery, V. J. & Kivelson, S. A. Superconductivity in Bad Metals. *Physical Review Letters* **74**, 3253–3256 (1995).

-
67. Bruin, J. A. N., Sakai, H., Perry, R. S. & Mackenzie, A. P. Similarity of Scattering Rates in Metals Showing T -Linear Resistivity. *Science* **339**, 804–807 (2013).
 68. Hartnoll, S. A. Theory of universal incoherent metallic transport. *Nature Physics* **11**, 54–61 (2015).
 69. Pines, D. & Nozières, P. *The Theory of Quantum Liquids - Normal Fermi Liquids* (Addison-Wesley, Redwood City, Calif., 1989).
 70. Gurzhi, R. Mutual Electron Correlations in Metal Optics. *Journal of Experimental and Theoretical Physics* **8**, 673 (1959).
 71. Stricker, D., Mravlje, J., Berthod, C., Fittipaldi, R., Vecchione, A., Georges, A. & van der Marel, D. Optical Response of Sr_2RuO_4 Reveals Universal Fermi-Liquid Scaling and Quasiparticles Beyond Landau Theory. *Physical Review Letters* **113**, 87404 (2014).
 72. Rischau, C. W., Lin, X., Grams, C. P., Finck, D., Harms, S., Engelmayer, J., Lorenz, T., Gallais, Y., Fauque, B., Hemberger, J. & Behnia, K. A ferroelectric quantum phase transition inside the superconducting dome of $\text{Sr}_{1-x}\text{Ca}_x\text{TiO}_{3-\delta}$. *Nature Physics* **13**, 643–648 (2017).
 73. Hamo, A., Benyamini, A., Shapir, I., Khivrich, I., Waissman, J., Kaasbjerg, K., Oreg, Y., von Oppen, F. & Ilani, S. Electron attraction mediated by Coulomb repulsion. *Nature* **535**, 395–400 (2016).
 74. Fratini, S & Ciuchi, S. Spectral properties and isotope effect in strongly interacting systems: Mott-Hubbard insulator versus polaronic semiconductor. *Physical Review B* **72**, 235107 (2005).
 75. Wark, K. *Thermodynamics* 5th ed. (McGraw-Hill, New York, 1988).
 76. Shimizu, Y., Miyagawa, K., Kanoda, K., Maesato, M. & Saito, G. Spin Liquid State in an Organic Mott Insulator with a Triangular Lattice. *Physical Review Letters* **91**, 107001 (2003).
 77. Shores, M. P., Nytko, E. A., Bartlett, B. M. & Nocera, D. G. A structurally perfect $S = (1/2)$ kagomé antiferromagnet. *Journal of the American Chemical Society* **127**, 13462–3 (2005).
 78. Shimizu, Y., Miyagawa, K., Kanoda, K., Maesato, M. & Saito, G. Emergence of inhomogeneous moments from spin liquid in the triangular-lattice Mott insulator $\kappa\text{-(ET)}_2\text{Cu}_2(\text{CN})_3$. *Physical Review B* **73**, 140407 (2006).
-

79. Mendels, P. & Bert, F. Quantum Kagome Antiferromagnet $\text{ZnCu}_3(\text{OH})_6\text{Cl}_2$. *Journal of the Physical Society of Japan* **79**, 11001 (2010).
80. Sun, W., Huang, Y.-X., Nokhrin, S., Pan, Y., Mi, J.-X., Mendels, P., Wills, A. S., Mi, J. X., Amato, A., van Tol, J., Ozarowski, A., Wills, A. S., Mendels, P. & Wills, A. S. Perfect Kagomé lattices in $\text{YCu}_3(\text{OH})_6\text{Cl}_3$: a new candidate for the quantum spin liquid state. *J. Mater. Chem. C* **4**, 8772–8777 (2016).
81. Norman, M. R. *Colloquium*: Herbertsmithite and the search for the quantum spin liquid. *Reviews of Modern Physics* **88**, 041002 (2016).
82. Puphal, P., Bolte, M., Sheptyakov, D., Pustogow, A., Kliemt, K., Dressel, M., Baenitz, M. & Krellner, C. Strong magnetic frustration in $\text{Y}_3\text{Cu}_9(\text{OH})_{19}\text{Cl}_8$: a distorted kagome antiferromagnet. *Journal of Materials Chemistry C* **5**, 2629–2635 (2017).
83. Anderson, P. W. Resonating valence bonds: A new kind of insulator? *Materials Research Bulletin* **8**, 153–160 (1973).
84. Anderson, P. W. The Resonating Valence Bond State in La_2CuO_4 and Superconductivity. *Science* **235**, 1196–1198 (1987).
85. Lee, P. A. An End to the Drought of Quantum Spin Liquids. *Science* **321**, 1306–1307 (2008).
86. Balents, L. Spin liquids in frustrated magnets. *Nature* **464**, 199–208 (2010).
87. Savary, L. & Balents, L. Quantum spin liquids: a review. *Reports on Progress in Physics* **80**, 016502 (2017).
88. Cano-Cortés, L., Merino, J. & Fratini, S. Quantum Critical Behavior of Electrons at the Edge of Charge Order. *Phys. Rev. Lett.* **105**, 36405 (2010).
89. Lefebvre, S., Wzietek, P., Brown, S., Bourbonnais, C., Jérôme, D., Mézière, C., Fourmigué, M. & Batail, P. Mott transition, antiferromagnetism, and unconventional superconductivity in layered organic superconductors. *Physical review letters* **85**, 5420–5423 (2000).
90. Vuletić, T., Héritier, M., Jérôme, D., Pasquier, C., Tomić, S., Bechgaard, K. & Auban-Senzier, P. Coexistence of superconductivity and spin density wave orderings in the organic superconductor $(\text{TMTSF})_2\text{PF}_6$. *The European Physical Journal B* **25**, 319–331 (2002).

-
91. Gati, E., Garst, M., Manna, R. S., Tutsch, U., Wolf, B., Bartosch, L., Schubert, H., Sasaki, T., Schlueter, J. A. & Lang, M. Breakdown of Hooke's law of elasticity at the Mott critical endpoint in an organic conductor. *Science Advances* **2**, e1601646 (2016).
 92. Uji, S., Terashima, T., Nishimura, M., Takahide, Y., Konoike, T., Enomoto, K., Cui, H., Kobayashi, H., Kobayashi, A., Tanaka, H., Tokumoto, M., Choi, E. S., Tokumoto, T., Graf, D. & Brooks, J. S. Vortex Dynamics and the Fulde-Ferrell-Larkin-Ovchinnikov State in a Magnetic-Field-Induced Organic Superconductor. *Physical Review Letters* **97**, 157001 (2006).
 93. Bergk, B., Demuer, A., Sheikin, I., Wang, Y., Wosnitza, J., Nakazawa, Y. & Lortz, R. Magnetic torque evidence for the Fulde-Ferrell-Larkin-Ovchinnikov state in the layered organic superconductor $\kappa - (\text{BEDT} - \text{TTF})_2\text{Cu}(\text{NCS})_2$. *Physical Review B* **83**, 64506 (2011).
 94. Coniglio, W. A., Winter, L. E., Cho, K., Agosta, C. C, Fravel, B & Montgomery, L. K. Superconducting phase diagram and FFLO signature in $\lambda - (\text{BETS})_2\text{GaCl}_4$ from rf penetration depth measurements. *Physical Review B* **83**, 224507 (2011).
 95. Agosta, C. C., Jin, J., Coniglio, W. A., Smith, B. E., Cho, K, Stroe, I, Martin, C, Tozer, S. W., Murphy, T. P., Palm, E. C., Schlueter, J. A. & Kurmoo, M. Experimental and semiempirical method to determine the Pauli-limiting field in quasi-two-dimensional superconductors as applied to $\kappa - (\text{BEDT} - \text{TTF})_2\text{Cu}(\text{NCS})_2$: Strong evidence of a FFLO state. *Physical Review B* **85**, 214514 (2012).
 96. Beyer, R., Bergk, B., Yasin, S., Schlueter, J. A. & Wosnitza, J. Angle-Dependent Evolution of the Fulde-Ferrell-Larkin-Ovchinnikov State in an Organic Superconductor. *Physical Review Letters* **109**, 27003 (2012).
 97. Mayaffre, H, Kramer, S, Horvatic, M, Berthier, C, Miyagawa, K, Kanoda, K & Mitrovic, V. F. Evidence of Andreev bound states as a hallmark of the FFLO phase in $\kappa - (\text{BEDT} - \text{TTF})_2\text{Cu}(\text{NCS})_2$. *Nature Physics* **10**, 928–932 (2014).
 98. Koutroulakis, G., Kühne, H., Schlueter, J. A., Wosnitza, J. & Brown, S. E. Microscopic Study of the Fulde-Ferrell-Larkin-Ovchinnikov State in an All-Organic Superconductor. *Physical Review Letters* **116**, 67003 (2016).
 99. Suda, M., Kato, R. & Yamamoto, H. M. Light-induced superconductivity using a photoactive electric double layer. *Science* **347**, 743–746 (2015).
-

100. Singla, R., Cotugno, G., Kaiser, S., Först, M., Mitrano, M., Liu, H. Y., Cartella, A., Manzoni, C., Okamoto, H., Hasegawa, T., Clark, S. R., Jaksch, D. & Cavalleri, A. THz-Frequency Modulation of the Hubbard U in an Organic Mott Insulator. *Physical Review Letters* **115**, 187401 (2015).
101. Sedlmeier, K., Elsässer, S., Neubauer, D., Beyer, R., Wu, D., Ivek, T., Tomić, S., Schlueter, J. A. & Dressel, M. Absence of charge order in the dimerized κ -phase BEDT-TTF salts. *Physical Review B* **86**, 245103 (2012).
102. Takabayashi, Y., Ganin, A. Y., Jeglic, P., Arcon, D., Takano, T., Iwasa, Y., Ohishi, Y., Takata, M., Takeshita, N., Prassides, K. & Rosseinsky, M. J. The Disorder-Free Non-BCS Superconductor Cs_3C_60 Emerges from an Antiferromagnetic Insulator Parent State. *Science* **323**, 1585–1590 (2009).
103. Dressel, M. Spin-charge separation in quasi one-dimensional organic conductors. *Die Naturwissenschaften* **90**, 337–44 (2003).
104. Holczer, K., Klein, O., Huang, S.-m., Kaner, R. B., Fu, K.-j., Whetten, R. L. & Diederich, F. Alkali-Fulleride Superconductors: Synthesis, Composition, and Diamagnetic Shielding. *Science* **252**, 1154–1157 (1991).
105. Limelette, P., Wzietek, P., Florens, S., Georges, A., Costi, T. A., Pasquier, C., Jérôme, D., Mézière, C & Batail, P. Mott Transition and Transport Crossovers in the Organic Compound κ -(BEDT-TTF) $_2$ Cu[N(CN) $_2$]Cl. *Physical Review Letters* **91**, 16401 (2003).
106. Alloul, H., Wzietek, P., Mito, T., Pontiroli, D., Aramini, M., Riccò, M., Itie, J. P. & Elkaim, E. Mott Transition in the A15 Phase of Cs_3C_{60} : Absence of a Pseudogap and Charge Order. *Physical Review Letters* **118**, 237601 (2017).
107. Mitrano, M., Cantaluppi, A., Nicoletti, D., Kaiser, S., Perucchi, A., Lupi, S., Di Pietro, P., Pontiroli, D., Riccò, M., Clark, S. R., Jaksch, D. & Cavalleri, A. Possible light-induced superconductivity in K_3C_{60} at high temperature. *Nature* **530**, 461–464 (2016).
108. Dengl, A. *Infrarot-Untersuchungen der elektronischen Ordnung organischer Metalle unter Druck* (1. Physikalisches Institut, Uni Stuttgart, Stuttgart, 2013).
109. Kozlov, M., Pokhodnia, K. & Yurchenko, A. The assignment of fundamental vibrations of BEDT-TTF and BEDT-TTF-d8. *Spectrochimica Acta Part A: Molecular Spectroscopy* **43**, 323–329 (1987).

110. Kozlov, M. E., Pokhodnia, K. I. & Yurchenko, A. A. Electron molecular vibration coupling in vibrational spectra of BEDT-TTF based radical cation salts. *Spectrochimica Acta Part A: Molecular Spectroscopy* **45**, 437–444 (1989).
111. Eldridge, J. E., Homes, C. C., Williams, J. M., Kini, A. M. & Wang, H. H. The assignment of the normal modes of the BEDT-TTF electron-donor molecule using the infrared and Raman spectra of several isotopic analogs. *Spectrochimica Acta Part A: Molecular and Biomolecular Spectroscopy* **51**, 947–960 (1995).
112. Demiralp, E. & Goddard, W. A. Vibrational Analysis and Isotope Shifts of BEDT-TTF Donor for Organic Superconductors. *The Journal of Physical Chemistry A* **102**, 2466–2471 (1998).
113. Dressel, M., Dumm, M., Knoblauch, T. & Masino, M. Comprehensive Optical Investigations of Charge Order in Organic Chain Compounds (TMTTF)₂X. en. *Crystals* **2**, 528–578 (2012).
114. Kato, R., Fukunaga, T., Yamamoto, H. M., Ueda, K. & Hengbo, C. Crystal structure and band parameters of mixed crystals derived from quantum spin liquid $\beta\text{-EtMe}_3\text{Sb}[\text{Pd}(\text{dmit})_2]_2$ (dmit = 1,3-dithiol-2-thione-4,5-dithiolate). *Physica Status Solidi (b)* **249**, 999–1003 (2012).
115. Kato, R. & Hengbo, C. *Cation Dependence of Crystal Structure and Band Parameters in a Series of Molecular Conductors, β' -(Cation)[Pd(dmit)₂]₂ (dmit = 1,3-dithiole-2-thione-4,5-dithiolate)* 2012.
116. Lee, S.-S. & Lee, P. A. U(1) Gauge Theory of the Hubbard Model: Spin Liquid States and Possible Application to κ -(BEDT-TTF)₂Cu₂(CN)₃. *Physical Review Letters* **95**, 36403 (2005).
117. Hiramatsu, T., Yoshida, Y., Saito, G., Otsuka, A., Yamochi, H., Maesato, M., Shimizu, Y., Ito, H., Nakamura, Y., Kishida, H., Watanabe, M. & Kumai, R. Design and Preparation of a Quantum Spin Liquid Candidate κ -(ET)₂Ag₂(CN)₃ Having a Nearby Superconductivity. *Bulletin of the Chemical Society of Japan* **90**, 1073–1082 (2017).
118. Kurosaki, Y., Shimizu, Y., Miyagawa, K., Kanoda, K. & Saito, G. Mott Transition from a Spin Liquid to a Fermi Liquid in the Spin-Frustrated Organic Conductor κ -(ET)₂Cu₂(CN)₃. *Physical Review Letters* **95**, 177001 (2005).

119. Pilon, D. V., Lui, C. H., Han, T. H., Shrekenhamer, D., Frenzel, A. J., Padilla, W. J., Lee, Y. S. & Gedik, N. Spin-Induced Optical Conductivity in the Spin-Liquid Candidate Herbertsmithite. *Physical Review Letters* **111**, 127401 (2013).
120. Kanoda, K. Recent progress in NMR studies on organic conductors. *Hyperfine Interactions* **104**, 235–249 (1997).
121. McKenzie, R. H. Similarities Between Organic and Cuprate Superconductors. *Science* **278**, 820–821 (1997).
122. Müller, J., Lang, M., Steglich, F., Schlueter, J. A., Kini, A. M. & Sasaki, T. Evidence for structural and electronic instabilities at intermediate temperatures in κ -(BEDT-TTF)₂X for X = Cu[N(CN)₂]Cl, Cu[N. *Physical Review B* **65**, 144521 (2002).
123. Dressel, M. Quantum criticality in organic conductors? Fermi liquid versus non-Fermi-liquid behaviour. *Journal of Physics: Condensed Matter* **23**, 293201 (2011).
124. Kawamoto, A., Miyagawa, K. & Kanoda, K. Deuterated κ -(BEDT-TTF)₂Cu [N(CN)₂]Br: A system on the border of the superconductor magnetic-insulator transition. *Physical Review B* **55**, 14140–14143 (1997).
125. Inokuchi, M., Tajima, H., Kobayashi, A., Ohta, T., Kuroda, H., Kato, R., Naito, T. & Kobayashi, H. Electrical and Optical Properties of α -(BETS)₂I₃ and α -(BEDT-STF)₂I₃. *Bulletin of the Chemical Society of Japan* **68**, 547–553 (1995).
126. Mori, H., Okano, T., Kamiya, M., Haemori, M., Suzuki, H., Tanaka, S., Tamura, M., Nishio, Y., Kajita, K., Kodani, M., Takimiya, K., Otsubo, T. & Moriyama, H. Control of electronic states by bandwidth and band filling in organic conductors. *Synthetic Metals* **120**, 979–980 (2001).
127. Merino, J., Greco, A., Drichko, N. & Dressel, M. Non-Fermi Liquid Behavior in Nearly Charge Ordered Layered Metals. *Physical Review Letters* **96**, 216402 (2006).
128. Kaiser, S., Yasin, S., Drichko, N., Dressel, M., Rõõm, T., Hübner, D., Nagel, U., Gard, G. L. & Schlueter, J. A. Optical investigations of the superconducting energy gap in β'' -(BEDT-TTF)₂SF₅CH₂CF₂SO₃. *Physica Status Solidi (b)* **249**, 985–990 (2012).

-
129. Drichko, N., Haas, P., Gorshunov, B., Schweitzer, D. & Dressel, M. Evidence of the superconducting energy gap in the optical spectra of $\alpha_t(\text{BEDT-TTF})_2\text{I}_3$. *Europhysics Letters* **59**, 774–778 (2002).
130. Wang, H. H., VanZile, M. L., Schlueter, J. A., Geiser, U., Kini, A. M., Sche, P. P., Koo, H.-J., Whangbo, M.-H., Nixon, P. G., Winter, R. W. & Gard, G. L. In-Plane ESR Microwave Conductivity Measurements and Electronic Band Structure Studies of the Organic Superconductor $\beta''\text{-(BEDT-TTF)}_2\text{SF}_5\text{CH}_2\text{-CF}_2\text{SO}_3$. *The Journal of Physical Chemistry B* **103**, 5493–5499 (1999).
131. Schlueter, J., Kini, A., Ward, B., Geiser, U., Wang, H., Mohtasham, J., Winter, R. & Gard, G. Universal inverse deuterium isotope effect on the T_c of BEDT-TTF-based molecular superconductors. *Physica C: Superconductivity* **351**, 261–273 (2001).
132. Geiser, U., Schlueter, J. A., Wang, H. H., Kini, A. M., Williams, J. M., Sche, P. P., Zakowicz, H. I., VanZile, M. L., Dudek, J. D., Nixon, P. G., Winter, R. W., Gard, G. L., Ren, J & Whangbo, M.-H. Superconductivity at 5.2 K in an Electron Donor Radical Salt of Bis(ethylenedithio)tetrathiafulvalene (BEDT-TTF) with the Novel Polyfluorinated Organic Anion $\text{SF}_5\text{CH}_2\text{CF}_2\text{SO}_3^-$. *Journal of the American Chemical Society* **118**, 9996–9997 (1996).
133. Dong, J., Musfeldt, J. L., Schlueter, J. A., Williams, J. M., Nixon, P. G., Winter, R. W. & Gard, G. L. Optical properties of $\beta''\text{-(ET)}_2\text{SF}_5\text{CH}_2\text{CF}_2\text{SO}_3$: A layered molecular superconductor with large discrete counterions. *Physical Review B* **60**, 4342–4350 (1999).
134. Girlando, A., Masino, M., Kaiser, S., Sun, Y., Drichko, N., Dressel, M. & Mori, H. Spectroscopic characterization of charge order fluctuations in BEDT-TTF metals and superconductors. *Physica Status Solidi (b)* **249**, 953–956 (2012).
135. Koutroulakis, G., Kühne, H., Wang, H. H., Schlueter, J. A., Wosnitza, J. & Brown, S. E. Charge fluctuations and superconductivity in organic conductors: the case of $\beta''\text{-(BEDT-TTF)}_2\text{SF}_5\text{CH}_2\text{CF}_2\text{SO}_3$. arXiv: [1601.06107](https://arxiv.org/abs/1601.06107) (2016).
136. Hirose, S., Kawamoto, A., Matsunaga, N., Nomura, K., Yamamoto, K. & Yakushi, K. Reexamination of ^{13}C -NMR in $(\text{TMTTF})_2\text{AsF}_6$: Comparison with infrared spectroscopy. *Physical Review B* **81**, 205107 (2010).
137. Guionneau, P., Kepert, C., Bravic, G., Chasseau, D., Truter, M., Kurmoo, M. & Day, P. Determining the charge distribution in BEDT-TTF salts. *Synthetic Metals* **86**, 1973–1974 (1997).
-

138. McKenzie, R. H., Merino, J., Marston, J. B. & Sushkov, O. P. Charge ordering and antiferromagnetic exchange in layered molecular crystals of the θ -type. *Physical Review B* **64**, 85109 (2001).
139. Chang, J., Blackburn, E., Holmes, A. T., Christensen, N. B., Larsen, J., Mesot, J., Liang, R., Bonn, D. A., Hardy, W. N., Watenphul, A., Zimmermann, M. v., Forgan, E. M. & Hayden, S. M. Direct observation of competition between superconductivity and charge density wave order in $\text{YBa}_2\text{Cu}_3\text{O}_{6.67}$. *Nature Physics* **8**, 871 (2012).
140. Kaiser, S. Light-induced superconductivity in high-Tc cuprates. *Physica Scripta* **92**, 103001 (2017).
141. Mori, H., Tanaka, S. & Mori, T. Systematic study of the electronic state in θ -type BEDT-TTF organic conductors by changing the electronic correlation. *Phys. Rev. B* **57**, 12023–12029 (1998).
142. Mori, H., Sakurai, N., Tanaka, S., Moriyama, H., Mori, T., Kobayashi, H. & Kobayashi, A. Control of Electronic State by Dihedral Angle in θ -type Bis(ethylenedithio)tetraselenafulvalene Salts. *Chemistry of Materials* **12**, 2984–2987 (2000).
143. Voloshenko, I. *Optical signatures of phase transitions in low-dimensional organic conductors* (1. Physikalisches Institut, Uni Stuttgart, Stuttgart, 2015).
144. Homes, C. C., Reedyk, M., Cradles, D. A. & Timusk, T. Technique for measuring the reflectance of irregular, submillimeter-sized samples. *Applied Optics* **32**, 2976–2983 (1993).
145. Gorshunov, B., Volkov, A., Spektor, I., Prokhorov, A., Mukhin, A., Dressel, M., Uchida, S. & Loidl, A. Terahertz BWO-Spectroscopy. *International Journal of Infrared and Millimeter Waves* **26**, 1217–1240 (2005).
146. Palik, E. D. *Handbook of Optical Constants* (Academic Press Inc., San Diego, CA, 1985).
147. Haynes, W. M. in *CRC Handbook of Chemistry and Physics* (ed Haynes, W. M.) 98th ed. (CRC Press, Taylor Francis Group, 2014).
148. Bain, G. A. & Berry, J. F. Diamagnetic Corrections and Pascal's Constants. *Journal of Chemical Education* **85**, 532 (2008).

-
149. Salameh, B., Nothardt, A., Balthes, E., Schmidt, W., Schweitzer, D., Strempler, J., Hinrichsen, B., Jansen, M. & Maude, D. K. Electronic properties of the organic metals Θ -(BEDT-TTF) $_2$ I $_3$ and Θ_T -(BEDT-TTF) $_2$ I $_3$. *Physical Review B* **75**, 54509 (2007).
150. Bories, M. *Optical Investigations on Spin Liquids* (1. Physikalisches Institut, Uni Stuttgart, Stuttgart, 2016).
151. Ferber, J., Foyevtsova, K., Jeschke, H. O. & Valentí, R. Unveiling the microscopic nature of correlated organic conductors: The case of κ -(ET) $_2$ Cu[N(CN) $_2$]Br $_x$ Cl $_{1-x}$. *Physical Review B* **89**, 205106 (2014).
152. Nakamura, Y., Hiramatsu, T., Yoshida, Y., Saito, G. & Kishida, H. Optical Properties of a Quantum Spin Liquid Candidate Material, κ -(BEDT-TTF) $_2$ Ag $_2$ (CN) $_3$. *Journal of the Physical Society of Japan* **86**, 14710 (2016).
153. Pinterić, M., Culo, M., Milat, O., Basletić, M., Korin-Hamzić, B., Tafra, E., Hamzić, A., Ivek, T., Peterseim, T., Miyagawa, K., Kanoda, K., Schlueter, J. A., Dressel, M. & Tomić, S. Anisotropic charge dynamics in the quantum spin-liquid candidate κ -(BEDT-TTF) $_2$ Cu $_2$ (CN) $_3$. *Physical Review B* **90**, 195139 (2014).
154. Pinterić, M., Lazić, P., Pustogow, A., Ivek, T., Kuvezdić, M., Milat, O., Gumhalter, B., Basletić, M., Culo, M., Korin-Hamzić, B., Löhle, A., Hübner, R., Sanz Alonso, M., Hiramatsu, T., Yoshida, Y., Saito, G., Dressel, M. & Tomić, S. Anion effects on electronic structure and electrodynamic properties of the Mott insulator κ -(BEDT - TTF) $_2$ Ag $_2$ (CN) $_3$. *Physical Review B* **94**, 161105 (2016).
155. Lazić, P., Pinterić, M., Góngora, D. R., Pustogow, A., Treptow, K., Ivek, T., Milat, O., Gumhalter, B., Doslić, N., Dressel, M. & Tomić, S. Importance of van der Waals interactions and cation-anion coupling in an organic quantum spin liquid. arXiv: [1710.01942](https://arxiv.org/abs/1710.01942) (2017).
156. Itou, T., Oyamada, A., Maegawa, S., Tamura, M. & Kato, R. Quantum spin liquid in the spin-1/2 triangular antiferromagnet EtMe $_3$ Sb[Pd(dmit) $_2$] $_2$. *Physical Review B* **77**, 104413 (2008).
157. Kanoda, K. & Kato, R. Mott Physics in Organic Conductors with Triangular Lattices. *Annual Review of Condensed Matter Physics* **2**, 167–188 (2011).
158. Hubbard, J. Electron Correlations in Narrow Energy Bands. III. An Improved Solution. *Proceedings of the Royal Society of London. Series A. Mathematical and Physical Sciences* **281**, 401–419 (1964).
-

159. Vollhardt, D. in *Correlated Electron Systems* (ed Emery, V. J.) 57 (World Scientific, Singapore, 1992).
160. Kandpal, H. C., Opahle, I., Zhang, Y.-Z., Jeschke, H. O. & Valentí, R. Revision of Model Parameters for κ -Type Charge Transfer Salts: An Ab Initio Study. *Physical Review Letters* **103**, 67004 (2009).
161. Merino, J, Dumm, M, Drichko, N, Dressel, M & McKenzie, R. H. Quasiparticles at the Verge of Localization near the Mott Metal-Insulator Transition in a Two-Dimensional Material. *Physical Review Letters* **100**, 86404 (2008).
162. Drichko, N., Beyer, R., Rose, E., Dressel, M., Schlueter, J. A., Turunova, S. A., Zhilyaeva, E. I. & Lyubovskaya, R. N. Metallic state and charge-order metal-insulator transition in the quasi-two-dimensional conductor κ -(BEDT-TTF)₂Hg(SCN)₂Cl. *Physical Review B* **89**, 75133 (2014).
163. Ivek, T., Beyer, R., Badalov, S., Culo, M., Tomić, S., Schlueter, J. A., Zhilyaeva, E. I., Lyubovskaya, R. N. & Dressel, M. Metal-insulator transition in the dimerized organic conductor κ - (BEDT-TTF)₂Hg(SCN)₂Br. *Physical Review B* **96**, 85116 (2017).
164. Dressel, M., Lazić, P., Pustogow, A., Zhukova, E., Gorshunov, B., Schlueter, J. A., Milat, O., Gumhalter, B. & Tomić, S. Lattice vibrations of the charge-transfer salt κ - (BEDT-TTF)₂Cu₂(CN)₃: Comprehensive explanation of the electrodynamic response in a spin-liquid compound. *Physical Review B* **93**, 81201 (2016).
165. Geiser, U., Wang, H. H., Carlson, K. D., Williams, J. M., Charlier, H. A., Heindl, J. E., Yaconi, G. A., Love, B. J., Lathrop, M. W., Schirber, J. E., Overmyer, D. L., Ren, J. & Whangbo, M.-H. Superconductivity at 2.8 K and 1.5 kbar in κ -(BEDT-TTF)₂Cu₂(CN)₃: the first organic superconductor containing a polymeric copper cyanide anion. *Inorganic Chemistry* **30**, 2586–2588 (1991).
166. Georges, A., Kotliar, G., Krauth, W. & Rozenberg, M. J. Dynamical mean-field theory of strongly correlated fermion systems and the limit of infinite dimensions. *Reviews of Modern Physics* **68**, 13–125 (1996).
167. Jarrell, M. & Gubernatis, J. E. Bayesian inference and the analytic continuation of imaginary-time quantum Monte Carlo data. *Physics Reports* **269**, 133–195 (1996).

-
168. Jeschke, H. O., de Souza, M., Valentí, R., Manna, R. S., Lang, M. & Schlueter, J. A. Temperature dependence of structural and electronic properties of the spin-liquid candidate κ -(BEDT-TTF)₂Cu₂(CN)₃. *Physical Review B* **85**, 35125 (2012).
169. Fournier, D., Poirier, M., Castonguay, M. & Truong, K. D. Mott Transition, Compressibility Divergence, and the P – T Phase Diagram of Layered Organic Superconductors: An Ultrasonic Investigation. *Physical Review Letters* **90**, 127002 (2003).
170. Schirber, J. E., Overmyer, D. L., Carlson, K. D., Williams, J. M., Kini, A. M., Wang, H. H., Charlier, H. A., Love, B. J., Watkins, D. M. & Yaconi, G. A. Pressure-temperature phase diagram, inverse isotope effect, and superconductivity in excess of 13 K in κ -(BEDT-TTF)₂Cu[N(CN)₂]Cl, where BEDT-TTF is bis(ethylenedithio)tetrathiafulvalene. *Physical Review B* **44**, 4666–4669 (1991).
171. Frikach, K., Poirier, M., Castonguay, M. & Truong, K. D. Elastic study of anti-ferromagnetic fluctuations in the layered organic superconductors κ -(BEDT-TTF)₂X. *Physical Review B* **61**, R6491–R6494 (2000).
172. Strack, C., Akinci, C., Pashchenko, V., Wolf, B., Uhrig, E., Assmus, W., Lang, M., Schreuer, J., Wiehl, L., Schlueter, J. A., Wosnitza, J., Schweitzer, D., Müller, J. & Wykhoff, J. Resistivity studies under hydrostatic pressure on a low-resistance variant of the quasi-two-dimensional organic superconductor κ -(BEDT-TTF)₂Cu[N(CN)₂]Cl. *Physical Review B* **72**, 54511 (2005).
173. Schirber, J. E., Venturini, E. L., Kini, A. M., Wang, H. H., Whitworth, J. R. & Williams, J. M. Effect of pressure on the superconducting transition temperature of κ -(BEDT-TTF)₂Cu(NCS)₂. *Physica C: Superconductivity* **152**, 157–158 (1988).
174. Kang, W., Jerome, D., Lenoir, C. & Batail, P. Some properties of the organic superconductor κ -(BEDT-TTF)₂Cu(SCN)₂ under pressure. *Journal of Physics: Condensed Matter* **2**, 1665 (1990).
175. Kato, R., Kobayashi, H., Kobayashi, A., Moriyama, S., Nishio, Y., Kajita, K. & Sasaki, W. A New Ambient-pressure Superconductor, κ -(BEDT-TTF)₂I₃. *Chemistry Letters* **16**, 507–510 (1987).
176. Guterding, D., Jeschke, H. O. & Valentí, R. Prospect of quantum anomalous Hall and quantum spin Hall effect in doped kagome lattice Mott insulators. *Scientific Reports* **6**, 25988 (2016).
-

177. Radonjić, M. M., Tanasković, D., Dobrosavljević, V., Haule, K. & Kotliar, G. Wigner-Mott scaling of transport near the two-dimensional metal-insulator transition. *Physical Review B* **85**, 85133 (2012).
178. Dobrosavljevic, V. & Tanaskovic, D. Wigner-Mott quantum criticality: from 2D-MIT to ^3He and Mott organics. arXiv: [1602.00131](https://arxiv.org/abs/1602.00131) (2016).
179. Wzietek, P., Mito, T., Alloul, H., Pontiroli, D., Aramini, M. & Riccò, M. NMR Study of the Superconducting Gap Variation near the Mott Transition in Cs_3C_{60} . *Physical Review Letters* **112**, 66401 (2014).
180. Baldassarre, L., Perucchi, A., Mitrano, M., Nicoletti, D., Marini, C., Pontiroli, D., Mazzani, M., Aramini, M., Riccò, M., Giovannetti, G., Capone, M. & Lupi, S. The strength of electron electron correlation in Cs_3C_{60} . **5**, 15240 (2015).
181. Harshman, D. R. & Fiory, A. T. High- T_c superconductivity in CS_3C_{60} compounds governed by local Cs- C_{60} Coulomb interactions. *Journal of Physics: Condensed Matter* **29**, 145602 (2017).
182. Taillefer, L. Scattering and Pairing in Cuprate Superconductors. *Annual Review of Condensed Matter Physics* **1**, 51–70 (2010).
183. Bozović, I., He, X., Wu, J. & Bollinger, A. T. Dependence of the critical temperature in overdoped copper oxides on superfluid density. *Nature* **536**, 309–311 (2016).
184. Sasaki, T. *Mott-Anderson Transition in Molecular Conductors: Influence of Randomness on Strongly Correlated Electrons in the κ -(BEDT-TTF) $_2X$ System* 2012.
185. Furukawa, T., Miyagawa, K., Ito, T., Ito, M., Taniguchi, H., Saito, M., Iguchi, S., Sasaki, T. & Kanoda, K. Quantum Spin Liquid Emerging from Antiferromagnetic Order by Introducing Disorder. *Physical Review Letters* **115**, 77001 (2015).
186. Belitz, D. & Kirkpatrick, T. R. The Anderson-Mott transition. *Reviews of Modern Physics* **66**, 261–380 (1994).
187. Pustogow, A., Zhukova, E., Gorshunov, B., Pinterić, M., Tomić, S., Schlueter, J. A. & Dressel, M. Low-Energy Excitations in the Quantum Spin-Liquid κ -(BEDT-TTF) $_2\text{Cu}_2(\text{CN})_3$. arXiv: [1412.4581](https://arxiv.org/abs/1412.4581) (2014).
188. Lee, S.-H., Kikuchi, H., Qiu, Y., Lake, B., Huang, Q., Habicht, K. & Kiefer, K. Quantum-spin-liquid states in the two-dimensional kagome antiferromagnets $\text{Zn}_x\text{Cu}_{4-x}(\text{OD})_6\text{Cl}_2$. *Nature Materials* **6**, 853–857 (2007).

-
189. Potter, A. C., Senthil, T. & Lee, P. A. Mechanisms for sub-gap optical conductivity in Herbertsmithite. *Physical Review B* **87**, 245106 (2013).
190. Sanz Alonso, M. *Effect of Disorder on the Optical Properties of Organic Quantum Spin-liquid Compounds* (1. Physikalisches Institut, Uni Stuttgart, Stuttgart, 2016).
191. Pashkin, A., Dressel, M., Hanfland, M. & Kuntscher, C. A. Deconfinement transition and dimensional crossover in the Bechgaard-Fabre salts: Pressure- and temperature-dependent optical investigations. *Physical Review B* **81**, 125109 (2010).
192. Uchida, S., Ido, T., Takagi, H., Arima, T., Tokura, Y. & Tajima, S. Optical spectra of $\text{La}_{2-x}\text{Sr}_x\text{CuO}_4$: Effect of carrier doping on the electronic structure of the CuO_2 plane. *Physical Review B* **43**, 7942–7954 (1991).
193. Nagel, U., Uleksin, T., Rößm, T., Lobo, R. P.S. M., Lejay, P., Homes, C. C., Hall, J. S., Kinross, A. W., Purdy, S. K., Munsie, T., Williams, T. J., Luke, G. M. & Timusk, T. Optical spectroscopy shows that the normal state of URu_2Si_2 is an anomalous Fermi liquid. *Proceedings of the National Academy of Sciences* **109**, 19161–19165 (2012).
194. Yang, J., Hwang, J., Timusk, T., Sefat, A. S. & Greedan, J. E. Temperature-dependent optical spectroscopy studies of $\text{Nd}_{1-x}\text{TiO}_3$. *Physical Review B* **73**, 195125 (2006).
195. Kaiser, S. *Interplay of Charge Order and Superconductivity* (1. Physikalisches Institut, Uni Stuttgart, Stuttgart, 2010).
196. Knoblauch, T. & Dressel, M. Charge disproportionation in $(\text{TMTTF})_2X$ ($X = \text{PF}_6, \text{AsF}_6$ and SbF_6) investigated by infrared spectroscopy. *Physica Status Solidi (c)* **9**, 1158–1160 (2012).
197. Treptow, K. *Optische Untersuchungen von korrelierten Isolatoren* (1. Physikalisches Institut, Uni Stuttgart, Stuttgart, 2017).
198. Olejniczak, I., Jones, B. R., Zhu, Z., Dong, J., Musfeldt, J. L., Schlueter, J. A., Morales, E., Geiser, U., Nixon, P. G., Winter, R. W. & Gard, G. L. Optical Properties of β'' -(ET) $_2$ SF $_5$ RSO $_3$ (R = CH $_2$ CF $_2$, CHF CF_2): Changing Physical Properties by Chemical Tuning of the Counterion. *Chemistry of Materials* **11**, 3160–3165 (1999).

199. Jones, B. R., Olejniczak, I., Dong, J., Pigos, J. M., Zhu, Z. T., Garlach, A. D., Musfeldt, J. L., Koo, H.-J., Whangbo, M.-H., Schlueter, J. A., Ward, B. H., Morales, E., Kini, A. M., Winter, R. W., Mohtasham, J & Gard, G. L. Optical Spectra and Electronic Band Structure Calculations of β'' -(ET)₂SF₅RSO₃ (R = CH₂CF₂, CHF₂CF₂, and CHF): Changing Electronic Properties by Chemical Tuning of the Counterion. *Chemistry of Materials* **12**, 2490–2495 (2000).
200. Oka, Y., Matsunaga, N., Nomura, K., Kawamoto, A., Yamamoto, K. & Yakushi, K. Charge Order in (TMTTF)₂TaF₆ by Infrared Spectroscopy. en. *Journal of the Physical Society of Japan* **84**, 114709 (2015).
201. Olejniczak, I., Barszcz, B., Szutarska, A., Graja, A., Wojciechowski, R., Schlueter, J. A., Hata, A. N. & Ward, B. H. IR and Raman spectra of β'' -(BEDT-TTF)₂RCH₂SO₃ (R = SF₅, CF₃): dimerization related to hydrogen bonding. *Physical Chemistry Chemical Physics* **11**, 3910–3920 (2009).
202. Olejniczak, I., Barszcz, B., Graja, A. & Schlueter, J. A. Optical study of β'' -(bis(ethylenedithio)tetrathiafulvalene)₂SF₅CH₂SO₃ Activation of intramolecular modes. *Materials Science Poland* **Vol. 27**, 619–627 (2009).
203. Auban-Senzier, P., Lenoir, C., Batail, P., Jérôme, D. & Tomić, S. Charge localization in organic conductors (TM)₂X: The influence of anion ordering. *The European Physical Journal B* **7**, 529–532 (1999).
204. Akutsu, H., Ishihara, K., Yamada, J.-i., Nakatsuji, S., Turner, S. S. & Nakazawa, Y. A strongly polarized organic conductor. *CrystEngComm* **18**, 8151–8154 (2016).
205. Jeschke, H. O. *First principles investigation of a purely organic class of charge-transfer salts* in ISCOM (2017).
206. Itou, T., Watanabe, E., Maegawa, S., Tajima, A., Tajima, N., Kubo, K., Kato, R. & Kanoda, K. Slow dynamics of electrons at a metal-Mott insulator boundary in an organic system with disorder. *Science Advances* **3** (2017).
207. Glied, M., Yasin, S., Kaiser, S., Drichko, N., Dressel, M., Wosnitza, J., Schlueter, J. & Gard, G. DC and high-frequency conductivity of the organic metals β -(BEDT-TTF)₂SF₅RSO₃ (R=CH₂CF₂ and CHF). *Synthetic Metals* **159**, 1043–1049 (2009).
208. Nad, F., Monceau, P., Nakamura, T. & Furukawa, K. The effect of deuteration on the transition into a charge ordered state of (TMTTF)₂X salts. en. *Journal of Physics: Condensed Matter* **17**, L399–L406 (2005).

-
209. Furukawa, K., Hara, T. & Nakamura, T. Deuteration Effect and Possible Origin of the Charge-Ordering Transition of $(\text{TMTTF})_2X$. *Journal of the Physical Society of Japan* **74**, 3288 (2005).
210. Pouget, J.-P., Foury-Leylekian, P., Le Bolloc'h, D., Hennion, B., Ravy, S., Coulon, C., Cardoso, V. & Moradpour, A. Neutron-Scattering Evidence for a Spin-Peierls Ground State in $(\text{TMTTF})_2\text{PF}_6$. *Journal of Low Temperature Physics* **142**, 147–152 (2006).
211. Isono, T., Kamo, H., Ueda, A., Takahashi, K., Nakao, A., Kumai, R., Nakao, H., Kobayashi, K., Murakami, Y. & Mori, H. Hydrogen bond-promoted metallic state in a purely organic single-component conductor under pressure. *Nature Communications* **4**, 1344 (2013).
212. Isono, T., Kamo, H., Ueda, A., Takahashi, K., Kimata, M., Tajima, H., Tsuchiya, S., Terashima, T., Uji, S. & Mori, H. Gapless Quantum Spin Liquid in an Organic Spin-1/2 Triangular-Lattice $\kappa\text{-H}_3(\text{Cat-EDT-TTF})_2$. *Physical Review Letters* **112**, 177201 (2014).
213. Ueda, A., Yamada, S., Isono, T., Kamo, H., Nakao, A., Kumai, R., Nakao, H., Murakami, Y., Yamamoto, K., Nishio, Y. & Mori, H. Hydrogen-Bond-Dynamics-Based Switching of Conductivity and Magnetism: A Phase Transition Caused by Deuterium and Electron Transfer in a Hydrogen-Bonded Purely Organic Conductor Crystal. *Journal of the American Chemical Society* **136**, 12184–12192 (2014).
214. Kagawa, F., Sato, T., Miyagawa, K., Kanoda, K., Tokura, Y., Kobayashi, K., Kumai, R. & Murakami, Y. Charge-cluster glass in an organic conductor. *Nature Physics* **9**, 419–422 (2013).
215. Oike, H., Kagawa, F., Ogawa, N., Ueda, A., Mori, H., Kawasaki, M. & Tokura, Y. Phase-change memory function of correlated electrons in organic conductors. *Physical Review B* **91**, 41101 (2015).
216. Sato, T., Miyagawa, K. & Kanoda, K. Electronic crystal growth. *Science* **357**, 1378–1381 (2017).
217. Kagawa, F. & Oike, H. Quenching of Charge and Spin Degrees of Freedom in Condensed Matter. *Advanced Materials* **29**, 1601979 (2017).
218. Kobayashi, H., Kato, R., Kobayashi, A., Nishio, Y., Kajita, K. & Sasaki, W. A NEW MOLECULAR SUPERCONDUCTOR, $(\text{BEDT-TTF})_2(\text{I}_3)_{1-x}(\text{AuI}_2)_x$ ($x < 0.02$). *Chemistry Letters* **15**, 789–792 (1986).
-

219. Tajima, N., Tajima, A., Tamura, M., Kato, R., Nishio, Y. & Kajita, K. Pressure control of transport property of organic conductors; α -, θ -(BEDT-TTF)₂I₃ and θ -(DIETS)₂[Au(CN)₄]. *Journal de Physique IV France* **114**, 263–267 (2004).
220. Yamamoto, T., Yamamoto, H. M., Kato, R., Uruichi, M., Yakushi, K., Akutsu, H., Sato-Akutsu, A., Kawamoto, A., Turner, S. S. & Day, P. Inhomogeneous site charges at the boundary between the insulating, superconducting, and metallic phases of β'' -type bis-ethylenedithio-tetrathiafulvalene molecular charge-transfer salts. *Physical Review B* **77**, 205120 (2008).
221. Kurmoo, M., Graham, A. W., Day, P., Coles, S. J., Hursthouse, M. B., Caulfield, J. L., Singleton, J., Pratt, F. L. & Hayes, W. Superconducting and Semiconducting Magnetic Charge Transfer Salts: (BEDT-TTF)₄AFe(C₂O₄)₃·C₆H₅CN (A = H₂O, K, NH₄). *Journal of the American Chemical Society* **117**, 12209–12217 (1995).
222. Akutsu, H., Akutsu-Sato, A., Turner, S. S., Le Pevelen, D., Day, P., Laukhin, V., Klehe, A.-K., Singleton, J., Tocher, D. A., Probert, M. R. & Howard, J. A. K. Effect of Included Guest Molecules on the Normal State Conductivity and Superconductivity of β'' -(ET)₄[(H₃O)Ga(C₂O₄)₃]·G (G = Pyridine, Nitrobenzene). *Journal of the American Chemical Society* **124**, 12430–12431 (2002).
223. Akutsu, H., Akutsu-Sato, A., Turner, S. S., Day, P., Tocher, D. A., Probert, M. R., Howard, J. A. K., Pevelen, D. L., Klehe, A.-K., Singleton, J. & Laukhin, V. N. Structures and properties of new superconductors, β'' -(ET)₄[(H₃O)Ga(C₂O₄)₃]·Sol [Sol = nitrobenzene and pyridine]. *Synthetic Metals* **137**, 1239–1240 (2003).
224. Coldea, A. I., Bangura, A. F., Singleton, J., Ardavan, A., Akutsu-Sato, A., Akutsu, H., Turner, S. S. & Day, P. Fermi-surface topology and the effects of intrinsic disorder in a class of charge-transfer salts containing magnetic ions: β -(BEDT-TTF)₄[(H₃O)M(C₂O₄)₃]Y (M = Ga, Cr, Fe; Y = C₅H₅N). *Physical Review B* **69**, 85112 (2004).
225. Fulde, P. & Ferrell, R. A. Superconductivity in a Strong Spin-Exchange Field. *Physical Review* **135**, A550–A563 (1964).
226. Larkin, A. I. & Ovchinnikov, Y. N. Inhomogeneous State of Superconductors. *Soviet Physics JETP-USSR* **20**, 762 (1965).

-
227. Botto, I. L., Baran, E. J. & Garcia, A. C. Thermal behaviour and vibrational spectra of $(\text{NH}_4)_3\text{Ga}(\text{C}_2\text{O}_4)_3 \cdot 3\text{H}_2\text{O}$ and $(\text{NH}_4)_3\text{Al}(\text{C}_2\text{O}_4)_3 \cdot 3\text{H}_2\text{O}$. *Journal of Thermal Analysis* **31**, 1301–1308 (1986).
228. Kuwae, A. & Machida, K. Vibrational spectra of nitrobenzene-d0, -p-d and -d5 and normal vibrations of nitrobenzene. *Spectrochimica Acta Part A: Molecular Spectroscopy* **35**, 27–33 (1979).
229. Clarkson, J. & Ewen Smith, W. A DFT analysis of the vibrational spectra of nitrobenzene. *Journal of Molecular Structure* **655**, 413–422 (2003).
230. Ihara, Y., Seki, H. & Kawamoto, A. ^{13}C NMR Study of Superconductivity near Charge Instability Realized in β'' -(BEDT-TTF) $_4$ [(H $_3$ O)Ga(C $_2$ O $_4$) $_3$] \cdot C $_6$ H $_5$ NO $_2$. *Journal of the Physical Society of Japan* **82**, 83701 (2013).
231. Ihara, Y., Jeong, M., Mayaffre, H., Berthier, C., Horvatić, M., Seki, H. & Kawamoto, A. ^{13}C NMR study of the charge-ordered state near the superconducting transition in the organic superconductor β'' -(BEDT-TTF) $_4$ [(H $_3$ O)Ga(C $_2$ O $_4$) $_3$] \cdot C $_6$ H $_5$ NO $_2$. *Physical Review B* **90**, 121106 (2014).
232. Ihara, Y., Futami, Y. & Kawamoto, A. High-Temperature Charge and Structure Anomalies in β'' -(BEDT-TTF) $_4$ [(H $_3$ O)Ga(C $_2$ O $_4$) $_3$] \cdot C $_6$ H $_5$ NO $_2$. *Journal of the Physical Society of Japan* **85**, 14601 (2016).
233. Pustogow, A., Li, Y., Bories, M., Dressel, M. & Valentí, R. Optical and Ab-Initio Study of Lattice Vibrations in the Kagome Compound Herbertsmithite. *in preparation* (2018).
234. Jérôme, D., Mazaud, A., Ribault, M. & Bechgaard, K. Superconductivity in a synthetic organic conductor (TMTSF) $_2$ PF $_6$. en. *Journal de Physique Lettres* **41**, 95–98 (1980).
235. Little, W. A. Possibility of Synthesizing an Organic Superconductor. *Physical Review* **134**, A1416–A1424 (1964).
236. Dressel, M. Ordering phenomena in quasi-one-dimensional organic conductors. *Die Naturwissenschaften* **94**, 527–41 (2007).
237. Köhler, B., Rose, E., Dumm, M., Untereiner, G. & Dressel, M. Comprehensive transport study of anisotropy and ordering phenomena in quasi-one-dimensional (TMTTF) $_2$ X salts ($X = \text{PF}_6, \text{AsF}_6, \text{SbF}_6, \text{BF}_4, \text{ClO}_4, \text{ReO}_4$). *Physical Review B* **84**, 035124 (2011).
-

238. Chow, D. S., Zamborszky, F, Alavi, B, Tantillo, D. J., Baur, A, Merlic, C. A. & Brown, S. E. Charge Ordering in the TMTTF Family of Molecular Conductors. *Physical Review Letters* **85**, 1698–1701 (2000).
239. Zamborszky, F, Yu, W, Raas, W, Brown, S. E., Alavi, B, Merlic, C. A. & Baur, A. Competition and coexistence of bond and charge orders in $(\text{TMTTF})_2\text{AsF}_6$. *Physical Review B* **66**, 81103 (2002).
240. Yu, W, Zhang, F, Zamborszky, F, Alavi, B, Baur, A, Merlic, C. A. & Brown, S. E. Electron-lattice coupling and broken symmetries of the molecular salt $(\text{TMTTF})_2\text{SbF}_6$. *Physical Review B* **70**, 121101 (2004).
241. Dumm, M., Salameh, B., Abaker, M., Montgomery, L. K. & Dressel, M. Magnetic and optical studies of spin and charge ordering in $(\text{TMTTF})_2\text{AsF}_6$. *Journal de Physique IV (Proceedings)* **114**, 57–60 (2004).
242. Dumm, M., Abaker, M. & Dressel, M. Mid-infrared response of charge-ordered quasi-1D organic conductors $(\text{TMTTF})_2X$. *Journal de Physique IV (Proceedings)* **131**, 55–58 (2005).
243. Dumm, M., Abaker, M., Dressel, M. & Montgomery, L. K. Charge Order in $(\text{TMTTF})_2\text{PF}_6$ Investigated by Infrared Spectroscopy. *Journal of Low Temperature Physics* **142**, 613–616 (2006).
244. Pashkin, A., Dressel, M., Ebbinghaus, S., Hanfland, M. & Kuntscher, C. Pressure-induced structural phase transition in the Bechgaard-Fabre salts. *Synthetic Metals* **159**, 2097–2100 (2009).
245. Dumm, M., Loidl, A., Alavi, B., Starkey, K. P., Montgomery, L. K. & Dressel, M. Comprehensive ESR study of the antiferromagnetic ground states in the one-dimensional spin systems $(\text{TMTSF})_2\text{PF}_6$, $(\text{TMTSF})_2\text{AsF}_6$, and $(\text{TMTTF})_2\text{Br}$. *Physical Review B* **62**, 6512–6520 (2000).
246. Dumm, M., Loidl, A., Fravel, B. W., Starkey, K. P., Montgomery, L. K. & Dressel, M. Electron spin resonance studies on the organic linear-chain compounds $(\text{TMTCF})_2X$ ($C = \text{S, Se}$; $X = \text{PF}_6, \text{AsF}_6, \text{ClO}_4, \text{Br}$). *Physical Review B* **61**, 511–521 (2000).
247. Nad, F., Monceau, P., Carcel, C. & Fabre, J. M. Charge and anion ordering phase transitions in $(\text{TMTTF})_2X$ salt conductors. en. *Journal of Physics: Condensed Matter* **13**, L717–L722 (2001).

-
248. Nakamura, T. Possible Charge Ordering Patterns of the Paramagnetic Insulating States in $(\text{TMTTF})_2X$. *Journal of the Physical Society of Japan* **72**, 213–216 (2003).
249. Nakamura, T., Furukawa, K. & Hara, T. ^{13}C NMR Analyses of Successive Charge Ordering in $(\text{TMTTF})_2\text{ReO}_4$. en. *Journal of the Physical Society of Japan* **75**, 013707 (2006).
250. Nogami, Y. & Nakamura, T. X-ray observation of $2k_{\text{F}}$ and $4k_{\text{F}}$ charge orderings in $(\text{TMTTF})_2\text{ReO}_4$ and $(\text{TMTTF})_2\text{SCN}$ associated with anion orderings. en. *Journal de Physique IV (Proceedings)* **12**, 145–148 (2002).
251. Nogami, Y., Ito, T., Yamamoto, K., Irie, N., Horita, S., Kambe, T., Nagao, N., Oshima, K., Ikeda, N. & Nakamura, T. X-ray structural study of charge and anion orderings of TMTTF salts. en. *Journal de Physique IV (Proceedings)* **131**, 39–42 (2005).
252. Salameh, B., Yasin, S., Dumm, M., Untereiner, G., Montgomery, L. & Dressel, M. Spin dynamics of the organic linear chain compounds $(\text{TMTTF})_2X$ ($X = \text{SbF}_6, \text{AsF}_6, \text{BF}_4, \text{ReO}_4$, and SCN). *Physical Review B* **83**, 205126 (2011).
253. Fujiyama, S. & Nakamura, T. Redistribution of Electronic Charges in Spin-Peierls State in $(\text{TMTTF})_2\text{AsF}_6$ Observed by ^{13}C NMR. en. *Journal of the Physical Society of Japan* **75**, 014705 (2006).
254. Nakamura, T., Furukawa, K. & Hara, T. Redistribution of Charge in the Proximity of the Spin-Peierls Transition: ^{13}C NMR Investigation of $(\text{TMTTF})_2\text{PF}_6$. *Journal of the Physical Society of Japan* **76**, 064715 (2007).
255. Pouget, J.-P. Structural Aspects of the Bechgaard and Fabre Salts: An Update. en. *Crystals* **2**, 466–520 (2012).
256. Pouget, J.-P. Bond and charge ordering in low-dimensional organic conductors. *Physica B: Condensed Matter* **407**, 1762–1770 (2012).
257. Liautard, B., Peytavin, S., Brun, G. & Maurin, M. Corrélations structurales dans la série $(\text{TMTTF})_2X$. *Journal de Physique* **43**, 1453–1459 (1982).
258. Kistenmacher, T. J. Cavity size versus anion size in $(\text{TMTSF})_2X$ salts: Possible implications for the uniqueness of $(\text{TMTSF})_2\text{ClO}_4$. *Solid State Communications* **50**, 729–733 (1984).
-

259. Galigné, J. L., Liautard, B., Peytavin, S., Brun, G., Maurin, M., Fabre, J. M., Torreilles, E. & Giral, L. Structure cristalline du fluoroborate de tétraméthyl-tétrathiafulvalène (TMTTF)₂BF₄ á 100 K et á température ambiante. *Acta Crystallographica Section B* **35**, 1129–1135 (1979).
260. Liautard, B., Peytavin, S., Brun, G., Chasseau, D., Fabre, J. M. & Giral, L. Structure du di(tétraméthyltétrathiafulvalénium) perchlorate (TMTTF)₂ClO₄. *Acta Crystallographica Section C* **40**, 1023–1026 (1984).
261. Kobayashi, H., Kobayashi, A., Sasaki, Y., Saito, G. & Inokuchi, H. The Crystal Structure of (TMTTF)₂ReO₄. *Bulletin of the Chemical Society of Japan* **57**, 2025–2026 (1984).
262. Williams, J., Ferraro, J., Thorn, R., Carlson, K., Geiser, U., Wang, H., Kini, A. & Whangbo, M. *Organic Superconductors* (Prentice Hall, Englewood Cliffs, NJ, 1992).
263. Takahashi, T., Nogami, Y. & Yakushi, K. Charge Ordering in Organic Conductors. en. *Journal of the Physical Society of Japan* **75**, 051008 (2006).
264. Rose, E. & Dressel, M. Coupling between molecular chains and anions in (TMTTF)₂X salts. *Physica B: Condensed Matter* **407**, 1787–1792 (2012).
265. Nad, F. & Monceau, P. Dielectric Response of the Charge Ordered State in Quasi-One-Dimensional Organic Conductors. *Journal of the Physical Society of Japan* **75**, 051005 (2006).
266. Meneghetti, M., Bozio, R., Zanon, I., Pecile, C., Ricotta, C. & Zanetti, M. Vibrational behavior of molecular constituents of organic superconductors: TMTSF, its radical cation and the sulphur analogs TMTTF and TMTTF⁺. *The Journal of Chemical Physics* **80**, 6210 (1984).
267. Dressel, M. & Drichko, N. Optical properties of two-dimensional organic conductors: signatures of charge ordering and correlation effects. *Chemical reviews* **104**, 5689–716 (2004).
268. Świetlik, R., Barszcz, B., Pustogow, A. & Dressel, M. Raman spectroscopy evidence of domain walls in the organic electronic ferroelectrics (TMTTF)₂X (X = SbF₆, AsF₆, PF₆). *Physical Review B* **95**, 85205 (2017).
269. Matsunaga, N., Hirose, S., Shimohara, N., Satoh, T., Isome, T., Yamamoto, M., Liu, Y., Kawamoto, A. & Nomura, K. Charge ordering and antiferromagnetism in (TMTTF)₂SbF₆. *Physical Review B* **87**, 144415 (2013).

-
270. Iwase, F., Sugiura, K., Furukawa, K. & Nakamura, T. ^{13}C NMR study of the magnetic properties of the quasi-one-dimensional conductor $(\text{TMTTF})_2\text{SbF}_6$. *Physical Review B* **84**, 115140 (2011).
271. Medjanik, K., de Souza, M., Kutnyakhov, D., Gloskovskii, A., Müller, J., Lang, M., Pouget, J.-P., Foury-Leylekian, P., Moradpour, A., Elmers, H.-J. & Schönhense, G. Hard X-ray photoemission study of the Fabre salts $(\text{TMTTF})_2X$ ($X = \text{SbF}_6$ and PF_6). *The European Physical Journal B* **87**, 256 (2014).
272. Monceau, P, Nad, F. Y. & Brazovskii, S. Ferroelectric Mott-Hubbard Phase of Organic $(\text{TMTTF})_2X$ Conductors. *Physical Review Letters* **86**, 4080–4083 (2001).
273. De Souza, M., Foury-Leylekian, P., Moradpour, A., Pouget, J.-P. & Lang, M. Evidence for Lattice Effects at the Charge-Ordering Transition in $(\text{TMTTF})_2X$. *Physical Review Letters* **101**, 216403 (2008).
274. Medjanik, K., Chernenkaya, A., Nepijko, S. A., Ohrwall, G., Foury-Leylekian, P., Alemany, P., Canadell, E., Schönhense, G. & Pouget, J.-P. Donor-anion interactions at the charge localization and charge ordering transitions of $(\text{TMTTF})_2\text{AsF}_6$ probed by NEXAFS. *Physical Chemistry Chemical Physics* **17**, 19202–19214 (2015).
275. Subías, G., Abbaz, T., Fabre, J. M. & Fraxedas, J. Characterization of the anion-ordering transition in $(\text{TMTTF})_2\text{ReO}_4$ x-ray absorption and photoemission spectroscopies. *Physical Review B* **76**, 085103 (2007).
276. Parkin, S. S. P., Mayerle, J. J. & Engler, E. M. Anion Ordering in $(\text{TMTTF})_2\text{-ReO}_4$: A Displacive Transition. *Le Journal de Physique Colloques* **44**, C3–1105–C3–1109 (1983).
277. Nakamura, T. ESR study of the charge ordering in $(\text{TMTTF})_2X$. *Physica B: Condensed Matter* **329-333**, 1148–1149 (2003).
278. Yamamoto, K. & Yakushi, K. Electron-molecular vibration coupling effect on the Raman spectrum of organic charge transfer salts. *Journal de Physique IV (Proceedings)* **114**, 153–155 (2004).
279. Seo, H. & Fukuyama, H. Antiferromagnetic Phases of One-Dimensional Quarter-Filled Organic Conductors. *Journal of the Physical Society of Japan* **66**, 1249–1252 (1997).
-

280. Jacko, A. C., Feldner, H., Rose, E., Lissner, F., Dressel, M., Valentí, R. & Jeschke, H. O. Electronic properties of Fabre charge-transfer salts under various temperature and pressure conditions. *Physical Review B* **87**, 155139 (2013).
281. Brazovskii, S. in *The Physics of Organic Superconductors and Conductors* (ed Lebed, A.) 313 (Springer-Verlag, Berlin, 2008).
282. Tomonaga, S.-i. Remarks on Bloch's Method of Sound Waves applied to Many-Fermion Problems. *Progress of Theoretical Physics* **5**, 544–569 (1950).
283. Luttinger, J. M. An Exactly Soluble Model of a Many-Fermion System. *Journal of Mathematical Physics* **4**, 1154 (1963).
284. Haldane, F. D. M. 'Luttinger liquid theory' of one-dimensional quantum fluids. I. Properties of the Luttinger model and their extension to the general 1D interacting spinless Fermi gas. en. *Journal of Physics C: Solid State Physics* **14**, 2585–2609 (1981).
285. Mastropietro, V. & Mattis, D. *Luttinger Model: The First 50 Years and Some New Directions* (World Scientific, Singapore, 2013).
286. Guan, X.-W., Batchelor, M. T. & Lee, C. Fermi gases in one dimension: From Bethe ansatz to experiments. *Reviews of Modern Physics* **85**, 1633–1691 (2013).
287. Hofferberth, S., Lesanovsky, I., Fischer, B., Schumm, T. & Schmiedmayer, J. Non-equilibrium coherence dynamics in one-dimensional Bose gases. *Nature* **449**, 324–327 (2007).
288. Widera, A., Trotzky, S., Cheinet, P., Fölling, S., Gerbier, F., Bloch, I., Gritsev, V., Lukin, M. D. & Demler, E. Quantum spin dynamics of mode-squeezed Luttinger liquids in two-component atomic gases. *Physical review letters* **100**, 140401 (2008).
289. Bockrath, M., Cobden, D. H., Lu, J., Rinzler, A. G., Smalley, R. E., Balents, L. & McEuen, P. L. Luttinger-liquid behaviour in carbon nanotubes. *Nature* **397**, 598–601 (1999).
290. Shi, Z., Hong, X., Bechtel, H. A., Zeng, B., Martin, M. C., Watanabe, K., Taniguchi, T., Shen, Y.-R. & Wang, F. Observation of a Luttinger-liquid plasmon in metallic single-walled carbon nanotubes. *Nature Photonics* **9**, 515–519 (2015).

-
291. Himpfel, F. J., Altmann, K. N., Bennewitz, R., Crain, J. N., Kirakosian, A., Lin, J.-L. & McChesney, J. L. One-dimensional electronic states at surfaces. *Journal of Physics: Condensed Matter* **13**, 11097 (2001).
292. Ohtsubo, Y., Kishi, J.-I., Hagiwara, K., Le Fèvre, P., Bertran, F., Taleb-Ibrahimi, A., Yamane, H., Ideta, S.-I., Matsunami, M., Tanaka, K. & Kimura, S.-I. Surface Tomonaga-Luttinger-Liquid State on Bi/InSb(001). *Physical review letters* **115**, 256404 (2015).
293. Kim, B. J., Koh, H., Rotenberg, E., Oh, S.-J., Eisaki, H., Motoyama, N., Uchida, S., Tohyama, T., Maekawa, S., Shen, Z.-X. & Kim, C. Distinct spinon and holon dispersions in photoemission spectral functions from one-dimensional SrCuO₂. *Nature Physics* **2**, 397–401 (2006).
294. Grioni, M., Pons, S. & Frantzeskakis, E. Recent ARPES experiments on quasi-1D bulk materials and artificial structures. en. *Journal of physics. Condensed matter : an Institute of Physics journal* **21**, 023201 (2009).
295. Voit, J. One-dimensional Fermi liquids. en. *Reports on Progress in Physics* **58**, 977–1116 (1995).
296. Giamarchi, T. *Quantum Physics in One Dimension* (Clarendon Press, Oxford, 2003).
297. Baeriswyl, D. & Degiorgi, L. *Strong interactions in low dimensions* (Kluwer Academic, Dordrecht; Boston; London, 2004).
298. Bourbonnais, C. Nuclear relaxation and electronic correlations in quasi-one-dimensional organic conductors. I. Scaling theory. en. *Journal de Physique I* **3**, 143–169 (1993).
299. Wzietek, P., Creuzet, F., Bourbonnais, C., Jérôme, D., Bechgaard, K. & Batail, P. Nuclear relaxation and electronic correlations in quasi-one-dimensional organic conductors. II. Experiments. en. *Journal de Physique I* **3**, 171–201 (1993).
300. Moser, J., Gabay, M., Auban-Senzier, P., Jérôme, D., Bechgaard, K. & Fabre, J. Transverse transport in organic conductors: possible evidence for a Luttinger liquid. *The European Physical Journal B* **1**, 39–46 (1998).
301. Dressel, M., Petukhov, K., Salameh, B., Zornoza, P. & Giamarchi, T. Scaling behavior of the longitudinal and transverse transport in quasi-one-dimensional organic conductors. *Physical Review B* **71**, 75104 (2005).
-

302. Giamarchi, T. Umklapp process and resistivity in one-dimensional fermion systems. *Physical Review B* **44**, 2905–2913 (1991).
303. Giamarchi, T. Resistivity of a one-dimensional interacting quantum fluid. *Physical Review B* **46**, 342–349 (1992).
304. Giamarchi, T. Mott transition in one dimension. *Physica B: Condensed Matter* **230-232**, 975–980 (1997).
305. Lee, P., Rice, T. & Anderson, P. Conductivity from charge or spin density waves. *Solid State Communications* **14**, 703–709 (1974).
306. Dardel, B., Malterre, D., Grioni, M., Weibel, P., Baer, Y., Voit, J. & Jérôme, D. Possible Observation of a Luttinger-Liquid Behaviour from Photoemission Spectroscopy of One-Dimensional Organic Conductors. *Europhysics Letters* **24**, 687 (1993).
307. Schwartz, A., Dressel, M., Grüner, G., Vescoli, V., Degiorgi, L. & Giamarchi, T. On-chain electrodynamics of metallic $(\text{TMTSF})_2X$ salts: Observation of Tomonaga-Luttinger liquid response. *Physical Review B* **58**, 1261–1271 (1998).
308. Vescoli, V, Zwick, F, Henderson, W, Degiorgi, L, Grioni, M, Gruner, G & Montgomery, L. K. Optical and photoemission evidence for a Tomonaga-Luttinger liquid in the Bechgaard salts. *The European Physical Journal B - Condensed Matter and Complex Systems* **13**, 503–511 (2000).
309. Pashkin, A., Dressel, M. & Kuntscher, C. A. Pressure-induced deconfinement of the charge transport in the quasi-one-dimensional Mott insulator $(\text{TMTTF})_2\text{AsF}_6$. *Physical Review B* **74**, 165118 (2006).
310. Biermann, S., Georges, A., Lichtenstein, A. & Giamarchi, T. Deconfinement Transition and Luttinger to Fermi Liquid Crossover in Quasi-One-Dimensional Systems. *Physical Review Letters* **87**, 276405 (2001).
311. Kim, C., Matsuura, A. Y., Shen, Z., Motoyama, N., Eisaki, H., Uchida, S., Tohyama, T. & Maekawa, S. Observation of Spin-Charge Separation in One-Dimensional SrCuO_2 . *Physical Review Letters* **77**, 4054–4057 (1996).
312. Rose, E., Loose, C., Kortus, J., Pashkin, A., Kuntscher, C. A., Ebbinghaus, S. G., Hanfland, M., Lissner, F., Schleid, T. & Dressel, M. Pressure-dependent structural and electronic properties of quasi-one-dimensional $(\text{TMTTF})_2\text{PF}_6$. *Journal of physics. Condensed matter : an Institute of Physics journal* **25**, 014006 (2013).

-
313. Pouget, J.-P. & Ravy, S. Structural Aspects of the Bechgaard Salts and Related Compounds. en. *Journal de Physique I* **6**, 1501–1525 (1996).
314. Pouget, J.-P. Interplay between electronic and structural degrees of freedom in quarter-filled low dimensional conductors. *Physica B: Condensed Matter* **460**, 45–52 (2015).
315. Nad, F., Monceau, P., Carcel, C. & Fabre, J. M. Dielectric response of the charge-induced correlated state in the quasi-one-dimensional conductor TM-TTF₂PF₆. *Physical Review B* **62**, 1753–1756 (2000).
316. Keilmann, F. & Hillenbrand, R. Near-field microscopy by elastic light scattering from a tip. *Philosophical transactions. Series A, Mathematical, physical, and engineering sciences* **362**, 787–805 (2004).
317. McLeod, A. S., van Heumen, E., Ramirez, J. G., Wang, S., Saerbeck, T., Guenon, S., Goldflam, M., Anderegg, L., Kelly, P., Mueller, A., Liu, M. K., Schuller, I. K. & Basov, D. N. Nanotextured phase coexistence in the correlated insulator V₂O₃. *Nature Physics* **13**, 80–86 (2016).
318. Lopes, M., Quintero, C. M., Hernández, E. M., Velázquez, V., Bartual-Murgui, C., Nicolazzi, W., Salmon, L., Molnár, G. & Bousseksou, A. Atomic force microscopy and near-field optical imaging of a spin transition. *Nanoscale* **5**, 7762 (2013).
319. Qazilbash, M. M., Brehm, M., Chae, B.-G., Ho, P.-C., Andreev, G. O., Kim, B.-J., Yun, S. J., Balatsky, A. V., Maple, M. B., Keilmann, F., Kim, H.-T. & Basov, D. N. Mott transition in VO₂ revealed by infrared spectroscopy and nano-imaging. *Science* **318**, 1750–3 (2007).
320. Qazilbash, M. M., Brehm, M., Andreev, G., Frenzel, A., Ho, P.-C., Chae, B.-G., Kim, B.-J., Yun, S., Kim, H.-T., Balatsky, A., Shpyrko, O., Maple, M., Keilmann, F. & Basov, D. Infrared spectroscopy and nano-imaging of the insulator-to-metal transition in vanadium dioxide. *Physical Review B* **79**, 075107 (2009).
321. Frenzel, A., Qazilbash, M., Brehm, M., Chae, B.-G., Kim, B.-J., Kim, H.-T., Balatsky, A., Keilmann, F. & Basov, D. Inhomogeneous electronic state near the insulator-to-metal transition in the correlated oxide VO₂. *Physical Review B* **80**, 115115 (2009).
-

322. Qazilbash, M. M., Tripathi, A., Schafgans, A. A., Kim, B.-J., Kim, H.-T., Cai, Z., Holt, M. V., Maser, J. M., Keilmann, F., Shpyrko, O. G. & Basov, D. N. Nanoscale imaging of the electronic and structural transitions in vanadium dioxide. *Physical Review B* **83**, 165108 (2011).
323. Dominguez, G., Mcleod, A. S., Gainsforth, Z., Kelly, P., Bechtel, H. A., Keilmann, F., Westphal, A., Thiemens, M. & Basov, D. N. Nanoscale infrared spectroscopy as a non-destructive probe of extraterrestrial samples. *Nature Communications* **5**, 5445 (2014).
324. Lucas, I. T., McLeod, A. S., Syzdek, J. S., Middlemiss, D. S., Grey, C. P., Basov, D. N. & Kostecki, R. IR Near-Field Spectroscopy and Imaging of Single Li_xFePO_4 Microcrystals. *Nano Letters* **15**, 1–7 (2015).
325. Liu, M., Sternbach, A. J., Wagner, M., Slusar, T. V., Kong, T., Bud'ko, S. L., Kittiwatanakul, S., Qazilbash, M. M., McLeod, A., Fei, Z., Abreu, E., Zhang, J., Goldflam, M., Dai, S., Ni, G.-X., Lu, J., Bechtel, H. A., Martin, M. C., Raschke, M. B., Averitt, R. D., Wolf, S. A., Kim, H.-T., Canfield, P. C. & Basov, D. N. Phase transition in bulk single crystals and thin films of VO_2 by nanoscale infrared spectroscopy and imaging. *Physical Review B* **91**, 245155 (2015).
326. Gatel, C., Warot-Fonrose, B., Biziere, N., Rodríguez, L. A., Reyes, D., Cours, R., Castiella, M. & Casanove, M. J. Inhomogeneous spatial distribution of the magnetic transition in an iron-rhodium thin film. *Nature Communications* **8**, 15703 (2017).
327. Ivek, T., Korin-Hamzić, B., Milat, O., Tomić, S., Clauss, C., Drichko, N., Schweitzer, D. & Dressel, M. Collective Excitations in the Charge-Ordered Phase of $\alpha\text{-(BEDT-TTF)}_2\text{I}_3$. *Physical Review Letters* **104**, 206406 (2010).
328. Yue, Y., Yamamoto, K., Uruichi, M., Nakano, C., Yakushi, K., Yamada, S., Hiejima, T. & Kawamoto, A. Nonuniform site-charge distribution and fluctuations of charge order in the metallic state of $\alpha\text{-(BEDT-TTF)}_2\text{I}_3$. *Physical Review B* **82**, 75134 (2010).
329. Ivek, T., Korin-Hamzić, B., Milat, O., Tomić, S., Clauss, C., Drichko, N., Schweitzer, D. & Dressel, M. Electrodynamic response of the charge ordering phase: Dielectric and optical studies of $\alpha\text{-(BEDT-TTF)}_2\text{I}_3$. *Physical Review B* **83**, 165128 (2011).
330. Tomić, S. & Dressel, M. Ferroelectricity in molecular solids: a review of electrodynamic properties. *Reports on Progress in Physics* **78**, 96501 (2015).

-
331. Beyer, R., Dengl, A., Peterseim, T., Wackerow, S., Ivek, T., Pronin, A. V., Schweitzer, D. & Dressel, M. Pressure-dependent optical investigations of α -(BEDT-TTF)₂I₃: Tuning charge order and narrow gap towards a Dirac semi-metal. *Physical Review B* **93**, 195116 (2016).
332. Tajima, N., Sugawara, S., Tamura, M., Nishio, Y. & Kajita, K. Electronic Phases in an Organic Conductor α -(BEDT-TTF)₂I₃: Ultra Narrow Gap Semiconductor, Superconductor, Metal, and Charge-Ordered Insulator. *Journal of the Physical Society of Japan* **75**, 51010 (2006).
333. Liu, D., Ishikawa, K., Takehara, R., Miyagawa, K., Tamura, M. & Kanoda, K. Insulating Nature of Strongly Correlated Massless Dirac Fermions in an Organic Crystal. *Physical Review Letters* **116**, 226401 (2016).
334. McLeod, A. S., Kelly, P., Goldflam, M. D., Gainsforth, Z., Westphal, A. J., Dominguez, G., Thiemens, M. H., Fogler, M. M. & Basov, D. N. Model for quantitative tip-enhanced spectroscopy and the extraction of nanoscale-resolved optical constants. *Physical Review B* **90**, 085136 (2014).
335. Matsukawa, M., Hashimoto, K., Yoshimoto, N., Yoshizawa, M., Kashiwaba, Y. & Noto, K. Thermal Conductivity in the *ab*-Plane of the Organic Conductor α -(BEDT-TTF)₂I₃. *Journal of the Physical Society of Japan* **64**, 2233–2234 (1995).
336. Yim, W. M. & Paff, R. J. Thermal expansion of AlN, sapphire, and silicon. *Journal of Applied Physics* **45**, 1456–1457 (1974).
337. Kondo, R., Kagoshima, S. & Harada, J. Crystal structure analysis under uniaxial strain at low temperature using a unique design of four-axis x-ray diffractometer with a fixed sample. *Review of Scientific Instruments* **76**, 93902 (2005).
338. Ishiguro, T., Kagoshima, S. & Anzai, H. Elastic Property of Tetrathiafulvalene-Tetracyanoquinodimethane (TTF-TCNQ). *Journal of the Physical Society of Japan* **42**, 365–366 (1977).
339. Heidmann, C.-P., Barnsteiner, A., Grob-Alltag, F., Chandrasekhar, B. & Hess, E. Anisotropic thermal expansion of the organic conductor α -(BEDT-TTF)₂I₃: New aspects of the metal-insulator transition. *Solid State Communications* **84**, 711–716 (1992).
-

340. Maesato, M., Kaga, Y., Kondo, R. & Kagoshima, S. Uniaxial strain method for soft crystals: Application to the control of the electronic properties of organic conductors. *Review of Scientific Instruments* **71**, 176–181 (1999).
341. Tajima, N., Ebina-Tajima, A., Tamura, M., Nishio, Y. & Kajita, K. Effects of Uniaxial Strain on Transport Properties of Organic Conductor α -(BEDT-TTF)₂I₃ and Discovery of Superconductivity. *Journal of the Physical Society of Japan* **71**, 1832–1835 (2002).
342. Liu, M. K., Wagner, M., Abreu, E., Kittiwatanakul, S., McLeod, A., Fei, Z., Goldflam, M., Dai, S., Fogler, M. M., Lu, J., Wolf, S. A., Averitt, R. D. & Basov, D. N. Anisotropic electronic state via spontaneous phase separation in strained vanadium dioxide films. *Physical Review Letters* **111**, 096602 (2013).

Declaration of originality

I hereby declare that this thesis and the work reported herein was composed by and originated entirely from me. Information derived from the published and unpublished work of others has been acknowledged in the text and references.

Andrej Pustogow

